SEQUENCE STRATIGRAPHY, FRACTURE CHARACTERIZATION, AND REBOUND HARDNESS ANALYSIS OF THE UNCONVENTIONAL "MISSISSIPPIAN LIMESTONE"/STACK PLAY, NORTH-CENTRAL OKLAHOMA, USA

By

YULUN WANG

Bachelor of Science in Petroleum Geology
Jilin University
Changchun, China
2012

Master of Science in Geology
The University of Tulsa
Tulsa, OK
2014

Submitted to the Faculty of the
Graduate College of the
Oklahoma State University
in partial fulfillment of
the requirements for
the Degree of
DOCTOR OF PHILOSOPHY
December, 2019

SEQUENCE STRATIGRAPHY, FRACTURE CHARACTERIZATION, AND REBOUND HARDNESS ANALYSIS OF THE UNCONVENTIONAL "MISSISSIPPIAN LIMESTONE"/STACK PLAY, NORTH-CENTRAL OKLAHOMA, USA

Dissertation Approved:

G. Michael Grammer

Dissertation Adviser

Jack Pashin

Daniel A. La ó D ávila

Gregor Eberli

Runar Nygaard

ACKNOWLEDGEMENTS

First and foremost, I would like to thank Dr. G. Michael Grammer for his mentorship within and beyond the classroom and our lab, which have taught me the way of being a researcher and a man with critical thinking, intellectual curiosity (the famous "so what"), and integrity. I would also like to thank my dissertation committee and Dr. Jim Puckette for their contribution to my research. My appreciation also extends to Dr. Mohamed Abdel-Salam and the administrative office in the school for their assistance. Center for Carbonate Research (CSL; University of Miami), especially Dr. Ralf Weger and Dr. Gregor Eberli, are thanked for kindly allowing me to study their Vaca Muerta samples and present my research. Tiptop Oil and Gas/SINOPEC (Oklahoma City, OK) is thanked for offering the internship opportunity, which provided invaluable industrial experience.

This dissertation is not possible without the support and assistance from several organizations and individuals. The "Mississippian Limestone"/STACK portion was supported by the Oklahoma State University Industry Consortium on the Reservoir Distribution and Characterization of the Mid-Continent Mississippian Carbonates – A Major Unconventional Resource Play, which was sponsored by the following companies: American Energy Partners, Chaparral Energy, Chesapeake Energy, Devon Energy, Longfellow Energy, Marathon Oil, Maverick Brothers, Newfield Exploration, SM Energy, Samson Energy, Sinopec/Tiptop, Red Fork Energy, Trey Resources, and Unit Petroleum. Additional financial support was provided by the Oklahoma Geological Foundation (Herbert G. and Shirley A. Davis Geology Fellowship), the American Association of Petroleum Geologists Foundation (Grants-in-Aid awards), and the Boone Pickens School of Geology. Appreciation is extended to the Powder XRD Core Facility at Department of Physics (Oklahoma State University) for assisting with the mineralogical analysis. For the subsurface fracture characterization, the authors gratefully acknowledge the valuable assistance from John Lorenz and comments from Julia Gale and one AAPG reviewer who helped significantly improve the manuscript. For the outcrop fracture characterization, Wayne Narr, one anonymous reviewer, and the volume editors of the SEPM Special Publication 112 (Eugene Rankey, Don McNeill) are specially thanked for their comments which significantly improved the manuscript. Julia Gale is thanked for her kind assistance on outcrop fracture characterization. For rebound hardness analysis, White Star Petroleum and MIDCON Data Service are thanked for their assistance in the rebound hardness test of the "Mississippian Limestone" cores. The Vaca Muerta samples were from the Industrial Associates Program of the CSL (Center for Carbonate Research) of the University of Miami.

Last but not least, I would like to thank my parents, my wife, and friends for their unconditional support and companionship, which have helped me survive and thrive.

Name: YULUN WANG

Date of Degree: DECEMBER, 2019

Title of Study: SEQUENCE STRATIGRAPHY, FRACTURE CHARACTERIZATION, AND REBOUND HARDNESS ANALYSIS OF THE UNCONVENTIONAL "MISSISSIPPIAN LIMESTONE"/STACK PLAY, NORTH-CENTRAL OKLAHOMA, USA

Major Field: GEOLOGY

Abstract: The "Mississippian Limestone"/STACK play in Oklahoma has been a prolific hydrocarbon play for decades. However, several critical aspects, all of which are valuable for reservoir characterization, such as core-based sequence stratigraphy and fracture distribution, and rebound hardness (RHN), are not well understood. To address these topics with an integrated approach, this study utilizes six cores from four counties in north-central Oklahoma and a time-equivalent outcrop in northwestern Arkansas, the latter of which is evaluated for a fracture analog.

In all cores combined, seven mudstone, siltstone, and silty limestone facies are present that exhibit vertical cyclicity at various scales, defining a hierarchical sequence stratigraphic framework. (Sub)vertical, naturally mineralized fractures are common in all cores, with the highest average fracture intensity corresponding to the silty limestone-rich intervals (i.e., regressive phases of "third-order" sequences), which commonly show distinctively low gamma-ray values. These observations imply the potential value of sequence stratigraphy in characterizing and predicting fracture distribution in these unconventional reservoirs. In the outcrop, which is composed of carbonate mudstone and chert, similar types of fractures are present, with overall higher fracture intensity in chert. The distribution pattern of attribute data (height, kinematic aperture, spacing) is affected by lithology, fracture type, and fracture height, pointing to a cooperative role of lithology, fracture type, and fracture-bedding relationships in affecting fracture attributes. Because of different dominant lithologies, this outcrop does not work as a direct fracture analog for the play areas of this study. For RHN analysis, plug samples from the Vaca Muerta Formation provide supplemental data. 2D crossplots between the collected RHN data and the rock data (mineralogy, porosity, sonic velocity, elastic parameters) show correlative trends with clustering by facies groups, implying the effect of facies in the statistical pattern and the value of RHN for rock typing. Variable correlation coefficient suggests variable capabilities of RHN in predicting rock properties, which can be related to the multivariate control of RHN as suggested by leverage analysis. In addition, regression analysis indicates that RHN can potentially assist in the prediction of certain rock properties. These observations imply the potential value of RHN in reservoir characterization.

TABLE OF CONTENTS

CHARACTERIZING THE DISTRIBUTION OF NATURAL FRACTURES FROM OUTCROP IN A MISSISSIPPIAN-AGED MIXED CARBONATE-CHERT SYSTEM, MID-CONTINENT, USA

Chapter Page

LIST OF TABLES

Table Page

LIST OF FIGURES

Figure Page

CHAPTER I

INTRODUCTION

The “Mississippian Limestone”/STACK play in north-central Oklahoma has been a prolific hydrocarbon play since the 1950s. Benefitting from the recent development in hydraulic fracturing and horizontal drilling, the play has been revived as an “unconventional” resource play characterized by low permeability (micro to nanodarcy-scale), with new discoveries extending further south, such as the STACK play (abbreviation for Sooner Trend, Anadarko basin, Canadian and Kingfisher counties) in central Oklahoma. However, several critical aspects are not well understood in various parts of the play, such as core-scale sequence stratigraphy, fracture distribution in core and outcrop, and rebound hardness (RHN), all of which can potentially enhance reservoir characterization and production design across a variety of scales (e.g., sub-meter, individual well, reservoir). In order to provide insight for these topics, this study utilizes six cores from four counties in north-central Oklahoma and a time-equivalent outcrop in northwestern Arkansas. These six cores, with a total footage of nearly 2400 feet (730 m), include three cores in the “Mississippian Limestone” play (shortened as MISS cores; Payne and Logan counties) and three cores in the STACK play (shortened as STACK cores; Kingfisher and Canadian counties) and serve as the primary subsurface rock data. In addition, two sets of outcrops, including a highly fractured outcrop with Mississippian-aged strata in northwestern Arkansas and outcrop plug samples from the Vaca Muerta Formation in Argentina, provide

supplemental fracture and petrophysical-rock mechanical data to the MISS/STACK cores, respectively.

Utilizing an integrated, rock-based approach, this dissertation project contains four overarching objectives:

1. Identify facies and establish a high-resolution sequence stratigraphic framework for the STACK cores, both of which serve as a basis for the subsequent sampling design and data integration;

2. Characterize the natural fractures in the STACK cores in terms of type, key attributes, and distribution. Along with the fracture data from the MISS cores (from Thompson, 2016), these key fracture parameters are tied with mineralogy, facies, and sequence stratigraphy to test the predictability of core-scale fracture distribution using a sequence stratigraphic approach (Chapter 2);

3. Characterize the natural fractures in time-equivalent rocks exposed in outcrop using a similar workflow as the one used for the fractures in the MISS/STACK cores to test if this outcrop can serve as a fracture analog for the subsurface (Chapter 3). This included testing the statistical relationships among fracture attributes, and comparison of the outcrop with the MISS/STACK cores from a rock type and rock mechanical perspective;

4. Collect rebound hardness data for the MISS/STACK cores and test the statistical relationships with facies, sequence stratigraphic framework , and the associated rock properties (e.g. mineralogy, porosity). The primary goal was to evaluate how RHN is affected by different rock properties and if RHN can therefore assist in predicting these properties (Chapter 4). Data of the plug samples from the Vaca Muerta Formation (Late Jurassic to Early Cretaceous) provide supplemental data (sonic velocity, elastic parameters), and are analyzed using the same workflow to further test the statistical relationships.

These research topics carry potential merits in terms of both basic and applied science:

1. Fracture networks, depending on whether the fractures are open or partially to totally mineralized, can not only produce reservoir compartmentalization by creating fluid flow anisotropy (as fluid flow barriers), but assist (as plane of weakness) or hinder production (as conduits for fluid loss and disruption for the growth of hydraulic fractures). Therefore, a detailed understanding of the distribution of natural fractures and the associated controlling factors across a variety of scales (e.g., core to seismic) is crucial for reservoir characterization and production design. However, the characterization and prediction of natural fracture systems is most commonly studied using seismic and structural attributes at a regional scale. Despite the recognition of stratigraphic control on fracture distribution, there is a general lack of detailed integration of fracture data into a high-resolution sequence stratigraphic framework at a core scale available in the literature. Such a knowledge gap, which also applies for the "Mississippian limestone"/STACK play in the U.S. southern midcontinent, can result in a limited understanding of fracture distribution and subsequent application of relevant datasets in predicting subsurface fractured zones at a sub-seismic scale. Correlating fracture distribution and intensity to a sequence stratigraphic framework can lead to the increased predictability of natural fractures in the subsurface.

2. Although cores from near-vertical wells can provide a continuous view of fracture distribution from a stratigraphic perspective, one critical shortcoming for core-based fracture analysis is related to the narrow width of the core (8.5 cm or 3.3 inches in this study), which creates a biased fracture dataset, particularly for the fracture attribute data from a lateral perspective. Therefore, a laterally extensive outcrop is ideal to further investigate the fracture attributes and lateral fracture distribution. Being generally time-equivalent to the subsurface from a chronostratigraphic perspective, an outcrop in northwestern Arkansas, which contains fresh exposure of laterally extensive, highly fractured Mississippian-aged strata, was selected to address such a limitation. In addition, because the outcrop strata in the "tri-state" region (northeastern Oklahoma, southwestern Missouri, northwestern Arkansas) are often considered as facies and stratigraphic analogs to the "Mississippian

Limestone"/STACK play, this portion of the project aims to examine if these outcrop strata (e.g. the outcrop included in this study) can serve as a fracture analog for the subsurface, which could provide guidance for reservoir characterization and production design (e.g., well spacing analysis).

3. Rebound hardness (RHN) is adopted in this research because it is a rock mechanical parameter that can be conveniently and timely tested using a portable device. Because of these advantages, RHN has gained considerable interest as a rock mechanical parameter in both academia and the petroleum industry in recent years, particularly in projects involving subsurface cores from unconventional reservoirs. Therefore, if RHN can be related to petrophysical and rock mechanical properties, it may serve as a valuable tool for estimating these properties with a faster, cheaper, and sample-conservative data delivery as compared to conventional laboratory analysis. Despite its increasingly common application in academia and industry over the past decade, there are few published studies focused on a comprehensive, detailed integration among RHN, facies, sequence stratigraphy , mineralogy, petrophysics (porosity, sonic velocity), and rock mechanical properties from core and wireline log data. In addition, few studies have integrated the observed statistical patterns of facies (i.e., rock texture, cementation pattern), followed by advanced statistical analysis to interpret the controlling factors of RHN and to test if RHN can predict rock properties. These issues significantly under-utilize the RHN data and are critical for testing the application of RHN to reservoir characterization and production design, which is the ultimate goal of this portion of the project.

Reference:

Thompson, T., 2016, Fracture characterization and prediction in the "Mississippian Limestone" in North-Central Oklahoma: unpublished Master thesis, Oklahoma State University, 139 p.

CHAPTER II

FRACTURE CHARACTERIZATION AND PREDICTION IN UNCONVENTIONAL RESERVOIRS OF THE "MISSISSIPPIAN LIMESTONE," NORTH-CENTRAL OKLAHOMA, UNITED STATES

2.0 Abstract

Natural fractures are common in several unconventional reservoirs in the U.S. and around the world and, even when sealed with cements, can facilitate the propagation of induced fractures during hydraulic fracturing. This study is focused on correlating fracture types and intensity to distinct petrophysically significant facies and to an established sequence stratigraphic framework in the unconventional carbonate reservoirs of the "Mississippian limestone" of the U.S. midcontinent region.

Four fracture types are observed: ptygmatic, vertical extension, shear, and mixed types of fractures. Most of the fractures have been completely sealed with predominantly calcite cement. Fractured zones are vertically heterogeneous at various scales, indicating the variability in rock mechanical properties. At the millimeter scale, fractures are commonly discontinuous and exhibit variable kinematic aperture. At the centimeter scale, ptygmatic fractures exhibit variable termination modes in relation to bedding planes, suggesting a mineralogical control on rock mechanical properties. At the meter scale, the highest fracture abundance corresponds to facies with the highest calcite content. The mineralogical control of fracture distribution is also

represented by the higher fracture intensity within the regressive phases of "third-order" sequences, indicating the value of sequence stratigraphic approach in characterizing and predicting fracture distribution in these unconventional reservoirs.

2.1 Introduction

In unconventional reservoirs characterized by low matrix permeability, natural fractures (abbreviated as "fractures" for the rest of this chapter), even when sealed with calcite cement, can aid in the propagation of induced fractures during hydraulic fracturing treatment by acting as planes of weakness (Babcock, 1978; Fisher et al., 2002; Gale et al., 2007, 2014), but may also pose a hindrance to production because of resulting fluid loss and impeding the growth of new hydraulic fractures during hydraulic fracturing treatment (e.g., Gale et al., 2014). Placement of deviated wells perpendicular to the dominant orientation of the naturally fractured system is a standard methodology, which helps to intersect the maximum possible number of fractures (Gale et al., 2007; Sonnenberg et al., 2011). As such, a detailed understanding of natural fracture distribution and the relevant controlling factors may enhance the understanding and prediction of production anomalies that could be associated with the reactivation of natural fractures during or following the hydraulic fracturing treatment (e.g., Gale et al., 2007, 2014). Efforts directed toward the characterization and prediction of natural fracture systems on a regional scale have been pervasive and are commonly focused on seismic and structural attributes (e.g., Padgett and Nester, 1991; Narr, 1996; Ericsson et al., 1998; Bafia and Spencer, 1999; Pérez et al., 1999; Bai and Pollard, 2000; Gale et al., 2004; Kelley and Jones, 2013; Holman, 2014; Grossi, 2015) and petrophysical data (Bafia and Spencer, 1999; Dagistanova et al., 2011). Although stratigraphic and mineralogical aspects (e.g., lithology) are commonly recognized as a key factor in controlling fracture distribution (e.g., Ladeira and Price, 1981; Corbett et al., 1987; Helgeson and Aydin, 1991; Gross et al., 1995; Hanks et al., 1997; Dershowitz et al., 1998; Ericsson et al., 1998; Friedman et al. 1994; Underwood et al., 2003; Gale et al., 2004, 2007; Laubach et al., 2009, 2010;

Sonnenberg et al., 2011) and can be the dominant control even over local structural deformation (Nelson and Serra, 1995; Hanks et al., 1997; Lorenz et al., 1997, 2002; Underwood et al., 2003), the lack of integration of fracture and mechanical stratigraphy into a high-resolution sequence stratigraphic framework may result in a limited understanding of the controlling factors of fracture distribution at the production scale, and a more limited application of relevant datasets in predicting subsurface fractured zones on an exploration or production scale. In addition, the impact of structural diagenesis on rock mechanical properties, from both a temporal and spatial perspective (e.g., Laubach et al., 2009), adds additional uncertainty when interpreting the mechanical stratigraphy during the time of formation of the natural fractures through the use of the present-day distribution of natural fractures.

In the unconventional "Mississippian limestone" play in the U.S. southern midcontinent, detailed core-based characterization of natural fractures has rarely been tied to a sequence stratigraphic framework. Correlating fracture distribution and intensity to a sequence stratigraphic framework may lead to the increased predictability of natural fractures in the subsurface, similar to which has been done in recent outcrop studies (e.g., Underwood et al., 2003; Cooke et al., 2006; Zahm and Hennings, 2009; Frost and Kerans, 2010; Zahm et al., 2010). The primary goal of this study is to characterize the type and distribution of natural fractures in the unconventional "Mississippian limestone," and to tie key fracture parameters (e.g., type, intensity, spacing) with variations in mineralogy, facies types, and the established sequence stratigraphic framework to examine the controlling factors of natural fracture distribution, and to test the potential for prediction of naturally fractured intervals using a sequence stratigraphic approach.

2.2 Geologic Background

The study area is located in north-central Oklahoma, part of the U.S. southern midcontinent (Figure 2.1A). During the Mississippian Epoch, this area was periodically covered by subtropical epeiric seas where a mixed carbonate–siliciclastic depositional system was developed. The

general depositional system is interpreted to have been a distally steepened ramp (Childress and Grammer, 2018; Price and Grammer, 2018), with the study area spanning both proximal and distal depositional positions on the Cherokee platform (Figure 2.1B). Structurally, the study area spans the region east and south-southwest of the Nemaha fault zone (i.e., Nemaha uplift and Nemaha Ridge; Figure 2.1B, C), which is a key structural feature in north-central Oklahoma possibly active during the Late Mississippian to Early Pennsylvanian (Gay, 2003a, b).

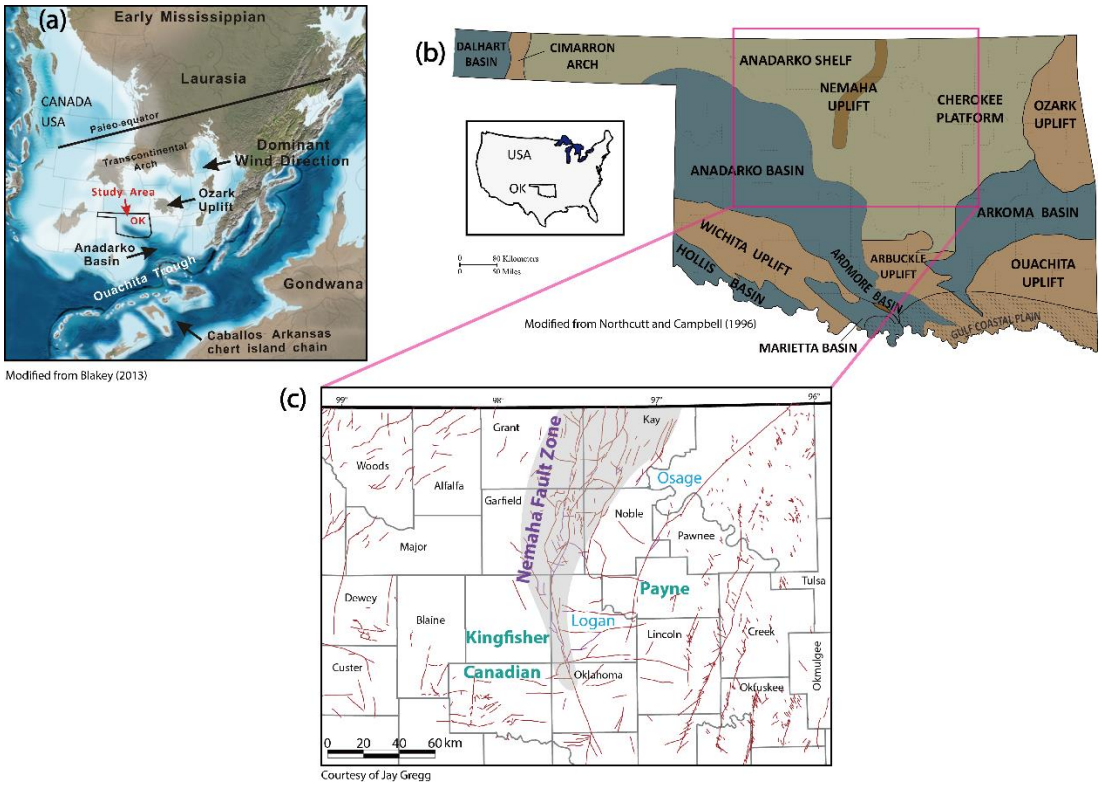

Figure 2.1. (A) Paleogeography, (B) regional depositional-structural elements, and (C) fault distribution of the study area. In structural map (C), counties involved in this study are highlighted with green (locations of cores for fracture description). Fault map is from Jay Gregg.

2.3 Methods

An integrated approach was utilized to derive a comprehensive dataset on natural fracture attributes and distribution at various scales using five subsurface cores in north-central Oklahoma (Figure 2.1). The dataset was then interpreted within the context of a sequence stratigraphic framework (Figure 2.2). The surface of the cores serves as the primary data source that is accompanied by data from petrographic thin sections and micro-CT imaging. Fracture attributes

such as height, kinematic aperture, spacing, termination style, and intensity were measured from the core surface. Because of the variable nature of kinematic aperture, which is defined as the accumulative opening of fracture, including opening space and cementation (Marrett et al., 1999), maximum values are estimated for subsequent analysis. To evaluate the fracture attributes beneath the core surface from a three-dimensional (3-D) perspective and at a finer scale, two 1.5 in. (3.8 cm) diameter core plugs were analyzed using micro-CT imaging technique at a resolution of 40 microns. Abundance of fractures is illustrated using fracture intensity, which refers to fracture count per meter of core (e.g., Ortega et al., 2006, 2010; Gale et al., 2014), and average fracture intensity is derived by dividing the fracture count by the corresponding footage of core of a selected interval (e.g., facies, depositional sequence). Mineralogical data from X-ray diffraction (XRD), such as calcite, quartz, and bulk clay content, add an additional facet to understanding the role of mineralogy in controlling the fracture distribution. These data were then compared with an established sequence stratigraphic framework to evaluate patterns that might assist with the prediction of fractures away from the well bore. The methodology utilized for fracture description and the definition of fracture attributes, as well as a means for distinguishing between induced fractures and natural fractures, are based on Kulander et al. (1990), Lorenz and Hill (1992), Nelson (2001), Lorenz et al. (2002), and Gale et al. (2007).

2.4 Results

2.4.1 Petrophysically Significant Facies

Seven lithofacies (five calcareous siltstones and two skeletal limestones) were defined based upon mineralogy, sedimentary structures, bioturbation intensity, and grain types (Figure 2.3), and interpreted to have been deposited on a distally steepened ramp. The lithofacies show repetitive vertical changes and apparent cyclicity that occur at various scales, which directly affect fracture distribution and reservoir compartmentalization. To present the rock data by highlighting potentially mineralogy controlled mechanical properties, five types of "petrophysically significant

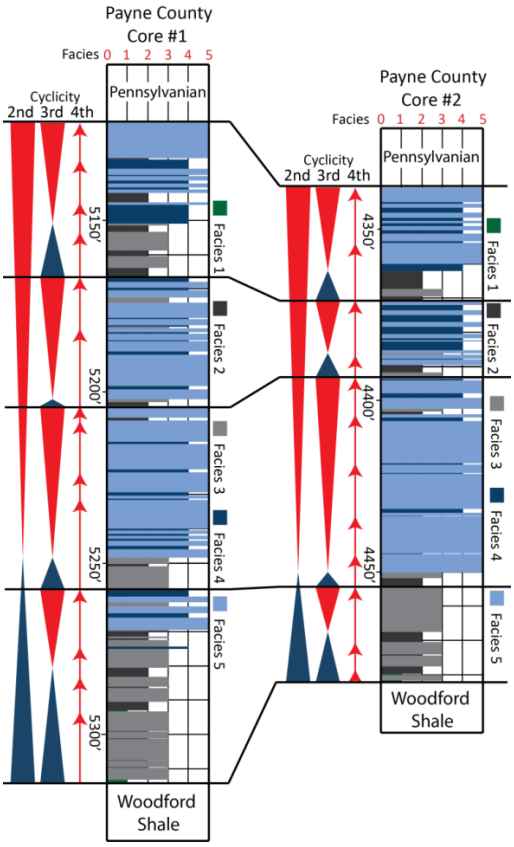

Figure 2.2. Sequence stratigraphic framework of two cores in the study area (Leblanc, 2014).

facies" (shortened as "P-Facies" for the rest of this chapter) are grouped based primarily upon the average XRD mineralogy and the extent of bioturbation (Figure 2.3). From P-Facies 1 to 5, general trends of increasing calcite content and decreasing clay content are observed, reflecting a generally shoaling-upward depositional trend (Figure 2.3). P-Facies 2, 3, and 4 exhibit similar mineralogical composition but were defined as separate facies petrophysically because of variations in the extent of bioturbation, which has been shown to possibly affect the resulting porosity and permeability values (e.g., Pemberton and Gingras, 2005; Gingras et al., 2012). The combination of the idealized vertical facies succession of depositional facies and the related succession of petrophysically significant facies (Figure 2.3) serves as the basis for constructing a hierarchical sequence stratigraphic framework, which is fundamental for integrating various datasets and testing the potential for increasing fracture predictability.

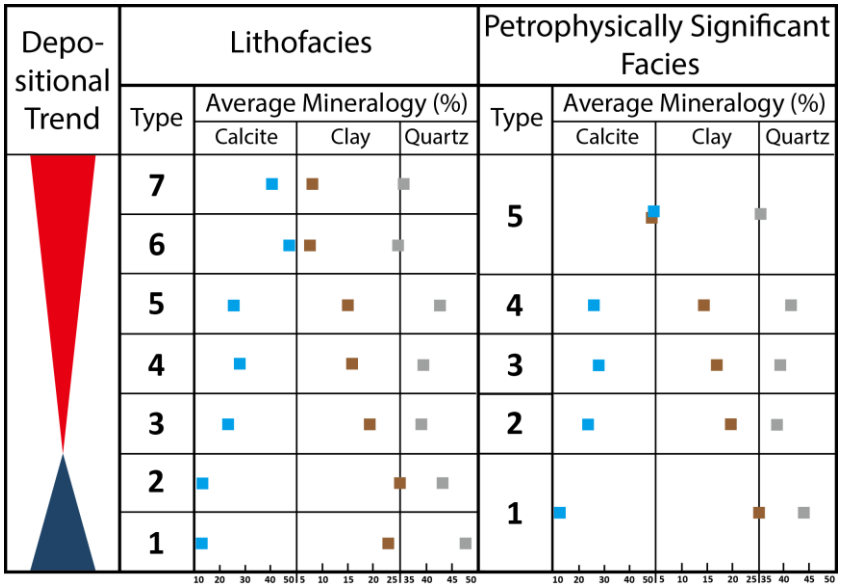

Figure 2.3. Diagram showing the relationship between lithofacies and petrophysically significant facies with average X-ray Diffraction (XRD) mineralogy and inferred depositional trends (blue and red triangle represents deepening and shallowing upward trend, respectively). Note the generally increasing calcite content and decreasing clay-quartz content from base to top in the vertical succession of both lithofacies and petrophysically significant facies.

2.4.1.1 P-Facies 1: Glauconitic Siltstone to Fine Sandstone and Massive-Bedded Siltstone

The glauconitic siltstone–fine sandstone facies is concentrated near the base of the Mississippian section and is volumetrically the most insignificant facies type. It varies from massive-bedded (Figure 2.4A, B) to locally laminated (Figure 2.4C), and is characterized by abundant fine sand-size glauconite grains (Figure 2.4D), which contributes to the distinct greenish color of this facies. Being subangular to subrounded and moderately sorted (Figure 2.4D), the glauconite grains possibly contain both transported and in situ components, the latter of which points to sediment starvation (Odin and Matter, 1981; Amorosi, 2012). Except for scarce *Teichichnus* (Figure 2.4B) and *Zoophycos* (Figure 2.4A) trace fossils, biogenic structures are rare. Similarly, the black-colored, massive-bedded siltstone facies rarely contains sedimentary or biogenic structures (Figure 2.4E) and is dominated by subangular to angular silt-size quartz grains (Figure 2.4F). With the highest average clay content (Figure 2.3), P-Facies 1 is interpreted as the facies

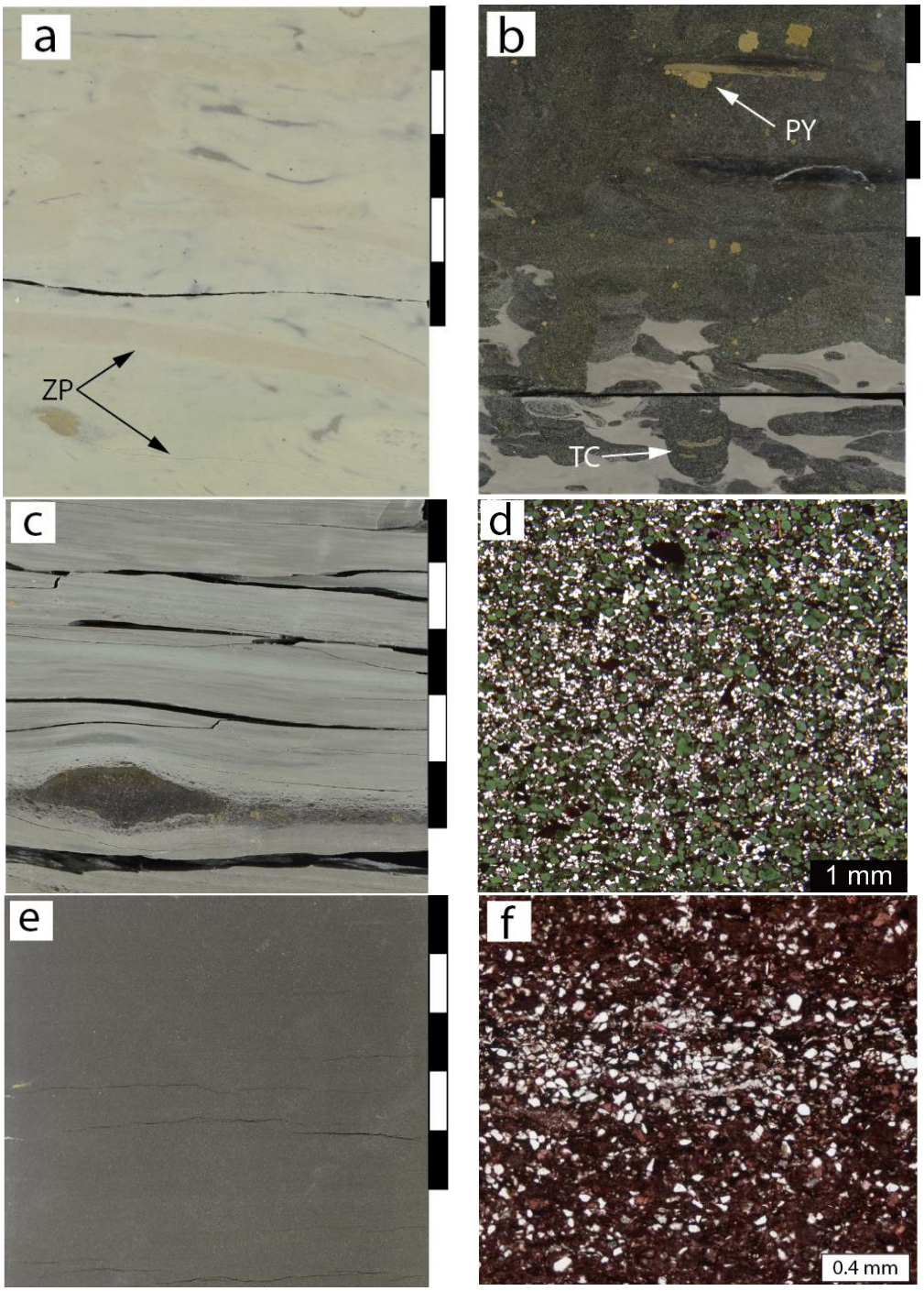

Figure 2.4. P-Facies 1—(A–D) Glauconitic siltstone to fine sandstone and (E, F) massive-bedded siltstone. The glauconitic siltstone to fine sandstone exhibits (A, B) massive-bedded and (C) laminated bedding structures with (D) abundant fine sand-size glauconite and (PY in B) scattered pyrite and trace fossils (ZP in A, TC in B). The massive-bedded siltstone is characterized by (E) massive-bedded structure, scarcity of bioturbation, and (F) dominance of silt-sized quartz and clay-sized particles. ZP: *Zoophycos*; TC: Teichichnus; PY: pyrite. Photos A, B, and C are within a two-meter-thick interval in the same core. Photos E and F are at the same depth. Scale bar is in centimeters.

with the lowest energy, being deposited in a distal outer ramp to basinal environment with generally restricted bottom waters.

2.4.1.2 P-Facies 2: Laminated Siltstone

The laminated siltstone facies is characterized by millimeter-thick, alternating clay-rich (darker colored) and calcite-rich (lighter colored) laminae (Figure 2.5A–C). The presence of millimeter-scale hummocky cross-stratification (HCS) in the calcite-rich laminae (Figure 2.5A) points to intermittent storm deposition as a potential mechanism of forming the calcite-rich layers (Cheel and Leckie, 1993). In this sense, variable proportions of the clay-rich and calcite-rich laminae (Figure 2.5A vs. 2.5C) suggest varying frequency and intensity of the storm events. The "rhythmic" appearance (Figure 2.5A, C) invokes the potential effects of tidal currents (Sarg, 2012), although the presence of HCS would likely negate that possibility. The laminated siltstone was likely deposited near storm wave base along the more proximal portion of the outer ramp relative to P-Facies 1.

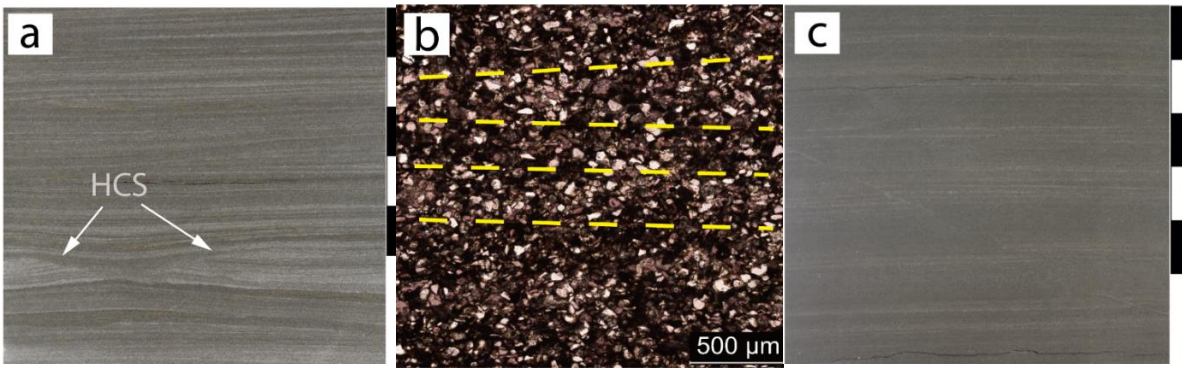

Figure 2.5. P-Facies 2—laminated siltstone. Note the truncated hummocky cross-stratification (HCS in A) and millimeter-scale laminations, the latter of which can be distinct (A) and subtle (C) and can be observed at petrographic scale (B). Photos A and B are about one meter apart in the same core. Scale bar is in centimeters.

2.4.1.3 P-Facies 3: Burrowed Calcareous Siltstone and P-Facies 4: Bioturbated Calcareous Siltstone

The primary difference between P-Facies 3 and P-Facies 4 lies in the intensity of bioturbation: ranging from relatively localized and isolated burrow clusters in P-Facies 3 (Figure 2.6A–C) to those that are commonly connected and form a more homogenized burrow network in P-Facies 4 (Figure 2.7A, B). Trace fossil assemblages are characterized by a low diversity but high abundance of traces. The dominance of *Phycosiphon* (Figures 2.6A, 2.7A–C) suggests an environment with low energy and a fine-grained substrate (Goldring et al., 1991; Wetzel and Bromley, 1994; MacEachern and Burton, 2000; Bednarz and Mcilroy, 2009). Localized *Zoophycos* (Figure 2.6C) may suggest the occasional presence of coarser-grained substrates, possibly related to storm deposits (Pemberton and Frey, 1984; Pemberton et al., 1992; MacEachern and Burton, 2000). *Teichichnus* occasionally penetrates the storm-related, hummocky cross-stratification - planar lamination (Figure 2.7D), illustrating their opportunistic nature in higher-energy environments. Additional evidence of fluctuating water conditions (e.g., oxygen levels and energy) includes variations in bioturbation intensity (Figure 2.7A) and the presence of carbonate-rich intervals (Figure 2.7B). Collectively, P-Facies 3 and P-Facies 4 are interpreted to have been deposited in a proximal outer ramp to distal middle ramp environment close to storm wave base.

2.4.1.4 P-Facies 5: Massive-bedded and Hummocky Cross-stratified (HCS)—Planar Laminated Packstone–Grainstone

P-Facies 5 contains the highest average calcite content (Figure 2.3) and is represented by two closely related subfacies. The massive-bedded facies (Figure 2.8A), which contains abundant peloids and crinoidal debris (Figure 2.8B), may be produced by storm- or earthquake-induced sediment liquefaction and transport by rapid sedimentation because of storms (Smith and Bustin, 1996; Boggs, 2006). For the hummocky cross-stratified, planar laminated packstone-grainstone facies, abundant HCS (Figure 2.8D) and planar laminations (Figure 2.8F) and scarce climbing ripples (Figure 2.8F) support an interpretation of rapid sedimentation during storms (Pemberton

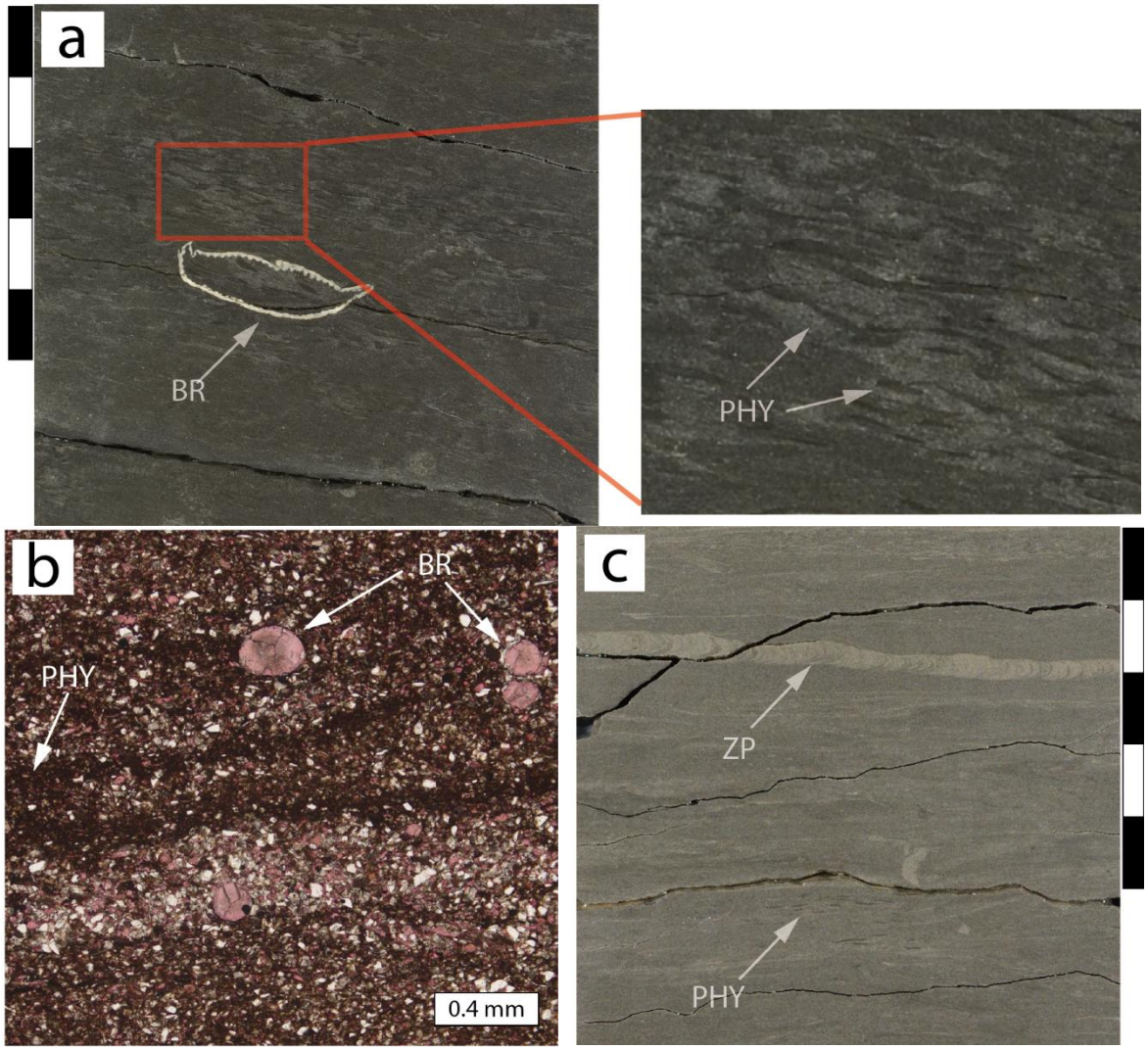

Figure 2.6. P-Facies 3—burrowed siltstone. It is characterized by generally scattered burrow clusters dominated by *Phycosiphon* (PHY in A, B, C), which can be (A) concentrated in places and (B) visible at petrographic scale. ZP: *Zoophycos*; BR: brachiopod. Photos A and B are about 0.7 meters apart in the same core. Scale bar is in centimeters.

et al., 1992; Cheel and Leckie, 1993; Pemberton and MacEachern, 1997). Energy conditions during deposition fluctuated, as indicated by relatively low-energy mud drapes (Figure 2.8D, E) and burrowed zones (Figure 2.8C), both of which may represent quiescence following storms. High energy HCS beds in the massive-bedded facies (Figure 2.8A) points to the episodic nature of sedimentation (sensu Dott, 1983). P-Facies 5 is interpreted as a series of sand bodies that were deposited in the proximal outer ramp to distal middle ramp around storm wave base.

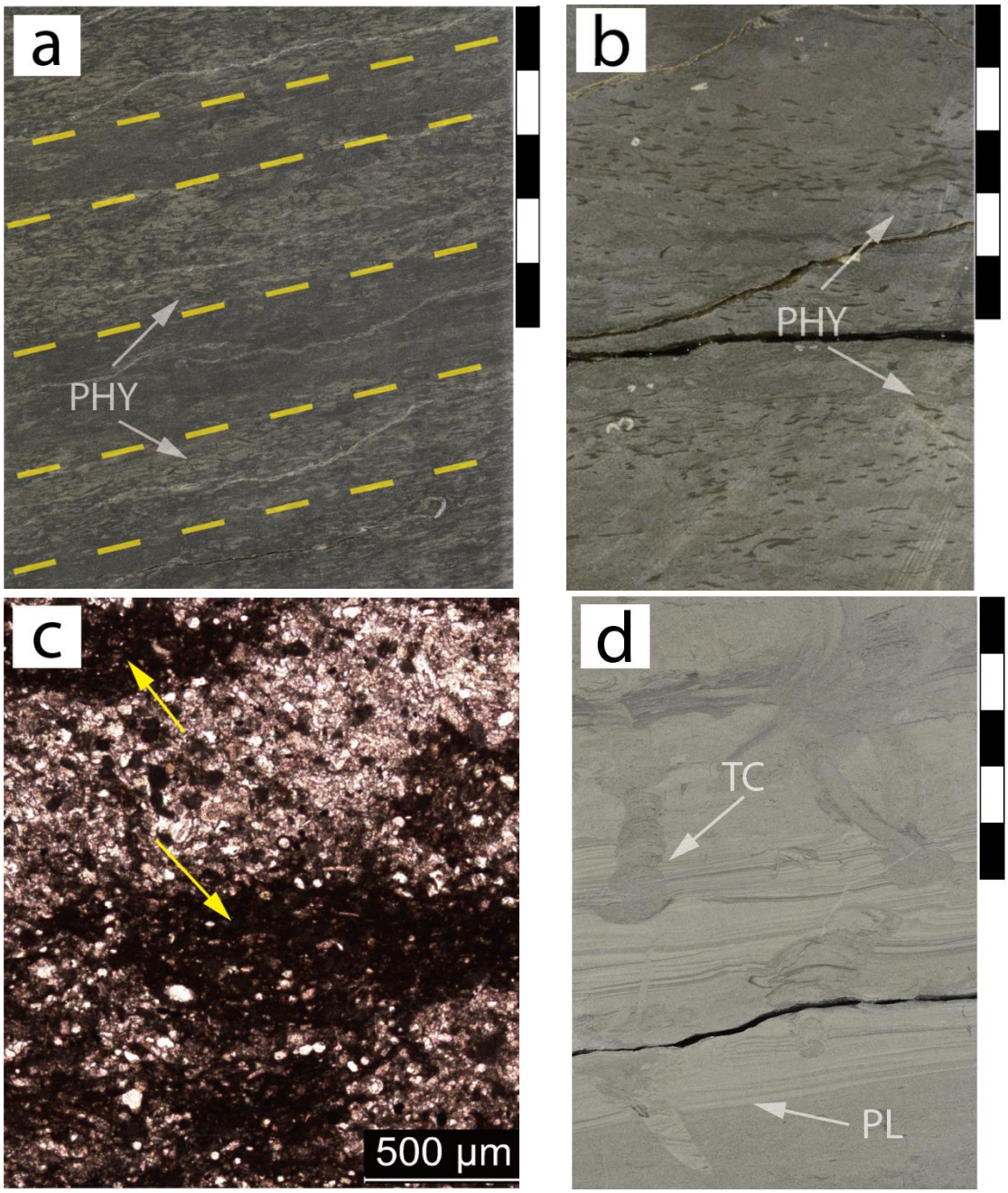

Figure 2.7. P-Facies 4—bioturbated siltstone. Compared to P-Facies 3 (burrowed siltstone), this facies is characterized by a connected bioturbation network dominated by *Phycosiphon*, which largely homogenizes the original rock fabric and is visible in both core (PHY in A and B) and petrographic scale (C, yellow arrows). Note the presence of cyclic variations in bioturbation intensity (A, yellow dashed lines), possibly suggesting variations in bottom water condition (e.g., oxygen, chemistry, and energy). In particular, the interval in (B) is characterized by 67% calcite and 19% quartz, both of which are significantly different from the average calcite (25%) and quartz (42%) content of this facies, likely because of the variability in the depositional system. Scattered storm-related, calcite-rich planar laminations (PL in D) are burrowed by escaping Teichichnus (TC in D). TC: Teichichnus; PL: planar lamination. Photos B and C are at the same depth. Scale bar is in centimeters.

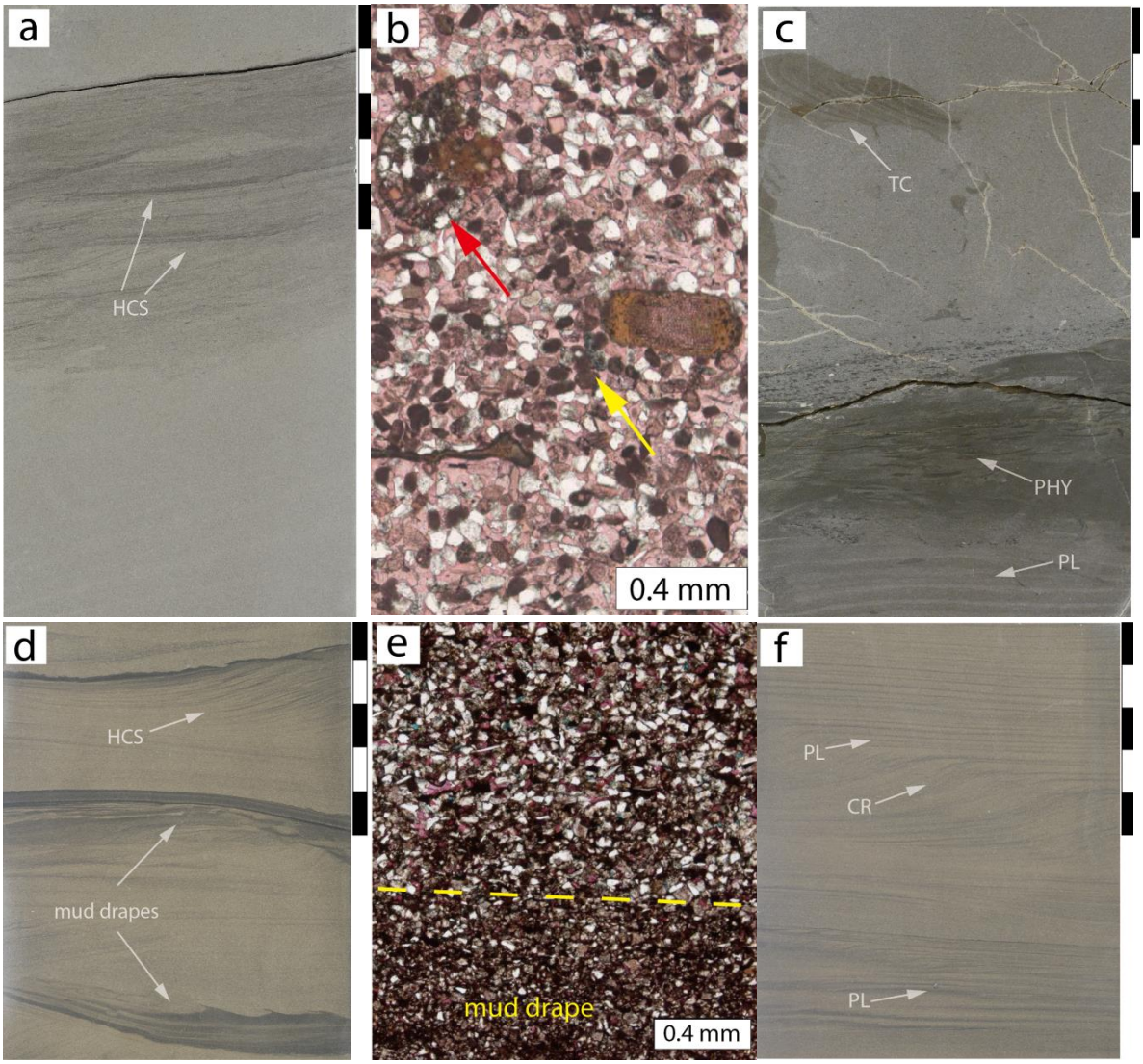

Figure 2.8. P-Facies 5—massive-bedded (A, B, C) and hummocky cross-stratified (HCS)-planar laminated (D, E, F) packstone–grainstone. In the massive-bedded packstone–grainstone, note the dominance of massive-bedded bedding structure (A, C) and abundant peloids (B, yellow arrow) and calcite cement (pink color in B) with scarce coral fragments (B, red arrow). Scattered hummocky cross-stratification (HCS in A), mud-filled Teichichnus (TC in C), burrowed bed with *Phycosiphon* (PHY in C), and wavy planar lamination (PL in C) point to fluctuating energy during deposition. Hummocky cross-stratified (HCS)-planar laminated packstone–grainstone is characterized by abundant HCS commonly truncated by mud drapes (D, E). Planar laminations (PL in F) and climbing ripples (CR in F) may be related to rapid sedimentation during storms. Photos A and B are about 7 m apart in the same core. Photos D and E are about 20 cm apart in the same core. Scale bar is in centimeters.

2.4.2 Fracture Types and Attributes

Based on morphological characteristics, four types of natural fractures were identified, including ptygmatic, vertical extension, shear, and zones with a mixed suite of fracture types (Figure 2.9).

These fracture types are present in all of the cores examined in this study, indicating their likely presence throughout the “Mississippian limestone” play in the southern midcontinent. In terms of abundance, the ptygmatic fractures are the most abundant fracture type observed, and shear fractures are the least abundant (Figure 2.9). The fractures are primarily vertical to subvertical in orientation, and are generally sealed with calcite cement, although partially open vertical extension fractures occur locally.

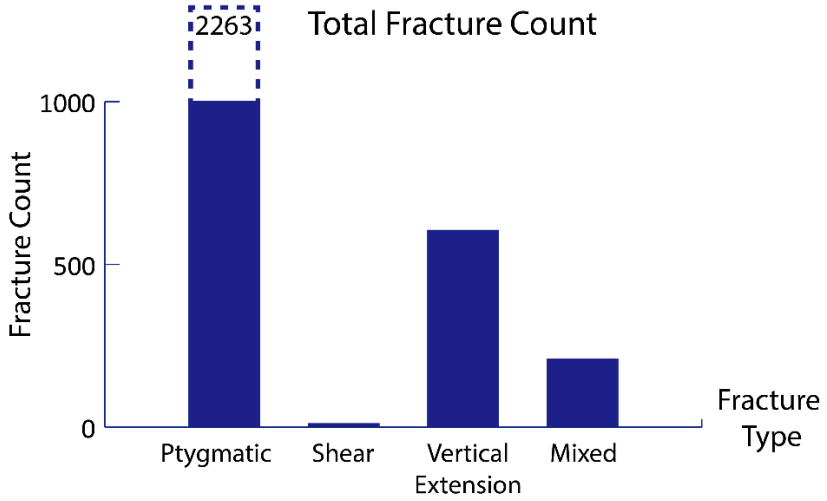

Figure 2.9. Total count of each fracture type identified in this study. Note that the total number of ptygmatic fractures is off the scale in the diagram (off-the-scale part is shown by dashed frame; total fracture count marked by number).

Excluding the ones with a missing or broken fracture wall, the estimated kinematic aperture ranges up to 11 mm, with an average of 0.4 mm (Figure 2.10). In particular, kinematic aperture is variable from a 3-D perspective, as revealed in the micro-CT imaging (Figure 2.11). Including the fractures terminated at the core edge and because of the absent of core pieces, the measured height ranges from 1 mm to 710 mm, averaging 38.4 mm (Figure 2.12). Observed termination style of the fractures are categorized into tapering (at top and base) or abruptly terminating (at top or base) in a seemingly homogeneous portion of the rock, termination related to variations in mineralogy at top or base, and terminations at the core edge or because of missing core pieces at top or base. In general, tapering at both the top and base is the more common termination pattern, accounting for 53.8% of the fracture population (Figure 2.13). For fractures occurring in sets

containing at least two individual fractures, which account for 19.5% of the fracture population, measured spacing ranges from 1 mm to 73 mm with an average of 18.2 mm (Figure 2.14), although the sampling bias related to the narrow core width (around 85 mm) should be considered.

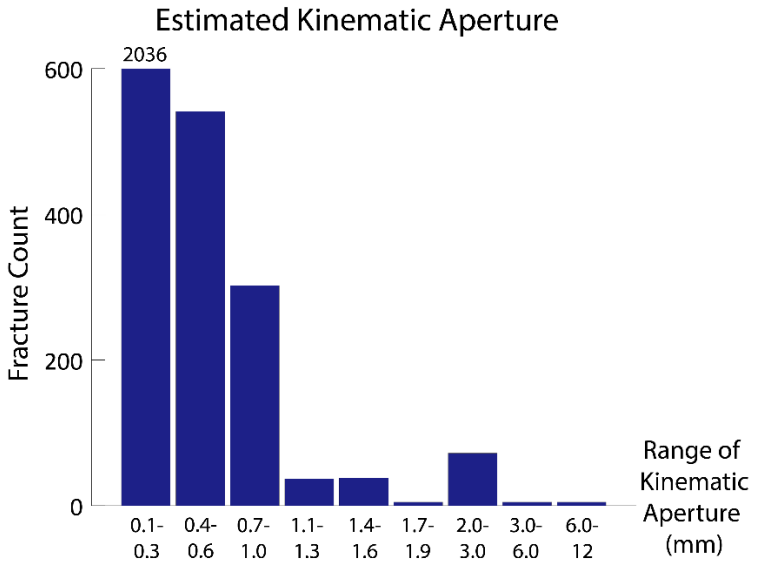

Figure 2.10. Histogram showing the distribution of estimated kinematic aperture by fracture count. Note that the total number of fractures with an estimated kinematic aperture in the range of 0.1–0.3 mm is off the scale (fracture count noted by number).

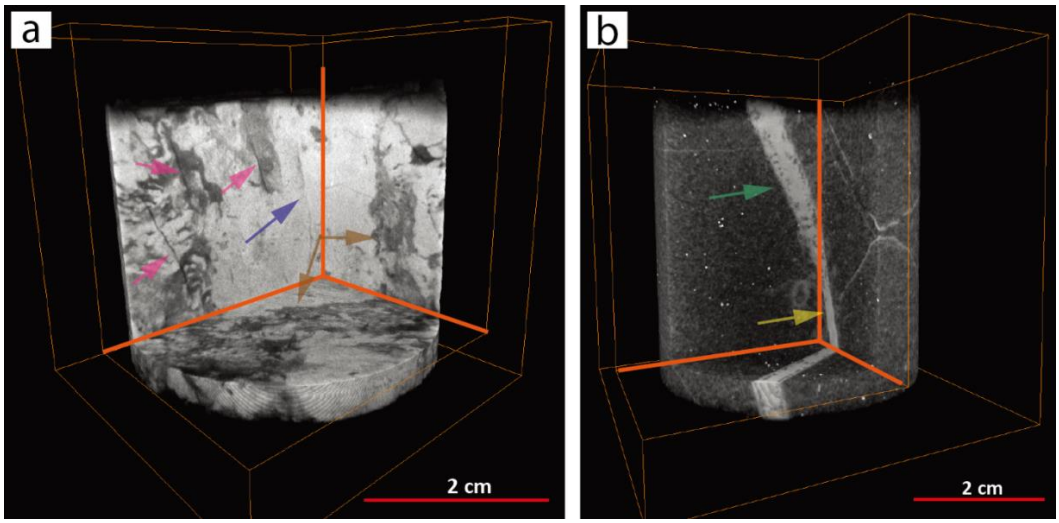

Figure 2.11. Micro-CT imaging of two core plugs obtained from one core, showing the discontinuity of fractures (A, dark blue arrow), disconnectedness of ptygmatic fracture set (A, pink and dark blue arrows), and variations in kinematic aperture along the length of a vertical extension fracture (B, green and yellow arrows). In the images, various hues of gray are associated with different densities of minerals—higher the density, lighter the gray color (Hu et al., 2014). Also note the strength of micro-CT imaging in revealing the bioturbation network from a 3-D perspective (A, brown arrows). A: P-Facies 4; B: P-Facies 5. Photos A and B are in the same core.

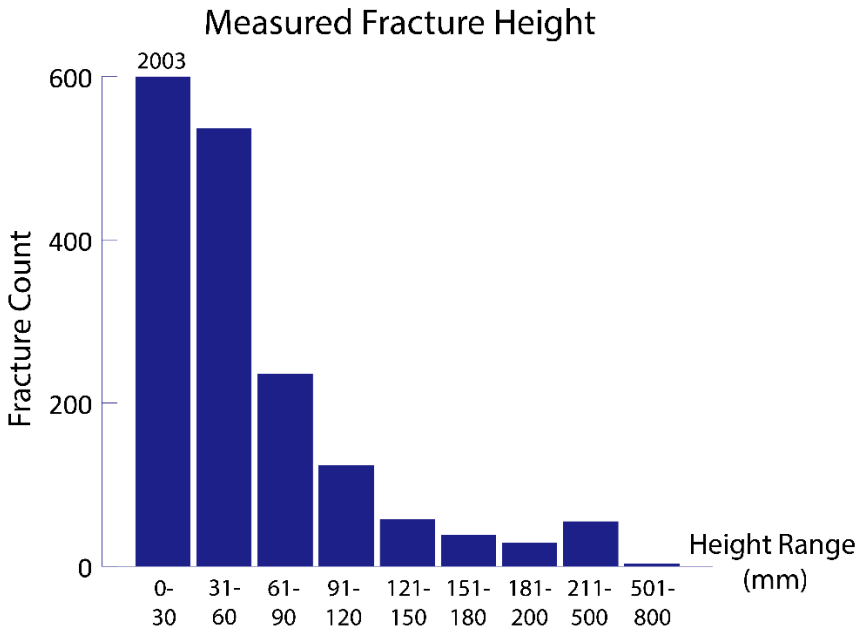

Figure 2.12. Histogram showing the distribution of measured fracture height by fracture count. Note that the total number of fractures with a measured height in the range of 0–30 mm is off the scale (fracture count noted by number).

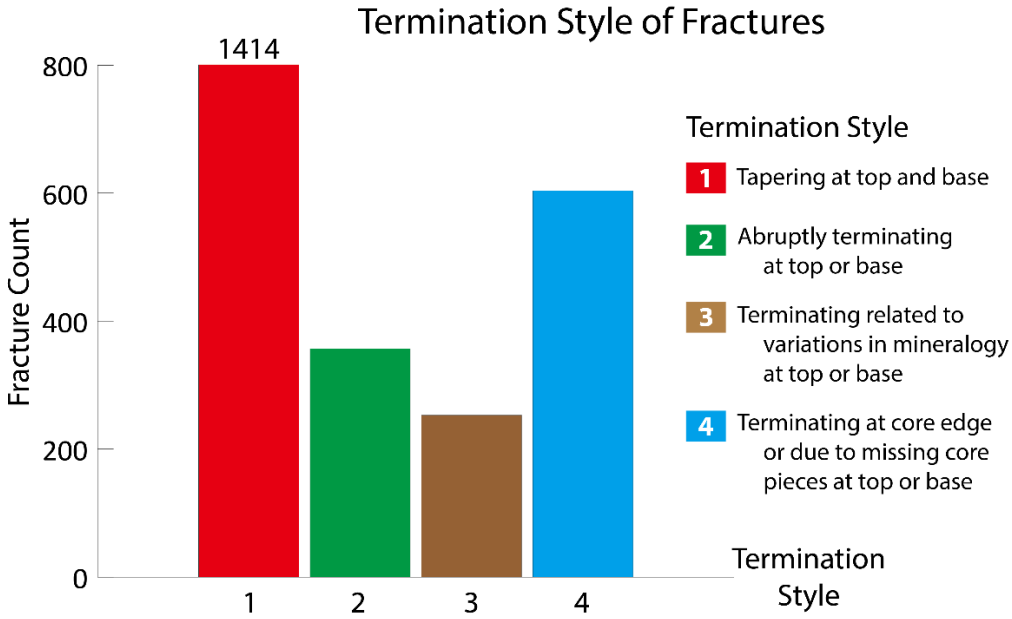

Figure 2.13. Histogram showing the distribution of termination style by fracture count. Note that the total number of fractures with a termination style of tapering at top and base is off the scale (fracture count noted by number).

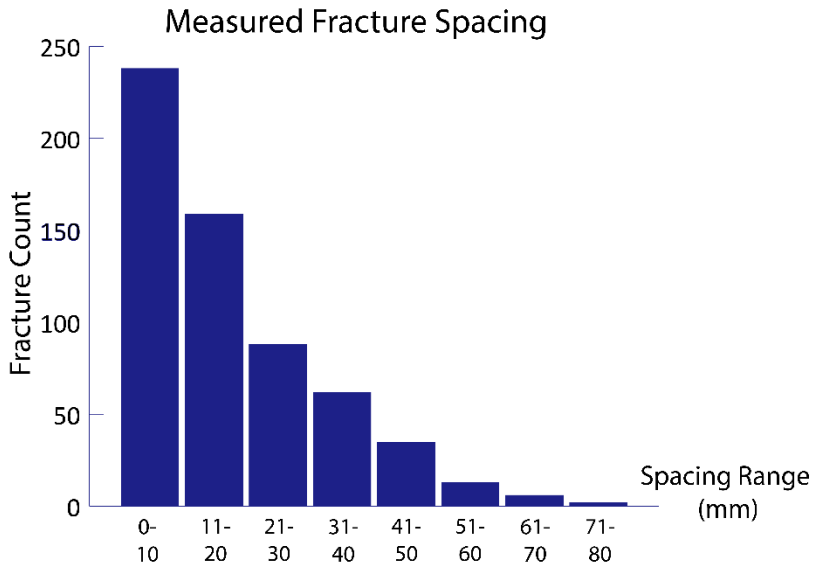

Figure 2.14. Histogram showing the distribution of measured fracture spacing by fracture count.

2.4.2.1 Ptygmatic Fractures

The ptygmatic fractures are characterized by a folded morphology (Figure 2.15A). They occur as solitary fractures (Figure 2.15A), sets of parallel fractures (Figure 2.15B), and fracture bundles at the petrographic scale (Figure 2.15C), and are often discontinuous at a submillimeter scale (Figure 2.15D). When cutting through mud-rich laminae, the ptygmatic fractures commonly become increasingly contorted (Figure 2.16A). Brittle failure of the ptygmatic fractures (Figures 2.16B, 2.15D), variations in the direction of propagation (Figure 2.16C), and the abrupt occurrence of highly fractured intervals (Figure 2.16D) are locally present. In relation to bedding, the ptygmatic fractures terminate within both relatively thin (Figure 2.17A) and thick (Figure 2.16A) relatively rigid intervals and within relatively ductile siltstone facies where mineralogical variations are not distinct (Figure 2.15A, B). The fractures locally deform finer-grained laminae in both upward and downward directions, which can be observed at both core (Figure 2.17B) and petrographic scales (Figure 2.17C). However, most ptygmatic fractures commonly extend across calcite-rich layers (Figure 2.18A). In rare cases, densely arrayed short ptygmatic fractures span across silica-rich bands in P-Facies 5, some of which are seemingly related to the presence of silicified *Zoophycos* trace fossils (Figure 2.18B, C).

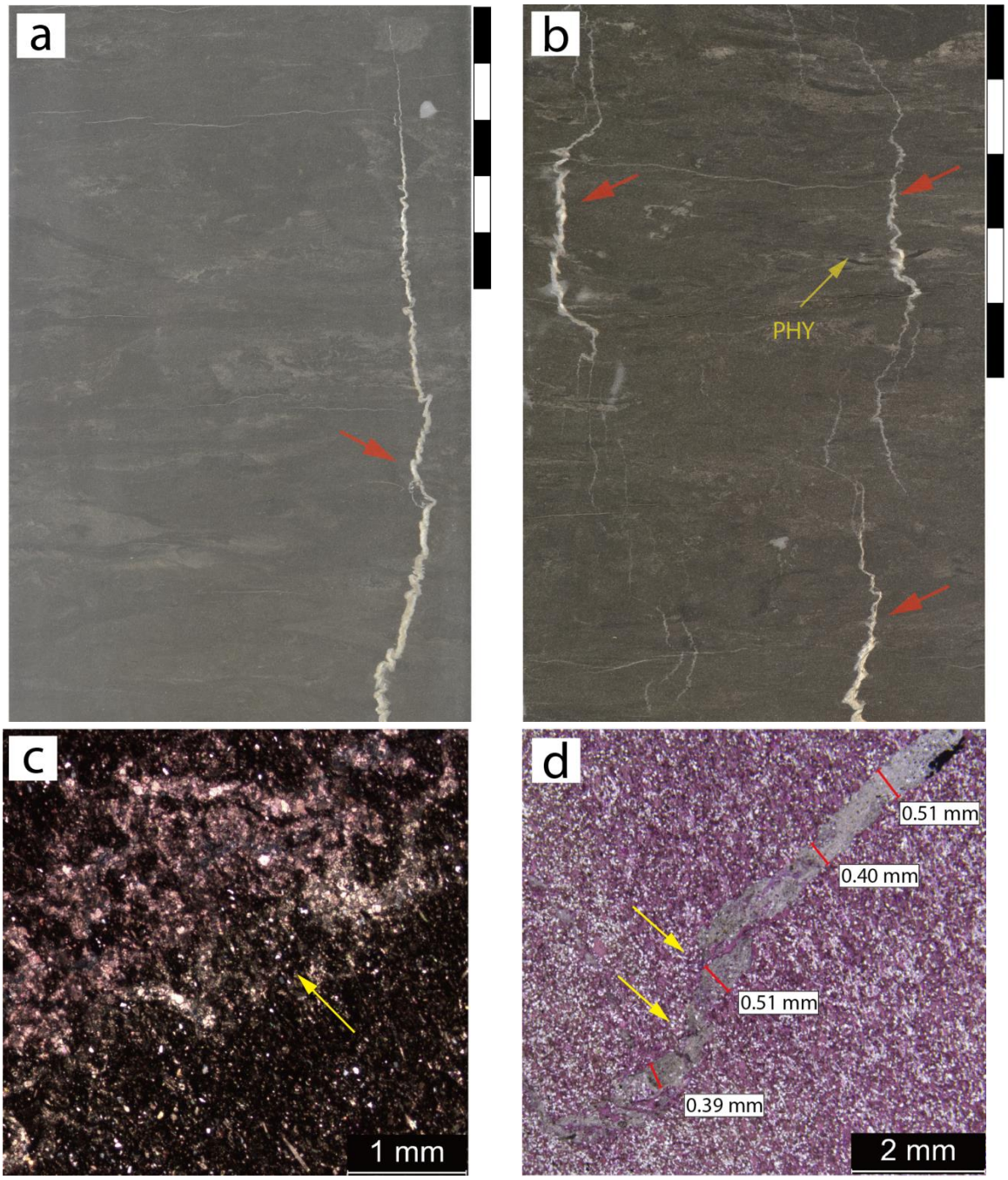

Figure 2.15. Occurrence of ptygmatic fractures as (A) single (red arrow), (B) sets (red arrows), and (C) bundles (yellow arrow). The fracture is commonly discontinuous at (D) millimeter scale (yellow arrows) and exhibits variable kinematic aperture (D). A: P-Facies 3; B: P-Facies 4; C: P-Facies 3; D: P-Facies 5; PHY: *Phycosiphon*. Scale bar is in centimeter.

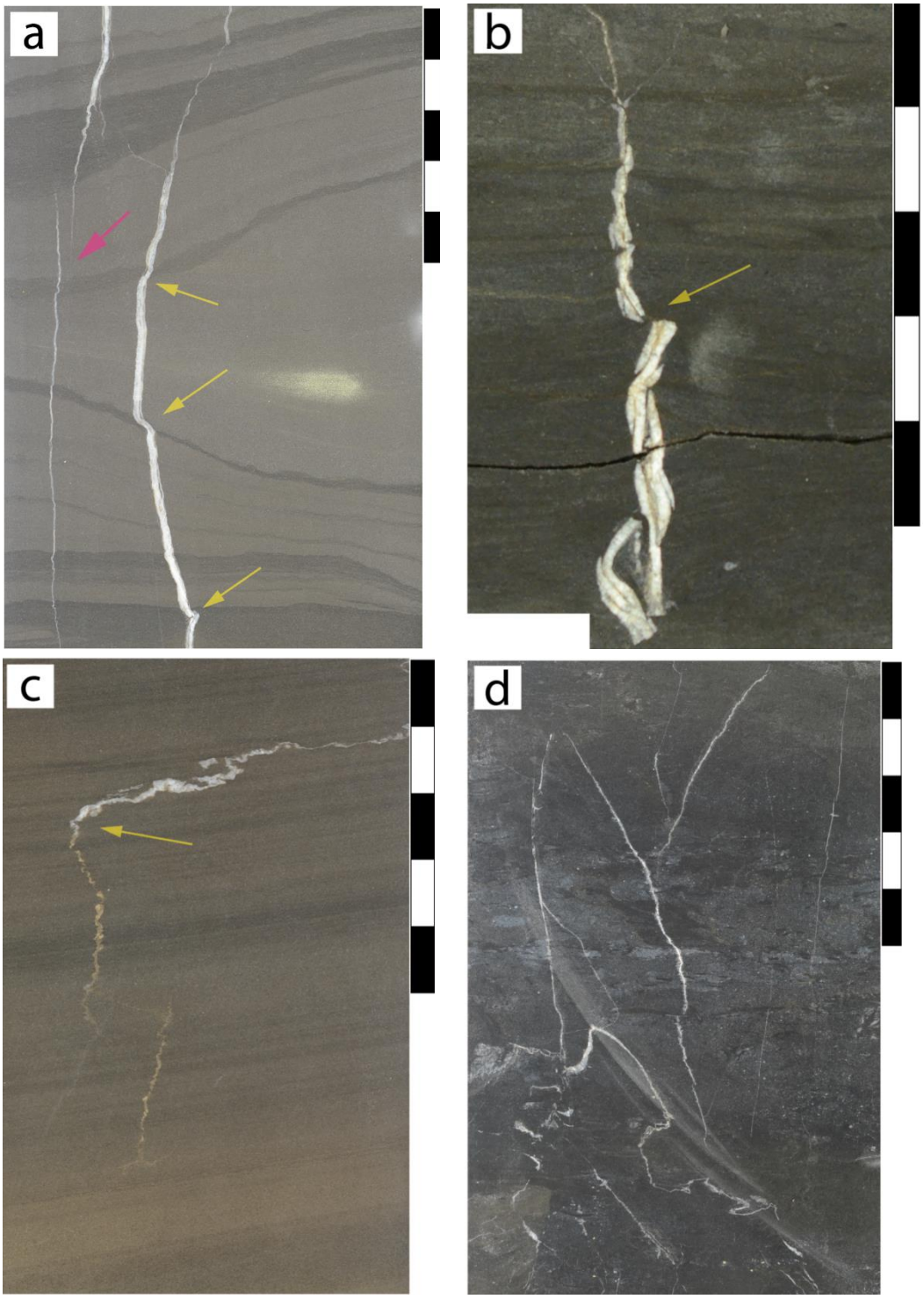

Figure 2.16. Possible evidence of ptygmatic fractures reacting to localized stress and evolution of rock mechanical properties, such as increasing contortion at (A) mud-rich laminae (yellow arrows), (B) brittle failure (yellow arrow), (C) abrupt change in propagation direction (yellow arrow), and (D) abrupt occurrence of highly fractured interval. Also note the termination of fracture within calcite-rich (A, pink arrow; C) and (D) silica-rich brittle layers. A: P-Facies 5; B: P-Facies 3; C: P-Facies 5; D: P-Facies 4. Scale bar is in centimeter.

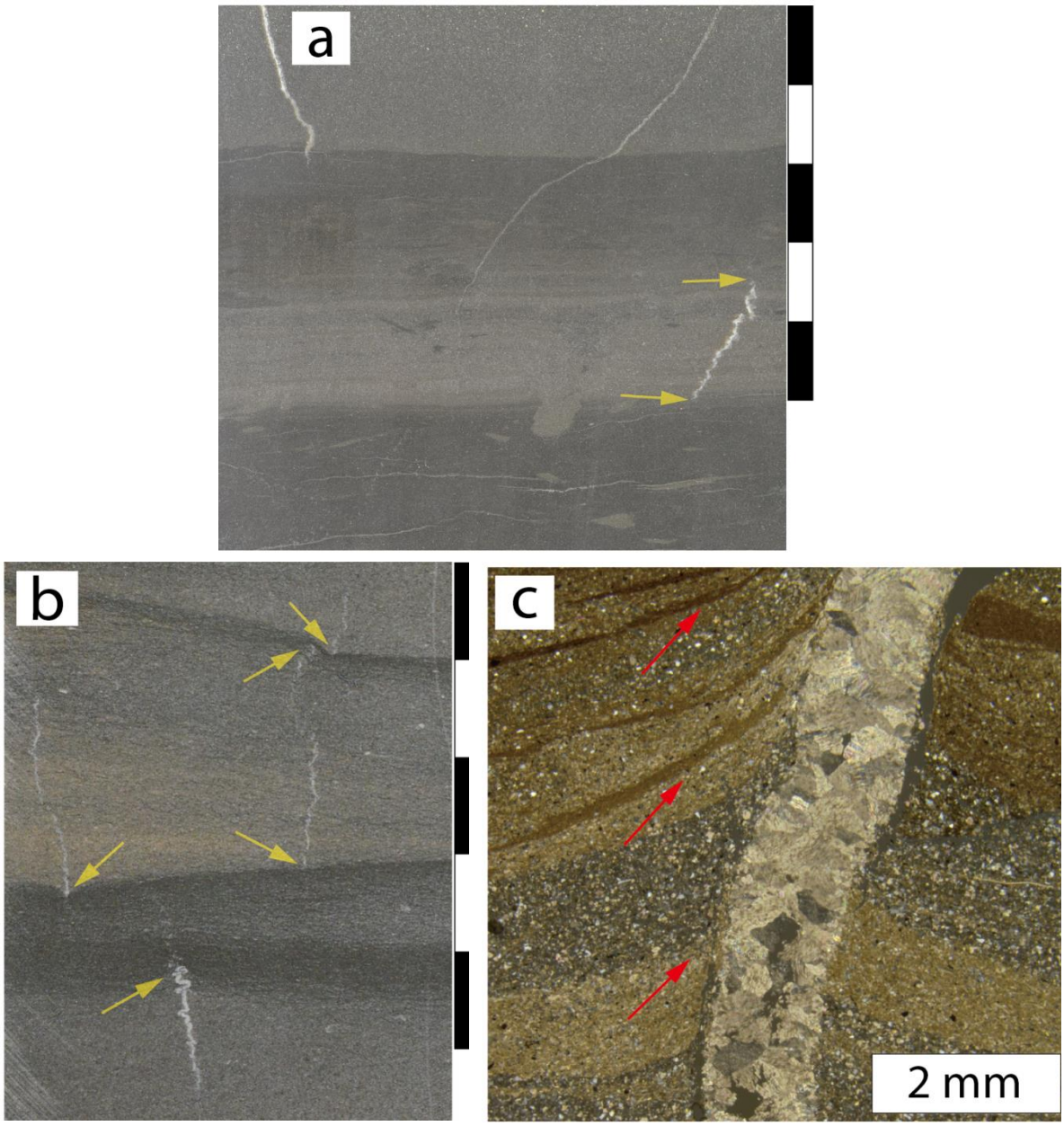

Figure 2.17. (A) Ptygmatic fractures can be completely confined within beds. (B, C) Also note the mud-rich laminae can be deformed by the fractures. A: P-Facies 3; B: P-Facies 5; C: P-Facies 5. Photos B and C are not in the same core. Scale bar is in centimeters.

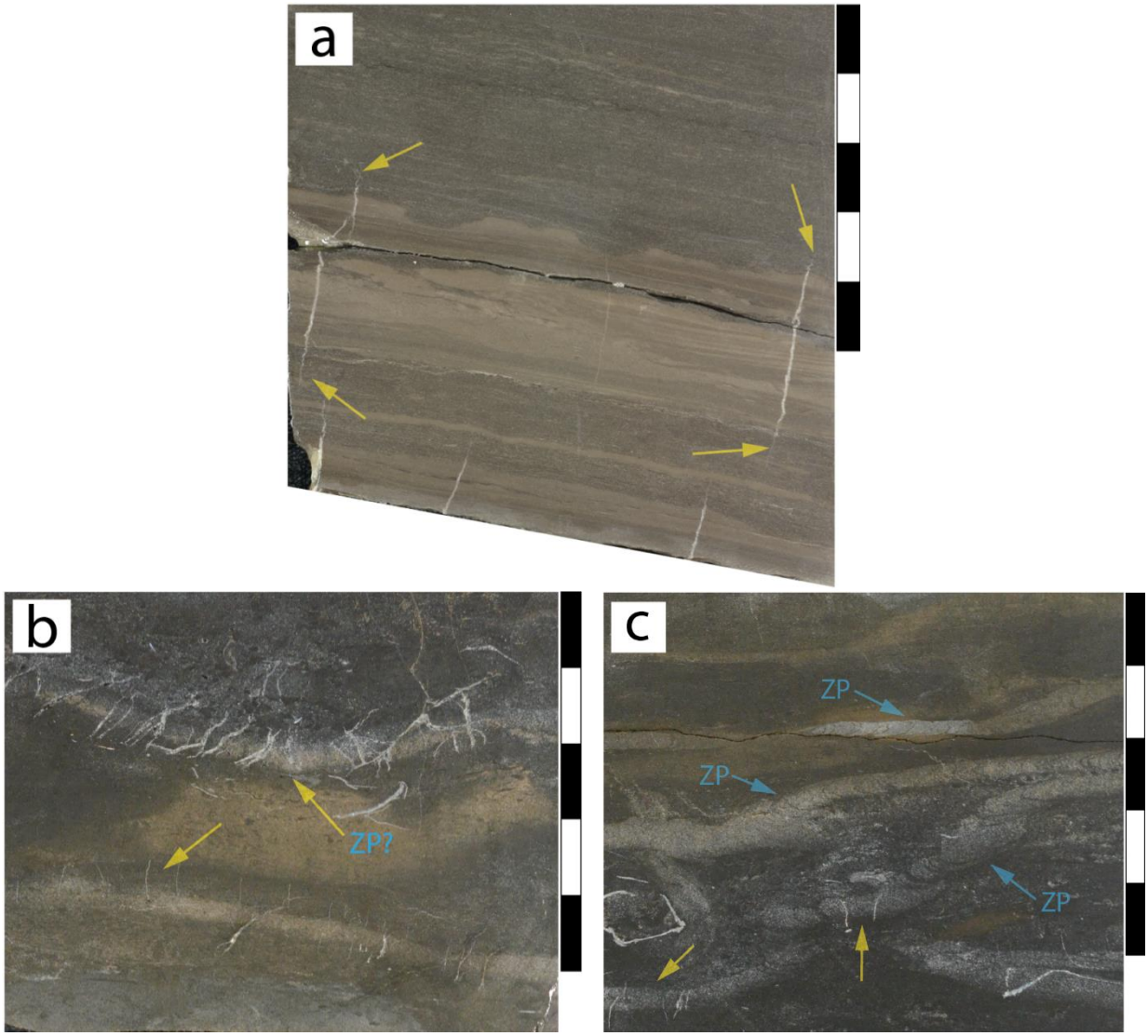

Figure 2.18. Ptygmatic fractures span across calcite-rich layers (A, yellow arrows). In particular, densely spaced short ptygmatic fractures span across silica-rich laminae (yellow arrows in B and C), some of which are seemingly silicified *Zoophycos* (ZP in B and C) trace fossils. A: P-Facies 3; B: P-Facies 5; C: P-Facies 5. The location of photo C is directly beneath B. Scale bar is in centimeters.

2.4.2.2 Vertical Extension Fractures

The vertical extension fractures are characterized by the absence of lateral offsets and straight fracture walls (Figure 2.19A). Locally, there are tall (e.g., over 80 mm in measured height) vertical extension fractures that, despite some calcite infill, are still partially open (Figure 2.19A). Without distinct evidence of dissolution at the contact between fracture-filling cement and fracture wall, the void space appears to be the result of a cessation of cementation. A variable

relationship between the rates of calcite cement precipitation that occurred during and after fracture growth and variable rates of fracturing opening may be present (e.g., Gale et al., 2004, 2014; Olson et al., 2009).

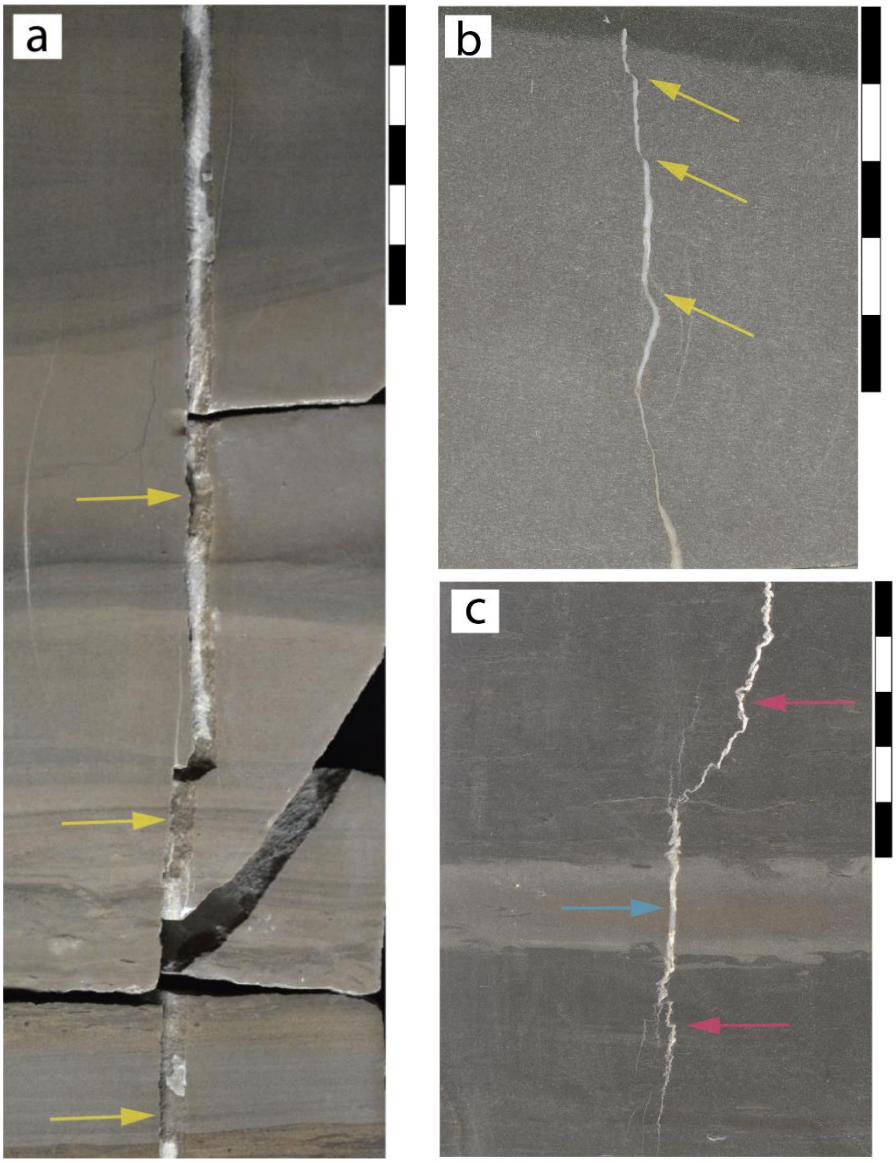

Figure 2.19. (A) Vertical extension, (B) shear, and (C) mixed fractures. Void space (A, yellow arrows), which is probably attributed to partial calcite mineralization, is occasionally observed in vertical extension fractures. The size of the fracture in Figure 19A is 89 mm in height and 0.2 to 1 mm in kinematic aperture. Shear fracture (nomenclature is from Cooper and Lorenz, 2012) is characterized by "pinch-and-swell" structure (B, yellow arrows). One type of mixed fractures includes a mixture of ptygmatic (C, pink arrows) and vertical extension (C, blue arrow) fractures, the latter of which cuts through a relatively brittle bed. A: P-Facies 5; B: P-Facies 5; C: P-Facies 4. Scale bar is in centimeter.

2.4.2.3 Shear and Mixed Fractures

Shear fractures (sensu Cooper and Lorenz, 2012) are characterized by a diagnostic "pinch-and-swell" structure (Figure 2.19B) that exhibits decreasing kinematic aperture at the inferred point where the shearing deformation occurred. In some cases, components of at least two of the three aforementioned fracture types coexist in a single fracture, which is herein defined as a "mixed" fracture type (Figure 2.19C). It should be noted that by "mixed type of fractures," we do not intend to define a fracture as "mixed-mode" (opening and shear; Gale et al., 2014). Both the shear and mixed fracture types are relatively uncommon in the studied units (Figure 2.9).

2.4.3 Fractures Related to Facies

The abundance of natural fractures is heterogeneously distributed and is controlled by the petrophysically significant facies types as well as the position within the sequence stratigraphic framework. In terms of facies control, P-Facies 5 (massive-bedded and HCS-planar laminated packstone–grainstone) exhibits the highest fracture count (Figure 2.20A) and average fracture intensity (Figure 2.20B) of all facies, which are correlated to the fact that P-Facies 5 has the highest average calcite content (Figure 2.3). This correlation between higher percentages of carbonate grains and more concentrated fracture distribution has been commonly documented and is thought to be associated with the higher strength because of the higher carbonate content or lower clay content in the more grain-supported textures in carbonate rocks (e.g., Corbett et al., 1987; Ericsson et al., 1988; Lorenz et al., 2002; Gale et al., 2007; Zahm et al., 2010). In addition, measured fracture spacing does not show a distinct separation among the P-Facies types (Figure 2.21).

2.4.4 Fractures Related to Sequence Stratigraphic Framework

The regressive phases of the interpreted "third-order" composite sequences generally exhibit ahigher fracture count and average fracture intensity than the associated transgressive phases, particularly as P-Facies 5 commonly defines the regressive phases (Figure 2.22A, B). Fracture

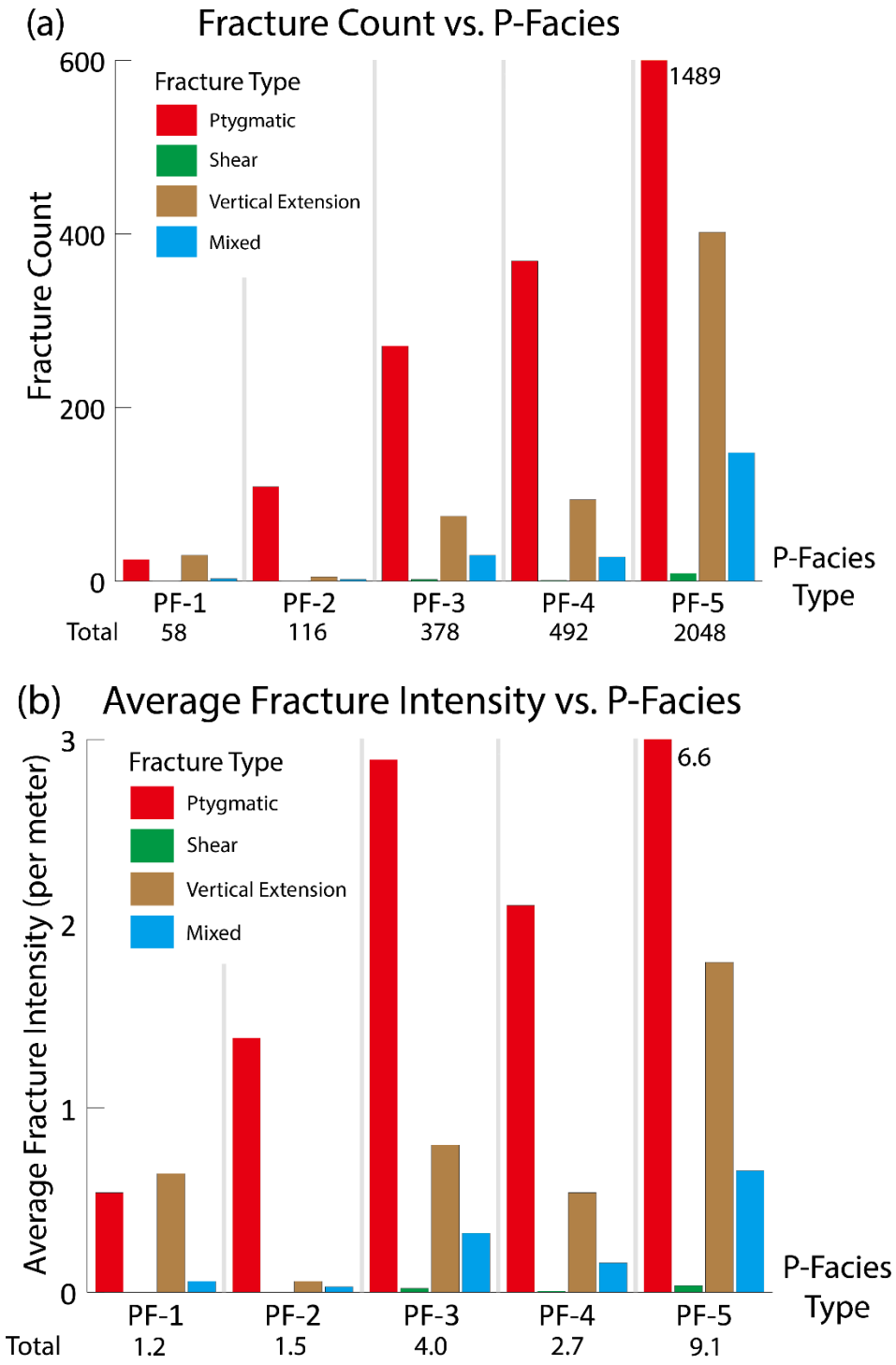

Figure 2.20. (A) Total count and (B) intensity of each fracture type in relationship to petrophysically significant facies. Note the (A) count and (B) average intensity of the ptygmatic fracture in P-Facies 5 are off the scale (total count and intensity marked by number).

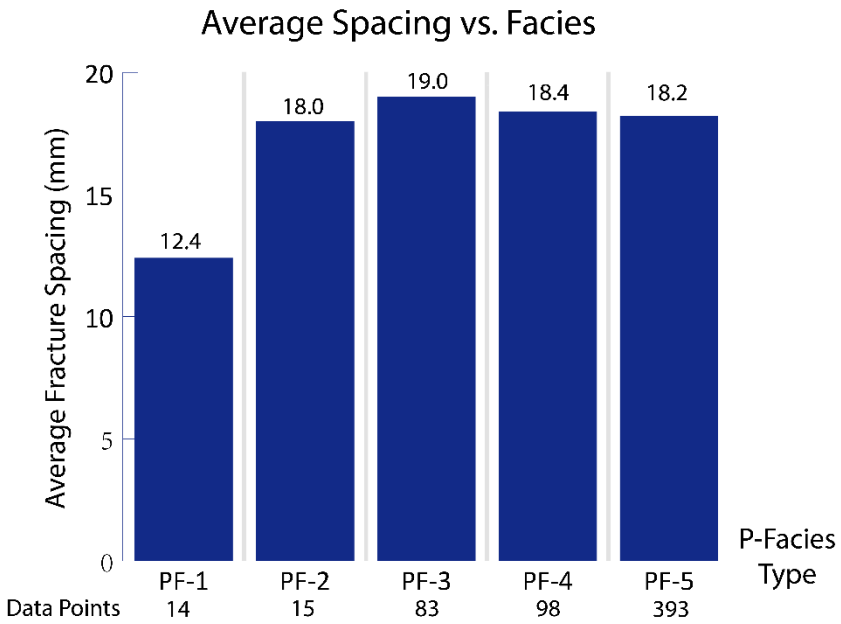

Figure 2.21. Average measured fracture spacing in relationship to petrophysically significant facies.

count and average intensity varies between sequences, invoking possible differences in the evolution of rock mechanical properties and intensity of structural deformation as external factors in addition to variable facies proportions, which are associated with fluctuations in the depositional system (e.g., water depth, oxygen level, and energy). Because the "third-order" sequences commonly show a clear upward-cleaning gamma-ray (GR) signature in this area (e.g., Puckette et al., 2018), the correlation between fracture intensity and the sequence stratigraphy may enhance the predictability of fractures in the subsurface in nearby uncored wells, although clustering of the fractures should be considered when extrapolating core-based fracture datasets into well logs and inter-well spaces. Similar trends between the sequence stratigraphic framework and fracture distribution have also been observed in pure carbonate systems such as the Devonian reef outcrops in the Canning Basin in western Australia (Frost and Kerans, 2010). Similar to the observation in facies, measured fracture spacing shows similar values in the transgressive and regressive phases of the "third-order" sequences (Figure 2.23).

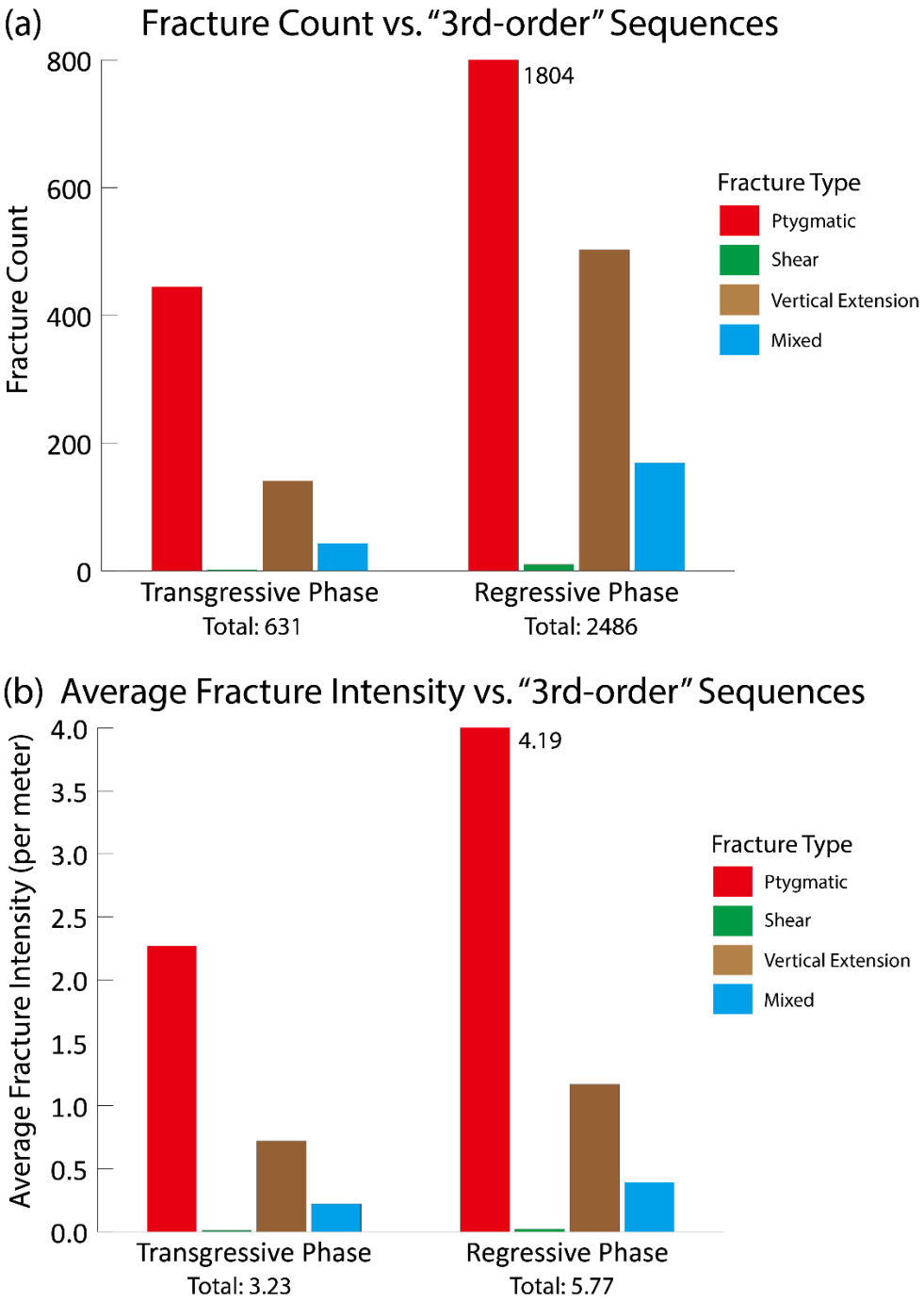

Figure 2.22. (A) Total count and (B) intensity of each fracture type in relationship to the "third-order" sequences. Note that regarding the ptygmatic fracture, the (A) count and (B) average intensity are off the scale in the regressive phase (total count and intensity marked by number).

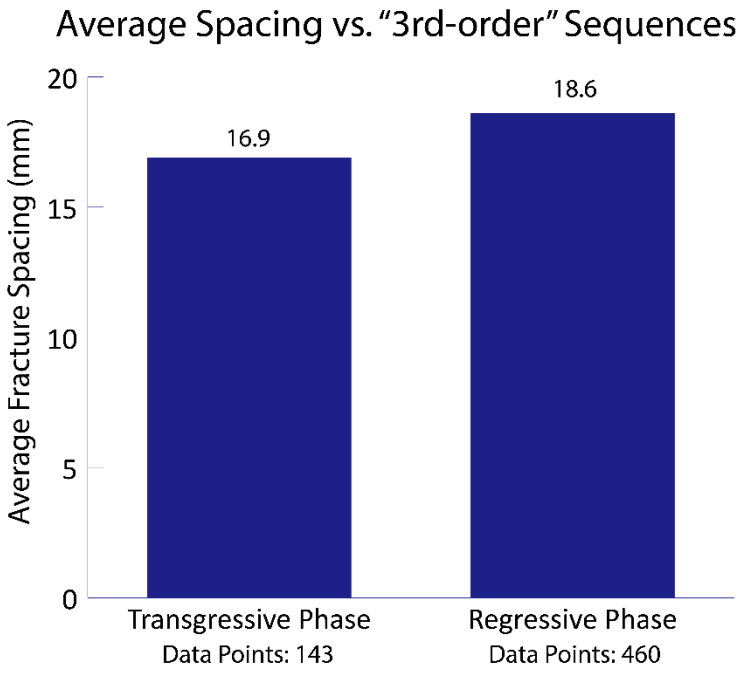

Figure 2.23. Average measured fracture spacing in relationship to the "third-order" sequences.

There are exceptions to the general pattern of fracture intensity being correlated to the "third-order" sequences, mostly seen when the "third-order" sequence may not be capped by packstone–grainstone facies, or when relatively abundant packstone–grainstone facies occur in the transgressive phases, most likely because of significant storm deposition. This illustrates the importance of rock data when calibrating well log data in predicting fracture distribution. At a finer scale, highly fractured intervals within the burrowed and bioturbated facies (Figure 2.15B, 2.16D) can further result in concentration of fractures in the transgressive phases. Similar patterns of higher fracture intensity in the "muddier" transgressive systems tract (TST) than the "grainier" highstand systems tract (HST) have also been documented in other units, for example, the Lower Cretaceous shallow-water limestones in south Texas (Zahm et al., 2010). Such fracture distribution is attributed to the lower unconfined strength and smaller bed or cycle thickness in the TST relative to those of the HST (Zahm et al., 2010). Variable evolution of rock mechanical properties may also play a role.

2.5 Discussion

2.5.1 Fractures and XRD Mineralogy

Mineralogical content, in particular, the calcite and clay content, directly controls yield strength and ductility and has been documented in several studies to affect fracture distribution (e.g., Corbett et al., 1987; Friedman et al., 1994; Gross, 1995; Rijken and Cooke 2001; Lorenz et al., 2002; Underwood et al., 2003; Lézin et al., 2009; Zahm et al., 2010). In this study, a general "first-order" mineralogical control of fracture distribution is observed. Average fracture intensity increases from P-Facies 1 to P-Facies 5 along with overall increasing calcite and decreasing clay content (Figure 2.24). Such a correlative relationship can be regarded as an average mineralogical representation of the facies as a control on fracture distribution. However, a detailed comparison between fracture count and whole-core XRD mineralogy (calcite and bulk clay content) is not successful. A key reason is the poorly defined sampling protocols (i.e., not aimed at specific facies or interval specific) that was used by the operator to sample once per unit interval or footage of core with variable sampling frequencies (from less than 1 m to more than 2 m [3–6.5 ft]). This nondirected sampling resulted in insufficient data points in thinly bedded intervals where facies variations frequently occur. Additional sampling bias is created when highly fractured intervals are skipped to filter out the potential impact of fracture-filling calcite cement on the mineralogy of the rock matrix. To test the relationship described earlier, high-frequency XRD data were collected from one of the cores in a 5 m- (16 ft-) thick "fourth-order" sequence to test the "high-resolution" (around 0.3 m [1 ft] per sample) mineralogical control on fracture distribution. This sequence contains all facies types except P-Facies 1 and exhibits well-constrained trend in facies-controlled fracture intensity. The results show a poorly constrained positive correlation between fracture intensity and calcite percentage, supporting the general premise that increasing calcite content leads to increased strength, even in the higher-frequency sequences or thinner units.

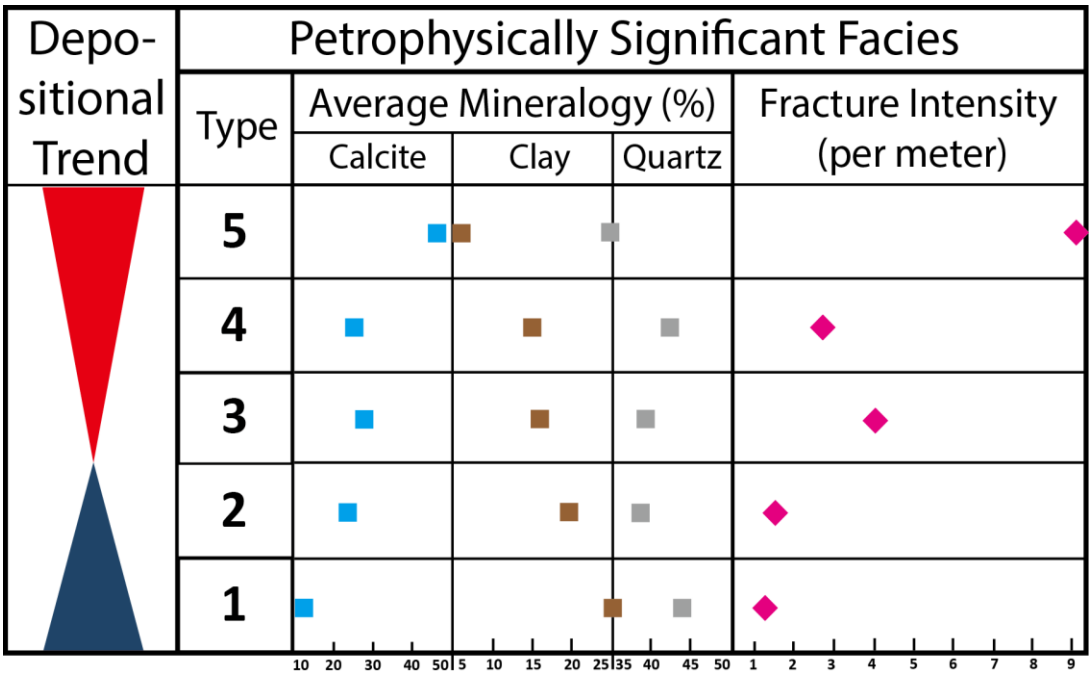

Figure 2.24. Comparison between average fracture intensity and average XRD mineralogy of each type of petrophysically significant facies. Note the generally positive correlation between average calcite content and fracture intensity, and the generally negative correlation between average clay and fracture intensity, both of which can be further related to the shoaling-upward depositional trend of the idealized vertical facies succession.

2.5.2 Origin of Fractures

The highly folded ptygmatic fractures commonly occur in many of the unconventional reservoirs currently being worked in the continental U.S. (Gale et al., 2014), including the Barnett Shale of the Fort Worth Basin (e.g., Gale et al., 2007), the "Mississippian limestone" play in the southern midcontinent (this study), and the Bakken play in the Williston Basin (e.g., Sonnenberg et al., 2011). However, the mechanism of formation for ptygmatic fractures remains poorly understood. One possible scenario involves a critical condition when the rock is behaving as a ductile medium but still has the strength to break at a relatively early stage post-deposition (Figure 2.25). Ductile compaction of fractures is evidenced by the intense distortion along the fracture length (Figure 2.15A, B) and is possibly a product of the viscosity and resistant strength of both the mineralized fracture and the less competent host rock (Ramberg, 1959; Shelley, 1968). The increasing extent of distortion as the ptygmatic fractures cut through mud-rich laminae (Figure 2.16A), which can

also be deformed (Figure 2.17B, C), supports this interpretation, pointing to the adaptive response of relatively ductile laminae to localized stress. In this sense, tortuosity of the ptygmatic fractures serves as a measurement of compressive strain (Ramberg, 1959; Shelley, 1968). Compaction at a relatively late stage is also likely present, as suggested by the brittle failure of the fracture (Figures 2.15D, 2.16B).

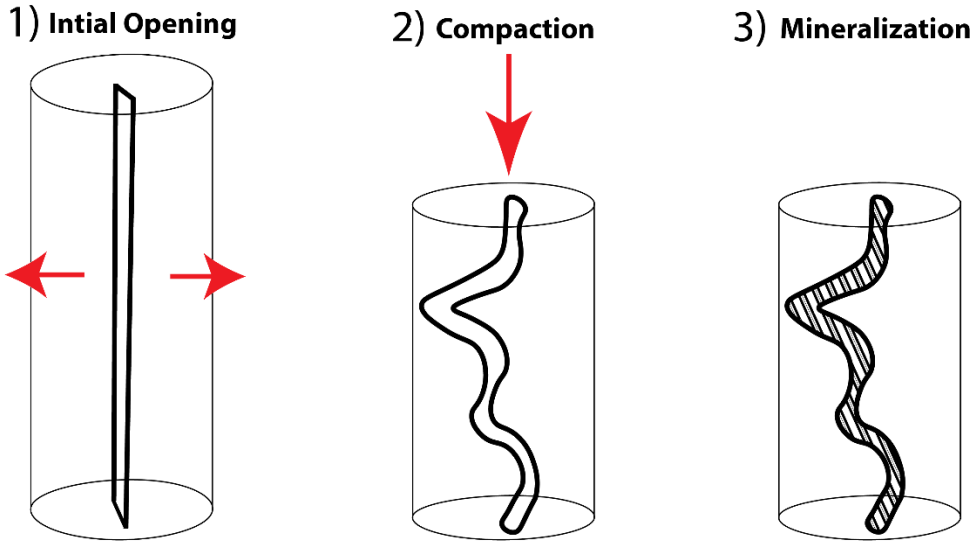

Figure 2.25. Schematic diagram showing the sequence of events that may contribute to the formation of ptygmatic fractures. See text for discussion.

In contrast, the vertical extension fractures, which are characterized by the relatively straight fracture walls (Figure 2.19A), are inferred to be formed at both a relatively early (postdeposition) and late (postburial) stage as the rock obtains sufficient strength to break via tensile failure (Olson et al., 2007), reflecting a sense of displacement perpendicular to fracture wall and a pure opening mode (mode I; e.g., Olson et al., 2009). In the shear fractures, the "pinch-and-swell" structure (Figure 2.19B) may reflect mode II sliding with lateral shear stress being oblique or orthogonal to fracture wall (e.g., Olson et al., 2009). Although the dominant stress regime can be difficult to determine in the intervals of mixed fracture types, difference in rock mechanical properties (e.g.,

strength) at the time of fracture propagation can be evident where transformation of the fracture type occurs (Figure 2.19C).

2.5.3 Structural Diagenesis

Temporal variations of rock mechanical properties (i.e., structural diagenesis) result in the fact that the present-day fracture distribution may not reflect the rock mechanical properties when the fractures were initially formed (e.g., Gale et al., 2004; Shackleton et al., 2005; Olson et al., 2007; Laubach et al., 2009, 2010). Interpreted to have been formed respectively at a relatively early and an early (postdeposition) to late (postburial) stage, the ptygmatic and vertical extension fractures seem to favor different rock strength, which is likely further affected by the susceptibility of different facies to diagenesis. The primary porosity of the coarser-grained, higher-energy P-Facies 5 was preferably filled with extensive calcite cements following deposition (Figure 2.8B), which adds strength to the rock (e.g., Shackleton et al., 2005) and facilitates the formation of the vertical extension fractures at both a relatively early and late stage. Therefore, the vertical, cyclic occurrence of facies that exhibit various susceptibilities to petrophysically significant calcite cementation contributes to the compartmentalization of rock mechanical properties and overall fracture distribution (e.g., Gale et al., 2004). In this sense, the coexistence of the ptygmatic and vertical extension fractures in the same facies suggests the temporal evolution of rock mechanical properties related to the type and extent of diagenetic modification that results in the present-day fracture and mechanical stratigraphy observed in the play.

Absence of natural fractures in certain intervals adjacent to highly fractured zones, such as in P-Facies 5 (e.g., Figure 2.8A) which contains the highest average fracture intensity (Figure 2.24), points to the potential role of different burial conditions in controlling the spatial distribution of fractures (e.g., Laubach et al., 2009) and the uncertainties when tying fracture stratigraphy with sequence stratigraphy. Although such a temporal offset between the formation of ptygmatic fractures and present-day rock mechanical properties results in potential difficulties in revealing

the rock and structural conditions at the time of fracturing and tying fracture stratigraphy with mechanical stratigraphy, pervasive diagenetic alteration of the mineralogical content in the rock matrix, such as dolomitization that can dominate over original mineralogy in controlling fracture intensity (e.g., Gale et al., 2004; Ortega et al., 2010), is not observed. This suggests that the distinct correlation between the fracture abundance and facies can be utilized to predict the fracture distribution using sequence stratigraphic approach in the subsurface Mississippian cores in this area. Although such a correlation could be overshadowed by postdepositional variations of rock mechanical properties (e.g., Olson et al., 2009), the grain texture, initial porosity, and mineralogical composition, all of which are affected by depositional environments and can be predicted by the relative positions in the sequence stratigraphic framework, are important to consider when addressing the issue of structural diagenesis when predicting and modeling fracture network.

In addition, structural diagenesis likely plays a key role in the clustering of fractures, which is difficult to evaluate when addressing the fracture dataset obtained from subsurface cores (e.g., Gale et al., 2014), and raises a challenge for upscaling the core-based data at a regional scale (e.g., Dershowitz et al., 1998). Among individual cores, the abundance of natural fractures is highly variable and can be partially explained by the various proportions of the petrophysically significant facies. Different potential for structural diagenesis (e.g., different spatial and temporal variations in rock mechanical properties; Laubach et al., 2009) affected by variations in facies distribution in different parts of the depositional system, as well as various activities relative to the structural elements in the area (e.g., fault distribution), is the other factor to consider. Although such sampling bias results in a challenge in predicting an exact fracture count in the subsurface, the correlative trend between fracture abundance and facies (Figure 2.20) and sequence stratigraphy (Figure 2.22) can provide insight for predicting the relative abundance of

natural fractures in both cores and uncored wells of the “Mississippian limestone” play in this area through the utilization of sequence stratigraphy.

2.5.4 Fracture Intensity, Spacing, and Height Related to Bed Thickness

In addition to mineralogically controlled variations in the strength of the rock units, attributes of mechanical interfaces (e.g., thickness) can also be critical in controlling fracture termination, height, spacing, and intensity, especially in relatively massive-bedded stratigraphic units with subtle stiffness variations (Underwood et al., 2003; Corbett et al., 1987). A positive correlation between fracture height and bed thickness has been commonly recognized (e.g., Schultz and Fossen, 2002) and is also observed in this study, particularly in cases where short ptygmatic fractures are confined within relatively thin brittle layers (Figure 2.17A). Such a pattern of fracture confinement in layers with higher calcite content has been commonly documented in both cores and outcrops of fractured sedimentary rocks (Pitman and Sprunt, 1986; Helgeson and Aydin, 1991; Gross et al., 1995; Frost and Kerans, 2010; Zahm et al., 2010) and in unconventional reservoirs (e.g., Corbett et al., 1987; Friedman et al., 1994; Cooke et al., 2006), and is thought to be related to the internal deformation of ductile layers and the local opening or sliding of weak interfaces (e.g., bedding planes), the latter of which reduces the stress singularity at the fracture tip and results in subcritical crack growth (e.g., Olson et al., 2009). Consequently, the fracture tip loses propagation impetus because of dissipation of stress concentration, and the fractures are then restricted to the brittle layers, which possess lower tensile strength than the ductile layers (Corbett et al., 1987; Helgeson and Aydin, 1991; Cooke and Underwood, 2001; Renshaw et al., 2003; Cooke et al., 2006). More commonly, the step-over of fractures into adjacent mud-rich, relatively ductile intervals (e.g., Figure 2.18A) may be associated with the strongly bonded nature of the contact with a relatively high cohesion and friction coefficient, which promotes fracture propagation (Cooke and Underwood, 2001), and with the nonelastic deformation within the ductile interval (Rijken and Cooke, 2001). Based on laboratory tests,

Friedman et al. (1994) proposed that the decreasing rate of fracture propagation and decreasing effective confining pressure, the latter of which may even transform the brittleness to ductility in mudrocks (Nygård et al., 2006), may also play a role. In cases where the ductile layers are relatively thin, stress at the fracture tip may not be dissipated by the internal deformation in the ductile layer so that fractures may continue to propagate into the next brittle layer (Figure 2.16A; Rijken and Cooke, 2001; Cooke et al., 2006), and waning propagation impetus at the fracture tip may be indicated by the decreasing kinematic aperture along the fracture length (Figure 2.16A). Although possibly affecting the average mineralogy of facies, the alternation of brittle and ductile layers can play a key role in determining the mechanical behavior of mudrocks (Gross and Engelder, 1995).

It has also been documented that thinner beds tend to contain more closely spaced short fractures than thicker beds with similar mechanical properties (e.g., McQuillan, 1973; Ladeira and Price, 1981; Corbett et al., 1987; Gross et al., 1995; Cooke et al., 2006; Sirat et al., 2007). In this study, closely spaced, relatively tall fractures (e.g., 15–30 cm [6-12 in.] in measured height) are present in thick (e.g., around 1 meter [3 ft]), massive-bedded intervals (Figure 2.16A), and singular, short fractures are common in thin calcite-rich layers (e.g., 1–5 cm in thickness; Figure 2.17A). However, an effort to delve into the relationship between bedding thickness and fracture attributes (e.g., height and spacing) was not successful, because of several reasons. The first and foremost is the difficulty to define beds in an unambiguous and definitive way, because of the common lacking of distinct variations in mineralogy (i.e., gradational contact) and common presence of thin laminae in a "bed." Consequently, the thickness of "a bed" commonly equals an interval of one facies type that can be several meters (several feet) thick with gradational contacts and contains fractures with highly variable height and complex stacking patterns (e.g., the top tip of one fracture is commonly adjacent to the basal tip of another fracture; Figure 2.16A). Such loosely constrained control of bedding on fracture distribution is a major reason that fracture

attributes are not reported along with fracture abundance in this study. As a result, the variable constraining relationship between fractures and bedding, when present, points to an overall poorly constrained relationship of bedding thickness to fracture height, further contributing to the uncertainties when relating bedding structures to mechanical layering. In addition, temporal evolution of rock mechanical properties and localized stress in intervals with similar mechanical properties may have further contributed to such a constraining relationship between bedding and fractures by producing a complex contrast of relative rigidity among units (e.g., Shackleton et al., 2005), which is illustrated by the deformed mud-rich laminae intersected by the ptygmatic fractures (Figure 2.17B, C). All of these factors may also be responsible for the tapering termination of fractures in zones seemingly without distinct mineralogical changes (Figure 2.15A, B) and the coexistence of various types of fractures in the same facies, illustrating the complexity in the attributes, distribution, and controlling factors of the fracture system, and the uncertainties when integrating fracture stratigraphy, mechanical stratigraphy, and sequence stratigraphy at a whole core scale. Timing of fracture development may also be a controlling factor, as "early" fractures tend to be independent of bedding thickness, and "late" fractures may be related to thickness of the brittle layers (e.g., Renshaw et al., 2003; Frost and Kerans, 2010).

2.5.5 Reservoir Considerations

Open fractures serve as key conduits for fluid migration, and therefore are crucial for reservoir permeability, especially when matrix porosity is extremely low (e.g., McQuillan, 1973). The localized presence of void space in the vertical extension fractures (Figure 2.19A) suggests that these type of fractures may be present as clusters in the subsurface similar to what has been inferred in the Barnett Shale and observed in the Austin Chalk (Gale et al., 2004; 2007). Therefore, these partially open vertical extension fractures may provide reservoir permeability at some scale, the quantitative extent of which is unknown. On the other hand, virtually, all of the ptygmatic and shear fractures are sealed with calcite cement and, therefore, likely to provide little,

if any, primary contribution to reservoir performance. These mineralized fractures, however, may promote the propagation of induced fractures during hydraulic fracturing treatments by serving as planes of weakness and reactivation (e.g., Gale et al., 2007; Hu et al., 2014).

2.5.6 Limitations

There are several potential limitations that must be considered in the application of the results reported in this study. The first and foremost relates to the nature of the core. The distance between the cores available for this study (ranging from several kilometers to tens of kilometers [several miles to tens of miles]) directly results in a sampling bias, which only reflects a clustered fracture distribution in the area. The narrow width of the core, which omits fractures with spacing wider than the core width, creates another sampling bias and potentially masks the "true" occurrence style and abundance of fractures (e.g., a singular fracture may be part of a fracture set not captured by the core; Figure 2.15A vs. B). All of these scenarios can lead to an incomplete picture of lateral fracture distribution, suggesting the scale-dependent nature of the fracture dataset. Gale et al. (2004) and Ortega et al. (2006, 2010) developed a scale-independent method to characterize fracture abundance with intensity and spacing data. Different from this study, their method was applied on outcrops and requires beds with a lateral extent that cannot be observed in core. In addition, average fracture spacing is commonly considered as the inverse of average fracture intensity in beds for closely spaced fractures (e.g., Ortega et al., 2006; Gale et al., 2007). Because of the highly variable and difficult nature of defining beds in much of these cores as discussed earlier, this trend was not observable in this study either. As such, the approach of counting fracture abundance from the perspective of unit length of core may be the best applicable method for the narrow subsurface cores, at least in this study.

The actual measurements of the fracture attributes may also be equivocal. For instance, true height of the fractures is underestimated when the fractures are observed terminating because of missing core pieces or at the core edge, which accounts for 23% of the fracture population

(Figure 2.13). This effect can be worsened by an inclined instead of a vertical orientation of the core. Because of this potential sampling bias, measured height of the fractures is not compared with facies and sequence stratigraphic framework. The kinematic aperture data of this study is estimated using a hand held millimeter-scale ruler, possibly resulting in some level of data imprecision. Ortega et al. (2006) used a microscope-calibrated comparator for accurate measurement of kinematic aperture. However, considering the highly variable kinematic aperture exhibited by the sinusoidal ptygmatic fractures (Figure 2.15A, B) that commonly taper (Figure 2.13), this comparator has its inherent limitation for this study. Examination of the "true" kinematic aperture can also be affected by the occasional breakage of core along fractures and the angle of the core surface intersecting the fracture plane. In addition, fractures terminating beneath the core surface, which are common based on micro-CT imaging results (Figure 2.11A) and petrography (Figure 2.15D), cannot be captured in a core surface-based investigation. Along with the variable 3-D kinematic aperture (Figure 2.11B), these features, which have also been observed in micro-CT imaging results in the Cretaceous Eagle Ford Formation (Hu et al., 2014), illustrate the necessity of incorporating 3-D imaging techniques as well as petrography, both of which may help upscale the fracture data (e.g., Gale et al., 2004) and reinforce the comprehensiveness of a core surface-based fracture dataset. Therefore, integrating fracture data at various scales from well log, outcrop, core surface, petrographic thin-sections, and high-frequency micro-CT imaging would be most applicable to developing a comprehensive natural fracture dataset. Further integration of fracture data with high-frequency porosity–permeability and rock mechanical data can be used to develop a composite geomechanical–reservoir model (Gale et al., 2004; Sirat et al., 2007; Zahm et al., 2010).

The final major limitation involves the observation of the mineralogical control of the fracture distribution and intensity, which suggests that nonsystematic sampling for XRD analysis may fail to capture the smaller-scale variability in fracture intensity related to bedding. More selective and

higher-frequency sampling would lead to a more reliable relationship between mineralogy and fracture distribution at the whole core scale.

2.6 Conclusions

This study illustrates the value of integrating a sequence stratigraphic approach into characterizing and predicting the distribution of natural fractures in the "Mississippian limestone" play in north-central Oklahoma. Four types of fractures are identified: ptygmatic fractures (most abundant), vertical extension fractures, shear fractures (least abundant), and zones of mixed types of fractures. The highly folded ptygmatic fractures are interpreted as forming relatively early via ductile buckling prior to lithification. As shown by micro-CT imaging, fractures are commonly discontinuous at the millimeter scale and terminate beneath the core surface, with a variable kinematic aperture from a 3-D perspective. The vast majority of the fractures are sealed with calcite cement with only local remnant void space observed in vertical extension fractures. These partially open vertical fractures likely contribute to reservoir permeability at some scale.

Results of this study indicate that the distribution of naturally fractured units in the "Mississippian limestone" play is heterogeneous and is controlled by both the facies types and the sequence stratigraphic framework. Among the five types of petrophysically significant facies, the massive-bedded and hummocky cross-stratified to planar laminated packstone–grainstone (P-Facies 5), which exhibits the highest calcite content, contains the most abundant fractures and the highest average fracture intensity, supporting the correlation between mineralogy and fracture distribution. From a sequence stratigraphic standpoint, the regressive phases of the "third-order" composite sequences exhibit higher fracture intensities than the associated transgressive phases when P-Facies 5 is the dominant facies. Because these "third-order" sequences can be identified by cleaning-upward GR patterns, the tie between fracture intensity and sequences that can be correlated sub-regionally provides a valuable tool to assist in the prediction of fractures in the subsurface away from cored wells.

2.7 References

Amorosi, A., 2012, The occurrence of glaucony in the stratigraphic record: Distribution patterns and sequence-stratigraphic significance: International Association of Sedimentologists Special Publication 45, p. 37–54.

Babcock, E. A., 1978, Measurement of subsurface fractures from dipmeter logs: AAPG Bulletin, v. 62, p. 1111–1126.

Bafia, D. J., and T. W. Spencer, 1999, Identifying fracture zones in the Austin Chalk: South Texas Geological Society Bulletin, v. 39, p. 9–15.

Bai, T., and D. D. Pollard, 2000, Fracture spacing in layered rocks: A new explanation based on the stress transition: Journal of Structural Geology, v. 22, p. 43–57.

Bednarz, M., and D. Mcilroy, 2009, Three-dimensional reconstruction of "*phycosiphoniform*" burrows: Implications for identification of trace fossils in core: Palaeontologia Electronica, v. 12, 15 p.

Blakey, R., 2013, Paleogeography and geologic evolution of North America: http://www2.nau.edu/rcb7/nam.html (accessed April 2016).

Boggs, S., 2006, Principles of sedimentology and stratigraphy: London, Pearson Education, 662 p.

Cheel, R. J., and D. A. Leckie, 1993, Hummocky cross-stratification, in V. P. Wright, ed., Sedimentology Review 1: Hoboken, New Jersey, Blackwell, p. 103–122.

Childress, M. and Grammer, G. M., 2018, Characteristics of debris flows and outrunner blocks: Evidence for Mississippian deposition on a distally steepened ramp, in G. M. Grammer, J. M.

Gregg, J. O. Puckette, P. Jaiswal, M. Pranter, S. J. Mazzullo, and R. H. Goldstein, eds., Mississippian reservoirs of the midcontinent, U.S.A.: AAPG Memoir 122, in press.

Cooke, M. L., J. A. Simo, C. A. Underwood, and P. Rijken, 2006, Mechanical stratigraphic controls on fracture patterns within carbonates and implications for groundwater flow: Sedimentary Geology, v. 184, p. 225–239.

Cooke, M. L., and C. A. Underwood, 2001, Fracture termination and step-over at bedding interfaces due to frictional slip and interface opening: Journal of Structural Geology, v. 23, p. 223–238.

Cooper, S., and J. Lorenz, 2012, Natural fracture characteristics in core from the Adkisson 1-33 SWD well, Logan County, Oklahoma: Devon Energy Confidential Report.

Corbett, K., M. Friedman, and J. Spang, 1987, Fracture development and mechanical stratigraphy of Austin Chalk, Texas: AAPG Bulletin, v. 71, p. 17–28.

Dagistanova, K., A. Aitzhanov, D. Belanger, P. Bateman, R. Camerlo, R. Fitzmorris, M. Hui, et al., 2011, Integration of dynamic data into characterization of the Tengiz reservoir: Tengiz slope: AAPG Search and Discovery Article #50399.

Dershowitz, B., P. LaPointe, T. Eiben, and L. Wei, 1998, Integration of discrete feature network methods with conventional simulator approaches: SPE Annual Technical Conference and Exhibition paper #49069, New Orleans, Louisiana, September 27–30, 1998.

Dott, R. H., 1983, 1982 SEPM presidential address: Episodic Sedimentation—How normal is average? How rare is rare? Does it matter?: Journal of Sedimentary Petrology, v. 53, p. 5–23.

Ericsson, J. B., H. C. McKean, and R. J. Hooper, 1998, Facies and curvature controlled 3D fracture models in a Cretaceous carbonate reservoir, Arabian Gulf, in G. Jones, Q. J. Fisher, and

R. J. Knipe, eds., Faulting, fault sealing and fluid flow in hydrocarbon reservoirs: Geological Society (London) Special Publication 147, p. 299–312.

Fisher, M. K., C. A. Wright, B. M. Davidson, A. K. Goodwin, E. O. Fielder, W. S. Buckler, and N. P. Steinsberger, 2002, Integrating fracture mapping technologies to optimize stimulations in the Barnett Shale: SPE Annual Technical Conference and Exhibition Article #77441, San Antonio, Texas, September 29–October 2, 2002.

Friedman, M., O. Kwon, and V. L. French, 1994, Containment of natural fractures in brittle beds of the Austin Chalk, in P. P. Nelson, and S. E. Laubach, eds., Proceedings of the first North American rock mechanics symposium: Rotterdam, Balkema, p. 833–840.

Frost, E. L., and C. Kerans, 2010, Controls on syndepositional fracture patterns, Devonian reef complexes, Canning Basin, Western Australia: Journal of Structural Geology, v. 32, p. 1231–1249.

Gale, J. F., S. E. Laubach, R. A. Marrett, J. E. Olson, J. Holder, and R. M. Reed, 2004, Predicting and characterizing fractures in dolostone reservoirs: Using the link between diagenesis and fracturing, in C. J. R. Braithwaite, G. Rizzi, and G. Darke, eds., The geometry and petrogenesis of dolomite hydrocarbon reservoirs: Geological Society (London) Special Publication 235, p. 177–192.

Gale, J. F., R. M. Reed, and J. Holder, 2007, Natural fractures in the Barnett Shale and their importance for hydraulic fracture treatments: AAPG Bulletin, v. 91, p. 603–622.

Gale, J. F. W., S. E. Laubach, J. E. Olson, P. Eichhubl, and A. Fall, 2014, Natural fractures in shale: A review and new observations: AAPG Bulletin, v. 98, p. 2165–2216.

Gay, S., Jr., 2003a, The Nemaha Trend—A system of compressional thrust-fold, strike-slip structural features in Kansas and Oklahoma, part 1: Shale Shaker, v. 54, p. 9–17.

Gay, S., Jr., 2003b, The Nemaha Trend—A system of compressional thrust-fold, strike-slip structural features in Kansas and Oklahoma, part 2, conclusion: Shale Shaker, v. 54, p. 39–49.

Gingras, M. K., G. Baniak, J. Gordon, J. Hovikoski, K. O. Konhauser, A. La Croix, R. Lemiski, et al., 2012, Porosity and permeability in bioturbated sediments: Developments in Sedimentology, v. 64, p. 837–868.

Goldring, R., J. E. Pollard, and A. M. Taylor, 1991, Anconichnus horizontalis: A pervasive ichnofabric-forming trace fossil in post-Paleozoic offshore siliciclastic facies: PALAIOS, v. 6, p. 250–263.

Gross, M. R., 1995, Fracture partitioning: Failure mode as a function of lithology in the Monterey Formation of coastal California: Geological Society of America Bulletin, v. 107, p. 779–792.

Gross, M. R., and T. Engelder, 1995, Strain accommodated by brittle failure in adjacent units of the Monterey Formation, USA: scale effects and evidence for uniform displacement boundary conditions: Journal of Structural Geology, v. 17, p. 1303–1318.

Gross, M. R., M. P. Fischer, T. Engelder, and R. J. Greenfield, 1995, Factors controlling joint spacing in interbedded sedimentary rocks: Integrating numerical models with field observations from the Monterey Formation, USA, in M. S. Ameen, ed., Fractography: Fracture topography as a tool in fracture mechanics and stress analysis: Geological Society (London) Special Publications 92, p. 215–233.

Grossi, P., 2015, Investigating natural fracture effects on well productivity: Eagle Ford, La Salle County, Texas: Unconventional Resources Technology Conference (URTeC) Article #2148347, San Antonio, Texas, July 20–22, 2015, 13 p.

Hanks, C. L., J. Lorenz, L. Teufel, and A. P. Krumhardt, 1997: Lithologic and structural controls on natural fracture distribution and behavior within the Lisburne Group, northeastern Brooks Range and North Slope subsurface, Alaska: AAPG bulletin, v. 81, p. 1700–1720.

Helgeson, D. E., and A. Aydin, 1991, Characteristics of joint propagation across layer interfaces in sedimentary rocks: Journal of Structural Geology, v. 13, p. 897–911.

Holman, R., 2014, Seismic characterization of fractured rock fabric in Mississippian Limestone, Payne County, Oklahoma: Unpublished M.S. thesis, Oklahoma State University, Stillwater, Oklahoma, 123 p.

Hu, D., L. Matzar, and V. N. Martysevich, 2014, Effect of natural fractures on Eagle Ford shale mechanical properties: SPE Annual Technical Conference and Exhibition Article #170651, Amsterdam, Netherlands, October 27–29, 2014, 16 p.

Kelley, C., and G. Jones, 2013, Investigating natural fracture effects on well productivity: Eagle Ford, La Salle County, Texas: Unconventional Resources Technology Conference (URTeC) Article #1607746, Denver, Colorado, August 12–14, 2013, 3 p.

Kulander, B. R., S. L. Dean, and B. J. Ward, 1990, Fractured core analysis: Interpretation, logging, and use of natural and induced fractures in core: AAPG Methods in Exploration 8, 88 p.

Laubach, S. E., P. Eichhubl, C. Hilgers, and R. H., Lander, 2010, Structural diagenesis: Journal of Structural Geology, v. 32, p. 1866–1872.

Laubach, S. E., J. E. Olson, and M. R. Gross, 2009, Mechanical and fracture stratigraphy: AAPG Bulletin, v. 93, p. 1413–1426.

Ladeira, F. L., and N. J. Price, 1981, Relationship between fracture spacing and bed thickness: Journal of Structural Geology, v. 3, p. 179–183.

LeBlanc, S., 2014, High resolution sequence stratigraphy and reservoir characterization of the "Mississippian Limestone" in north-central Oklahoma: M.S. thesis, Oklahoma State University, Stillwater, Oklahoma, 443 p.

Lézin, C., F. Odonne, G. J. Massonnat, and G. Escadeillas, 2009, Dependence of joint spacing on rock properties in carbonate strata: AAPG Bulletin, v. 93, p. 271–290.

Lorenz, J. C., and R. E. Hill, 1992, Measurement and analysis of fractures in core, in J. W. Schmoker, E. B. Coalson, and C. A. Brown, eds., Geological studies relevant to horizontal Drilling: Examples from western North America: Denver, Colorado, Rocky Mountain Association of Geologists, p. 47–60.

Lorenz, J. C., W. D. Rizer, H. E. Farrell, M. D. Sonnenfeld, and C. L. Hanks, 1997, Characteristics of natural fractures in carbonate strata, in I. Palaz, and K. J. Marfurt, eds., Carbonate seismology: Society of Exploration Geophysicists Geophysical Development Series 6, p. 179–201.

Lorenz, J. C., J. L. Sterling, D. S. Schechter, C. L. Whigham, and J. J. Jensen, 2002, Natural fractures in the Spraberry Formation, Midland Basin, Texas: The effects of mechanical stratigraphy on fracture variability and reservoir behavior: AAPG Bulletin, v. 86, p. 505–524.

MacEachern, J. A., and J. A. Burton, 2000, Firmground *Zoophycos* in the Lower Cretaceous Viking Formation, Alberta: A distal expression of the Glossifungites ichnofacies: PALAIOS, v. 15, p. 387–398.

Marrett, R., O.J. Ortega, and C.M. Kelsey, 1999, Extent of power-law scaling for natural fractures in rock: Geology, v. 27, p. 799-802.

McQuillan, H., 1973, Small-scale fracture density in Asmari Formation of southwest Iran and its relation to bed thickness and structural setting: AAPG Bulletin, v. 57, p. 2367–2385.

Narr, W., 1996, Estimating average fracture spacing in subsurface rock: AAPG bulletin, v. 80, p. 1565–1585.

Nelson, R. A., 2001, Geological analysis of naturally fractured reservoirs, 2nd edition: New York, Elsevier, 332 p.

Nelson, R. A., and S. Serra, 1995, Vertical and lateral variations in fracture spacing in folded carbonate sections and its relation to locating horizontal wells: Canadian SPE/CIM/CANMET International Conference on Recent Advances in Horizontal Well Applications Paper HWC94-41, Calgary, Canada, March 20–23, 1994, 10 p.

Nygård, R., M. Gutierrez, R. K. Bratli, and K. Høeg, 2006, Brittle–ductile transition, shear failure and leakage in shales and mudrocks: Marine and Petroleum Geology, v. 23, p. 201–212.

Northcutt, R. A., and J. A. Campbell, 1996, Geologic Provinces of Oklahoma: Transactions of the 1995 AAPG Mid-Continent Section Meeting, p. 128-134.

Odin, G. S., and A. Matter, 1981, De glauconiarum origine: Sedimentology, v. 28, p. 611–641.

Olson, J. E., S. E. Laubach, and R. H. Lander, 2007, Combining diagenesis and mechanics to quantify fracture aperture distributions and fracture pattern permeability, in L. Lonergan, R. J. H. Jolly, K. Rawnsley, and D. J. Sanderson, eds., Fractured reservoirs: Geological Society (London) Special Publication 270, p. 101–116.

Olson, J. E., S. E. Laubach, and R. H. Lander, 2009, Natural Fracture characterization in tight gas sandstones: Integrating mechanics and diagenesis: AAPG Bulletin, v. 93, p. 1535–1549.

Ortega, O. J., J. F. W. Gale, and R. Marrett, 2010, Quantifying diagenetic and stratigraphic controls on fracture intensity in platform carbonates: An example from the Sierra Madre Oriental, northeast Mexico: Journal of Structural Geology, v. 32, p. 1943–1959.

Ortega, O. J., R. A. Marrett, and S. E. Laubach, 2006, A scale-independent approach to fracture intensity and average spacing measurement: AAPG Bulletin, v. 90, p. 193–208.

Padgett, M. J., and D. C. Nester, 1991, Fracture evaluation of Block P-0315, Point Arguello Field, Offshore California, Using core, outcrop, seismic data and curved space analysis: Fractured reservoirs: Origin, description, evaluation, in R. Sneider, W. Massell, R. Mathis, D. Loren, P. Wichmann, eds., The integration of geology, geophysics, petrophysics and petroleum engineering in reservoir delineation, description and management: AAPG Special Volume 26, p. 242–268.

Pemberton, S. G., and R. W. Frey, 1984, Ichnology of storm-influenced shallow marine sequence: Cardium Formation (Upper Cretaceous) at Seebe, Alberta, in D. F. Scott and D. J. Glass, eds., The Mesozoic of Middle North America: Canadian Society of Petroleum Geologists Memoir 9, p. 281–304.

Pemberton, S. G., and J. A. MacEachern, 1997, The ichnological signature of storm deposits: The use of trace fossils in event stratigraphy, in C. E. Brett and G. C. Baird, eds., Paleontological events: Stratigraphic, ecological, and evolutionary implications: New York, Columbia University Press, p. 73–109.

Pemberton, S. G., J. A. MacEachern, and R. W. Frey, 1992, Trace fossil facies models: Environmental and allostratigraphic significance, in R. G. Walker and N. P. James, eds., Facies models: Response to sea level change: St. John's, Newfoundland, Geological Association of Canada, p. 47–72.

Pemberton, S. G., and M. K. Gingras, 2005, Classification and characterizations of biogenically enhanced permeability: AAPG Bulletin, v. 89, p. 1493–1517.

Pérez, M. A., V. Grechka, and R. J. Michelena, 1999, Fracture detection in a carbonate reservoir using a variety of seismic methods: Geophysics, v. 64, p. 1266–1276.

Pitman, J. K., and E. S. Sprunt, 1986, Origin and distribution of fractures in Lower Tertiary and Upper Cretaceous rocks, Piceance Basin, Colorado, and their relation to the occurrence of hydrocarbons, in C. W. Spencer, R. F. Mast, eds., Geology of tight gas reservoirs: AAPG Studies in Geology 24, p. 221–233.

Price, B. J., and G. M. Grammer, 2018, High resolution sequence stratigraphic architecture and reservoir characterization of the Mississippian Burlington–Keokuk Formation, northwestern Arkansas, U.S.A., in G. M. Grammer, J. M. Gregg, J. O. Puckette, P. Jaiswal, M. Pranter, S. J. Mazzullo, and R. H. Goldstein, eds., Mississippian reservoirs of the midcontinent, U.S.A.: AAPG Memoir 122, in press.

Puckette, J., S. LeBlanc, B. Price, J. Bertalott, J. Bynum, L. Jaeckel, K. Flinton, Y. Wang, and G. M. Grammer, 2018, High resolution sequence stratigraphy and reservoir characterization of the Mississippian limestone in the subsurface, Northeastern Oklahoma, in G. M. Grammer, J. M. Gregg, J. O. Puckette, P. Jaiswal, M. Pranter, S. J. Mazzullo, and R. H. Goldstein, eds., Mississippian reservoirs of the midcontinent, U.S.A.: AAPG Memoir 122, in press.

Ramberg, H., 1959, Evolution of ptygmatic folding: Norsk Geologisk Tidsskrift, v. 39, p. 99–152.

Renshaw, C. E., T. A. Myse, and S. R. Brown, 2003, Role of heterogeneity in elastic properties and layer thickness in the jointing of layered sedimentary rocks: Geophysical Research Letters, v. 30, p. 13-1–13-4.

Rijken, P., and M. L. Cooke, 2001, Role of shale thickness on vertical connectivity of fractures in the Austin Chalk, Texas: application of crack-bridging theory: Tectonophysics, v. 337, p. 117–133.

Sarg, J. F., 2012, The Bakken—an unconventional petroleum and reservoir system: Final scientific/technical report: United States Department of Energy, 65 p.

Schultz, R. A., and H. Fossen, 2002, Displacement–length scaling in three dimensions: The importance of aspect ratio and application to deformation bands: Journal of Structural Geology, v. 24, p. 1389–1411.

Shackleton, J. R., M. L. Cooke, and A. J. Sussman, 2005, Evidence for temporally changing mechanical stratigraphy and effects on joint-network architecture: Geology, v. 33, p. 101–104.

Shelley, D., 1968, Ptygma-like veins in graywacke, mudstone, and low-grade schist from New Zealand: The Journal of Geology, v. 76, p. 692–701.

Sirat, M., S. Salman, and S. Bellah, 2007, Fracturing mechanism and fracture systems analysis of carbonate reservoir from Abu Dhabi, UAE: SPE/EAGE reservoir characterization and simulation conference Article #111397, Abu Dhabi, October 28–31, 2007, 9 p.

Smith, M. G., and R. M. Bustin, 1996, Lithofacies and paleoenvironments of the Late Devonian and Early Mississippian Bakken Formation, Williston Basin: Bulletin of Canadian Petroleum Geology, v. 44, p. 495–507.

Sonnenberg, S. A., J. A. LeFever, and R. J. Hill, 2011, Fracturing in the Bakken petroleum system, Williston Basin, in J. W. Roberson, J. A. LeFever, and S. B. Gaswirth, eds., The Bakken–Three Forks Petroleum System in the Williston Basin: Denver, Colorado, Rocky Mountain Association of Geologists, p. 393–417.

Underwood, C. A., M. L. Cooke, J. A. Simo, and M. A. Muldoon, 2003, Stratigraphic controls on vertical fracture patterns in Silurian dolomite, northeastern Wisconsin: AAPG Bulletin, v. 87, p. 121–142.

Wetzel, A., and R. G. Bromley, 1994, *Phycosiphon incertum* revisited: Anconichnus horizontalis is its junior subjective synonym: Journal of Paleontology, v. 68, p. 1396–1402.

Zahm, C. K., and P. H. Hennings, 2009, Complex fracture development related to stratigraphic architecture: Challenges for structural deformation prediction, Tensleep sandstone at the Alcova anticline, Wyoming: AAPG Bulletin, v. 93, p. 1427–1446.

Zahm, C. K., L. C. Zahm, and J. A. Bellian, 2010, Integrated fracture prediction using sequence stratigraphy within a carbonate fault damage zone, Texas, USA: Journal of Structural Geology, v. 32, p. 1363–1374.

CHAPTER III

CHARACTERIZING THE DISTRIBUTION OF NATURAL FRACTURES FROM OUTCROP IN A MISSISSIPPIAN-AGED MIXED CARBONATE-CHERT SYSTEM, MID-CONTINENT, USA

3.0 Abstract

Natural fractures are common in the unconventional "Mississippian Limestone" play of the U.S. Southern Mid-Continent region. Due to their narrow width, vertical cores provide limited data on the distribution of fracture attributes (e.g., kinematic aperture, height, and spacing) in relation to fracture abundance. For the purpose of searching for an outcrop analog that provides an extensive view of lateral fracture distribution, this study utilizes an outcrop with Mississippian-aged strata in northwestern Arkansas. Targeting the Reeds Spring Formation, this study aims to characterize the type, attributes, and distribution of natural fractures, and to test the outcrop's suitability as a fracture analog for the subsurface. In the outcrop, planar and nodular beds of lime mudstone and chert contain near-vertical cemented fractures. Fracture types mainly include ptygmatic and opening-mode fractures. Ptygmatic fractures are the most common fracture type in both lime mudstone and chert, whereas the opening-mode fractures are present mostly in chert. Bedding structures, which are defined by lime mudstone-chert variations, affect fracture growth, as indicated by the observation that perfect bed-bounded, top- or base-bounded, and confined fractures collectively account for the majority of the fracture population. In terms of fracture

intensity, chert shows a higher average value as compared to lime mudstone. Negative exponential and power law are present as the statistical patterns between cumulative frequency and fracture height, kinematic aperture, aspect ratio, and spacing. The best-fitting distribution pattern and the coefficient of determination vary with lithology, fracture type, and fracture height. These patterns likely point to a cooperative role of lithology, fracture type, and fracture-bedding relationships, as well as the dynamics of rock mechanical properties, in affecting these fracture attributes. In comparison with the cores, this outcrop may serve as a fracture analog for the "Mississippian Limestone" play in northernmost Oklahoma-southernmost Kansas where cherty facies are widespread, but not for the play areas in north-central Oklahoma which are dominated by mixed carbonate-siliciclastic facies.

3.1 Introduction

3.1.1 Previous Work, Significance, and Objective

Natural fractures are prevalent in unconventional hydrocarbon reservoirs, such as Bakken (e.g., Sonnenberg et al., 2011), Vaca Muerta (e.g., Hernández-Bilbao, 2016), Barnett Shale (e.g., Gale et al., 2007), and the "Mississippian Limestone" (e.g., Thompson, 2016; Wang et al., 2019, in press). Throughout the life span of production wells, production can initiate with high flow rates followed by rapid and significant declines in production within the first year (decline rates can be greater than 60% for the "Mississippian Limestone" play; Chesapeake Energy Investor Presentation, 2015; Figure 3.1). Considering the generally low matrix permeability which commonly is at a nanodarcy scale (unpublished data), the presence of natural fractures likely creates production anomalies in some play areas (Montgomery et al., 1998). As such, producing these unconventional reservoirs requires considering the attributes and distribution of open natural fractures which can create flow anisotropy and reservoir compartmentalization at multiple scales (Nelson, 2001). Sealed natural fractures at certain scales can be critical for production and engineering design as well, as they may modify the propagation of induced fractures during

hydraulic fracturing by serving as planes of weakness-reactivation or conduits for fluid loss (Gale et al., 2007, 2014). Therefore, the natural fracture system, either open or sealed, is a crucial component of reservoir characterization and modeling workflow.

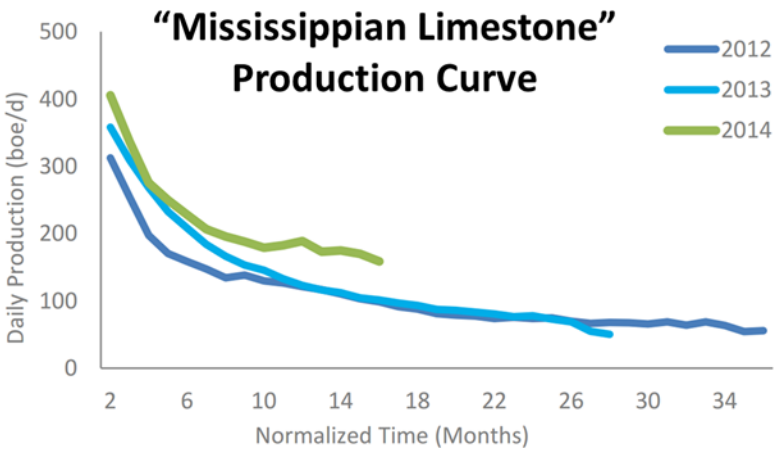

Figure 3.1. Production curve of the unconventional "Mississippian Limestone" play (Chesapeake Energy Investor Presentation, 2015). Note the sharp decline of production within the first year.

Despite its being a subject of numerous academic and industrial research projects in the past fifty years, core-scale fracture system of the "Mississippian Limestone" play has not been well studied. In cores located in north-central Oklahoma (Figure 3.2A), natural fractures, which are mostly near-vertical in dip and in relation to bedding, show a vertically and laterally compartmentalized distribution at multiple scales (e.g., Wang et al., 2019, in press). However, the narrow width of core (8.5 cm) hampers the acquisition of fracture spacing and the lateral distribution of fracture size (kinematic aperture, height) that can guide fluid flow modeling and production design (Bonnet et al., 2001; Gale et al., 2014; ; Wang et al., 2019, in press). To overcome this limitation, outcrops with laterally extensive exposures are ideal for acquiring fracture size and spacing data which may provide insight for deciphering the subsurface fracture system. Studies aiming for a systematic evaluation of the natural fracture system in the Mississippian-aged strata in outcrops (Figure 3.2B) have only recently been initiated (e.g., Burberry and Peppers, 2017). In addition, outcrops of Mississippian-aged strata exposed in northeastern Oklahoma, southwestern Missouri, and northwestern Arkansas have been utilized as

analogs for the subsurface (e.g., Mazzullo et al., 2011) for rock types, depositional system, and stratigraphic architecture. By comparing the outcrop of this study with different parts of the play, we aim to test if this outcrop is a suitable analog for the subsurface, in terms of lithology, rock mechanical aspects, and fracture distribution.

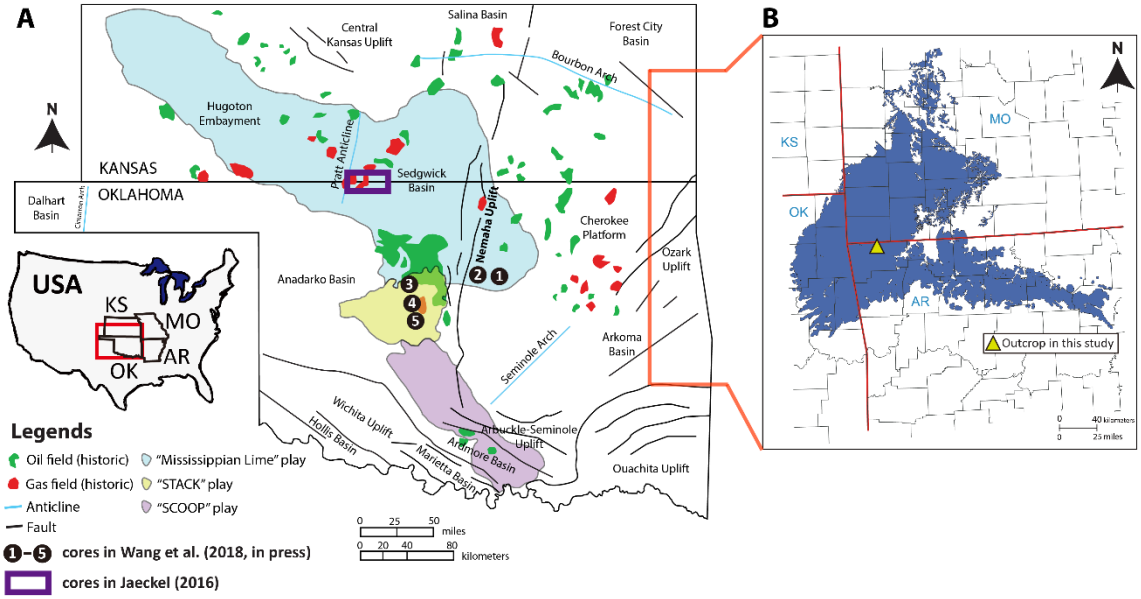

Figure 3.2. The Mississippian-aged "unconventional" reservoirs in the US southern mid-continent (A) mainly include the "Mississippian Limestone" play (blue) and the "STACK" play (yellow), along with the "chat" reservoirs (partly shown by the small bold box; Jaeckel, 2016). The generally time-equivalent rocks crop out further northeast in the "tri-state" area (blue areas in b), where the outcrop of this study is located (yellow triangle in b). The base map of (A) is courtesy of John Hunt. (B) is modified from Mazzullo et al. (2011).

3.1.2 Study Target

"Mississippian Limestone" is an informal name for much of the Mississippian-aged strata in the U.S. southern mid-continent. It includes subsurface hydrocarbon reservoirs in southern Kansas and central Oklahoma (some at depths of greater than 10,000 feet; Figure 3.2A) and extends northeastward as outcrop exposures in the "tri-state" area of southwestern Missouri, northwestern Arkansas, and northeastern Oklahoma (Figure 3.2B). The reservoirs, generally referred to as the "Mississippian Limestone" play, have become a major unconventional resource play in the continental U.S. (e.g., Matson, 2013).

In this study, a road-cut outcrop located in northwestern Arkansas (Figure 3.2B, Figure 3.3A) is characterized in terms of the distribution of fracture size (kinematic aperture, height) and spacing and the controlling factors, and tested for its suitability as a fracture analog for the subsurface. There are several reasons that this outcrop was selected. The lower part of the Reeds Spring Formation, the focus of this study (Figure 3.3A, B), contains abundant cemented fractures in layers of lime mudstone (henceforth noted as "mudstone" for brevity) and chert (Figure 3.3C, D, E). These fractures are similar in many ways to the natural fractures documented in cores in the north-central Oklahoma part of the play (Wang et al., 2019, in press), providing a possible direct analog from the perspective of fracture geometry. In addition, the nodular geometry of the fracture-hosting layers provides a unique opportunity to evaluate the fracture characteristics in non-planar bedding strata and to test the fracture distribution patterns described in other studies. Furthermore, if similar lithologies and fracture distributions are present in the subsurface, the findings of this study may help constrain fracture models and provide insight for fracture prediction and production.

3.2 Methodology

3.2.1 Description of Fractures

In this study, fractures are interpreted as natural if they are partially to fully mineralized (Figure 3.3C, E; 3.4A). In other mudstone reservoirs (e.g., siliciclastic mudstone reservoirs in the Barnett Shale), open ("barren") natural fractures indicate that the determination of natural and induced fractures solely by the presence of cements can be problematic (e.g., Gale et al., 2014). In this study, the fractures interpreted as "induced" exhibit several characteristics that do not appear to be natural in origin. To begin with, the walls of these fractures show a fresh appearance without stain or mineral lining (Figure 3.4B). In addition, there is no systematic surface texture that indicates relative movement of fracture walls (e.g., slicken sides). Although barren fractures with small-scale mineral lining on their walls can occur in outcrop (e.g., Gale et al. 2014; Ukar et al.,

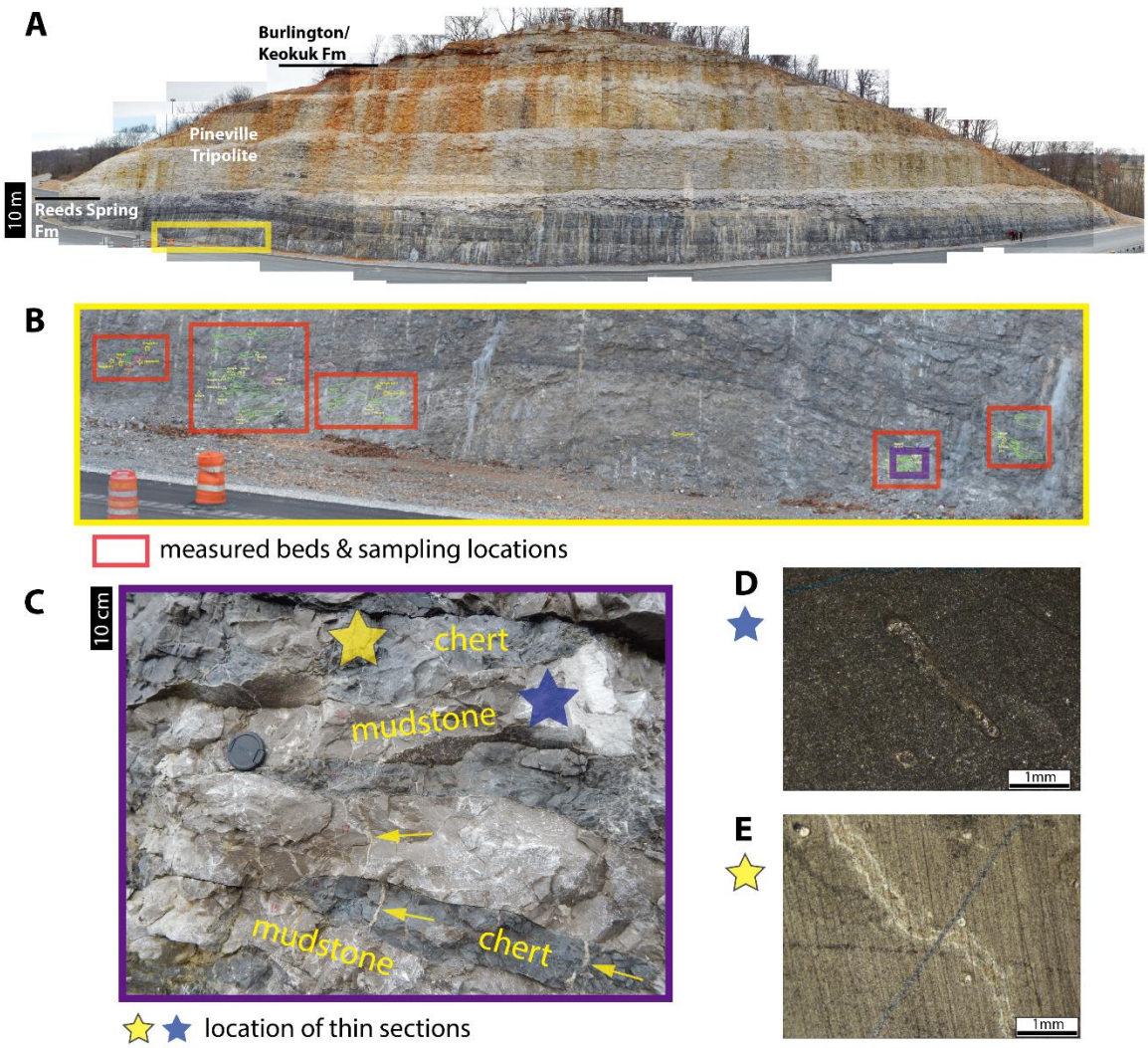

Figure 3.3. At the largest scale, the outcrop represents (A) a recent (minimally weathered) road-cut. The portion of the outcrop investigated is shown by the yellow boxes in (A) and (B), and is within the lower part of the Reeds Spring Formation. It consists of planar and nodular beds of lime mudstone (C, D) and chert (C, E). In (B), locations of measured beds and samples are shown with red boxes (safety cone for scale). (C) is zoomed-in from a bolder box near the lower right corner of (B). Note the presence of calcite-filled fractures in both mudstone and chert (arrows). (D) and (E) are thin section photomicrographs of mudstone and chert, respectively, with sampling locations being marked by stars in (C). Parallel near-vertical stripes in (D) and € are artifacts from sample preparation. Photos in (A) and (B) are courtesy of Ahmed El Belasy

2017), the abundance of artificially-induced fractures that are created by explosives during the construction of the road-cut likely have mingled with or disrupted the network of naturally occurring barren fractures, making identification of any such natural fractures problematic. Therefore, this study uses a conservative approach and interprets only the fractures with cements visible along the fracture walls as natural, recognizing uncertainties are possible.

For the interpreted natural fractures, the methodology for collecting the fracture data follows on the workflow defined by several previous studies, such as Kulander et al. (1990), Lorenz and Hill (1992), Nelson (2001), Ortega et al. (2006), Gale et al. (2007), and McGinnis et al. (2017). The investigated portion of the outcrop is composed of near-vertical exposure without a pavement view. Considering the dominantly near-vertical dip of the investigated fractures (see section below, Results – Fracture Characteristics), the linear scanline method, as opposed to the circular scanline method (which requires a pavement view, e.g., Mauldon et al., 2001; Sanderson and Nixon, 2015; Procter and Sanderson, 2018), was utilized to guide the acquisition of fracture data. Individual scanline (millimeter-scale measuring tape) is placed at a fixed position being normal to the intersected fractures (e.g., Putz-Perrier and Sanderson, 2008; Hooker et al., 2013). Length of the scanline is defined as the length between the first and last fracture that is intersected by a single scanline. Because the vast majority of the fractures in the outcrop are near vertical, the length of a scanline generally equals the sum of the fracture spacing.

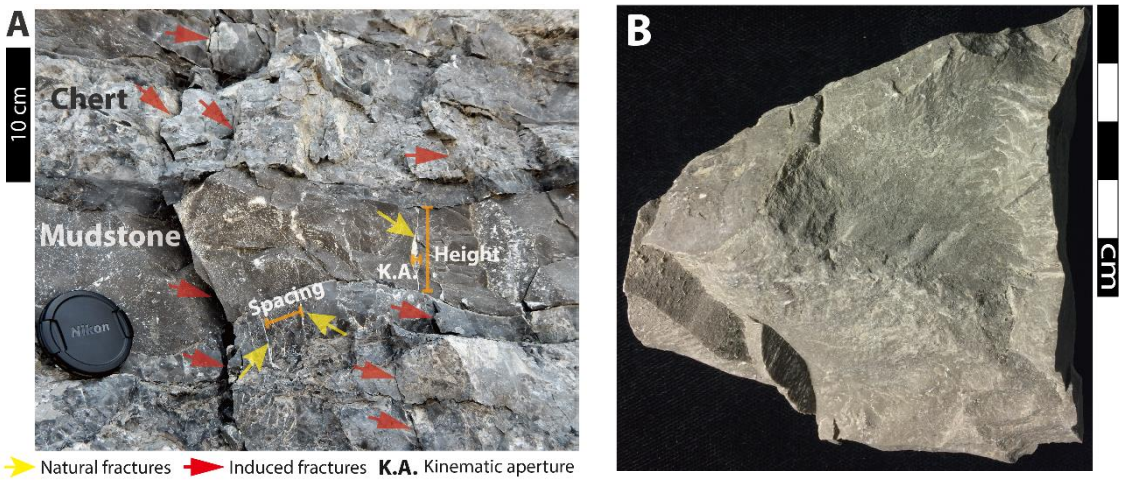

Figure 3.4. (A) outcrop photo showing the interpreted natural and induced fractures. For the interpreted natural fractures, some of the documented parameters shown here include kinematic aperture, height, and spacing. (B) photo of a lime mudstone sample showing the wall of the interpreted induced fracture.

After the scanline was placed, the attributes of the fractures intersected by the scanline were recorded, including type of fractures, orientation (vertical or sub-vertical, dip angle), mineral fill (extent and composition), kinematic aperture (using a comparator), height (using a centimeter

ruler), spacing (using a centimeter ruler), and termination style (Figure 3.4A). Fracture type is defined by morphology and inferred mode of formation (e.g., Olson et al., 2009). Kinematic aperture is defined as the accumulative opening of a fracture (including cement and opening space; Marrett et al., 1999). Aspect ratio is calculated from a ratio between kinematic aperture and height. Fracture spacing is the distance from a fracture to its adjacent fracture to the left on the scanline. Termination style include tapered at fracture tip, abrupt but random termination within bed, and abrupt due to lithological variations. As for the definition of fracture sets, common criteria include orientation, openness, scale, cement composition, and inferred timing (e.g., Hooker et al., 2013; Burberry and Peppers, 2017). In this outcrop, fractures are mostly near-vertical in dip direction without a systematic cross-cutting pattern. Because of the distinctive host lithologies, fractures are grouped by lime mudstone and chert, and integrated with measured and derived fracture data to test for statistical relationships.

The abundance of fractures is evaluated by fracture intensity. Because of the linear scanline method being applied to a cross-sectional view, fracture intensity is defined as the number of fractures per unit length of scanline (e.g., fractures per meter in this study; see Ortega et al., 2006; Gale et al., 2007; McGinnis et al., 2017). Because fracture intensity can vary based upon the scale of investigation (i.e., macro-fractures vs. micro-fractures), it is necessary to incorporate fracture size (kinematic aperture, height) with fracture intensity data (Marrett et al., 1999; Ortega et al., 2006; Hooker et al., 2013; Laubach et al., 2018). To achieve this, one effective means is the cumulative frequency diagram, which has been used to test the correlation between fracture attributes and abundance (Bonnet et al., 2001; Putz-Perrier and Sanderson 2008; Marrett et al., 1999; Ortega et al., 2006; Hooker et al. 2013). To calculate the cumulative fracture frequency, fractures are sorted from the maximum to minimum value of size (kinematic aperture, height) or spacing. In this study, because fractures with the same size or spacing are present in different lithologies (lime mudstone and chert), one of the fractures with the same size or spacing is

retained for each lithology for a simplified data population covering both lithologies. Sequential cumulative numbers (1, 2, 3, etc) are then assigned to the fractures arranged from the largest to the smallest size or spacing. Lastly, the cumulative numbers are divided by the length of the corresponding scanline to calculate cumulative fracture frequency, which can be plotted with fracture size or spacing data for a cumulative frequency diagram. By connecting fracture data at multiple scales, cumulative frequency diagram links fracture intensity with fracture size and spacing and allows for the prediction of the distribution of these data at multiple scales (e.g., Marrett et al., 1999; Bonnet et al., 2001; Ortega et al., 2006).

3.2.2 Spacing Regularity and Strain Homogeneity

Fracture spacing data can be utilized to quantify the distribution pattern of fractures along a 2D line – random, clustered, or regular. One parameter is spacing regularity (C_v) (Gillespie et al., 1999; Odling et al., 1999; Supak et al., 2006).

$$C_v = r / Savg$$

where r is standard deviation of spacing and Savg is mean of spacing. A C_v value equals to 1 means a random distribution, larger than 1 suggests a clustered distribution, and smaller than 1 implies a regular distribution. For relatively small populations, a modified spacing regularity (C_v*) is recommended (Gillespie, 2003) and is utilized in this study.

$$C_v^* = C_v [(N+1)/(N-1)]^{1/2}$$

where N is number of fractures on the scanline. Additional data type that can be quantified for an array of fractures is strain homogeneity (V'), which reflects the distribution of strain by relating cumulative kinematic aperture to the position of fractures on a scanline (Putz-Perrier and Sanderson, 2008). On a cross-plot of cumulative kinematic aperture against the position of fractures on a scanline, the straight line connecting the two fractures on two ends of the scanline represents a pattern of homogeneous strain. By comparing the measured data with the values on

this homogeneous strain line, the ratio between the absolute values of the maximum and minimum difference is referred to as strain homogeneity (V'). Ranging between 0 and 1, V' provides a quantification of strain distribution – the higher the value, the more heterogeneous the strain distribution along the scanline. Although there is no absolute standard to evaluate the exact extent of strain homogeneity, V' can be compared among fracture arrays for a relative comparison. Both the spacing regularity and strain homogeneity are calculated for each scanline when possible and are compared between mudstone and chert.

3.2.3 Bedding and its Relationship to Fractures

In addition to fracture characteristics, the nature of bedding and its relationship to fractures were documented. Because of the distinctive contrast in lithologies (lime mudstone and chert) and the absence of transitional lithology in the investigated strata, a "bedding plane" is defined at the contact between mudstone and chert. For each bed, lithology and geometry is documented, and the nature of the bedding plane is described from outcrop, hand samples, and petrographic thin sections. Because of the common nodular bedding geometry with variable thickness, bed thickness is measured along the length of all fractures intersected by the scanline using a centimeter-scale ruler.

Fracture height can reflect the confining relationship between fractures and bedding, and may be utilized to characterize the hierarchy of mechanical stratigraphy (e.g., Laubach et al., 2018). However, many studies fail to incorporate a systematic characterization of fracture height, resulting in an incomplete fracture attribute dataset (e.g., Hooker et al., 2013; Laubach et al., 2018). Based upon "fracture bed boundedness," Hooker et al. (2013) proposed a classification scheme which groups fractures into perfect bed-bounded, top bounded, hierarchical, and unbounded members. To classify the fracture height data into individual, non-overlapping end members, we modify the classification of Hooker et al. (2013) by considering all nine possible scenarios between one near-vertical fracture and one bed, and group these scenarios into four

categories: perfect bed-bounded (both top and base tips in a fracture terminate at bedding planes), top- or base-bounded, confined (both fracture tips do not reach bedding planes), and unbounded (at least one of the tips in one fracture extend beyond bedding planes) (Figure 3.5). Among different categories, relative abundance is compared between mudstone and chert. Fracture size (height, kinematic aperture) and spacing are also compared for these four categories to test for the effect of fracture-bedding-relationship on fracture patterns.

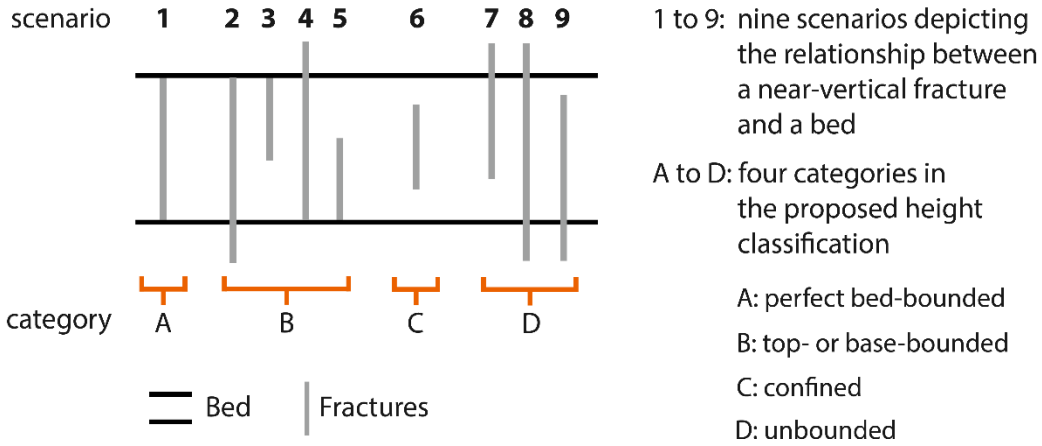

Figure 3.5. schematic diagram showing fracture height classification proposed in this study. Based upon the relationship between fracture tips and bedding planes, fractures are grouped into four categories: perfect bed-bounded, top- or base-bounded, confined, and unbounded.

3.2.4 Rebound Hardness

To compare the rock strength between fracture-hosting lithologies and compare the outcrop values with core data (Core #3, 4, 5 in Figure 3.2A), samples were collected from the measured beds and nearby portions of the outcrop, with float samples in the same areas collected as supporting data. Samples with satisfactory bulk volume (around five to ten centimeters in length, width, height) were cut with a flat base and top (not necessarily following stratigraphic-upward direction), and rebound hardness was tested using the Equotip Piccolo 2 Unit-D hardness tester. The samples were placed on a stable benchtop, or a fine grained sand-filled container to ensure stabilization of the sample during testing. Testing spots were selected near the center of the sample surface for maximum sample mass and stability, avoiding visible cracks and holes. For each data point, five measurements with a less-than-50 (unit: HLD) difference between the

maximum and minimum reading were selected and used to calculate the arithmetic mean , which is the rebound hardness value. Although taken from the same beds in which fracture data were acquired, these samples are not necessarily covered by the scanline.

3.3 Results

3.3.1 Nature of Bedding

A total of 25 beds have been measured, including 11 mudstone beds and 14 chert beds. Bedding geometry varies from planar to more commonly nodular for both mudstone and chert (e.g., Figure 3.3C). Measured bed thickness (along fracture length) ranges from 10 mm to 210 mm, and mudstone and chert show similar range, average value, and standard deviation (Table 3.1). Along bedding planes, stylolites with associated extension gash and V-shaped fracture (Figure 3.6A) and microfaults (Figure 3.6B) are present, although these features do not seem to be common. In chert, mud-filled trace fossils commonly occur as relatively uncompacted, silicified networks (Figure 3.6C), which may reflect the dynamics of rock mechanical properties. In terms of rebound hardness, chert shows distinctively higher values than mudstone (Table 3.2).

Lithology	Average	Maximum	Minimum	Data Points	Standard Deviation
mudstone	98.9	200	10	55	42.7
chert	97	210	30	125	43.8

Table 3.1. Measured bed thickness data of mudstone and chert beds in terms of average, maximum, and minimum values (all in millimeters), along with data points and standard deviation. Note the similar average value, range, and standard deviation between mudstone and chert.

3.3.2 Fracture Characteristics

Within the outcrop, large-scale faults or joints are absent. Most of the fractures that are interpreted as natural exhibit a near vertical dip. The few places where the fracture plane is exposed reveal a strike close to NE-SW. However, a systematic documentation of strike is not feasible because of the absence of a pavement view. These natural fractures are filled with calcite

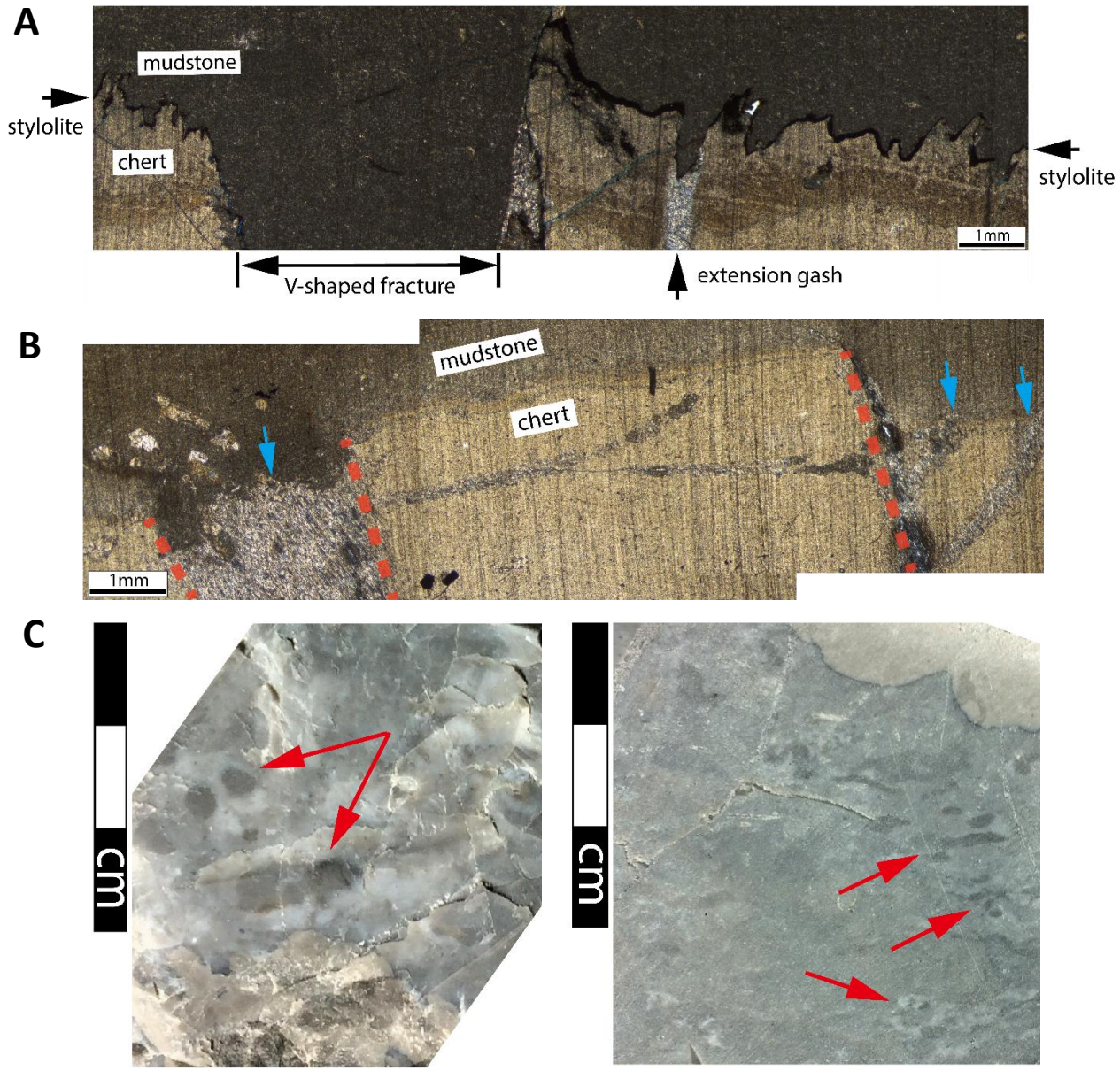

Figure 3.6. (A) and (B) are stitched thin section photomicrographs showing the presence of stylolite (A), V-shaped fracture (A), extension gash (A), and micro-fault (B; dashed lines) at the contact between lime mudstone and chert. In (A), only the upper part of the "V-shape" fracture is shown. In (B), note the offset created by the microfaults (dashed lines) and the fractures bounding the protruded fault block (arrows). At the left margin of the fault block, the fracture is partly filled with mudstone at the top (arrow at the left margin of the fault block), indicating a syndepositional origin of the fault. (C) includes two photos showing chert samples with uncompacted trace fossils (arrows; likely *Phycosiphon incertum*) which contain mud-filled cores (dark color) and silicified outer rims (lighter color), indicating that the silicification occurred prior to burial. Near-vertical stripes in (A) and (B) are artifacts created from sample preparation. All photos are taken at a stratigraphic upward direction.

Lithology	Average	Maximum	Minimum	Data Points	Standard Deviation
mudstone	659.6	687	590	12	27.4
chert	903.6	956	847	16	31.5

Table 3.2. Rebound hardness data of mudstone and chert samples in terms of average, maximum, and minimum values (all in HLD), along with data points and standard deviation. Note the distinctively higher average rebound hardness value and data range in chert as compared to mudstone.

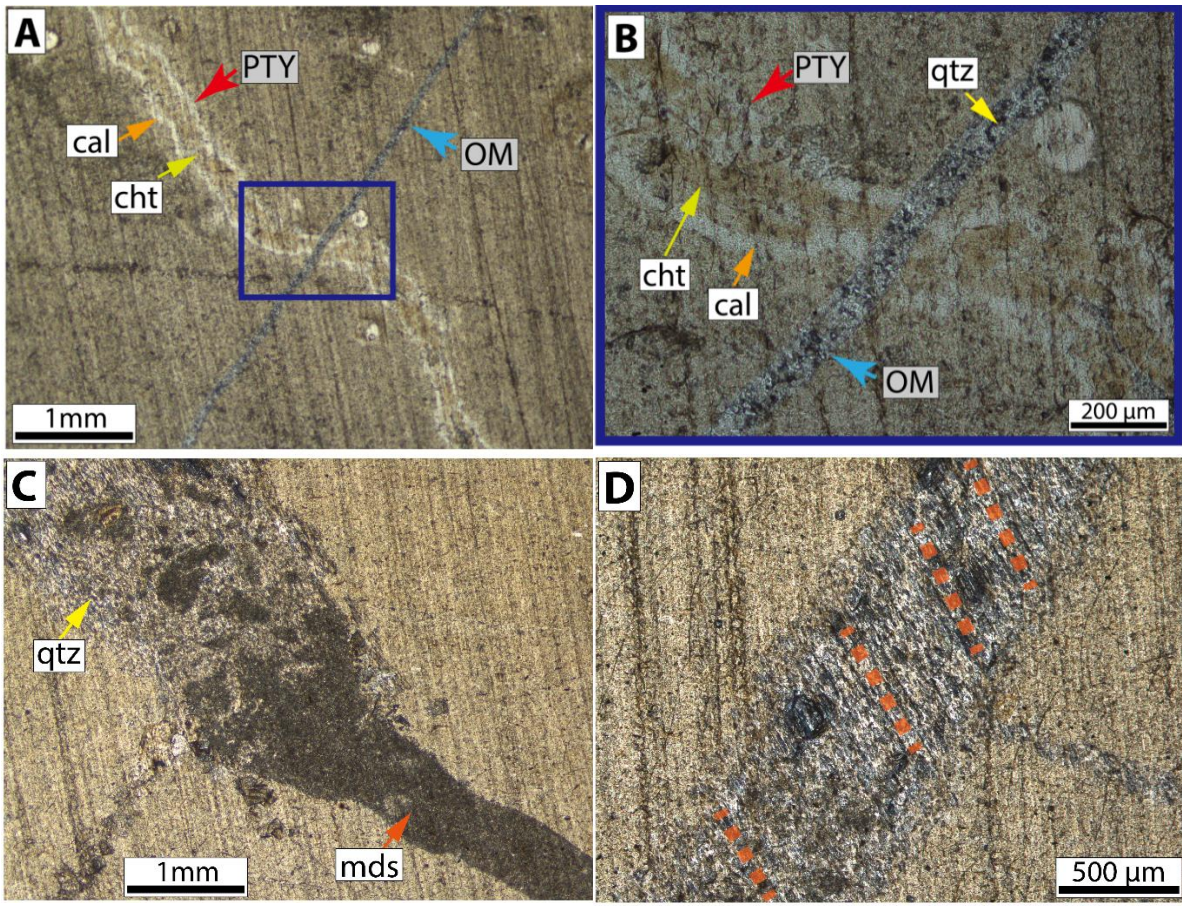

Figure 3.7. Thin section photomicrographs of chert samples showing the mineralization within the fractures. (A) and (B) show a ptygmatic fracture (PTY) intersected by a thinner opening-mode fracture (OM). The ptygmatic fracture (PTY) is filled with light-colored calcite cement (cal) around the fracture wall and darker-colored chert cement (cht) between the fracture walls. The opening-mode fracture (OM) is filled with quartz cement (qtz). (C) shows a fracture filled with darker-colored muddy sediment (mds) in the lower part and a mixture of quartz cement (qtz) and clusters of muddy sediment in the upper part. This fracture is near the base of left margin of the micro-fault as shown in Figure 6b (the lower part of the fracture marked by arrow). (D) shows that the crystal of quartz cement within a fracture aligns at a high angle (dashed lines) to the fracture wall. All photos are oriented with stratigraphic up to the top of the page. Near-vertical stripes in all photos are artifacts created from sample preparation. (B) is zoomed-in from (A), as shown with a box in (A).

and quartz cement (Figure 3.7A, B), and less commonly filled with carbonate mud (Figure 3.7C) and chert cement (Figure 3.7B). For quartz cements, the crystals can be at a high angle to the fracture wall (Figure 3.7D).

A total of 181 measured fractures show a wide size range, with measured kinematic aperture ranging from 0.095 to 7 millimeters and height ranging from 10 to 133 millimeters. Kinematic aperture are mostly less than 1 millimeter, and model height data range from 20 to 60 millimeters in both mudstone and chert (Figure 3.8A, B). Fracture height:bed thickness ratios range from 0.06 to 2.2, and are mostly less than 1, for both mudstone and chert (Figure 3.8C). The most common type of fracture termination style is abrupt termination due to lithological variations, accounting for 59.3% in the lime mudstone and 53.8% in chert (Figure 3.8D). Fracture intensity ranges from 4.3 to 71, with a higher average value in chert (33.5) than in mudstone (8.5) and a similar variation trend between mudstone and chert (Figure 3.9). Measured fracture spacing ranges from 3 to 60 millimeter, with a lower average value in chert (29.9 mm) than in mudstone (116.5 mm). Spacing regularity (C_v*) shows a maximum and minimum value of 2.41 and 0.47, respectively, with similar average values around 1.27 in mudstone and chert. Strain homogeneity (V') ranges from 0.043 to 0.74, with a higher average value in chert (0.42) than in mudstone (0.33). Both C_v* and V' show a similar range without separation between mudstone and chert.

Based on morphological features, two types of structurally originated fractures are inferred, including ptygmatic and opening-mode fractures. Ptygmatic fractures are folded along fracture length (Figure 3.10A). Another type of fracture contains relatively planar walls which imply an opening direction perpendicular to the fracture wall, and are referred to as opening-mode fractures (Figure 3.10B; Pollard and Aydin, 1988; Bonnet et al., 2001; Olson et al., 2009). Rarely, components of these two fractures coexist, and are collectively defined as a hybrid fracture. Ptygmatic fractures are present in both chert and mudstone (Figure 3.10A). It is also the most common type, with intensities of 17.8 and 4.4 in chert and mudstone, respectively (Figure 3.11).

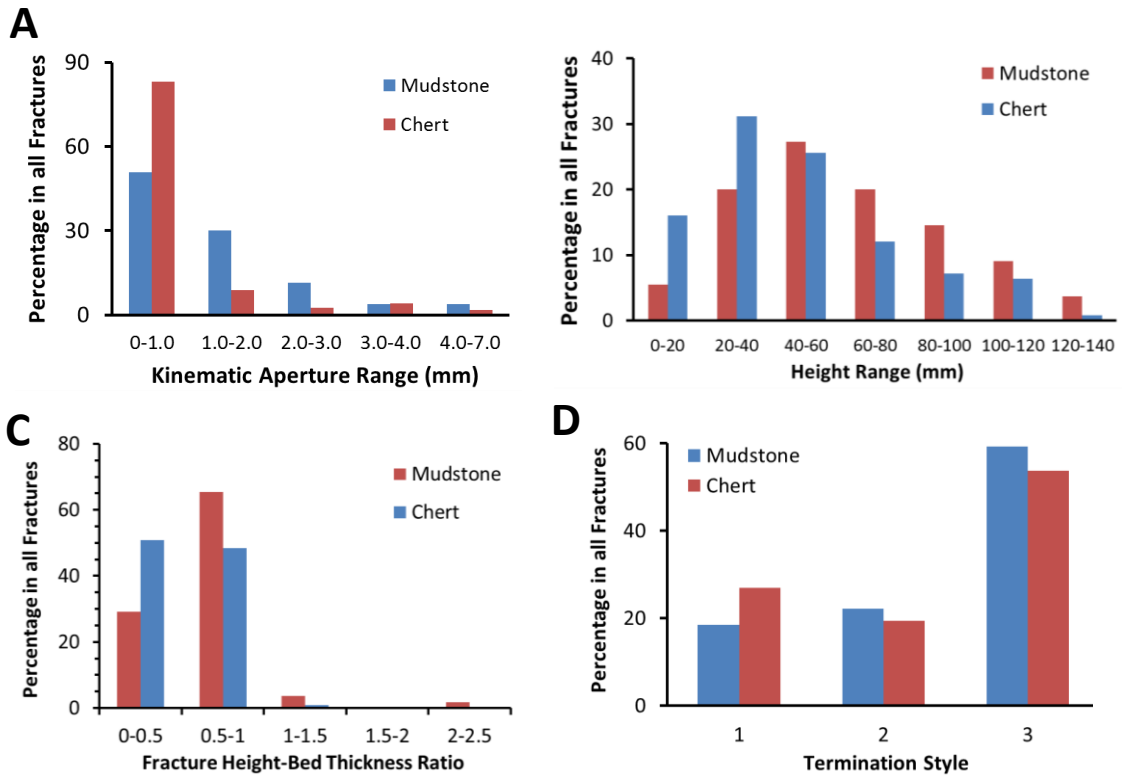

Figure 3.8. Histogram showing (A) kinematic aperture, (B) height, (C) height-bed thickness ratio, and (D) observed termination style of fractures of mudstone and chert. For all four parameters, neither mudstone nor chert exhibits overall higher values than the other. For termination style, type 1 means the fracture is tapered at top and base; type 2 means the fracture is abruptly terminated at top or base in a random place; type 3 means the fracture is abruptly terminated at top or base due to lithological variations.

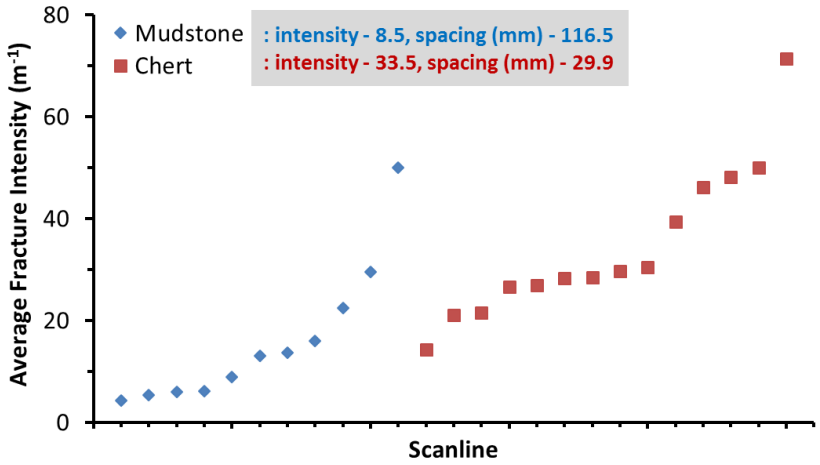

Figure 3.9. Cross-plot showing the average fracture intensity of mudstone and chert, with the average intensity and spacing values marked to the right of lithology key. For both lithologies, fracture intensity is sorted from lowest to highest, with the scanline numbers being consequently placed in a low-to-high order. Note the distinctively higher average fracture intensity and lower average fracture spacing in chert than mudstone.

Chert hosts the vast majority of the opening-mode fractures (98.2%), with an intensity of 14.3 (versus 0.16 in mudstone) (Figure 3.11). Hybrid fractures, being the least common type as observed in this study, are observed only in chert (intensity: 1.3; Figure 3.11). Because the hybrid fractures are rare, they will not be addressed in detail for the rest of this paper. In other parts of the outcrop, some fractures show a brecciated appearance (Figure 3.12A) and near-horizontal orientation (Figure 3.12B). Based on the fluid inclusion and stable C/O isotope data from the fracture-filling cements (e.g., Mohammadi et al. 2019, in press), these brecciated fractures are potentially hydrothermal in origin. In this sense, these fractures likely reflect different diagenetic and structural processes, and therefore, are treated as a separate fracture system and are not further addressed in this study.

3.3.3 Fracture Size and Spacing Distribution

3.3.3.1 By Lithology and Fracture Type

For fractures with a minimum measured kinematic aperture of 0.95 mm (lowest measured value

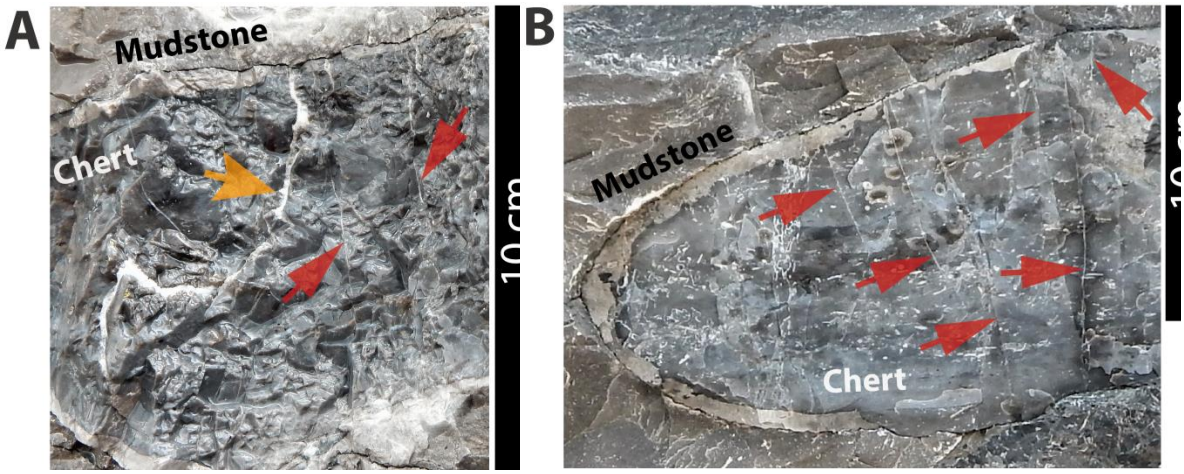

Figure 3.10. Outcrop photos showing two main types of natural fractures: ptygmatic (thicker arrow in a) and opening-mode (thinner arrows in A and B) fractures. In (A), note the folded geometry of the ptygmatic fracture. The coexistence of ptygmatic and opening-mode fractures in chert (A) likely indicates the temporal evolution of rock mechanical properties that facilitates the formation of these two types of fractures during different time frames. In (B), note that the opening-mode fractures terminate against the white- to cream-colored upper rim of the chert nodule, in a direction generally perpendicular to the tangential line of the curved lithologic interface. All photos are taken at a stratigraphic upward direction.

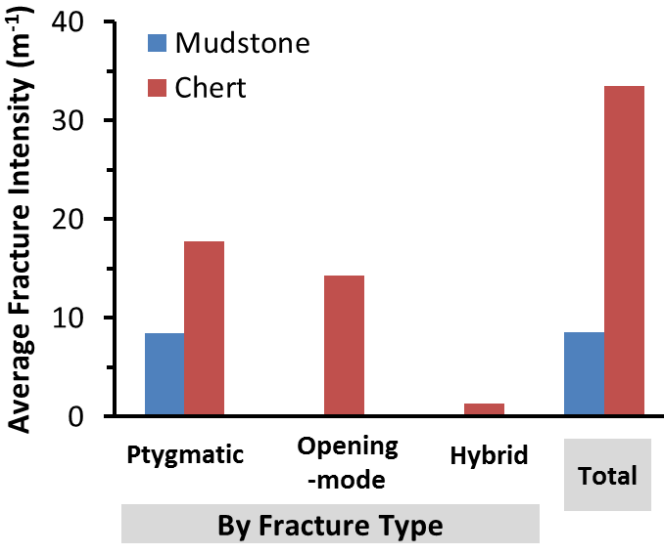

Figure 3.11. Histogram showing the average fracture intensity of the three fracture types and of all fractures as whole. Ptygmatic fractures are present in both mudstone and chert, whereas opening-mode fractures are mostly present in chert, indicating an impact of lithology on fracture types. In addition, chert shows a distinctively higher average fracture intensity, suggesting the effect of lithology on fracture abundance.

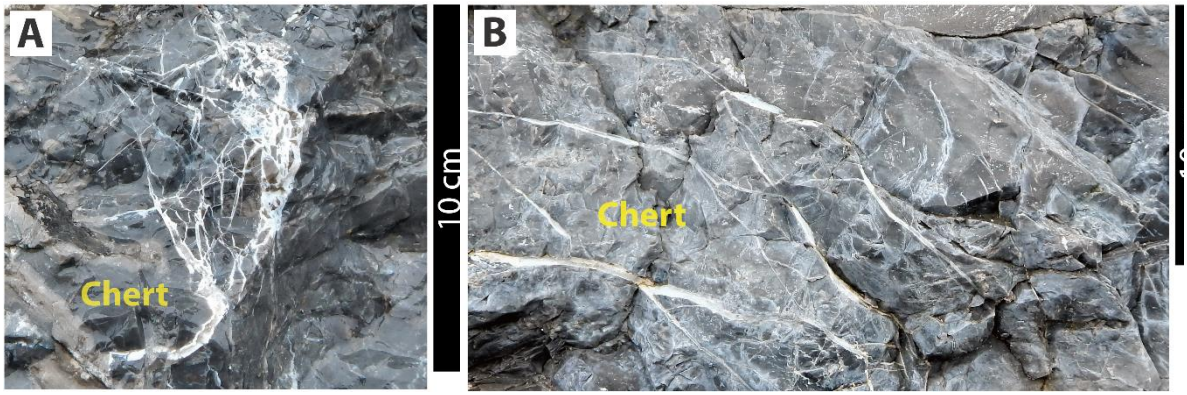

Figure 3.12. Outcrop photos showing the (A) brecciated and (B) near-horizontal fractures. Formed from likely different diagenetic and structural process as compared to the ptygmatic and opening-mode fractures, they are not further addressed in this study. All photos are taken at a stratigraphic upward direction.

in this study), the distribution of kinematic aperture (i.e., correlation with cumulative frequency) is better fit by negative exponential as compared to power-law for all data as a whole (Figure 3.13A) and between mudstone and chert with a similar data range (Figure 3.13B), as indicated by a higher value of coefficient of determination (R^2) in chert (0.76) than mudstone (0.57) (Figure 3.13B). When grouping the data by fracture types (Figure 3.13C, D), ptygmatic fractures show a

best-fitting trend of negative exponential in both mudstone and chert, with a higher R^2 in chert (0.78) than in mudstone (0.57). In contrast, a power law distribution fits best for the opening-mode fractures in chert with a similar R^2 value (0.78) with ptygmatic fracture.

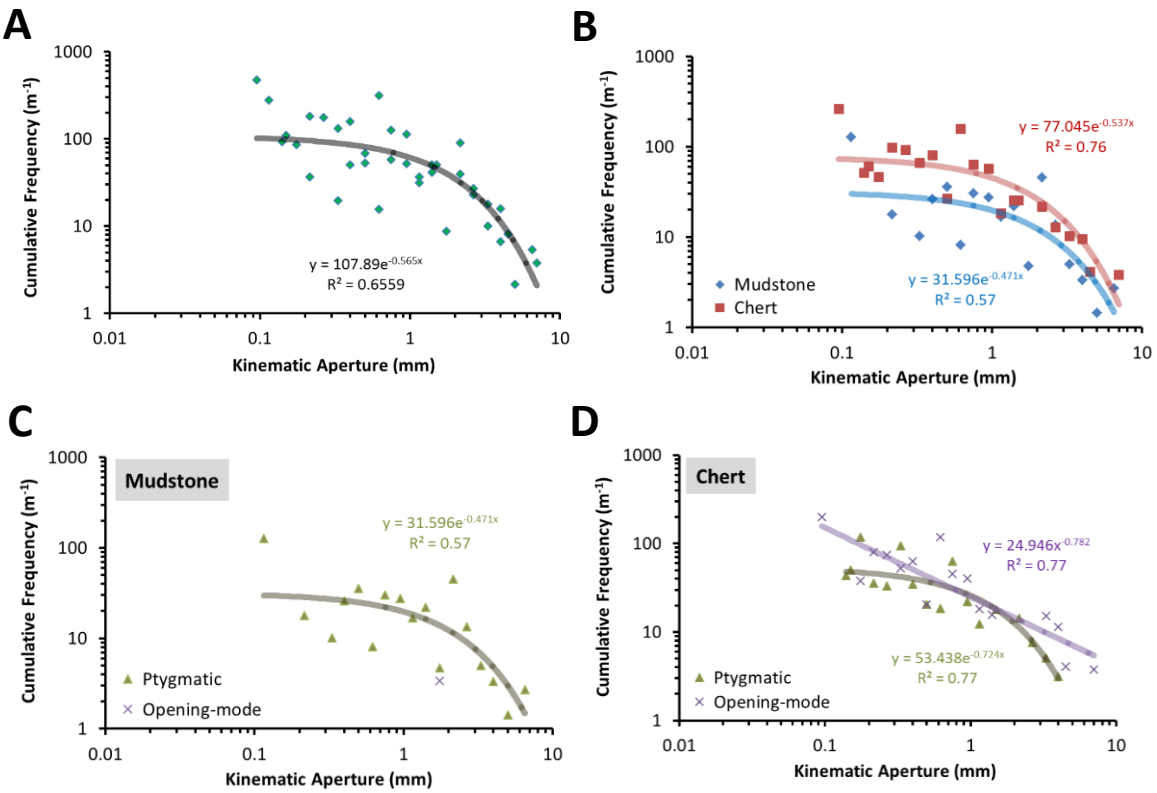

Figure 3.13. Cross-plots showing the distribution of kinematic aperture (A) of all data as a whole and arranged (B) by lithology and (C, D) by fracture type. See text for further discussion.

For fractures with a minimum measured height of 10 mm (lowest measured value in this study), negative exponential fits best with cumulative frequency for all data plotted together (Figure 3.14A) and arranged by lithology (Figure 3.14B). Particularly, data of lime mudstone and chert show different distribution trends as suggested by crosscutting data groups (Figure 3.14B) with closely ranged R^2 (mudstone: 0.65, chert: 0.61). Further grouping the data by fracture type (Figure 3.14C, D), negative exponential fits best for ptygmatic fractures in both mudstone and chert, whereas power law fits best for opening-mode fractures in chert.

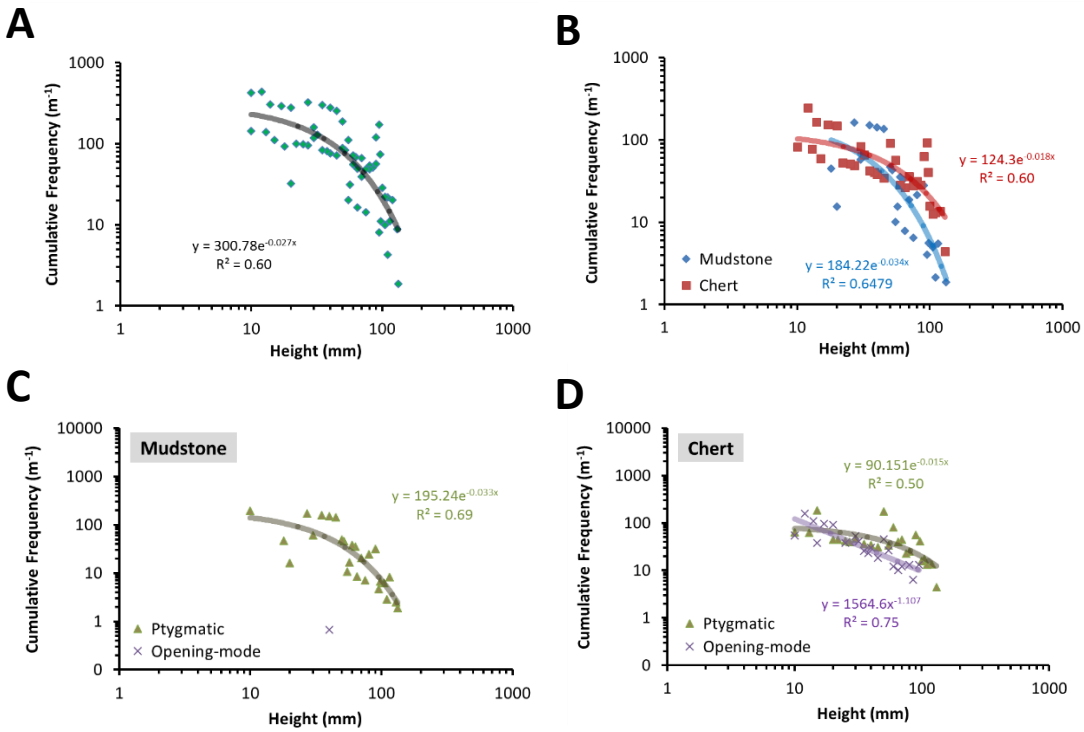

Figure 3.14. Cross-plots showing the distribution of height (A) of all data as a whole and arranged (B) by lithology and (C, D) by fracture type. See text for further discussion.

A mixture of best-fitting trends occurs in aspect ratios when correlated to cumulative frequency. A power law fit applies to the situations of all data (Figure 3.15A), chert (Figure 3.15B), and for ptygmatic and opening-mode fractures in chert (Figure 3.15D). For mudstone (Figure 3.15B) and ptygmatic fractures in mudstone (Figure 3.15C), negative exponential fits best with similar R^2 values (0.49 and 0.48, respectively). Particularly, the data of ptygmatic and opening-mode fractures in chert largely overlap (Figure 3.15D).

With a minimum measured value of 3 mm (lowest measured value in this study), spacing shows a best-fitting trend of negative exponential with cumulative frequency for all data (Figure 3.16A) and between two lithologies (Figure 3.16B) and two fracture types (Figure 3.16C, D). Similar to fracture height (Figure 3.14B), mudstone and chert exhibit crosscutting pattern with similar R^2 values (mudstone: 0.78, chert: 0.71; Figure 3.16B). Similar to aspect ratios (Figure 3.15D), data

of ptygmatic and opening-mode fractures largely overlap, despite a higher R^2 in ptygmatic fractures (0.79) than opening-mode fractures (0.67) (Figure 3.16D).

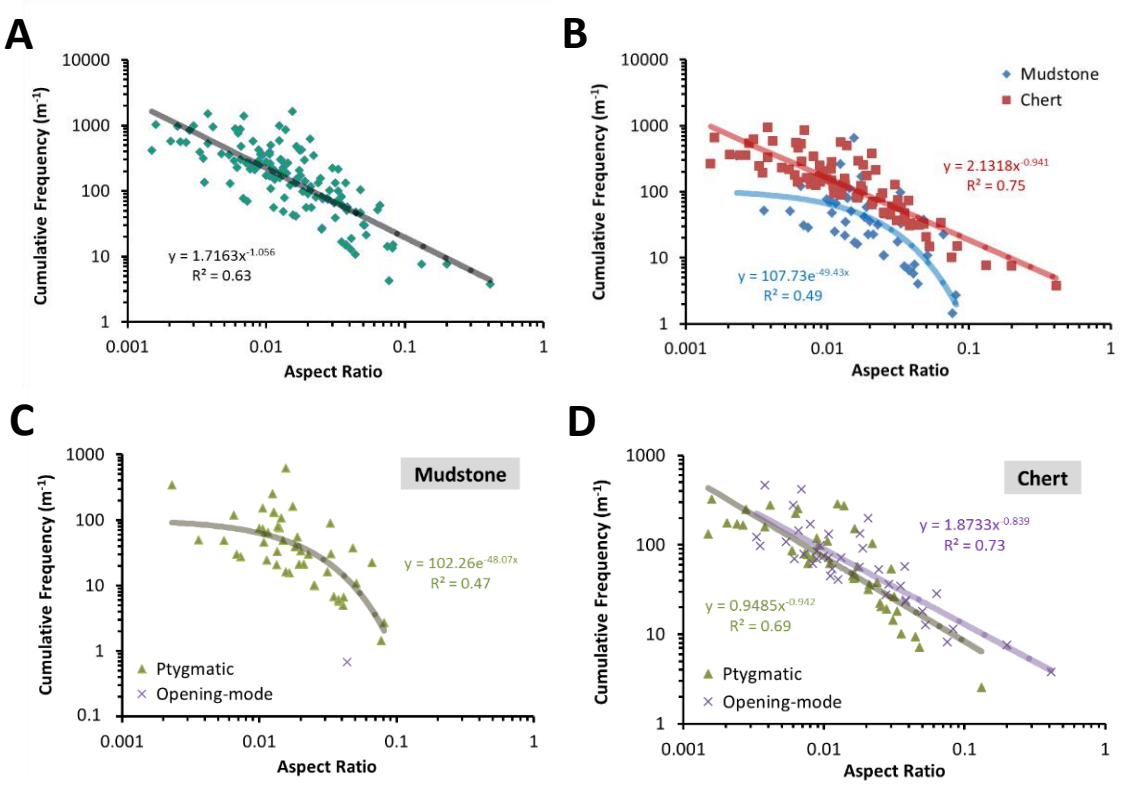

Figure 3.15. Cross-plots showing the distribution of aspect ratio (A) of all data as a whole and arranged (B) by lithology and (C, D) by fracture type. See text for further discussion.

3.3.3.2 By Height Classification

When grouped using the proposed height classification (Figure 3.5), fractures extending beyond both bedding planes (#8 in Category D; Figure 3.5) are not observed in this study. Category B and C (top- or base-bounded and confined fractures) account for the majority of all fractures as a whole (Figure 3.17A; 86%) and in mudstone and chert (Figure 3.17B; 45.5% for mudstone, 92% for chert). All categories show similar ranges of height values, with the Category D (unbounded fractures) showing the highest average value (Category A: 81.7 mm, Category B: 51.4 mm, Category C: 48.3 mm, Category D: 91.7 mm). Because of the limited data (Figure 3.17A; 1.7% in all fractures), Category D fractures will not be discussed in detail for the rest of this paper.

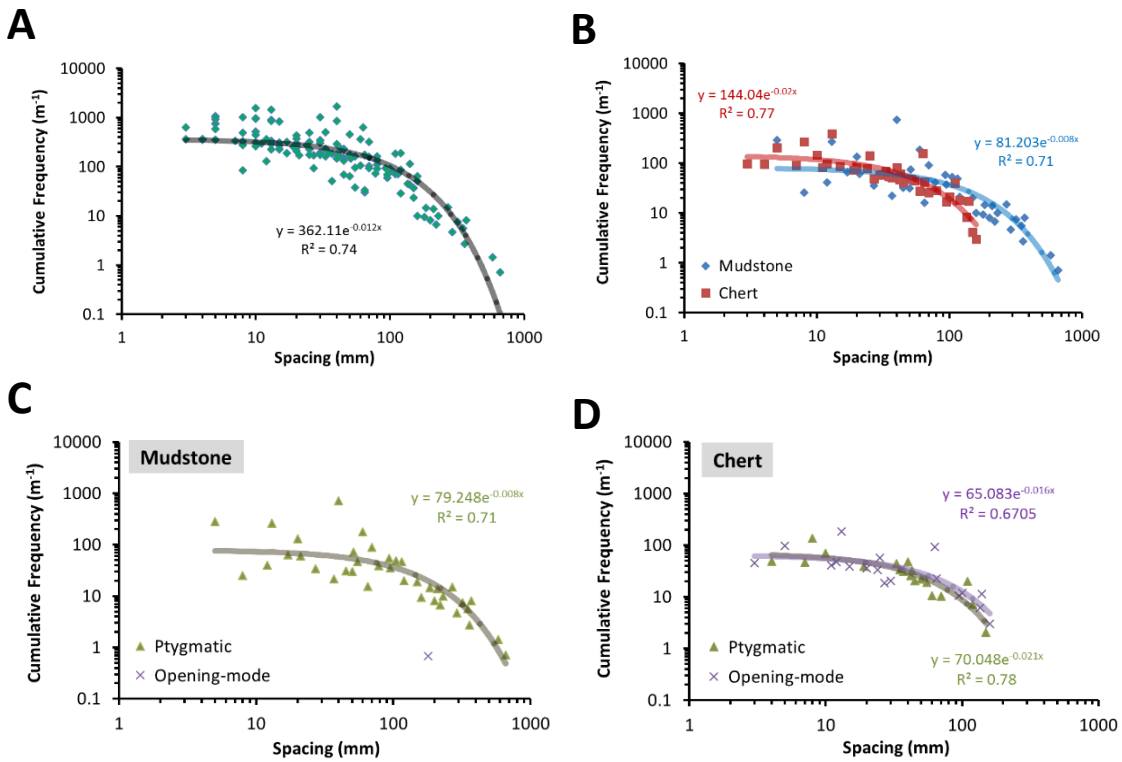

Figure 3.16. Cross-plots showing the distribution of spacing (A) of all data as a whole and arranged (B) by lithology and (C, D) fracture type. See text for further discussion.

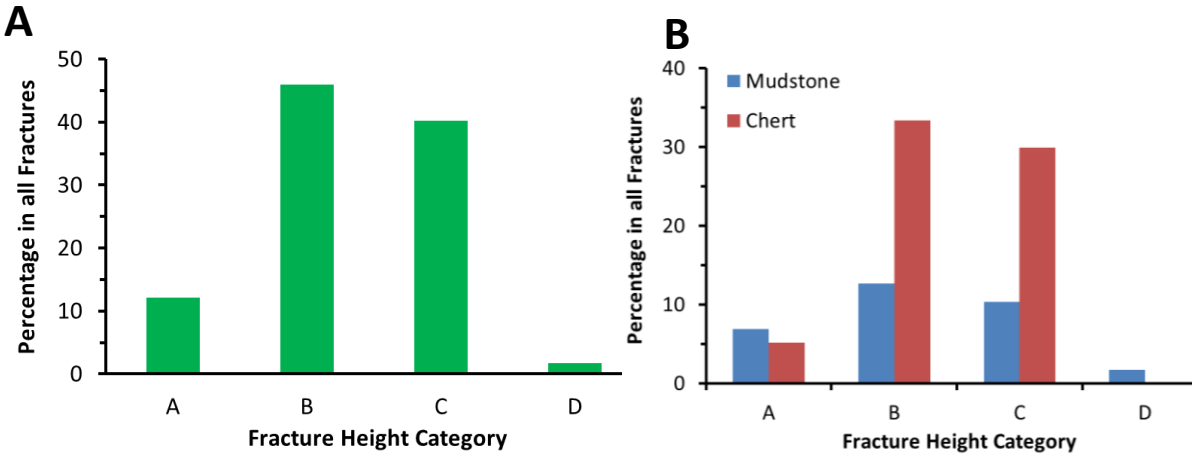

Figure 3.17. Histograms showing the distribution of the fracture height categories. For (A) all fractures as a whole and for (B) both mudstone and chert, Category B and C (top- or base-bounded and confined fractures) account for the majority of the population, indicating the effect of bedding plane on fracture termination.

In addition, the distribution of kinematic aperture, height, and spacing shows variable patterns when grouped by the height classification. Power law and negative exponential fits best for

kinematic aperture (Figure 3.18) and height data (Figure 3.19), respectively. In contrast, spacing data (Figure 3.20) show variable best-fitting trends: power law for Category A and negative exponential for Category B and C. Correlating spacing with height, kinematic aperture, and bed thickness reveals a lack of separation among different fracture categories.

3.4 Discussion

3.4.1 Controlling Factors of Fracture Pattern

For the frequency distribution of fracture attribute data, common non-clustering patterns include negative exponential, log-normal, gamma, and power law (Bonnet et al., 2001). In particular, the power law distribution appears to be the most common pattern in many studies (e.g., Marrett et al., 1999; Ortega et al., 2006; Hooker et al., 2013; Santos et al., 2015). Factors responsible for these variations include dynamics of rock mechanical properties (e.g., elastic moduli), effective stress, flaws within the rock, lithology-controlled layering thickness, properties of the mechanical interfaces (Narr and Suppe, 1991; Gross and Engelder, 1995; Gross et al., 1995; Bai and Pollard,

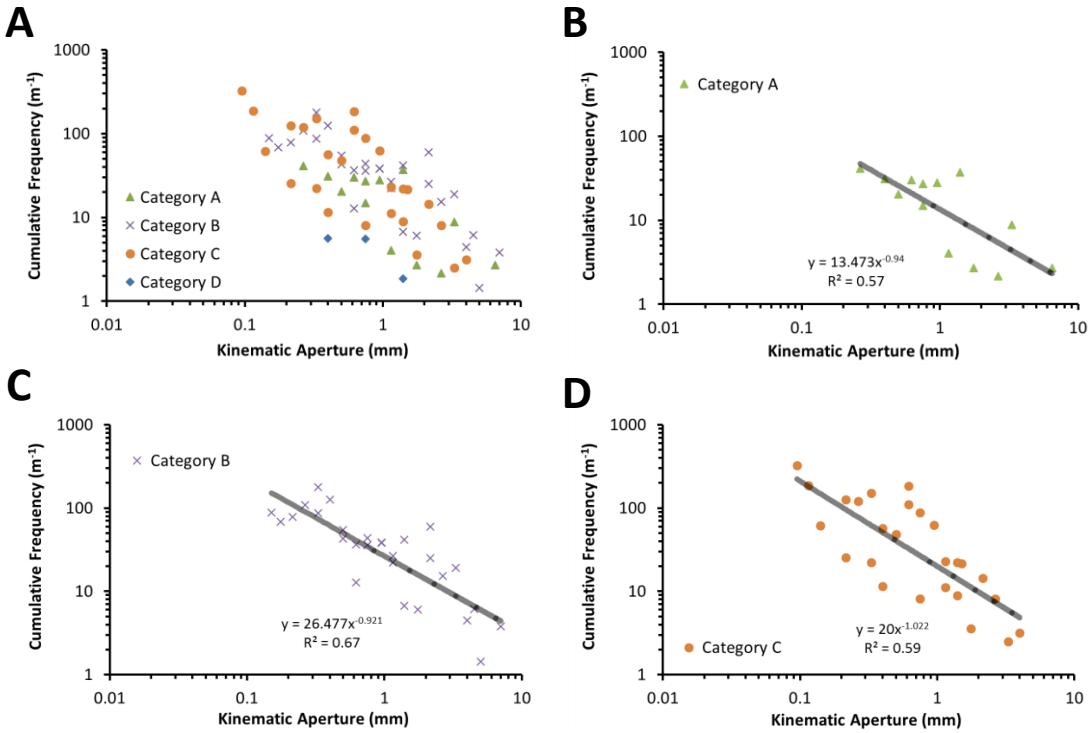

Figure 3.18. Cross-plots showing the distribution of kinematic aperture arranged by the four height categories. See text for further discussion.

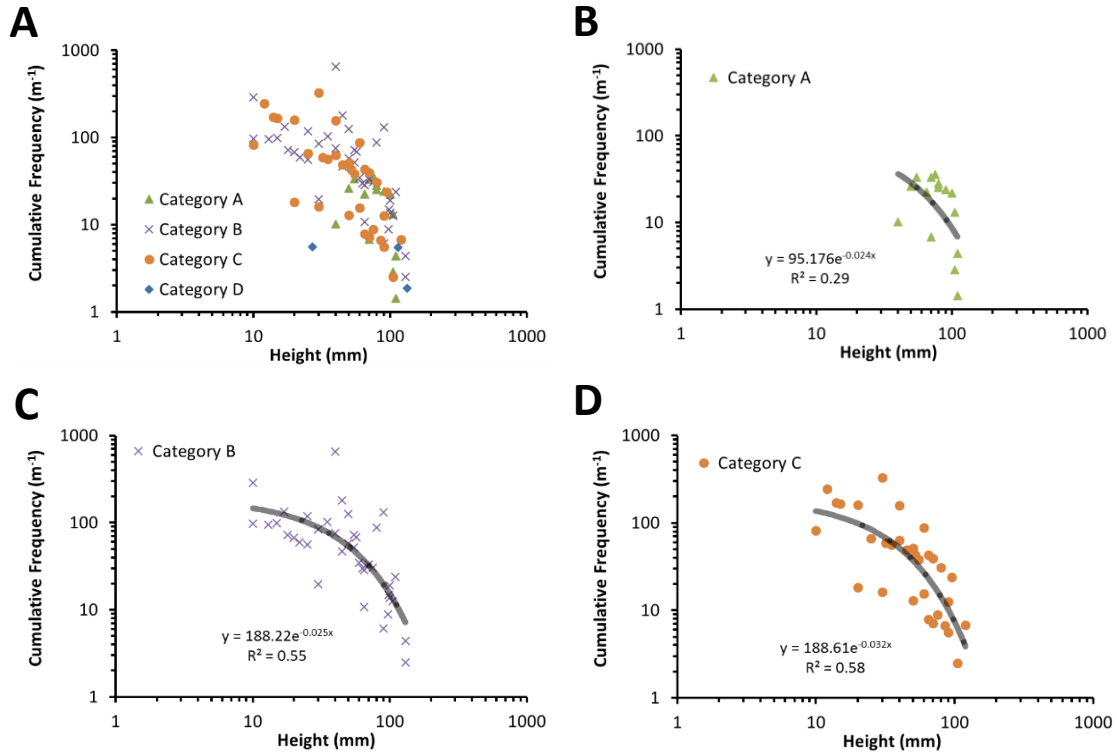

Figure 3.19. Cross-plots showing the distribution of height arranged by the four height categories. See text for further discussion.

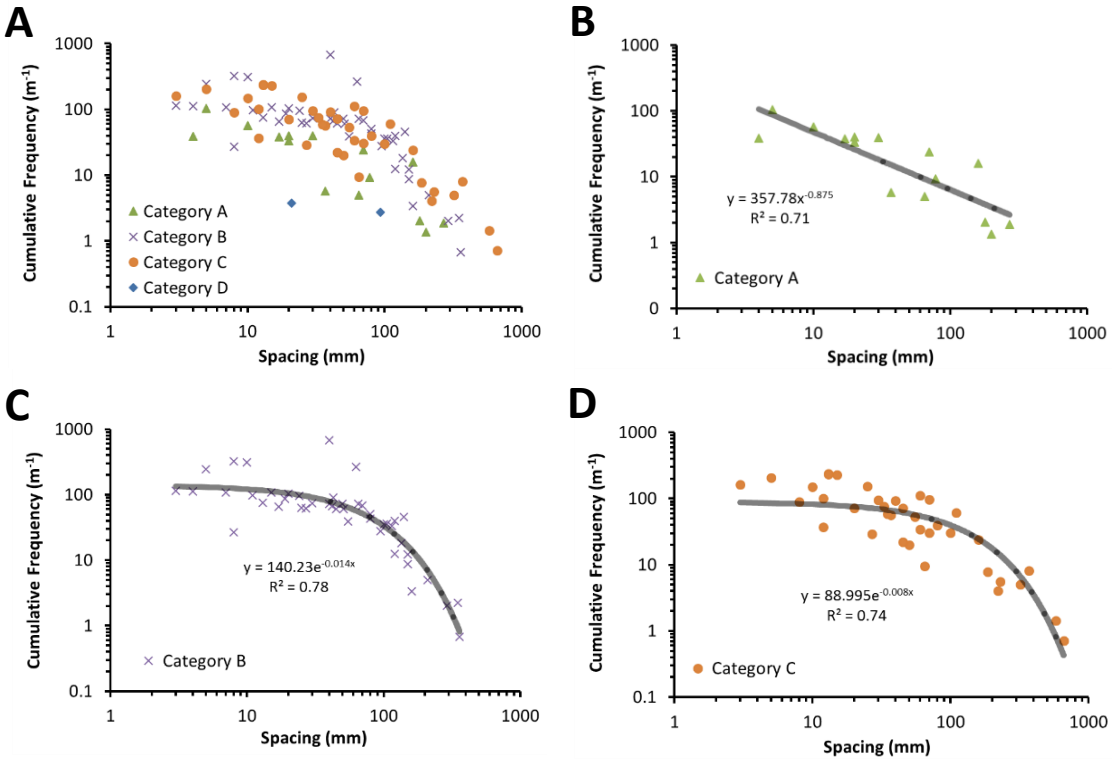

Figure 3.20. Cross-plots showing the distribution of spacing arranged by the four height categories. See text for further discussion.

2000 a, b; Gillespie et al., 2001), burial history (Hooker et al., 2013), and the interaction between fracture growth and cement precipitation (Olson et al., 2009; Laubach et al., 2010; Hooker et al., 2013).

In this study, fractures exhibit a non-clustering distribution in both lithologies. Negative exponential and power law distributions are the best-fitting trends for all data as a whole, and for groupings by lithology, fracture types (Figures 3.13 to 3.16), and height classification (Figure 3.18 to 3.20). By relating fracture abundance (cumulative frequency) with fracture attributes (kinematic aperture, height, spacing), these correlations suggest a potential of predicting fracture size and spacing distribution within the presented range of data in other parts of this outcrop. In other words, for the fractures in other parts of this outcrop with the fracture attributes (kinematic aperture, height, spacing) falling within the range of these correlations, the range of their cumulative frequency and its connection with these attributes can potentially be estimated using the statistical relationships presented. Variations of these patterns are present, likely related to a combination of lithology, fracture type, fracture height category, evolving mechanical properties, and sampling (data) bias. As for the causes of these statistical patterns, negative exponential may be related to a uniform stress field (Dershowitz and Einstein, 1988) and fracture growth processes at an early stage (Bonnet et al., 2001), the former of which is unlikely for this study as indicated by a wide range of strain homogeneity (V') values in both mudstone and chert (0.043 to 0.74). For power law scaling, an absence of characteristic scales of fracture length during fracture growth can be a factor (Bonnet et al., 2001).

3.4.2 Lithology, Fracture Type, and Fracture Height Classification

3.4.2.1 Lithology and Fracture Type

When kinematic aperture, fracture height, fracture height-bed thickness ratio, and termination style of fractures are grouped by mudstone and chert, neither lithology invariably exhibits higher

values than the other (Figure 3.8). In particular, the wide range of spacing-bed thickness ratio in mudstone and chert is different from the data presented by Narr and Suppe (1991) which documents a similar ratio for the same rock type. For spacing regularity (C_v*) and strain homogeneity (V'), an overall larger-than-1 C_v* in both mudstone and chert (average: 1.27) indicates variations in fracture spacing, but lacks clustering. In addition, C_v* spans across the line of 1 with a wide range, suggesting a mixture of clustered and regular distribution, and the caveat of using an average spacing-to-layer thickness relationship in interpreting fracture spacing distribution (e.g., Li et al., 2018). Similar V' in mudstone (0.33) and chert (0.42) suggest an overall similar extent of homogeneity in strain distribution, and may be responsible for the exponential distribution patterns as discussed above (e.g., Dershowitz and Einstein, 1988). Within the limited data of this study, a higher average V' in chert may suggest that chert has overall higher strain heterogeneity, which may imply more mechanical flaws within the rock and a lower strain level required for fracturing (Gross et al., 1995). This interpretation may explain the higher average fracture intensity in chert than in mudstone (Figure 3.11), which is similar to the scenarios as documented by Gross et al. (1995) in the Monterey Formation.

On the other hand, the impact of lithology is evident in the relative abundance of different types of fractures (Figure 3.11) as well as in fracture intensity (Figure 3.11). These observations are different from those of Narr (1991) and Gross et al. (1995), who documented fracture-free mudstone in outcrops of the Monterey Formation. Different best-fitting trends and R^2 in kinematic aperture (Figure 3.13), height (Figure 3.14), and spacing (Figure 3.16) distributions suggest the impact of lithology and fracture types in these variations. In more detail, for kinematic aperture, height, and aspect ratio, the R^2 values of certain distributions show a variation in the order of 0.01 (Table 3.3, marked in gray). In this sense, these distributions may be fitted more-or-less equally by power law or negative exponential. For other distributions where the

Data Trends and R^2 of Size and Spacing Distribution			Kinematic Aperture			Height		
			P.L.	N.E.	Diff.	P.L.	N.E.	Diff.
All Data			0.66	0.66	0.03	0.52	0.61	0.09
By Lithology		Mudstone	0.53	0.57	0.04	0.52	0.65	0.13
		Chert	0.74	0.76	0.02	0.57	0.61	0.04
By Fracture Type	Mud-stone	Ptygmatic	0.53	0.57	0.04	0.57	0.69	0.12
	Chert	Ptygmatic	0.73	0.78	0.05	0.39	0.5	0.11
		Opening-mode	0.78	0.73	0.05	0.75	0.76	0.01
By Height Category		A	0.58	0.44	0.14	0.21	0.29	0.08
		B	0.68	0.65	0.03	0.44	0.56	0.12
		C	0.59	0.58	0.01	0.53	0.58	0.05

			Aspect Ratio			Spacing		
			P.L.	N.E.	Diff.	P.L.	N.E.	Diff.
All Data			0.63	0.37	0.26	0.63	0.75	0.12
By Lithology		Mudstone	0.46	0.49	0.03	0.61	0.72	0.11
		Chert	0.76	0.46	0.3	0.61	0.78	0.17
By Fracture Type	Mud-stone	Ptygmatic	0.44	0.48	0.04	0.61	0.71	0.1
	Chert	Ptygmatic	0.69	0.64	0.05	0.63	0.79	0.16
		Opening-mode	0.74	0.47	0.27	0.55	0.67	0.12
By Height Category		A				0.71	0.69	0.02
		B				0.54	0.78	0.24
		C				0.72	0.74	0.02

Table 3.3. Table showing the R2 values of kinematic aperture, height, aspect ratio, and spacing data for all data as a whole and when grouped by lithology, fracture type, and height categories, in terms of power law and negative exponential distribution. The types of trends with the highest R2 values are highlighted in red. The distributions where difference in R2 is on the order of 0.01, which are considered as interchangeable between power law and negative exponential, are highlighted in gray. P.L.: power law. N.E.: negative exponential; Diff.: difference in R2 between power law and negative exponential.

difference in R^2 is in the order of 0.1 (Table 3.3), the certainty for the best-fitting statistical pattern is potentially higher.

In addition, different statistical patterns – including crosscutting, overlapping, and overall non-overlapping with similar or different geometries of trend lines – are present among different data populations (Table 3.4), further illustrating the impact of lithology and the formation process of fractures in fracture size and spacing distribution. Also, when arranged by lithology, the data largely show distinct separations (crosscutting, largely non-overlapping), as opposed to being arranged by fracture types (Table 3.4), probably pointing to a more dominant role of lithology over fracture type in resulting in such patterns. In particular, for kinematic aperture and aspect ratio, chert data overlie on top of mudstone data (Figure 3.13B, 3.15B). One possible reason is that for a certain value of kinematic aperture and aspect ratio, chert tends to show an overall higher cumulative frequency (i.e., higher abundance) than mudstone. In contrast, the data groups of height (Figure 3.14B) and spacing (Figure 3.16B) of mudstone and chert and height between ptygmatic and opening-mode fractures in chert (Figure 3.14D) crosscut each other. For ptygmatic and opening-mode fractures in chert, kinematic aperture (Figure 3.13D), aspect ratio (Figure 3.15D), and spacing (Figure 3.16D) overlap, indicating a potential dominance of lithology over fracture types on these distributions when these two types of fracture coexist in a particular lithology. In contrast, the best-fitting trend lines of ptygmatic fracture data is largely similar between mudstone and chert (Figure 3.13, 3.14, 3.16; C, D), suggesting that fracture type is the dominant factor over lithology in these statistical relationships. Collectively, these observations

likely point to a variable role of lithology and fracture types on the distribution of fracture size (kinematic aperture, height, aspect ratio) and spacing data.

Relationships Between Data Clusters by Lithology and by Fracture Types		By Lithology	By Fracture Type
Crosscutting		height, spacing	height
Overlapping		N/A	kinematic aperture, aspect ratio, spacing
Largely non-overlapping	**Similar geometry in trend line**	kinematic aperture	N/A
	Different geometries in trend line	aspect ratio	N/A

Table 3.4. Table showing the relationships between data clusters (crosscutting, overlapping, largely non-overlapping) when grouped by lithology and by fracture types. Variations in these three patterns among different lithologies and fracture types may indicate the impact of lithology and the formation process of fractures in the distribution of fracture attribute data.

3.4.2.2 Height Classification

Similar to the data distributions arranged by lithology and fracture types, different types of best-fitting trends are observed when data are separated by height categories. For kinematic aperture, height, and spacing (Figure 3.18, 3.19, 3.20), Category B, C, and B respectively show more closely constrained data pattern as compared to other categories (Table 3.3). Between power law and negative exponential, Category A, B, and B respectively show a difference in R^2 values of > 0.1 (Table 3.3). These variabilities in statistical pattern among different height categories indicate the effect of the fracture height-bedding relationship in the distribution of these fracture data. In particular, Category A (perfect bed-bounded), which is a common assumption in many fracture modeling workflows (Laubach et al., 2018), only accounts for 12% of the total fracture population (Figure 3.17A), suggesting the importance of considering the variable patterns between fracture height and bedding at multiple scales in modeling workflows.

Bedding structures may not constrain fracture growth, as documented by studies that bedding planes do not necessarily act as mechanical interfaces by which fractures are bounded (Gross, 1993; Gross and Engelder, 1995; Laubach et al., 2006; Burberry and Peppers, 2017). In this study, Category A, B, and C fractures, the growth of which are completely (Category A and C) and partially (Category B) related to bedding, collectively account for nearly 98% of total fractures measured in this study (Figure 3.17A), indicating the effect of lithology-controlled bedding plane on fracture growth. In addition, because the measured fractures in this study do not penetrate multiple beds and the relatively simple, end-member lithologies (lime mudstone and chert) do not show a hierarchical interbedded architecture, it is likely that bedding planes act as mechanical interfaces, with the lime mudstone and chert beds being the elements for mechanical layering.

In addition, it is commonly documented that bed thickness correlates to fracture spacing (positive correlation; Gross et al., 1995; Cooke et al., 2006) and height (positive correlation; e.g., Schultz and Fossen, 2002). In this study, a systematic relationship is not observed when comparing bed thickness with fracture spacing and height. One key reason is likely because the beds examined in this study are mostly nodular in geometry, which shows variable bed thickness for individual fractures. When cross-plotting the bed thickness measured along the height of each individual fractures against fracture spacing, which is recorded as the distance from a fracture to the fracture to its left, no distinct pattern is observed for mudstone or chert. Despite the overall similar statistics of bed thickness in these two lithologies (Table 3.1) and the effect of bedding on fracture growth (i.e., Category A, B and C account for nearly 98% of total fractures; Figure 3.17A), such a lack of pattern further indicates the variabilities in fracture spacing (Figure 3.9) and height categories (Figure 3.17B) in both lithologies and the complex relationship of bed thickness with fracture spacing and height in a nonplanar-bedded setting.

3.4.3 Process and Timing of Fracture Formation and Dynamics of Mechanical Properties

As mentioned earlier, fractures of this study show seemingly similar strike directions without systematic cross-cutting patterns. In such settings, it can be difficult to infer the timing of fracture formation based upon fracture network architecture. On the other hand, geometry and distribution of ptygmatic and opening-mode fractures may provide information on their relative timing and the rock mechanical dynamics of the fracture-hosting rock.

The geometries of the folded ptygmatic and planar opening-mode fractures suggest that they are favored as the rock behaves as a more plastic and more brittle medium, respectively (Ramsay and Huber, 1983). In chert, uncompacted silicified trace fossil (Figure 3.6C) suggests that the silicification occurs at a near-surface condition prior to compaction (e.g., shallow burial). Such an early origin of chert has been documented in other chert formations (e.g., Lawrence, 1993; Chatellier, 2015). Therefore, it is possible that chert evolves from a plastic to a brittle medium at an early stage following deposition, which favors the formation of ptygmatic fractures followed by opening-mode fractures. As burial progresses and rock strength increases with time, more opening-mode fractures may form and fill in the space between the earlier-formed fractures ("sequential infilling"; sensu Gross, 1993). During this process, an uneven stress distribution may be present at the rim of the nodular chert, as suggested by the fractures terminating against the rim in a direction generally perpendicular to the tangential line of the curved lithologic interface (Figure 3.10B). Being more prone to differential compaction, the nodular geometry of the chert, along with the increasingly higher rock strength as burial continues, could facilitate additional opening-mode fractures at a later stage. In contrast, mudstone likely retained a more plastic condition at an early stage following deposition, favoring the formation of ptygmatic fractures. Only when the rock gained sufficient strength during later burial did opening-mode fractures form in mudstone. Therefore, it is possible that there is a temporal offset in terms of the formation timing of these two types of fractures as the rock mechanical properties evolve, with potential overlaps being present. Further considering the coexistence of ptygmatic and opening-mode

fractures in mudstone and chert (Figure 3.10A), a dynamic evolution of rock mechanical properties is likely present. These dynamics in rock mechanical and fracture growth history, which have been documented as part of structural diagenesis (e.g., Shackleton et al., 2005; Laubach et al., 2009, 2010), likely contributes to the higher average fracture intensity in chert (Figure 3.11), as well as to different distribution patterns of the spacing data between mudstone and chert (Figure 3.16B). In addition, stylolites at mudstone-chert contacts (Figure 3.6A), which can indicate compaction in low-porosity zones, points to potentially different rock strength across the contact (Nelson, 2001). The extension gash and V-shaped opening-mode fracture associated with the stylolite (Figure 3.6A) indicate lateral extension in addition to uniaxial compaction (Nelson, 2001), the latter of which likely creates the folded geometry of the ptygmatic fracture (Figure 3.7A, B; 3.10A). In addition, the micro-fault at the mudstone-chert contact, where the overlying mudstone penetrates into the fractures bounding the fault block (arrow at the left margin of the fault block; Figure 3.6B), likely is syndepositional in origin. These observations and interpretations suggest a dynamic deformation history at the bedding surfaces as well. In the opening-mode fractures, the high angle of the crystals relative to the fracture walls (Figure 3.7D) indicates that a shear component parallel to fracture wall likely is present in addition to the extension perpendicular to the fracture walls (e.g., Hancock, 1985), creating a mixture of mode I (pure opening-mode) and mode III (scissoring) (Olson et al., 2009). These complex histories of fracture development and cement growth, along with a dynamic history of rock mechanical properties as discussed above, likely play a cooperative role in the distribution of fracture size and spacing data (Olson et al., 2009; Laubach et al., 2010; Hooker et al., 2013), which, in this study, may be further suggested by the variable best-fitting trends (Table 3.3) and data patterns (Table 3.4).

On the other hand, there are evidence that the rock mechanical contrast at the time of fracture formation has been retained, at least partially, into the present-day outcrop. As compared to

mudstone, higher average fracture intensity in chert (Figure 3.11) does correspond to higher rebound hardness (Table 3.2), connecting higher fracture abundance with higher rock strength. In contrast, Burberry and Peppers (2017) documented a higher fracture intensity in less competent layers (e.g., mudstone) in the same chronostratigraphic units in the same region. In their study, nodular chert is encased in a spectrum of limestone facies which show similar ranges of rock strength. More importantly, these chert units do not occur as nodules or layers as mechanical layering. In our study, the limestone facies and the associated diagenetic overprints as described in Burberry and Peppers (2017), which control mechanical stratigraphy, are not present. Instead, chert and mudstone, which show distinct contrasts in rock strength (Table 3.2), have likely served as the elements of mechanical layering since the formation of the earliest fractures. This way, different evolving paths of rock mechanical stratigraphy, and consequently, different distribution patterns of fractures, are likely responsible for the different observations in this study as compared to Burberry and Peppers (2017). Without additional data acquisition and statistical tests, applying the findings of this study to other outcrops with similar lithology distribution should proceed with caution. Potential limitations due to not only the type of lithology, but the layering characteristics, are critical factors in predicting fracture distribution using established statistical relationships, particularly for subsurface datasets (e.g., core samples) which provides a limited lateral view of bedding geometry.

3.4.4 Effect of Sampling and Data Bias on the Distribution of Fracture Size and Spacing Data

Several limitations related to the data acquisition method and the nature of outcrop could bias data and interpretations. To begin with, the 2D surface of the outcrop exposure reveals "apparent", instead of "true", kinematic aperture and fracture spacing (e.g., Gillespie et al., 1999; Zeeb et al., 2013; Watkins et al., 2015). For fractures tapering at tip(s), only the kinematic aperture intersected by the scanlines are captured. In addition, length of the scanline is limited

inherently due to the lateral termination of bedding and the spatial extent of the outcrop ("censoring" problem in Pickering et al., 1995 and Bonnet et al., 2001). In this study, because of the dominant nodular bedding geometry, the lateral extent of the measured bed can generally be covered by a 1 meter measuring tape, which partially mitigates this issue. Compared to other studies (e.g., Ortega et al., 2006; Hooker et al., 2013; Santos et al., 2015), the results of this study exhibit a more loosely constrained data population (i.e., lower R^2 values; Figure 3.13, 3.14, 3.15, 3.16). This can be related to the likelihood of measuring the same kinematic aperture, height, and spacing values in mudstone and chert. Consequently, multiple cumulative frequency values can be present for fractures with the same values of kinematic aperture, height, and spacing, widening the data range and lowering the R^2 values (Figure 3.13, 3.14, 3.15, 3.16). One possible reason is that multiple fracture attributes (kinematic aperture, height, spacing) and lithology play a cooperative role when being related to fracture abundance (cumulative frequency). In this sense, multivariate statistical analysis may help determine the relative importance of different fracture attributes in relation to fracture abundance under different data grouping schemes (e.g., by lithology, fracture type, or height category) and the statistical pattern involving multiple fracture attributes. In addition, the gaps between the data points (Figure 3.13, 3.14, 3.15, 3.16) may be related to the notion that the saturation of fracture formation has not been reached (Narr and Suppe, 1991; Bai and Pollard, 2000 a; Burberry and Peppers, 2017). Furthermore, as suggested by minor differences in R^2 (in the order of 0.01) (e.g., kinematic aperture, height, spacing; Table 3.3), the observed negative exponential trend may be part of an incomplete power law distribution (Bonnet et al., 2001), adding uncertainties in the predictability of fracture data. This may be partly attributed to the limited data quantity and the limited size range of fractures characterized. Considering the fracture attributes and distribution pattern at an outcrop scale may not be representative of the fractures at microscopic scale ("left-hand truncation" problem in Pickering et al., 1995; Gross and Engelder, 1995; Ortega et al., 2006; Bonnet et al., 2001; Hooker et al., 2013; Zeeb et al., 2013), the potential of predicting fracture distribution from the correlations

presented (Figure 3.13 to 3.16, 3.18 to 3.20) is currently limited to the fractures in this outcrop within the statistical range presented in this paper. To further test the predictability for fractures beyond the scale of the fractures presented in this study, additional data acquisition for the fractures that are at the microscopic scale and in a similar size range in other parts of the outcrop can be helpful, the former of which can reveal the fractures being present within the outcrop exposure. For fractures at a larger scale (e.g., faults), they would require different approaches and are beyond the scope of this study. Integrating multiple fracture attributes with fracture abundance (i.e., multivariate analysis) may also help determine the best-fitting statistical relationships to further test the predictability of fracture data. Lastly, the definition of fracture set may also play a role. Because the measured fractures in this study are grouped by the hosting lithology, the data that may belong to different "true" fracture sets are merged (Figure 3.13 to 3.16), creating potential uncertainties in the statistical pattern.

3.4.5 Comparison between Outcrop and Subsurface

A primary motivation of this study was to evaluate an outcrop analog for the fractured "Mississippian Limestone" play in north-central Oklahoma, which is dominated by siltstone and silty limestone with scattered chert layers (Wang et al., 2019, in press). In comparison, ptygmatic and opening-mode fractures ("vertical extension fractures" in Wang et al., 2019, in press) are common for both the outcrop of this study and this part of the play. In addition, mudstone and chert in the outcrop show similar average rebound hardness values with (calcareous) siltstone – silty limestone and chert layers in core (Figure 3.21). In cores, the chert layers can be more fractured than surrounding layers (Wang et al., 2019, in press), similar to the findings of this study where chert shows a higher average fracture intensity than mudstone (Figure 3.11). However, the silty limestone, which is a primary facies volumetrically and has the highest average fracture intensity in core (Wang et al., 2019, in press), is not present in this outcrop

(Figure 3.21). Because of the variability in dominant lithologies, the outcrop of this study is not deemed a suitable direct fracture analog for this part of the play.

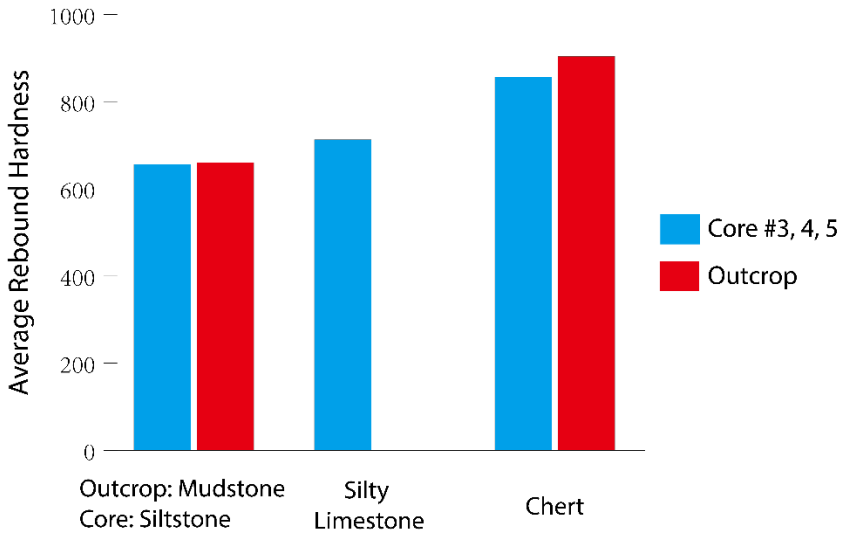

Figure 3.21. Histogram comparing the lithology and average rebound hardness of this outcrop with the cores in Wang et al. (2019, in press). Despite the similar average rebound hardness values, different dominant lithologies indicate that this outcrop is not a suitable direct fracture analog for the "Mississippian Limestone" play in north-central Oklahoma.

On the other hand, results of this study may have application to the Mississippian-aged "Chat" reservoirs at northernmost Oklahoma-southernmost Kansas (Figure 3.2A). In this part of the play, fractured cherty zones are widespread and can exhibit higher abundance of fractures than surrounding layers (unpublished data; Franseen, 2006). Assuming that a similar geometry of fracture-prone cherty zones is present in these reservoirs, the outcrop of this study may provide first-order insights to lateral fracture distribution and varying fracture intensity, both of which can be critical for production design (e.g., horizontal drilling, hydraulic fracturing). However, surface weathering and different exhumation histories can create new fractures and widen the existing fractures in outcrop (Gale et al., 2014), and consequently, result in potentially different data ranges and statistical patterns, as well as different fluid flow properties and rock strength (Bonnet et al., 2001). Therefore, extrapolating outcrop fracture patterns into the subsurface to guide reservoir characterization and production should be treated with caution. Different types of lithology (and lithofacies) and diagenetic overprints of these Mississippian-aged rocks across the

outcrop and different parts of the play, which can be linked to variable depositional and diagenetic environments and structural histories, are likely additional contributing factors.

3.5 Conclusions

In the Mississippian Reeds Spring Formation, an outcrop of strata equivalent to part of the "Mississippian Limestone" play, planar and nodular beds of lime mudstone and chert contain near-vertical, calcite- and quartz-cemented fractures. Two primary types of fractures include ptygmatic and opening-mode fractures. Ptygmatic fractures are the most common type in both mudstone and chert, whereas opening-mode fractures are present mostly in chert. When grouped by the relationship to bedding, the perfect bed-bounded, top- or base-bounded, and confined fractures account for 98.2 % of the total fracture population, suggesting the role of bedding structures in affecting fracture growth. The perfect bed-bounded fractures (Category A), which are commonly assumed in modeling workflows, exhibit a relatively well-constrained correlation between spacing and cumulative frequency.

Lithology plays a role in fracture intensity, as suggested by a higher average value for fracture intensity in chert than mudstone. Examining individual fracture attributes (kinematic aperture, height, termination style) reveals variability of fracture spacing (spacing regularity), and the distribution of strain (strain homogeneity), but no distinct separation between lime mudstone and chert. A similar pattern is observed in correlating among kinematic aperture, height, spacing, and bed thickness by lithology and by fracture types. However, trends of negative exponential and power law are present in fracture size and spacing distributions, suggesting a potential of predicting fracture size and spacing distribution in this outcrop within the presented data range under these situations. The type of best-fitting trend and R^2 values are different between mudstone and chert, between ptygmatic and opening-mode fractures, and among different fracture height categories, all of which are likely a product of lithology, fracture types, and different fracture height categories. In addition, the ptygmatic and opening-mode fractures, the

relative abundance of which can be related to lithology, likely form during different time frames as rock mechanical properties evolve. Further considering the presence of stylolites with associated extension gash and syndepositional micro-faults at bedding surfaces, and the high angle of the crystal orientation relative to fracture wall, these observations collectively point to a dynamic rock mechanical history, which potentially contributes to the different distribution patterns of fracture size and spacing data. On the other hand, higher average fracture intensity in chert does correspond to higher rebound hardness than mudstone, pointing to a linkage between lithology, rock mechanical properties, and fracture distribution.

Compared with the "Mississippian Limestone" play in north-central Oklahoma, the difference in the dominant lithologies indicates that this outcrop is not a suitable direct fracture analog for this part of the play. However, this outcrop may provide insight for the fracture distribution for the play area in northernmost Oklahoma-southernmost Kansas where fractured cherty facies are widespread. Because of the potential differences in the ranges and the resultant statistical patterns of fracture size and spacing data, as well as dominant lithologies and structural and diagenetic histories, the extrapolation of outcrop fracture data for guiding subsurface fracture prediction and modeling should proceed with caution.

3.6 References

Bai, T., and Pollard, D.D., 2000 a, Closely spaced fractures in layered rocks: initiation mechanism and propagation kinematics: Journal of Structural Geology, v. 22, p. 1409-1425.

Bai, T., and Pollard, D.D., 2000 b, Fracture spacing in layered rocks: a new explanation based on the stress transition: Journal of Structural Geology, v. 22, p. 43-57.

Bonnet, E., Bour, O., Odling, N.E., Davy, P., Main, I., Cowie, P., and Berkowitz, B., 2001, Scaling of fracture systems in geological media: Review of Geophysics, v. 39, p. 347-383.

Burberry, C.M., and Peppers, M.H., 2017, Fracture characterization in tight carbonates: An example from the Ozark Plateau, Arkansas: AAPG Bulletin, v. 101, p. 1675-1696.

Chatellier, J., 2015, Chert, a diagenetic and sedimentological indicator often misunderstood or forgotten, Mississippian from Alberta and world analogues: AAPG Search and Discovery Article #41597.

Chesapeake Energy Investor Presentation 1Q'15, online, May 6 2015.

Cooke, M.L., Simo, J.A., Underwood, C.A., and Rijken, P., 2006, Mechanical stratigraphic controls on fracture patterns within carbonates and implications for groundwater flow: Sedimentary Geology, v. 184, p. 225–239.

Dershowitz, W.S., and Einstein, H.H., 1988, Characterizing rock joint geometry with joint system models: Rock Mechanics and Rock Engineering, v. 21, p. 21-51.

Franseen, E.K., 2006, Mississippian (Osagean) shallow-water, mid-latitude siliceous sponge spicule and heterozoan carbonate facies: An example from Kansas with implications for regional controls and distribution of potential reservoir facies: Current Research in Earth Sciences, Bulletin 252, part I, 23 p.

Gale, J.F.W., Reed, R.M., and Holder, J., 2007, Natural fractures in the Barnett Shale and their importance for hydraulic fracture treatments: AAPG bulletin, v. 91, p. 603-622.

Gale, J.F.W., Laubach, S.E., Olson, J.E., Eichhubl, P., and Fall, A., 2014, Natural Fractures in shale: A review and new observations: AAPG Bulletin, v. 98, p. 2165-2216.

Gillespie, P.A., Johnston, J.D., Loriga, M.A., McCaffrey, K.J.W., Walsh, J.J., and Watterson, J., 1999, Influence of layering on vein systematics in line samples: Geological Society, London, Special Publications, v. 155, p. 35-56.

Gillespie, P.A., Walsh, J.J., and Watterson, J., Bonson, C.G., and Manzocchi, T., 2001, Scaling relationships of joint and vein arrays from The Burren, Co. Clare, Ireland: Journal of Structural Geology, v. 23, p. 183-201.

Gillespie, P., 2003, Comment on "The geometric and statistical evolution of normal fault systems: an experimental study of the effects of mechanical layer thickness on scaling laws" by Ackermann, R.V., Schlische, R.W., Withjack, M.O.: Journal of Structural Geology v. 25, p. 819-822.

Gross, M.R., 1993, The origin and spacing of cross joints: examples from the Monterey Formation, Santa Barbara Coastline, California: Journal of Structural Geology, v. 15, p. 737-751.

Gross, M. R., and Engelder, T., 1995, Strain accommodated by brittle failure in adjacent units of the Monterey Formation, USA: scale effects and evidence for uniform displacement boundary conditions: Journal of Structural Geology, v. 17, p. 1303-1318.

Gross, M. R., Fischer, M. P., Engelder, T., and Greenfield, R. J., 1995, Factors controlling joint spacing in interbedded sedimentary rocks: integrating numerical models with field observations from the Monterey Formation, USA: Geological Society, London, Special Publications, v. 92, p.215-233.

Hancock, P.L., 1985, Brittle microtectonics: principles and practice: Journal of Structural Geology, v. 7, p. 437-457.

Hernández-Bilbao, E., 2016, High-resolution chemostratigraphy, sequence stratigraphic correlation, porosity and fracture characterization of the Vaca Muerta Formation, Neuquén Basin, Argentina: Colorado School of Mines PhD dissertation, 195 p.

Hooker, J. N., Laubach, S.E., and Marrett, R., 2013, Fracture-aperture size—Frequency, spatial distribution, and growth processes in strata-bounded and non-strata-bounded fractures, Cambrian Mesón Group, NW Argentina: Journal of Structural Geology, v. 54, p. 54-71.

Jaeckel, L., 2016, High resolution sequence stratigraphy and reservoir characterization of Mid-Continent Mississippian carbonates in north-central Oklahoma and south-central Kansas: unpublished Master Thesis, Oklahoma State University.

Kulander, B. R., Dean, S. L., and Ward, B. J., 1990, Fractured core analysis: Interpretation, logging, and use of natural and induced fractures in core: AAPG Methods in Exploration, No. 8, 88 p.

Laubach, S.E., Olson, J.E., and Gross, M.R., 2009, Mechanical and fracture stratigraphy: AAPG Bulletin, v. 87, p. 561-579.

Laubach, S.E., Eichhubl, P., Hilgers, C., and Lander, R.H., 2010, Structural Diagenesis: Journal of Structural Geology, v. 32, p. 1866-1872.

Laubach, S.E., Lamarche, J., Gauthier, B.D.M., Dunne, W.M., and Sanderson, D.J., 2018, Spatial arrangement of faults and opening-mode fractures: Journal of Structural Geology, v. 108, p. 2-15.

Lawrence, M.J.F., 1993, Sedimentology and petrography of early diagenetic chert and dolomite in the Late Cretaceous - early Tertiary Amuri Limestone Group, eastern Marlborough, New Zealand: New Zealand Journal of Geology and Geophysics, v. 36, p. 9-25.

Li, J.Z., Laubach, S.E., Gale, J.F.W., and Marrett, R.A., 2018, Quantifying opening-mode fracture spatial organization in horizontal wellbore image logs, core and outcrop: Application to Upper Cretaceous Frontier Formation tight gas sandstones, USA: Journal of Structural Geology, v. 108, p. 137-156.

Lorenz, J. C., and Hill, R. E., 1992, Measurement and analysis of fractures in core, in J.W. Schmoker, E.B. Coalson, and C.A. Brown, eds, Geological Studies Relevant to Horizontal Drilling: Examples from Western North America: Rocky Mountain Association of Geologists, p. 47-60.

Marrett, R., Ortega, O.J., and Kelsey, C.M., 1999, Extent of power-law scaling for natural fractures in rock: Geology, v. 27, p. 177-802.

Matson, S.E., 2013, Mississippi Lime Play: from outcrop to subsurface - the evolution of a play: AAPG Search and Discovery Article #110170.

Mauldon, M., Dunneb, W.M., and Rohrbaugh, M.B., Jr., 2001, Circular scanlines and circular windows: new tools for characterizing the geometry of fracture traces: Journal of Structural Geology, v. 23, p. 247-258.

Mazzullo, S.J., Wilhite, B.W., and Boardman, D.R., 2011, Lithostratigraphic architecture of the Mississippian Reeds Spring Formation (Middle Osagean) in southwest Missouri, northwest Arkansas, and northeast Oklahoma: Outcrop analog of subsurface petroleum reservoirs: Shale Shaker, March/April 2011, p. 254-269.

McGinnis, R.N., Ferrill, D.A., Morris, A.P., Smart, K.J., and Lehrmann, 2017, D., Mechanical stratigraphic controls on natural fracture spacing and penetration: Journal of Structural Geology, v. 95, p. 160-170.

Mohammadi, S., Gregg, J.M., Shelton, K.L., Appold, M.S., and Puckette, J.O., 2019 (in press), Influence of late diagenetic fluids on Mississippian carbonate rocks on the Cherokee – Ozark Platform, NE Oklahoma, NW Arkansas, SW Missouri, and SE Kansas, in G.M. Grammer, J. M. Gregg, J.O. Puckette, P. Jaiswal, M. Pranter, S.J. Mazzullo, and R.H. Goldstein, eds.,

Mississippian Reservoirs of the Mid-Continent, U.S.A.: American Association of Petroleum Geologist (AAPG) Memoir, 10.1306/13632154M1163791.

Montgomery, S.L., Mullarkey, J.C., Longman, M.W., Colleary, W. M., and Rogers, J.P., 1998, Mississippian “chat” reservoirs, south Kansas: Low-resistivity pay in a complex chert reservoir: AAPG Bulletin, v. 82, p. 187–205.

Narr, W., and Suppe, 1991, J., Joint spacing in sedimentary rocks: Journal of Structural Geology, v. 13, p. 1037-1048.

Nelson, R.A., 2001, Geological analysis of naturally fractured reservoirs, 2nd edition: Gulf Professional Publishing, 332 p.

Odling, N.E., Gillespie, P., Bourgine, B., Castaing, C., Chiles, J.P., Christensen, N.P., Fillion, E., Genter, A., Olsen, C., Thrane, L., Trice, R., Aarseth, E., Walsh, J.J., and Watterson, J., 1999, Variations in fracture system geometry and their implications for fluid flow in fractures hydrocarbon reservoirs: Petroleum Geoscience, v. 5, p. 373-384.

Olson, J.E., Laubach, S.E., and Lander, R.H., 2009, Natural Fracture characterization in tight gas sandstones: Integrating mechanics and diagenesis: AAPG Bulletin, v. 93, p. 1535-1549.

Ortega, O.J., Marrett, R., and Laubach, S.E., 2006, A scale-independent approach to fracture intensity and average spacing measurement: AAPG Bulletin, v. 90, p. 193-208.

Pickering, G., Bull, J.M., and Sanderson, D.J., 1995, Sampling power-law distributions: Tectonophysics, v. 248, p. 1-20.

Pollard, D.D., and Aydin, A., 1988, Progress in understanding jointing over the past century: Geological Society of America Bulletin, v. 100, p. 1181-1204.

Procter, A., and Sanderson, D.J., 2018, Spatial and layer-controlled variability in fracture networks: Journal of Structural Geology, v. 108, p. 52-65.

Putz-Perrier, M.W., and Sanderson, D.J., 2008, Spatial distribution of brittle strain in layered sequences: Journal of Structural Geology, v. 30, p. 50-54.

Ramsay, J. G., and Huber, M.I., 1983, The techniques of modern structural geology Vol. 1: Strain analysis: Academic Press, 307 p.

Sanderson, D.J., and Nixon, C.W., 2015, The use of topology in fracture network characterization: Journal of Structural Geology, v. 72, p. 55-66.

Santos, R.F., Miranda, T.S., Barbosa, J.A., Gomes, I.F., Matos, G.C., Gale, J.F.W., Neumann, V.H., and Guimar ães, L.J., 2015, Characterization of natural fracture systems: Analysis of uncertainty effects in linear scanline results: AAPG Bulletin, v. 99, p.2203-2219.

Schultz, R.A., and Fossen, H., 2002, Displacement–length scaling in three dimensions: The importance of aspect ratio and application to deformation bands: Journal of Structural Geology, v. 24, p. 1389–1411.

Shackleton, J.R., Cooke, M.L., and Sussman, A.J., 2005, Evidence for temporally changing mechanical stratigraphy and effects on joint-network architecture: Geology, v. 33, p. 101-104.

Sonnenberg, S.A., LeFever, J.A., and Hill, R.J., 2011, Fracturing in the Bakken petroleum system, Williston Basin, in J.W. Roberson, J.A. LeFever, and S.B. Gaswirth, eds, The Bakken-Three Forks Petroleum System in the Williston Basin: Rocky Mountain Association of Geologist, p. 393-417.

Supak S., Bohnenstiehl, D.R., and Buck, W.R., 2006, Flexing is not stretching: An analogue study of flexure-induced fault populations: Earth and Plnatery Science Letters, v. 246, p. 125-137.

Thompson, T., 2016, Fracture characterization and prediction in the “Mississippian Limestone” in north-central Oklahoma: Oklahoma State University Master thesis, 139 p.

Ukar, E., Lopez, R. G., Laubach, S. E., Gale, J.F.W., Manceda, R., and Marrett, R., 2017: Microfractures in bed-parallel veins (beef) as predictors of vertical macrofractures in shale: Vaca Muerta Formation, Agrio Fold-and-Thrust Belt, Argentina: Journal of South American Earth Sciences, v. 79, p. 152-169.

Wang, Y., Thompson, T., and Grammer, G.M., 2019 (in press), Fracture characterization and prediction in unconventional reservoirs of the “Mississippian limestone”, north-central Oklahoma, USA, in G.M. Grammer, J. M. Gregg, J.O. Puckette, P. Jaiswal, M. Pranter, S.J. Mazzullo, and R.H. Goldstein, eds., Mississippian Reservoirs of the Mid-Continent, U.S.A.: American Association of Petroleum Geologist (AAPG) Memoir, DOI:10.1306/13632151M1163789.

Watkins, H., Bond, C.E., Healy, D., Butler, R.W.H., 2015, Appraisal of fracture sampling methods and a new workflow to characterise heterogeneous fracture networks at outcrop: Journal of Structural Geology, v. 72, p. 67-82.

Zeeb, C., Gomez-Rivas, E., Bons, P. D., and Blum, P., 2013, Evaluation of sampling methods for fracture network characterization using outcrops: AAPG Bulletin, v. 97, p. 1545-1566.

CHAPTER IV

TESTING THE VALUE OF REBOUND HARDNESS IN ESTIMATING PETROPHYSICAL AND ROCK MECHANICAL PROPERTIES FROM CORE AND WIRELINE LOGS: EXAMPLES FROM THE "MISSISSIPPIAN LIMESTONE"/STACK PLAY (U.S. MIDCONTINENT) AND THE VACA MUERTA FORMATION (ARGENTINA)

4.0 Abstract

Rebound hardness (RHN) has become a widely applied rock mechanical parameter in the petroleum industry, in large part due to the low-cost of the equipment and the easy-to-perform testing procedures. However, the RHN data is often under-utilized due to a lack of detailed integration with rock properties. Targeting the unconventional "Mississippian Limestone"/STACK play in north-central Oklahoma, USA, and outcrops of the Vaca Muerta Formation (Late Jurassic to Early Cretaceous) in Argentina, this study aims to test the value of RHN in reservoir characterization and production design by evaluating the statistical relationship between RHN and petrophysical and rock mechanical properties from core and wireline logs.

RHN can be a valuable parameter in assisting petrophysical rock typing and sample selection for detailed laboratory analyses of petrophysical and rock mechanical properties, both of which are critical for core-based reservoir characterization and production design projects. RHN data collected from the "Mississippian Limestone"/STACK cores show correlative trends with mineralogy and porosity, indicating RHN may help estimate these parameters in a faster, cheaper,

and sample-conservative way relative to conventional laboratory analyses. All the correlations show clusters by facies groups, with mineralogy and porosity showing variable significance levels in affecting RHN in different facies grouping schemes. This implies the effect of rock fabric in the statistical pattern and the value of RHN for rock typing, and therefore, the importance of a core-based facies description in this workflow, which directs a facies-based sampling and testing protocol that is critical to capture facies variability across a variety of scales. Correlative trends are also observed when correlating RHN collected from the Vaca Muerta plug samples with the associated data (mineralogy, porosity, sonic velocity, elastic parameters), illustrating the utility of RHN in characterizing similar types of mixed carbonate-siliciclastic reservoirs. Despite the correlative trends in the aforementioned 2D correlations, the correlation coefficient is highly variable, ranging from around 0.3 to approaching 0.9. This points to the presence of significant scatter in the data, leading to overlapping data ranges among different facies, which in turn, contributes to the lack of pattern between RHN and the sequence stratigraphic framework. As further indicated by the lack of distinct trends between RHN and the wireline log data, RHN exhibits variable capabilities in predicting rock properties using 2D cross-plots for these complex mixed carbonate-siliciclastic rocks. On the other hand, forward regression analysis indicates that RHN can potentially assist in the prediction of certain rock properties, indicating the potential value of RHN in modeling these properties from a multivariate perspective.

4.1 Introduction

In rock mechanical analysis, which is critical for production design (e.g., horizontal drilling, hydraulic fracturing) and the evaluation of reservoir performance following the hydraulic fracturing treatment, data with high sampling frequency is not commonly achievable due to its high cost, sample-destructive nature, and the difficult and time-consuming analytical procedures involved (e.g., Sachpazis, 1990; Verwall and Mulder, 1993; Lee et al., 2014, 2016; Zahm and

Enderlin, 2010; Brooks et al., 2016). Originally developed for metal and concrete materials in civil engineering, rebound hardness (i.e., Leeb hardness) has gained considerable interest as a rock mechanical parameter in the petroleum industry and in academia over the past decade, particularly in research involving the mixed carbonate-siliciclastic, "unconventional" reservoir rocks. This is due to the relatively low-cost of the equipment, and the time-efficient and overall non-destructive data acquisition procedures (e.g., Aoki and Matsukura, 2008).

Many studies have conducted rebound hardness (RHN) analyses targeting "unconventional" reservoir rocks. Some studies attempt to relate RHN to unconfined compressive strength (UCS; e.g., Verwall and Mulder, 1993; Katz et al., 2000; Aoki and Matsukura, 2008; Zahm and Enderlin, 2010; Lee et al., 2016) and Young's modulus (Sachpazis, 1990). All of these studies derive a conversion with relatively high coefficient of determination (>0.7 R^2), indicating the potential role of rebound hardness in estimating unconfined compressive strength. However, by deriving one conversion for data acquired from samples with a variety of lithology and facies types, these studies do not address the potential role of rock fabric in affecting the statistical patterns in detail. One caveat for merging the data is that different mineralogy, cementation patterns (extent, composition), pore architecture (e.g., pore type, pore sizes and relationships to grains and matrix), all of which can be related to specific lithology and facies, can create variabilities in the relative role of different rock properties in affecting rock strength, resulting in different statistical patterns when relating rock strength index (e.g., RHN) to other rock mechanical properties (e.g., UCS). This scenario is applicable for common "end-member" rock types, such as sandstone, limestone, and granite, as compared to the commonly mixed carbonate-siliciclastic, "unconventional" reservoir rocks, and also for the "unconventional" reservoir rocks with similar composition and "appearance" at wireline log, core, and petrographic scales. Some studies have attempted to compare RHN with petrophysical properties from wireline logs, core, and CT-scanning, with the goal of documenting a generalized relationship between RHN and mineralogy (clay and

calcareous components) and porosity for various types of carbonate rocks (e.g., Yaşar and Erdoğan, 2004; Aoki and Matsukura, 2008; Zahm and Enderlin, 2010; Daniels et al., 2012; Baumgardner et al., 2014; Ritz et al., 2014; Brooks et al., 2016). Other studies have targeted the relationship of organic content and porosity with rock strength (Sone and Zoback, 2013b), sonic velocity (Eberli et al., 2003; Baechle et al., 2005, 2008; Fournier et al., 2011; Sone and Zoback, 2013a; Altowairqi et al., 2015; Abatan et al., 2016), and elastic parameters (Fournier et al., 2011; Sone and Zoback, 2013a, b).

However, few published studies focus on a comprehensive, detailed integration among RHN, mineralogy, petrophysics (porosity, sonic velocity), and rock mechanical properties from core and wireline log data, and relating the observed statistical patterns to facies (i.e., rock fabric, cementation pattern) and sequence stratigraphic framework accompanied with detailed statistical analysis to interpret the controlling factors of RHN, and to test if RHN can predict reservoir properties, all of which are critical topics to tackle for applying RHN to reservoir characterization. Some studies (e.g., Katz et al., 2000; Yaşar and Erdoğan, 2004) tend to draw their conclusions from sparse data ($n<10$), although the correlation is strong (>0.8 R^2). These issues result in a significant under-utilization of the RHN data in terms of reservoir characterization and production aspects, such as modeling reservoir properties and locating target zones from both a reservoir quality and rock mechanical perspective. In particular, if well-defined statistical relationships are present between RHN and petrophysical (e.g., porosity, sonic velocity) and rock mechanical properties (e.g., elastic parameters), RHN can not only be a convenient and valuable tool in mapping reservoir distribution and guiding production design, but provide a more time- and cost-efficient and a sample-conservative means of estimating these properties at a significantly higher data density as compared to the current capabilities and economics of conventional laboratory analysis.

Focusing on the “Mississippian Limestone”/STACK play in north-central Oklahoma with supplemental data from the outcrop Vaca Muerta Formation in Argentina (Late Jurassic to Early Cretaceous), this study aims to test if RHN can assist in reservoir characterization and production design by evaluating the statistical relationship of RHN with mineralogy, porosity, sonic velocity, and elastic parameters. By tying the statistical patterns with facies and sequence stratigraphic framework described from cores from the “Mississippian Limestone” play (abbreviated as MISS cores) from the STACK play (abbreviated as STACK cores), this study analyzes the effect of facies variability in these correlations. Considering that petrophysical properties, such as sonic velocity, are commonly affected by a combination of rock properties (as previously mentioned), such a multivariate control also likely applies to RHN. To test this hypothesis, this study aims to evaluate how RHN is affected by different rock properties, and if RHN can help predict these properties from a multivariate perspective. Lastly, because the plug samples from the Vaca Muerta Formation exhibit variable thickness, this study tests how sample size affects RHN and its statistical pattern with rock properties, which lacks a detailed documentation in published literature.

4.2 Data and Methodology

4.2.1 Rebound Hardness Test

For the “Mississippian Limestone”/STACK cores (Figure 4.1), the dataset includes core slabs (2415 feet/736 m in total footage) and the associated XRD mineralogy (calcite, quartz, bulk clay) and total porosity (Table 4.1) from three MISS cores and three STACK cores. In addition, plug samples from outcrop cores of the Vaca Muerta Formation and the associated plug data (calcite content, porosity, sonic velocity, and calculated elastic parameters) serve as the supplemental data (Table 4.1). Wireline log data are from the MISS wells (Well #1, 2, and 3 in Figure 4.1), and include mineralogy (calcite, quartz, clay), sonic velocity, porosity, and elastic parameters. Rebound hardness (RHN) data was collected from the core slab and plug samples using an

Equotip Piccolo 2 Unit-D hardness tester (Figure 4.2a) – a portable device that provides overall non-destructive, time-efficient, and easy-to-perform tests of hardness. RHN is tested by hitting a testing tip (0.5 to 1 millimeter in diameter) onto the testing surface in a perpendicular direction (Figure 4.2b). As it rebounds back, the rebound (Vr) and impact (Vi) velocities are recorded. The ratio of these two velocities, which reflects the energy loss during the impact, is then converted into RHN by multiplying the ratio by 1000 (Figure 4.2b; dimensionless unit in HLD or HL). Such a measurement process is different from several other hardness testing methods which measure the depth of indentation (e.g., Rockwell hardness; Frank et al., 2016) or the relative rebound height (e.g., Shore hardness; Committee on Standardization of Laboratory Tests, 1978). Therefore, although having "hardness" in its name, RHN is a proxy for rock strength by providing "a measure of the resistance of a surface to impact penetration of a plunger tip" (Aydin and Basu, 2005), rather than a physically defined hardness parameter. Because of its unitless nature, RHN can be conveniently compared with other types of rock data (e.g., mineralogy, porosity, sonic velocity, rock mechanical properties).

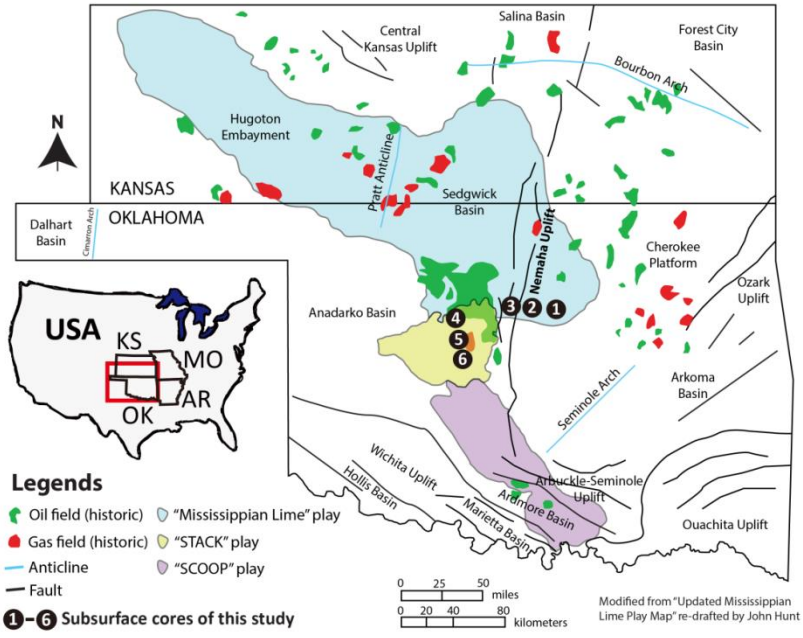

Figure 4.1. For the six MISS/STACK cores of this study, three (#1, 2, 3) are from the historic "Mississippian Limestone" play (light blue area) which spans across north-central Oklahoma and southern Kansas, and three (#4, 5, 6) are from the STACK play (yellow area).

<table>
<tr><th colspan="3">Sample and Data</th><th colspan="3">MISS/STACK (subsurface)</th><th>Vaca Muerta (outcrop)</th></tr>
<tr><td rowspan="2">Sample</td><td colspan="2">Inventory</td><td colspan="3">736 m/2415 ft of core slabs</td><td>25 core plugs</td></tr>
<tr><td colspan="2">Size</td><td colspan="3">width: 8.5 cm,
thickness: 2.3 cm</td><td>diameter: 2.5 cm/1 inch, height: 16.9 to 51.7 mm</td></tr>
<tr><td rowspan="10" colspan="2">Data Inventory</td><td rowspan="7">Core (Slab, Plugs)</td><td colspan="2">Rebound Hardness</td><td>N=3358</td><td>N=25</td></tr>
<tr><td rowspan="3">Mineralogy</td><td>Calcite/CO_3</td><td rowspan="3">N=385 *calcite; XRD</td><td>N=25 *CO_3; dissolved</td></tr>
<tr><td>Quartz</td><td>N=0</td></tr>
<tr><td>Bulk Clay</td><td>N=0</td></tr>
<tr><td colspan="2">Porosity</td><td>N=243</td><td>N=25</td></tr>
<tr><td rowspan="2">Sonic Velocity (wet)</td><td>Vp</td><td rowspan="2">N=0</td><td rowspan="2">N=25</td></tr>
<tr><td>Vs</td></tr>
<tr><td rowspan="4">Elastic Parameters (dynamic; calculated from sonic velocity)</td><td>Young’s Modulus</td><td rowspan="4">N=0</td><td rowspan="4">N=25</td></tr>
<tr><td>Poisson’s Ratio</td></tr>
<tr><td>Bulk Modulus</td></tr>
<tr><td>Shear Modulus</td></tr>
<tr><td rowspan="4">Wireline Log</td><td colspan="2">Mineralogy</td><td rowspan="4">N=3 (MISS wells)</td><td rowspan="4">N=0</td></tr>
<tr><td colspan="2">Sonic Velocity</td></tr>
<tr><td colspan="2">Porosity</td></tr>
<tr><td colspan="2">Elastic Parameters</td></tr>
</table>

Table 4.1. For the MISS/STACK and Vaca Muerta samples, the type and amount of data are different, with a much more limited data in the Vaca Muerta samples. The MISS/STACK data are mostly from all six cores, with porosity being unavailable for Core #6. Wireline log data are from the three MISS wells (well #1, 2, and 3 in Figure 1), and include mineralogy (calcite, quartz, clay), sonic velocity (Vp, Vs), porosity (neutron, density), and elastic parameters (Young’s modulus, Poisson’s ratio, bulk modulus, shear modulus). For the Vaca Muerta data, the elastic parameters are calculated from sonic velocity. CO_3: carbonate content.

The testing procedures of RHN, as discussed below, are based upon and modified from several sources, including ASTM Standard (2005), Aoki and Matsukura (2008), Aydin (2008), Zahm and Enderlin (2010), and Brooks et al. (2016). Prior to testing, it is critical to visually inspect the

sample and the testing surface to ensure the following requirements are met: the sample is largely complete in terms of surface area and total volume without significant hollow interior; sample is stabilized with the testing surface being dry and horizontal; testing location should be relatively well-polished and lacks extensive surface markings (e.g., saw marks) without cracks or fractures, holes (e.g., macroporosity), or excessive dirt being in contact with the testing tip. For each data point, the RHN value is derived from the arithmetic average of at least five measurements that are tested at separate locations. For the core slab samples, these measurements were conducted along the center line of the sample and away from the sample edge (by at least 1 to 2 centimeters) (Figure 4.2c), for the purpose of ensuring sufficient sample stability during testing and filtering out the negative effect of proximity to sample edge on the RHN results (e.g., Amaral et al., 1999; Aydin, 2008). For intervals that are massive-bedded or contain relatively thick layers (Figure 4.2c), the measurements for individual data points were conducted within a small circular-shaped area (less than 1 cm2 in size; yellow circles in Figure 4.2c), as opposed to evenly across the transect (red box in Figure 4.2c). For intervals where the layering is thinner than 1 cm, the measurements are conducted along the layering while being close to the center line of the sample as much as possible (green arrow in Figure 4.2c). For plug samples, RHN are tested within a circular-shaped area (less than 1 cm^2 in size) near the center of the circular transect of the samples. To enhance data consistency and validity, only the measurements of individual data points in which the difference between the maximum and minimum result is no larger than 50 HLD were used, wherever possible. In particular, the effect of cracks in producing anomalously low RHN values has been commonly documented (e.g., Hack et al., 1993; Amaral et al., 1999; Katz et al., 2000; Aydin and Basu, 2005). As observed in this study, RHN tested on top of a crack is lower by at least 50 to 100 HLD than the result tested at the adjacent location within the same circular testing area (Figure 4.2c). Although it is possible that the higher-than-50 HLD-difference does not necessarily correspond to invalid RHN results, but rather is resultant from the actual variability of RHN, using such an arbitrary cut-off to filter out the potentially invalid RHN data

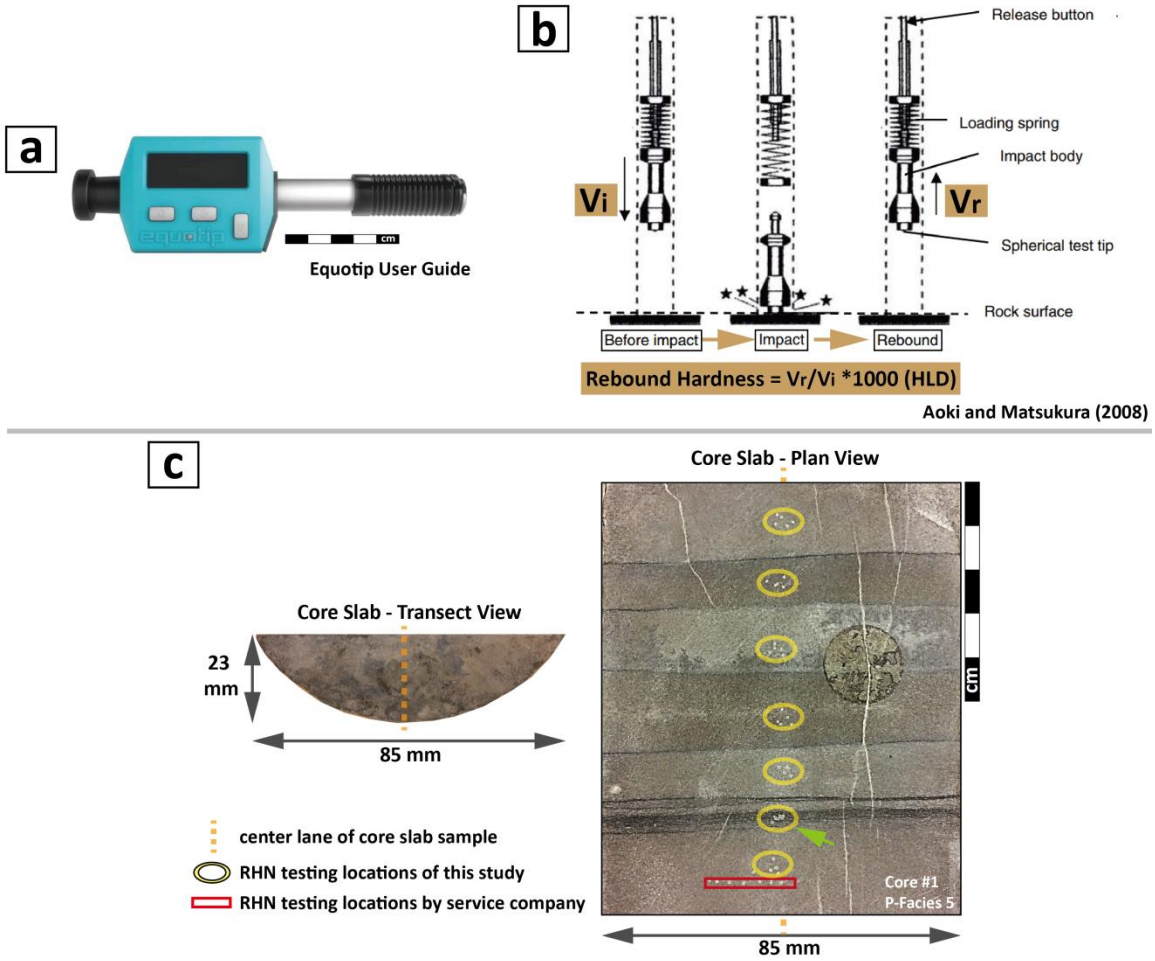

Figure 4.2. (a) The Equotip Piccolo 2 Unit-D hardness tester is a portable device for quick and easy-to-perform hardness tests; (b) rebound hardness is calculated using the rebound (Vr) and impact (Vi) velocities recorded by the device as it hits the testing surface; (c) to maximize sample mass and stability, rebound hardness was tested along center line of core slab samples (marked by dashed line). For each data point, which is averaged from at least five measurements, the testing locations of these individual measurements are overall confined within circular areas (white dots confined by the yellow circles in c) that are aligned with the center line of the sample and are less than 1 cm^2 in area. For layers that are too thin for such a circular area, the measurements are conducted along the layering while being close to the centerline as much as possible (marked by green arrow in c). In (c), the horizontal row of dents that aligns along a straight line (marked by a red box near the base of the right photo) is left from the tests conducted by service company. Such a method is not adopted in this study, because the variable thickness due to the curvy base core slab sample can potentially introduce variability in the RHN measurements. (a) is from the user guide of the testing device.

may be the most feasible and safest practice, at least for this study. For the core slab samples, RHN was tested at a sampling frequency ranging from a few centimeters to less than half a meter (1 foot), based upon the distribution of sedimentary structures (e.g., laminations, bedding,

bioturbation) and facies, along with the location of the existing core data (XRD mineralogy, porosity). For the plug samples, one RHN data point was collected for the individual samples which show one type of facies. For the plug samples that exhibit varying rock types, RHN values from the dominant facies in the plugged location in core is adopted for subsequent data analyses. In addition, because of the variable height of the plug samples (Table 4.1) and the potential effect of sample size on RHN results, it is necessary to filter out the samples that are under the "minimum height" threshold, which likely bear higher probability in producing invalid RHN results. To achieve this, the RHN results tested from plugs are compared with the RHN tested in the same core on the same facies. Using the same criterion with the MISS/STACK core slab samples, only the plugs that exhibit such a difference in RHN being lower than 50 HLD (n=25; as opposed to a total of 85 samples) are selected for subsequent analysis (more details will be addressed in Discussion).

To minimize sample vibration during the RHN test, a supportive medium is critical for stabilizing the sample. For commercial core slab samples, they are commonly supported by styrofoam in cardboard boxes (shortened as “core box” for brevity; Figure 4.3a), with an unpolished and curvy base (Figure 4.2c) that is not feasible for the coupling procedure recommended by the manufacturer for concrete and metal samples with a flat base. A common alternative solution is to use a container filled with fine sand (shortened as “sand box” for brevity; Figure 4.3b) to stabilize the sample. In this study, when comparing the results tested in core box with the ones tested in sand box, the RHN values tested at the same location on the same sample largely overlap with statistically insignificant discrepancies (Figure 4.3c), indicating that the RHN data tested on these two types of supporting mediums are interchangeable. The reason is likely that, due to storage , the supporting styrofoam has been well molded to accommodate the rugged basal surface of core slab samples and provides sufficient support for stabilizing the sample. Therefore, RHN is tested by maintaining the slab samples in the styrofoam, on the premise that the core slab samples are in

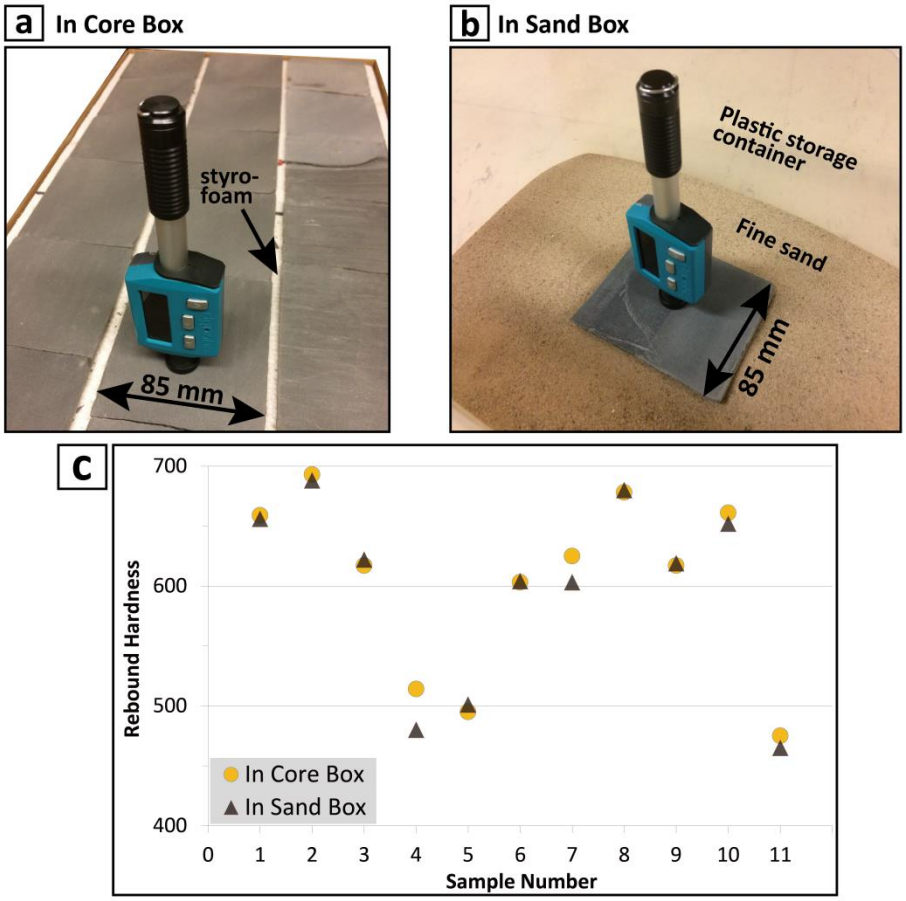

Figure 4.3. By comparing the rebound hardness results tested by keeping the core slab samples in core box (a) with the results tested by placing the samples in sand box (b), both of which are tested in the same location on the same sample, the data largely overlap with statistically insignificant difference (c). A total of eleven samples were used, including six samples from Core #5 and five samples from Core #6.

solid contact at the base. Some studies utilize an arc-shaped machined slot as a stabilizing medium for the core slab samples (Aydin, 2008). However, the significant ruggedness at the base of the core slab samples will create an uneven contact at its interface with the smooth metal surface of the slot, which can create sample vibration during testing and lower the RHN results. In contrast, by testing the samples in a well-supported styrofoam, it not only provides sufficient cushioning for the slab sample, but minimizes the potential damage to sample integrity that can occur during the transport of fractured samples, which are common for “unconventional reservoir rocks”, from the core box to another medium. It has also been documented that placing the sample in a supporting medium being softer than the specimen can lower the RHN results (Aydin

and Basu, 2005). However, because this study aims for a relative analysis of RHN, not precise calculations using absolute values, we think that testing the core slab samples with consistent thickness in the core box is a feasible method for this study. For the plug samples, they are placed in a sand box, in which at least three quarters the plug height is covered by the fine sand.

For testing locations, the manufacturer recommends that they should be along a straight line across the two edges of the sample (Frank et al., 2016). However, this is for relatively large, regular-shaped (e.g., cylindrical, rectangular) samples. For the core slab samples, because of their narrow width (8.5 cm) and curvy lateral shape (Figure 4.2c), testing along the diameter will place the testing points on parts of the sample where the sample thickness drastically decreases away from the center line of the sample (Figure 4.2c; also see Daniels et al., 2012 and Ritz et al., 2014), adding undesirable variability to the results. In addition, by testing along a straight line along the width, it is possible that all the testing locations can land on a horizontal crack, which can be difficult to identify by naked eye. By testing within a circular area along the center line of the core slab sample, it can minimize the impact of variable sample thickness on the testing results, and also help filter out the invalid results related to cracks. Regarding the number of tests for each data point, several studies (e.g., Aydin, 2008; Zahm and Enderlin, 2010; Brooks et al., 2016) recommend a method of conducting ten to twenty measurements and deleting the maximum and minimum results, followed by the averaging of the remaining data. However, such amount of measurements for individual data point will create significant damage on the testing surface within the circular area as proposed in this study (yellow circles in Figure 4.2c), which will impede repetitive testing. Perhaps more importantly, when testing on samples with satisfactory conditions as discussed above, manually deleting the maximum and minimum data points will impair the data integrity associated with the actual variability of rock properties (also in Amaral et al., 1999; Aydin and Basu, 2005; Aydin, 2008). In this study, by inspecting the testing surface, the potentially invalid data points are manually filtered out to the most extent resolvable to the

naked eye during the testing process, despite the fewer measurements of individual data points. Therefore, the testing protocol as discussed above can not only allow for the detection of potentially invalid RHN results related to unsatisfactory sample conditions, but enhance data consistency and testing efficiency and allow for iterative testing by minimizing the number of tests performed at a particular location.

4.2.2 Statistical Analysis

After the RHN data are collected, two phases of statistical analysis are conducted. The first phase is to plot RHN against mineralogy, porosity, sonic velocity, and elastic parameters from core and against wireline log data from the MISS wells in 2D cross-plots to test for their bivariate correlation. The correlation coefficient (*r*), which reflects both the type (positive or negative) and the strength of linear correlations, is utilized to quantify the correlation. Based upon detailed facies description from core, the data are also plotted by facies types to evaluate potential clustering among facies (groups), and if this exists, to define what the statistical relationships (type of best-fitting trends and *r*) are among facies types (or groups). The data of each facies type (or group) was then tied to rock fabric (composition and size of grains, matrix, and cement) to account for the effect of facies variability on the observed statistical relationship. In addition, the RHN data is further plotted by depth for individual core to compare with the sequence stratigraphic framework defined from the MISS/STACK cores, to examine if the RHN data exhibit trends among sequences. Facies descriptions of the MISS cores and the Vaca Muerta Formation are from Leblanc (2014) and Thompson (2016), and in part from Eberli et al. (2017), respectively.

The second phase of statistical analysis includes multivariate and fit modeling analysis, both of which are conducted using the JMP® software (v.13). Multivariate analysis allows for a visualization of the bivariate statistical patterns of all parameters by compiling the correlations in a scatterplot matrix. As with the first phase of the statistical analysis, the correlation coefficient (*r*)

is calculated for each correlation to evaluate the correlation strength and to guide the subsequent analysis. To examine the impact of input parameters in affecting an output parameter, fit modeling, including leverage analysis and forward regression analysis, was conducted. Leverage analysis allows for the visualization of including individual variable(s) as input in predicting an output parameter using a linear hypothesis, as well as the relative significance of these variables in such predictions (Sall, 1990). There are two types of leverage analysis: effect leverage analysis (targeting individual parameters when all input parameters are included) and whole model leverage analysis (targeting all input parameters as a whole). For the purpose of evaluating the relative significance of individual parameters in affecting RHN (output), effect leverage analysis was conducted for the MISS/STACK data (XRD mineralogy and porosity as input) and Vaca Muerta data (carbonate content, porosity, Vp as input). Specifically, the significance level of individual parameters is evaluated by *p*-value, by which a <0.01 value is considered as "substantially significant " in supporting the test hypothesis (i.e., in predicting the output parameter). To aid in the graphical visualization of *p*-value, which can be in the order of 10^{-4} to 10^{-7}, the p-values are transformed to LogWorth scale ($-\log_{10}$(p-value)): the higher the LogWorth value, the more significant the associated parameter is in supporting the testing hypothesis (JMP® User Guide), with a >2 LogWorth value indicating a substantial significance level of the corresponding input parameter. In addition, it has been proposed that the false discovery rate (FDR) *p*-value provides an enhanced evaluation by adjusting the *p*-values to control the FDR for multiple tests (Benjamini and Hochberg, 1995). In this study, the FDR *p*-value (automatically calculated by JMP®) and the corresponding FDR LogWorth values are adopted. For the statistical details, readers are referred to Benjamini and Hochberg (1995).

The second and final step for fit modeling is forward regression analysis, which uses all input parameters in different combinations by gradually increasing the number of variables (i.e., "forward") to predict an output parameter. In this sense, forward regression analysis can be

considered as an extension of the leverage analysis – being the "effect leverage analysis" when only one input parameter is included and being the "whole model leverage analysis" when at least two of the input parameters are included. Different from the bivariate and multivariate analyses which utilize correlation coefficient (r), adjusted coefficient of determination (adjusted R^2) is used in forward regression analysis to evaluate the confidence level of a given combination of input parameter(s) in predicting the output parameter. As compared to coefficient of determination (R^2), adjusted R^2 is more appropriate for forward regression analysis because it allows for the comparison of correlation strength among models with different numbers of variables, which is the scenario in forward regression analysis, by including the degree of freedom in its computation (JMP® User Guide). Therefore, comparing adjusted R^2 among different models allows for the evaluation of the optimal combination of input parameters in predicting the output parameter – the higher the adjusted R^2 value, the higher the confidence level. For the MISS/STACK data, RHN and XRD mineralogy (calcite, quartz, bulk clay) were set as the input parameter to test the prediction of porosity (i.e., output parameter). For the Vaca Muerta, two sets of forward regression analysis were conducted: RHN, carbonate content, and Vp (input) to test the prediction of porosity (output); RHN, carbonate content, and porosity (input) to predict Vp (output).

4.3 Geologic Background

Based on mineralogy, grain types, sedimentary structures, and the extent of bioturbation, a total of seven facies are identified in the "Mississippian-Limestone"/STACK cores, including five mudstone-siltstone (Figure 4.4, 4.5, 4.6) and two silty limestone facies (Figure 4.7a to h). Supported by a black- to brown-colored, clay-rich matrix, the siltstone facies include glauconitic siltstone-fine sandstone (Figure 4.4a to 4.4d), massive-bedded mudstone-siltstone (Figure 4.4e, 4.4f), laminated siltstone (Figure 4.5), burrowed siltstone (Figure 4.6a to 4.6c), and bioturbated siltstone (Figure 4.6d to 4.6f). In contrast, the silty limestone facies, which are generally lighter in

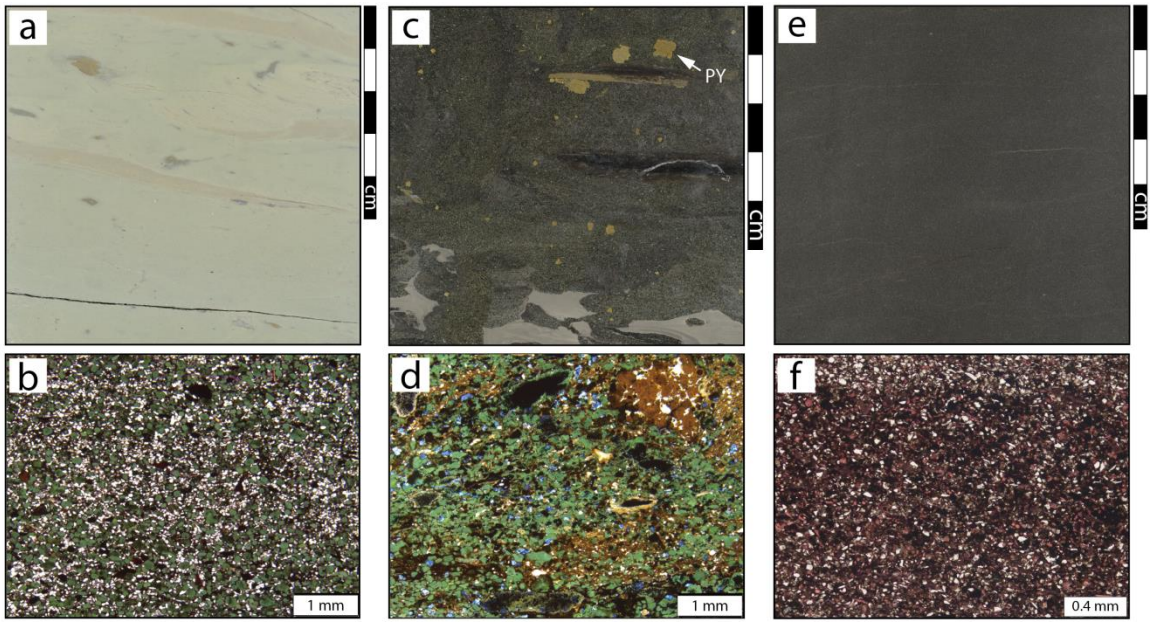

Figure 4.4. Core (a, c, e) and thin section (b, d, f) photos of P-Facies 1 identified in the MISS/STACK cores. P-Facies 1 includes two facies: glauconitic siltstone- fine sandstone (a, b, c, d) and massive-bedded mudstone-siltstone (e, f). The glauconitic facies is characterized by abundant glauconite grains and pyrite (PY in c), the former of which produce a distinctive greenish color in both core and thin sections. The massive-bedded mudstone-siltstone facies typically lacks sedimentary structures. In (b) and (f), the white grains are silt-sized quartz. In (f), the pink grains are skeletal fragments. In (d), note the much more abundant pores in (blue portions) as compared to (b). Only (e) and (f) are from the same sample in the same core.

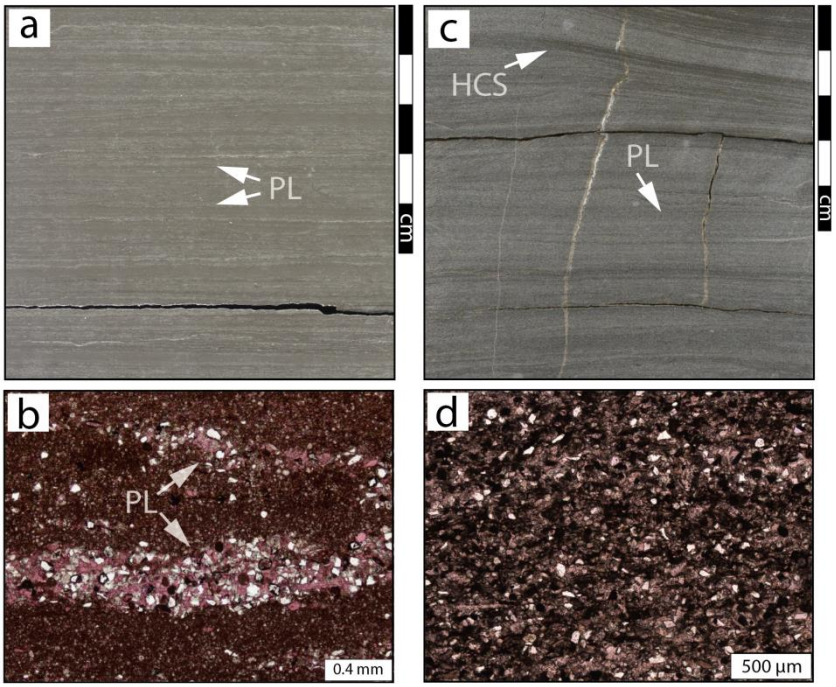

Figure 4.5. Core (a, c) and thin section (b, d) photos of P-Facies 2 identified in the MISS/STACK cores. P-Facies 2 only includes the laminated siltstone facies, which is dominated by millimeter-

thick planar lamination (PL in a, b, c) consisting of alternating, millimeter-thick calcite-rich (lighter-colored in a, c) and clay-rich (darker-colored in a, c) laminae. Typically, the calcite-rich laminae show a lower area percentage relative to the clay-rich laminae (a, b; b: 35% calcite, 18% bulk clay). However, there are scattered places where the calcite-rich laminae are more dominant over the clay-rich laminae (c, d; d: 69% calcite, 4% bulk clay). Hummocky cross-stratifications (HCS in c) are present, likely pointing to high-energy storm events (Cheel and Leckie, 1993). (a) and (b) are 0.4 m/1.3 ft apart in the same core. (c) and (d) are nearly 1 m/3 ft apart in the same core.

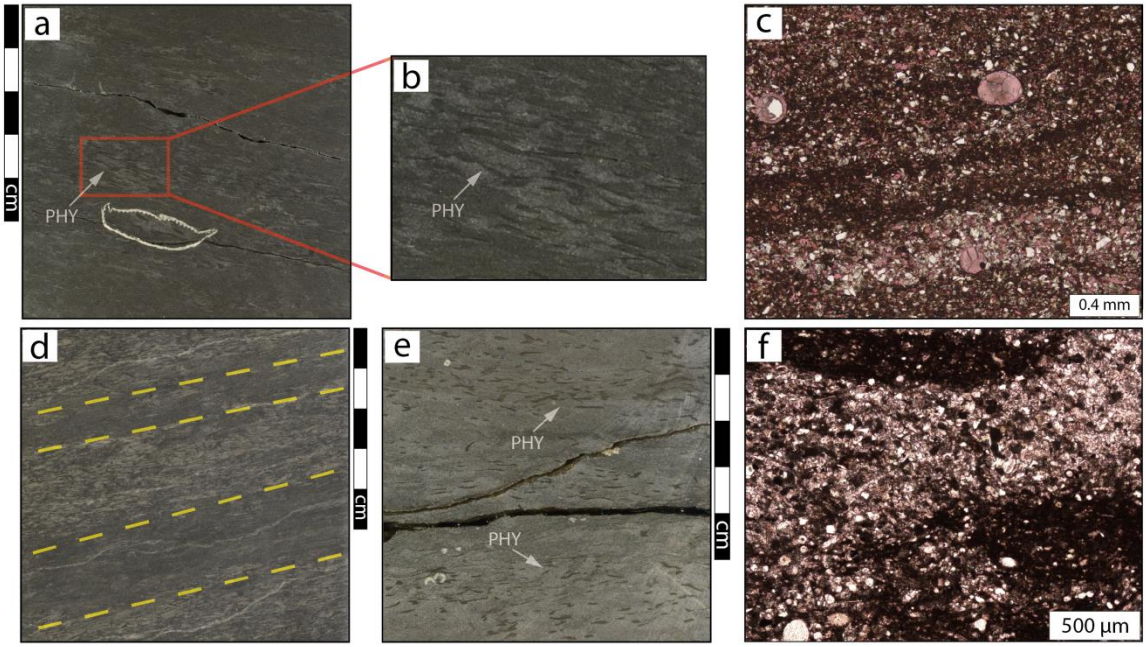

Figure 4.6. Core (a, b, d, e) and thin section (c, f) photos of P-Facies 3 and 4 identified in the MISS/STACK cores. P-Facies 3 is the burrowed siltstone (a, b, c), and P-Facies 4 is bioturbated siltstone (d, e, f). These two P-Facies typically share the same rock fabric with the same dominant trace fossil (*Phycosiphon*; PHY in a, b, e) and are differentiated by the relatively isolated burrows in P-Facies 3 and connected burrows in P-Facies 4. A clay-rich matrix typically dominates these two P-Facies (c: 26% calcite, 21% bulk clay), with a calcite-rich framework occasionally present in P-Facies 4 (f: 67% calcite, 5% bulk clay). In (d), note the variable extent of bioturbation (marked by dashed lines). (b) is zoomed in from part of (a). (a) and (c) are 0.7 m/2.5 ft apart in the same core. (e) and (f) are from the same sample.

color, are characterized by abundant skeletal and peloidal grains with calcite cement at interparticle spaces (Figure 4.7a to 4.7h), indicating higher energy during deposition (e.g., storm events) as compared to the siltstone facies. Two silty limestone facies are identified, including massive-bedded packstone-grainstone (Figure 4.7a to 4.7d) and probable hummocky cross-stratified (HCS; Figure 4.7e, 4.7f)-planar laminated packstone-grainstone (Figure 4.7g, 4.7h), and are differentiated by different dominant sedimentary structures. All of these facies, which are

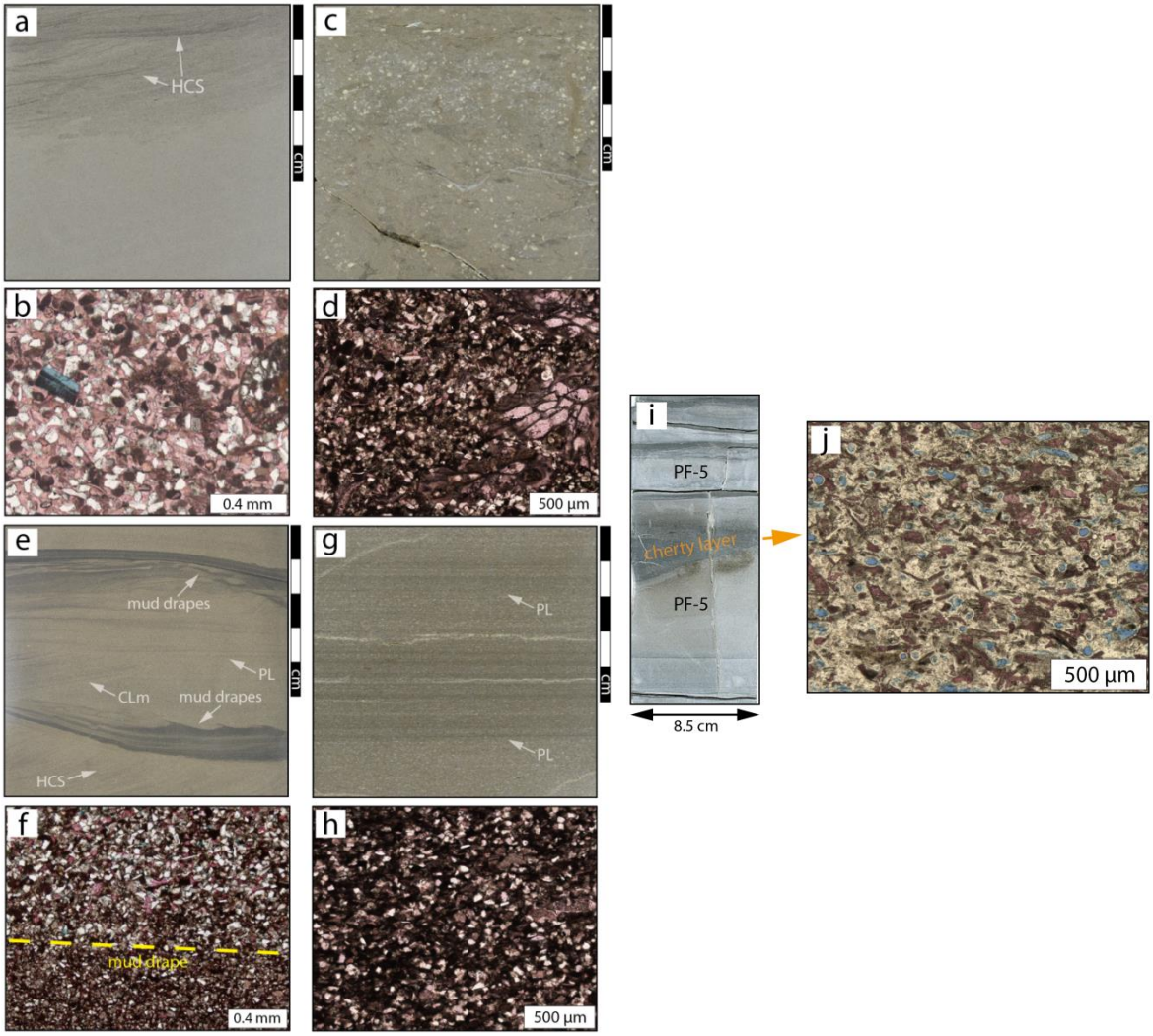

Figure 4.7. Core (a, c, e, g, i) and thin section (b, d, f, h, j) photos of P-Facies 5 (a to h) and cherty layers (i, j) identified in the MISS/STACK cores. P-Facies 5 includes two silty limestone facies: massive-bedded packstone-grainstone (a to d) and hummocky cross-stratified (HCS)-planar laminated packstone-grainstone (e to h). Both facies typically contain abundant calcite cement at interparticle space (a, b, e, f) with abundant silt-sized quartz (white grains), peloids (dark-colored grains), and skeletal fragments (mainly crinoid and brachiopod) (b: 58% calcite, 3% bulk clay; f: 50% calcite, 4% bulk clay). On the other hand, both facies contain muddier variants (c, d, g, h) that are characterized by lower calcite content (d: 34% calcite, h: 33% calcite) and higher bulk clay content (d and h: 7% bulk clay). For the cherty layers, they are scattered as dark-gray to black, thin layers (a few centimeters thick) in most of the P-Facies (i) and contains abundant silica cements (j; 68% quartz, 26% calcite, 1% clay). In (e), HCS (also in a) and planar lamination (PL; also in g) are likely associated with the high-energy storm events (Cheel and Leckie, 1993) and are interlayered with mud drapes (e; dashed line in f) and rare planar cross-lamination (CLm in e), all of which point to fluctuating energy condition during deposition. (a) and (b) are 5.8 m/19 ft apart in the same core. (c) and (d) are 9 cm/0.3 ft apart in the same core. (e) and (f) are 12 cm/0.4 ft apart in the same core. (g) and (h) are from the same sample. (j) is from Leblanc (2014).

commonly observed in the "Mississippian" intervals of this region (Gao and Wang, 2017; Wang et al., 2019, in press), contain abundant silt-sized quartz grains with variable skeletal and clay content and likely represent deposition around the middle to outer parts of a regionally defined, distally steepened ramp (e.g., Childress and Grammer, 2019, in press). Dark gray to black cherty zones are present as centimeter-scale layers (generally 1 to 10 cm thick) in most of the P-Facies throughout all six cores (Figure 4.7i, 4.7j), and are treated separately relative to the seven siltstone-to-limestone facies because of its distinctive rock strength and overall scattered nature within the rocks.

For the purpose of highlighting their potential difference in petrophysical properties, these seven facies are grouped into five types of "petrophysically significant facies" (shortened as P-Facies or PF for brevity; Figure 4.8) based upon mineralogy (average calcite and clay content) and the extent of bioturbation, both of which have been documented to be potential factors in affecting the petrophysical properties (e.g., Gingras et al., 2012). From PF-1 to PF-5, well-defined trends of increasing average calcite content and decreasing average clay content are present (Figure 4.8), suggesting an increasingly higher depositional energy which matches the interpretation from sedimentary structures and rock fabric. The vertically repetitive occurrence of these facies, as depicted by such an idealized vertical facies succession (Figure 4.8), allows for the definition of commonly shallowing-upward, "third-order" sequences in individual cores, which constructs a regionally defined sequence stratigraphic framework (Figure 4.9; also in Gao and Wang, 2017; Wang et al., 2019, in press) . On the other hand, mineralogy of all facies covers a wide range (horizontal gray bars in Figure 4.8), likely related to the variable energy conditions and water depth during deposition. In terms of reservoir quality, visible pores are absent on the core surface, with scattered pores visible by optical microscopy in P-Facies 5. Based upon limited data, the highest average porosity values are observed in PF-1 and PF-2 (Figure 4.8). For the Vaca Muerta Formation, which is Late Jurassic to Early Cretaceous in age, the samples of this study contain a

similar mixed carbonate-siliciclastic facies assemblage, such as carbonate mudstone (calcareous, mixed carbonate/siliceous) and wackestone (Eberli et al., 2017).

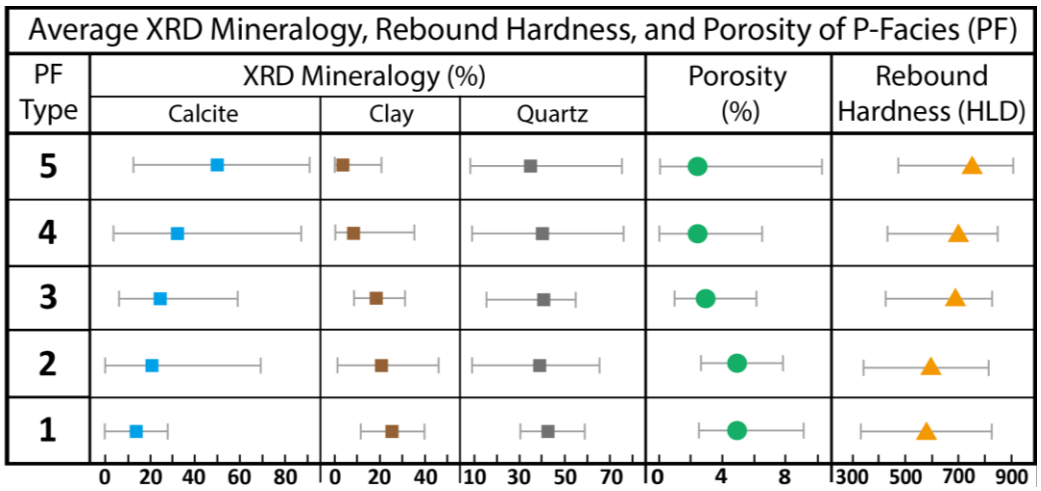

Data Points by P-Facies	XRD Mineralogy	Rebound Hardness	Porosity
PF-5	140	1367	95
PF-4	124	931	80
PF-3	43	515	20
PF-2	53	340	27
PF-1	25	205	10

Figure 4.8. XRD mineralogy (calcite, bulk clay, quartz), rebound hardness (RHN), and porosity of individual P-Facies in the MISS/STACK cores regarding average value and data range (gray horizontal lines; upper figure), along with the number of data points (lower table). No data from cherty zones are included. For each P-Facies type, the data quantity is consistent across the three mineralogy types. The standard deviation values of RHN exhibits a decreasing trend from PF-1 to PF-5 (94.1, 104.3, 65.3, 56.2, 51.4). Total data points of XRD mineralogy and porosity of each P-Facies type are the same with the subsequent analyses (e.g., 2D cross-plots, multivariate and fit modeling analyses).

4.4 Results

4.4.1 Rebound Hardness vs. Rock Properties and Sequence Stratigraphic Framework

Overall, the MISS/STACK rebound hardness (RHN) data follow a normal distribution (n=243; Figure 4.10a). In contrast, the Vaca Muerta data show a bimodal distribution (n=26) with a distinctively different data range (Figure 4.10b), which may be an effect of different facies types and/or the distinctively smaller data set for the Vaca Muerta as compared to the MISS/STACK

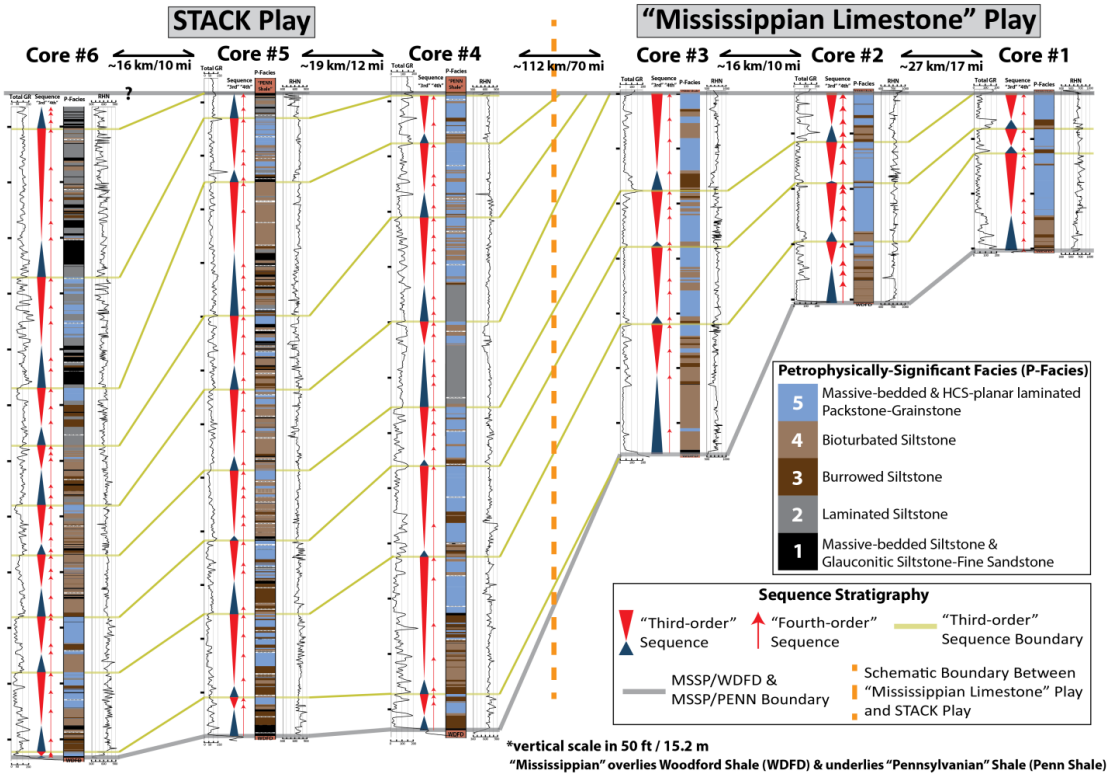

Figure 4.9. Stratigraphic cross-section consisting of the six cores of this study across the "Mississippian Lime" (core #1, 2, 3) and STACK (core #4, 5, 6) play areas showing the gamma-ray log (GR; first column to the left), sequence stratigraphy (second column to the left with triangles showing the "third-order" sequences and vertical arrows showing the "fourth-order" sequences), facies description (third column to the left with color blocks), and rebound hardness (RHN; fourth column to the left) in individual well/core. Note that PF-5 (light blue blocks in the right column of each core) commonly show distinctively low gamma-ray (GR) values and defines the top of the "third-order" sequences in core, producing a "cleaning-upward" GR signature that assists regional-scale correlation. Also note the lack of pattern in the RHN data among sequences in individual cores, and the variations in facies types and stratigraphic architecture (stratal thickness, number and thickness of individual "third-order" sequences) across the "Mississippian Limestone" play (core #1, 2, 3; at northeast) and STACK play (core #4, 5, 6; at southwest). Facies description of Core #1, 2, and 3 are from Leblanc (2014) and Thompson (2016). Correlations within and across the MISS and STACK play areas are achieved by tying the cores of this study with closely spaced wireline logs in the uncored wells in-between the cores.

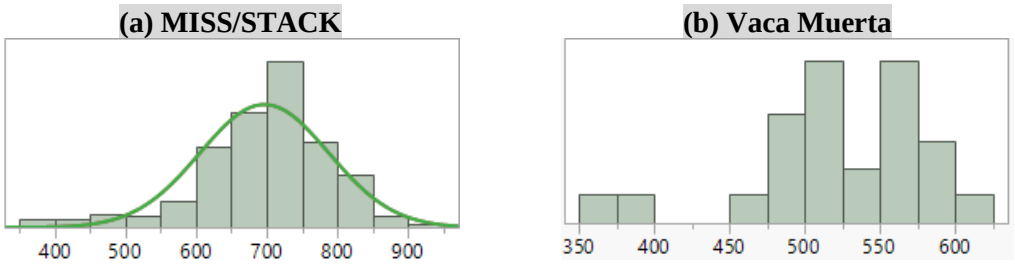

Figure 4.10. For the rebound hardness (RHN) data, MISS/STACK shows a normal distribution (a) and Vaca Muerta shows a bimodal distribution (b). The range of the RHN data is also distinctively different.

data. When compared with core analysis data, the average RHN of the MISS/STACK data shows a positive trend with increasing calcite and negative trend with increasing clay content (Figure 4.8). As shown in Figure 4.11, trends are also observed with correlating RHN with total quartz content (positive trend) and with total porosity (negative trend). The four correlations illustrated in Figure 4.11 show an overall linear trend and clustering by the same facies groups: PF-1 and PF-2 (PF-1/2 for clarity and brevity), PF-3 and PF-4 (PF-3/4 for clarity and brevity), and PF-5, all of which show different statistical patterns (Figure 4.12). Among the three mineralogy types, bulk clay shows the highest correlation coefficient (r) in all PF combined (r=-0.78; Figure 4.11) and in PF-1/2 (r=-0.84; Figure 4.12) and PF-3/4 (r=-0.64; Figure 4.12), with quartz showing the highest R in PF-5 (r=0.45; Figure 4.12). In particular, calcite of PF-5 is the only scenario where the data of a particular PF group exhibits an inverse trend with all PF combined (r=-0.25 in PF-5, Figure 4.12; r=0.35 in all PF combined; Figure 4.11). For porosity, the data in PF-3/4 exhibit the highest r value (r=-0.61; Figure 4.12), followed by all PF combined (r=-0.48; Figure 4.11). Several data points show distinctively high RHN values (approaching 900 HLD, marked as "PF-4 Cherty" and "PF-5 Cherty"; Figure 4.11), and are from the cherty layers (Figure 4.7i, j). Because the data is limited (Figure 4.11), these cherty zones were not included in the subsequent statistical analysis.

The statistical pattern of porosity is different in the MISS and STACK data, with more distinctive negative trend and a lower correlation coefficient in the STACK data (r=-0.46) as compared to the MISS data (r=-0.68) (Figure 4.13). When RHN is cross-plotted against the wireline log data (well #1, 2, 3 in Figure 4.1), no distinct pattern is observed (not shown here). Similar to the MISS/STACK data (Figure 4.11), the Vaca Muerta RHN data show a positive trend with carbonate content and a negative trend with porosity (Figure 4.14). In addition, sonic velocity (Figure 4.14) and three of the four elastic parameters (Young's modulus, bulk modulus, shear modulus; Figure 4.15) exhibit positive trends with RHN. An overall linear trend is present in all of these correlations except for Poisson's ratio (Figure 4.15). The data are also clustered by facies,

but the highest amount of data is only present for two facies with around ten data points showing overall linear trends. Several of these correlations show *r* values being close to 0.75 (Figure 4.14, 4.15), with the other parameters ranging from 0.4 to 0.7 (Figure 4.15). For both the MISS/STACK (Figure 4.11, 4.12) and Vaca Muerta data (Figure 4.14, 4.15), an overall scattered data pattern with overlapping data ranges are observed in all facies combined and among different facies (groups). When plotted by location of the data against the sequence stratigraphic framework defined from the MISS/STACK cores, the RHN data does not show distinctive trends among sequences within individual cores (Figure 4.9).

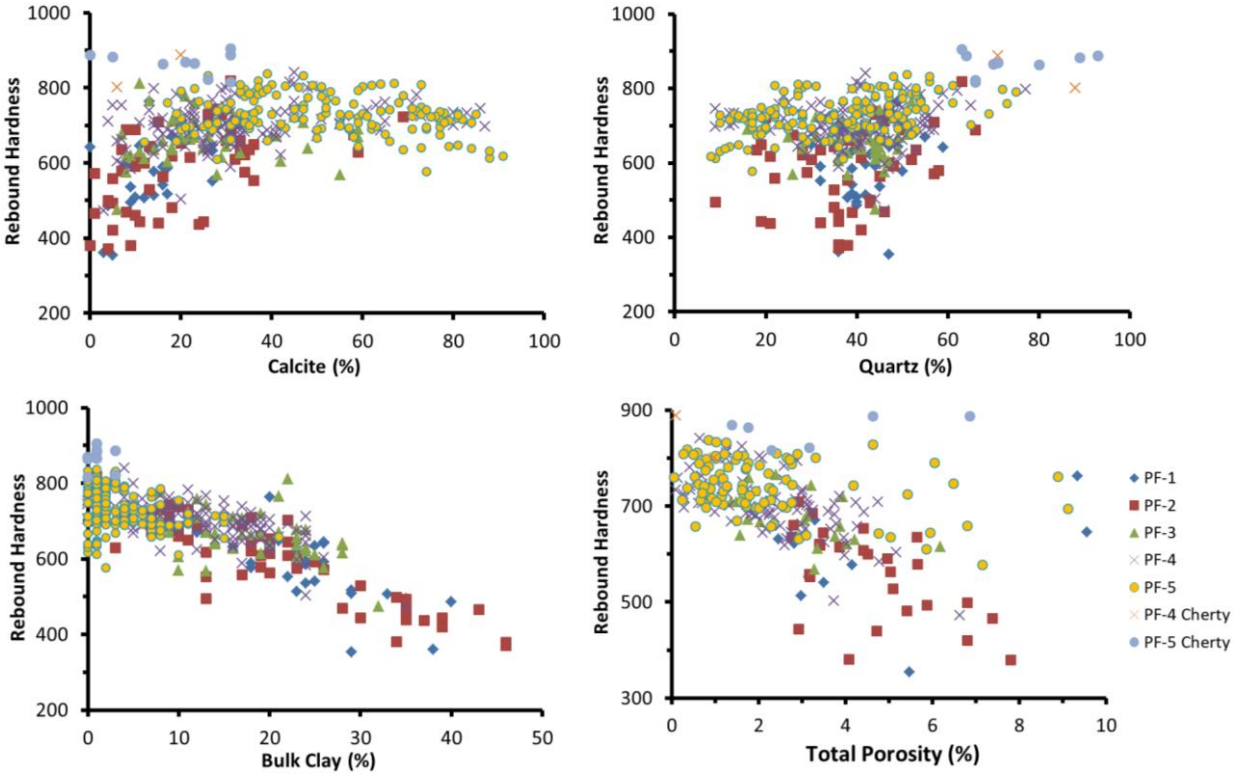

r Values_All PF Combined _MISS/STACK	Calcite	Quartz
	0.35	0.24
	Bulk Clay	**Porosity**
	-0.78	-0.48

Figure 4.11. Cross-plots showing the correlation between rebound hardness and XRD mineralogy and porosity of the MISS-STACK cores, accompanied with the *r* values (table). Bulk clay shows the strongest correlation (*r*=-0.78, blue cell in table).

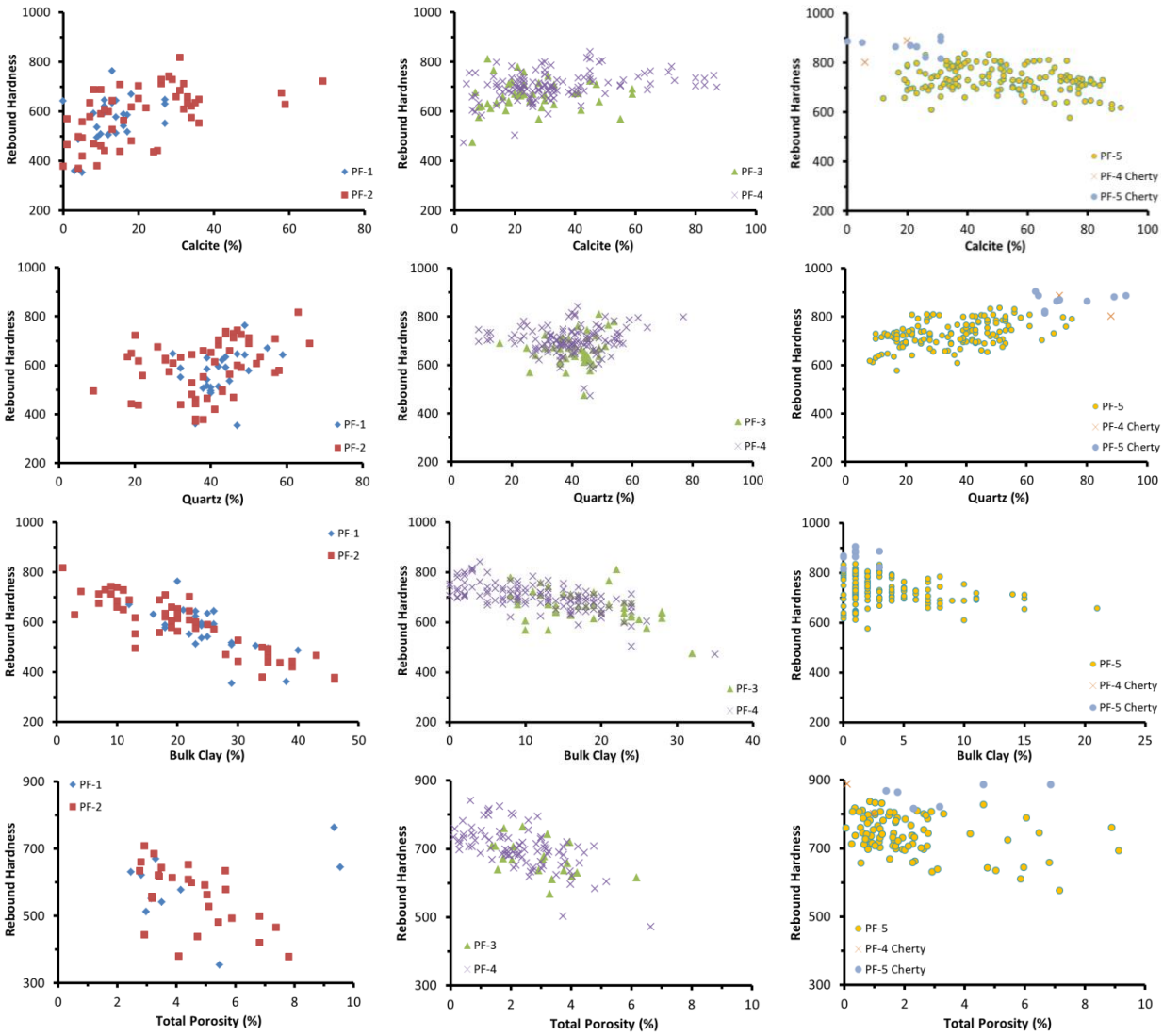

r Values_By PF Group_MISS/STACK	PF-1 + PF-2	PF-3 + PF-4	PF-5
Calcite	0.51	0.31	-0.25
Quartz	0.31	0.05	0.45
Bulk Clay	-0.84	-0.64	-0.27
Porosity	-0.18	-0.61	-0.28

Figure 4.12. Cross-plots showing the correlation of rebound hardness with XRD mineralogy and with porosity of individual P-Facies groups in the MISS/STACK cores, accompanied with the r values of each correlation (table). Bulk clay in PF-1 and PF-2 exhibits the strongest correlation among all P-Facies groups (*r*=-0.84; blue cell under "PF-1 + PF-2"). In PF-3 and PF-4, bulk clay and porosity (gray cells in table) show the highest and close-to-highest absolute *r* values. In PF-5, quartz (gray cell) shows the highest absolute *r* value.

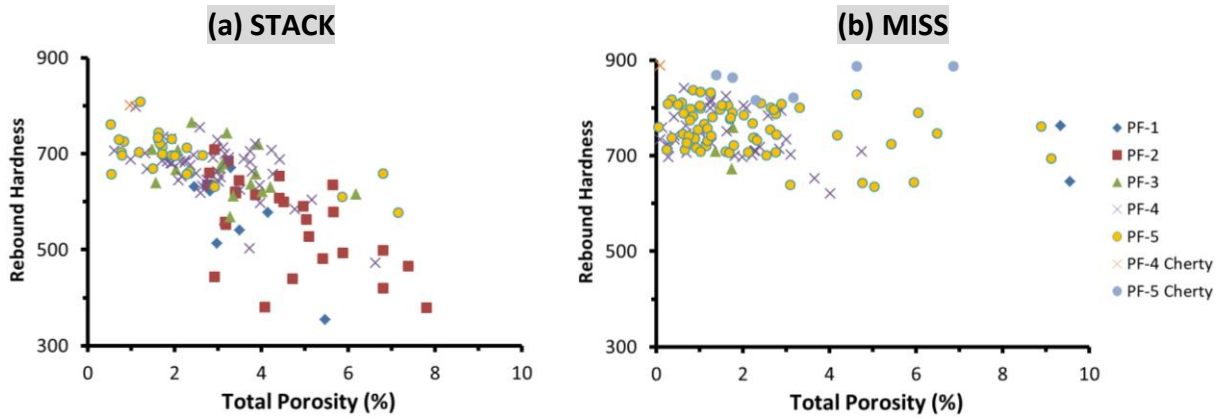

Figure 4.13. When arranging the RHN-to-porosity correlation by the STACK (a) and the MISS cores (b), the STACK data (a) show a more distinctive negative trend, but with a lower absolute r value (*r*=-0.46; *r*=-0.68 for MISS data).

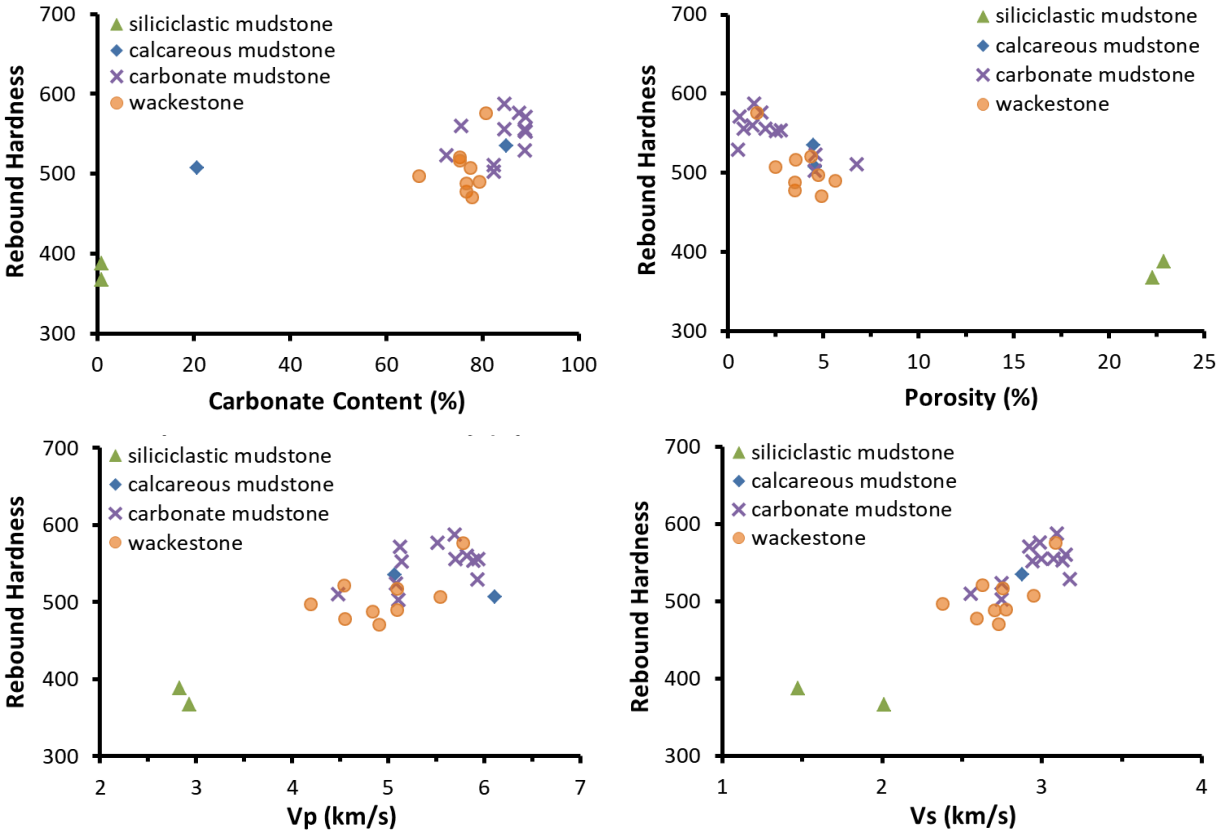

r Values_All Facies Combined_VM	CO_3%	Porosity
	0.51	-0.74
	Vp	Vs
	0.74	0.77

Figure 4.14. Cross-plots showing the correlation of rebound hardness with carbonate content, porosity, and compressional (Vp) and shear (Vs) wave velocity of the Vaca Muerta data,

accompanied with the r values of each correlation (table). Highest (gray cells in table) and close-to-highest (lower by less than 0.5) absolute *r* values (blue cell in table) are present in porosity, Vp, and Vs. VM: Vaca Muerta.

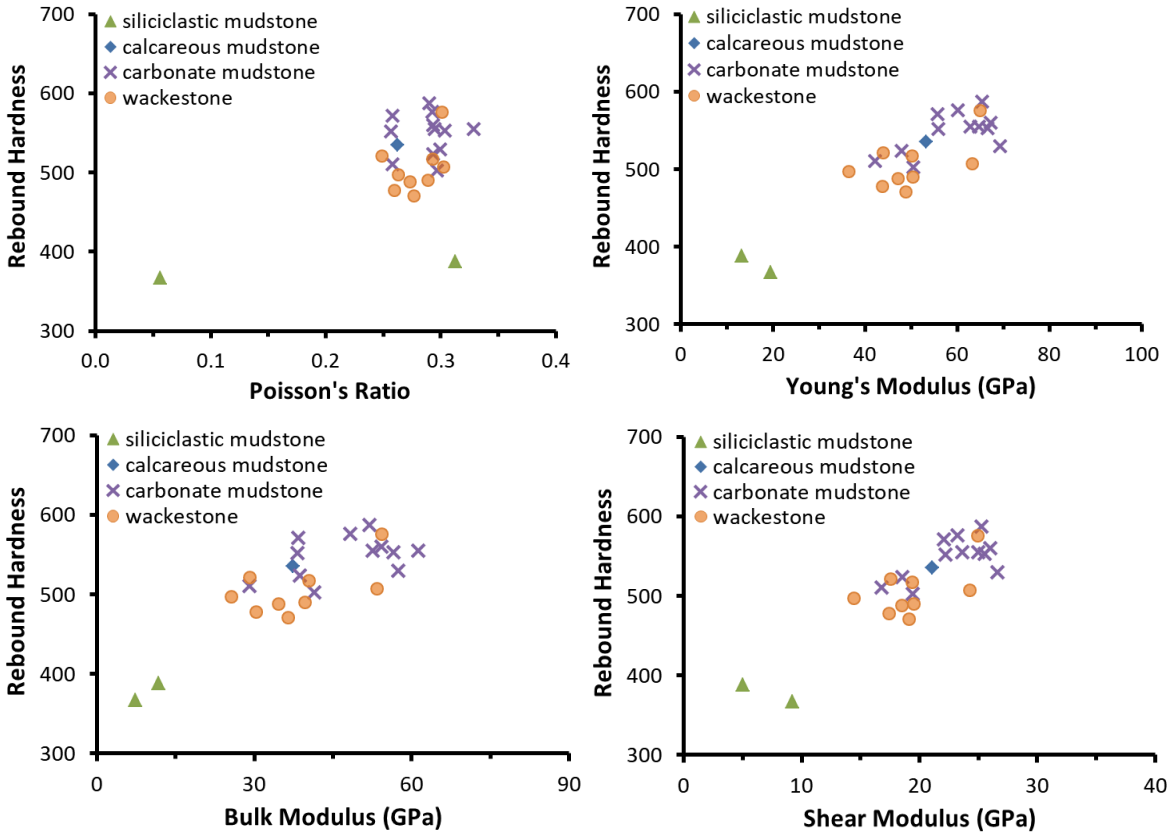

r Values_All Facies Combined_VM	Poisson's Ratio	Young's Modulus
	0.47	0.73
	Bulk Modulus	**Shear Modulus**
	0.63	0.74

Figure 4.15. Cross-plots showing the correlation of rebound hardness with the elastic parameters of the Vaca Muerta data, accompanied with the *r* values of each correlation (table). Young's modulus and shear modulus show the highest *r* values (0.73 and 0.74; blue cells in table). VM: Vaca Muerta.

4.4.2 Statistical Analysis

Because of the overall linear trends between RHN and mineralogy, porosity, sonic velocity, and elastic parameters (Figure 4.11 to 4.15), it is suitable to conduct multivariate and fit modeling analyses for these data, both of which are based upon linear hypothesis (JMP® User Guide). For both MISS/STACK and Vaca Muerta data, multivariate analysis reveals a similar pattern of

bivariate *r* for all facies combined (Figure 4.16, 4.17) as compared to Figure 4.11, 4.14, and 4.15. However, it should be noted that the *r* values in the multivariate analysis of the MISS/STACK data (Figure 4.16) are slightly different (<0.3 in *r* values) as compared to the correlations in Figure 4.10, because certain samples are not tested with XRD mineralogy or porosity. In the MISS/STACK data (Figure 4.16), calcite exhibits strong correlation with quartz (*r*=-0.73) and bulk clay (*r*=-0.72), and porosity shows moderate correlation with calcite (*r*=-0.46) and bulk clay (*r*=0.49). In the Vaca Muerta data (Figure 4.17), strong correlation is present in carbonate content with porosity (*r*=-0.92) and sonic velocity (*r*=0.8 for Vp and Vs; Figure 4.17). In addition, Vp shows strong correlation with Vs (*r*=0.97) and three of the four elastic parameters (Young's modulus, *r*=0.99; bulk modulus, *r*=0.98; shear modulus, *r*=0.98; Figure 4.18). Because of these relationships (i.e., multicollinearity), which is due to the calculated elastic parameters from Vp and Vs, Vs and elastic parameters are not included in the subsequent fit modeling analysis. For the leverage analysis of the MISS/STACK data, bulk clay shows the highest FDR LogWorth in all PF combined and PF-1/2, and porosity shows the highest FDR LogWorth in PF-3/4 and in PF-5 (Figure 4.17). In all of these four cases, the highest FDR LogWorth are greatly >2, and such a scenario being present for only one parameter in PF-1/2, PF-3/4, and in PF-5 (Figure 4.18). In addition, bulk clay, porosity, and quartz content of all PF combined show comparable >2 FDR LogWorth (Figure 4.18). For the Vaca Muerta data, carbonate content and porosity barely reach 2 in FDR LogWorth, with Vp showing <2 FDR LogWorth (Figure 4.18).

When using RHN and XRD mineralogy of all PF combined to predict the MISS/STACK porosity, six out of the fifteen possible models exhibit the highest and close-to-highest (lower by less than 0.5 than highest) adjusted R^2 around 0.36 (blue and gray cells in "All PF" column; Table 4.2). For individual PF groups, the number of models showing the highest and close-to-highest adjusted R^2 is different: three models in PF-1/2 (adj. R^2: 0.50 to 0.52), five models in PF-3/4 (adj. R^2: 0.65 to 0.69), and three models in PF-5 (adj. R^2: 0.27 to 0.32) (blue and gray cells in the columns of "PF-

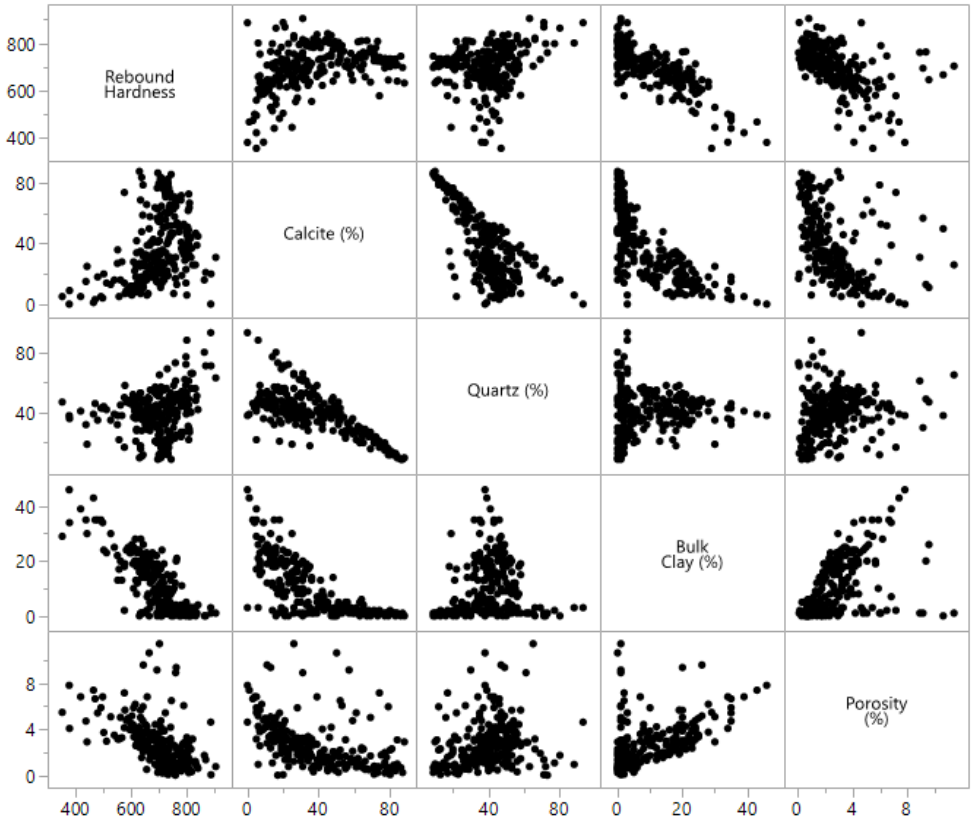

***r* Values of Multivariate Correlations _MISS/STACK**	**RHN**	**Calcite**	**Quartz**	**Bulk Clay**	**Porosity**
RHN	*1.00*	0.37	0.22	-0.78	-0.52
Calcite	0.37	*1.00*	-0.73	-0.72	-0.46
Quartz	0.22	-0.73	*1.00*	0.13	0.19
Bulk Clay	-0.78	-0.72	0.13	*1.00*	0.49
Porosity	-0.52	-0.46	0.19	0.49	*1.00*

Figure 4.16. Scatterplot matrix showing the multivariate analysis involving rebound hardness, XRD mineralogy (calcite, quartz, bulk clay; %), and porosity (%) of the MISS/STACK data, accompanied with the *r* values of each correlation (table). The highest and close-to-highest (lower by less than 0.5) *r* values are observed in correlations of RHN-to-bulk clay (*r*=-0.78), calcite-to-quartz (*r*=-0.73), and calcite-to-bulk clay (*r*=-0.72) (blue and gray cells in table). *r* values in gray texts correspond to the repetitive *r* values with the ones in black, both of which are derived from the same correlations. *r* values in blue italic texts (1.00) denote the correlations between the same parameter.

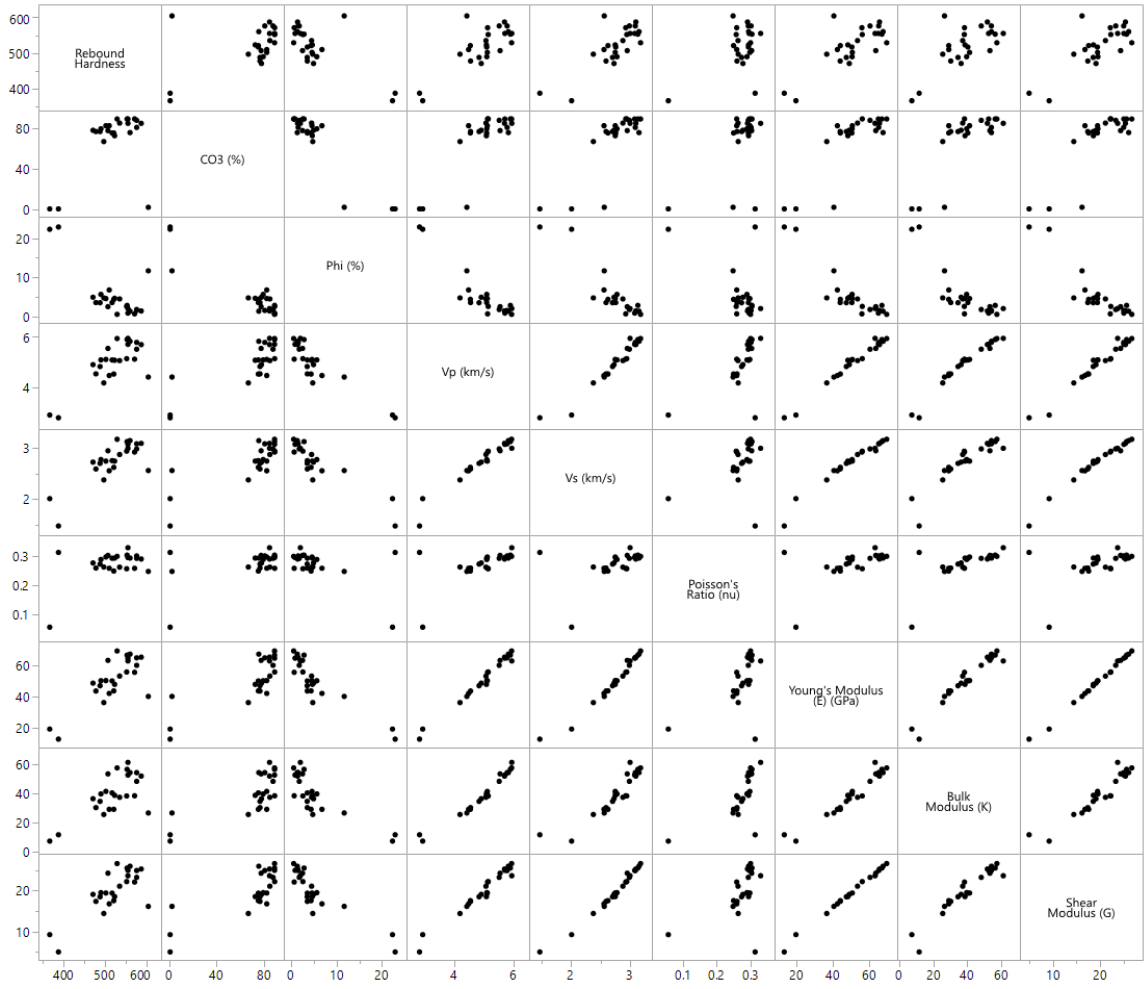

r Values of Multivariate Correlations _Vaca Muerta	RHN	CO_3	Porosity	Vp	Vs	Poisson's Ratio	Young's Modulus	Bulk Modulus	Shear Modulus
RHN	*1.00*	0.52	-0.74	0.78	0.79	0.48	0.77	0.69	0.77
CO_3	0.52	*1.00*	-0.92	0.80	0.80	0.52	0.79	0.73	0.79
Porosity	-0.74	-0.92	*1.00*	-0.90	-0.90	-0.56	-0.89	-0.81	-0.88
Vp	0.78	0.80	-0.90	*1.00*	0.97	0.62	0.99	0.98	0.98
Vs	0.79	0.80	-0.90	0.97	*1.00*	0.43	0.98	0.90	0.99
Poisson's Ratio	0.48	0.52	-0.56	0.62	0.43	*1.00*	0.54	0.65	0.49
Young's Modulus	0.77	0.79	-0.89	0.99	0.98	0.54	*1.00*	0.96	1.00
Bulk Modulus	0.69	0.73	-0.81	0.98	0.90	0.65	0.96	*1.00*	0.95
Shear Modulus	0.77	0.79	-0.88	0.98	0.99	0.49	1.00	0.95	*1.00*

Figure 4.17. Scatterplot matrix showing the multivariate analysis involving rebound hardness, carbonate content (CO_3; %), porosity (%), Vp, Vs, Poisson's ratio, Young's modulus, bulk modulus, and shear modulus. Strong correlations are observed in carbonate content-to-porosity (*r* =-0.92) and porosity-to-sonic velocity (*r*=-0.90) (blue cells in the column of "CO_3" and "Porosity" in table). In contrast, lower but decent r values are observed when correlating RHN with porosity (*r*=-0.74), sonic velocity (*r*=0.78 and 0.79), Young's modulus (*r* =0.77), and shear modulus (*r*=0.77). Also note the overall excellent correlation (*r* being no lower than 0.9) among Vp, Vs, and elastic parameters (excluding Poisson's ratio; blue and gray cells in the columns of "Vp" and "Vs" in table). *r* values in gray texts correspond to the repetitive r values with the ones in black, both of which are derived from the same correlations. *r* values in blue italic texts (1.00) denote the correlation between the same parameter. In table, blue and gray texts respectively denote the highest *r* and close-to-highest *r* in the corresponding categories.

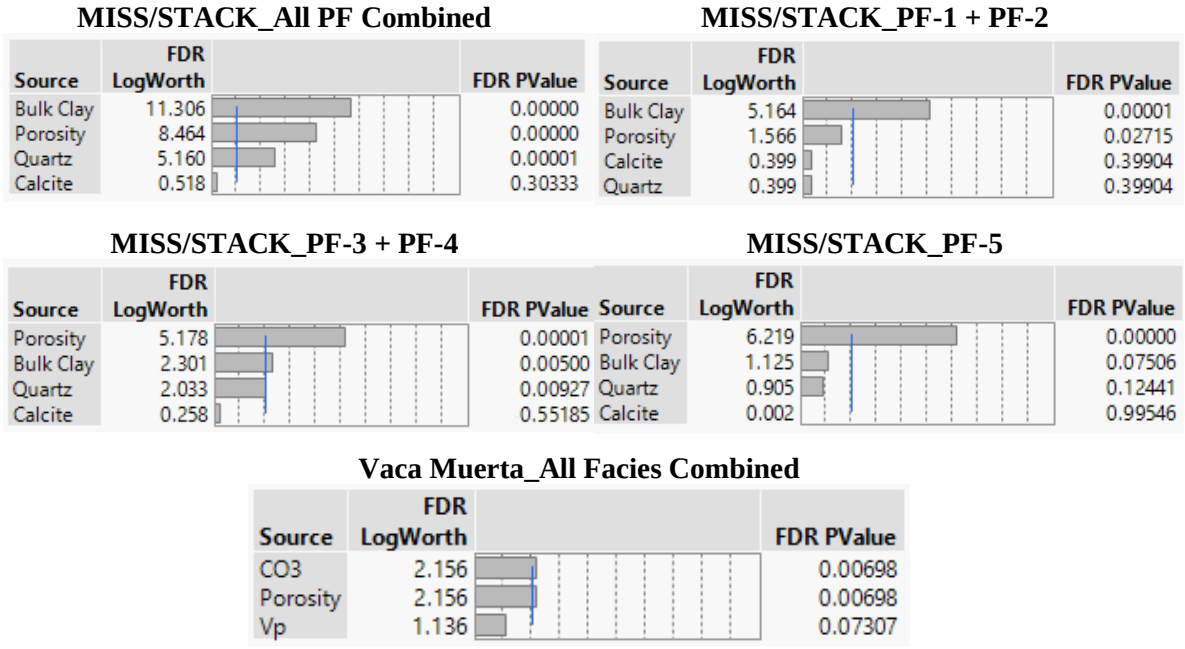

Figure 4.18. Leverage analytical results of MISS/STACK and Vaca Muerta data showing the FDR LogWorth values of individual input parameters ("source" in figures) in predicting rebound hardness. *P*-value is set as 0.01, which corresponds to "2" in FDR LogWorth. In all five scenarios, the blue vertical lines in the FDR LogWorth column indicate a value of 2, above which indicates a substantial significance level of a particular input parameter in determining rebound hardness. See text for discussion.

1 + PF-2", "PF-3 + PF-4", and "PF-5", respectively; Table 4.2). When predicting porosity of the Vaca Muerta data (Table 4.3a), combining RHN with carbonate content and with carbonate content and Vp yield the highest adjusted R^2 of 0.93, being close to the scenario of including carbonate content and Vp (adj. R^2 = 0.91) (blue and gray cells). For the prediction of Vp (Table 4.3b), combining RHN with porosity and with carbonate content and porosity show the highest

adjusted R^2 (0.81; blue cells). For both predictions, the lowest adjusted R^2 is observed when only including RHN (0.53 for porosity, 0.59 for Vp; Table 4.3).

Forward Regression_MISS/STACK _ Input: RHN, XRD; Output: Porosity	**Number of Variables**	**Adj.R^2 _All PF**	**Adj.R^2 _PF-1+2**	**Adj.R^2 _PF-3+4**	**Adj.R^2 _PF-5**
RHN	1	0.27	0.01	0.37	0.15
Bulk Clay	1	0.23	0.29	0.42	-0.01
Calcite	1	0.23	0.35	0.58	0.01
Quartz	1	0.06	0.09	0.29	-0.003
RHN, Quartz	2	0.36	0.14	0.64	0.24
RHN, Calcite	2	0.35	0.34	0.68	0.21
RHN, Bulk Clay	2	0.28	0.42	0.47	0.14
Calcite, Bulk Clay	2	0.26	0.39	0.59	0.001
Quartz, Bulk Clay	2	0.25	0.43	0.53	-0.01
Calcite, Quartz	2	0.25	0.34	0.62	0.01
RHN, Quartz, Bulk Clay	3	0.36	0.50	0.65	0.27
RHN, Calcite, Bulk Clay	3	0.36	0.51	0.69	0.31
RHN, Calcite, Quartz	3	0.36	0.32	0.68	0.24
Calcite, Quartz, Bulk Clay	3	0.26	0.43	0.61	0.07
RHN, Calcite, Quartz, Bulk Clay	4	0.36	0.52	0.69	0.32

Table 4.2. Table showing the adjusted R^2 (adj. R^2) from the forward regression analysis of the MISS/STACK data with different combinations of input parameters (XRD mineralogy, RHN) in predicting the MISS/STACK porosity. The blue and gray cells respectively indicate the highest and close-to-highest (lower by less than 0.5) adjusted R^2 of a particular facies grouping scheme. See text for discussion.

4.5 Discussion

4.5.1 Rebound Hardness vs. Rock Properties: An Overview

As suggested by the positive trend with calcite/carbonate content (Figure 4.11, 4.14) and the negative trend with bulk clay content (Figure 4.11), RHN can aid in an estimation of the relative abundance of mineralogy. Among the three types of XRD mineralogy, bulk clay in the MISS/STACK data exhibits a distinctive negative trend and is the only mineralogy type with a

(a) VM _Input: RHN, CO_3, Vp; Output: Porosity	Number of Variables	Adj.R^2
CO_3	1	0.84
Vp	1	0.79
RHN	1	0.53
RHN, CO_3	2	0.93
CO_3, Vp	2	0.91
RHN, Vp	2	0.79
RHN, CO_3, Vp	3	0.93

(b) VM_ Input: RHN, CO_3, Porosity; Output: Vp	Number of Variables	Adj.R^2
Porosity	1	0.79
CO_3	1	0.63
RHN	1	0.59
RHN, Porosity	2	0.81
RHN, CO_3	2	0.80
CO_3, Porosity	2	0.79
RHN, CO_3, Porosity	3	0.81

Table 4.3. Table showing the adjusted R^2 (Adj. R^2) from the forward regression analysis of the Vaca Muerta data with different combinations of input parameters in predicting porosity (a, left) and Vp (b, right). The blue and gray cells respectively indicate the highest and close-to-highest (lower by less than 0.5) adjusted R^2 for the prediction of porosity (a, left) and Vp (b, right). CO_3: carbonate content. See text for discussion.

relatively robust correlation (r=-0.78, Figure 11; r=-0.84 for PF-1 and PF-2, Figure 4.12), which can potentially allow for the derivation of conversion to aid in statistical modeling. Therefore, RHN is most effective for estimating bulk clay content, which can be crucial for evaluating reservoir performance and completion issues related to fine migration and swelling clay. On the other hand, such a correlation also indicates that bulk clay can help estimate RHN. Considering the potential conversion from RHN to unconfined compressive strength (UCS) as demonstrated by many studies (in Introduction), RHN can be a valuable parameter for production design, such as horizontal drilling and hydraulic fracturing. However, it is important to note that we do not advocate for applying the RHN-to-UCS conversion to directly calculate the UCS for the MISS/STACK and the Vaca Muerta samples of this study. One key reason is that, because of the unique geological background of each basin (e.g., depositional setting, sea-level history, burial history, diagenesis), it is highly problematic to use an uniform conversion which is inclusive of these unique aspects of one particular basin, across multiple basins and different parts of the same basin. This is particularly important for the mixed carbonate-siliciclastic reservoir rocks, which

can appear almost identical in rock samples and wireline log signatures. Also, the experimental protocols of these studies are highly variable with different amount and types of samples used to constrain the conversion, which can lead to variable statistical validity for their results. Therefore, it is critical to derive the RHN-to-UCS conversion on a case-by-case basis. In addition, a similar pattern between RHN and clay content has been reported in other mixed carbonate-siliciclastic reservoirs, such as the Wolfcamp/Leonard strata in the Midland Basin (Baumgardner et al., 2014; unpublished data), pointing to the value of this workflow in other "unconventional" reservoirs.

As further suggested by the trend of average RHN with calcite and bulk clay content at a PF scale (Figure 4.8), such a connection between present-day rock strength and mineralogy implies that the rock strength determined at a syndepositional and early diagenetic stage has likely been preserved into the present-day. In this sense, the present-day rock mechanical properties are likely a combination of relatively early "unaltered" and late "altered" signals, implying a dynamic evolution history of the rock mechanical properties. Similarly, RHN can potentially provide a first-order estimation for the range of total porosity (r=-0.48, Figure 4.11; r=-0.61 for PF-3 and PF-4, Figure 4.14), sonic velocity (r=0.78 for Vp, r=0.79 for Vs, Figure 4.14), and certain elastic parameters (r=0.77 for Young's modulus, r=0.77 for shear modulus, Figure 4.15). Because of the rapid turnaround time of the collection of RHN data, these observations indicate that RHN can potentially provide a more time- and cost-efficient estimation of certain rock properties as compared to conventional laboratory analysis. For the MISS/STACK data, the similar clustering patterns of data by PF groups in mineralogy and porosity (i.e., PF-1 and -2, PF-3 and -4, PF-5; Figure 4.12) potentially point to a systematic variation of mineralogy and porosity among these PF groups. In addition, different statistical patterns among different facies (groups) (Figure 4.11, 4.12, 4.14, 4.15) suggest RHN can potentially aid in petrophysical rock typing and sample selection for more detailed laboratory analyses, both of which are critical for core-based reservoir characterization project at the earlier stages of reservoir analysis. Also, the clustering of data by

facies further indicates that variability of facies affects the statistical pattern in these correlations. Therefore, it is important to select the testing locations of RHN in this workflow based upon a detailed facies description in core.

In particular, several studies document that sonic velocity and elastic properties are affected by variations in mineralogy and pore architecture (porosity, pore shape, pore size) in both carbonate (e.g., Eberli et al., 2003; Baechle et al., 2005, 2008; Fournier et al., 2011) and mixed carbonate-siliciclastic rocks (e.g., Chang et al., 2006; Sone and Zoback, 2013a, b; Altowairqi et al., 2015; Abatan et al., 2016; Vanden Berg and Grammer, 2019, in press). Therefore, the clustering and trend of data in carbonate content and porosity of the Vaca Muerta data (Figure 4.14) can explain the clustering of data in sonic velocity (Figure 4.14) and elastic parameters (Figure 4.15). In particular, Poisson's ratio is the only elastic parameter lacking a distinctive pattern with RHN (Figure 4.15). Considering the negative trend between RHN and bulk clay content in the MISS/STACK data (Figure 4.11), which may also present in the Vaca Muerta data, such a lack of pattern in the RHN-to-Poisson's ratio correlation (Figure 4.15) is consistent with results from Sone and Zoback (2013a) which documents the lack of a pattern between Poisson's ratio and clay content in mixed carbonate-siliciclastic rocks. It is also important to note that the relationship between RHN and elastic parameters may not be as straightforward as it appears in the 2D cross-plots (Figure 4.15), because rock failure consists of a dynamic process which involves the coalescence of microfractures, and the correlation between rock strength and elastic moduli cannot be captured by "simple elastic models" (e.g., unconfined compressive strength vs. Young's modulus; Sone and Zoback, 2013b). In addition, Hack et al. (1993) reported that the competitive relationship between the crushing of sample surface during the RHN test and rock strength can affect the correlation between RHN and elastic parameters. In this sense, RHN may show a more closely constrained correlation with elastic parameters in stronger rocks, which tend to experience less crushing at the testing location as compared to weaker rocks. Such an empirical

relationship may further contribute to the grouping of rock mechanical data by facies types with variable rock strength (Figure 4.15), even at an average scale (Figure 4.8). However, because of the limited quantity of the Vaca Muerta data (Table 4.1), the statistical patterns of individual parameters are not analyzed by facies types.

4.5.2 Clustering of Data by P-Facies Groups: MISS/STACK Data

4.5.2.1 Mineralogy

For the MISS/STACK data, the clustering of calcite, quartz, and clay content by P-Facies groups (PF-5, PF-3/4, and PF-1/2; Figure 4.12) can be related to rock fabric (e.g., composition and form of presence of grains and cement or matrix) and diagenesis (e.g., evolution of rock fabric), which collectively determines the present-day rock strength (i.e., RHN). For PF-5, RHN shows a relatively consistent pattern despite the variations of all three mineralogy types (Figure 4.12). This can be related to the rock fabric of PF-5, which is the only PF with abundant skeletal fragments, peloidal grains, and calcite cements within interparticle space (Figures 4.7b, f), all of which contribute to its highest average calcite contents (Figure 4.8) and correspond to its interpreted highest overall depositional energy among all PF. With little evidence of dissolution and recrystallization, these interstitial calcite cements have likely constructed a calcite-rich framework which provides rigidity to the rock via syndepositional marine cementation, which can be formed within weeks to months at both shallower and deeper water depths (Grammer et al., 1999; Eberli et al., 2003). In addition, additional interlocking of the calcite-dominated skeletal fragments by these cements, such as the syntaxial overgrowth of crinoid fragments which can potentially be interconnected from a 3D perspective, provides additional rigidity to this framework. During subsequent early burial, this framework has likely provided resistance to compaction, and therefore, contributed to the preservation of the “unaltered” signal of rock mechanical properties from the syndepositional and early diagenetic stage. It should be noted that the variation of porosity during the compaction and early burial stage will affect the rock strength.

However, despite the wide range of total porosity of PF-5 (almost 0 to nearly 10%; Figure 4.12), the RHN values of PF-5 are relatively consistent with respect to mineralogy as compared to other P-Facies (Figure 4.12), implying the critical role of the calcite-rich rock framework in maintaining the rock strength. This interpretation is also supported by the low significance level of mineralogy in determining the RHN of PF-5, none of which exhibit substantial significance (i.e., distinctively lower-than-2 FDR LogWorth values; Figure 4.18).

In contrast, PF-1/2 and PF-3/4 consistently show positive trends in calcite content and negative trends in quartz content (Figure 4.12). These mudstone to siltstone facies are dominated by a mud-dominated framework (Figure 4.4, 4.5, 4.6) which likely behaves as a relatively plastic medium at the syndepositional stage when the rigid, calcite-rich framework was formed in PF-5, and is likely more sensitive to mineralogical variations and compaction at the subsequent burial stage. In addition, the bulk clay content of these two PF groups exhibits distinctive negative trends with the most closely constrained correlation among the three mineralogy types (Figure 4.12), which is consistent with the pattern in all P-Facies combined (Figure 4.11). In more detail, the data of PF-3/4 show a separation with PF-1/2, with PF-3/4 exhibiting an overall higher RHN with higher calcite content and lower clay content (Figure 4.12). This can be related to the difference in rock fabric between these two PF groups. For PF-3/4, they contain calcite-rich burrow networks dominated by *Phycosiphon* (PHY in Figure 4.6), which is the primary trace fossil in these two P-Facies. It consists of a muddy core enclosed by a calcite-rich rim (Figure 4.6b), which was likely formed at a syndepositional stage because it is believed that the calcite was expelled by the organism (Bednarz and McIlroy, 2009). Even for PF-3 where the burrows appear relatively isolated on the core surface (Figure 4.6a), these burrow networks can potentially be interconnected from a 3D perspective (Bednarz and McIlroy, 2009). Therefore, it is possible that these burrow networks can form a calcite-rich framework in both PF-3 and PF-4 and provide rock strength early in the syndepositional stage in a similar way with PF-5. Such a hypothesis is

supported by the largely non-significant role of mineralogy in determining RHN in both PF-3/4 and PF-5 (Figure 4.18). These potential similarities in the rock framework of PF-3/4 and PF-5 can explain the relatively consistent RHN relative to calcite content in both PF groups and the partially overlapping data between these two PF groups (Figure 4.11). On the other hand, unlike the interstitial cements in PF-5 which are precipitated from fluids at interparticle space and support the grains (Figures 4.7b), the framework formed by burrow networks in PF-3/4 (Figure 4.6) are likely not as prevalent from a 3D perspective. As further suggested by the lack of additional interlocking of skeletal grains (e.g., syntaxial overgrowth of the crinoid fragments in PF-5), the clay-rich matrix in PF-3/4 can potentially intersect through the burrow network and play a role in determining the rock strength. This interpretation is supported by the distinctive negative trend with moderate correlation strength between bulk clay content and RHN (r=-0.64 in PF-3/4, Figure 4.12) and the close-to-2 FDR LogWorth of bulk clay in determining the RHN of PF-3/4 (Figure 4.18). For PF-1/2, the most distinctive negative trend with the highest r (-0.84) in bulk clay content in all facies grouping schemes (Figure 4.11, 4.12) indicates that RHN provides the most effective estimation of the bulk clay content of PF-1 and PF-2. This suggests that the dominantly clay-rich mud matrix in these two P-Facies (Figure 4.5), which lack the interstitial calcite cement of PF-5 (Figure 4.7) and the burrow network in PF-3/4 (Figure 4.6), plays an critical role in affecting RHN. This observation is further supported by the role of bulk clay in being the only mineralogy type with substantial significance of in determining the RHN of PF-1/2 (distinctively higher-than-2 FDR LogWorth; Figure 4.18). Therefore, such a framework likely exhibits the highest sensitivity to mineralogy variation and compaction as compared to other P-Facies, corresponding to the distinctive trends in all mineralogy types (Figure 4.12).

Quartz content shows positive trends in all facies grouping schemes (Figure 4.11, 4.12), with the highest *r* in PF-5 (0.45; Figure 4.12). However, quartz appears as floating grains in the clay-rich matrix of PF-1 to PF-4 (Figure 4.4, 4.5, 4.6) and in the calcite cements of PF-5 (Figure 4.7). In

this case, these quartz grains may serve as a contributor to rock strength by being in contact from a 3D perspective due to compaction. Such a hypothesis can be supported by the most distinctive positive trend of quartz content in PF-1/2 (r=0.31; Figure 4.12). For PF-5, the positive trend in quartz content (Figure 4.12) may be related to the interlocking of quartz grains by interstitial calcite cement (Figure 4.7b), which can particularly be important for rock strength when the calcite content is relatively low (e.g., 30%; Figure 4.7d, f, h). The only other case where quartz is a primary contributor to rock strength is the cherty zones where the silica cements are abundant at interparticle space (Figure 4.7j). Such a rigid rock framework likely behaves in a similar way with the calcite-rich framework of P-Facies 5, corresponding well to the consistent, high RHN values of these cherty zones (approaching 900 HLD; Figure 4.12).

4.5.2.2 Porosity

Considering that RHN is calculated by the ratio of rebound and impact velocities (Figure 4.2b), such a ratio is partially determined by the energy loss during a single test. Assuming the relative consistency of other rock properties (e.g., mineralogy), higher porosity will lead to higher energy loss during a single impact, which results in a lower rebound velocity, and hence a lower RHN value. On the other hand, the consistent negative trend between RHN and porosity (Figure 4.11, 4.12, 4.14) indicates that such an assumption is valid in interpreting the impact of porosity on RHN. At a PF scale, PF-1/2 show overall higher porosity than PF-3/4 and PF-5 (Figure 4.8, 4.12). Because visible pores are rare at a core and petrographic scale, such higher porosity in PF-1/2 is likely a result of abundant microporosity in the clay minerals which further result in overall lower RHN, despite their higher average bulk clay content (Figure 4.8). In particular, there are two data points from PF-1 which show distinctively high porosity (approaching 10%; Figure 4.12). They are from the glauconitic siltstone-sandstone facies (part of P-Facies 1; Figure 4.4a to d), which is concentrated directly above the base of the Mississippian section and is volumetrically the most insignificant MISS/STACK facies identified this study (mostly less than 10 feet/3 meters thick).

From a regional scale, the different statistical patterns of RHN-to-porosity correlation between the MISS and STACK cores are partially represented by a group of PF-5 data points from the MISS cores with distinctively high RHN and high porosity (Figure 4.11, 4.13). This may indicate the variable reservoir quality of a particular facies across different parts of the play, although such a discrepancy can be an artifact of sampling bias. In addition, the STACK data exhibit a wider range of RHN related to the overall low RHN of PF-2 (Figure 4.13), which is not identified the MISS cores. As further suggested by the more distinctive negative trend with a lower *r* (-0.46) as compared to the MISS data (-0.68) (Figure 4.13), these differences indicate the caveat of using one RHN-to-porosity conversion for different parts of the play.

4.5.3 Controlling Factors of Statistical Relationship

4.5.3.1 Scale Difference of Data, Heterogeneity of Rock Properties, and Potential Experimental Errors

Despite the correlative trends with core data, the correlation coefficient of 70% of all 24 correlations in the MISS/STACK and Vaca Muerta data combined is far less than 0.8 (Figure 4.11 to 4.15), pointing to the presence of significant scatter in the data. This further leads to overlapping data ranges among different facies, which likely attributes to the lack of distinctive trends when comparing the RHN data among individual sequences (Figure 4.9). As further indicated by the lack of a clear pattern between RHN and wireline log data from the three MISS wells (well #1, 2, 3; Figure 4.1), rebound hardness carries variable capabilities in predicting rock properties of these unconventional reservoirs using 2D cross-plots, and therefore, cannot serve as a substitute to the conventional laboratory tests for these reservoir properties. There are several reasons that may explain such a scattered data pattern. Firstly, core and wireline log data are acquired using an averaging method within a certain sampled volume. Specifically, XRD mineralogy is analyzed using powdered sample (e.g., a few grams), and porosity is tested using crushed or plug samples (e.g., 3.8 cm/1.5 inch in diameter, 5 cm/2 inch in height). For wireline

log data, they are averaged in either a horizontal (e.g., gamma-ray, neutron, density) or a vertical interval (e.g., sonic) with a range of at least 0.5 meters. In comparison, individual RHN data point is tested in a <1 cm^2 area on the core surface (Figure 4.2c). Such an offset in the scale of these data is likely a key factor in the overall loosely constrained data pattern in the core data (also in Ritz et al., 2014) and the lack of statistically robust patterns when correlating RHN with the wireline log data from the MISS wells.

Secondly, core and wireline log data are not capable of accurately representing the rock properties in certain intervals, such as the end-member components with distinctively different mineralogy which are commonly present at the sub-centimeter scale. In these cases, the resultant heterogeneity in rock properties (e.g., reservoir quality, sonic velocity) can be well below the presumed sample volume and resolution of core and wireline log data. Also, the rock properties can vary from both a vertical (i.e., stratigraphic) and a lateral (i.e., in-between wells) perspective, pointing to the inherently biased nature of core and wireline log data in representing the actual rock properties at the marked data locations. Typical examples include thinly layered facies (Figure 4.5b and 4.7e), burrowed/bioturbated intervals (Figure 4.6), and debris flow deposits (Figure 4.19), which are respectively composed of millimeter-thick calcite-rich and clay-rich layers, centimeter-scale calcite-rich burrow network in clay-rich matrix, and a m-range of clasts floating in matrix with a variety of size and composition. As the samples are processed (e.g., grinded for mineralogy analysis), these end-member components will be mixed together, resulting in a "mixed" or an averaged result which underrepresents the actual distribution of rock properties within the sampled volume. Although unavailable at such a sub-centimeter scale, porosity can also be different for these components and further results in variations in other rock properties (e.g., sonic velocity). One example is the presence of PF-1 and PF-3 as centimeter-scale layers in P-Facies 5, all of which may exhibit different porosity (Figure 4.8). Considering the effect of burrows in porosity (e.g., Gingras et al., 2012), the intervals with varying amounts of

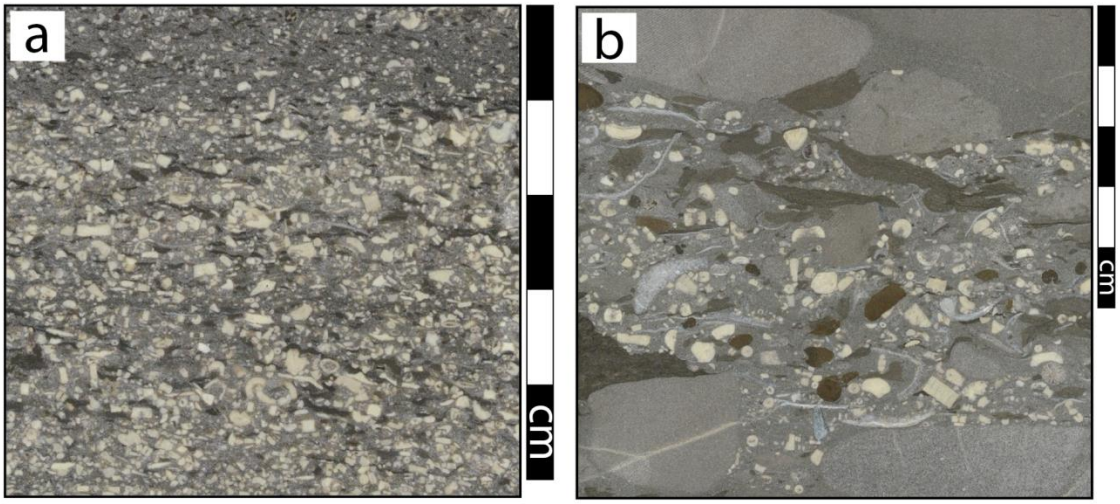

Figure 4.19. Debris flow deposits, which are scattered in the MISS/STACK cores, are composed of millimeter-scale (a) and centimeter-scale (b) clasts floating in muddier (a) and grainier (b) matrix. They can be either unsuitable (a) or suitable (b) for rebound hardness test, which is respectively due to the closely packed, sand-sized skeletal grains with a similar size range (0.5 to 2 mm) that is close to the size of the testing tip of the equipment (less than 1 mm) (a) and the presence of gravel-sized clasts (can be larger than 1 cm in size) (b).

bioturbation, which is common in the MISS/STACK cores (Figure 4.6d), can be compartmentalized in porosity as well. Such a mismatch between the heterogeneity of rock properties and the averaging of core data can further contribute to the scattered data pattern as observed in this study. In addition to potentially variable petrophysical properties, these end-member components can also create heterogeneity in rock strength at a millimeter to centimeter scale (also in Zahm and Enderlin, 2010), which further contributes to the scatter in the data. Evidence includes higher RHN in the burrow network (Figure 4.20a), in the calcite-rich layers (Figure 4.20b), and in a special case, in the cherty layers (Figure 4.20c). Hack et al. (1993) and Brooks et al. (2016) document a similar effect of contrasting grain size and bioturbation, respectively, in creating a scattered data pattern when correlating RHN to unconfined compressive strength. These observations further illustrate the importance of selecting the testing locations based upon a detailed, core-based facies description across a variety of scales (e.g., centimeter to meter) to capture the variability of rock strength in these thinly layered intervals, rather than using a fixed testing frequency (e.g., 1 meter of core per data; see Daniels et al., 2012,

Ritz et al., 2014). In addition to the scattered data pattern, the RHN data exhibit overlapping data ranges among individual facies (groups) (Figure 4.8, 4.11, 4.12, 4.14, 4.15). For example, there are data points of PF-5 where the calcite content is around 30% and the quartz content is approaching 50% (Figure 4.7g, h), with both mineralogy falling within the data range PF-1 and PF-2. For PF-4, calcite content can be higher than 60% (Figure 4.6e, f), corresponding to a higher abundance of the calcite-rich burrow network and interstitial calcite cement. In these two cases, these seemingly "outlier" data points represent the siliciclastic-rich and calcite-rich variants of the typical PF-5 and PF-4, respectively. Such an overlapping data pattern among different PF groups reflects the variability of rock properties across a variety of scales (e.g., centimeter to meters) within the same and among different facies, further indicating the caveat of applying the same conversion regardless of facies and rock types.

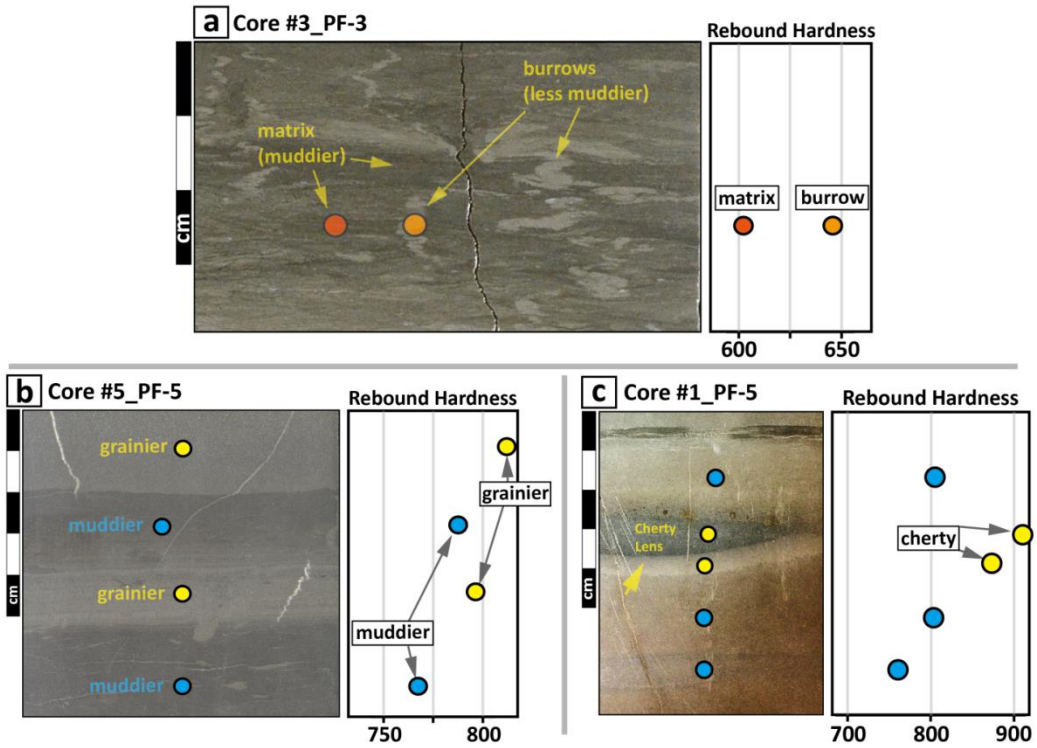

Figure 4.20. From a stratigraphic perspective, rebound hardness (RHN) values can show variability across a variety of scales, which, at a centimeter scale, can be related to the presence of burrows (a) and alternation between grainier and muddier layers (b, c). Burrows, when being more grainer than the mud-rich matrix, can show high RHN values (a). For layered intervals, grainer layers can show higher or similar RHN values as compared to muddier layers (b). In a special case, cherty layers show distinctively higher RHN values than the surrounding less-chertier or non-cherty layers (c).

Despite the presence of these potentially "outlier" data points, a strict definition of outliers is challenging and potentially problematic to achieve. Because the XRD mineralogy and porosity data from the MISS/STACK cores were sampled using a fixed frequency by service companies (largely spaced at intervals of 2 meters to 5 meters within the core per sample), the quantity of the data points does not reflect the relative thickness of the facies types where these data were sampled. Even if the data were sampled based upon the distribution of facies, it is difficult to evaluate if certain data points are truly outliers or not solely based upon the amount of the data relative to the thickness of corresponding facies within individual cores. This can be further complicated by the variable mineralogy within a particular facies (e.g., burrow network vs. matrix in PF-4, calcite-rich vs. clay-rich laminae in PF-5; Figure 4.6d, e; 4.7e), and the changing facies types and porosity vertically within individual wells and laterally among individual wells within a larger-scale stratigraphic architecture that is changing across different parts of the play (Figure 4.9). Perhaps more importantly, these "outliers" can actually reflect the variabilities in rock properties. Examples include the high porosity data points of P-Facies 1 (Figure 4.4d, 4.12), calcite-rich data points of P-Facies 4 (Figure 4.6e), mud-rich data points of P-Facies 5 (Figure 4.7c), and cherty zones with distinctively high RHN values (Figure 4.20c), all of which reflect the inherent depositional dynamics and the unique diagenesis and porosity development. Therefore, removing these data points, simply because of their "anomalous" values without understanding the mechanism behind these values, will create significant bias in the data and the resultant modeling results. In this sense, this study adopts a conservative approach by including all of the data points in the statistical analysis, for maximizing the data integrity as discussed above. On the other hand, despite such an effort in capturing the rock strength of these end-member components, it is questionable how the RHN of these components can be integrated with the "averaged" rock data, because it is not meaningful to derive an arithmetic mean of RHN for these components (e.g., Aydin, 2008). In this study, certain mineralogy and porosity data of these intervals were

sampled from a range of depths in core (i.e., 7 cm/0.25 ft) by service companies. In this case, the RHN data were tested around the middle point within such intervals, which appear to be the most viable way to minimize data bias. Because of such uncertainties in establishing the connection between RHN and the compositional and petrophysical heterogeneity of certain intervals at a fine scale, plotting RHN from a stratigraphic perspective (i.e., by depth) appears to be the most feasible way to capture the variability in rock strength of these intervals.

Thirdly, the overlapping and scattered data pattern may simply be a function of overlapping and scattering in the petrophysical properties and elastic parameters in different facies. This can be related to diagenetic alteration (Chang et al., 2006), variabilities in pore types (i.e., same porosity does not necessarily produce same sonic velocity for different pore types; Eberli et al., 2003) and mineralogical variations (Chang et al., 2006; Sone and Zoback, 2013a), and the interactive effect of these rock properties in determining RHN (Figure 4.11, 4.14, 4.15), the latter of which is suggested by the data trends in all the correlations (Figure 4.11, 4.12, 4.14, 4.15). In other words, RHN is possibly controlled by multiple petrophysical and rock mechanical parameters (also in Sachpazis, 1990; Ritz et al., 2014), and such a multivariate control can further contribute to the scatter and overlapping data pattern. In this sense, fit modeling analysis is necessary to evaluate the controlling factors of RHN, which will be addressed in the following sections. Lastly, potential experimental errors may further contribute to the loosely constrained data pattern. To begin with, core data (e.g., mineralogy, porosity) and RHN are not necessarily tested in the exact same sample. Samples for core data are often acquired at the edge or bottom of the core slab samples, which are not suitable for RHN test. Also, the core slab samples can be shifted during storage and transportation, making it difficult to achieve a precisely consistent sampling location between RHN and core data. For porosity measurements, cracks can develop during the sample preparation and measurement process, particularly for samples with high clay content (e.g., PF-1), and result in the overestimation of porosity. This can be a particularly critical issue for the

MISS/STACK porosity data, many of which are measured from crushed samples. However, because these data were provided by service companies, it is almost impossible to evaluate the sample condition for individual data points. When testing RHN for rocks with low strength (e.g., PF-1 and PF-2), cracks can be generated beneath the core surface during the impact, lowering the RHN value by a certain extent (also in Aydin, 2008).

4.5.3.2 Effect of Diagenesis and Burial Condition

Although the statistical patterns between RHN and mineralogy can be related to generalized rock fabric, there are diagenetic processes related to variable fluid composition and burial-exhumation cycles, many of which are difficult to resolve, that can affect rock mechanical properties. These events, such as compaction, pressure dissolution, and recrystallization, are undoubtedly critical in determining rock mechanical properties at different stages in a dynamic way, leading to the present-day rock mechanical stratigraphy and porosity distribution. On the other hand, the diagenetic processes that can significantly alter the original sedimentary structures, such as pervasive dolomitization and exposure-related porosity alteration, are not observed in this study. Even for the facies that consists of a rock framework dominated by clay-rich matrix (e.g., PF-1), which points to potentially the highest vulnerability of porosity loss due to compaction, the negative trend between RHN and porosity (PF-1 in Figure 4.12) indicate that burial did not homogenize the porosity to create consistent porosity values. These observations make it valid to relate present-day rock strength (i.e., RHN) with facies.

When interpreting the statistical pattern between RHN and rock properties, another challenge is the variabilities of petrophysical and rock mechanical properties at surface and reservoir conditions. Notably, an offset in testing condition is present for core and wireline log data (surface vs. reservoir conditions), and may have further contributed to the lack of pattern in RHN-to-log correlation. In addition, the presence of differential stress, variable fluid composition and saturation, and rock-fluid interaction in the subsurface can affect acoustic anisotropy (e.g., Vp-Vs

ratio) and elastic properties (e.g., bulk modulus, shear modulus) (Han et al., 1986; Baechle et al., 2005; Sone and Zoback, 2013a, b; Altowairqi et al., 2015). Therefore, the petrophysical (e.g., porosity, sonic velocity) and rock mechanical properties (e.g., RHN, elastic parameters) are expected to exhibit variability at reservoir conditions as compared to surface conditions, and may even possibly be "reversed" for certain rock types (e.g., Nygård et al., 2006). In this sense, how the statistical patterns as presented in this study can be applicable at reservoir condition is questionable. In addition, differential burial condition may have homogenized the rock mechanical properties among different facies, which may have contributed to the overlapping data pattern. In specific, certain data points of PF-1 and PF-2 exhibit RHN values that approach the higher end of PF-5 (800 HLD; Figure 4.12). The RHN values can also be similar between the end-member components with distinct mineralogical contrast, such as between the calcite-rich and clay-rich layers (Figure 4.20b). More "enhanced" compaction associated with the mud-supported rock framework may be a contributing factor, and may explain the observations in Zahm and Enderlin (2010) that tight siliceous mudstone exhibit similar unconfined compressive strength with porous grainstone.

4.5.3.3 Definition of Facies

In addition to the potential effect of rock fabric and diagenesis on RHN, the definition of facies directly affects the statistical pattern at a facies group scale (Figure 4.12). Because of the descriptive criterion and the "transitional" mineralogy of certain facies, designating an unambiguous facies type is challenging for certain intervals, which is further accentuated by the lack of clear-cut, distinctive contacts between certain facies. Consequently, certain data points can be equivocally defined as multiple types of P-Facies, which may have artificially widened the data range of certain facies (i.e., "outlier" data) and resulted in the scattered and overlapped data pattern. Examples include the coexistence of burrowed and bioturbated intervals (Figure 4.6d) and the presence of calcite-rich PF-4 (Figure 4.6e), and siliciclastic-rich PF-5 (Figure 4.7c, g),

which may alternatively be interpreted as bioturbated PF-5, and PF-3 or PF-2, respectively. These scenarios reflect a lack of distinctive variations in depositional energy associated with the relatively deeper water setting, which is common for mixed carbonate-siliciclastic, "unconventional" reservoir rocks (e.g., Bakken play; Sarg, 2012). Because the similar appearance of these intervals in core, even possibly in wireline logs (e.g., gamma-ray logs; Figure 4.9), it is critical to tie detailed core-based facies descriptions with wireline log data prior to conducting rock typing solely based upon wireline log signature. On the other hand, because of their overall consistent rock fabric and dominant sedimentary structures as compared to the "typical facies", these "outlier" facies are included as part of the "typical" facies. In cases where thin layers of multiple types of facies are alternatively present within a certain interval (e.g., Figure 4.6d), the dominant facies is designated using the facies with the highest area percentage in core, when possible. Despite these potential uncertainties, the mudstone-siltstone (PF-1 to PF-4) and silty limestone (PF-5) assemblages can be differentiated with relatively high confidence in core and wireline logs (Figure 4.9). From the perspective of reservoir characterization at a play scale, these are the facies divisions that exhibit distinct wireline log response (e.g., distinctively low GR values for "typical" PF-5; Figure 4.9) and define the "third-order" sequences which are the basic stratigraphic unit for regional- to sub-regional-scale correlation (Figure 4.9; also in Gao and Wang, 2017; Wang et al., 2019, in press). As further suggested by the distinctively different statistical pattern with core data at a facies group scale (PF-1 to PF-4 vs. PF-5), RHN analyzed within a proper facies grouping scheme can be valuable in reservoir studies, as discussed in the previous sections.

4.5.3.4 Effect of Sample Size

Sample size has been documented as a factor that affects RHN, although most studies use a Schmidt Hammer to test block rock samples (e.g., Verwall and Mulder, 1993; Amaral et al., 1999; Demirdag et al., 2008; Ritz et al., 2014; Brooks et al., 2016). Brooks et al. (2016) documented a

threshold volume (187 cm^3) for core plug samples, under which the RHN values decrease drastically. Using the Vaca Muerta plug samples which exhibit highly variable heights (Table 4.1), this study reveals a similar effect of plug height on RHN. When comparing RHN tested in plugs with the ones tested within the same core at the same facies (adjacent to the location of plug samples separated by a distance of 2 to 10 cm, when possible), the difference in RHN values firstly shows a decreasing trend as the plug height increases (Figure 4.21). As the plug length approaches 3.16 cm, which is the height of a particular plug sample, the value of this difference largely stabilizes within 100 HLD (Figure 4.21). Therefore, this "3.16 cm" threshold is considered as the "minimum plug height" for the plug samples to yield valid RHN results in this study. To make the data selection criteria consistent with the one used for the MISS/STACK core slab samples, only the plug samples showing a less-than-50 HLD in such difference (horizontal dashed line in Figure 4.21) are adopted for the statistical analysis. Considering the binned nature of the plug height of the Vaca Muerta samples, it is questionable how the "3.16 cm" cut-off accurately corresponds to the "minimum sample height" for valid RHN results in different facies types. On the other hand, as suggested by Figure 4.21, it appears that this value is above the minimum threshold for valid RHN results, and therefore, can be used as a generalized guidance for sample preparation, at least for the Vaca Muerta samples of this study. In addition, the corresponding threshold plug volume (15.5 cm^3; 1 inch/2.5 cm in diameter, 3.16 cm in height) is distinctively smaller than the one reported by Brooks et al. (2016) and the recommendation of ASTM Standard (2005) for NX-sized plug (123 cm^3 for plug samples with a diameter of 2.16 inch/5.48 cm and a height of 5.2 inch/10.9 cm), for which this study was not able to test due to the limited size range of the plug samples available. In addition to affecting the RHN results, plug size also affects the statistical pattern between RHN and rock properties. As compared with the data from all plug samples (n=135), the plug samples above the "3.16 cm" threshold (n=25) exhibits similar linear trends but with higher R when correlated with the data in Figure 4.14 and Figure 4.15, although this may simply be a function of fewer data points.

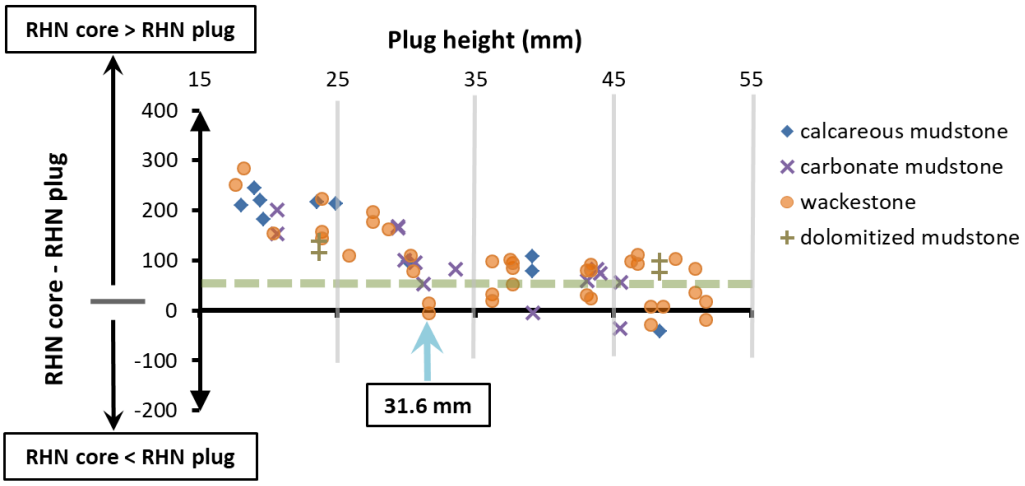

Figure 4.21. Cross-plot showing the relationship between the height of Vaca Muerta plug samples (horizontal axis) and the difference between RHN tested in plug and in the same core (adjacent to the location of plug samples, when possible) at the same facies (vertical axis). As the plug height passes 31.6 millimeters (vertical blue arrow), which is the height of a particular plug sample, the value of such a difference largely stabilizes within the range of 100 HLD. To make the selection criterion of "valid RHN data" consistent with the one used for the MISS/STACK data, only the plugs exhibiting less-than-50 HLD in such a difference (dashed bold horizontal line) are utilized for statistical analyses. For reference, thickness of the Vaca Muerta and MISS/STACK core is 49 mm and 23 mm, respectively.

For the MISS/STACK core slab samples, they exhibit a relatively consistent thickness of around 2.3 centimeters. Because of the proprietary nature of these samples, the effect of slab sample size cannot be tested in this study. Although this thickness is far less than the thickness (25 cm) recommended by the manufacturer for block concrete and metal samples that are lighter than 5 kg, the RHN tested from the slab samples of this study can be valid for a relative evaluation, as long as the sample thickness at the testing location of RHN is consistent (Amaral et al., 1999). This is achieved by testing along the center line of the core slab samples and avoiding the sample edge to maximize sample mass and minimize sample vibration, as discussed in previous sections (Data and Method; Figure 4.2c).

4.5.4 Multivariate, Leverage, and Forward Regression Analyses

4.5.4.1 Multivariate Analysis

Regarding the statistical relationship among the other rock properties, porosity of the MISS/STACK data exhibits similar absolute r values with RHN (r=-0.52), calcite content (r=-0.46), and bulk clay content (r=0.49) (Figure 4.16). This pattern may explain the similar clustering of data by P-Facies groups in porosity and mineralogy (Figure 4.12). In addition, considering that the calcite content is largely contributed by skeletal components and interstitial cements, the strong negative correlations of calcite content with quartz (r=-0.73) and bulk clay content (r=-0.72) (Figure 4.16) point to the reciprocal relationship of carbonate production with siliciclastic input. Despite the relatively low correlation strength (r=0.49), a significant part of the clay content data show strong positive correlation with porosity (Figure 4.16). With a similar trend that has been documented in other studies on "unconventional" reservoir rocks (e.g., Sone and Zoback, 2013a), this pattern indicates that the clay minerals, which contain abundant micropores, are a primary contributor to reservoir quality.

In the Vaca Muerta data, sonic velocity shows a strong correlation with porosity (r=-0.90 for Vp and Vs) and carbonate content (r=0.80 for Vp and Vs) (Figure 4.17), indicating that porosity and carbonate content affect sonic velocity, which has been documented in several other studies (e.g., Eberli et al., 2003). Similar to the porosity-to-calcite relationship in the MISS/STACK data, porosity exhibits a negative trend with carbonate content, but with a much more substantial correlation (r=-0.92, as compared to -0.46 in MISS/STACK data; Figure 4.17). Considering the reciprocal relationship between carbonate and clay content, this trend potentially provides indirect evidence for the critical contribution of clay to the reservoir quality of the Vaca Muerta. Lastly, the strong negative correlation between porosity and elastic parameters (Young's modulus, bulk modulus, and shear modulus; Figure 4.17) has also been documented in several studies targeting the mixed carbonate-siliciclastic rocks (e.g., Eberli et al., 2003; Baechle et al., 2005, 2008; Fournier et al., 2011; Altowairqi et al., 2015; Abatan et al., 2016).

4.5.4.2 Leverage Analysis

As mentioned in previous sections (Sect. 4.5.3.1), RHN is likely resultant from the interaction of multiple rock properties. This hypothesis is supported by the results of leverage analysis. When predicting the RHN of both MISS/STACK and VM, different amounts and types of input parameters exhibit substantial significance in different facies grouping schemes (Figure 4.18), confirming that RHN is resultant from the interaction of multiple rock properties (i.e., multivariate control), which may also contributes to the lack of distinctive trends between the RHN data and the sequence stratigraphic framework (Figure 4.9) . More importantly, this indicates that these parameters exhibit variable significance in affecting RHN which points to a complex relationship between rebound hardness and rock properties, and that a detailed, core-based facies characterization is critical in this workflow. In addition, parameters with substantial significance are clearly defined in MISS/STACK, whereas such parameters are absent in Vaca Muerta (Figure 4.18). Such a discrepancy is likely related to the distinctive difference in the type and quantity of data between these two sample sets (Table 4.1), the latter of which is the reason why the leverage analysis is not successful for the individual Vaca Muerta facies. Another observation worth noting is that the parameter with the highest significance level in determining RHN does not necessarily correspond to the highest correlation coefficient (r) from a bivariate and multivariate perspective. In the MISS/STACK data, bulk clay shows the highest significance and highest r in all PF combined and PF-1/2 (Table 4.4). For PF-3/4 and PF-5, porosity exhibits the highest significance, whereas bulk clay and quartz respectively show the highest r (Table 4.4). Such variabilities in the analytical results between effect leverage and bivariate/multivariate analyses suggests that it can be problematic to infer the relative significance of these parameters in determining RHN solely based upon r. On the other hand, when ranked by r from both a bivariate and multivariate perspective, the four parameters (i.e., three XRD mineralogy, porosity) are in the same order for all facies grouping schemes (Table 4.4), indicating the relatively consistent r values using a bivariate (i.e., 2D cross-plots) and multivariate approach. The difference in r values are minor for individual parameters (no larger than 0.1; Table 4.4), which is

likely due to the inconsistent data quantity in bivariate (Figure 4.11, 4.12) and multivariate analysis (Figure 4.13). In addition, the difference in FDR LogWorth values of porosity with bulk clay and quartz content of the MISS/STACK data is distinctively higher in PF-5 than in PF-3/4 (Figure 4.18), indicating that porosity exerts the most predominant significance on RHN in PF-5. This may explain the negative trend between RHN and calcite content in PF-5 (r=-0.25), which is the only case where the statistical trend of a certain PF group is inverse with the trends in other PF groups (Figure 4.12) and all PF combined (Figure 4.11). This hypothesis can be further supported by the negative trends of calcite content of PF-5 with quartz (*r*=-0.90), bulk clay (*r*=-0.51), and porosity (*r*=-0.15), all of which indicate that these three parameters do not exhibit an inversing effect on the statistical pattern of the RHN-to-calcite correlation of PF-5.

4.5.4.3 Forward Regression Analysis

For the MISS/STACK data, three models (i.e., RHN, quartz, bulk clay; RHN, calcite, bulk clay; RHN, calcite, quartz, bulk clay) show the highest and close-to-highest adjusted R^2 across all

Relative Order of Parameters Ranked By FDR LogWorth and R	**FDR LogWorth**	***r* (bivariate;** Figure 11, 12**)**	***r* (multivariate;** Figure 16, 17**)**
All PF combined	clay (>>2), ϕ (>>2), qtz (>>2), cal	clay (-0.78), ϕ (-0.48), cal (0.35), qtz (0.24)	clay (-0.78), ϕ (-0.52), cal (0.37), qtz (0.22)
PF-1 and PF-2	clay (>>2), ϕ, qtz, cal	clay (-0.84), cal (0.51), qtz (0.31), ϕ (-0.18)	clay (-0.77), cal (0.42), qtz (0.25), ϕ (-0.18)
PF-3 and PF-4	ϕ (>>2), clay, qtz, cal	clay (-0.64), ϕ (-0.61), cal (0.31), qtz (0.05)	clay (-0.69), ϕ (-0.61), cal (0.41), qtz (-0.03)
PF-5	ϕ (>>2), clay, qtz, cal	qtz (0.45), ϕ (-0.28), clay (-0.27), cal (-0.25)	qtz (0.48), ϕ (-0.39), clay (-0.29), cal (0.27)

Table 4.4. Table showing the ranking of the four input parameters of the MISS/STACK data (calcite, quartz, bulk clay, porosity) in terms of relative significance (FDR LogWorth values) and correlation coefficient (*r*) from a bivariate and multivariate perspective. Bivariate *r* values are from Figure 11 and Figure 12. Multivariate *r* values are from the multivariate analysis of individual P-Facies groups (not shown here). For FDR LogWorth, the data types showing distinctively higher-than-2 values are marked in gray. For bivariate and multivariate *r*, the data

types showing the highest absolute *R* values are highlighted in gray. cal: calcite content. qtz: quartz content. ϕ: porosity. For FDR LogWorth values, ">>2" means "distinctively higher than 2". See text for discussion.

facies grouping schemes (Table 4.2). This suggests that a similar suite of input parameters may be applicable in predicting porosity at a whole core scale. For these three models, similar adjusted R^2 are observed in all PF combined (around 0.35) with PF-5 (around 0.3) and in PF-1/2 and PF-3/4 (0.5 to 0.7), the latter of which show an increase in adjusted R^2 values (blue and gray cells; Table 4.2). Such variations in correlation strength among different facies grouping schemes further illustrate the importance of facies types in predicting porosity from RHN and mineralogy. For all facies grouping schemes (Table 4.2), adding RHN enhances the prediction of porosity by increasing the adjusted R^2 by around 0.1 (e.g., all PF combined - RHN with quartz and bulk clay) to >0.3 (e.g., PF-3/4 - RHN with quartz), indicating the potential value of RHN in assisting the modeling of porosity. However, the <0.5 adjusted R2 in most of these models indicates that RHN and the three types of XRD mineralogy available in this study are not sufficient to yield substantial prediction for porosity. In contrast, compared to the MISS/STACK data when all P-Facies is combined (adjusted R^2 values are around 0.35; Table 4.2), the correlation confidence of the Vaca Muerta data is distinctively more substantial, as indicated by close-to-0.9 in highest adjusted R^2 when predicting porosity and close-to-0.8 in highest adjusted R^2 when predicting Vp (Table 4.3), indicating the potential value of these combinations in such predictions. On the other hand, by adding RHN in the model, the increase in the adjusted R^2 values range from close to 0 (porosity – from Vp to RHN and Vp) to 0.18 (Vp – from carbonate content to RHN and carbonate content), with such an increase being mostly <0.1 (Table 4.3). In this sense, the effect of RHN in enhancing the prediction of rock properties in the Vaca Muerta data does not appear as significant as the MISS/STACK data. In particular, a similar combination of RHN with calcite content in the MISS/STACK data and with the carbonate content in the Vaca Muerta data respectively yields the highest and close-to-highest adjusted R^2 in predicting porosity in the MISS/STACK data (Table 4.2) and in predicting porosity and Vp in the Vaca Muerta data (Table 4.3). This indicates

the potential value of this combination of parameters in modeling petrophysical properties in similar types of mixed carbonate-siliciclastic reservoirs.

For the effect leverage and forward regression analyses of this study, discrepancy in data type and quantity can create uncertainties in the analytical results, such as the lack of input parameters showing substantial significance in the Vaca Muerta data (Figure 4.18). Between the MISS/STACK and Vaca Muerta data, sonic velocity and elastic parameters are missing in the MISS/STACK data, whereas bulk clay and quartz content are missing in the Vaca Muerta data (Table 4.1). Therefore, the relative significance of these "missing" parameters in determining RHN, as wells as how these "missing" parameters will affect the relative significance of the existing parameters in determining RHN and the prediction of porosity and sonic velocity, need to be further tested. Also, the data quantity of the Vaca Muerta data is far more limited (n=25) as compared to the MISS/STACK data (n=243) (Table 4.1), which can create additional uncertainties to the analytical results of the Vaca Muerta data. To address this issue, the most ideal situation in sample and data preparation is analyzing the same data types with a similar, "decent" amount of data in each data type for both areas.

4.5.5 Summary: the Impact of Facies Variability and Sequence Stratigraphic Framework on Rebound Hardness Analyses

In particular, the importance of a detailed, core-based facies characterization is illustrated in both the bivariate correlation between RHN and rock properties and the fit modeling analysis. Specifically, the facies types and corresponding relative abundance not only show vertical variations within a depositional sequence (sub-meter in scale), among individual sequences (meters in scale), and at a formation scale within individual well (tens of meters in scale), but exhibit variabilities among individual wells across different parts of the basin at a sub-regional to regional scale (tens of square miles/kilometers in size) (also in Gao and Wang, 2017). This further implies that the vertical stacking and lateral variability of these facies and associated

porosity variations, both of which can be characterized and potentially predicted using a core-based sequence stratigraphic framework (Wang et al., 2019, in press), play a vital role in the reservoir characterization and modeling from both a petrophysical and rock mechanical perspective across a variety of scales. As further indicated by the statistical trends among mineralogy, reservoir quality, and RHN, an integration of these data within a core-based sequence stratigraphic framework can potentially guide the mapping and predicting the optimal targeted zones at multiple scales and the production design from both a reservoir quality and stimulation perspective, with a more time- and cost-efficient and sample-conservative delivery of relevant data as compared to conventional laboratory analyses. On the other hand, despite the partition of data by facies groups (Figure 4.11 to 4.15), the lack of distinctive patterns between RHN and the sequence stratigraphic framework (Figure 4.9) implies the complex controlling factors of RHN, which is corroborated by the scattered, overlapped data pattern in 2D cross-plots (Figure 4.11 to 4.15) and the observations in the leverage analysis (Figure 4.18).

4.6 Conclusions

Despite the limitations in the bivariate correlations with rock properties, rebound hardness (RHN) can be a valuable tool for reservoir characterization and production design. Correlative trends are present between RHN and XRD mineralogy, porosity, and elastic parameters from the "Mississippian Lime"/STACK play and the Vaca Muerta Formation, with scatter and overlapped data ranges being present among different facies with highly variable correlation coefficient, which is likely responsible for the lack of distinctive trends when comparing RHN with the sequence stratigraphic framework defined from the "Mississippian Lime"/STACK cores. These observations indicate that RHN carries variable capacities in accurately predicting reservoir properties from a bivariate perspective, and therefore, cannot serve as a substitute for conventional laboratory tests for these parameters. However, certain parameters, such as bulk clay content in the MISS/STACK data and porosity in the Vaca Muerta data, exhibit strong

correlation with absolute *r* values approaching 0.8, indicating that RHN can potentially be a valuable tool in providing a timely estimation of these parameters. In addition, the clustering of data by P-Facies groups in these correlations, which can be tied with rock fabric of individual P-Facies groups, suggests that RHN can aid in designing an integrated rock typing scheme from a petrophysical and rock mechanical perspective and the importance of a facies-based sampling protocol. This also indicates that RHN can provide valuable guidance for selecting core plug samples for detailed laboratory analysis, which is crucial in the early stage of core-based exploration projects but can be difficult and expensive to achieve with high data density for the low-porosity and low-permeability "unconventional" reservoir rocks. The statistical trends between RHN and rock properties point to a multivariate control of RHN, which is confirmed by fit modeling analysis. Leverage analysis suggests that bulk clay content and porosity exhibits the most significant control on RHN for the MISS/STACK data, with variabilities being present in different facies grouping schemes. This further illustrates the importance of a systematic facies characterization for interpreting the controlling factors of RHN. Forward regression analysis reveals that the confidence level of predicting porosity and Vp can be enhanced when combining RHN with mineralogy and sonic velocity, indicating the potential value of such combination of parameters in modeling reservoir properties.

4.7 References

Abatan, A.O., O.D. Akinyemi, J.A. Olowofela, G.A. Ajiboye, and F.K. Salako, 2016, Experimental investigation of factors affecting compressional and shear wave velocities in shale and limestone of Ewekoro formation of Southern Nigeria sedimentary basin: Environmental Earth Sciences, 75: 1442, 20p.

Altowairqi, Y., R. Rezaee, B. Evans, and M. Urosevic, 2015, Shale elastic property relationships as a function of total organic carbon content using synthetic samples: Journal of Petroleum Science and Engineering, v. 133, p. 392-400.

Amaral, P. M., L. Guerra Rosa, and J. Cruz Fernandes, 1999, Determination of Schmidt rebound hardness consistency in granite: International Journal of Rock Mechanics and Mining Sciences, v. 36, p. 833-837.

Aoki, H. and Y. Matsukura, 2008, Estimating the unconfined compressive strength of intact rocks from Equotip hardness: Bulletin of Engineering Geology and the Environment, v. 67, p. 23-29.

Aydin, A., and A. Basu, 2005, The Schmidt hammer in rock material characterization: Engineering Geology, v. 81, p. 1-14.

Aydin, A., 2008, ISRM suggested method for determination of the Schmidt hammer rebound hardness: revised version, in R. Ulusay, ed., The ISRM Suggested Methods for Rock Characterization, Testing and Monitoring: 2007-2014, p. 25-33.

Baechle, G.T., R.J. Weger, G.P. Eberli, J.L. Massaferro, and Y.F. Sun, 2005, Changes of shear moduli in carbonate rocks: Implications for Gassmann applicability: The Leading Edge, v. 24, p. 507-510.

Baechle, G.T., A. Colpaert, G.P. Eberli, and R.J. Weger, 2008, Effects of microporosity on sonic velocity in carbonate rocks: The Leading Edge, v. 27, p. 1012-1018.

Baumgardner, R.W., H.S. Hamlin, and H.D. Rowe, 2014, High-Resolution Core Studies of Wolfcamp/Leonard Basinal Facies, Southern Midland Basin, Texas: AAPG Search and Discovery Article 10607.

Bednarz, M. and D. McIlroy, 2009, Three-dimensional reconstruction of "*phycosiphoniform*" burrows: implications for identification of trace fossils in core: Palaeontologia Electronica, v. 12, 15p.

Benjamini, Y. and Y. Hochberg, 1995, Controlling the False Discovery Rate: A Practical and Powerful Approach to Multiple Testing: Journal of the Royal Statistical Society, Series B57, p. 289–300.

Brooks, D., X. Janson, and C. Zahm, 2016, The effect of sample volume on micro-rebound hammer UCS measurements in Gulf Coast Cretaceous carbonate cores: Gulf Coast Association of Geological Societies (GCAGS) Journal, v. 5, p. 189-202.

Chang, C., M.D. Zoback, and A. Khaksar, 2006, Empirical relations between rock strength and physical properties in sedimentary rocks: Journal of Petroleum Science and Engineering, v. 51, p. 223-237.

Cheel, R.J. and D.A. Leckie, 1993, Hummocky cross-stratification: Sedimentology Review 1, v. 1, p. 103-122.

Childress, M. and G.M. Grammer, 2019, Mass transport deposits deposited along a Mississippian ramp, Mid-Continent, U.S.A., in G.M. Grammer, J. M. Gregg, J.O. Puckette, P. Jaiswal, M. Pranter, S.J. Mazzullo, and R.H. Goldstein, eds., Mississippian Reservoirs of the Mid-Continent, U.S.A.: American Association of Petroleum Geologists Memoir 116, in press.

Committee on Standardization of Laboratory Tests, 1978, Suggested methods for determining hardness and abrasiveness of rocks: International Journal of Rock Mechanics and Mining Sciences and Geomechanics Abstracts, v. 15, p. 89-97.

Daniels, G., C.A. Mcphee, Y.C. Sorrentino, and P. McCurdy, 2012, Non-destructive strength index testing applications for sand failure evaluation, SPE Asia Pacific Oil and Gas Conference and Exhibition conference paper 158326.

Demirdag, S., H. Yavuz, and R. Altindag, 2009, The effect of sample size on Schmidt rebound hardness value of rocks: International Journal of Rock Mechanics and Mining Sciences, v. 46, p. 725-730.

Eberli, G.P., G.T. Baechle, F.S. Anselmetti, and M.L. Incze, 2003, Factors controlling elastic properties in carbonate sediments and rocks: The Leading Edge, v. 22, p. 654-660.

Eberli, G.P., R.J. Weger, M. Tenaglia, L. Rueda, L. Rodriguez, M. Zeller, D. McNeill, S. Murray, and P.K. Swart, 2017, The Unconventional Play in the Neuquén Basin, Argentina – Insights From the Outcrop for the Subsurface: Unconventional Resources Technology Conference (URTeC) paper 2687581.

Fournier, F., P. Leonide, K. Biscarrat, A. Gallois, J. Borgomano, and A. Foubert, 2011, Elastic properties of microporous cemented grainstones: Geophysics, v. 76, p. E211-E226.

Frank, S., C. Frehner, and A. Akhlaghi, 2016, Portable Hardness Testing: Leeb, Portable Rockwell and UCI: Equotip Application Booklet, Proceq SA.

Gao, Z.J., and Y. Wang, 2017, Sequence stratigraphic architecture and reservoir characteristics of the “Mississippian Limestone”, north-central Oklahoma, USA, Unconventional Resources Technology Conference (URTeC) DOI 10.15530/urtec-2017-2670748.

Gingras, M. K., G. Baniak, J. Gordon, J. Hovikoski, K.O. Konhauser, A. La Croix, R. Lemiski, C. Mendoza, S.G. Pemberton, C. Polo, and J.P. Zonneveld, 2012, Porosity and permeability in bioturbated sediments: Developments in Sedimentology, v. 64, p. 837-868.

Grammer, G.M., C. M. Crescini, D. McNeill, and L.H. Taylor, 1999, Quantifying rates of syndepositional marine cementation in deeper platform environments – new insight into a fundamental process: Journal of Sedimentary Research, v. 69, p. 202-207.

Hack, H.R.G.K., J. Hingira, and W. Verwaal, 1993, Determination of discontinuity wall strength by Equotip and ball rebound tests: International Journal of Rock Mechanics and Mining Sciences and Geomechanics Abstracts, v. 30, pp. 151-155.

Han, D.H., A. Nur, and D. Morgan, 1986, Effects of porosity and clay content on wave velocities in sandstones: Geophysics, v. 51, p. 2093-2107.

JMP® User Guide: JMP® 13 Fitting Linear Models, 2016, SAS Institute Inc.

Katz, O., Z. Reches, and J.-C. Roegiers, 2000, Evaluation of mechanical rock properties using a Schmidt Hammer: International Journal of Rock Mechanics and Mining Sciences v. 37, p. 723-728.

LeBlanc, S., 2014, High resolution sequence stratigraphy and reservoir characterization of the "Mississippian Limestone" in north-central Oklahoma: Oklahoma State University unpublished Master thesis, 443 p.

Lee, J.S., L. Smallwood, and E. Morgan, 2014, New application of rebound hardness numbers to generate logging of unconfined compressive strength in laminated shale formations: 48th U.S. Rock Mechanics/Geomechanics Symposium conference paper ARMA-2014-6972.

Lee, J.S., J. Kieschnick, C. Geyer, J. Brumley, and L. DeSpain, 2016, Comparison of different methods to estimate uniaxial compressive strength in a Barnett Shale: 50th U.S. Rock Mechanics/Geomechanics Symposium conference paper ARMA-2016-455.

Nygård, R., M. Gutierrez, R.K. Bratli, and K. Høeg, 2006, Brittle-ductile transition, shear failure and leakage in shales and mudrocks: Marine and Petroleum Geology, v. 23, p. 201-212.

Ritz, E., M. Honarpour, W.F. Dula, and J.P. Dvorkin, 2014, Core Hardness Testing and Data Integration for Unconventionals, Unconventional Resources Technology Conference (URTeC) paper 1916004.

Sachpazis, C.I., 1991, Correlating Schmidt hardness with compressive strength and Young's modulus of carbonate rocks: International Association of Engineering Geology Bulletin, v. 42, p. 75–83.

Sall, J., 1990, Leverage plots for general linear hypotheses: The American Statistician, v. 44, p. 308-315.

Sarg, J.F., 2012, The Bakken – An unconventional petroleum and reservoir system: Final Scientific/Technical Report, Colorado School of Mines Bakken Consortium, Oil and Natural Gas Technology, National Energy Technology Laboratory, Office of Fossil Energy, 65 p.

Standard Test Method for Determination of Rock Hardness by Rebound Hammer Method, ASTM Standard 2005 (D5873 − 05).

Sone, H. and M.D. Zoback, 2013a, Mechanical properties of shale-gas reservoir rocks - Part 1: Static and dynamic elastic properties and anisotropy: Geophysics, v. 78, p. D381-D392.

Sone, H. and M.D. Zoback, 2013b, Mechanical properties of shale-gas reservoir rocks - Part 2: Ductile creep, brittle strength, and their relation to the elastic modulus: Geophysics, v. 78, p. D393-D402.

Thompson, T., 2016, Fracture Characterization and Prediction in the “Mississippian Limestone” in North-Central Oklahoma: Oklahoma State University unpublished Master Thesis, 139 p.

Vanden Berg, B., S. LeBlanc, and G.M. Grammer, 2019, Integrated reservoir characterization to provide insight into porosity and permeability in a mixed carbonate-siliciclastic reservoir, in G.M.

Grammer et al., eds, American Association of Petroleum Geologist Memoir 116, Mississippian Reservoirs of the Mid-Continent, U.S.A., in press.

Verwaal, W. and A. Mulder, 1993, Estimating rock strength with the Equotip hardness tester: International Journal of Rock Mechanics and Mining Sciences and Geomechanics Abstracts v. 30, p. 659-662.

Wang, Y., T. Thompson, and G.M. Grammer, 2019, Fracture characterization and prediction in unconventional reservoirs of the "Mississippian Limestone", north-central Oklahoma, USA, in G.M. Grammer et al., eds, American Association of Petroleum Geologist Memoir 116, Mississippian Reservoirs of the Mid-Continent, U.S.A., in press.

Yaşar, E. and Y. Erdoğan, 2004, Estimation of rock physicomechanical properties using hardness methods: Engineering Geology, v. 71, p. 281-288.

Zahm, C.K. and M. Enderlin, 2010, Characterization of rock strength in Cretaceous strata along the Stuart City Trend, Texas: Gulf Coast Association of Geological Societies (GCAGS) Transactions, v. 60, p. 693-702.

CHAPTER VI

CONCLUSIONS

Part 1 (Chapter 2): Fracture Characterization and Prediction in Unconventional Reservoirs of the "Mississippian Limestone," North-Central Oklahoma, USA

1. In the six cores from the "Mississippian limestone"/STACK play in north-central Oklahoma, the vast majority of the natural fractures are mineralized with calcite cement. Four types of fractures are identified: ptygmatic fractures (most abundant), vertical extension fractures, shear fractures (least abundant), and zones of mixed types of fractures.

2. Fracture distribution is controlled by facies types and the sequence stratigraphic framework. The massive-bedded and hummocky cross-stratified to planar laminated packstone–grainstone (P-Facies 5) exhibits the most abundant fractures and the highest average fracture intensity. The regressive phases of the "third-order" composite sequences, which can contain abundant P-Facies 5, and are characterized by distinctively low gamma-ray values, exhibit overall higher fracture intensities than the associated transgressive phases.

3. Because these "third-order" sequences are regionally traceable by cleaning-upward gamma-ray patterns, the tie between fracture intensity and these sequences provides a valuable tool to assist in the prediction of fractures in the subsurface away from cored wells.

Part 2 (Chapter 3): Characterizing the distribution of natural fractures from outcrop in a Mississippian-aged mixed carbonate-chert system, Mid-Continent, USA

1. In the Mississippian Reeds Spring Formation, planar and nodular beds of lime mudstone and chert contain near-vertical, calcite- and quartz-cemented fractures. Fracture types are similar to the "Mississippian limestone"/STACK cores, mainly including ptygmatic and opening-mode fractures ("vertical extension fractures" in cores).

2. Chert exhibits higher average fracture intensity than mudstone, suggesting that lithology plays a role in fracture intensity. Ptygmatic fractures are the most common type in both mudstone and chert, whereas opening-mode fractures are present mostly in chert.

3. For the distribution of kinematic aperture, height, and spacing data, trends of negative exponential and power law are present, suggesting a potential of predicting fracture size and spacing distribution in this outcrop within the presented data range. The type of best-fitting trend and R^2 values vary by lithology, fracture types, and fracture height categories, pointing to a corporative effect of lithology, fracture types, and fracture-to-layering relationship on the corresponding variability.

4. The ptygmatic and opening-mode fractures likely form during different time frames as rock mechanical properties evolve. As further indicated by the different hosting lithologies, a dynamic rock mechanical history is inferred.

5. Compared with the "Mississippian Limestone"/STACK play in north-central Oklahoma, the difference in the dominant lithologies indicates that this outcrop is not a suitable direct fracture analog for this part of the play.

Part 3 (Chapter 4): Testing the Value of Rebound Hardness in Estimating Petrophysical and Rock Mechanical Properties from Core and Wireline Logs: Examples from the

“Mississippian Limestone”/STACK Play (U.S. Midcontinent) and the Vaca Muerta Formation (Argentina)

1. Correlative trends are present between rebound hardness (RHN) and XRD mineralogy, porosity, and elastic parameters for the “Mississippian Lime”/STACK play and the Vaca Muerta samples.

2. All correlations show clustering of data by facies groups, suggesting that RHN can aid in petrophysical rock typing and that a facies-based sampling protocol is important for this workflow. This also indicates that RHN can guide the sample selection for detailed laboratory analysis.

3. The scatter in these correlations indicates that RHN carries an overall limited capability in accurately predicting reservoir properties from a bivariate perspective, and therefore, cannot serve as a substitute for conventional laboratory tests for these parameters. This likely contributes to the lack of distinctive trends between RHN and sequence stratigraphic framework .

3. As suggested by the statistical trends between RHN and various rock properties, RHN is affected by multiple rock properties, and such a multivariate control of RHN is further confirmed by fit modeling analysis.

4. Leverage analysis suggests that bulk clay content and porosity exhibits the most significant control on RHN for the MISS/STACK data. Forward regression analysis reveals that the confidence level of predicting porosity and Vp can be enhanced when combining RHN with mineralogy and sonic velocity, indicating the potential value of such combination of parameters in modeling reservoir properties

APPENDICES

APPENDIX 1

ILLUSTRATIVE CORE DESCRIPTIONS

CORE #4, 5, 6

For the core description of core #1, 2, and 3, readers are referred to Leblanc (2014) and Thompson (2016).

* Leblanc, S., 2014, High resolution sequence stratigraphy and reservoir characterization of the "Mississippian Limestone" in north-central Oklahoma: unpublished Master thesis, Oklahoma State University, 443 p.
Thompson, T., 2016, Fracture characterization and prediction in the "Mississippian Limestone" in North-Central Oklahoma: unpublished Master thesis, Oklahoma State University, 139 p.

Idealized Vertical Facies Succession

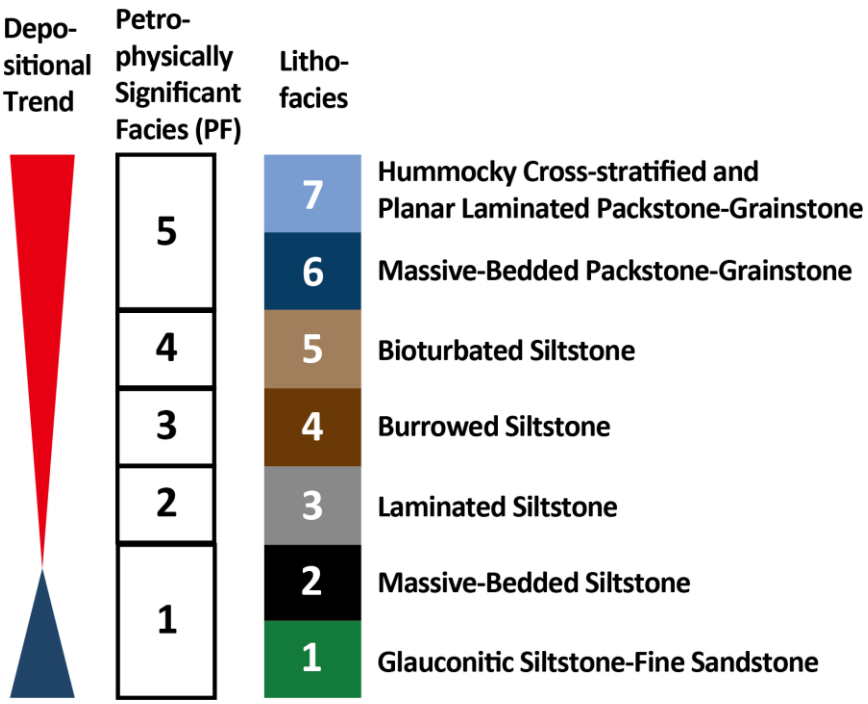

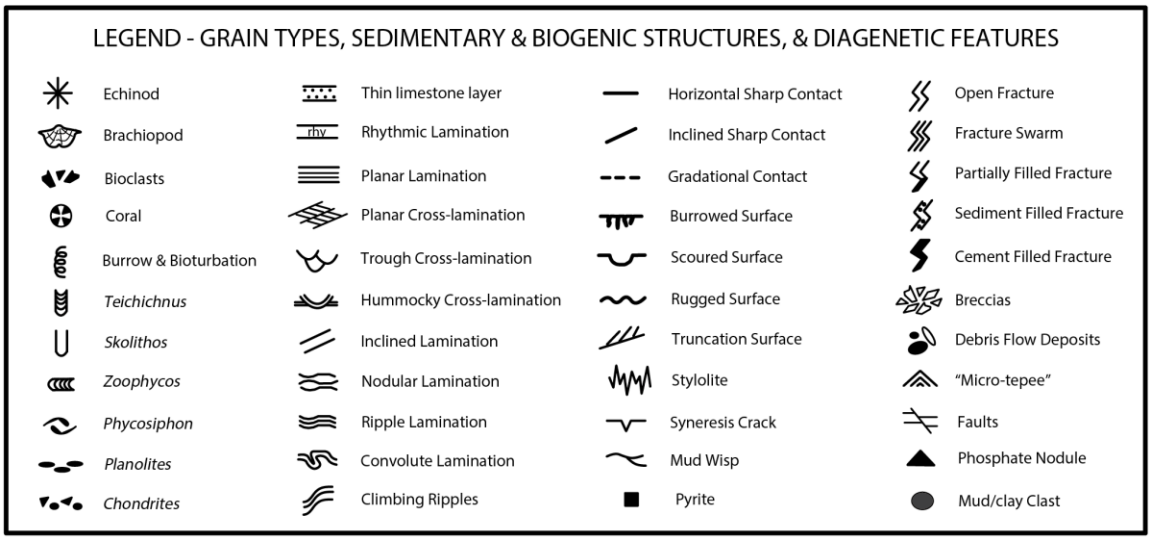

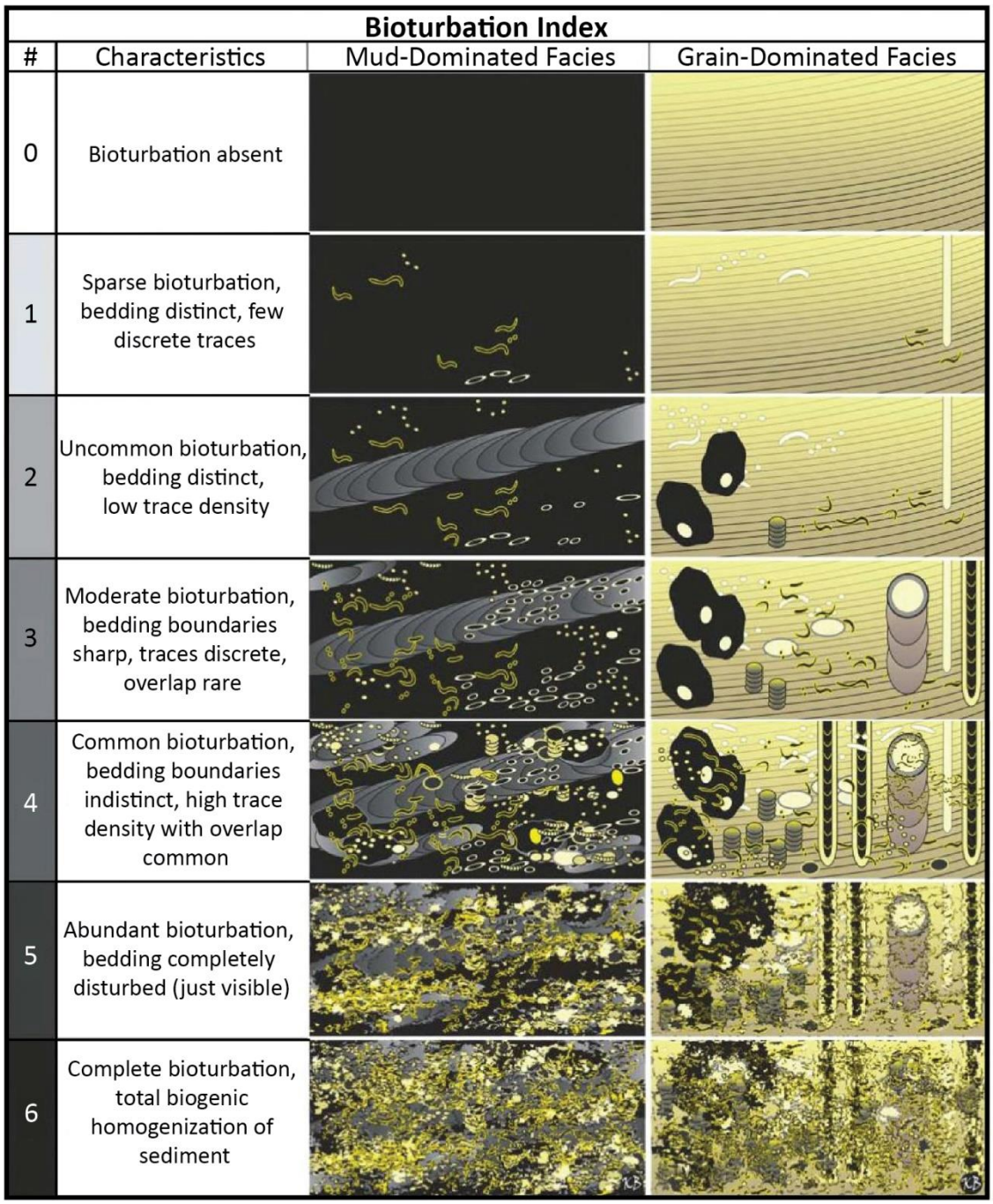

Schematic representation of bioturbation index (BI) values (from MacEachern and Bann, 2008)

*MacEachern, J.A., Bann, 2008, K.L., The role of ichnology in refining shallow marine facies models, *in* Hampson, G.J., Steel, R.J., Burgess, P.M. and Dalrymple, R.W., eds, Recent advances in models of siliciclastic shallow-marine stratigraphy, Society for Sedimentary Geology (SEPM) Special Publication 90, p. 73-116.

Core #4, Kingfisher County, Oklahoma

Formation: Mississippian Limestone

Mississippian Interval: 8590.88'-9168.05'

Core #1: 8568'-9019'
Core #2: 9019'-9261.8'

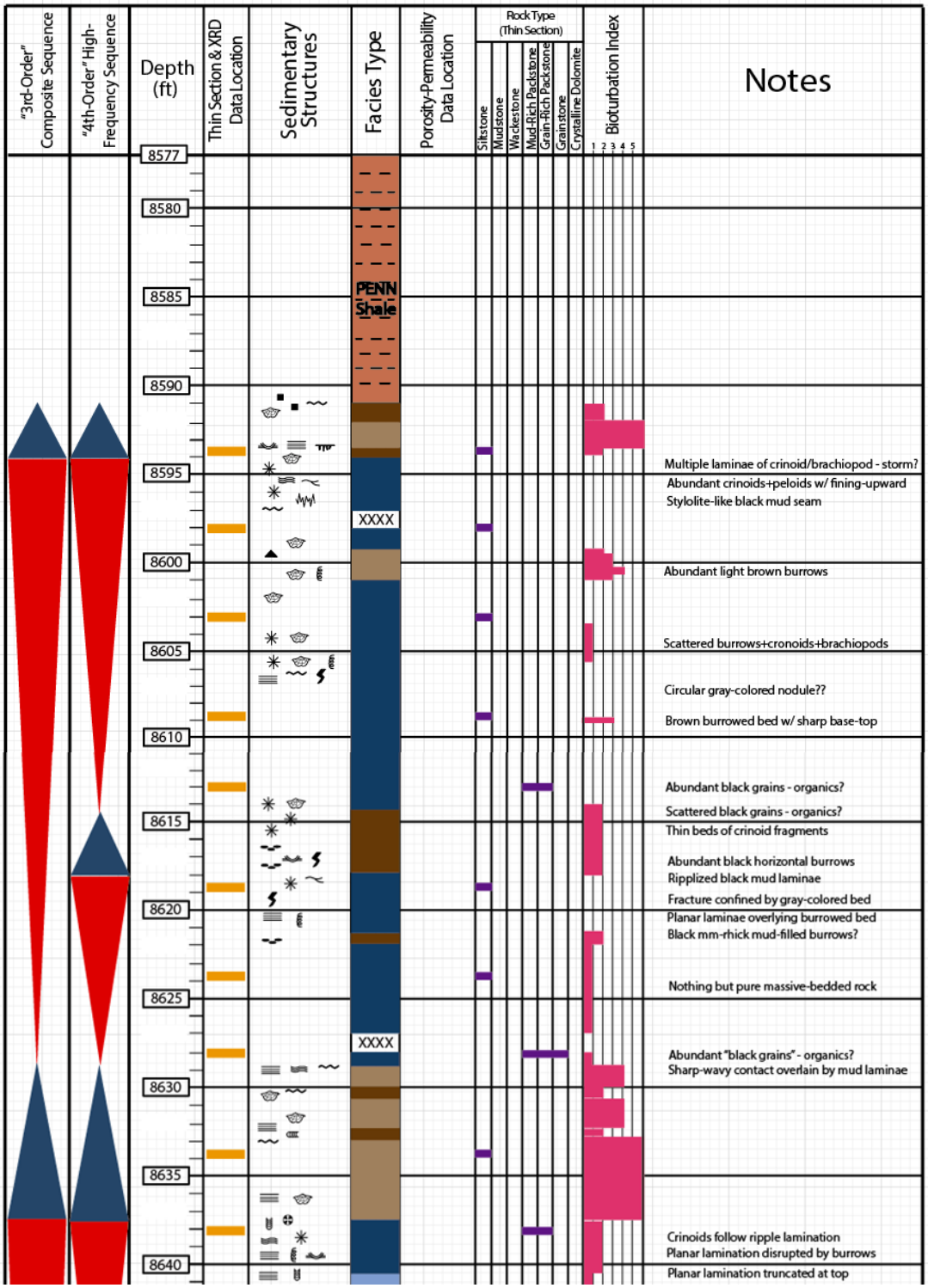

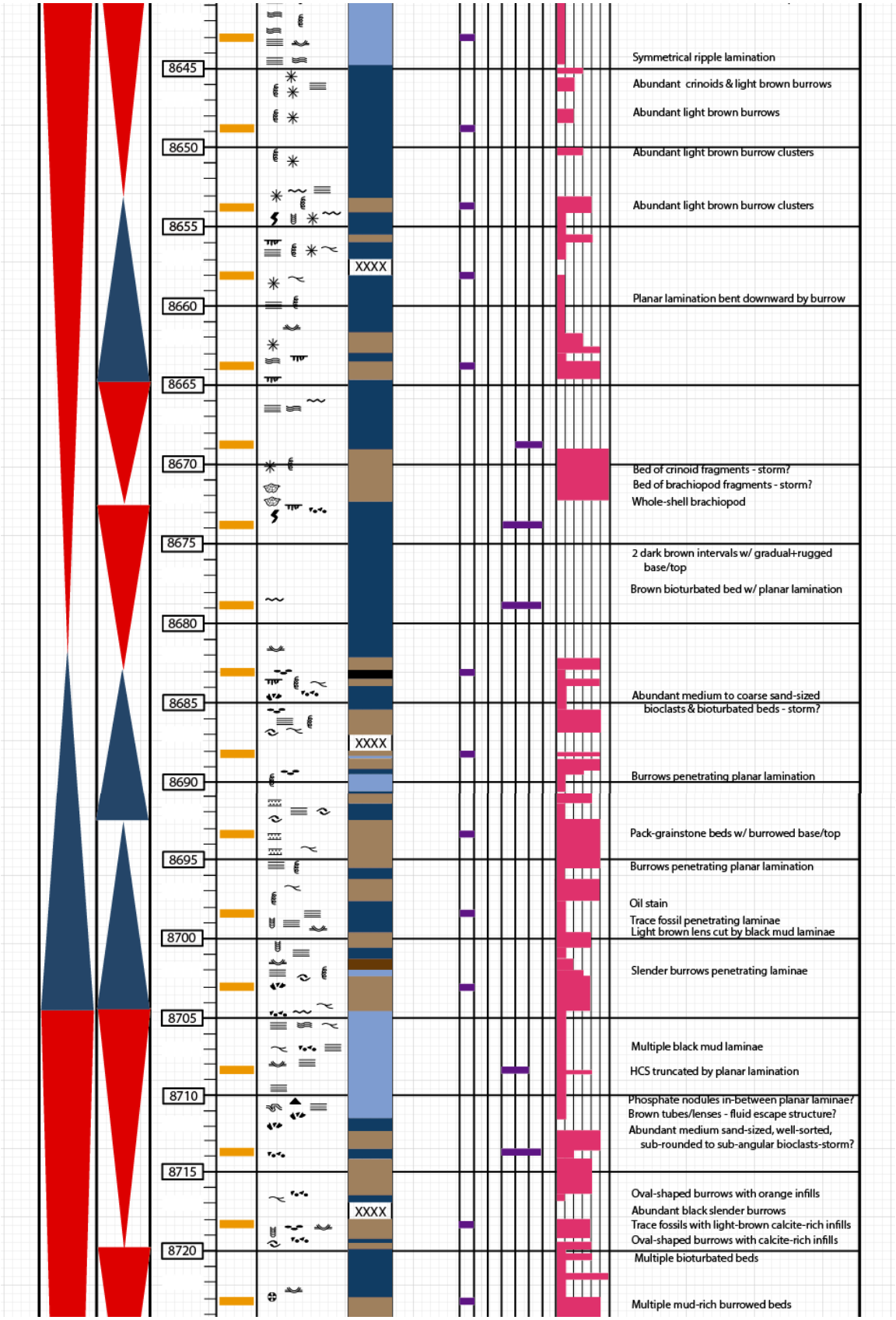
8645
8650
8655
8660
8665
8670
8675
8680
8685
8690
8695
8700
8705
8710
8715
8720
XXXX
XXXX
XXXX
Symmetrical ripple lamination
Abundant crinoids & light brown burrows
Abundant light brown burrows
Abundant light brown burrow clusters
Abundant light brown burrow clusters
Planar lamination bent downward by burrow
Bed of crinoid fragments - storm?
Bed of brachiopod fragments - storm?
Whole-shell brachiopod
2 dark brown intervals w/ gradual+rugged base/top
Brown bioturbated bed w/ planar lamination
Abundant medium to coarse sand-sized bioclasts & bioturbated beds - storm?
Burrows penetrating planar lamination
Pack-grainstone beds w/ burrowed base/top
Burrows penetrating planar lamination
Oil stain
Trace fossil penetrating laminae
Light brown lens cut by black mud laminae
Slender burrows penetrating laminae
Multiple black mud laminae
HCS truncated by planar lamination
Phosphate nodules in-between planar laminae?
Brown tubes/lenses - fluid escape structure?
Abundant medium sand-sized, well-sorted, sub-rounded to sub-angular bioclasts-storm?
Oval-shaped burrows with orange infills
Abundant black slender burrows
Trace fossils with light-brown calcite-rich infills
Oval-shaped burrows with calcite-rich infills
Multiple bioturbated beds
Multiple mud-rich burrowed beds

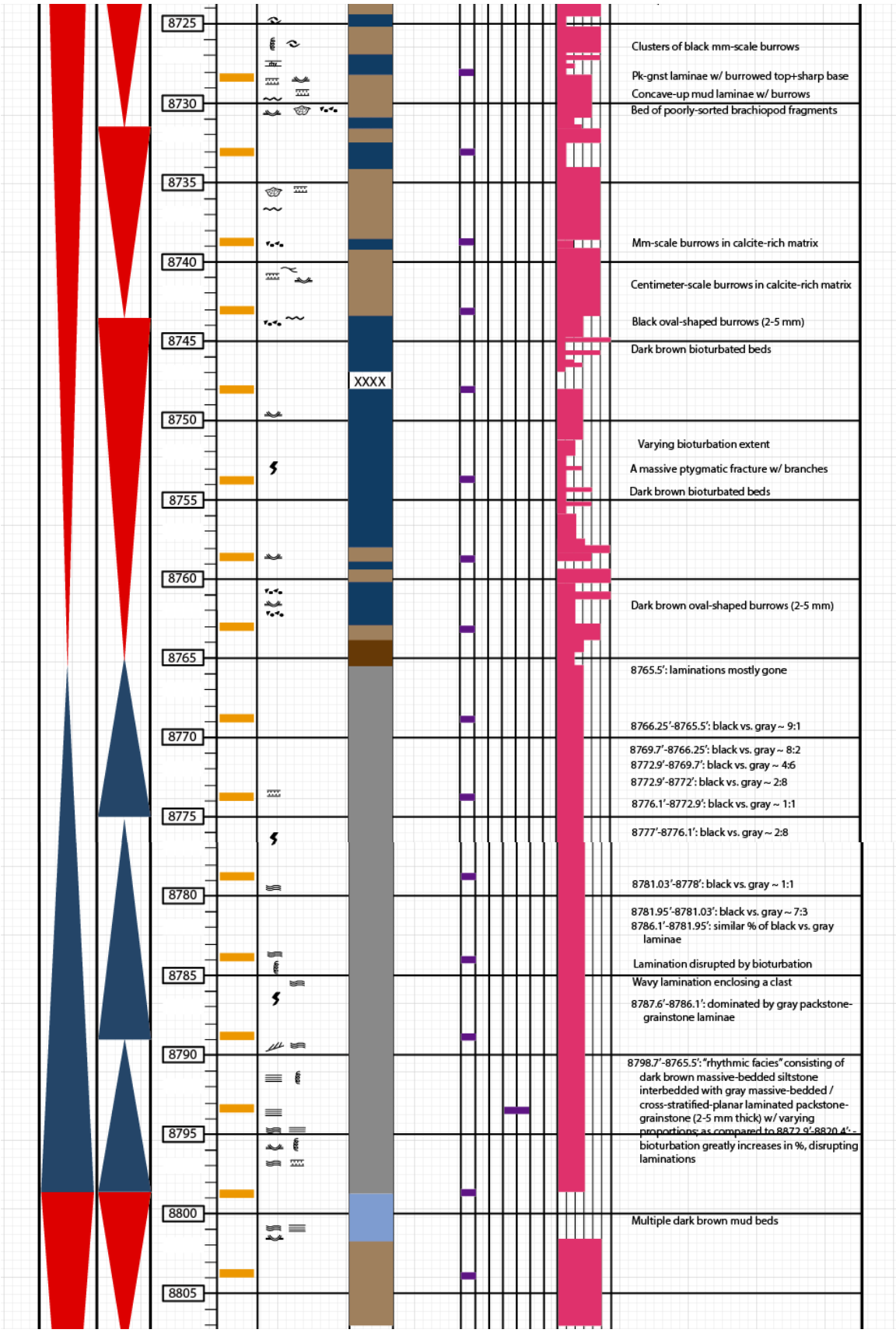
8725
8730
8735
8740
8745
8750
8755
8760
8765
8770
8775
8780
8785
8790
8795
8800
8805
XXXX
Clusters of black mm-scale burrows
Pk-gnst laminae w/ burrowed top+sharp base
Concave-up mud laminae w/ burrows
Bed of poorly-sorted brachiopod fragments
Mm-scale burrows in calcite-rich matrix
Centimeter-scale burrows in calcite-rich matrix
Black oval-shaped burrows (2-5 mm)
Dark brown bioturbated beds
Varying bioturbation extent
A massive ptygmatic fracture w/ branches
Dark brown bioturbated beds
Dark brown oval-shaped burrows (2-5 mm)
8765.5': laminations mostly gone
8766.25'-8765.5': black vs. gray ~ 9:1
8769.7'-8766.25': black vs. gray ~ 8:2
8772.9'-8769.7': black vs. gray ~ 4:6
8772.9'-8772': black vs. gray ~ 2:8
8776.1'-8772.9': black vs. gray ~ 1:1
8777'-8776.1': black vs. gray ~ 2:8
8781.03'-8778': black vs. gray ~ 1:1
8781.95'-8781.03': black vs. gray ~ 7:3
8786.1'-8781.95': similar % of black vs. gray laminae
Lamination disrupted by bioturbation
Wavy lamination enclosing a clast
8787.6'-8786.1': dominated by gray packstone-grainstone laminae
8798.7'-8765.5': "rhythmic facies" consisting of dark brown massive-bedded siltstone interbedded with gray massive-bedded / cross-stratified-planar laminated packstone-grainstone (2-5 mm thick) w/ varying proportions; as compared to 8872.9'-8820.4': - bioturbation greatly increases in %, disrupting laminations
Multiple dark brown mud beds

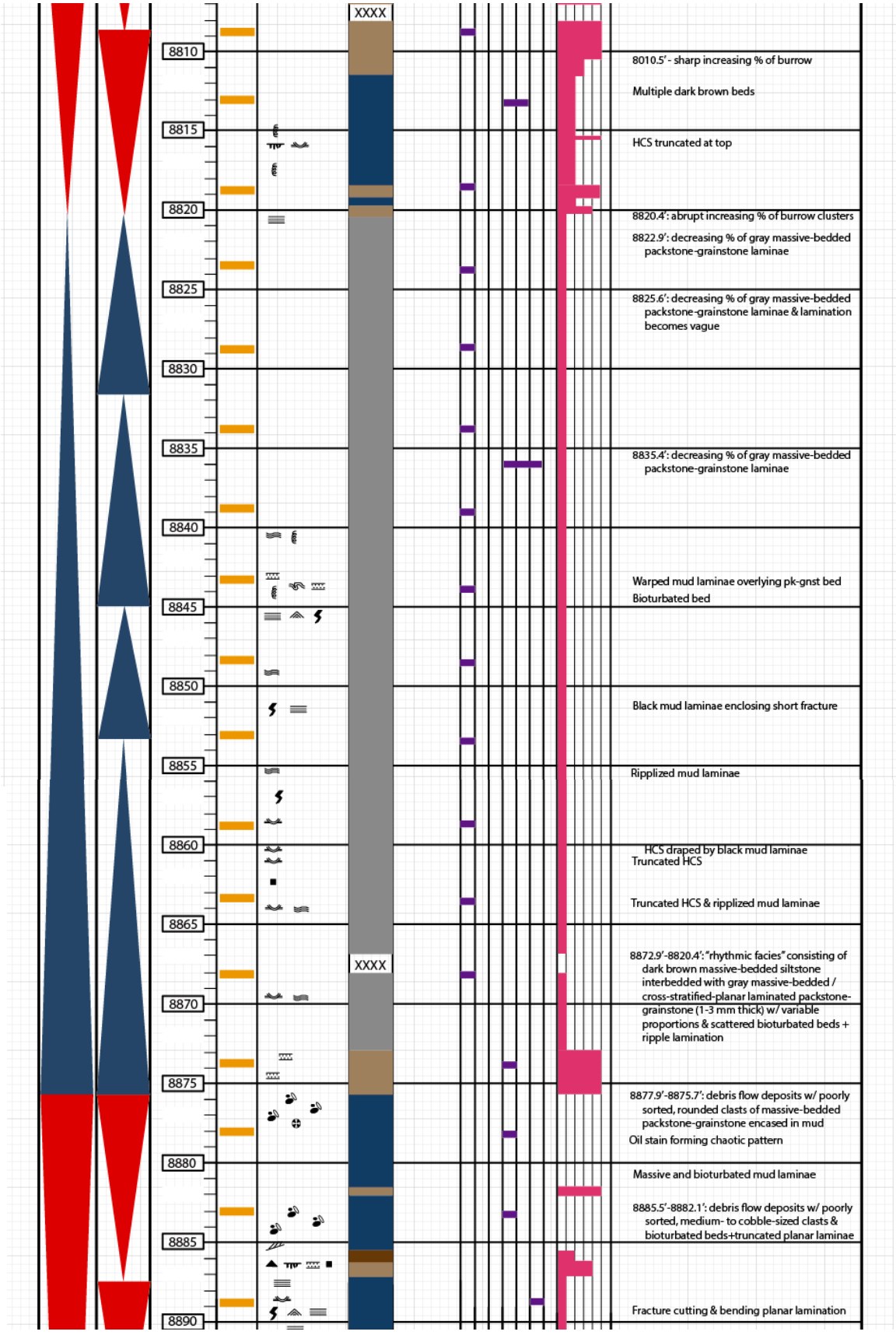
XXXX
8810
8815
8820
8825
8830
8835
8840
8845
8850
8855
8860
8865
XXXX
8870
8875
8880
8885
8890
8010.5' - sharp increasing % of burrow
Multiple dark brown beds
HCS truncated at top
8820.4': abrupt increasing % of burrow clusters
8822.9': decreasing % of gray massive-bedded packstone-grainstone laminae
8825.6': decreasing % of gray massive-bedded packstone-grainstone laminae & lamination becomes vague
8835.4': decreasing % of gray massive-bedded packstone-grainstone laminae
Warped mud laminae overlying pk-gnst bed
Bioturbated bed
Black mud laminae enclosing short fracture
Ripplized mud laminae
HCS draped by black mud laminae
Truncated HCS
Truncated HCS & ripplized mud laminae
8872.9'-8820.4': "rhythmic facies" consisting of dark brown massive-bedded siltstone interbedded with gray massive-bedded / cross-stratified-planar laminated packstone-grainstone (1-3 mm thick) w/ variable proportions & scattered bioturbated beds + ripple lamination
8877.9'-8875.7': debris flow deposits w/ poorly sorted, rounded clasts of massive-bedded packstone-grainstone encased in mud
Oil stain forming chaotic pattern
Massive and bioturbated mud laminae
8885.5'-8882.1': debris flow deposits w/ poorly sorted, medium- to cobble-sized clasts & bioturbated beds+truncated planar laminae
Fracture cutting & bending planar lamination

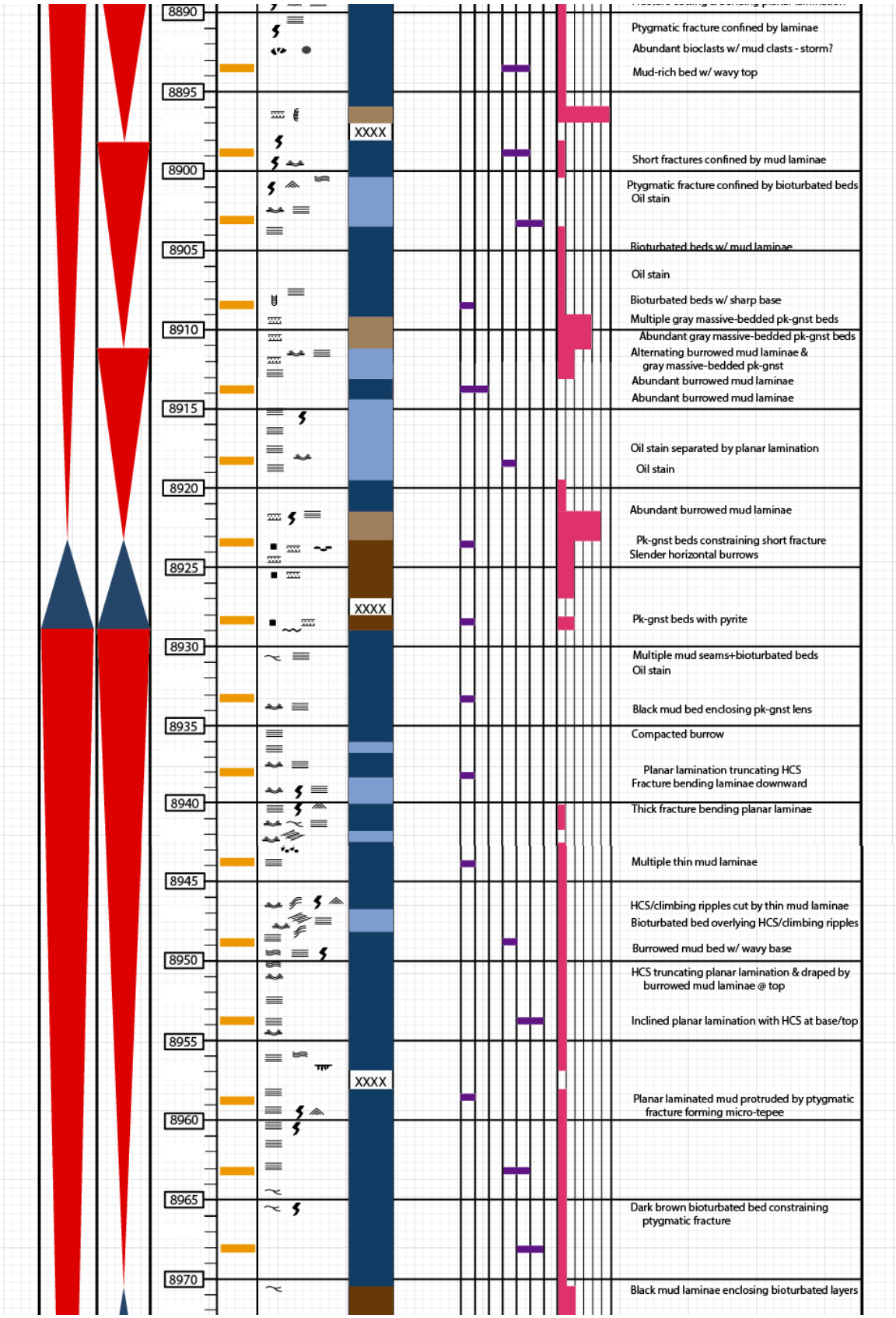
8890
8895
8900
8905
8910
8915
8920
8925
8930
8935
8940
8945
8950
8955
8960
8965
8970
XXXX
XXXX
XXXX
Ptygmatic fracture confined by laminae
Abundant bioclasts w/ mud clasts - storm?
Mud-rich bed w/ wavy top
Short fractures confined by mud laminae
Ptygmatic fracture confined by bioturbated beds
Oil stain
Bioturbated beds w/ mud laminae
Oil stain
Bioturbated beds w/ sharp base
Multiple gray massive-bedded pk-gnst beds
Abundant gray massive-bedded pk-gnst beds
Alternating burrowed mud laminae &
gray massive-bedded pk-gnst
Abundant burrowed mud laminae
Abundant burrowed mud laminae
Oil stain separated by planar lamination
Oil stain
Abundant burrowed mud laminae
Pk-gnst beds constraining short fracture
Slender horizontal burrows
Pk-gnst beds with pyrite
Multiple mud seams+bioturbated beds
Oil stain
Black mud bed enclosing pk-gnst lens
Compacted burrow
Planar lamination truncating HCS
Fracture bending laminae downward
Thick fracture bending planar laminae
Multiple thin mud laminae
HCS/climbing ripples cut by thin mud laminae
Bioturbated bed overlying HCS/climbing ripples
Burrowed mud bed w/ wavy base
HCS truncating planar lamination & draped by
burrowed mud laminae @ top
Inclined planar lamination with HCS at base/top
Planar laminated mud protruded by ptygmatic
fracture forming micro-tepee
Dark brown bioturbated bed constraining
ptygmatic fracture
Black mud laminae enclosing bioturbated layers

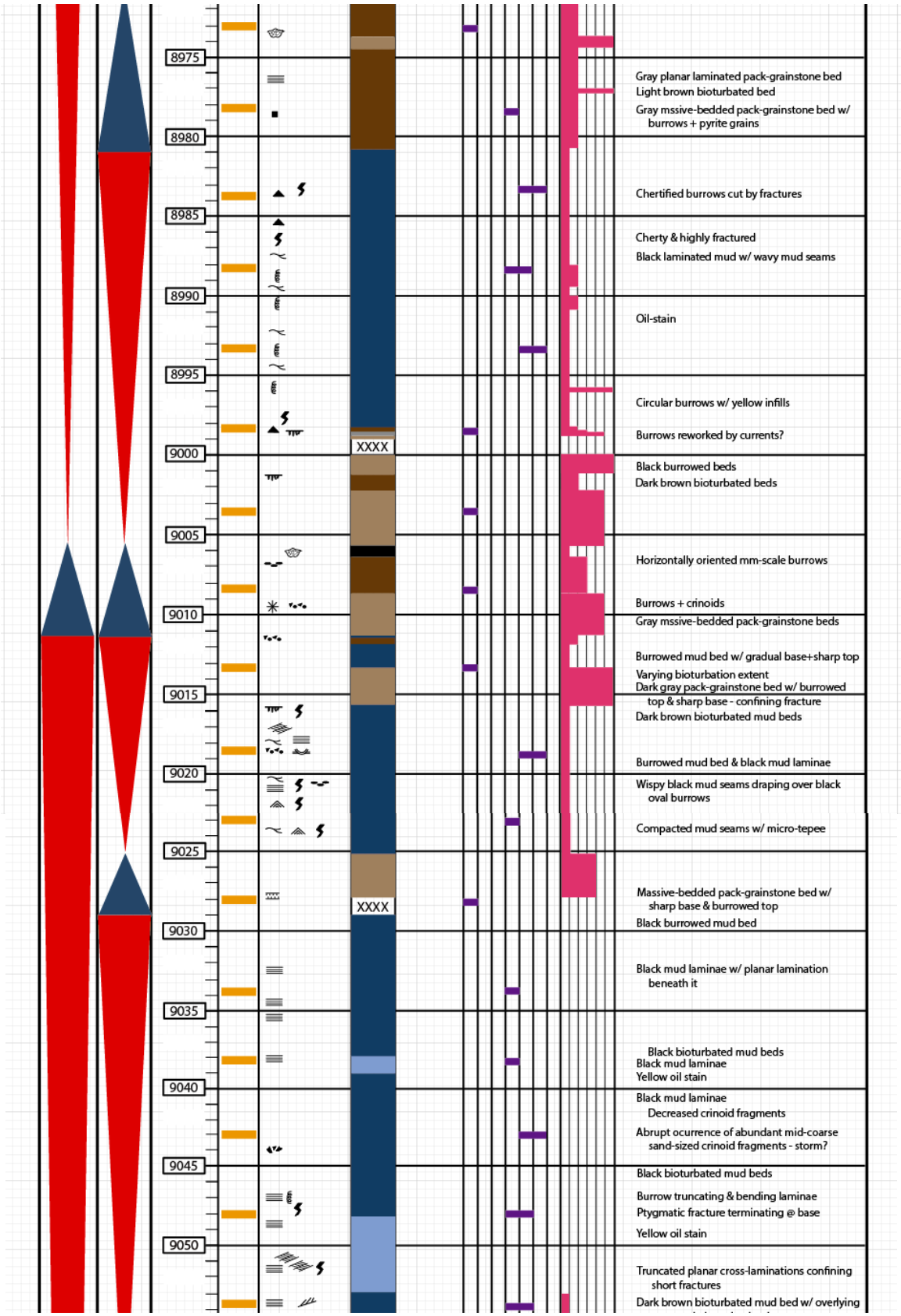
8975
8980
8985
8990
8995
9000
9005
9010
9015
9020
9025
9030
9035
9040
9045
9050
XXXX
XXXX
Gray planar laminated pack-grainstone bed
Light brown bioturbated bed
Gray mssive-bedded pack-grainstone bed w/ burrows + pyrite grains
Chertified burrows cut by fractures
Cherty & highly fractured
Black laminated mud w/ wavy mud seams
Oil-stain
Circular burrows w/ yellow infills
Burrows reworked by currents?
Black burrowed beds
Dark brown bioturbated beds
Horizontally oriented mm-scale burrows
Burrows + crinoids
Gray mssive-bedded pack-grainstone beds
Burrowed mud bed w/ gradual base+sharp top
Varying bioturbation extent
Dark gray pack-grainstone bed w/ burrowed top & sharp base - confining fracture
Dark brown bioturbated mud beds
Burrowed mud bed & black mud laminae
Wispy black mud seams draping over black oval burrows
Compacted mud seams w/ micro-tepee
Massive-bedded pack-grainstone bed w/ sharp base & burrowed top
Black burrowed mud bed
Black mud laminae w/ planar lamination beneath it
Black bioturbated mud beds
Black mud laminae
Yellow oil stain
Black mud laminae
Decreased crinoid fragments
Abrupt ocurrence of abundant mid-coarse sand-sized crinoid fragments - storm?
Black bioturbated mud beds
Burrow truncating & bending laminae
Ptygmatic fracture terminating @ base
Yellow oil stain
Truncated planar cross-laminations confining short fractures
Dark brown bioturbated mud bed w/ overlying

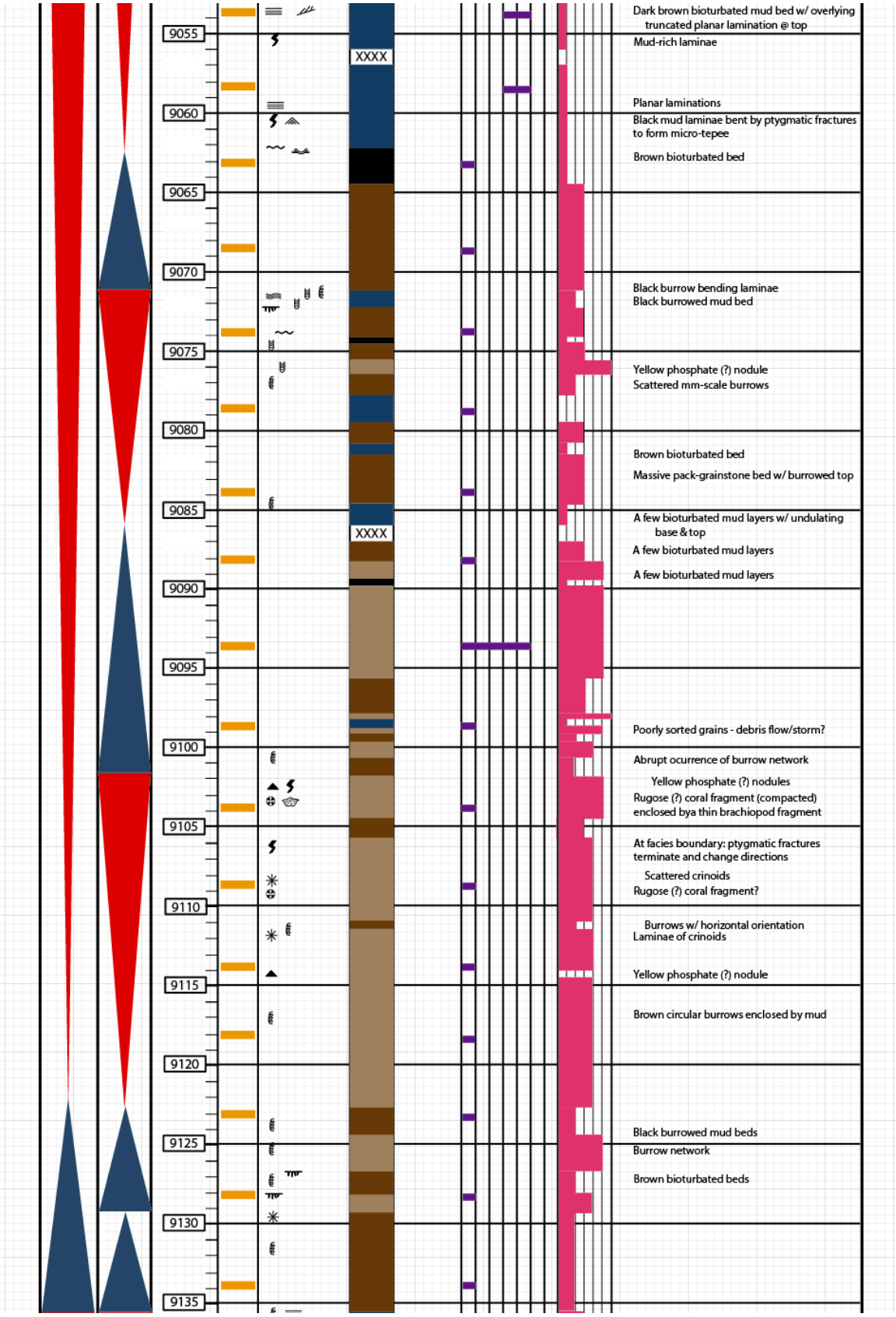
9055
9060
9065
9070
9075
9080
9085
9090
9095
9100
9105
9110
9115
9120
9125
9130
9135
XXXX
XXXX
Dark brown bioturbated mud bed w/ overlying truncated planar lamination @ top
Mud-rich laminae
Planar laminations
Black mud laminae bent by ptygmatic fractures to form micro-tepee
Brown bioturbated bed
Black burrow bending laminae
Black burrowed mud bed
Yellow phosphate (?) nodule
Scattered mm-scale burrows
Brown bioturbated bed
Massive pack-grainstone bed w/ burrowed top
A few bioturbated mud layers w/ undulating base & top
A few bioturbated mud layers
A few bioturbated mud layers
Poorly sorted grains - debris flow/storm?
Abrupt ocurrence of burrow network
Yellow phosphate (?) nodules
Rugose (?) coral fragment (compacted) enclosed bya thin brachiopod fragment
At facies boundary: ptygmatic fractures terminate and change directions
Scattered crinoids
Rugose (?) coral fragment?
Burrows w/ horizontal orientation
Laminae of crinoids
Yellow phosphate (?) nodule
Brown circular burrows enclosed by mud
Black burrowed mud beds
Burrow network
Brown bioturbated beds

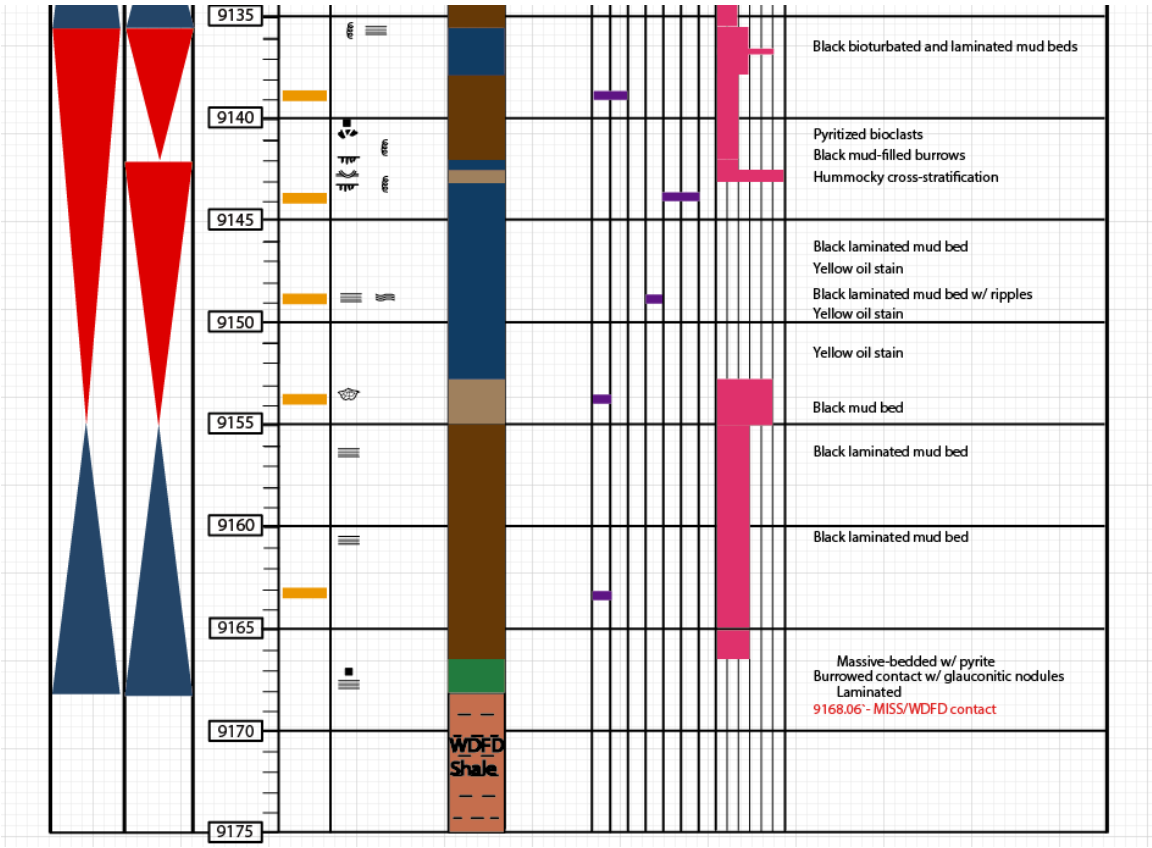
9135
9140
9145
9150
9155
9160
9165
9170
9175
WDFD Shale
Black bioturbated and laminated mud beds
Pyritized bioclasts
Black mud-filled burrows
Hummocky cross-stratification
Black laminated mud bed
Yellow oil stain
Black laminated mud bed w/ ripples
Yellow oil stain
Yellow oil stain
Black mud bed
Black laminated mud bed
Black laminated mud bed
Massive-bedded w/ pyrite
Burrowed contact w/ glauconitic nodules
Laminated
9168.06`- MISS/WDFD contact

Core #5, Kingfisher County, Oklahoma

Formation: "Mississippian Limestone"

Mississippian Interval: 8791.6'-9390.5'

Core #1: 8777'-8988.9'
Core #2: 8989'-9201.2'
Core #3: 9202'-9334.6'
Core #4: 9335'-9389'

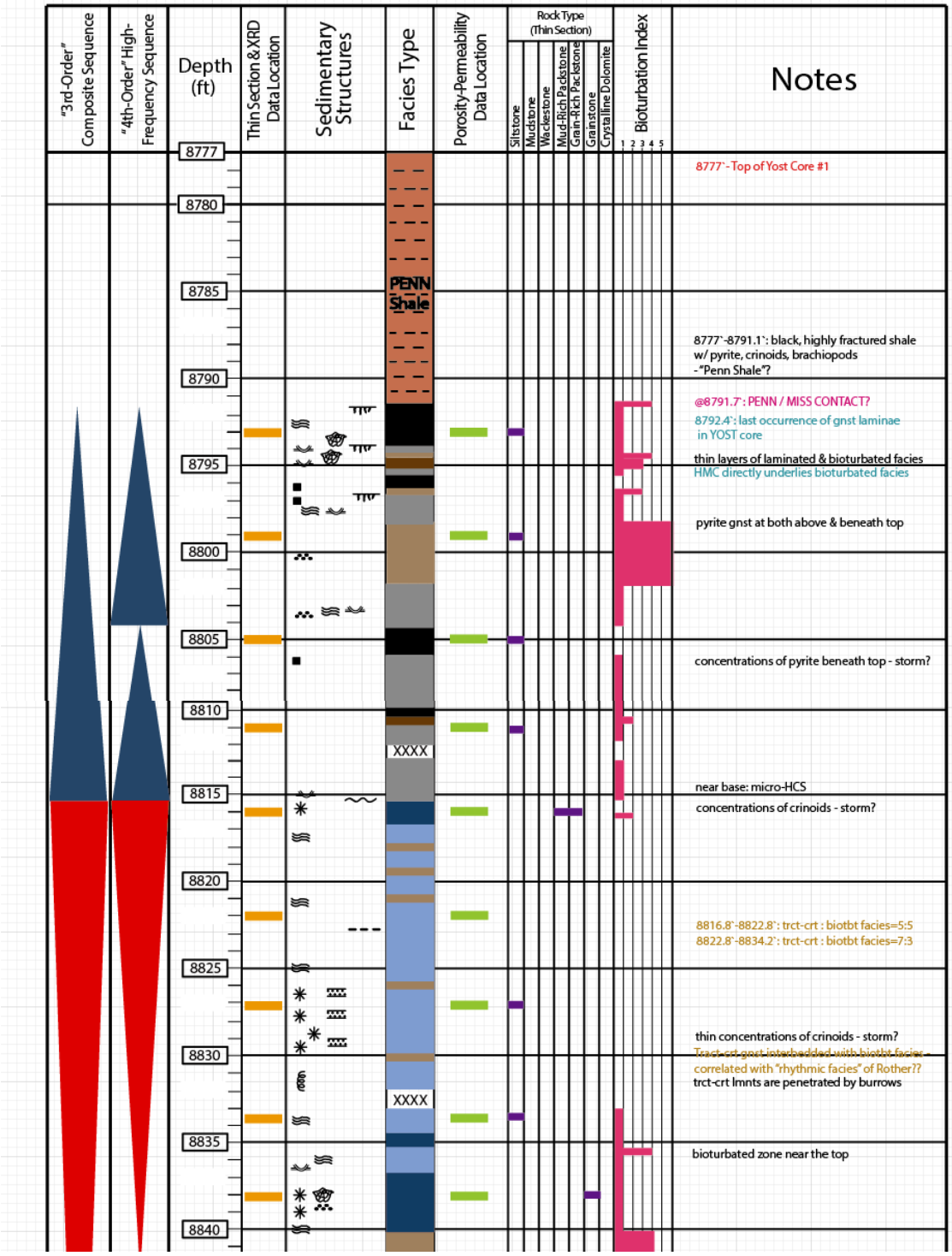

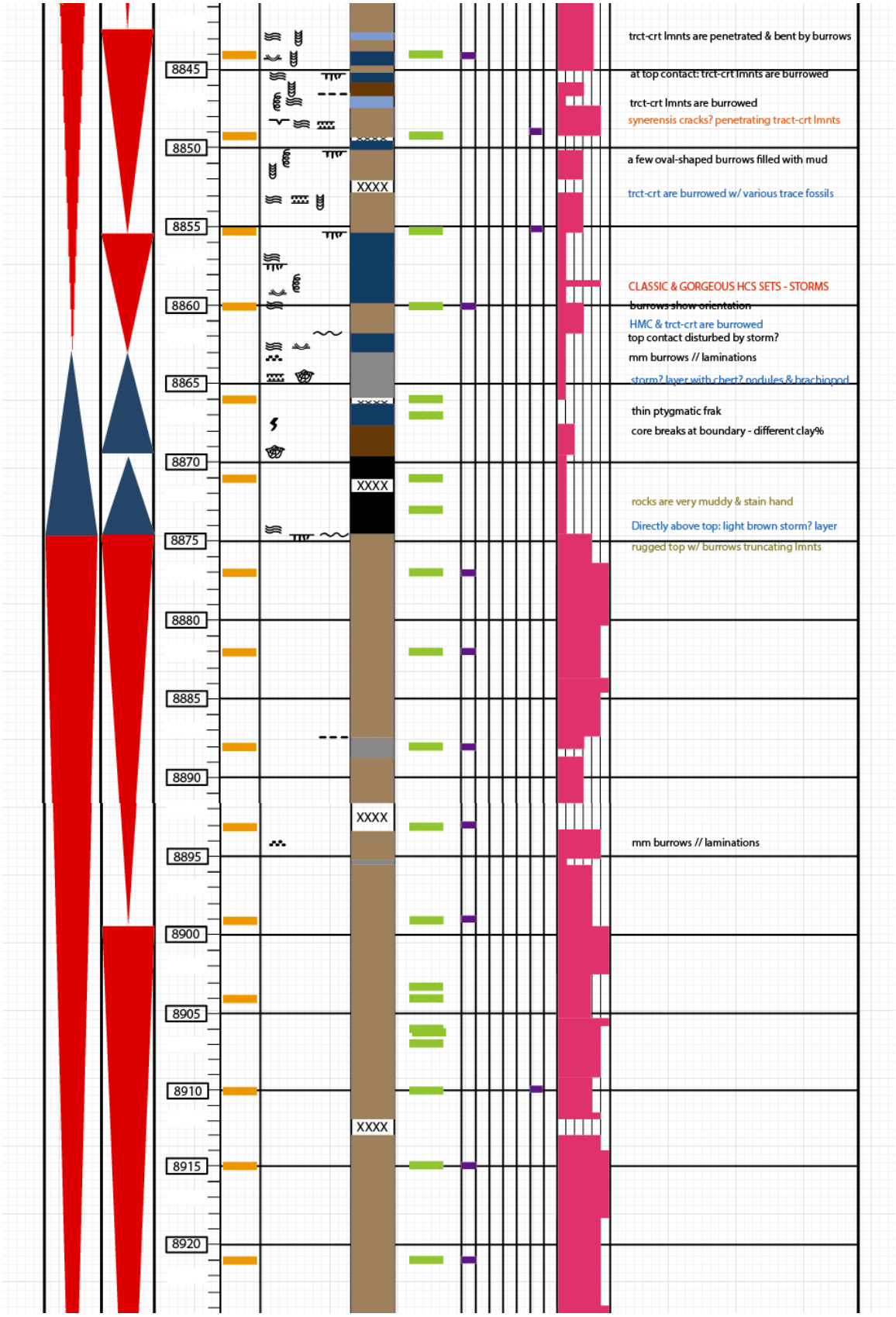
8845
8850
8855
8860
8865
8870
8875
8880
8885
8890
8895
8900
8905
8910
8915
8920
XXXX
XXXX
XXXX
XXXX
trct-crt lmnts are penetrated & bent by burrows
at top contact: trct-crt lmnts are burrowed
trct-crt lmnts are burrowed
synerensis cracks? penetrating tract-crt lmnts
a few oval-shaped burrows filled with mud
trct-crt are burrowed w/ various trace fossils
CLASSIC & GORGEOUS HCS SETS - STORMS
burrows show orientation
HMC & trct-crt are burrowed
top contact disturbed by storm?
mm burrows // laminations
storm? layer with chert? nodules & brachiopod
thin ptygmatic frak
core breaks at boundary - different clay%
rocks are very muddy & stain hand
Directly above top: light brown storm? layer
rugged top w/ burrows truncating lmnts
mm burrows // laminations

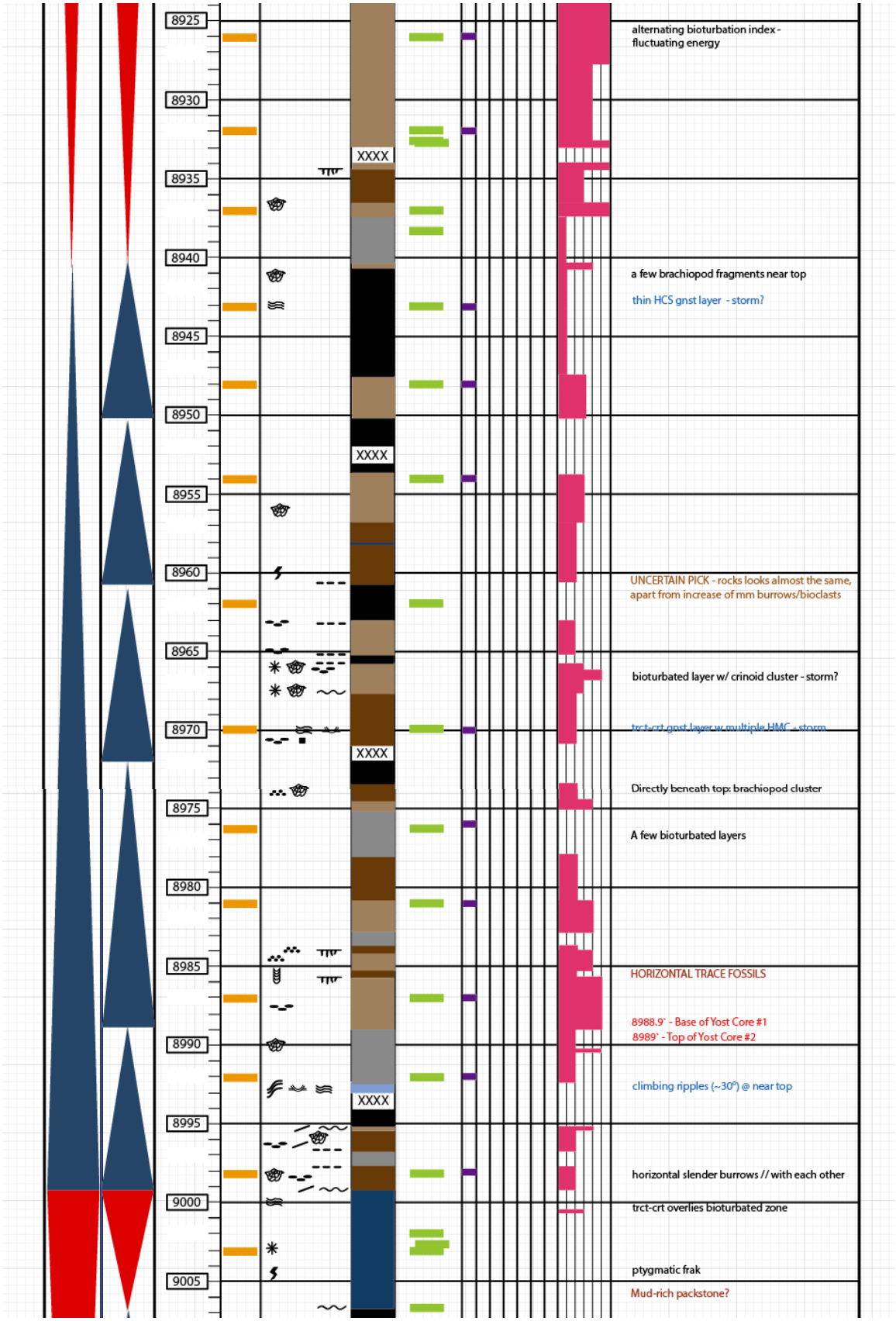
8925
8930
8935
8940
8945
8950
8955
8960
8965
8970
8975
8980
8985
8990
8995
9000
9005
XXXX
XXXX
XXXX
XXXX
alternating bioturbation index - fluctuating energy
a few brachiopod fragments near top
thin HCS gnst layer - storm?
UNCERTAIN PICK - rocks looks almost the same, apart from increase of mm burrows/bioclasts
bioturbated layer w/ crinoid cluster - storm?
trct-crt gnst layer w multiple HMC - storm
Directly beneath top: brachiopod cluster
A few bioturbated layers
HORIZONTAL TRACE FOSSILS
8988.9' - Base of Yost Core #1
8989' - Top of Yost Core #2
climbing ripples (~30°) @ near top
horizontal slender burrows // with each other
trct-crt overlies bioturbated zone
ptygmatic frak
Mud-rich packstone?

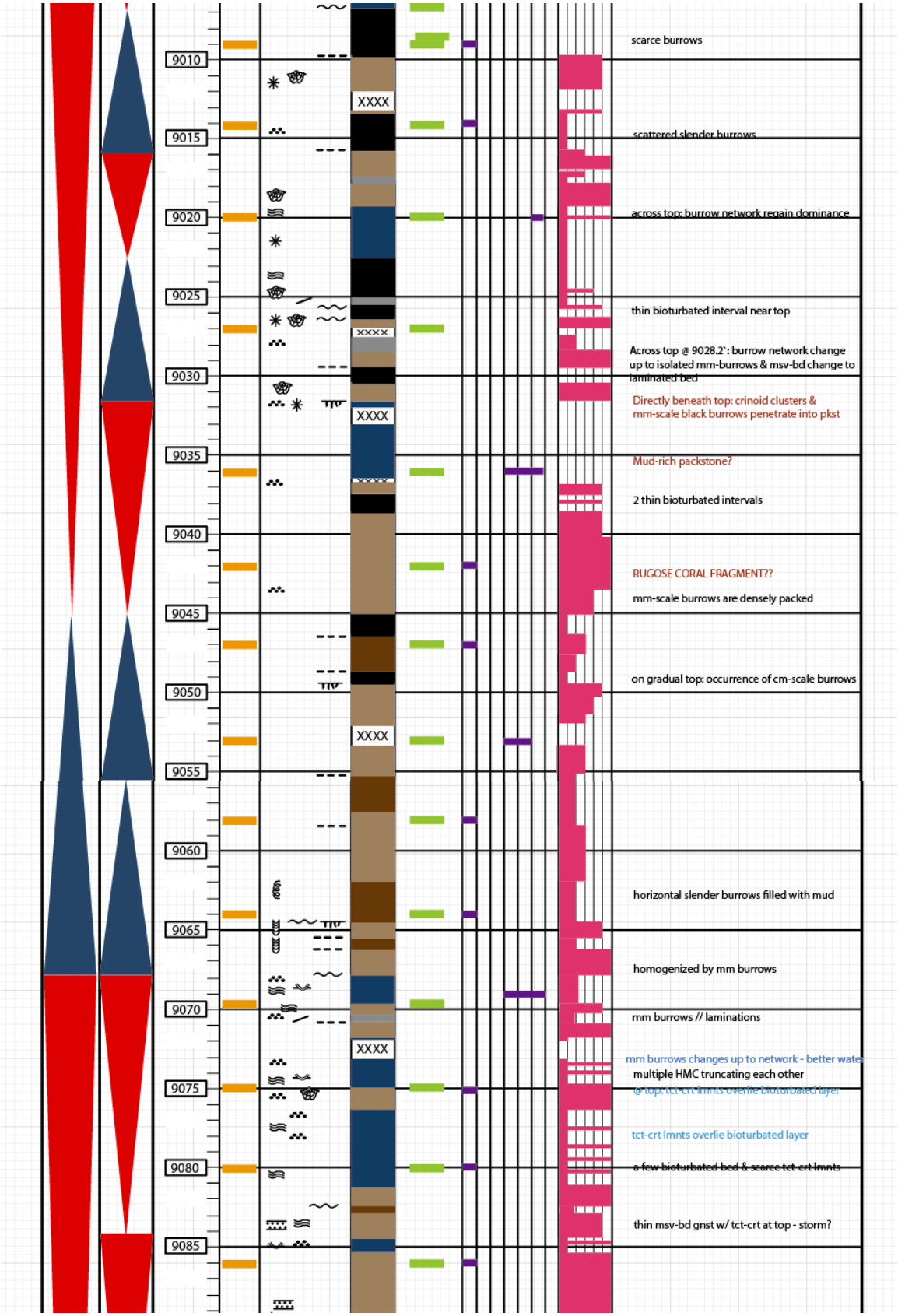
9010
9015
9020
9025
9030
9035
9040
9045
9050
9055
9060
9065
9070
9075
9080
9085
XXXX
scarce burrows
scattered slender burrows
across top: burrow network regain dominance
thin bioturbated interval near top
Across top @ 9028.2': burrow network change up to isolated mm-burrows & msv-bd change to laminated bed
Directly beneath top: crinoid clusters & mm-scale black burrows penetrate into pkst
Mud-rich packstone?
2 thin bioturbated intervals
RUGOSE CORAL FRAGMENT??
mm-scale burrows are densely packed
on gradual top: occurrence of cm-scale burrows
horizontal slender burrows filled with mud
homogenized by mm burrows
mm burrows // laminations
mm burrows changes up to network - better wate
multiple HMC truncating each other
tct-crt lmnts overlie bioturbated layer
thin msv-bd gnst w/ tct-crt at top - storm?

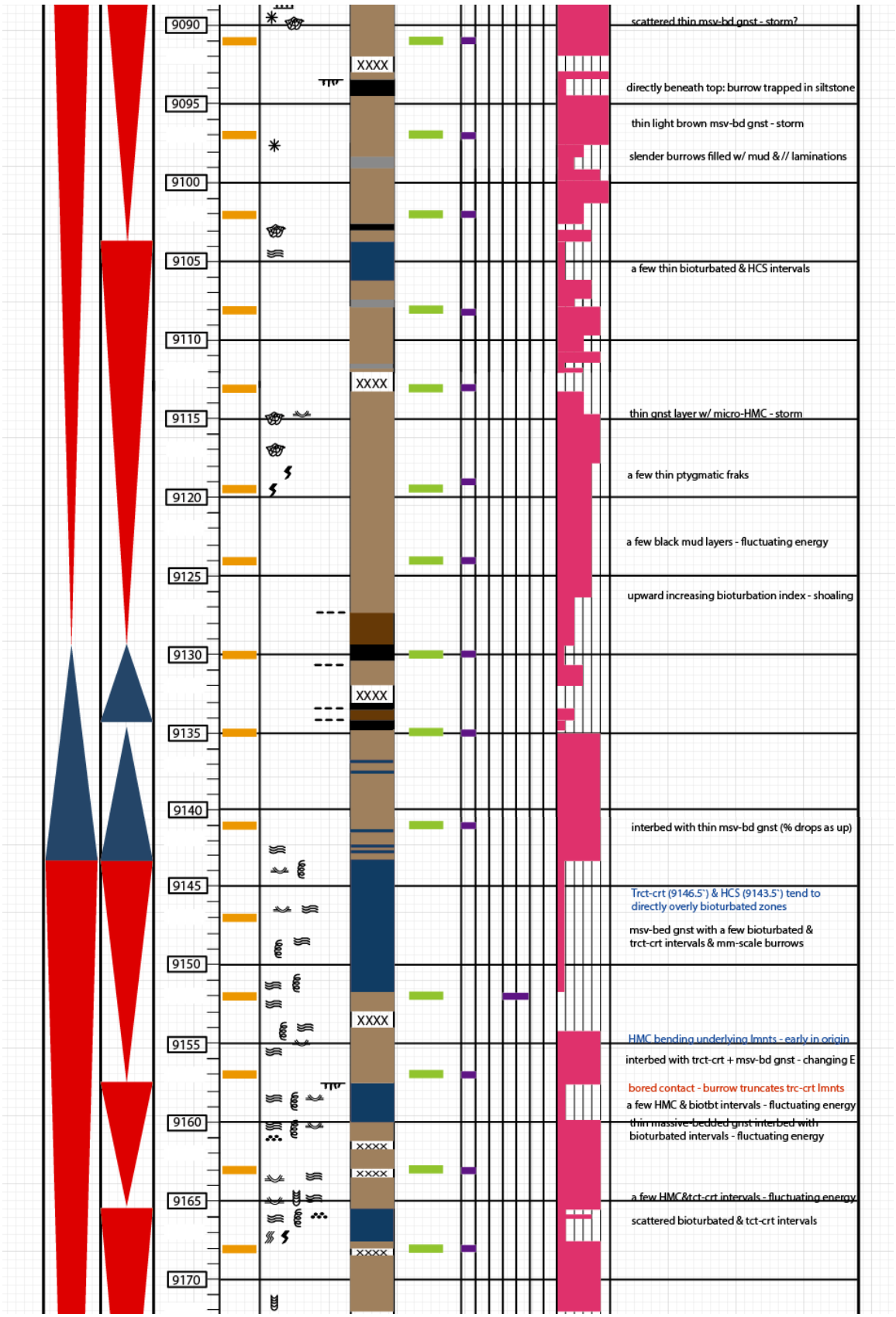
9090
9095
9100
9105
9110
9115
9120
9125
9130
9135
9140
9145
9150
9155
9160
9165
9170
XXXX
scattered thin msv-bd gnst - storm?
directly beneath top: burrow trapped in siltstone
thin light brown msv-bd gnst - storm
slender burrows filled w/ mud & // laminations
a few thin bioturbated & HCS intervals
thin gnst layer w/ micro-HMC - storm
a few thin ptygmatic fraks
a few black mud layers - fluctuating energy
upward increasing bioturbation index - shoaling
interbed with thin msv-bd gnst (% drops as up)
Trct-crt (9146.5') & HCS (9143.5') tend to directly overly bioturbated zones
msv-bed gnst with a few bioturbated & trct-crt intervals & mm-scale burrows
HMC bending underlying lmnts - early in origin
interbed with trct-crt + msv-bd gnst - changing E
bored contact - burrow truncates trc-crt lmnts
a few HMC & biotbt intervals - fluctuating energy
thin massive-bedded gnst interbed with bioturbated intervals - fluctuating energy
a few HMC&tct-crt intervals - fluctuating energy
scattered bioturbated & tct-crt intervals

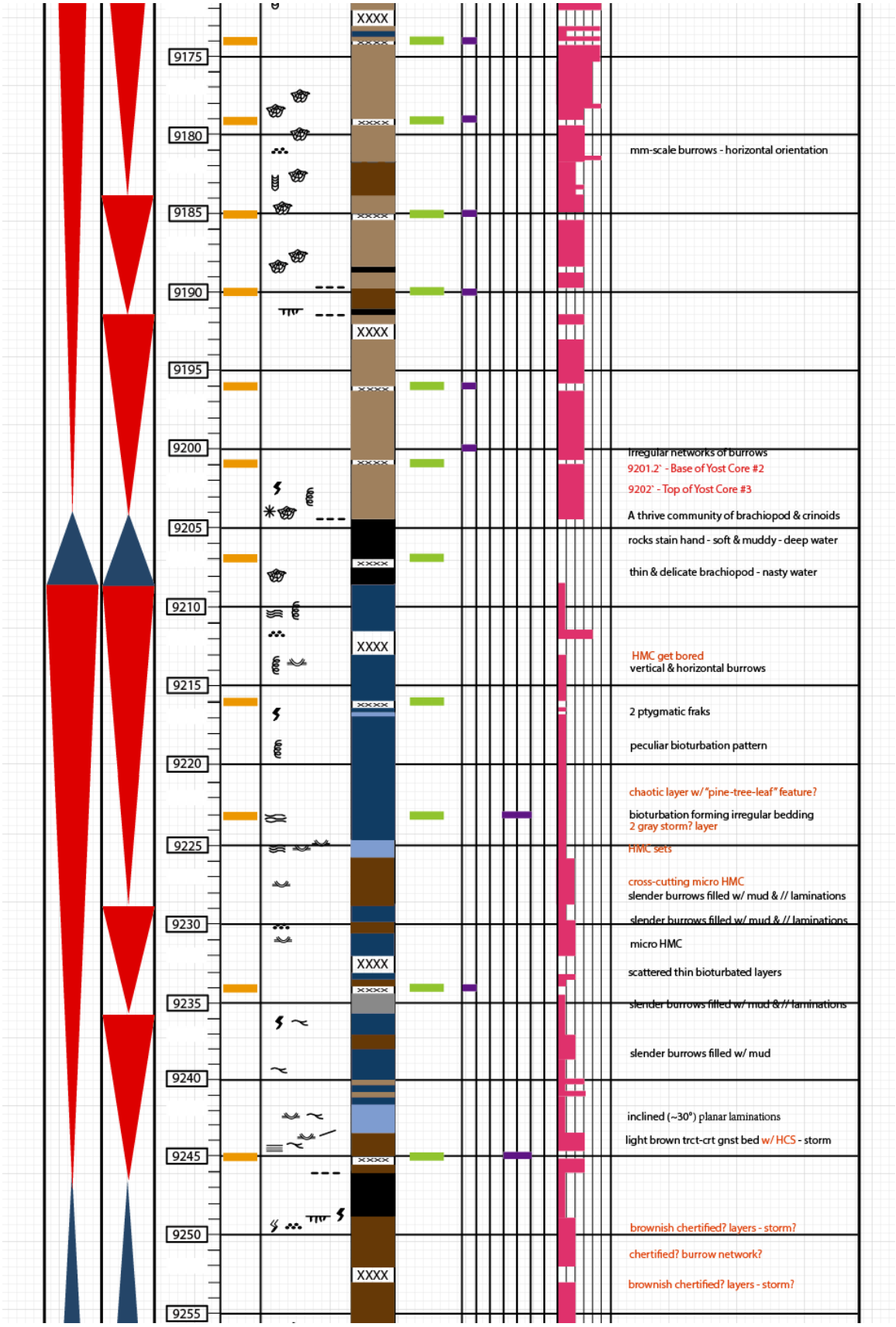
9175
9180
9185
9190
9195
9200
9205
9210
9215
9220
9225
9230
9235
9240
9245
9250
9255
XXXX
XXXX
XXXX
XXXX
mm-scale burrows - horizontal orientation
Irregular networks of burrows
9201.2' - Base of Yost Core #2
9202' - Top of Yost Core #3
A thrive community of brachiopod & crinoids
rocks stain hand - soft & muddy - deep water
thin & delicate brachiopod - nasty water
HMC get bored
vertical & horizontal burrows
2 ptygmatic fraks
peculiar bioturbation pattern
chaotic layer w/ "pine-tree-leaf" feature?
bioturbation forming irregular bedding
2 gray storm? layer
HMC sets
cross-cutting micro HMC
slender burrows filled w/ mud & // laminations
slender burrows filled w/ mud & // laminations
micro HMC
scattered thin bioturbated layers
slender burrows filled w/ mud & // laminations
slender burrows filled w/ mud
inclined (~30°) planar laminations
light brown trct-crt gnst bed w/ HCS - storm
brownish chertified? layers - storm?
chertified? burrow network?
brownish chertified? layers - storm?

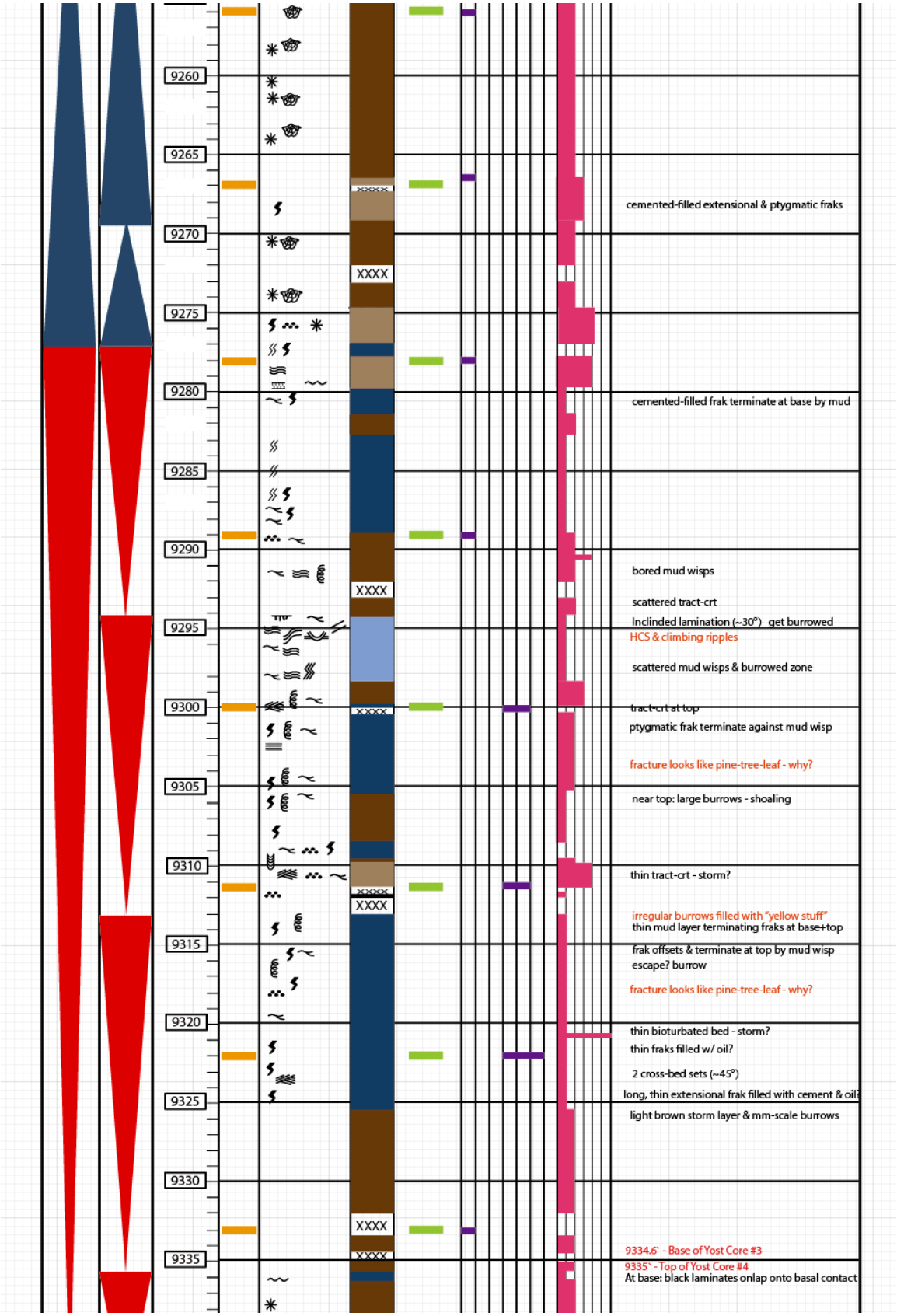
9260
9265
9270
9275
9280
9285
9290
9295
9300
9305
9310
9315
9320
9325
9330
9335
XXXX
cemented-filled extensional & ptygmatic fraks
cemented-filled frak terminate at base by mud
bored mud wisps
scattered tract-crt
Inclinded lamination (~30°) get burrowed
HCS & climbing ripples
scattered mud wisps & burrowed zone
tract-crt at top
ptygmatic frak terminate against mud wisp
fracture looks like pine-tree-leaf - why?
near top: large burrows - shoaling
thin tract-crt - storm?
irregular burrows filled with "yellow stuff"
thin mud layer terminating fraks at base+top
frak offsets & terminate at top by mud wisp
escape? burrow
fracture looks like pine-tree-leaf - why?
thin bioturbated bed - storm?
thin fraks filled w/ oil?
2 cross-bed sets (~45°)
long, thin extensional frak filled with cement & oil?
light brown storm layer & mm-scale burrows
9334.6' - Base of Yost Core #3
9335' - Top of Yost Core #4
At base: black laminates onlap onto basal contact

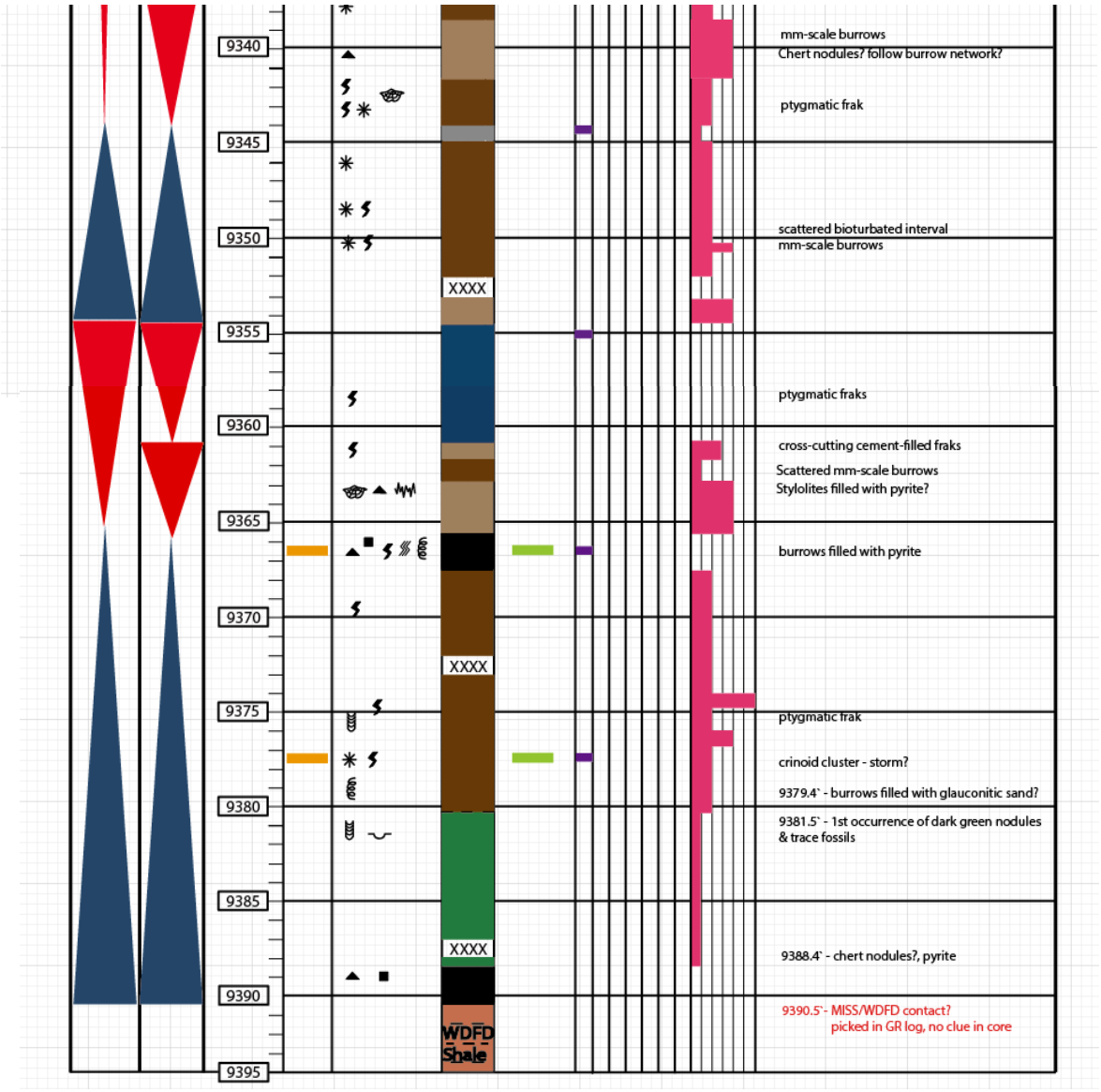
9340
9345
9350
9355
9360
9365
9370
9375
9380
9385
9390
9395
XXXX
XXXX
XXXX
WDFD
Shale
mm-scale burrows
Chert nodules? follow burrow network?
ptygmatic frak
scattered bioturbated interval
mm-scale burrows
ptygmatic fraks
cross-cutting cement-filled fraks
Scattered mm-scale burrows
Stylolites filled with pyrite?
burrows filled with pyrite
ptygmatic frak
crinoid cluster - storm?
9379.4` - burrows filled with glauconitic sand?
9381.5` - 1st occurrence of dark green nodules
& trace fossils
9388.4` - chert nodules?, pyrite
9390.5`- MISS/WDFD contact?
picked in GR log, no clue in core

Core #6, Canadian County, Oklahoma

Formation: "Mississippian Limestone"

Mississippian Interval: 9732'-10312' (top is not in core)

Core #1: 9732'-9969.4'

Core #2: 9970'-10316.3'

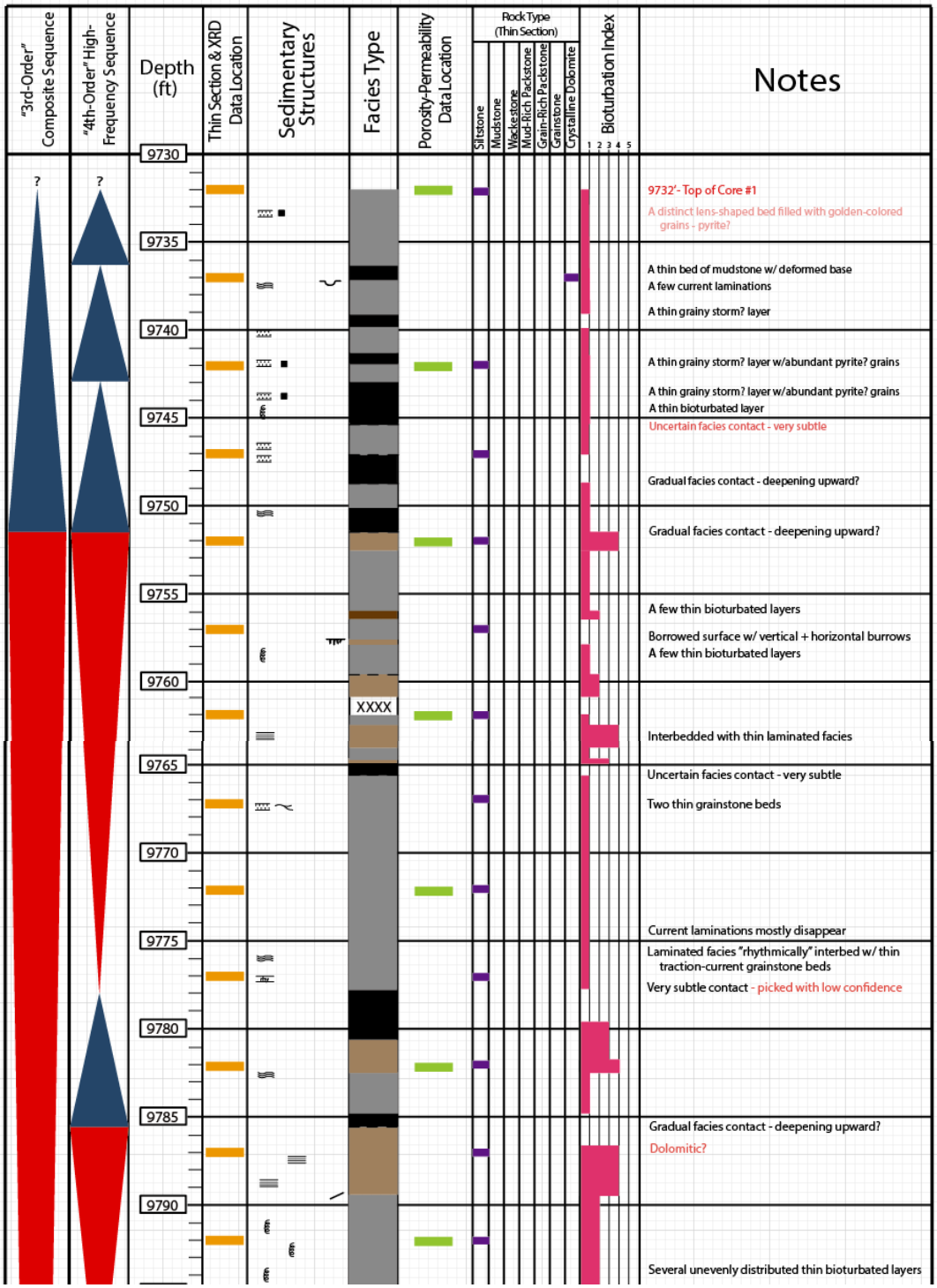

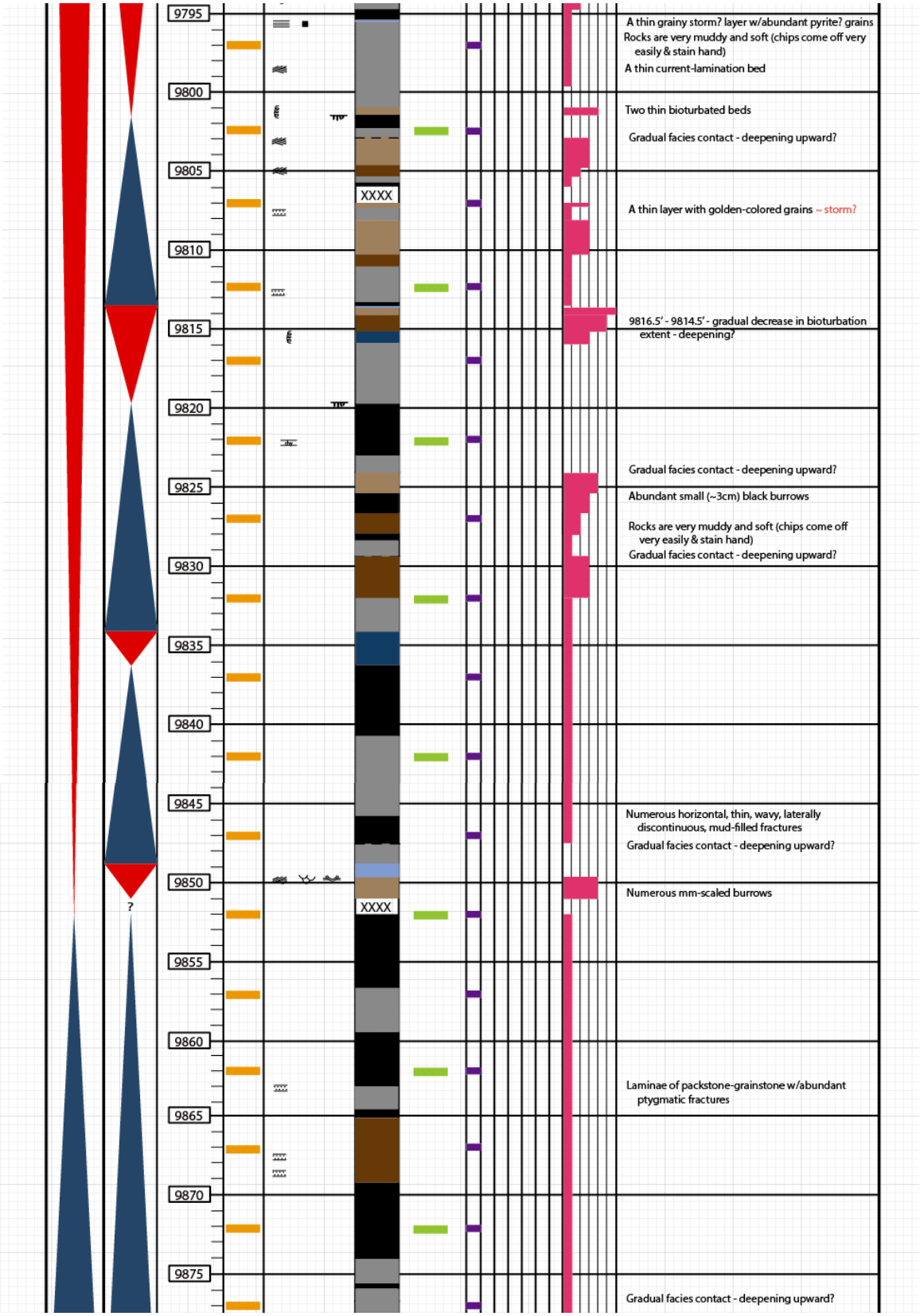
9795
9800
9805
9810
9815
9820
9825
9830
9835
9840
9845
9850
9855
9860
9865
9870
9875
XXXX
XXXX
?
A thin grainy storm? layer w/abundant pyrite? grains
Rocks are very muddy and soft (chips come off very easily & stain hand)
A thin current-lamination bed
Two thin bioturbated beds
Gradual facies contact - deepening upward?
A thin layer with golden-colored grains ~ storm?
9816.5' - 9814.5' - gradual decrease in bioturbation extent - deepening?
Gradual facies contact - deepening upward?
Abundant small (~3cm) black burrows
Rocks are very muddy and soft (chips come off very easily & stain hand)
Gradual facies contact - deepening upward?
Numerous horizontal, thin, wavy, laterally discontinuous, mud-filled fractures
Gradual facies contact - deepening upward?
Numerous mm-scaled burrows
Laminae of packstone-grainstone w/abundant ptygmatic fractures
Gradual facies contact - deepening upward?

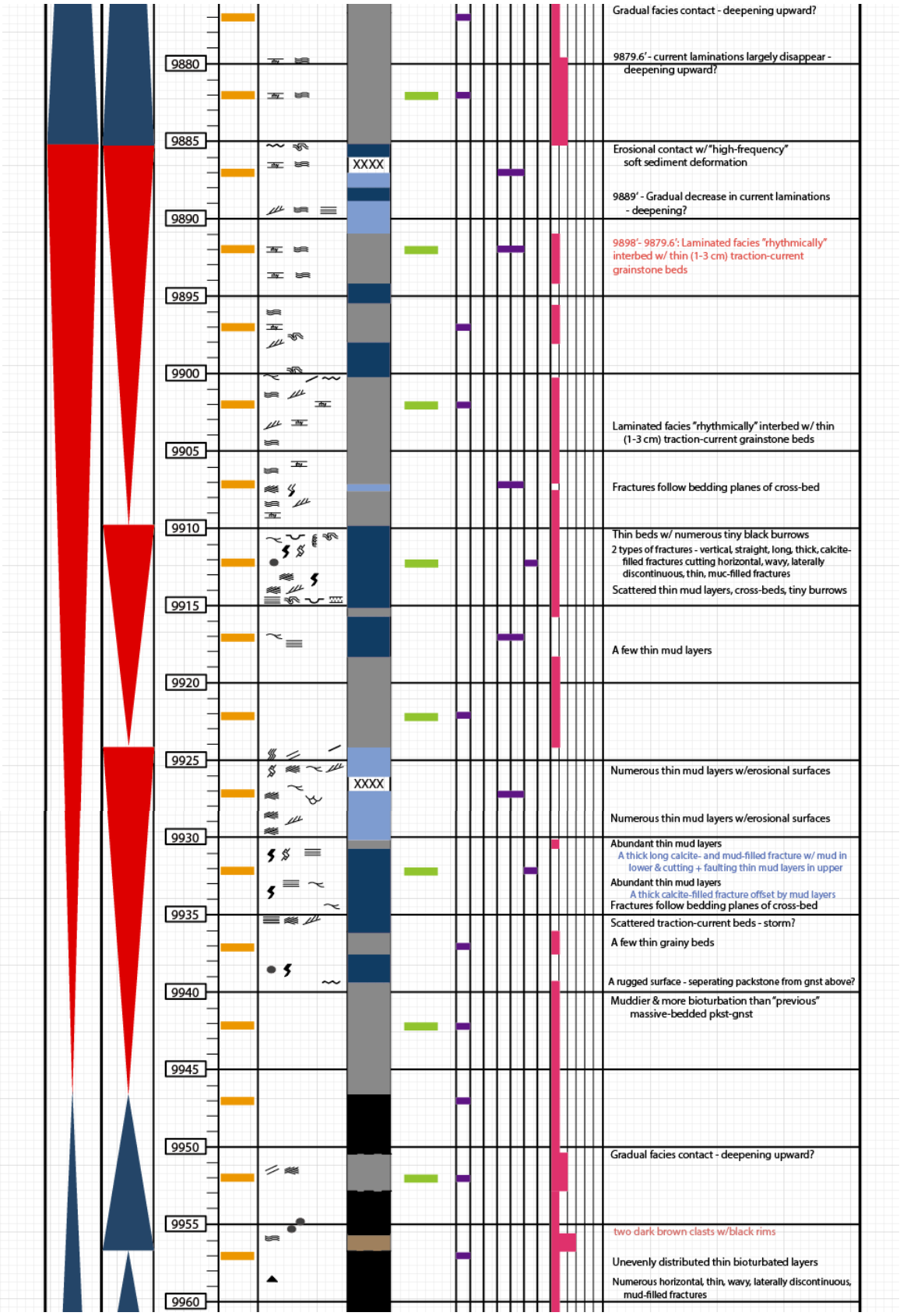
9880
9885
9890
9895
9900
9905
9910
9915
9920
9925
9930
9935
9940
9945
9950
9955
9960
XXXX
XXXX
Gradual facies contact - deepening upward?
9879.6' - current laminations largely disappear - deepening upward?
Erosional contact w/"high-frequency" soft sediment deformation
9889' - Gradual decrease in current laminations - deepening?
9898'- 9879.6': Laminated facies "rhythmically" interbed w/ thin (1-3 cm) traction-current grainstone beds
Laminated facies "rhythmically" interbed w/ thin (1-3 cm) traction-current grainstone beds
Fractures follow bedding planes of cross-bed
Thin beds w/ numerous tiny black burrows
2 types of fractures - vertical, straight, long, thick, calcite-filled fractures cutting horizontal, wavy, laterally discontinuous, thin, muc-filled fractures
Scattered thin mud layers, cross-beds, tiny burrows
A few thin mud layers
Numerous thin mud layers w/erosional surfaces
Numerous thin mud layers w/erosional surfaces
Abundant thin mud layers
A thick long calcite- and mud-filled fracture w/ mud in lower & cutting + faulting thin mud layers in upper
Abundant thin mud layers
A thick calcite-filled fracture offset by mud layers
Fractures follow bedding planes of cross-bed
Scattered traction-current beds - storm?
A few thin grainy beds
A rugged surface - seperating packstone from gnst above?
Muddier & more bioturbation than "previous" massive-bedded pkst-gnst
Gradual facies contact - deepening upward?
two dark brown clasts w/black rims
Unevenly distributed thin bioturbated layers
Numerous horizontal, thin, wavy, laterally discontinuous, mud-filled fractures

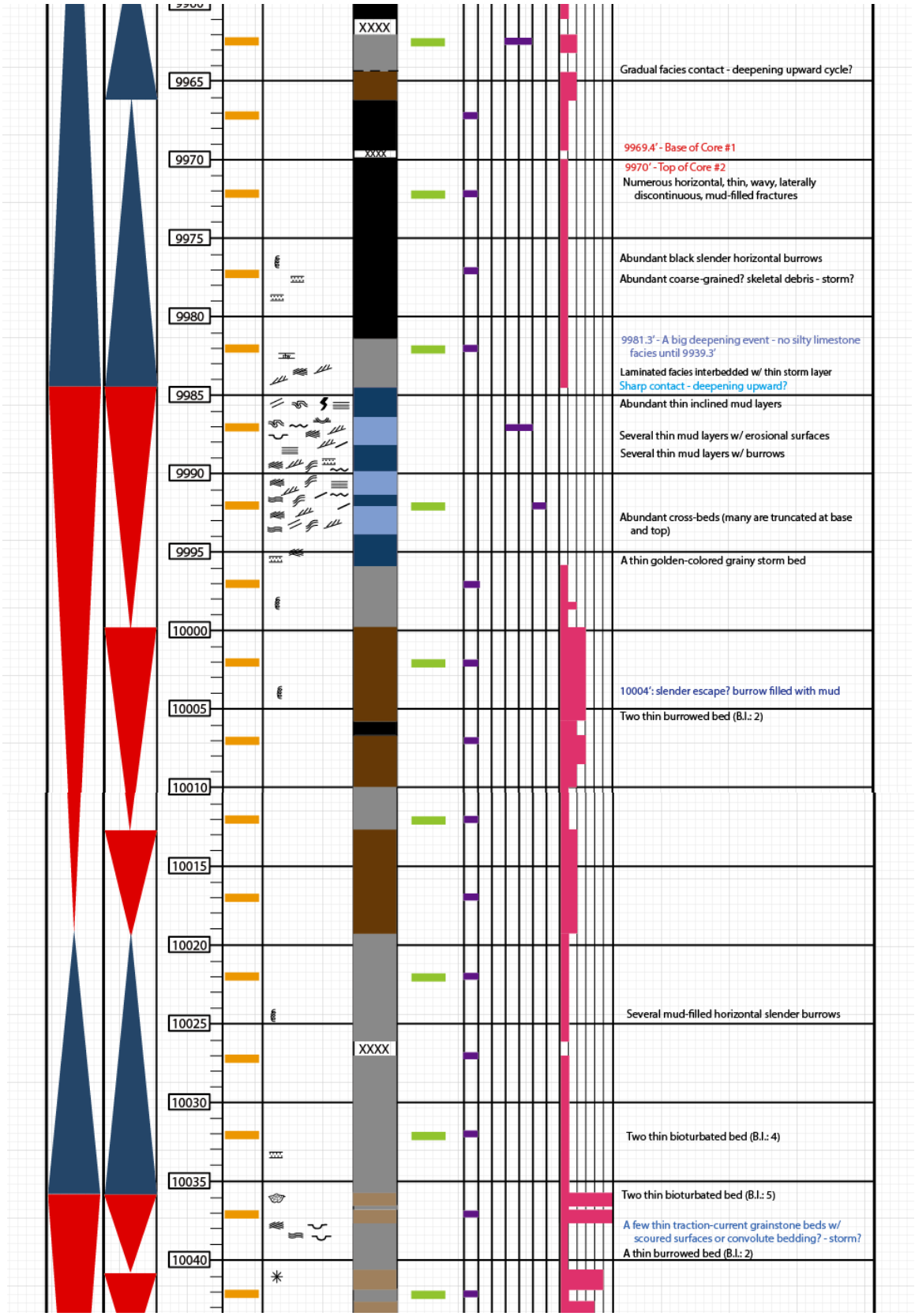
XXXX
9965
9970
9975
9980
9985
9990
9995
10000
10005
10010
10015
10020
10025
10030
10035
10040
Gradual facies contact - deepening upward cycle?
9969.4' - Base of Core #1
9970' - Top of Core #2
Numerous horizontal, thin, wavy, laterally discontinuous, mud-filled fractures
Abundant black slender horizontal burrows
Abundant coarse-grained? skeletal debris - storm?
9981.3' - A big deepening event - no silty limestone facies until 9939.3'
Laminated facies interbedded w/ thin storm layer
Sharp contact - deepening upward?
Abundant thin inclined mud layers
Several thin mud layers w/ erosional surfaces
Several thin mud layers w/ burrows
Abundant cross-beds (many are truncated at base and top)
A thin golden-colored grainy storm bed
10004': slender escape? burrow filled with mud
Two thin burrowed bed (B.I.: 2)
Several mud-filled horizontal slender burrows
Two thin bioturbated bed (B.I.: 4)
Two thin bioturbated bed (B.I.: 5)
A few thin traction-current grainstone beds w/ scoured surfaces or convolute bedding? - storm?
A thin burrowed bed (B.I.: 2)

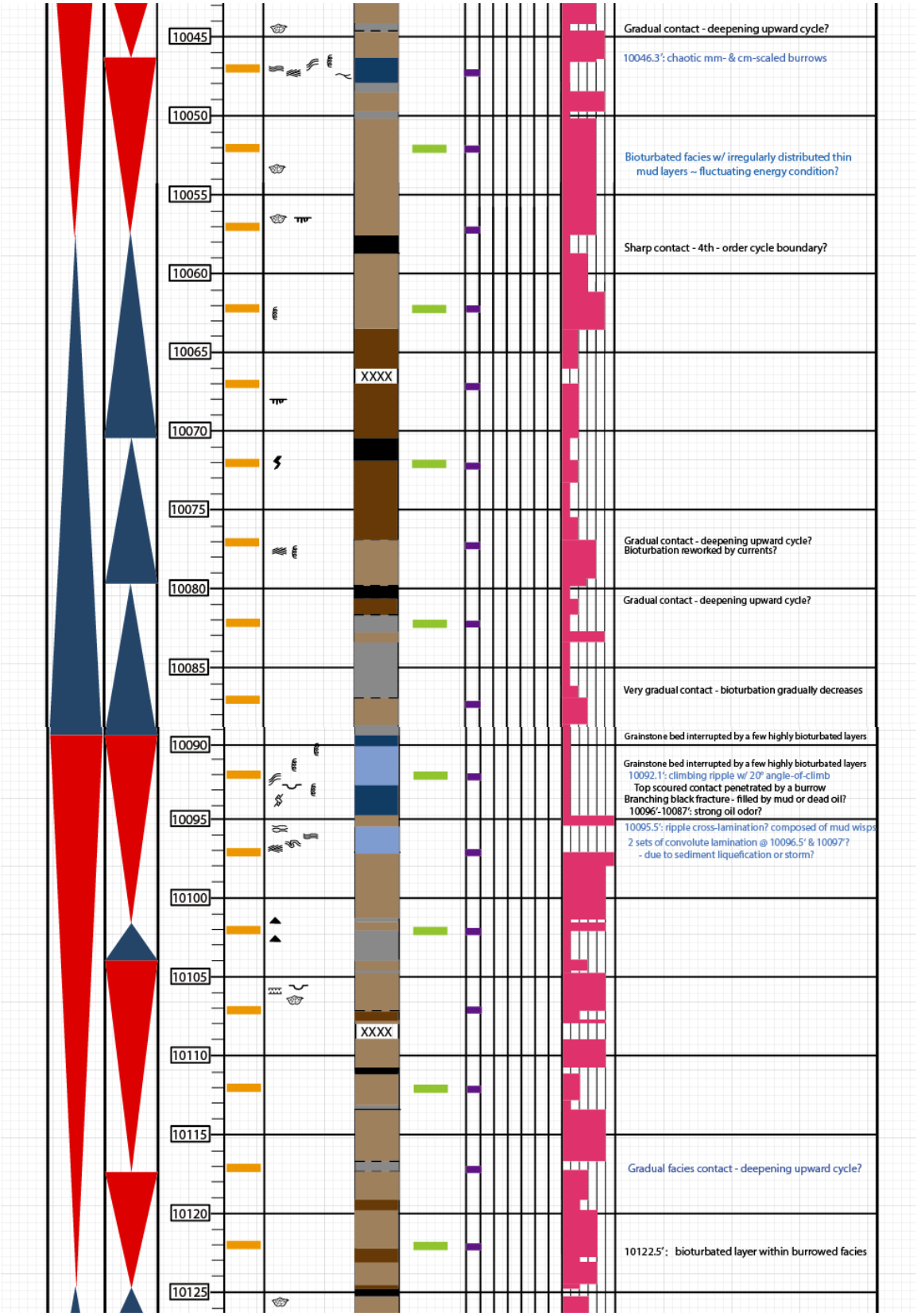
10045
10050
10055
10060
10065
10070
10075
10080
10085
10090
10095
10100
10105
10110
10115
10120
10125
XXXX
XXXX
Gradual contact - deepening upward cycle?
10046.3': chaotic mm- & cm-scaled burrows
Bioturbated facies w/ irregularly distributed thin mud layers ~ fluctuating energy condition?
Sharp contact - 4th - order cycle boundary?
Gradual contact - deepening upward cycle?
Bioturbation reworked by currents?
Gradual contact - deepening upward cycle?
Very gradual contact - bioturbation gradually decreases
Grainstone bed interrupted by a few highly bioturbated layers
Grainstone bed interrupted by a few highly bioturbated layers
10092.1': climbing ripple w/ 20° angle-of-climb
Top scoured contact penetrated by a burrow
Branching black fracture - filled by mud or dead oil?
10096'-10087': strong oil odor?
10095.5': ripple cross-lamination? composed of mud wisps
2 sets of convolute lamination @ 10096.5' & 10097'?
- due to sediment liquefication or storm?
Gradual facies contact - deepening upward cycle?
10122.5': bioturbated layer within burrowed facies

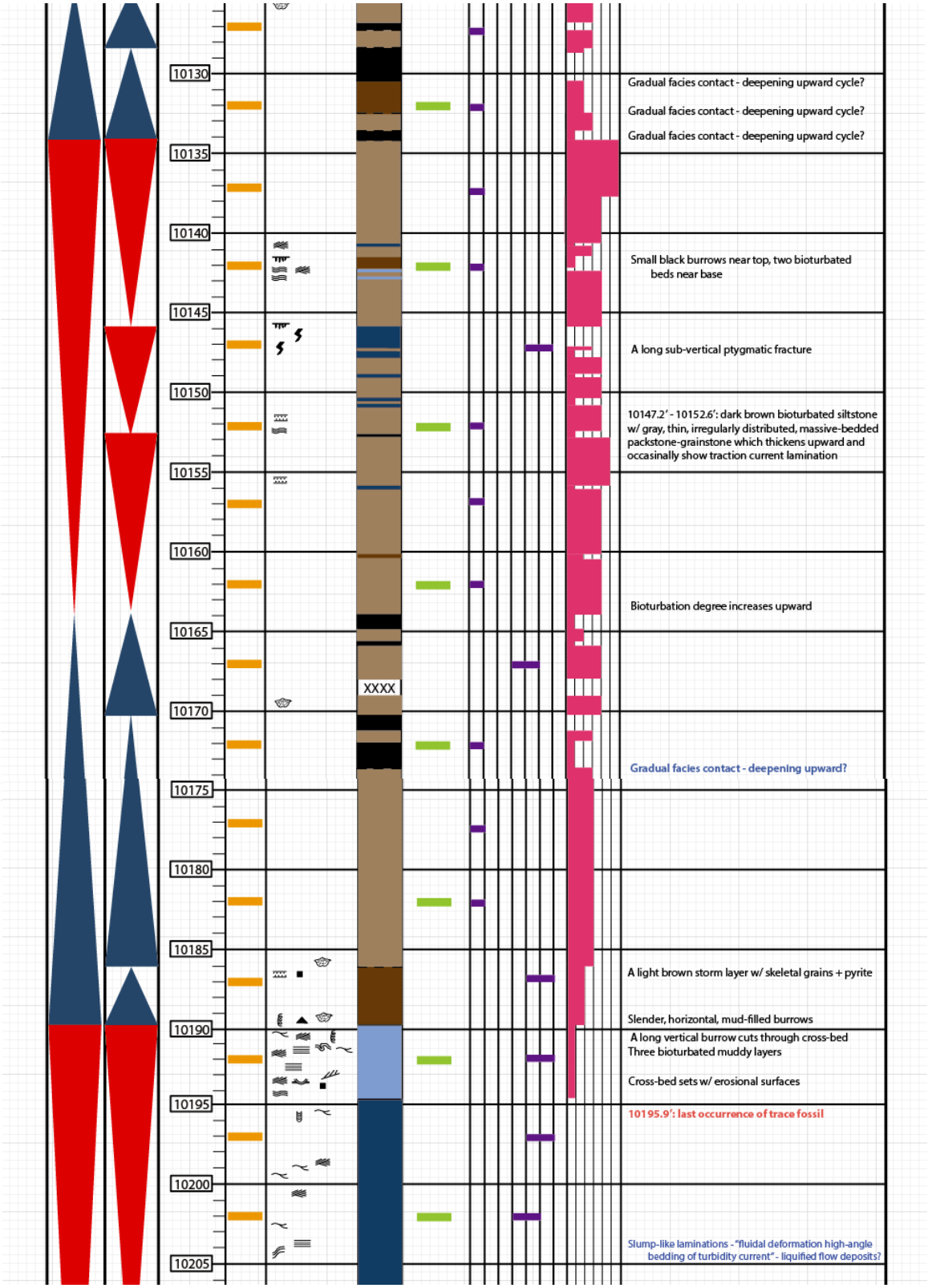
10130
10135
10140
10145
10150
10155
10160
10165
10170
10175
10180
10185
10190
10195
10200
10205
XXXX
Gradual facies contact - deepening upward cycle?
Gradual facies contact - deepening upward cycle?
Gradual facies contact - deepening upward cycle?
Small black burrows near top, two bioturbated beds near base
A long sub-vertical ptygmatic fracture
10147.2' - 10152.6': dark brown bioturbated siltstone w/ gray, thin, irregularly distributed, massive-bedded packstone-grainstone which thickens upward and occasinally show traction current lamination
Bioturbation degree increases upward
Gradual facies contact - deepening upward?
A light brown storm layer w/ skeletal grains + pyrite
Slender, horizontal, mud-filled burrows
A long vertical burrow cuts through cross-bed
Three bioturbated muddy layers
Cross-bed sets w/ erosional surfaces
10195.9': last occurrence of trace fossil
Slump-like laminations - "fluidal deformation high-angle bedding of turbidity current" - liquified flow deposits?

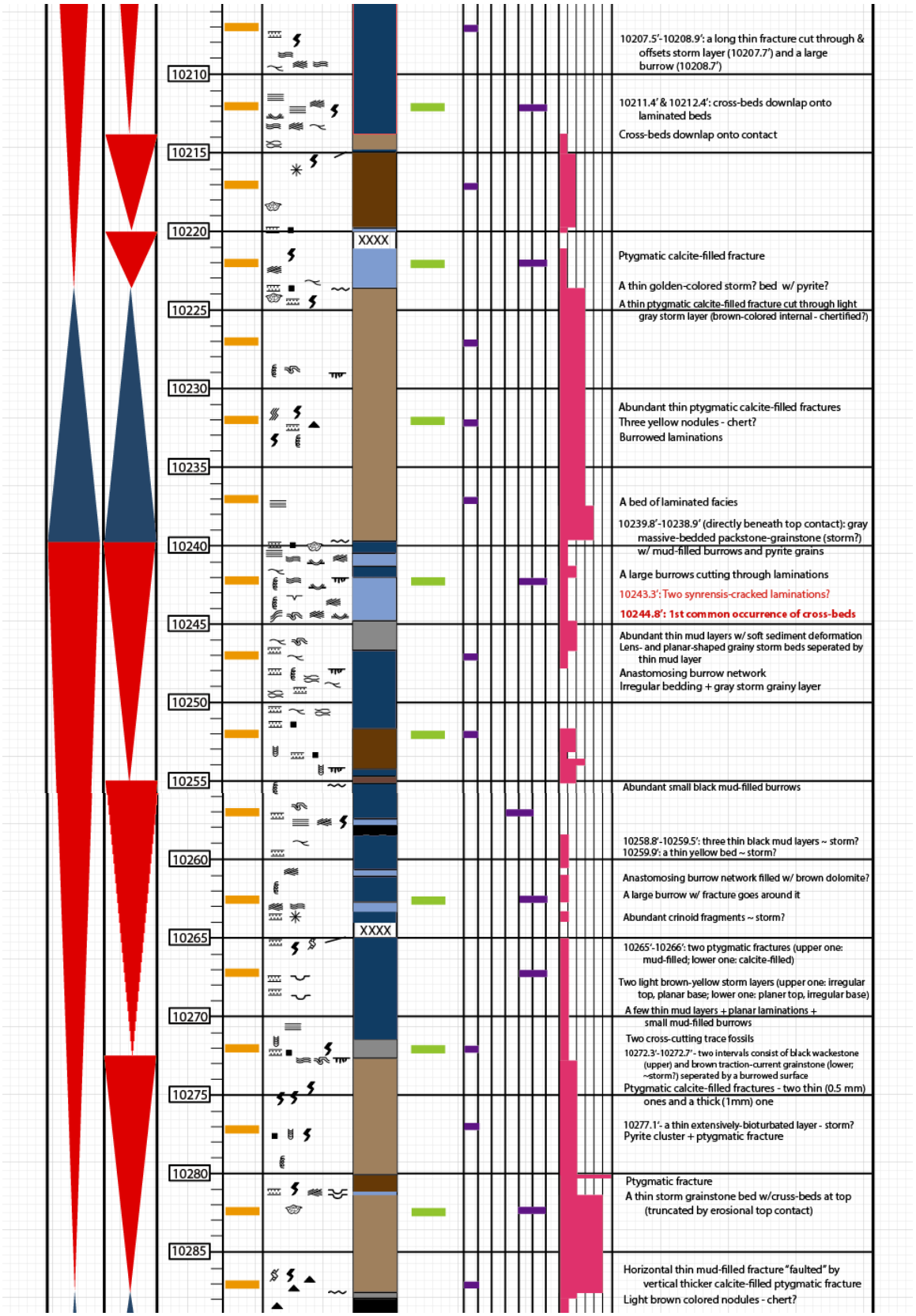
10210
10215
10220
10225
10230
10235
10240
10245
10250
10255
10260
10265
10270
10275
10280
10285
XXXX
XXXX
10207.5'-10208.9': a long thin fracture cut through & offsets storm layer (10207.7') and a large burrow (10208.7')
10211.4' & 10212.4': cross-beds downlap onto laminated beds
Cross-beds downlap onto contact
Ptygmatic calcite-filled fracture
A thin golden-colored storm? bed w/ pyrite?
A thin ptygmatic calcite-filled fracture cut through light gray storm layer (brown-colored internal - chertified?)
Abundant thin ptygmatic calcite-filled fractures
Three yellow nodules - chert?
Burrowed laminations
A bed of laminated facies
10239.8'-10238.9' (directly beneath top contact): gray massive-bedded packstone-grainstone (storm?) w/ mud-filled burrows and pyrite grains
A large burrows cutting through laminations
10243.3': Two synrensis-cracked laminations?
10244.8': 1st common occurrence of cross-beds
Abundant thin mud layers w/ soft sediment deformation
Lens- and planar-shaped grainy storm beds seperated by thin mud layer
Anastomosing burrow network
Irregular bedding + gray storm grainy layer
Abundant small black mud-filled burrows
10258.8'-10259.5': three thin black mud layers ~ storm?
10259.9': a thin yellow bed ~ storm?
Anastomosing burrow network filled w/ brown dolomite?
A large burrow w/ fracture goes around it
Abundant crinoid fragments ~ storm?
10265'-10266': two ptygmatic fractures (upper one: mud-filled; lower one: calcite-filled)
Two light brown-yellow storm layers (upper one: irregular top, planar base; lower one: planer top, irregular base)
A few thin mud layers + planar laminations + small mud-filled burrows
Two cross-cutting trace fossils
10272.3'-10272.7' - two intervals consist of black wackestone (upper) and brown traction-current grainstone (lower; ~storm?) seperated by a burrowed surface
Ptygmatic calcite-filled fractures - two thin (0.5 mm) ones and a thick (1mm) one
10277.1'- a thin extensively-bioturbated layer - storm?
Pyrite cluster + ptygmatic fracture
Ptygmatic fracture
A thin storm grainstone bed w/cruss-beds at top (truncated by erosional top contact)
Horizontal thin mud-filled fracture "faulted" by vertical thicker calcite-filled ptygmatic fracture
Light brown colored nodules - chert?

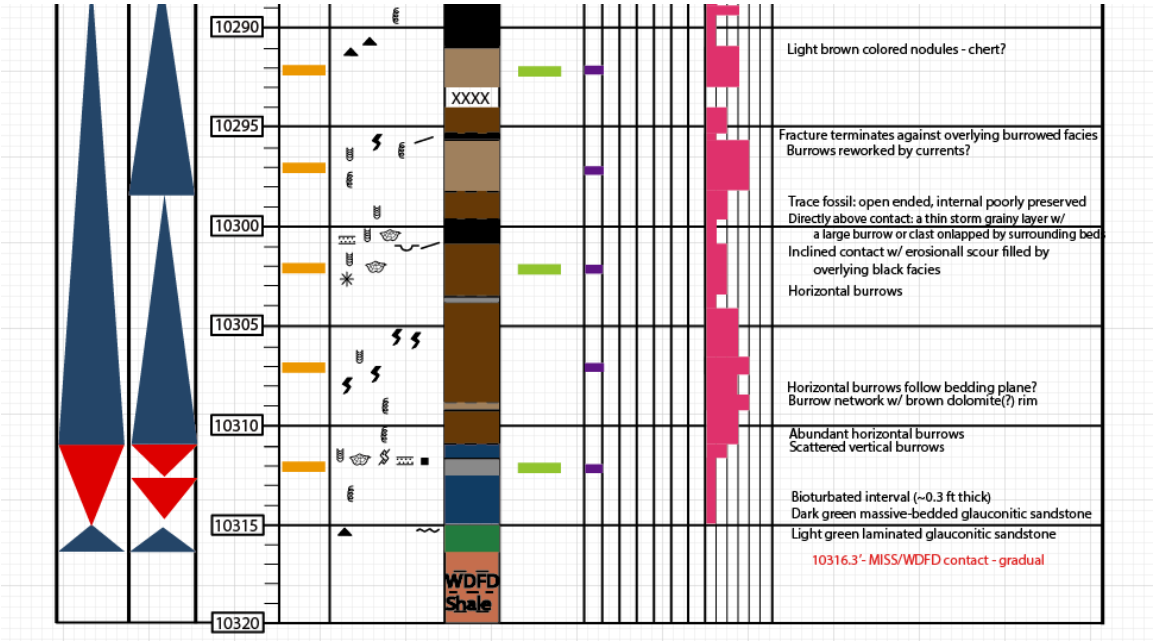
10290
10295
10300
10305
10310
10315
10320
XXXX
WDFD Shale
Light brown colored nodules - chert?
Fracture terminates against overlying burrowed facies
Burrows reworked by currents?
Trace fossil: open ended, internal poorly preserved
Directly above contact: a thin storm grainy layer w/ a large burrow or clast onlapped by surrounding bed
Inclined contact w/ erosionall scour filled by overlying black facies
Horizontal burrows
Horizontal burrows follow bedding plane?
Burrow network w/ brown dolomite(?) rim
Abundant horizontal burrows
Scattered vertical burrows
Bioturbated interval (~0.3 ft thick)
Dark green massive-bedded glauconitic sandstone
Light green laminated glauconitic sandstone
10316.3'- MISS/WDFD contact - gradual

APPENDICES

APPENDIX 2

FRACTURE DATA – STACK CORES (CORE #4, 5, 6)

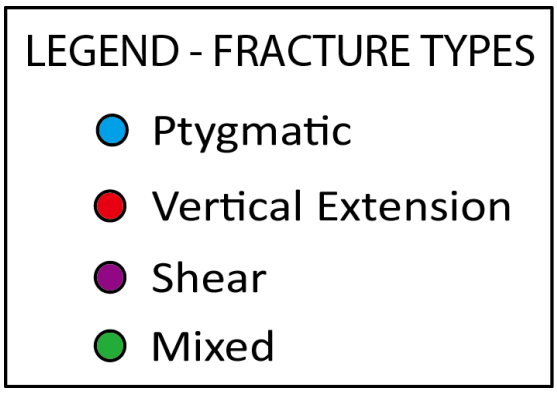

In fracture data spreadsheet:
fracture types include ptygmatic (P), vertical extension (VE), and shear (S); for mixed type of fractures, individual types are noted (e.g., VE+P), with the type being noted first is the type showing higher proportion within the fracture (e.g., in "VE+P", "VE" is the more dominant type);
orientation is documented as vertical (V) or sub-vertical (SV);
observed termination styles are categorized into tapering (at top and base; noted as "1") or abruptly terminating (at top or base; noted as "2") in a seemingly homogeneous portion of the rock, termination related to variations in mineralogy at top or base (noted as "3"), and terminations at the core edge or because of missing core pieces at top or base (noted as "4");
fracture spacing is documented as the distance between two adjacent fractures, starting from the left edge of the core, if there are several measurements at the same depth.

For fracture data of core #1, 2, and 3, readers are referred to Thompson (2016).
*Thompson, T., 2016, Fracture characterization and prediction in the "Mississippian Limestone" in North-Central Oklahoma: unpublished Master thesis, Oklahoma State University, 139 p.

Core #4 – Fracture Type and Frequency

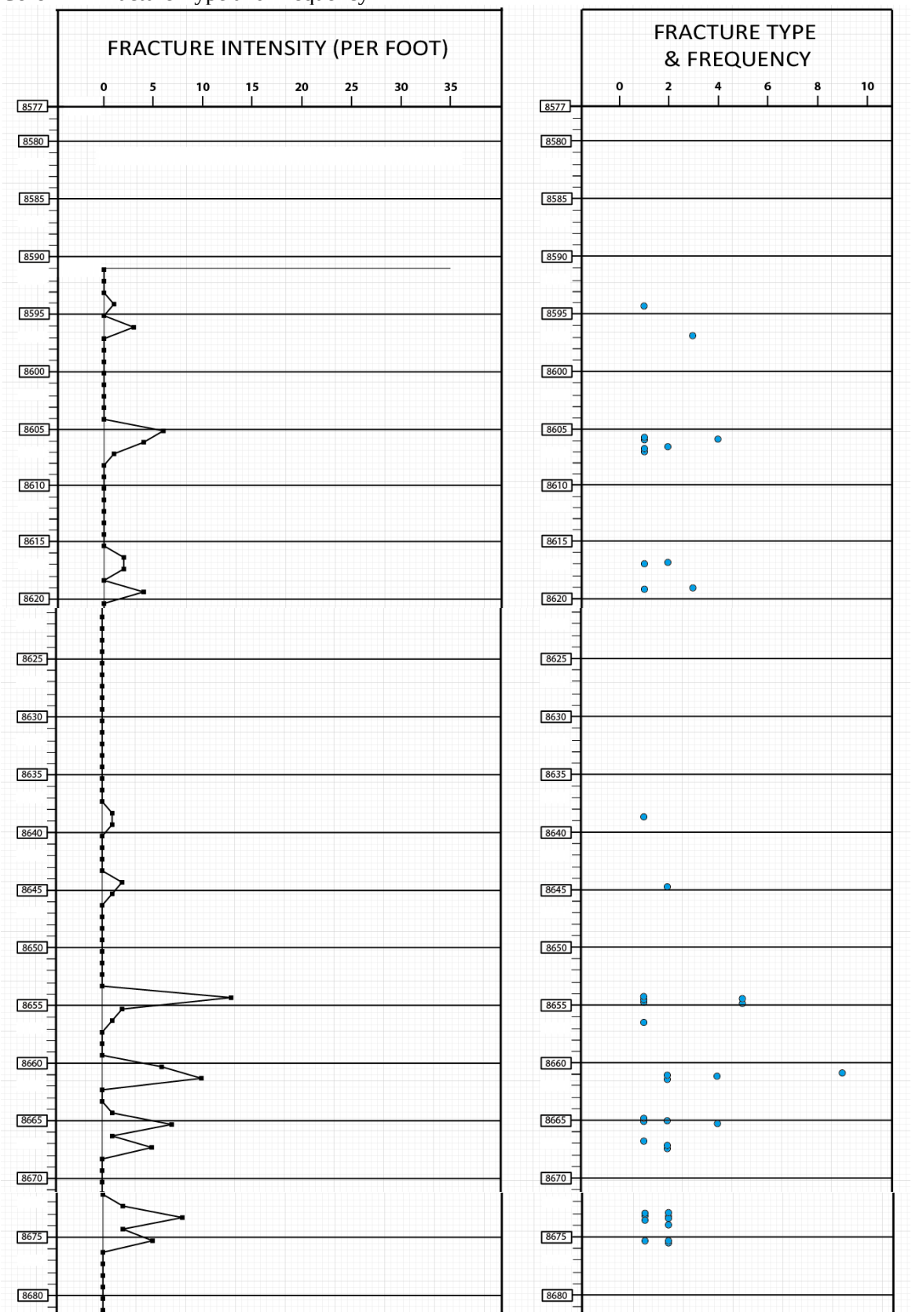

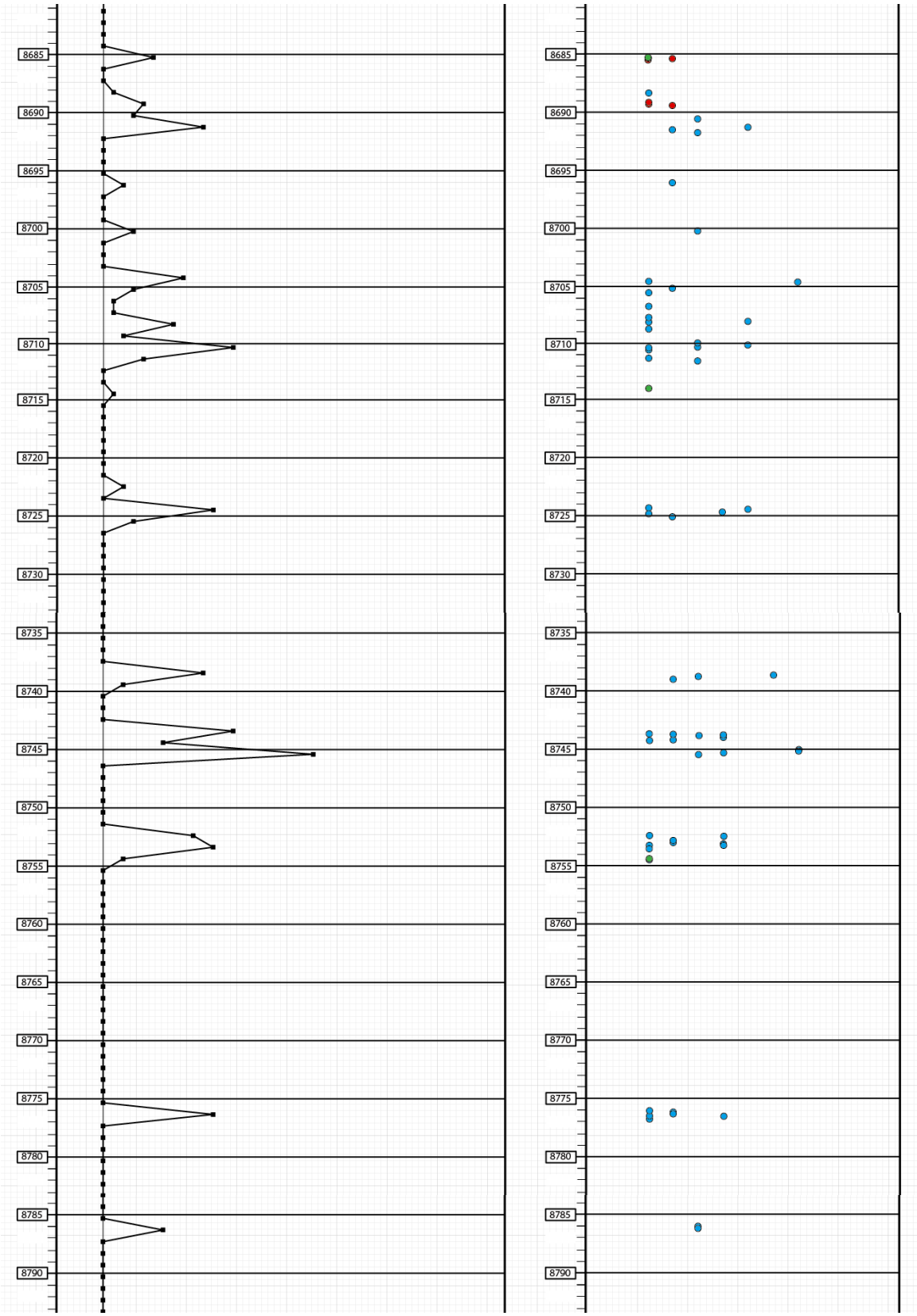
8685
8690
8695
8700
8705
8710
8715
8720
8725
8730
8735
8740
8745
8750
8755
8760
8765
8770
8775
8780
8785
8790

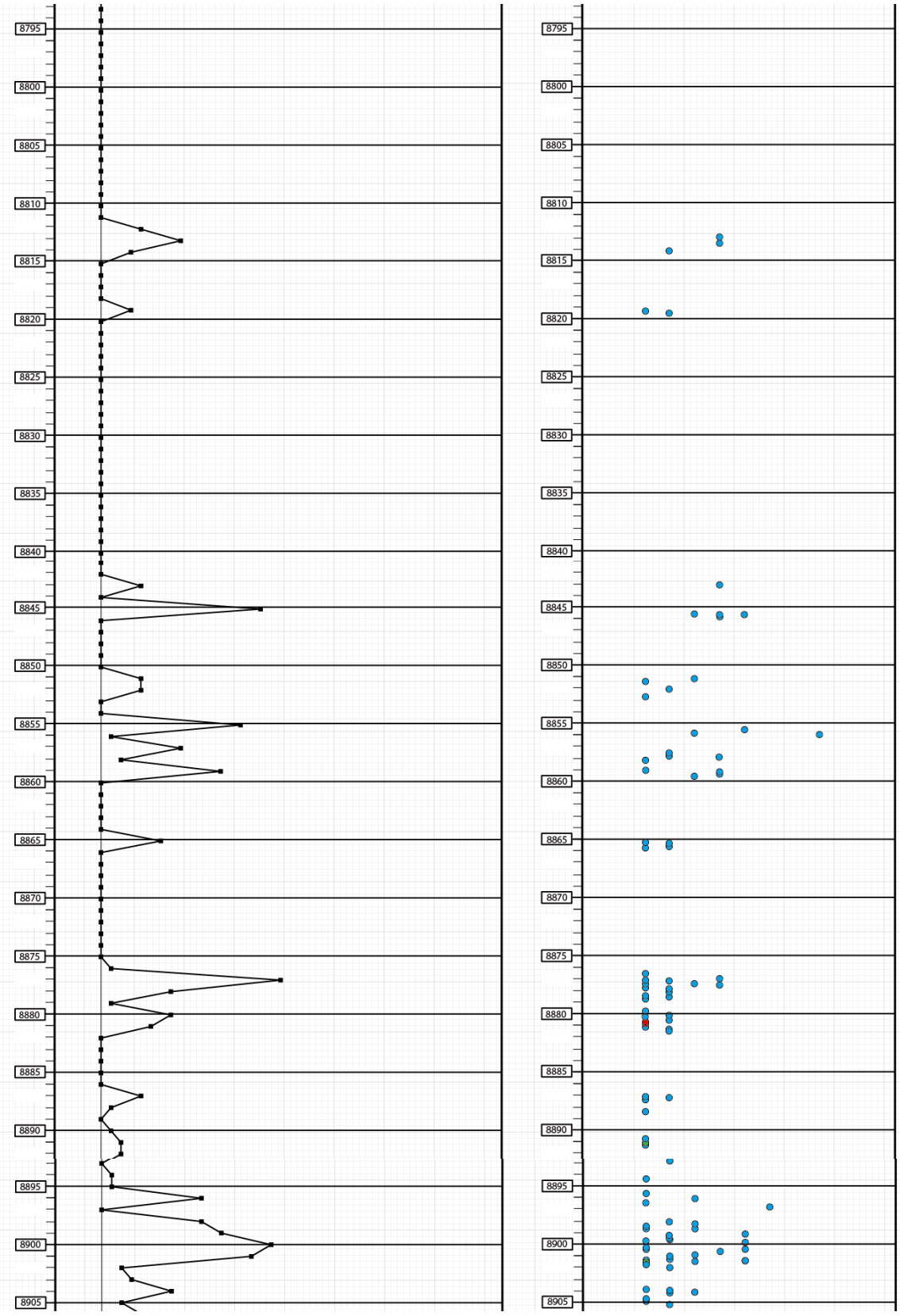
8795
8800
8805
8810
8815
8820
8825
8830
8835
8840
8845
8850
8855
8860
8865
8870
8875
8880
8885
8890
8895
8900
8905

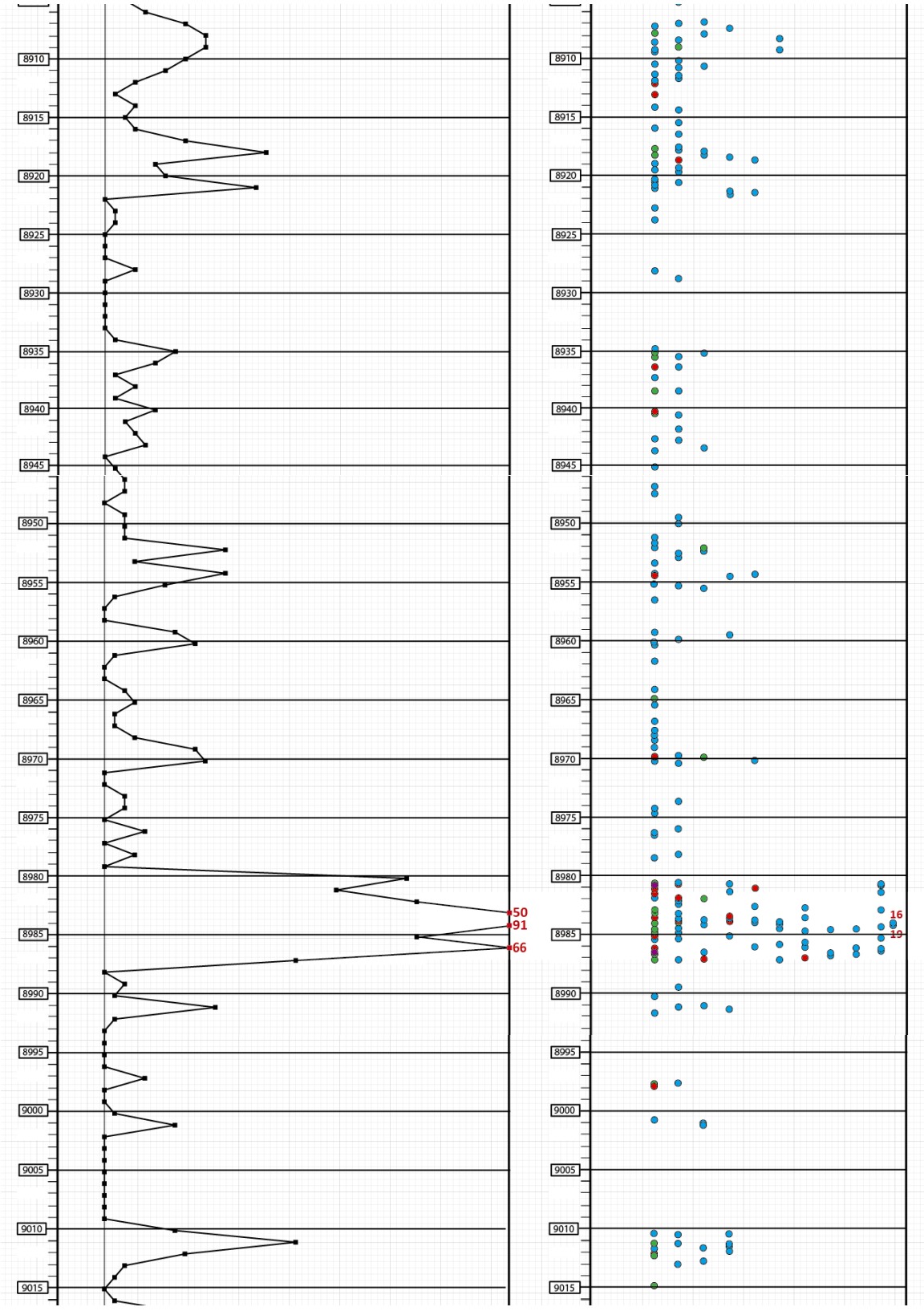
8910
8915
8920
8925
8930
8935
8940
8945
8950
8955
8960
8965
8970
8975
8980
8985
8990
8995
9000
9005
9010
9015
50
91
66
16
19

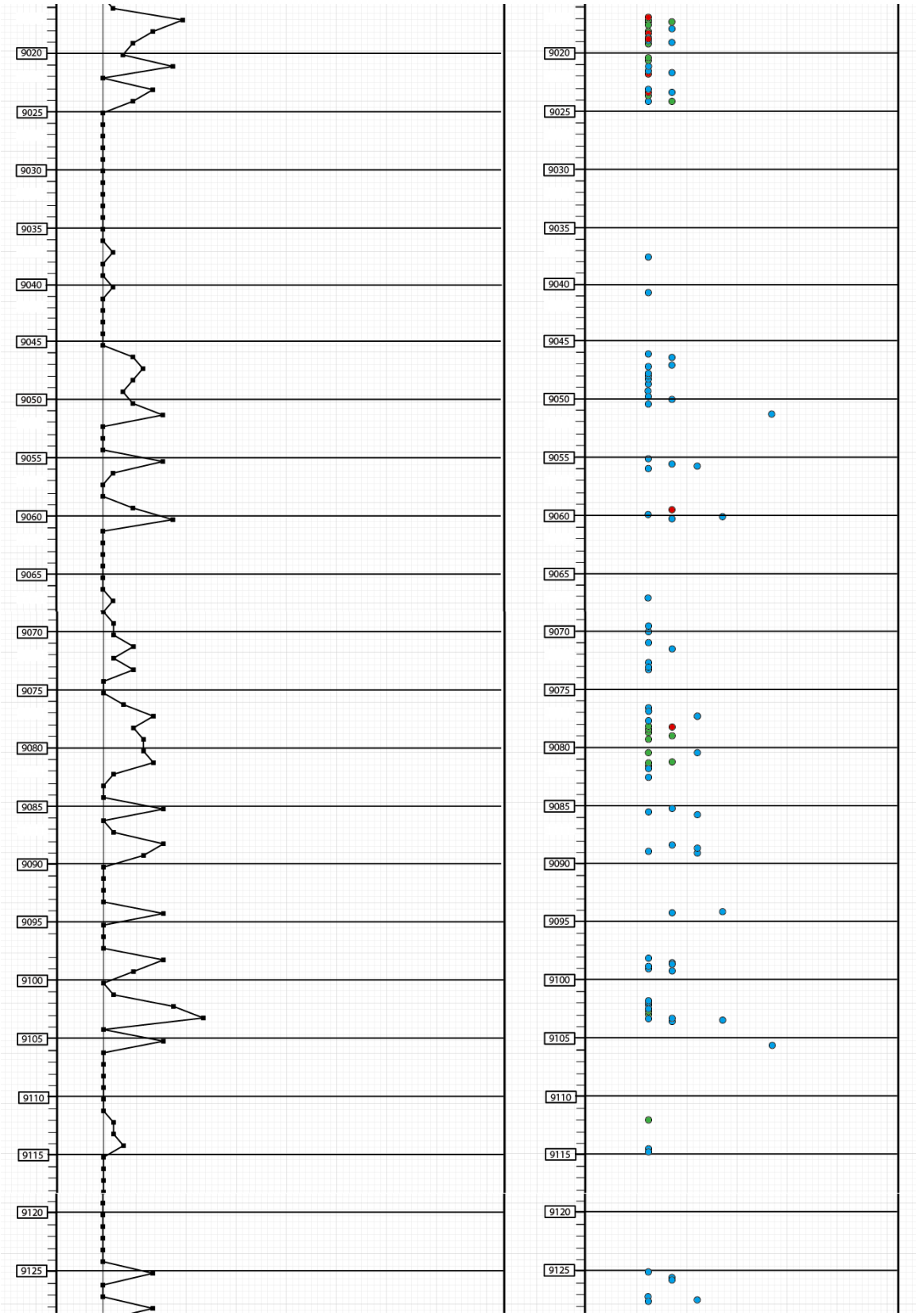
9020
9025
9030
9035
9040
9045
9050
9055
9060
9065
9070
9075
9080
9085
9090
9095
9100
9105
9110
9115
9120
9125

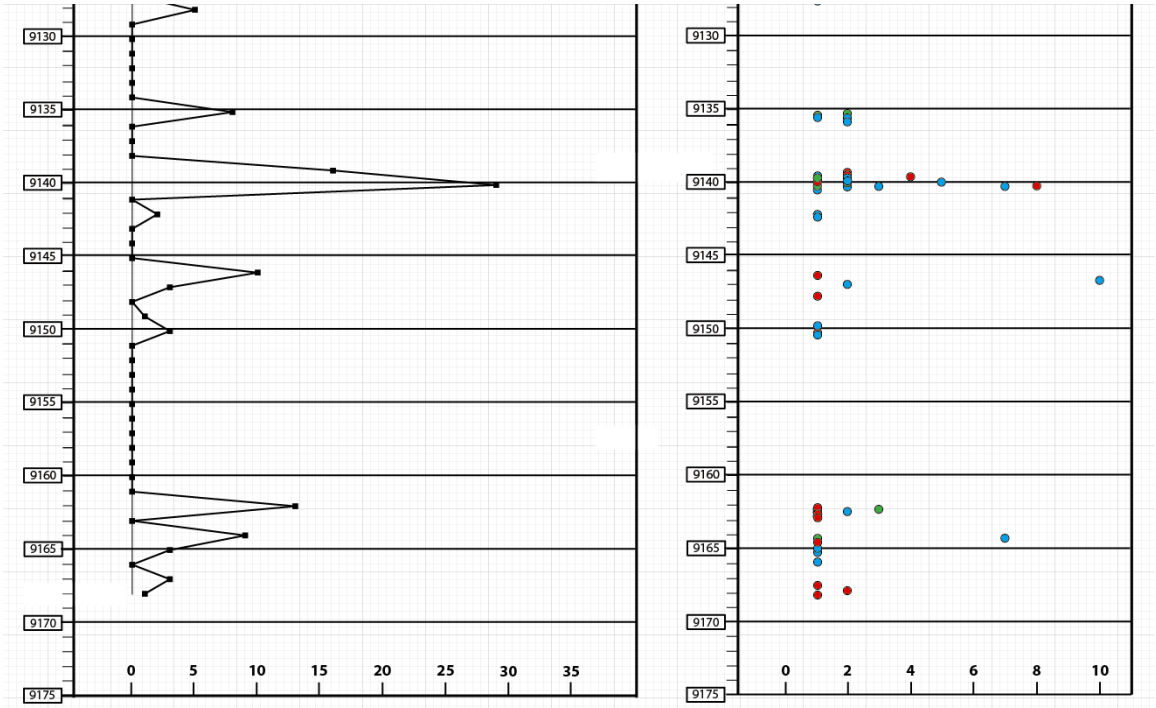
9130
9135
9140
9145
9150
9155
9160
9165
9170
9175
0
5
10
15
20
25
30
35
9130
9135
9140
9145
9150
9155
9160
9165
9170
9175
0
2
4
6
8
10

Core #5 – Fracture Type and Frequency

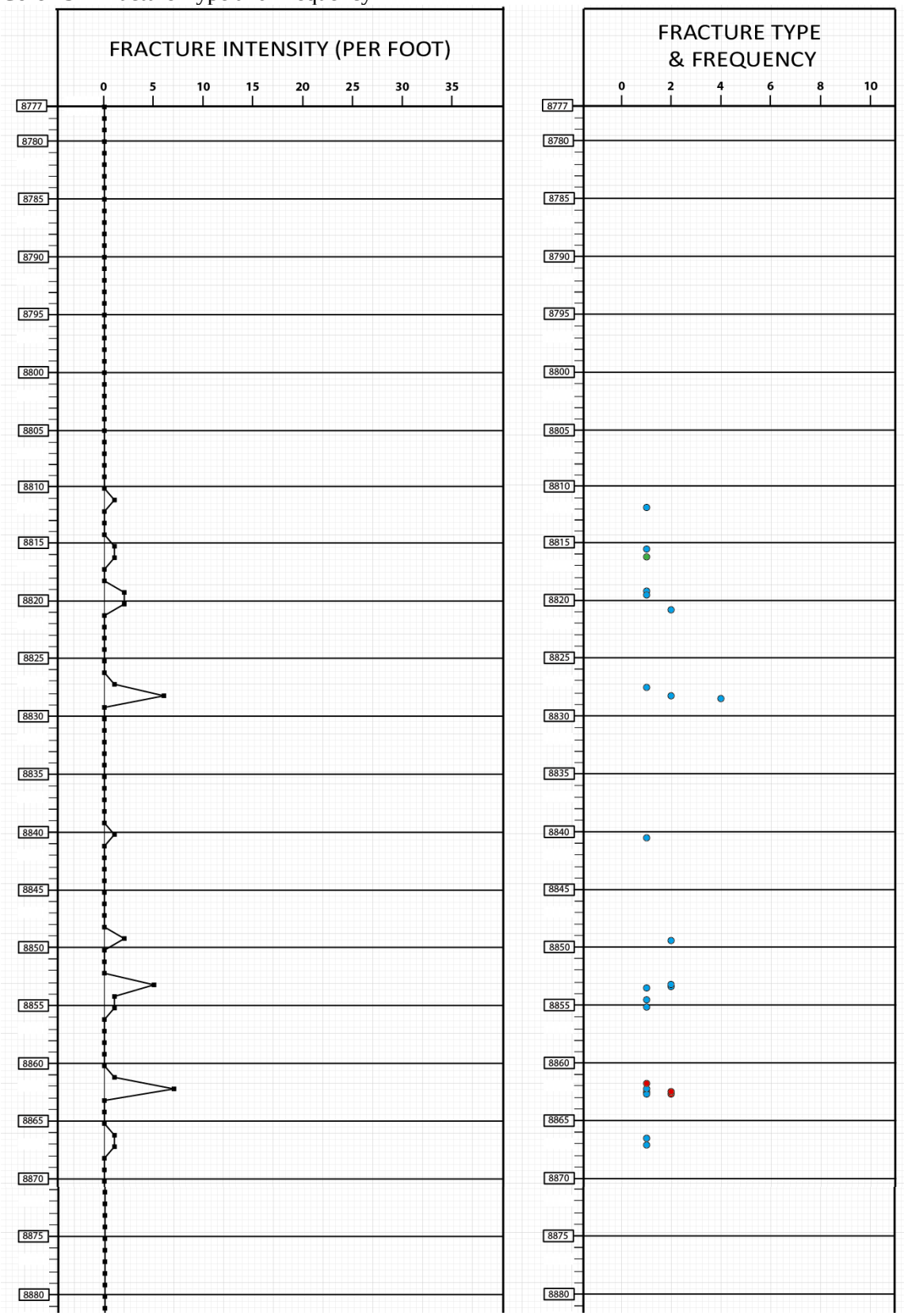

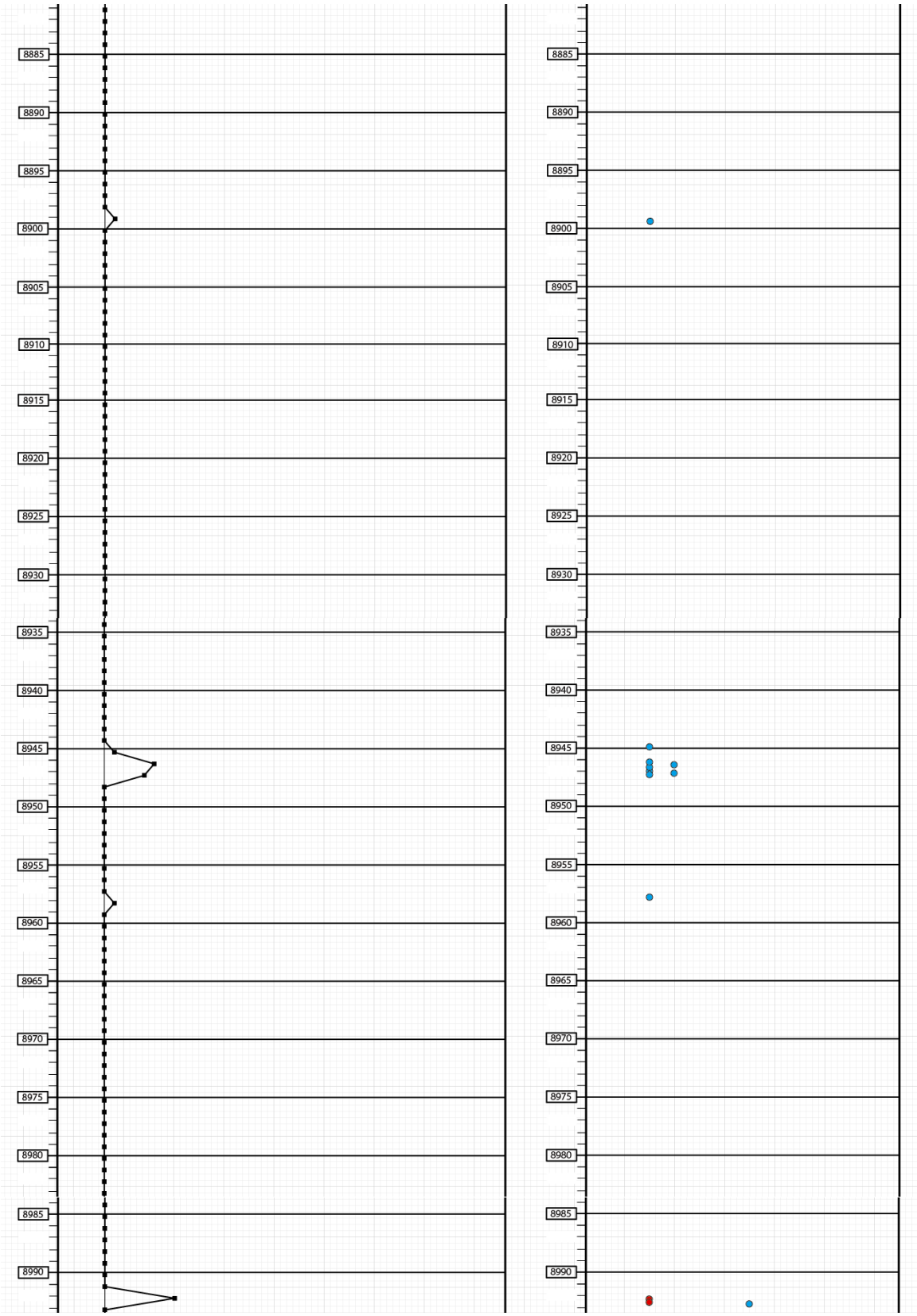
8885
8890
8895
8900
8905
8910
8915
8920
8925
8930
8935
8940
8945
8950
8955
8960
8965
8970
8975
8980
8985
8990

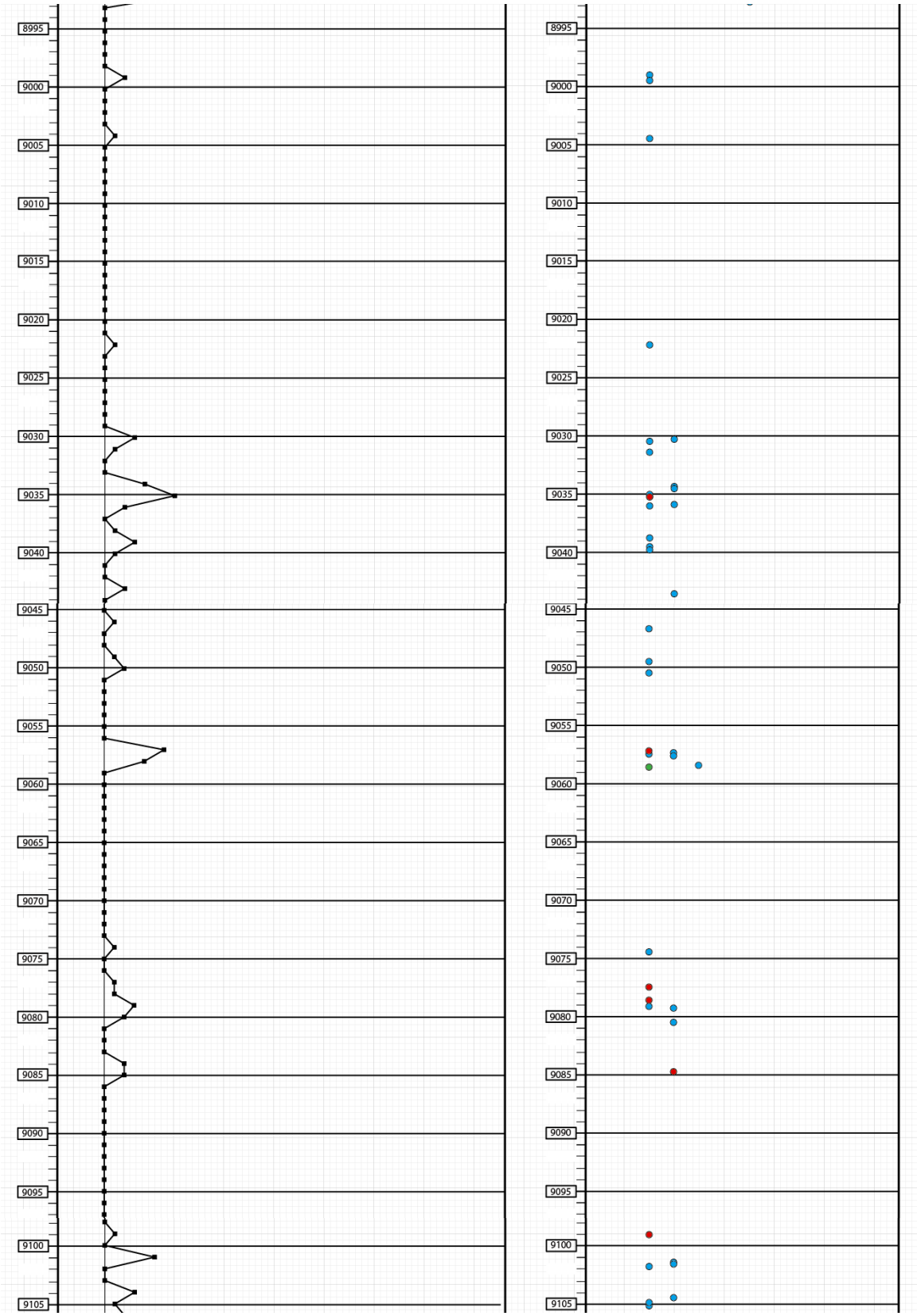
8995
9000
9005
9010
9015
9020
9025
9030
9035
9040
9045
9050
9055
9060
9065
9070
9075
9080
9085
9090
9095
9100
9105

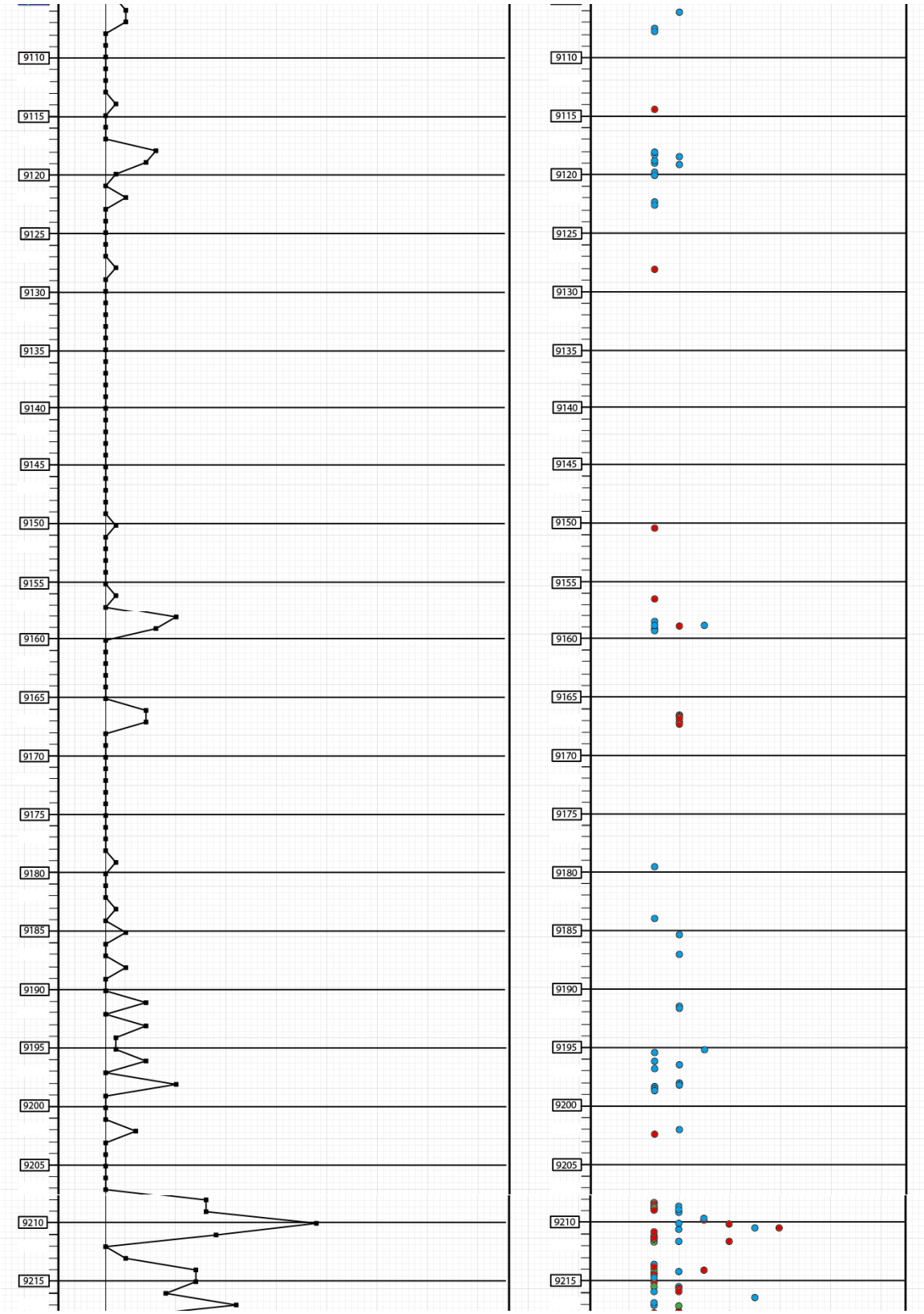
9110
9115
9120
9125
9130
9135
9140
9145
9150
9155
9160
9165
9170
9175
9180
9185
9190
9195
9200
9205
9210
9215

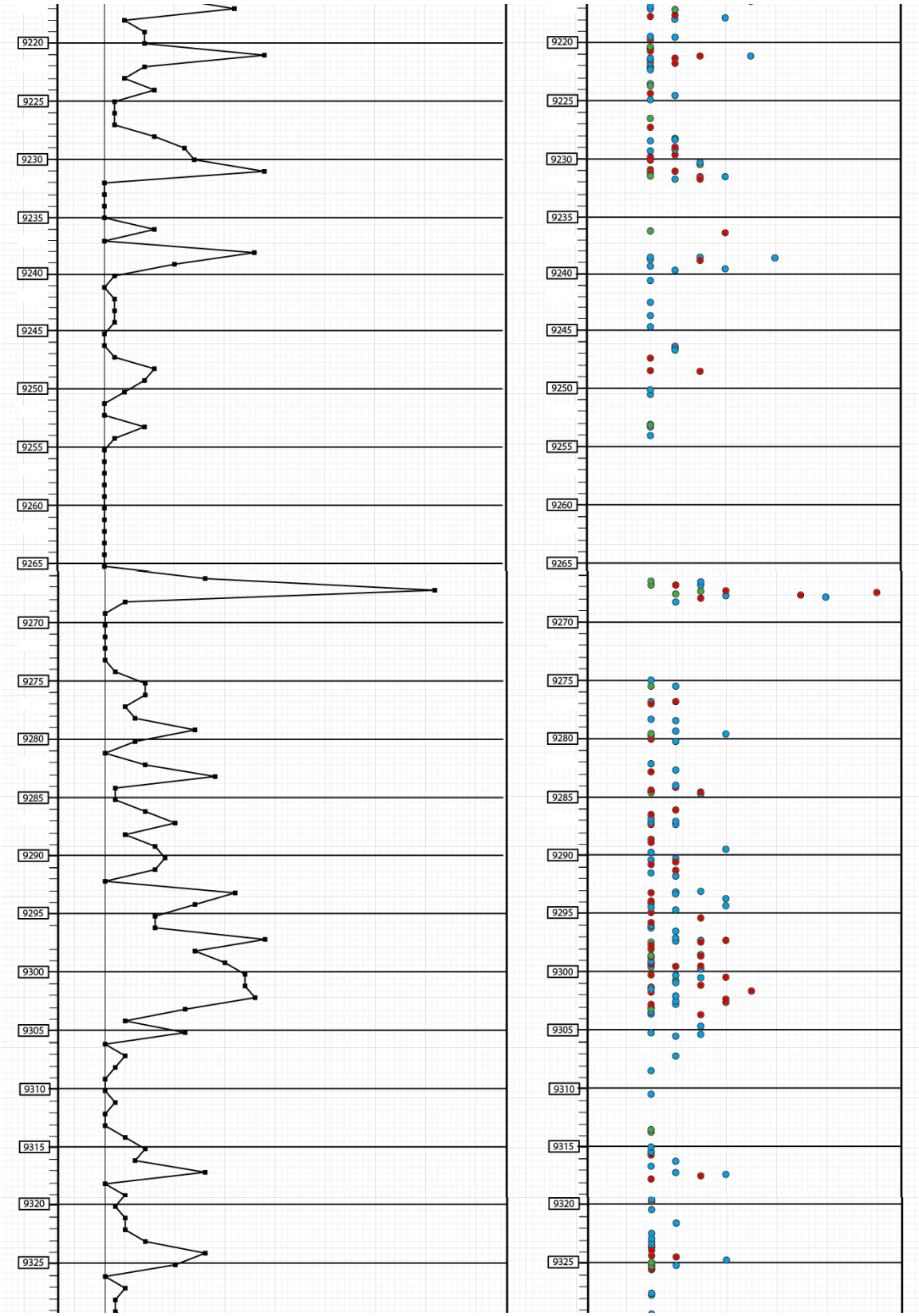
9220
9225
9230
9235
9240
9245
9250
9255
9260
9265
9270
9275
9280
9285
9290
9295
9300
9305
9310
9315
9320
9325

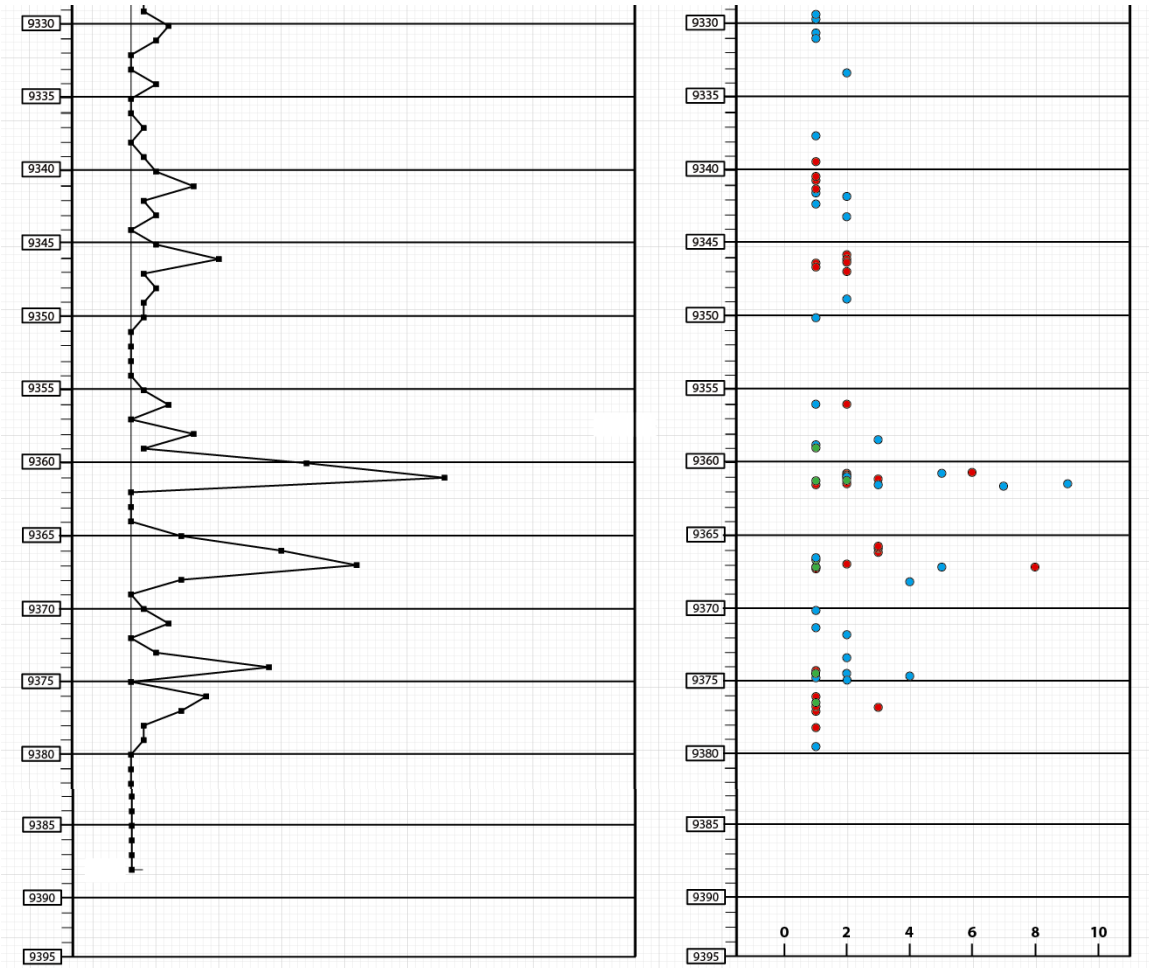
9330
9335
9340
9345
9350
9355
9360
9365
9370
9375
9380
9385
9390
9395
0
2
4
6
8
10

Core #6 – Fracture Type and Frequency

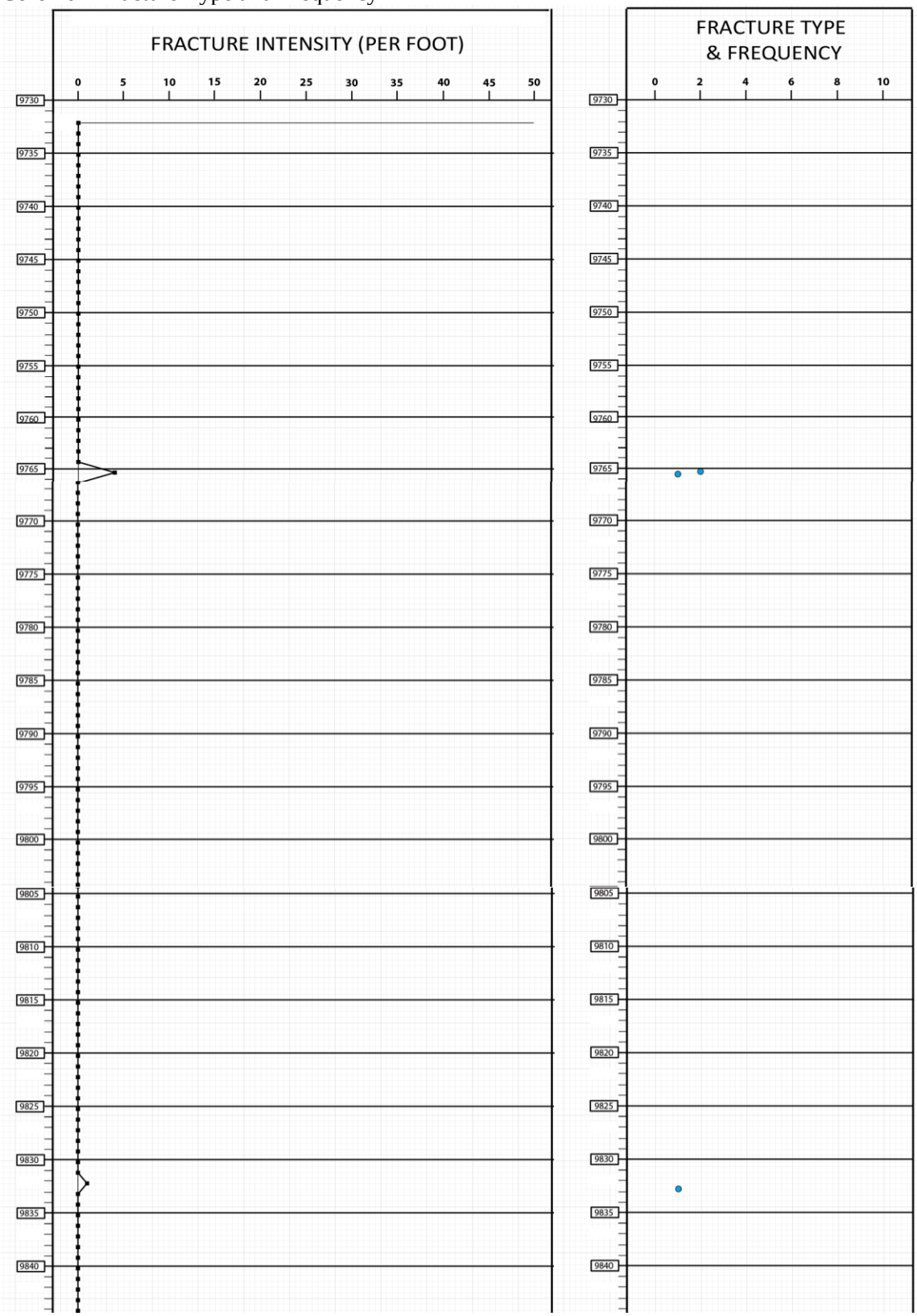

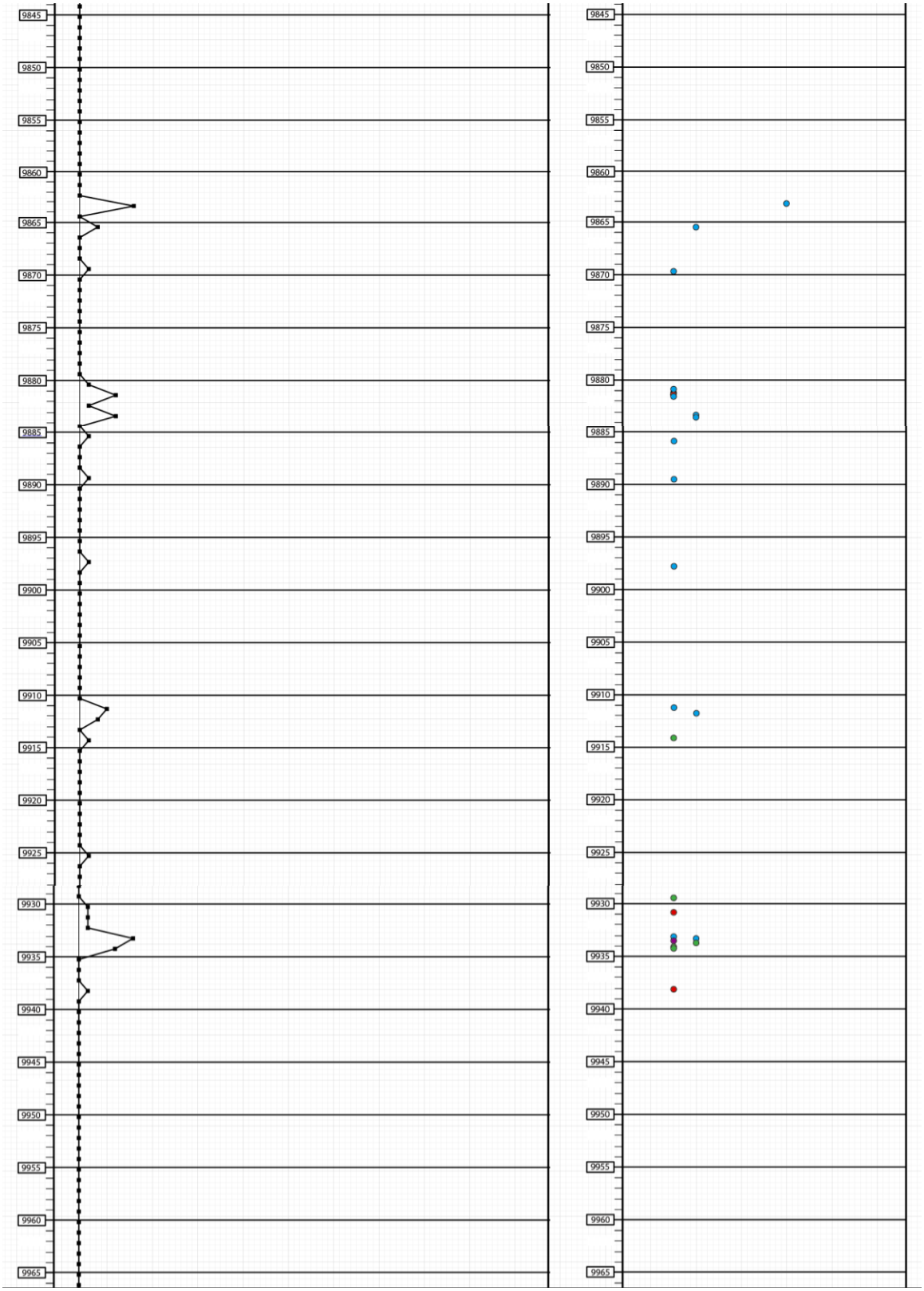
9845
9850
9855
9860
9865
9870
9875
9880
9885
9890
9895
9900
9905
9910
9915
9920
9925
9930
9935
9940
9945
9950
9955
9960
9965


9970
9975
9980
9985
9990
9995
10000
10005
10010
10015
10020
10025
10030
10035
10040
10045
10050
10055
10060
10065
10070
10075
10080
10085

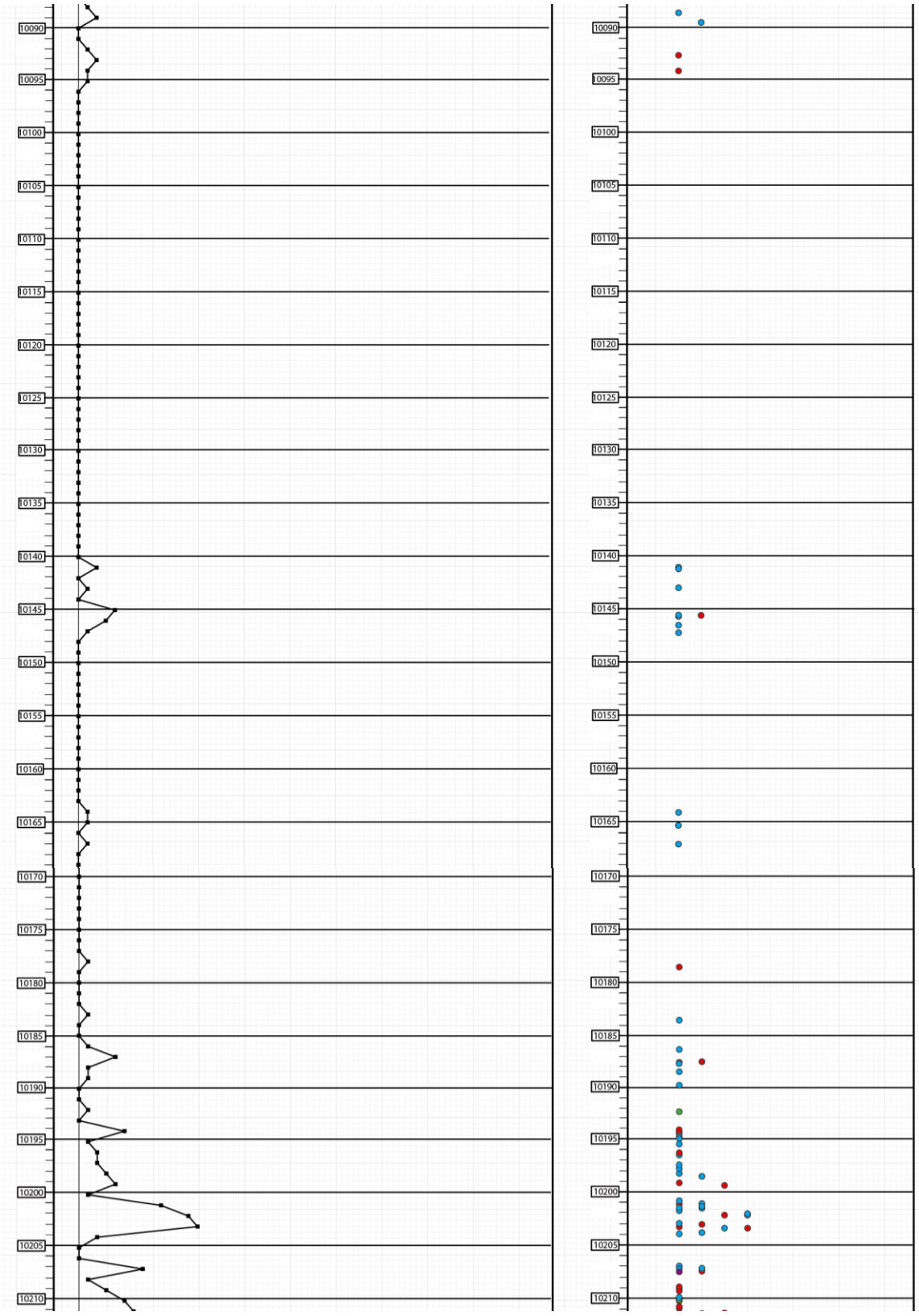
10090
10095
10100
10105
10110
10115
10120
10125
10130
10135
10140
10145
10150
10155
10160
10165
10170
10175
10180
10185
10190
10195
10200
10205
10210

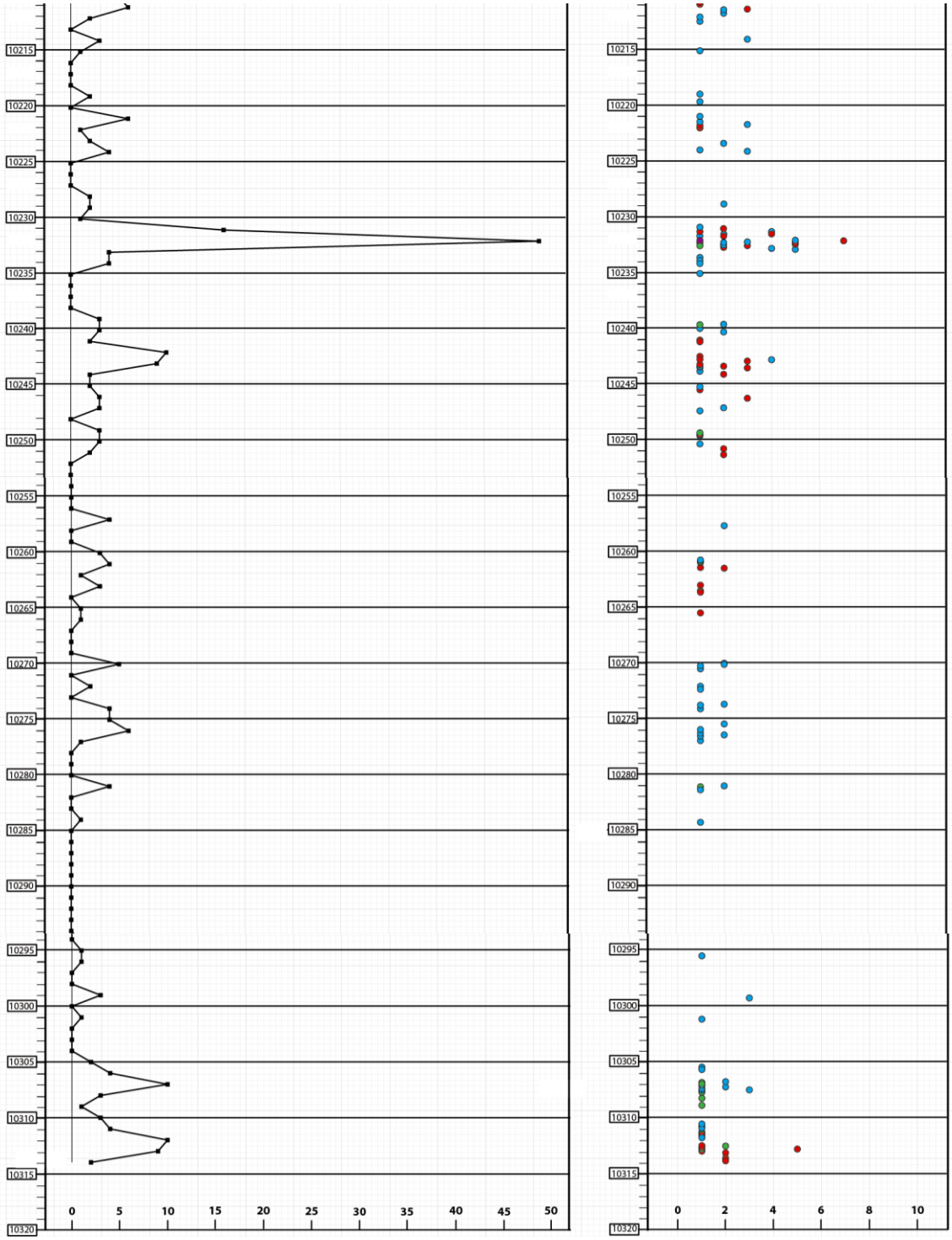
10215
10220
10225
10230
10235
10240
10245
10250
10255
10260
10265
10270
10275
10280
10285
10290
10295
10300
10305
10310
10315
10320
0
5
10
15
20
25
30
35
40
45
50
0
2
4
6
8
10

Core #4 – Fracture type and frequency by facies

Core #	Box #	Facies	Ptygmatic	Shear	Vertical Extension	Mixed	Mixed Types
2	17	1			4		
		2					
		3					
		4	9		1	2	P+VE
		5					
		6					
		7					
2	16	1					
		2					
		3					
		4	8		4	1	P+VE
		5					
		6					
		7					
2	15	1					
		2					
		3					
		4					
		5					
		6	14		3		
		7					
2	14	1					
		2					
		3					
		4	26		17	1	VE+P
						3	P+S
		5					
		6					
		7					
2	13	1					
		2					
		3					
		4	6			3	P+VE
		5					
		6	4				
		7					
2	12	1					
		2					
		3					
		4					
		5	5				
		6					
		7					

Core #	Box #	Facies	Ptygmatic	Shear	Vertical Extension	Mixed	Mixed Types
2	11	1					
		2					
		3					
		4					
		5	2			1	VE+P
		6					
		7					
2	10	1					
		2					
		3					
		4					
		5	22			1	VE+P
						1	P+VE
		6					
		7					
2	9	1					
		2					
		3					
		4	2				
		5	10				
		6	3				
		7					
2	8	1					
		2					
		3					
		4	1				
		5	9				
		6	6				
		7					
2	7	1					
		2					
		3					
		4	11			2	P+VE
		5					
		6	1		2	3	P+VE
						6	VE+P
		7					

Core #	Box #	Facies	Ptygmatic	Shear	Vertical Extension	Mixed	Mixed Types
2	6	1					
		2					
		3					
		4	5				
		5					
		6	2				
		7					
2	5	1					
		2					
		3					
		4					
		5					
		6	14		2		
		7					
2	4	1					
		2					
		3					
		4					
		5					
		6	8				
		7	13				
2	3	1					
		2					
		3					
		4					
		5					
		6	2				
		7					
2	1	1					
		2					
		3					
		4					
		5					
		6	11		2	4	P+VE
						2	VE+P
		7					
1	51	1					
		2					
		3					
		4					
		5					
		6	2		1	1	P+VE
						1	VE+P
		7					

Core #	Box #	Facies	Ptygmatic	Shear	Vertical Extension	Mixed	Mixed Types
1	50	1					
		2					
		3					
		4	15			1	P+S
						1	P+VE
		5	9				
		6	7		3	3	VE+P
						2	P+VE
						1	P+S
		7					
1	49	1					
		2					
		3					
		4					
		5	7				
		6					
		7					
1	48	1					
		2					
		3					
		4					
		5					
		6	12		1	1	P+VE
1	47	1					
		2					
		3					
		4					
		5					
		6	257	1	25	4	P+VE
						8	VE+P
						4	P+S
						1	VE+S
		7					
1	46	1					
		2					
		3					
		4	11				
		5					
		6	40		8	1	VE+S
						2	VE+P
		7					

Core #	Box #	Facies	Ptygmatic	Shear	Vertical Extension	Mixed	Mixed Types
1	45	1					
		2					
		3					
		4	1				
		5					
		6	18		1	3	VE+P
						1	P+VE
		7					
1	44	1					
		2					
		3					
		4					
		5					
		6	17				
		7					
1	43	1					
		2					
		3					
		4					
		5					
		6	25		1	1	P+VE
						1	VE+P
						2	P+S
		7	3				
1	42	1					
		2					
		3					
		4					
		5					
		6	11		1	1	VE+P
		7	4			1	VE+P
1	41	1					
		2					
		3					
		4	3				
		5					
		6	6			2	VE+P
		7	2		1		
1	40	1					
		2					
		3					
		4				1	P+VE
		5	3				
		6	20				
		7	2				

Core #	Box #	Facies	Ptygmatic	Shear	Vertical Extension	Mixed	Mixed Types
1	39	1					
		2					
		3					
		4					
		5	8				
		6	3		1		
		7	31	1	3	1	P+S
1	38	1					
		2					
		3					
		4					
		5	6				
		6	42			3	VE+P
		7	16			1	VE+P
1	37	1					
		2					
		3					
		4					
		5	10				
		6	31				
		7	14				
1	36	1					
		2					
		3					
		4					
		5	2				
		6	6				
		7					
1	35	1					
		2					
		3					
		4					
		5					
		6	36		2		
		7					
1	34	1					
		2					
		3	6				
		4					
		5					
		6					
		7					

Core #	Box #	Facies	Ptygmatic	Shear	Vertical Extension	Mixed	Mixed Types
1	33	1					
		2					
		3	23				
		4					
		5					
		6					
		7					
1	32	1					
		2					
		3	21				
		4					
		5					
		6					
		7					
1	31	1					
		2					
		3	20				
		4					
		5					
		6					
		7					
1	28	1					
		2					
		3					
		4					
		5					
		6	13				
		7					
1	25	1					
		2					
		3					
		4					
		5					
		6	6				
		7					
1	24	1					
		2					
		3	11				
		4					
		5					
		6					
		7					

Core #	Box #	Facies	Ptygmatic	Shear	Vertical Extension	Mixed	Mixed Types
1	21	1					
		2					
		3					
		4					
		5					
		6	21				
		7					
1	20	1					
		2					
		3					
		4					
		5					
		6	39				
		7					
1	19	1					
		2					
		3					
		4					
		5					
		6	10				
		7					
1	18	1					
		2					
		3					
		4					
		5					
		6	13				
		7					
1	17	1					
		2					
		3					
		4					
		5					
		6	1				
		7					
1	16	1					
		2					
		3					
		4					
		5					
		6	3				
		7	35				

Core #	Box #	Facies	Ptygmatic	Shear	Vertical Extension	Mixed	Mixed Types
1	15	1					
		2					
		3					
		4					
		5	3				
		6	2				
		7					
1	14	1					
		2					
		3					
		4					
		5	8				
		6	7		5	2	VE+P
		7	1				
1	12	1					
		2					
		3					
		4					
		5					
		6	20				
		7					
1	11	1					
		2					
		3					
		4					
		5					
		6	26				
		7					
1	10	1					
		2					
		3					
		4					
		5					
		6	14				
		7					
1	9	1					
		2					
		3					
		4					
		5					
		6	2				
		7					

Core #	Box #	Facies	Ptygmatic	Shear	Vertical Extension	Mixed	Mixed Types
1	8	1					
		2					
		3					
		4					
		5					
		6	1				
		7					
1	6	1					
		2					
		3					
		4	3				
		5					
		6	4				
		7					
1	5	1					
		2					
		3					
		4					
		5					
		6	10				
		7					
1	4	1					
		2					
		3					
		4					
		5					
		6	3				
		7					
1	3	1					
		2					
		3					
		4					
		5					
		6	1				
		7					

Core #5 – Fracture type and frequency by facies

Core #	Box #	Facies	Ptygmatic	Shear	Vertical Extension	Mixed	Mixed Types
4	5	1					
		2					
		3					
		4	26		8	1	P+VE
		5					
		6					
		7					
4	4	1					
		2	7		21	1	VE+P
		3					
		4	5				
		5					
		6					
		7					
4	3	1					
		2					
		3					
		4	5				
		5	20		19	2	VE+P
						1	P+S
						1	P+VE
		6	5		5		
		7					
4	2	1					
		2					
		3					
		4	5		10		
		5					
		6					
		7					
4	1	1					
		2					
		3	6				
		4	1				
		5			4		
		6					
		7					
3	15	1					
		2					
		3					
		4	4		5		
		5					
		6					
		7					

Core #	Box #	Facies	Ptygmatic	Shear	Vertical Extension	Mixed	Mixed Types
3	14	1					
		2					
		3					
		4	3		1		
		5					
		6	16		7	2	VE+P
		7					
3	13	1					
		2					
		3					
		4					
		5					
		6	12		6	1	P+S
						1	VE+S
		7					
3	12	1					
		2					
		3					
		4	9				
		5					
		6	16		22	2	VE+P
		7					
3	11	1					
		2					
		3					
		4	20	1	11	2	VE+P
						1	P+VE
		5					
		6	7		5	2	VE+P
		7	19		13	1	VE+P
3	10	1					
		2					
		3					
		4	11		5		
		5					
		6	14		12	1	VE+P
		7					
3	9	1					
		2					
		3					
		4	1				
		5	9		2		
		6	8		6	1	VE+P
		7					

Core #	Box #	Facies	Ptygmatic	Shear	Vertical Extension	Mixed	Mixed Types
3	8	1					
		2					
		3					
		4					
		5	21		21	3	P+VE
						4	VE+P
						1	P+S
		6					
		7					
3	6	1					
		2	5		5		
		3					
		4	6			1	VE+P
		5					
		6					
		7					
3	5	1					
		2					
		3					
		4	2				
		5					
		6	20		3		
		7	1				
3	4	1					
		2					
		3					
		4			4		
		5					
		6	12		18	5	VE+P
		7					
3	3	1					
		2					
		3					
		4	7		1	1	VE+P
		5					
		6	10		14	1	VE+P
		7	3				
3	2	1					
		2					
		3					
		4					
		5	2		4	1	P+VE
		6	23		16	4	VE+P
		7	4				

Core #	Box #	Facies	Ptygmatic	Shear	Vertical Extension	Mixed	Mixed Types
3	1	1	1				
		2					
		3					
		4					
		5	2		1		
		6	19		18		
		7					
2	24	1					
		2					
		3					
		4					
		5	11				
		6					
		7					
2	23	1					
		2					
		3					
		4					
		5	10				
		6					
		7					
2	22	1					
		2					
		3					
		4					
		5	4				
		6					
		7					
2	20	1					
		2					
		3					
		4					
		5					
		6	2		7		
		7					
2	19	1					
		2					
		3					
		4					
		5			1		
		6	8		2		
		7					

Core #	Box #	Facies	Ptygmatic	Shear	Vertical Extension	Mixed	Mixed Types
2	18	1					
		2					
		3					
		4					
		5					
		6			1		
		7					
2	16	1					
		2					
		3					
		4			1		
		5					
		6					
		7					
2	15	1					
		2					
		3					
		4					
		5	12				
		6					
		7					
2	14	1					
		2					
		3	1				
		4					
		5	4			1	VE+P
		6	2				
		7					
2	13	1					
		2					
		3					
		4					
		5	5		1		
		6	4				
		7					
2	11	1					
		2					
		3					
		4					
		5	2				
		6	6		2		
		7					

Core #	Box #	Facies	Ptygmatic	Shear	Vertical Extension	Mixed	Mixed Types
2	10	1					
		2					
		3					
		4					
		5					
		6	1		1		
		7					
2	8	1					
		2					
		3					
		4	5		1		
		5	4				
		6					
		7					
2	7	1					
		2					
		3					
		4					
		5	6				
		6					
		7					
2	6	1					
		2					
		3					
		4					
		5	3				
		6	9		1		
		7					
2	5	1					
		2					
		3					
		4					
		5	4				
		6	2				
		7					
2	4	1					
		2	1				
		3					
		4					
		5					
		6	1				
		7					

Core #	Box #	Facies	Ptygmatic	Shear	Vertical Extension	Mixed	Mixed Types
2	2	1					
		2					
		3					
		4					
		5					
		6	3				
		7					
2	1	1					
		2					
		3					
		4					
		5					
		6					
		7	5		2		
1	22	1					
		2					
		3					
		4	1				
		5					
		6					
		7					
1	21	1					
		2					
		3					
		4	2				
		5					
		6					
		7					
1	19	1					
		2	8				
		3					
		4					
		5	1				
		6					
		7					
1	14	1					
		2					
		3					
		4					
		5	1				
		6					
		7					

Core #	Box #	Facies	Ptygmatic	Shear	Vertical Extension	Mixed	Mixed Types
1	11	1					
		2					
		3					
		4					
		5					
		6	1				
		7					
1	10	1					
		2					
		3					
		4					
		5					
		6	3		5	1	VE+P
		7					
1	9	1					
		2					
		3					
		4					
		5	6				
		6	2				
		7					
1	8	1					
		2					
		3					
		4					
		5	1				
		6					
		7					
1	6	1					
		2					
		3					
		4					
		5					
		6					
		7	7				
1	5	1					
		2					
		3					
		4					
		5					
		6	1			1	VE+P
		7	4				

Core #6 – Fracture type and frequency by facies

Core #	Box #	Facies	Ptygmatic	Shear	Vertical Extension	Mixed	Mixed Types
2	39	1					
		2					
		3					
		4					
		5					
		6			16	1	VE+P
		7					
2	38	1					
		2					
		3	1				
		4	14			2	P+S
						2	P+VE
		5	3			1	VE+P
		6	2		1	1	VE+P
		7					
2	37	1					
		2					
		3	1				
		4	3				
		5	1				
		6					
		7					
2	35	1					
		2					
		3					
		4	6				
		5	2				
		6	2				
		7					
2	34	1					
		2					
		3				1	VE+P
		4	8				
		5					
		6	7				
		7					
2	33	1					
		2					
		3					
		4					
		5					
		6	3		5	1	P+VE
						1	VE+P
		7	1		1	1	VE+P

Core #	Box #	Facies	Ptygmatic	Shear	Vertical Extension	Mixed	Mixed Types
2	32	1					
		2					
		3					
		4					
		5					
		6	2		5	1	VE+P
		7	2				
2	31	1					
		2					
		3	1		4		
		4					
		5					
		6	6				
		7	7		16		
2	30	1					
		2					
		3					
		4					
		5	37	1	30	1	P+VE
						1	VE+S
		6	2				
		7					
2	29	1					
		2					
		3					
		4					
		5	14				
		6	2		1		
		7					
2	28	1					
		2					
		3					
		4	6				
		5					
		6	5		1		
		7					
2	27	1					
		2					
		3					
		4					
		5					
		6	16	1	8		
		7					

Core #	Box #	Facies	Ptygmatic	Shear	Vertical Extension	Mixed	Mixed Types
2	26	1					
		2					
		3					
		4					
		5					
		6	31		16		
		7					
2	25	1					
		2					
		3					
		4	3		3		
		5					
		6	2		1		
		7	1		2	1	VE+P
2	24	1					
		2					
		3					
		4					
		5	0		0		
		6					
		7					
2	22	1					
		2	1				
		3					
		4					
		5	2				
		6					
		7					
2	20	1					
		2					
		3					
		4					
		5	5		2		
		6	2				
		7					
2	14	1					
		2					
		3	0				
		4					
		5	4				
		6	2		0		
		7					

Core #	Box #	Facies	Ptygmatic	Shear	Vertical Extension	Mixed	Mixed Types
2	12	1					
		2				1	VE+P
		3					
		4	4	1		1	VE+P
		5					
		6					
		7					
2	11	1					
		2					
		3					
		4	10		1		
		5	3				
		6					
		7					
2	10	1					
		2					
		3					
		4					
		5	1				
		6					
		7					
2	9	1					
		2					
		3					
		4					
		5					
		6	11				
		7					
2	3	1					
		2					
		3					
		4					
		5					
		6			1	1	P+S
		7					
2	2	1					
		2					
		3			1	1	P+VE
		4					
		5					
		6	1	5	1	2	P+S
		7					

Core #	Box #	Facies	Ptygmatic	Shear	Vertical Extension	Mixed	Mixed Types
1	23	1					
		2					
		3					
		4					
		5					
		6	2	1	2	4	P+S
		7					
1	22	1					
		2					
		3					
		4					
		5					
		6					
		7				1	VE+P+S
1	21	1					
		2					
		3					
		4					
		5					
		6				0	unknown
		7					
1	20	1					
		2					
		3					
		4					
		5					
		6	4				
		7					
1	19	1					
		2					
		3	1				
		4					
		5					
		6					
		7					
1	18	1					
		2					
		3	1				
		4					
		5					
		6	1				
		7					

Core #	Box #	Facies	Ptygmatic	Shear	Vertical Extension	Mixed	Mixed Types
1	17	1					
		2					
		3	0		0		
		4					
		5					
		6					
		7					
1	16	1					
		2	1				
		3					
		4					
		5					
		6					
		7					
1	15	1					
		2					
		3	6				
		4	0				
		5					
		6					
		7					
1	12	1					
		2					
		3	1				
		4					
		5					
		6					
		7					
1	4	1					
		2	2				
		3	2				
		4					
		5					
		6					
		7					

Core #4 – Fracture intensity

Core#	Box#	Depth (ft)	Fracture Intensity	Notes
1	3	8591	0	
		8592	0	
		8593	0	
		8594	1	
1	4	8595	0	
		8596	3	
		8597	0	NO CORE
		8598	0	
		8599	0	
		8600	0	
		8601	0	
		8602	0	
		8603	0	
1	5	8604	0	
		8605	6	
		8606	4	
		8607	1	
		8608	0	
		8609	0	
		8610	0	
		8611	0	
		8612	0	
1	6	8613	0	
		8614	0	
		8615	0	
		8616	2	
		8617	2	
		8618	0	
		8619	4	
		8620	0	
		8621	0	
1	7	8622	0	
		8623	0	
		8624	0	
		8625	0	
		8626	0	
		8627	0	
		8628	0	
		8629	0	
		8630	0	

Core#	Box#	Depth (ft)	Fracture Intensity	Notes
1	8	8631	0	
		8632	0	
		8633	0	
		8634	0	
		8635	0	
		8636	0	
		8637	0	
		8638	1	
		8639	1	
1	9	8640	0	
		8641	0	
		8642	0	
		8643	0	
		8644	2	
		8645	1	
		8646	0	
		8647	0	
		8648	0	
1	10	8649	0	
		8650	0	
		8651	0	
		8652	0	
		8653	0	
		8654	13	
		8655	2	
		8656	1	
		8657	0	NO CORE
1	11	8658	0	
		8659	0	
		8660	6	
		8661	10	
		8662	0	
1	12	8667	5	
		8668	0	
		8669	0	
		8670	0	
		8671	0	
		8672	2	
		8673	8	
		8674	2	
		8675	5	

Core#	Box#	Depth (ft)	Fracture Intensity	Notes
1	13	8676	0	
		8677	0	
		8678	0	
		8679	0	
		8680	0	
		8681	0	
		8682	0	
		8683	0	
		8684	0	
1	14	8685	5	
		8686	0	
		8687	0	NO CORE
		8688	1	
		8689	4	
		8690	3	
		8691	10	
		8692	0	
		8693	0	
1	15	8694	0	
		8695	0	
		8696	2	
		8697	0	
		8698	0	
		8699	0	
		8700	3	
		8701	0	
		8702	0	
1	16	8703	0	
		8704	8	
		8705	3	
		8706	1	
		8707	1	
		8708	7	
		8709	2	
		8710	13	
		8711	4	
1	17	8712	0	
		8713	0	
		8714	1	
		8715	0	
		8716	0	
		8717	0	NO CORE
		8718	0	
		8719	0	
		8720	0	

Core#	Box#	Depth (ft)	Fracture Intensity	Notes
1	18	8721	0	
		8722	2	
		8723	0	
		8724	11	
		8725	3	
		8726	0	
		8727	0	
		8728	0	
		8729	0	
1	19	8730	0	
		8731	0	
		8732	0	
		8733	0	
		8734	0	
		8735	0	
		8736	0	
		8737	0	
		8738	10	
1	20	8739	2	
		8740	0	
		8741	0	
		8742	0	
		8743	13	
		8744	6	
		8745	21	
		8746	0	
		8747	0	NO CORE
1	21	8748	0	
		8749	0	
		8750	0	
		8751	0	
		8752	9	
		8753	11	
		8754	2	
		8755	0	
		8756	0	
1	22	8757	0	
		8758	0	
		8759	0	
		8760	0	
		8761	0	
		8762	0	
		8763	0	
		8764	0	
		8765	0	

Core#	Box#	Depth (ft)	Fracture Intensity	Notes
1	23	8766	0	
		8767	0	
		8768	0	
		8769	0	
		8770	0	
		8771	0	
		8772	0	
		8773	0	
		8774	0	
1	24	8775	0	
		8776	11	
		8777	0	NO CORE
		8778	0	
		8779	0	
		8780	0	
		8781	0	
		8782	0	
		8783	0	
1	25	8784	0	
		8785	0	
		8786	6	
		8787	0	
		8788	0	
		8789	0	
		8790	0	
		8791	0	
		8792	0	
1	26	8793	0	
		8794	0	
		8795	0	
		8796	0	
		8797	0	
		8798	0	
		8799	0	
		8800	0	
		8801	0	
1	27	8802	0	
		8803	0	
		8804	0	
		8805	0	
		8806	0	
		8807	0	
		8808	0	
		8809	0	
		8810	0	

Core#	Box#	Depth (ft)	Fracture Intensity	Notes
1	28	8811	0	
		8812	4	
		8813	8	
		8814	3	
		8815	0	
		8816	0	
		8817	0	
		8818	0	
		8819	3	
1	29	8820	0	
		8821	0	
		8822	0	
		8823	0	
		8824	0	
		8825	0	
		8826	0	
		8827	0	
		8828	0	
1	30	8829	0	
		8830	0	
		8831	0	
		8832	0	
		8833	0	
		8834	0	
		8835	0	
		8836	0	
		8837	0	
1	31	8838	0	
		8839	0	
		8840	0	
		8841	0	
		8842	0	
		8843	4	
		8844	0	
		8845	16	
		8846	0	
1	32	8847	0	
		8848	0	
		8849	0	
		8850	0	
		8851	4	
		8852	4	
		8853	0	
		8854	0	
		8855	14	

Core#	Box#	Depth (ft)	Fracture Intensity	Notes
1	33	8856	1	
		8857	8	
		8858	2	
		8859	12	
		8860	0	
		8861	0	
		8862	0	
		8863	0	
		8864	0	
1	34	8865	6	
		8866	0	
		8867	0	NO CORE
		8868	0	
		8869	0	
		8870	0	
		8871	0	
		8872	0	
		8873	0	
1	35	8874	0	
		8875	0	
		8876	1	
		8877	18	
		8878	7	
		8879	1	
		8880	7	
		8881	5	
		8882	0	
1	36	8883	0	
		8884	0	
		8885	0	
		8886	0	
		8887	4	
		8888	1	
		8889	0	
		8890	1	
		8891	2	
1	37	8892	2	
		8893	0	
		8894	1	
		8895	1	
		8896	10	
		8897	0	NO CORE
		8898	10	
		8899	12	
		8900	17	

Core#	Box#	Depth (ft)	Fracture Intensity	Notes
1	38	8901	15	
		8902	2	
		8903	3	
		8904	7	
		8905	2	
		8906	4	
		8907	8	
		8908	10	
		8909	10	
1	39	8910	8	
		8911	6	
		8912	3	
		8913	1	
		8914	3	
		8915	2	
		8916	3	
		8917	8	
		8918	16	
1	40	8919	5	
		8920	6	
		8921	15	
		8922	0	
		8923	1	
		8924	1	
		8925	0	
		8926	0	
		8927	0	NO CORE
1	41	8928	3	
		8929	0	
		8930	0	
		8931	0	
		8932	0	
		8933	0	
		8934	1	
		8935	7	
		8936	5	
1	42	8937	1	
		8938	3	
		8939	1	
		8940	5	
		8941	2	
		8942	3	
		8943	4	
		8944	0	
		8945	1	

Core#	Box#	Depth (ft)	Fracture Intensity	Notes
1	43	8946	2	
		8947	2	
		8948	0	
		8949	2	
		8950	2	
		8951	2	
		8952	12	
		8953	3	
		8954	12	
1	44	8955	6	
		8956	1	
		8957	0	NO CORE
		8958	0	
		8959	7	
		8960	9	
		8961	1	
		8962	0	
		8963	0	
1	45	8964	2	
		8965	3	
		8966	1	
		8967	1	
		8968	3	
		8969	9	
		8970	10	
		8971	0	
		8972	0	
1	46	8973	2	
		8974	2	
		8975	0	
		8976	4	
		8977	0	
		8978	3	
		8979	0	
		8980	30	
		8981	23	
1	47	8982	31	
		8983	50	
		8984	91	
		8985	31	
		8986	66	
		8987	19	
		8988	0	
		8989	2	
		8990	1	

Core#	Box#	Depth (ft)	Fracture Intensity	Notes
1	48	8991	11	
		8992	1	
		8993	0	
		8994	0	
		8995	0	
		8996	0	
		8997	4	
		8998	0	
		8999	0	NO CORE
1	49	9000	1	
		9001	7	
		9002	0	
		9003	0	
		9004	0	
		9005	0	
		9006	0	
		9007	0	
		9008	0	
1	50	9009	0	
		9010	7	
		9011	19	
		9012	8	
		9013	2	
		9014	1	
		9015	0	
		9016	1	
		9017	8	
1	51	9018	5	
2	1	9019	3	
		9020	2	
		9021	7	
		9022	0	
		9023	5	
		9024	3	
		9025	0	
		9026	0	
		9027	0	
2	2	9028	0	
		9029	0	
		9030	0	
		9031	0	
		9032	0	
		9033	0	
		9034	0	
		9035	0	
		9036	0	

Core#	Box#	Depth (ft)	Fracture Intensity	Notes
2	3	9037	1	
		9038	0	
		9039	0	
		9040	1	
		9041	0	
		9042	0	
		9043	0	
		9044	0	
		9045	0	
2	4	9046	3	
		9047	4	
		9048	3	
		9049	2	
		9050	3	
		9051	6	
		9052	0	
		9053	0	
		9054	0	
2	5	9055	6	
		9056	1	
		9057	0	NO CORE
		9058	0	
		9059	3	
		9060	7	
		9061	0	
		9062	0	
		9063	0	
2	6	9064	0	
		9065	0	
		9066	0	
		9067	1	
		9068	0	
		9069	1	
		9070	1	
		9071	3	
		9072	1	
2	7	9073	3	
		9074	0	
		9075	0	
		9076	2	
		9077	5	
		9078	3	
		9079	4	
		9080	4	
		9081	5	

Core#	Box#	Depth (ft)	Fracture Intensity	Notes
2	8	9082	1	
		9083	0	
		9084	0	
		9085	6	
		9086	0	NO CORE
		9087	1	
		9088	6	
		9089	4	
		9090	0	
2	9	9091	0	
		9092	0	
		9093	0	
		9094	6	
		9095	0	
		9096	0	
		9097	0	
		9098	6	
		9099	3	
2	10	9100	0	
		9101	1	
		9102	7	
		9103	10	
		9104	0	
		9105	6	
		9106	0	
		9107	0	
		9108	0	
2	11	9109	0	
		9110	0	
		9111	0	
		9112	1	
		9113	1	
		9114	2	
		9115	0	NO CORE
		9116	0	
		9117	0	
2	12	9118	0	
		9119	0	
		9120	0	
		9121	0	
		9122	0	
		9123	0	
		9124	0	
		9125	5	
		9126	0	

Core#	Box#	Depth (ft)	Fracture Intensity	Notes
2	13	9127	0	
		9128	5	
		9129	0	
		9130	0	
		9131	0	
		9132	0	
		9133	0	
		9134	0	
		9135	8	
2	14	9136	0	
		9137	0	
		9138	0	
		9139	16	
		9140	29	
		9141	0	
		9142	2	
		9143	0	
		9144	0	NO CORE
2	15	9145	0	
		9146	10	
		9147	3	
		9148	0	
		9149	1	
		9150	3	
		9151	0	
		9152	0	
		9153	0	
2	16	9154	0	
		9155	0	
		9156	0	
		9157	0	
		9158	0	
		9159	0	
		9160	0	
		9161	0	
		9162	13	
2	17	9163	0	
		9164	9	
		9165	3	
		9166	0	
		9167	3	
		9168	1	

Core #5 – Fracture intensity

Core#	Box#	Depth (ft)	Fracture Intensity	Notes
1	1	8777	0	
		8778	0	
		8779	0	
		8780	0	
		8781	0	
		8782	0	
		8783	0	
		8784	0	
		8785	0	
1	2	8786	0	
		8787	0	
		8788	0	
		8789	0	
		8790	0	
		8791	0	
		8792	0	
		8793	0	
		8794	0	
1	3	8795	0	
		8796	0	
		8797	0	
		8798	0	
		8799	0	
		8800	0	
		8801	0	
		8802	0	
		8803	0	
1	4	8804	0	
		8805	0	
		8806	0	
		8807	0	
		8808	0	
		8809	0	
		8810	0	
		8811	0	
		8812	0	NO CORE
1	5	8813	0	
		8814	0	
		8815	1	
		8816	1	
		8817	0	
		8818	0	
		8819	2	
		8820	2	
		8821	0	

Core#	Box#	Depth (ft)	Fracture Intensity	Notes
1	6	8822	0	
		8823	0	
		8824	0	
		8825	0	
		8826	0	
		8827	1	
		8828	6	
		8829	0	
		8830	0	
1	7	8831	0	
		8832	0	
		8833	0	
		8834	0	
		8835	0	
		8836	0	
		8837	0	
		8838	0	
		8839	0	
1	8	8840	1	
		8841	0	
		8842	0	
		8843	0	
		8844	0	
		8845	0	
		8846	0	
		8847	0	
		8848	0	
1	9	8849	1	
		8850	0	
		8851	0	
		8852	0	NO CORE
		8853	5	
		8854	1	
		8855	1	
		8856	0	
		8857	0	
1	10	8858	0	
		8859	0	
		8860	0	
		8861	1	
		8862	7	
		8863	0	
		8864	0	
		8865	0	
		8866	1	

Core#	Box#	Depth (ft)	Fracture Intensity	Notes
1	11	8867	1	
		8868	0	
		8869	0	
		8870	0	
		8871	0	
		8872	0	
		8873	0	
		8874	0	
		8875	0	
1	12	8876	0	
		8877	0	
		8878	0	
		8879	0	
		8880	0	
		8881	0	
		8882	0	
		8883	0	
		8884	0	
1	13	8885	0	
		8886	0	
		8887	0	
		8888	0	
		8889	0	
		8890	0	
		8891	0	
		8892	0	
		8893	0	
1	14	8894	0	
		8895	0	
		8896	0	
		8897	0	
		8898	0	
		8899	1	
		8900	0	
		8901	0	
		8902	0	
1	15	8903	0	
		8904	0	
		8905	0	
		8906	0	
		8907	0	
		8908	0	
		8909	0	
		8910	0	
		8911	0	

Core#	Box#	Depth (ft)	Fracture Intensity	Notes
1	16	8912	0	
		8913	0	
		8914	0	
		8915	0	
		8916	0	
		8917	0	
		8918	0	
		8919	0	
		8920	0	
1	17	8921	0	
		8922	0	
		8923	0	
		8924	0	
		8925	0	
		8926	0	
		8927	0	
		8928	0	
		8929	0	
1	18	8930	0	
		8931	0	
		8932	0	
		8933	0	
		8934	0	
		8935	0	
		8936	0	
		8937	0	
		8938	0	
1	19	8939	0	
		8940	0	
		8941	0	
		8942	0	
		8943	0	
		8944	0	
		8945	1	
		8946	5	
		8947	4	
1	20	8948	0	
		8949	0	
		8950	0	
		8951	0	
		8952	0	
		8953	0	
		8954	0	
		8955	0	
		8956	0	

Core#	Box#	Depth (ft)	Fracture Intensity	Notes
1	21	8957	1	
		8958	2	
		8959	0	
		8960	0	
		8961	0	
		8962	0	
		8963	0	
		8964	0	
		8965	0	
1	22	8966	0	
		8967	0	
		8968	0	
		8969	0	
		8970	0	
		8971	0	1
		8972	0	NO CORE
		8973	0	
		8974	0	
1	23	8975	0	
		8976	0	
		8977	0	
		8978	0	
		8979	0	
		8980	0	
		8981	0	
		8982	0	
		8983	0	
1	24	8984	0	
		8985	0	
		8986	0	
		8987	0	
		8988	0	
2	1	8989	0	
		8990	0	
		8991	0	
		8992	7	
		8993	0	NO CORE
		8994	0	
		8995	0	
		8996	0	
		8997	0	

Core#	Box#	Depth (ft)	Fracture Intensity	Notes
2	2	8998	0	
		8999	2	
		9000	0	
		9001	0	
		9002	0	
		9003	0	
		9004	1	
		9005	0	
		9006	0	
2	3	9007	0	
		9008	0	
		9009	0	
		9010	0	
		9011	0	
		9012	0	
		9013	0	
		9014	0	
		9015	0	
2	4	9016	0	
		9017	0	
		9018	0	
		9019	0	
		9020	0	
		9021	0	
		9022	1	
		9023	1	
		9024	0	
2	5	9025	0	
		9026	1	
		9027	0	
		9028	0	
		9029	0	
		9030	3	
		9031	2	
		9032	0	NO CORE
		9033	0	
2	6	9034	4	
		9035	7	
		9036	2	
		9037	0	
		9038	1	
		9039	3	
		9040	1	
		9041	0	
		9042	0	

Core#	Box#	Depth (ft)	Fracture Intensity	Notes
2	7	9043	2	
		9044	0	
		9045	0	
		9046	0	
		9047	0	
		9048	0	
		9049	1	
		9050	4	
		9051	0	
2	8	9052	0	NO CORE
		9053	0	
		9054	0	
		9055	0	
		9056	0	
		9057	6	
		9058	4	
		9059	0	
		9060	0	
2	9	9061	0	
		9062	0	
		9063	0	
		9064	0	
		9065	0	
		9066	0	
		9067	0	
		9068	0	
		9069	0	
2	10	9070	0	
		9071	0	
		9072	0	NO CORE
		9073	0	
		9074	1	
		9075	0	
		9076	0	
		9077	0	
		9078	1	
2	11	9079	6	
		9080	2	
		9081	0	
		9082	0	
		9083	0	
		9084	2	
		9085	2	
		9086	0	
		9087	0	

Core#	Box#	Depth (ft)	Fracture Intensity	Notes
2	12	9088	0	
		9089	0	
		9090	0	
		9091	0	
		9092	0	
		9093	0	
		9094	0	
		9095	0	
		9096	0	
2	13	9097	0	
		9098	0	
		9099	1	
		9100	0	
		9101	5	
		9102	0	
		9103	0	
		9104	3	
		9105	1	
2	14	9106	2	
		9107	2	
		9108	0	
		9109	0	
		9110	0	
		9111	0	
		9112	0	
		9113	0	
		9114	4	
2	15	9115	0	
		9116	0	
		9117	0	
		9118	5	
		9119	4	
		9120	1	
		9121	0	
		9122	2	
		9123	0	
2	17	9133	0	
		9134	0	
		9135	0	
		9136	0	
		9137	0	
		9138	0	
		9139	0	
		9140	0	
		9141	0	

Core#	Box#	Depth (ft)	Fracture Intensity	Notes
2	18	9142	0	
		9143	0	
		9144	0	
		9145	0	
		9146	0	
		9147	0	
		9148	0	
		9149	0	
		9150	1	
2	19	9151	0	
		9152	0	
		9153	0	
		9154	0	
		9155	0	
		9156	1	
		9157	0	
		9158	7	
		9159	6	
2	20	9160	0	
		9161	0	
		9162	0	
		9163	0	
		9164	0	
		9165	0	
		9166	4	
		9167	4	
		9168	0	
2	21	9169	0	
		9170	0	
		9171	0	
		9172	0	
		9173	0	
		9174	0	
		9175	0	
		9176	0	
		9177	0	
2	22	9178	0	
		9179	1	
		9180	0	
		9181	0	
		9182	0	
		9183	1	
		9184	0	
		9185	2	
		9186	0	

Core#	Box#	Depth (ft)	Fracture Intensity	Notes
2	23	9187	0	
		9188	2	
		9189	0	
		9190	0	
		9191	4	
		9192	0	NO CORE
		9193	4	
		9194	1	
		9195	1	
2	24	9196	4	
		9197	0	
		9198	7	
		9199	0	
		9200	0	
		9201	0	NO CORE
3	1	9202	3	
		9203	0	
		9204	0	
		9205	0	
		9206	0	
		9207	0	
		9208	10	
		9209	10	
		9210	21	
3	2	9211	12	
		9212	0	NO CORE
		9213	2	
		9214	9	
		9215	9	
		9216	6	
		9217	13	
		9218	2	
		9219	4	
3	3	9220	4	
		9221	16	
		9222	4	
		9223	2	
		9224	5	
		9225	1	
		9226	1	
		9227	1	
		9228	7	

Core#	Box#	Depth (ft)	Fracture Intensity	Notes
3	4	9229	8	
		9230	9	
		9231	16	
		9232	0	NO CORE
		9233	0	
		9234	0	
		9235	0	
		9236	5	
		9237	0	
3	5	9238	15	
		9239	7	
		9240	1	
		9241	0	
		9242	1	
		9243	1	
		9244	1	
		9245	0	
		9246	0	
3	6	9247	1	
		9248	5	
		9249	4	
		9250	2	
		9251	0	
		9252	0	NO CORE
		9253	4	
		9254	1	
		9255	0	
3	7	9256	0	
		9257	0	
		9258	0	
		9259	0	
		9260	0	
		9261	0	
		9262	0	
		9263	0	
		9264	0	
3	8	9265	0	
		9266	10	
		9267	33	
		9268	2	
		9269	0	
		9270	0	
		9271	0	
		9272	0	NO CORE
		9273	0	

Core#	Box#	Depth (ft)	Fracture Intensity	Notes
3	9	9274	1	
		9275	4	
		9276	4	
		9277	2	
		9278	3	
		9279	9	
		9280	3	
		9281	0	
		9282	4	
3	10	9283	14	
		9284	1	
		9285	1	
		9286	4	
		9287	7	
		9288	2	
		9289	5	
		9290	6	
		9291	5	
3	11	9292	0	NO CORE
		9293	13	
		9294	9	
		9295	5	
		9296	5	
		9297	16	
		9298	9	
		9299	12	
		9300	14	
3	12	9301	14	
		9302	15	
		9303	8	
		9304	2	
		9305	10	
		9306	0	
		9307	2	
		9308	1	
		9309	0	
3	13	9310	0	
		9311	1	
		9312	0	NO CORE
		9313	0	
		9314	2	
		9315	4	
		9316	3	
		9317	10	
		9318	0	

Core#	Box#	Depth (ft)	Fracture Intensity	Notes
3	14	9319	2	
		9320	1	
		9321	2	
		9322	3	
		9323	5	
		9324	10	
		9325	7	
		9326	0	
		9327	2	
3	15	9328	1	
		9329	1	
		9330	6	
		9331	2	
		9332	0	NO CORE
		9333	0	
		9334	2	
4	1	9335	0	
		9336	0	
		9337	1	
		9338	0	
		9339	1	
		9340	2	
		9341	5	
		9342	1	
		9343	2	
4	2	9344	0	
		9345	4	
		9346	7	
		9347	1	
		9348	2	
		9349	1	
		9350	1	
		9351	0	
		9352	0	NO CORE
4	3	9353	0	
		9354	0	
		9355	1	
		9356	3	
		9357	0	
		9358	7	
		9359	1	
		9360	14	
		9361	25	

Core#	Box#	Depth (ft)	Fracture Intensity	Notes
4	4	9362	0	
		9363	0	
		9364	0	
		9365	4	
		9366	12	
		9367	18	
		9368	4	
		9369	0	
		9370	1	
4	5	9371	5	
		9372	0	NO CORE
		9373	5	
		9374	11	
		9375	0	
		9376	10	
		9377	4	
		9378	1	
		9379	1	
4	6	9380	0	
		9381	0	
		9382	0	
		9383	0	
		9384	0	
		9385	0	
		9386	0	
		9387	0	
		9388	0	

Core #6 – Fracture intensity

Core#	Box#	Depth (ft)	Fracture Intensity	Notes
1	1	9732	0	
		9733	0	
		9734	0	
		9735	0	
		9736	0	
		9737	0	
		9738	0	
		9739	0	
		9740	0	
1	2	9741	0	
		9742	0	
		9743	0	
		9744	0	
		9745	0	
		9746	0	
		9747	0	
		9748	0	
		9749	0	
1	3	9750	0	
		9751	0	
		9752	0	
		9753	0	
		9754	0	
		9755	0	
		9756	0	
		9757	0	
		9758	0	
1	4	9759	0	
		9760	0	
		9761	0	
		9762	0	
		9763	0	
		9764	0	
		9765	4	
		9766	0	
		9767	0	
1	5	9768	0	
		9769	0	
		9770	0	
		9771	0	
		9772	0	
		9773	0	
		9774	0	
		9775	0	
		9776	0	

Core#	Box#	Depth (ft)	Fracture Intensity	Notes
1	6	9777	0	
		9778	0	
		9779	0	
		9780	0	
		9781	0	
		9782	0	
		9783	0	
		9784	0	
		9785	0	
1	7	9786	0	
		9787	0	
		9788	0	
		9789	0	
		9790	0	
		9791	0	
		9792	0	
		9793	0	
		9794	0	
1	8	9795	0	
		9796	0	
		9797	0	
		9798	0	
		9799	0	
		9800	0	
		9801	0	
		9802	0	
		9803	0	
1	9	9804	0	
		9805	0	
		9806	0	
		9807	0	
		9808	0	
		9809	0	
		9810	0	
		9811	0	
		9812	0	
1	10	9813	0	
		9814	0	
		9815	0	
		9816	0	
		9817	0	
		9818	0	
		9819	0	
		9820	0	
		9821	0	

Core#	Box#	Depth (ft)	Fracture Intensity	Notes
1	11	9822	0	
		9823	0	
		9824	0	
		9825	0	
		9826	0	
		9827	0	
		9828	0	
		9829	0	
		9830	0	
1	12	9831	0	
		9832	1	
		9833	0	
		9834	0	
		9835	0	
		9836	0	
		9837	0	
		9838	0	
		9839	0	
1	13	9840	0	
		9841	0	
		9842	0	
		9843	0	
		9844	0	
		9845	0	
		9846	0	
		9847	0	
		9848	0	
1	14	9849	0	
		9850	0	
		9851	0	NO CORE
		9852	0	
		9853	0	
		9854	0	
		9855	0	
		9856	0	
		9857	0	
1	15	9858	0	
		9859	0	
		9860	0	
		9861	0	
		9862	0	
		9863	6	
		9864	0	
		9865	0	
		9866	0	

Core#	Box#	Depth (ft)	Fracture Intensity	Notes
1	16	9867	0	
		9868	0	
		9869	1	
		9870	0	
		9871	0	
		9872	0	
		9873	0	
		9874	0	
		9875	0	
1	17	9876	0	
		9877	0	
		9878	0	
		9879	0	
		9880	0	
		9881	0	
		9882	0	
		9883	0	
		9884	0	
1	18	9885	1	
		9886	0	NO CORE
		9887	0	
		9888	0	
		9889	1	
		9890	0	
		9891	0	
		9892	0	
		9893	0	
1	19	9894	0	
		9895	0	
		9896	0	
		9897	1	
		9898	0	
		9899	0	
		9900	0	
		9901	0	
		9902	0	
1	20	9903	0	
		9904	0	
		9905	0	
		9906	0	
		9907	0	
		9908	0	
		9909	0	
		9910	0	
		9911	4	

Core#	Box#	Depth (ft)	Fracture Intensity	Notes
1	21	9912	2	
		9913	0	
		9914	0	
		9915	0	
		9916	0	
		9917	0	
		9918	0	
		9919	0	
		9920	0	
1	22	9921	0	
		9922	0	
		9923	0	
		9924	0	
		9925	1	
		9926	0	NO CORE
		9927	0	
		9928	0	
		9929	0	
1	23	9930	0	
		9931	1	
		9932	2	
		9933	6	
		9934	4	
		9935	0	
		9936	0	
		9937	0	
		9938	1	
1	24	9939	0	
		9940	0	
		9941	0	
		9942	0	
		9943	0	
		9944	0	
		9945	0	
		9946	0	
		9947	0	
1	25	9948	0	
		9949	0	
		9950	0	
		9951	0	
		9952	0	
		9953	0	
		9954	0	
		9955	0	
		9956	0	

Core#	Box#	Depth (ft)	Fracture Intensity	Notes
1	26	9957	0	
		9958	0	
		9959	0	
		9960	0	
		9961	0	
		9962	0	
		9963	0	
		9964	0	
		9965	0	
1	27	9966	0	
		9967	0	
		9968	0	
		9969	0	
2	1	9970	0	
		9971	0	
		9972	0	
		9973	0	
		9974	0	
		9975	0	
		9976	0	
		9977	0	
		9978	0	
2	2	9979	0	
		9980	0	
		9981	0	
		9982	0	
		9983	0	
		9984	4	
		9985	9	
		9986	1	
		9987	0	
2	3	9988	2	
		9989	0	
		9990	0	
		9991	0	
		9992	0	
		9993	0	
		9994	0	
		9995	0	
		9996	0	

Core#	Box#	Depth (ft)	Fracture Intensity	Notes
2	4	9997	0	
		9998	0	
		9999	0	
		10000	0	
		10001	0	
		10002	0	
		10003	0	
		10004	0	
		10005	0	
2	5	10006	0	
		10007	0	
		10008	0	
		10009	0	
		10010	0	
		10011	0	
		10012	0	
		10013	0	
		10014	0	
2	6	10015	0	
		10016	0	
		10017	0	
		10018	0	
		10019	0	
		10020	0	
		10021	0	
		10022	0	
		10023	0	
2	7	10024	0	
		10025	0	
		10026	0	
		10027	0	
		10028	0	
		10029	0	
		10030	0	
		10031	0	
		10032	0	
2	8	10033	0	
		10034	0	
		10035	0	
		10036	0	
		10037	0	
		10038	0	
		10039	0	
		10040	0	
		10041	0	

Core#	Box#	Depth (ft)	Fracture Intensity	Notes
2	9	10042	0	
		10043	0	
		10044	0	
		10045	0	
		10046	6	
		10047	5	
		10048	0	
		10049	0	
		10050	0	
2	10	10051	0	
		10052	0	
		10053	0	
		10054	0	
		10055	0	
		10056	0	
		10057	0	
		10058	1	
		10059	1	
2	11	10060	0	
		10061	3	
		10062	0	
		10063	0	
		10064	3	
		10065	4	
		10066	0	
		10067	0	
		10068	4	
2	12	10069	0	
		10070	3	
		10071	1	NO CORE
		10072	1	
		10073	2	
		10074	0	
		10075	1	
		10076	0	
		10077	0	
2	13	10078	0	
		10079	0	
		10080	0	
		10081	0	
		10082	0	
		10083	0	
		10084	0	
		10085	0	
		10086	0	

Core#	Box#	Depth (ft)	Fracture Intensity	Notes
2	14	10087	0	
		10088	0	
		10089	2	
		10090	0	
		10091	0	
		10092	0	
		10093	0	
		10094	0	
		10095	4	
2	15	10096	0	
		10097	0	
		10098	0	
		10099	0	
		10100	0	
		10101	0	
		10102	0	
		10103	0	
		10104	0	
2	16	10105	0	
		10106	0	
		10107	0	
		10108	0	
		10109	0	
		10110	0	
		10111	0	
		10112	0	
		10113	0	
2	17	10114	0	
		10115	0	
		10116	0	
		10117	0	
		10118	0	
		10119	0	
		10120	0	
		10121	0	
		10122	0	
2	18	10123	0	
		10124	0	
		10125	0	
		10126	0	
		10127	0	
		10128	0	
		10129	0	
		10130	0	
		10131	0	

Core#	Box#	Depth (ft)	Fracture Intensity	Notes
2	19	10132	0	
		10133	0	
		10134	0	
		10135	0	
		10136	0	
		10137	0	
		10138	0	
		10139	0	
		10140	0	
2	20	10141	2	
		10142	0	
		10143	1	
		10144	0	
		10145	4	
		10146	3	
		10147	1	
		10148	0	
		10149	0	
2	21	10150	0	
		10151	0	
		10152	0	
		10153	0	
		10154	0	
		10155	0	
		10156	0	
		10157	0	
		10158	0	
2	22	10159	0	
		10160	0	
		10161	0	
		10162	0	
		10163	0	
		10164	1	
		10165	1	
		10166	0	
		10167	1	
2	23	10168	0	
		10169	0	
		10170	0	
		10171	0	
		10172	0	
		10173	0	
		10174	0	
		10175	0	
		10176	0	

Core#	Box#	Depth (ft)	Fracture Intensity	Notes
2	24	10177	0	
		10178	0	
		10179	0	
		10180	0	
		10181	0	
		10182	0	
		10183	0	
		10184	0	
		10185	0	
2	25	10186	1	
		10187	4	
		10188	1	
		10189	1	
		10190	0	
		10191	0	
		10192	1	
		10193	0	
		10194	5	
2	26	10195	1	
		10196	2	
		10197	2	
		10198	3	
		10199	4	
		10200	1	
		10201	9	
		10202	12	
		10203	13	
2	27	10204	2	
		10205	0	
		10206	0	
		10207	7	
		10208	1	
		10209	3	
		10210	5	
		10211	6	
		10212	2	
2	28	10213	0	
		10214	3	
		10215	1	
		10216	0	
		10217	0	
		10218	0	
		10219	2	
		10220	0	
		10221	6	

Core#	Box#	Depth (ft)	Fracture Intensity	Notes
2	29	10222	1	
		10223	3	
		10224	9	
		10225	0	NO CORE
		10226	0	
		10227	0	
		10228	2	
		10229	2	
		10230	1	
2	30	10231	16	
		10232	49	
		10233	4	
		10234	4	
		10235	0	
		10236	0	
		10237	0	
		10238	0	
		10239	3	
2	31	10240	3	
		10241	2	
		10242	10	
		10243	9	
		10244	2	
		10245	2	
		10246	3	
		10247	3	
		10248	0	
2	32	10249	3	
		10250	3	
		10251	2	
		10252	0	
		10253	0	
		10254	0	
		10255	0	
		10256	0	
		10257	4	
2	33	10258	0	
		10259	0	
		10260	3	
		10261	4	
		10262	1	
		10263	3	
		10264	0	
		10265	3	
		10266	2	

Core#	Box#	Depth (ft)	Fracture Intensity	Notes
2	34	10267	0	
		10268	0	
		10269	0	NO CORE
		10270	5	
		10271	0	
		10272	3	
		10273	0	
		10274	4	
		10275	4	
2	35	10276	6	
		10277	1	
		10278	0	
		10279	0	
		10280	0	
		10281	4	
		10282	0	
		10283	0	
		10284	1	
2	36	10285	0	
		10286	0	
		10287	0	
		10288	0	
		10289	0	
		10290	0	
		10291	0	
		10292	0	
		10293	0	
2	37	10294	0	
		10295	1	
		10296	1	
		10297	0	
		10298	0	
		10299	3	
		10300	0	
		10301	1	
		10302	0	
2	38	10303	0	
		10304	0	
		10305	2	
		10306	4	
		10307	10	
		10308	4	
		10309	4	
		10310	3	
		10311	4	

Core#	Box#	Depth (ft)	Fracture Intensity	Notes
2	39	10312	10	
		10313	9	
		10314	2	
		10315	0	
		10316	0	

Core #4 – Fracture measurement data

Depth (ft; top)	Type	Height (mm)	Vertical /sub-vertical	Dip (near 90 °if blank)	Kinematic aperture (mm)		Single/ branch-ing	Termination	
					Min (0.1 if blank)	Max		Top	Base
9168.03	VE	154	V			0.1	SG	4	4
67.45	VE	130	V			0.1	SG	4	4
67.8	VE	35	V			0.1	SG	4	4
67.9	VE	30	V			0.1	SG	4	4
65.93	P	10	V			0.3	SG	1	1
0.23	P	80	V		0.6	1	SG	1	4
0.0	P	10	V			0.3	SG	4	1
64.2	P	35	V			0.2	SG	4	4
0.19	P	17	V			0.2	SG	4	4
0.31	P+VE	85	V			0.1	SG	1	1
0.5	VE	8	V			0.3	SG	2	4
0.19	P	140	V			0.2	SG	1	1
0.25	P	118	V			0.2	SG	1	1
0.19	P	37	V			0.2	BR	1	1
0.28	P+VE	135	V			0.5	BR	1	1
0.23	P	17	V			0.2	SG	1	1
9162.22	P	6	V			0.3	SG	4	4
0.28	P	40	V			0.2	SG	1	1
0.32	P+VE	85	V			0.2	SG	1	1
0.32	P+VE	40	V			0.2	SG	1	4
0.45	P+VE	52	V			0.2	SG	1	1
0.38	P+VE	160	V			0.2	BR	1	1
0.39	P	9	V			0.2	SG	1	1
0.4	P	90	V			0.4	SG	1	1
0.65	P	60	V			0.2	SG	1	1
0.14	VE	88	V			0.1	SG	1	1
0.44	VE	35	V			0.1	SG	1	1
0.62	VE	10	V			0.1	SG	1	1
0.8	VE	35	V			0.1	SG	1	1
9150.23	VE	235	V			0.5	SG	?	
0.4	P	59	V			?	SG	?	
9148.98	P	230	V			0.5	SG	1	1
0.47	P	23	V			0.2	SG	1	3
0.0	P	22	V			0.2	SG	1	3
47.73	VE	60	V			0.2	SG	1	1
46.38	VE	12	V			0.3	SG	1	1
0.85	P	28	V		0.3	3	BR	1	1
0.85	P	28	V			3	BR	1	1
0.85	P	28	V			3	BR	1	1
0.85	P	28	V			3	BR	1	1

Depth (ft; top)	Type	Height (mm)	Vertical /sub-vertical	Dip (near 90 °if blank)	Kinematic aperture (mm)		Single/ branch-ing	Termination	
					Min (0.1 if blank)	Max		Top	Base
0.85	P	28	V			3	BR	1	1
0.85	P	28	V			3	BR	1	1
0.85	P	28	V			3	BR	1	1
0.85	P	28	V			3	BR	1	1
0.85	P	28	V			3	BR	1	1
0.85	P	28	V			3	BR	1	1
9142.1	P	30	V			0.2	SG	1	1
0.17	P	68	V			0.2	SG	1	1
40.55	P	4	SV			1	SG	2	4
0.16	P	37	V		0.2	1	SG	2	2
0.19	P	40	V			0.1	SG	1	4
0.19	VE+P	29	V			0.2	SG	1	1
0.17	VE	19	V			0.2	BR	1	1
0.27	P	5	V			0.1	SG	1	1
0.26	P	5	V			0.1	SG	1	1
0.2	P	7	V			0.1	SG	1	1
0.11	VE	19	V			0.1	SG	1	1
0.2	VE	17	V			0.1	SG	1	1
0.23	VE	8	V			0.1	SG	1	1
9140.2	VE	16	V			0.1	SG	1	1
0.19	VE	23	V			0.2	BR	1	1
0.19	VE	14	V			0.5	SG	1	1
0.2	VE	20	V			0.1	SG	1	1
0.25	P	5	V			0.1	SG	1	1
0.25	P	5	V			0.1	SG	1	1
0.28	P	8	V			0.1	SG	1	1
0.3	P	7	V			0.2	SG	1	1
0.27	P	10	V			1	SG	4	2
0.27	P	5	V			0.1	SG	1	1
0.28	P	10	V			0.1	SG	1	1
0.06	P	11	V			0.2	SG	4	4
0.06	P	10	SV		0.1	1	SG	2	2
0.02	P	38	V		0.1	1	BR	1	1
0.02	P	12	SV		0.1	1	SG	1	4
0.04	P+S	26	V		0.1	1	SG	2	1
0.07	P	4	V		0.1	1	SG	4	2
0.08	P+S	19	V		0.3	1	SG	4	2
9139.3	VE	35	V			0.1	SG	1	1
0.3	VE	32	V			0.1	SG	1	1
0.37	VE	20	V			0.1	SG	1	1
0.51	P	30	V		0.1	1	SG	1	1
0.5	VE	8	V			0.3	SG	4	1
0.68	VE	6	V			0.1	SG	4	2

Depth (ft; top)	Type	Height (mm)	Vertical /sub-vertical	Dip (near 90 °if blank)	Kinematic aperture (mm)		Single/ branch-ing	Termination	
					Min (0.1 if blank)	Max		Top	Base
0.69	VE	5	V			0.1	SG	2	2
0.7	VE	5	V			0.1	SG	2	2
0.89	P	13	V			0.2	SG	2	2
0.97	VE	10	V			0.1	SG	2	2
0.83	P+S	45	V			0.2	SG	4	2
0.83	P	52	V			0.2	SG	4	2
0.87	P	21	V			0.2	BR	1	1
0.95	P	15	V			0.2	BR	1	1
0.89	VE	8	V			0.1	SG	1	1
0.86	P	6	V			0.2	SG	4	1
9135.26	P+VE	60	V			0.2	SG	1	1
0.43	P+VE	155	V			3	BR	1	1
0.21	P+VE	129	V			0.3	SG	1	1
0.51	P	59	V			0.3	BR	1	1
0.58	P	5	V			0.2	SG	1	1
0.59	P	10	V			0.2	SG	4	4
0.87	P	33	V			1	SG	1	1
0.81	P	16	V		0.5	1	SG	4	4
27.13	P	103	V			0.5	SG	1	4
0.46	P	11	V			0.2	SG	4	1
0.46	P	27	V			1	SG	1	1
0.49	P	35	V			1	SG	1	1
0.55	P	17	V			0.5	SG	1	1
9125.04	P	170	V			0.2	SG	1	1
0.57	P	2	V			0.2	SG	1	1
0.58	P	17	V			0.3	SG	2	4
0.7	P	15	V			0.2	SG	4	4
0.79	P	11	V			0.2	SG	1	4
9114.58	P	122	V		0.3	1	SG	1	1
0.92	P	18	V			0.5	SG	1	1
12.01	VE	480	V			? - NO LEFT WALL	BR	1	1
9105.69	P	20	V		0.5	1	SG	2	2
0.71	P	11	V			0.5	SG	2	2
0.69	P	9	V		0.5	2	BR	2	2
0.7	P	6	V		0.5	1	SG	2	2
0.71	P	4	V		0.5	1	SG	2	2
0.66	P	26	V		0.2	5	BR	4	1
0.69	VE	5	V			0.1	SG	2	2
9103.66	P	50	V		0.5	1	SG	1	1
0.45	P	15	V		0.1	0.5	SG	1	4
0.5	P	12	V		0.1	0.2	SG	4	1

Depth (ft; top)	Type	Height (mm)	Vertical /sub-vertical	Dip (near 90 °if blank)	Kinematic aperture (mm)		Single/ branch-ing	Termination	
					Min (0.1 if blank)	Max		Top	Base
0.39	P	20	V			0.2	SG	1	1
0.39	P	30	V			0.1	SG	1	1
0.4	P	9	V			0.2	SG	1	1
0.18	P	14	V			0.5	SG	1	1
0.19	P	13	V			0.4	SG	1	1
0.26	P	5	V			0.5	SG	1	1
0.3	P	7	V			0.5	SG	1	1
9102.69	VE+P	92	V			0.2	BR	1	4
0.85	P+VE	50	V			0.2	BR	1	4
0.55	P	25	V		0.5	3.5	SG	1	1
0.61	P	46	V		1	2	SG	2	2
0.26	P	17	V			2	SG	1	1
0.15	P	20	V			2	SG	1	1
0.02	P	13	V			2	SG	4	1
9101.87	P	80	V		1	2	SG	4	2
9099.02	P	70	V			1	SG	1	1
0.22	P	36	V			0.3	SG	1	1
0.35	P	32	V			0.3	SG	1	1
98.53	P	5	V			0.2	SG	4	4
0.62	P	43	V			0.3	SG	4	4
0.69	P	15	V			0.2	SG	4	1
0.73	P	50	V			0.2	SG	1	4
0.9	P	14	V			0.2	SG	4	1
0.1	P	85	V		0.3	1	SG	4	4
94.07	P	32	V			0.1	SG	1	4
0.05	P	10	V			0.1	SG	4	1
0.06	P	30	V			0.1	SG	1	4
0.1	P	30	V			0.2	SG	4	1
0.22	P	10	V			0.2	SG	4	1
0.25	P	45	V			0.2	SG	1	1
9089.02	P	40	V			0.2	SG	1	1
88.88	P	65	V			0.2	SG	1	1
0.98	P	118	V			0.2	BR	1	1
0.68	P	58	V			0.1	SG	1	1
0.6	P	116	V		0.5	1	SG	1	1
0.57	P	47	V			1	SG	1	1
0.25	P	20	V			0.7	SG	3	3
0.31	P	60	V			? - NO CORE SURFACE	SG	1	1
0.95	P	11	SV		0.1	1	SG	1	4
85.21	P	65	V		0.1	0.2	SG	4	1

Depth (ft; top)	Type	Height (mm)	Vertical /sub-vertical	Dip (near 90 °if blank)	Kinematic aperture (mm)		Single/ branch-ing	Termination	
					Min (0.1 if blank)	Max		Top	Base
0.18	P	160	V		0.1	0.2	SG	1	1
0.55	P	79	V			0.2	SG	1	1
0.79	P	5	V			0.1	SG	1	1
0.82	P	5	V			0.1	SG	1	1
0.78	P	65	V			0.1	SG	1	4
82.58	P	33	SV			1	SG	4	1
9081.86	P	39	V			0.2	SG	1	4
0.68	P+VE	50	V			0.2	SG	1	1
0.49	P+VE	68	V			0.1	SG	1	1
0.18	P+VE	155	V			0.1	SG	1	1
0.15	P+VE	125	V			0.1	SG	1	1
80.46	P	32	V			1	SG	1	1
0.44	P	5	V			0.5	SG	3	3
0.34	P	7	V			0.5	SG	3	3
0	P+VE	27	V			0.5	SG	4	1
79.35	VE+P	35	V			0.2	SG	4	4
0	VE+P	20	V			0.2	SG	4	4
0	VE+P	10	V			0.2	SG	4	4
78.75	VE+P	165	V			0.2	SG	1	4
0.49	VE+P	81	V			0.2	SG	1	1
0.17	VE	110	V			0.2	SG	4	4
0.15	VE+P	107	V			0.2	SG	1	1
0.1	VE	13	V			0.1	SG	1	1
9077.71	P	18	V			0.1	SG	4	1
0.38	P	7	V			0.1	SG	1	4
0.32	P	8	V			0.1	SG	1	1
0.33	P	23	V			0.1	SG	4	1
76.65	P	65	V		0.5	3	BR	1	2
0.85	P	94	V		0.1	3	SG	2	4
73.06	P	72	V			0.1	SG	1	1
0.31	P	25	V			0.1	SG	1	1
9072.73	P	112	V			0.2	SG	1	1
71.57	P	55	V			0.2	SG	1	4
0.65	P	18	V			0.2	SG	1	4
0	P	19	V			0.2	SG	1	4
70.0	P	62	V			0.2	SG	4	2
69.55	P	15	V		0.5	1	SG	4	1
67.12	P	70	V			0.2	SG	4	1
9060.26	P	100	V			0.6	SG	4	1
0.03	P	22	V			0.3	SG	2	3
0.12	P	13	V			1	SG	3	1
0.06	P	12	V			0.5	SG	1	3
0.2	P	3	V			0.5	SG	3	1

Depth (ft; top)	Type	Height (mm)	Vertical /sub-vertical	Dip (near 90 °if blank)	Kinematic aperture (mm)		Single/ branch-ing	Termination	
					Min (0.1 if blank)	Max		Top	Base
0.1	P	6	V			0.5	SG	2	3
59.98	P	23	V			0.5	SG	3	4
0.4	VE	52	V			0.2	SG	4	1
0.55	VE	28	V			0.2	SG	4	1
56	P	40	V			0.5	SG	1	1
55.8	P	50	V		0.5	1	SG	4	4
0.85	P	35	V			0.3	SG	4	4
0.74	P	29	V			0.3	SG	4	4
0.62	P	32	V			0.3	SG	4	4
0.63	P	24	V			0.5	SG	4	4
0.14	P	42	SV	40	0.1	6	SG	2	1
9051.27	P	25	V		0.3	1	SG	3	3
0.26	P	10	V			0.2	SG	3	3
0.25	P	19	V		0.2	1	SG	3	3
0.18	P	7	SV		0.2	1	SG	3	4
0.18	P	11	SV			0.2	SG	3	3
0.18	P	11	SV		0.3	2	SG	3	3
50.43	P	40	SV		4	10	SG	2	4
0.06	P	15	V			0.1	SG	1	1
0	P	8	V			0.2	SG	1	1
49.3	P	192	V			1	BR	1	1
0.89	P	25	V		0.5	1	SG	1	1
48.75	P	59	V			0.6	SG	1	1
0.23	P	29	V			0.2	SG	4	1
0	P	60	V		0.1	2	SG	4	3
47.89	P	31	V		1	1.5	SG	4	4
0.19	P	50	V			0.1	SG	1	1
0.08	P	65	V			0.1	SG	1	1
0.07	P	48	V			0.1	SG	1	4
46.54	P	165	V			0.2	SG	1	1
0.4	P	23	V			0.1	SG	3	4
0.1	P	17	V			0.1	SG	1	4
9040.7	P	7	V			1	SG	2	2
37.62	P	52	V		0.1	0.5	SG	1	2
9024.12	P+VE	120	V			0.2	SG	1	1
0.05	P+VE	165	V		0.1	1	BR	3	4
0.09	P	92	V			0.2	BR	3	1
23.69	VE+P	15	V			1	SG	4	4
0.34	VE	8	V			0.1	SG	1	3
0.39	P	11	V			0.2	SG	3	3
0.21	P	30	V			0.2	SG	4	3
0.05	P	23	V		0.2	0.5	SG	1	4
21.89	VE	25	V			1	SG	3	4

Depth (ft; top)	Type	Height (mm)	Vertical /sub-vertical	Dip (near 90 °if blank)	Kinematic aperture (mm)		Single/ branch-ing	Termination	
					Min (0.1 if blank)	Max		Top	Base
0.73	P	20	V			0.5	SG	1	1
0.75	P	7	V			0.2	SG	1	1
0.54	P	15	V			0.3	SG	2	2
0.18	P	11	V			0.2	SG	1	1
0.16	P	20	V			0.2	SG	1	1
20.68	VE+P	140	V			0.1	SG	1	1
0.38	P+VE	21	V		0.5	1	SG	3	3
19.16	P+VE	192	V		0.1	1	SG	1	1
0.02	P	6	V			0.1	SG	3	3
0.02	P	9	V			0.2	SG	3	3
9018.11	P+VE	43	V			0.6	SG	4	1
0.12	VE	20	V			0.1	SG	1	1
0.69	P	25	V			0.2	SG	3	4
0.93	P	15	V			0.2	SG	3	4
0.87	VE+P	45	V			0.5	SG	1	4
9017.88	P	27	V			0.2	SG	3	1
0.88	P	35	V			0.3	SG	3	1
0.18	VE+P	180	V		0.2	0.5	SG	4	1
0.29	VE	85	V			0.1	SG	1	1
0.59	P+VE	27	V			0.5	SG	2	1
0.17	VE+P	26	V			0.2	SG	4	1
0.25	VE+P	92	V			0.2	SG	1	4
16.97	VE	45	V			0.2	SG	4	4
14.92	P+VE	23	V			0.5	SG	1	4
13.02	P	40	V			0.2	SG	1	1
0	P	73	V			0.5	SG	1	1
12.81	P	32	V			0.5	SG	1	1
0.83	P	17	V			0.2	SG	1	1
0.83	P	25	V			0.3	SG	1	1
0.1	VE	13	V			0.2	SG	2	2
0.16	P+S	50	V		0.2	0.5	SG	2	4
9011.52	P	52	V		0.2	0.5	BR	4	4
0.63	P	165	V			0.2	BR	1	3
0.69	P	130	V			0.3	SG	1	1
0.56	P	43	V			0.1	SG	1	1
0.65	P	200	V			0.1	BR	1	4
0.51	P	202	V			0.5	BR	1	1
0.89	P+S	95	V			0.1	SG	1	1
0.89	P	95	V			0.1	SG	1	1
0.94	P	75	V			0.1	SG	1	1
0.7	P	52	V			0.1	SG	1	1
0.62	P	70	V			0.1	SG	1	4
0.83	P	102	V			0.1	SG	1	1

Depth (ft; top)	Type	Height (mm)	Vertical /sub-vertical	Dip (near 90 °if blank)	Kinematic aperture (mm)		Single/ branch-ing	Termination	
					Min (0.1 if blank)	Max		Top	Base
0.37	P	15	V			0.1	SG	1	1
0.18	P+VE	65	V			0.3	BR	1	4
0.43	P	22	V			0.6	SG	4	1
0.48	P	14	V			0.2	SG	1	4
0.46	P	13	V			0.2	SG	4	1
0.23	P	42	V			0.1	SG	1	1
20	P	62	V			0.2	SG	1	4
9010.48	P	17	V			0.1	SG	1	1
0.37	P	5	V			0.1	SG	1	1
0.47	P	30	V			0.5	SG	1	1
0.53	P	15	V			0.3	SG	1	1
0.52	P	5	V			0.3	SG	1	1
0.14	P	28	V			0.2	SG	1	1
0.14	P	16	V			0.2	SG	1	1
9001	P	5	V			0.1	SG	1	1
0.01	P	12	V			0.5	SG	1	1
0.06	P	30	SV		0.1	1	SG	1	1
0.2	P	40	V			0.5	SG	1	1
0.19	P	12	V			0.3	SG	1	1
0.23	P	19	V			0.1	SG	1	1
9000.9	P	75	V		0.1	1	BR	1	1
8997.61	P	15	SV			0.3	SG	1	1
0.67	P	7	V			0.1	SG	3	3
0.69	P+VE	65	SV			0.2	BR	1	1
0.81	VE	28	V			0.1	SG	1	1
91.81	P	75	V			0.5	SG	1	1
0	P	15	V			0.5	BR	4	1
0.06	P	20	V			0.2	SG	1	1
0.08	P	7	V			0.2	SG	1	1
0.1	P	25	V			0.5	BR	4	4
0.15	P	24	V			0.5	SG	1	4
0.35	P	6	V			0.2	SG	4	1
0.37	P	16	V			0.2	SG	1	1
0.37	P	15	V			0.3	SG	4	1
43	P	20	V			0.5	SG	1	1
8990.22	P	19	V			0.4	SG	4	4
89.53	P	28	V			0.6	SG	3	1
0.6	P	110	V			? - NO CORE FACE	SG	2	4
8987.02	VE	5	V			0.1	SG	3	1
0.02	VE	5	V			0.1	SG	3	1
0.02	VE	5	V			0.1	SG	3	1

Depth (ft; top)	Type	Height (mm)	Vertical /sub-vertical	Dip (near 90 °if blank)	Kinematic aperture (mm)		Single/ branch-ing	Termination	
					Min (0.1 if blank)	Max		Top	Base
0.02	VE	5	V			0.1	SG	3	1
0.02	VE	5	V			0.1	SG	3	1
0.02	VE	5	V			0.1	SG	3	1
0.02	VE	5	V			0.1	SG	3	1
0.03	VE+P	13	V			0.1	SG	3	1
0.06	P	7	V			0.1	SG	1	1
0.08	P	5	V			0.1	SG	1	1
0.09	P	5	V			0.1	SG	1	1
0.09	P	5	V			0.1	SG	1	1
0.09	P	5	V			0.1	SG	1	1
0.09	P	5	V			0.1	SG	1	1
0.15	VE	6	V			0.1	SG	1	1
0.17	P	6	V			0.1	SG	1	1
0.16	VE	7	V			0.1	SG	1	1
0.16	VE	7	V			0.1	SG	1	1
0.17	P	5	V			0.1	SG	1	1
86.86	P	5	V			0.3	SG	1	1
0.86	P	5	V			0.3	SG	1	1
0.86	P	5	V			0.3	SG	1	1
0.81	P	7	V			0.3	SG	1	1
0.78	P	10	V			0.3	BR	1	1
0.79	P	10	V			0.2	SG	4	1
0.81	P	2	V			0.1	SG	4	1
0.82	P	3	V			0.1	SG	1	1
0.72	P	33	V			0.1	SG	1	1
0.73	P	8	V			0.3	SG	1	1
0.75	P	4	V			0.1	SG	1	1
0.75	P	9	V			0.1	SG	1	1
86.73	P	4	V			0.1	SG	1	1
0.73	P	4	V			0.2	SG	1	1
0.73	P	4	V			0.1	SG	1	1
0.73	P	4	V			0.1	SG	1	1
0.73	P	4	V			0.1	SG	1	1
0.65	P	3	V			0.1	SG	1	1
0.65	P	3	V			0.1	SG	1	1
0.65	P	3	V			0.1	SG	1	1
0.65	P	3	V			0.1	SG	1	1
0.65	P	2	V			0.1	SG	1	1
0.65	P	2	V			0.1	SG	1	1
0.65	P	5	V			0.1	SG	1	1
0.55	P	6	V			0.1	SG	2	1
0.54	P	12	SV			0.1	SG	1	1
0.48	P	20	V			0.1	SG	1	1

Depth (ft; top)	Type	Height (mm)	Vertical /sub-vertical	Dip (near 90 °if blank)	Kinematic aperture (mm)		Single/ branch-ing	Termination	
					Min (0.1 if blank)	Max		Top	Base
0.52	S	3	V			0.1	SG	2	2
0.51	VE	13	V			0.1	SG	2	4
0.44	P	5	V			0.4	SG	2	1
0.35	P	31	V			0.1	SG	4	1
0.4	P	3	V			0.3	SG	2	2
0.39	P	3	V			0.2	SG	2	2
0.39	P	3	V			0.2	SG	2	2
0.39	P	3	V			0.2	SG	2	2
0.39	P	3	V			0.2	SG	2	2
0.29	P+VE	33	V			0.1	SG	1	3
0.37	P	3	V			0.2	SG	2	2
0.37	P	3	V			0.2	SG	2	2
0.37	P	3	V			0.2	SG	2	2
0.37	P	3	V			0.2	SG	4	2
0.33	P	13	V			0.1	SG	1	1
0.35	P	5	V			0.1	SG	1	1
0.32	P	5	V			0.2	SG	2	2
0.3	P	3	V			0.1	SG	1	1
0.3	P	3	V			0.1	SG	1	1
0.29	P	4	V			0.3	SG	1	1
0.29	P	5	V			0.3	SG	1	1
0.23	P	4	V			0.2	SG	1	1
0.23	P	4	V			0.2	SG	1	1
0.23	P	4	V			0.2	SG	1	1
0.23	P	4	V			0.2	SG	1	1
0.25	P	5	V			0.3	SG	1	2
0.23	P	3	V			0.1	SG	1	1
0.22	P	15	V			0.3	SG	1	1
0.22	P	11	V			0.1	SG	1	1
20	P	4	V			0.1	SG	1	1
0.18	VE	5	V			0.1	SG	1	2
8986.06	P	8	V			0.1	SG	1	1
0.06	P	10	V			0.1	SG	1	1
0.06	P	6	V			0.1	SG	1	1
0.07	P	6	V			0.1	SG	1	1
0.08	P	3	V			0.1	SG	1	1
0.08	P	4	V			0.1	SG	1	1
0.08	P	4	V			0.1	SG	1	1
0.3	P	15	V			0.5	BR	1	1
0.3	P	20	V			0.5	BR	1	1
0.3	P	22	V			0.5	BR	1	1
0.02	P	29	V			0.5	SG	1	1
0.02	P	7	V			0.1	SG	1	1

Depth (ft; top)	Type	Height (mm)	Vertical /sub-vertical	Dip (near 90 °if blank)	Kinematic aperture (mm)		Single/ branch-ing	Termination	
					Min (0.1 if blank)	Max		Top	Base
0.02	P	7	V			0.1	SG	1	1
0.01	P+VE	4	V			0.1	SG	1	1
0	P	4	V			0.2	SG	2	2
85.91	P	3	V			0.3	SG	1	1
0.91	P	6	V			0.3	SG	1	2
0.91	P	3	V			0.3	SG	1	1
0.91	P	5	V			0.3	SG	1	1
0.9	P	9	V			0.3	BR	1	1
0.8	P	3	V			0.2	SG	1	1
0.73	P	2	V			0.1	SG	1	1
0.73	P	3	V			0.1	SG	1	1
0.73	P	4	V			0.1	SG	1	1
0.73	P	4	V			0.1	SG	1	1
0.66	P	3	V			0.1	SG	1	1
0.66	P	5	V			0.1	SG	1	1
0.64	P	4	V			0.1	SG	1	1
0.48	P	84	V			0.2	SG	2	4
0.38	P	5	V		0.5	1	SG	2	2
0.39	P	8	V		0.5	1	SG	2	2
0.29	P	9	V			0.1	SG	1	1
0.28	P	5	V			0.2	SG	1	1
0.28	P	5	V			0.2	SG	1	1
0.28	P	5	V			0.2	SG	1	1
0.28	P	5	V			0.2	SG	1	1
0.28	P	5	V			0.2	SG	1	1
0.28	P	5	V			0.2	SG	1	1
0.28	P	5	V			0.2	SG	1	1
0.27	P	21	V			0.2	SG	1	1
0.27	P	21	V			0.2	SG	1	1
0.7	P	14	V		0.1	0.3	SG	1	1
0.05	P	10	V		0.1	0.3	SG	1	1
0.06	P	15	V			0.1	SG	1	1
0.05	VE	40	V			0.1	SG	1	1
0.06	P	19	V		0.1	0.2	BR	4	1
8984.89	P	16	V			0.5	SG	3	1
0.92	VE+P	8	V			0.3	SG	1	1
0.72	P	10	V			0.3	SG	1	1
0.72	P	5	V			0.3	SG	1	1
0.72	P	5	V			0.3	SG	1	1
0.72	P	10	V			0.3	SG	1	1
0.02	P	7	V			0.1	SG	1	1
0.65	VE+P	5	V			0.2	SG	1	1
0.64	P	16	V			0.5	SG	1	3

Depth (ft; top)	Type	Height (mm)	Vertical /sub-vertical	Dip (near 90 °if blank)	Kinematic aperture (mm)		Single/ branch-ing	Termination	
					Min (0.1 if blank)	Max		Top	Base
0.64	P	12	V			0.5	SG	1	3
0.67	P	5	V			0.1	SG	1	3
0.58	P	4	V			0.1	SG	1	1
0.58	P	4	V			0.1	SG	1	3
0.57	P	3	V			0.1	SG	3	1
0.57	P	3	V			0.1	SG	3	1
0.62	P	4	V			0.1	SG	1	1
0.62	P	4	V			0.1	SG	1	1
0.62	P	4	V			0.1	SG	1	1
0.62	P	4	V			0.1	SG	1	1
0.52	P	4	V			0.1	SG	1	1
0.52	P	4	V			0.1	SG	1	1
0.52	P	4	V			0.1	SG	1	1
0.52	P	4	V			0.1	SG	1	1
0.52	P	4	V			0.1	SG	1	1
0.52	P	4	V			0.1	SG	1	1
0.51	P	3	V			0.1	SG	1	1
0.51	P	3	V			0.1	SG	1	1
0.51	P	3	V			0.1	SG	1	1
0.5	P	4	V			0.2	SG	2	2
0.5	P	3	V			0.1	SG	1	1
0.5	P	3	V			0.1	SG	1	1
0.5	P	3	V			0.1	SG	1	1
0.49	P	5	V			0.1	SG	1	1
0.48	P	8	V			0.2	SG	1	4
0.43	P	3	V			0.1	SG	1	1
0.43	P	3	V			0.1	SG	1	1
0.4	P	4	SV			0.1	SG	1	1
0.3	P	11	SV			0.2	BR	1	1
0.3	P	5	SV			0.2	BR	1	1
0.3	P	5	SV			0.2	BR	1	1
0.3	P	5	SV			0.2	BR	1	1
0.3	P	5	SV			0.2	BR	1	1
0.3	P	5	SV			0.2	BR	1	1
0.3	P	5	SV			0.2	BR	1	1
0.3	P	5	SV			0.2	BR	1	1
0.3	P	5	SV			0.2	BR	1	1
0.3	P	5	SV			0.2	BR	1	1
0.19	P	4	V			0.1	SG	2	2
0.19	P	4	V			0.1	SG	2	2
0.19	P	4	V			0.1	SG	2	2
0.19	P	4	V			0.1	SG	2	2
0.19	P	4	V			0.1	SG	2	2

Depth (ft; top)	Type	Height (mm)	Vertical /sub-vertical	Dip (near 90 °if blank)	Kinematic aperture (mm)		Single/ branch-ing	Termination	
					Min (0.1 if blank)	Max		Top	Base
0.19	P	4	V			0.1	SG	2	2
0.19	P	4	V			0.1	SG	2	2
0.19	P	4	V			0.1	SG	2	2
0.19	P	4	V			0.1	SG	2	2
0.19	P	4	V			0.1	SG	2	2
0.19	P	4	V			0.1	SG	2	2
0.19	P	4	V			0.1	SG	2	2
0.19	P	4	V			0.1	SG	2	2
0.19	P	4	V			0.1	SG	2	2
0.19	P	4	V			0.1	SG	2	2
0.19	P	4	V			0.1	SG	2	2
0.1	P	5	V			0.5	BR	1	1
0.1	P	5	V			0.5	BR	1	1
0.1	P	5	V			0.5	BR	1	1
0.1	P	5	V			0.5	BR	1	1
0.1	P	5	V			0.5	BR	1	1
0.1	P	5	V			0.5	BR	1	1
0.1	P	5	V			0.5	BR	1	1
0.1	P	5	V			0.5	BR	1	1
0.1	P	5	V			0.5	BR	1	1
0.1	P	5	V			0.5	BR	1	1
0.1	P	5	V			0.5	BR	1	1
0.1	P	5	V			0.5	BR	1	1
0.1	P	5	V			0.5	BR	1	1
0.1	P	5	V			0.5	BR	1	1
0.1	P	5	V			0.5	BR	1	1
0.1	P	5	V			0.5	BR	1	1
0.1	P	5	V			0.5	BR	1	1
0.1	P	5	V			0.5	BR	1	1
0.1	P	5	V			0.5	BR	1	1
0.1	P	5	V			0.5	BR	1	1
0.1	P	5	V			0.5	BR	1	1
0.14	P	4	SV			0.2	SG	1	1
0.14	P	4	SV			0.2	SG	1	1
0.14	P	4	SV			0.2	SG	1	1
8984.02	P	3	V			0.2	SG	1	1
0.02	P	3	V			0.2	SG	1	1
0.03	P	7	SV			0.6	BR	1	1
0.04	P	9	SV			1	SG	1	1
0.04	P	3	V			0.1	SG	1	1
0.02	VE+P	44	V			0.1	BR	1	1
0.06	P	8	V			1	BR	4	1
83.98	P	5	V			0.2	SG	4	1
0.93	P	30	V			0.2	SG	1	1
0.93	P	13	V			0.2	SG	1	1

Depth (ft; top)	Type	Height (mm)	Vertical /sub-vertical	Dip (near 90 °if blank)	Kinematic aperture (mm)		Single/ branch-ing	Termination	
					Min (0.1 if blank)	Max		Top	Base
0.93	P	10	V			0.2	SG	1	1
0.93	P	9	V			0.2	SG	1	1
0.99	P+S	6	V			0.1	SG	2	2
0.99	P+S	11	V			0.6	SG	4	2
0.97	VE	22	V			0.1	SG	4	1
0.97	VE	11	V			0.1	SG	4	1
94	VE	4	V			0.1	SG	4	1
83.89	VE	5	V			0.1	SG	1	1
0.88	P	1	V			0.1	SG	2	2
0.88	P	1	V			0.1	SG	2	2
0.88	P	1	V			0.1	SG	2	2
0.88	P	3	V			0.1	SG	2	2
0.88	P	3	V			0.1	SG	2	2
0.8	P	30	V			0.5	SG	4	1
0.83	P	10	V			0.5	SG	1	1
0.83	P	10	V			0.5	SG	1	1
0.85	P	21	V			0.5	SG	2	4
0.89	VE	13	V			0.1	SG	1	4
0.73	P	56	V			0.3	BR	1	1
0.75	P+VE	13	V			0.5	SG	1	1
0.86	VE	5	V			0.2	SG	1	1
0.78	P	5	V			0.1	SG	1	1
0.78	P	5	V			0.1	SG	1	1
0.73	P	6	V			0.2	SG	1	1
8983.68	P	14	V			0.1	SG	4	4
0.68	P	19	V			0.2	BR	1	1
0.69	P	9	V			0.2	BR	1	1
0.68	VE	3	V			0.1	SG	1	1
0.68	VE	3	V			0.1	SG	1	1
0.68	VE	3	V			0.1	SG	1	1
0.68	VE	6	V			0.1	SG	1	1
0.67	P	5	V			0.1	SG	1	1
0.55	P	5	V			1	SG	2	2
0.56	P	3	V			0.1	SG	2	2
0.54	P	4	V			0.2	SG	2	2
0.5	P	3	V			0.2	SG	2	2
0.5	P	3	V			0.2	BR	2	2
0.5	P	6	V			0.5	BR	2	2
0.5	P	2	V			0.1	SG	2	2
0.5	VE	11	V			0.1	SG	1	1
0.47	VE+S	10	V			0.2	SG	1	1
0.45	VE+S	5	V			0.1	SG	1	1
0.39	P	22	V			0.1	SG	4	1

Depth (ft; top)	Type	Height (mm)	Vertical /sub-vertical	Dip (near 90 °if blank)	Kinematic aperture (mm)		Single/ branch-ing	Termination	
					Min (0.1 if blank)	Max		Top	Base
0.39	P	24	V			0.1	SG	4	1
0.11	VE+P	130	V			0.5	SG	2	2
0.1	P	2	V			0.2	SG	2	2
0.09	P	3	V			0.2	SG	2	2
0	P	2	V			0.2	SG	2	2
0	P	2	V			0.2	SG	2	2
82.99	P	3	SV			0.1	SG	2	2
0.99	P	3	V			0.2	SG	2	2
0.99	P	3	V			0.2	SG	2	2
0.9	P	24	V			0.1	SG	3	1
8982.95	P	11	V			0.3	SG	2	3
0.95	P	9	V			0.2	SG	2	3
0.98	P	6	V			0.2	SG	2	3
0.98	P	5	V			0.5	SG	2	3
0.92	P	8	V			0.6	SG	2	1
0.83	P+S	20	V			0.8	SG	2	3
0.76	P	12	V			0.1	SG	1	1
0.69	P	2	V			0.2	SG	2	2
0.69	P	2	V			0.2	SG	2	2
0.69	P	2	V			0.2	SG	2	2
0.69	P	5	V			1	SG	2	2
0.69	P	2	H			0.5	SG	1	1
0.7	P	2	H			0.2	SG	1	1
0.6	P	4	SV			0.5	SG	1	1
0.59	P	6	V			0.3	SG	1	1
0.59	P	9	V			0.3	SG	1	1
0.56	P	7	V			1	SG	1	1
0.58	P	2	SV			0.5	SG	1	1
0.4	P	70	V			0.2	SG	1	1
0.46	P	5	SV			0.1	SG	1	1
0.12	P	5	SV			0.2	SG	1	1
0.15	P	8	SV			0.2	SG	1	1
8982.06	P	6	V			0.2	SG	2	2
0.01	VE+P	23	V			0.3	SG	2	2
0.08	VE	3	V			0.5	SG	2	2
0.09	VE+P	9	V			0.1	SG	2	2
0.05	VE+P	14	V			0.3	SG	2	2
8981.59	P	10	V			0.1	SG	4	1
0.51	VE	2	SV			0.1	SG	1	1
0.51	P	7	V			0.1	SG	1	1
0.5	P	3	V			0.1	SG	1	1
0.49	P	4	V			0.2	SG	1	1
0.48	P	4	V			0.1	SG	1	1

Depth (ft; top)	Type	Height (mm)	Vertical /sub-vertical	Dip (near 90 °if blank)	Kinematic aperture (mm)		Single/ branch-ing	Termination	
					Min (0.1 if blank)	Max		Top	Base
0.47	P	3	V			0.1	SG	1	1
0.47	P	3	V			0.1	SG	1	1
0.48	P	4	V			0.1	SG	1	1
0.46	P	7	V			0.2	SG	1	1
0.49	P	10	V			0.1	SG	1	1
0.3	P	3	V			0.2	SG	1	1
0.3	P	3	V			0.2	SG	1	1
0.3	P	6	V			0.3	SG	1	1
0.28	P	5	V			0.3	SG	1	1
0.9	VE	15	V			0.1	SG	1	1
0.08	VE	11	V			0.1	SG	1	1
0.06	VE	13	V			0.1	SG	1	1
0	VE	27	V			0.1	SG	1	1
0.17	VE	9	V			0.1	SG	1	1
0.09	VE+S	8	V			0.1	SG	1	1
0.7	VE	7	V			0.1	SG	1	1
80.88	VE+P	52	V			0.1	SG	1	1
8980.77	VE	57	V			0.1	SG	3	4
0.8	VE+P	12	V			0.2	SG	1	1
0.79	P	3	SV			0.1	SG	1	1
0.75	P	2	V			0.2	SG	1	1
0.88	P	5	V			0.9	SG	1	1
0.87	P	3	SV			0.2	SG	1	1
0.85	P	6	V			0.1	SG	4	2
0.84	P	2	SV			0.2	SG	2	2
0.82	P	10	V		0.1	1	BR	1	1
0.82	P	4	V			1	SG	1	1
0.82	P	4	V			1	SG	1	1
0.86	P	2	SV			0.2	SG	2	1
0.82	P	4	V			0.5	SG	2	2
0.8	P	2	V			0.1	SG	1	2
0.79	P	2	SV			0.2	SG	1	2
0.79	P	2	SV			0.2	SG	1	2
0.78	P	2	V			0.5	BR	1	2
0.78	P	1	V			0.5	BR	3	1
0.78	P	9	V			0.5	BR	3	1
0.78	P	1	V			1	BR	3	1
0.77	P	1	V			0.3	SG	3	1
0.79	P	3	SV			0.1	SG	2	2
0.78	P	4	V			0.2	SG	2	2
0.78	P	6	V			0.5	SG	2	2
0.78	P	3	V			0.2	SG	2	2
0.8	P	2	SV			0.5	SG	2	2

Depth (ft; top)	Type	Height (mm)	Vertical /sub-vertical	Dip (near 90 °if blank)	Kinematic aperture (mm)		Single/ branch-ing	Termination	
					Min (0.1 if blank)	Max		Top	Base
0.8	P	3	SV			0.5	SG	2	2
0.8	P	3	SV			0.5	SG	2	2
8978.45	P	5	V			0.2	SG	4	1
0.22	P	3	V			0.1	SG	2	2
0.21	P	7	V			0.2	SG	4	4
96.63	P	82	V			0.2	SG	1	1
0.42	P	10	V			0.1	SG	4	4
0.04	P	4	V			0.2	SG	1	4
0.02	P	8	V			0.2	SG	1	4
74.7	P	24	V			0.5	SG	4	1
0.28	P	14	V			0.2	SG	1	1
73.66	P	12	V			0.3	SG	1	2
0.69	P	24	V			0.3	SG	1	4
8970.16	P	83	V			1	SG	4	1
0.16	P	10	V			0.2	SG	4	3
0.16	P	10	V			0.2	SG	4	3
0.16	P	10	V			0.2	SG	4	3
0.4	P	14	V			0.2	SG	2	2
0.23	P	35	V			0.2	SG	3	1
0.23	P	25	V			0.3	SG	3	1
0.12	P	7	V			0.2	SG	3	4
69.93	P	52	V			1	SG	4	4
0.9	VE+P	103	V			1	SG	4	3
0.9	VE+P	26	V			0.3	BR	4	4
0.9	VE+P	27	V			0.3	BR	4	4
0.9	VE	15	V			0.3	SG	4	2
0.8	P	36	V			0.3	SG	4	4
0.71	P	66	V			1.5	SG	1	4
0.07	P	24	V			0.2	SG	4	4
68.44	P	256	V			0.2	SG	?	4
67.99	P	187	V			0.2	SG	4	4
0.6	P	237	V			0.3	SG	4	4
66.81	P	78	V			0.5	SG	1	1
64.98	P+VE	158	V			2	BR	4	3
65.45	P	2	V			0.7	SG	2	2
0.48	P	1	V			0.7	SG	2	2
64.02	P	30	V			1	SG	1	1
8961.78	P	54	V		0.3	1	BR	3	4
60.3	P	50	V			0.3	SG	1	1
0.17	P	8	V			0.3	SG	3	3
59.28	P	206	V			1.5	SG	3	1
0.51	P	108	V			0.5	SG	1	1
0.5	P	182	V			0.5	SG	1	1

Depth (ft; top)	Type	Height (mm)	Vertical /sub-vertical	Dip (near 90 °if blank)	Kinematic aperture (mm)		Single/ branch-ing	Termination	
					Min (0.1 if blank)	Max		Top	Base
0.62	P	125	V			0.5	SG	4	1
0.62	P	144	V			0.1	SG	4	1
0.85	P	55	V			0.1	SG	1	1
0.95	P	38	V			0.1	SG	1	1
56.65	P	45	V			0.1	SG	1	1
55.65	P	75	V			0.1	SG	1	1
0.55	P	32	V			0.1	SG	1	1
0.4	P	45	V			0.1	SG	1	1
0.37	P	42	V			0.2	SG	4	1
0.51	P	12	V			0.2	SG	1	4
0.13	P	40	V			0.1	SG	1	1
8954.61	P	28	V			0.1	SG	3	1
0.61	P	110	V			? – PARTIAL FACE	?	2	4
0.61	P	36	V			1	BR	3	1
0.34	P	74	V			0.6	SG	1	3
0.36	VE	23	V			0.1	SG	1	3
0.27	P	70	V			0.3	BR	1	1
0.3	P	20	V			0.1	SG	1	1
0.33	P	76	V			0.5	BR	1	3
0.57	P	?	sv			0.4	SG	1	1
0.26	P	16	V			0.1	SG	1	1
0.37	P	42	V			0.1	SG	1	1
0.28	P	33	V			0.3	SG	1	4
53.38	P	88	V			0.2	SG	1	4
52.9	P	60	V			0.2	SG	4	1
0.9	P	130	V			0.1	SG	4	1
8952.62	P	14	V			0.5	SG	2	1
0.63	P	11	V			0.1	SG	1	1
0.43	P	4	V			0.2	SG	1	1
0.43	P	5	V			0.1	SG	1	1
0.21	VE+P	18	V			0.5	SG	4	1
0.18	P+S	14	V			0.5	SG	3	1
0.18	P+S	38	V			1.5	SG	3	1
0.27	P	5	V			0.1	SG	1	1
0.13	P	3	V			0.1	SG	1	1
51.15	P	249	V			0.2	SG	4	1
0.71	P	65	V			0.2	SG	1	4

Depth (ft; top)	Type	Height (mm)	Vertical /sub-vertical	Dip (near 90 °if blank)	Kinematic aperture (mm)		Single/ branch-ing	Termination	
					Min (0.1 if blank)	Max		Top	Base
50.03	P	25	V			? - INCOMPLETE WALL	?	?	?
0.05	P	20	V			0.5	SG	1	1
49.54	P	36	V			1	SG	3	3
0.51	P	5	V			0.2	SG	3	1
8947.55	P	41	V			0.2	SG	3	1
46.95	P	126	V			0.1	SG	4	1
0.8	P	55	V			0.1	SG	1	1
8945.12	P	45	V			1	SG	3	3
43.75	P	15	V			0.2	SG	1	3
0.5	P	22	V			0.2	SG	1	4
0.5	P	28	V			0.2	SG	4	1
0.52	P	15	V			0.1	SG	1	1
42.98	P	16	V			0.2	SG	1	3
0.94	P	3	V			0.2	SG	1	1
0.78	P	78	V			0.2	SG	1	3
41.82	P	52	V			0.2	SG	4	4
0.87	P	36	V			0.2	SG	1	4
40.62	P	25	V			0.2	SG	2	2
0.68	P	16	V			0.2	SG	2	2
0.28	VE	83	V			0.8	BR	1	3
0.55	VE+P	17	V		0.5	1	SG	3	3
38.53	VE+P	632	V			3	BR	4	3
0.67	P	53	V			1	SG	1	3
0.53	P	21	V			0.2	SG	1	1
8937.28	P	10	V			0.2	SG	1	1
8936.32	P	23	V			0.2	SG	2	2
0.37	P	48	V			0.2	SG	2	4
0.22	VE	35	V			0.2	SG	4	1
35.45	P	98	V			0.1	SG	3	1
0.12	VE+P	93	V		0.2	1.5	BR	3	3
0.42	P	345	V		0.2	0.5	BR	3	4
0.42	VE+P	192	V			0.5	BR	3	4
0.12	P	17	V			0.2	BR	4	2
0.17	P	12	V			0.2	SG	2	2
0.22	P	47	V			0.2	SG	2	4
34.78	P	42	V			0.1	SG	4	4
8928.8	P	30	V			0.2	SG	2	2
0.73	P	20	V			0.1	SG	2	2
0.1	P	20	V			0.3	SG	2	2

Depth (ft; top)	Type	Height (mm)	Vertical /sub-vertical	Dip (near 90 °if blank)	Kinematic aperture (mm)		Single/ branch-ing	Termination	
					Min (0.1 if blank)	Max		Top	Base
8923.8	P+VE	11	V			0.2	SG	1	2
22.72	P	19	V			0.1	SG	1	1
21.69	P	3	V			0.1	SG	3	3
0.63	P	5	V			0.1	SG	3	3
0.63	P	5	V			0.1	SG	3	3
0.63	P	5	V			0.2	SG	3	3
0.53	P	11	V			0.1	SG	3	3
0.53	P	11	V			0.1	SG	3	3
0.48	P	10	V			0.1	SG	3	3
0.52	P	20	V			0.5	SG	4	3
0.46	P	7	V			0.2	SG	2	1
0.28	P	50	V			0.3	SG	3	2
0.02	P	26	V			0.1	SG	1	4
0.24	P	3	V			0.1	SG	1	1
0.25	P	3	V			0.1	SG	1	1
0.27	P	3	V			0.1	SG	1	1
20.6	P	52	V			0.1	SG	1	1
0.74	P	42	V			0.2	SG	1	3
0.74	P	17	V			0.2	SG	4	4
0.89	P	40	V			0.2	SG	3	4
0.35	P	110	V			0.2	SG	3	1
8919.82	P	160	V			0.3	SG	1	3
0.75	P	15	V			0.2	SG	1	1
0.58	P	95	V			0.5	SG	4	1
0.35	P	62	V			0.3	SG	4	1
0.22	P	22	V			0.3	SG	1	2
8918.98	P	5	V			0.7	SG	2	2
0.76	VE	42	V			0.2	SG	1	4
0.68	VE	35	V			0.1	SG	2	2
0.62	P	6	SV			0.1	SG	4	4
0.62	P	8	SV			0.1	SG	1	1
0.57	P	55	V			0.1	SG	4	1
0.62	P	11	SV			0.1	SG	1	1
0.52	P	53	V			0.7	BR	4	1
0.47	P	7	V			0.3	SG	2	4
0.47	P	7	V			0.5	SG	2	4
0.48	P	3	V			0.1	SG	2	4
0.48	P	3	V			0.1	SG	2	4
0.2	P+S	21	V			0.8	SG	1	1
0.16	P	14	V			0.5	SG	4	1
0.16	P	36	V			1	BR	4	1
0.13	P	5	V			0.5	SG	3	4
17.9	P	23	V			0.2	SG	1	1

Depth (ft; top)	Type	Height (mm)	Vertical /sub-vertical	Dip (near 90 °if blank)	Kinematic aperture (mm)		Single/ branch-ing	Termination	
					Min (0.1 if blank)	Max		Top	Base
0.9	P	15	V			0.2	SG	1	1
0.9	P	13	V			0.2	SG	1	1
0.82	P	4	SV			0.5	SG	4	1
0.82	P	4	V			0.5	SG	4	1
0.77	S	8	V			0.2	SG	1	1
0.68	P	26	V			0.1	SG	4	1
0.53	P	30	V			0.1	SG	1	1
8916.55	P	20	V			0.1	SG	1	1
0.59	P	58	V			0.1	SG	1	1
0	P	123	V			0.5	SG	4	1
15.59	P	43	V			0.5	SG	2	2
0.45	P	17	V		0.2	0.5	SG	3	3
14.43	P	9	V			0.2	SG	3	3
0.43	P	9	V			0.2	SG	3	3
0.14	P	35	V			0.5	SG	3	4
13.03	VE	22	V			0.5	SG	1	2
12.18	VE	113	V			?-MISSING FACE	SG	1	1
11.92	P	33	V			0.2	SG	1	1
0.78	P	83	V			0.6	BR	4	3
0.62	P	90	V			0.2	SG	3	4
0.48	P	42	V			0.1	SG	1	3
0.48	P	101	V			0.1	SG	1	3
0.3	P	98	V			0.3	BR	1	1
8910.84	P	17	V			0.2	SG	1	1
0.84	P	13	V			0.2	SG	2	2
0.73	P	15	V			0.2	SG	2	2
0.51	P	12	V			0.2	SG	2	2
0.19	P	9	V			0.2	SG	2	2
0.19	P	15	V			0.2	SG	2	2
0.7	P	4	V			0.1	SG	1	1
0.71	P	2	V			0.1	SG	1	1
89.09	P	27	V			0.5	SG	1	1
0.17	P	13	V			0.5	SG	1	1
0.18	P	8	V			0.2	SG	1	1
0.18	P	10	V			0.2	SG	1	1
0.18	P	10	V			0.5	SG	1	1
0.12	P	8	V			0.1	SG	1	1
0.14	P	9	V			0.1	SG	1	1
0.01	VE+P	28	V			0.3	SG	1	1
0.0	P	30	V			0.3	SG	2	4

Depth (ft; top)	Type	Height (mm)	Vertical /sub-vertical	Dip (near 90 °if blank)	Kinematic aperture (mm)		Single/ branch-ing	Termination	
					Min (0.1 if blank)	Max		Top	Base
8.98	VE+P	17	V			0.3	SG	1	1
0.55	P	69	V			?-BROKEN FACE	SG	?	?
0.37	P	5	V			0.1	SG	2	1
0.37	P	10	V			0.1	BR	2	1
0.24	P	28	V			0.3	SG	1	1
0.21	P	11	V			0.2	SG	1	1
0.2	P	44	V		0.5	2	SG	2	1
0.21	P	36	V		0.5	1	SG	2	2
0.21	P	2	SV			0.5	SG	2	2
0.22	P	28	V			0.5	SG	1	1
8907.86	P	40	V		0.2	1	SG	1	3
0.84	P	3	V			0.1	SG	2	1
0.84	P	3	V			0.1	SG	1	1
0.79	P+VE	11	V			0.1	SG	4	1
0.38	P	26	V			0.2	SG	1	1
0.33	P	20	V			0.3	SG	1	1
0.43	P	8	V			0.1	SG	1	1
0.35	P	45	V			1	BR	1	1
0.23	P	13	V			0.5	SG	1	4
0	P	13	V			0.5	SG	4	1
0	P	13	V			1	SG	4	1
6.89	P	4	V			0.2	SG	1	1
6.84	P	22	V			0.2	SG	3	2
0.84	P	9	V		0.2	1	SG	3	2
0.84	P	16	V			0.2	SG	3	2
5.16	P	17	V			0.2	SG	4	3
0.1	P	16	V			0.1	SG	1	4
4.88	P	25	V			0.1	SG	1	1
0.71	P	30	V			0.1	SG	1	1
0.05	P	21	V			0.1	SG	4	1
0.12	P	4	V			0.1	SG	1	4
0.18	P	18	V			0.1	SG	1	3
8904	P	15	V			0.5	SG	4	1
0.03	P	5	V			0.2	SG	1	4
3.99	P	2	V			0.6	SG	2	2
0.98	P	3	V			0.6	BR	2	2
0.82	P	21	V		0.2	0.6	SG	1	1
2.04	P	4	V			0.2	SG	1	1
0.07	P	128	V			0.2	SG	1	1
1.45	P	11	V			0.2	SG	2	2

Depth (ft; top)	Type	Height (mm)	Vertical /sub-vertical	Dip (near 90 °if blank)	Kinematic aperture (mm)		Single/ branch-ing	Termination	
					Min (0.1 if blank)	Max		Top	Base
0.42	P	5	V			0.2	SG	2	2
0.4	P	2	V			0.1	SG	2	2
0.4	P	3	V			0.1	SG	2	2
0.4	P	10	V		0.1	3	SG	3	1
0.34	P	4	V			0.1	SG	1	1
0.2	P	8	V			0.1	SG	2	1
0.15	P	5	SV			0.1	SG	2	2
0.05	P	15	V			0.2	SG	2	2
0	P	13	SV		0.5	2	SG	4	4
0.46	P	13	V			0.2	SG	1	2
0.5	P	5	V			0.1	SG	2	2
0.54	P	8	V			0.4	BR	2	2
0.57	VE+P	58	V		0.1	1	SG	1	4
0.78	P	32	V			0.5	SG	2	2
8900.94	P	6	V			0.2	SG	1	1
0.96	P	7	V			0.2	SG	2	2
0.98	P	4	V			0.2	SG	2	4
0.67	P	48	V			1	BR	2	2
0.58	P	21	V			0.5	SG	2	2
0.66	P	8	V			0.3	SG	2	2
0.7	P	9	V			0.1	SG	1	1
0.47	P	23	V			0.1	BR	2	1
0.46	P	27	V			0.2	BR	2	1
0.45	P	44	V			0.2	BR	2	1
0.43	P	46	V			0.4	BR	2	1
0.38	P	23	V			0.2	SG	1	1
0.22	P	30	V			0.5	SG	1	1
0.35	P	20	SV			0.5	SG	1	1
8899.92	P	83	V			0.3	SG	2	2
0.88	P	6	V			0.3	SG	2	2
0.86	P	16	V			0.3	SG	2	2
0.85	P	50	V			0.2	SG	2	2
0.84	P	89	V			0.1	SG	2	4
8899.71	P	39	V			1	SG	1	2
0.64	P	15	V			0.2	SG	4	1
0.61	P	24	V			0.2	BR	4	4
0.51	P	56	V			0.3	SG	4	1
0.43	P	78	V			0.1	SG	4	1
0.21	P	2	V			0.3	SG	2	2
0.1	P	27	V			0.1	SG	1	1
0.08	P	18	V			0.2	SG	1	1
0.05	P	12	V			0.1	BR	1	1
0.03	P	10	V			0.1	SG	1	1

Depth (ft; top)	Type	Height (mm)	Vertical /sub-vertical	Dip (near 90 °if blank)	Kinematic aperture (mm)		Single/ branch-ing	Termination	
					Min (0.1 if blank)	Max		Top	Base
0.01	P	12	V			0.5	SG	4	1
0.01	P	19	V			0.6	SG	4	4
98.72	P	53	V			0.2	SG	1	1
0.73	P	73	V			0.1	SG	1	4
0.73	P	9	V			0.3	SG	4	2
0.6	P	20	V			0.3	SG	2	1
0.49	P	113	V		0.5	7	BR	4	4
0.21	P	19	V			0.2	SG	1	1
0.14	P	18	V			0.2	SG	1	1
0.14	P	18	V			0.2	SG	1	1
0.01	P	39	V		0.5	1	BR	2	2
0	P	29	V		1	2	BR	4	2
8896.87	P	24	V			0.3	SG	2	2
0.88	P	5	V			0.2	SG	3	2
0.88	P	8	V			0.2	SG	3	2
0.83	P	6	V			0.2	SG	1	2
0.83	P	6	V			0.2	SG	1	2
0.84	P	4	V			0.1	SG	2	2
0.48	P	27	V			0.2	SG	1	1
0.15	P	27	V			0.2	SG	1	1
0.15	P	27	V			0.1	SG	1	1
0.14	P	2	V			0.2	SG	2	2
95.7	P	65	V			?-MISSING FACE	SG	2	2
94.39	P	184	V		0.1	0.3	BR	1	4
92.88	P	5	V			0.5	SG	2	2
0.87	P	5	V			0.1	SG	1	1
8891.22	P	28	V			0.5	BR	4	2
0.15	P	63	V		0.5	2	BR	2	2
90.78	P	4	V			0.3	SG	2	2
88.34	P	113	V			0.2	SG	1	1
87.38	P	10	V			0.2	SG	4	2
0.21	P	8	V			0.3	SG	2	2
0.12	P	5	V			0.1	SG	1	1
0.05	P	5	V			0.1	SG	1	1
8881.34	P	17	V			0.1	SG	3	1
0.35	P	49	V			0.1	SG	1	1
0.41	P	8	V			0.1	SG	2	2
0.44	P	10	V			0.1	SG	1	1
0.21	P	16	SV		1	2	SG	3	3
8880.91	P	19	V			0.2	BR	4	1

Depth (ft; top)	Type	Height (mm)	Vertical /sub-vertical	Dip (near 90 °if blank)	Kinematic aperture (mm)		Single/ branch-ing	Termination	
					Min (0.1 if blank)	Max		Top	Base
0.77	P	20	V			0.2	SG	4	4
0.57	P	14	V			0.5	SG	4	2
0.55	P	20	V			0.5	SG	1	1
0.27	P	25	V		0.1	1	SG	4	1
0.03	P	29	V			0.1	SG	4	1
0.12	P	57	V			0.1	SG	1	4
79.84	P	13	V			0.1	SG	4	1
8878.72	P	5	SV		0.5	2	SG	2	2
0.59	P	19	V			0.2	SG	2	2
0.5	P	19	V			0.2	SG	1	1
0.37	P	30	V			0.1	SG	3	1
0.13	P	14	SV			0.5	BR	2	2
0.1	P	9	V			0.1	SG	1	1
77.92	P	6	V			0.1	SG	3	1
0.92	P	67	V			0.1	SG	3	1
0.75	P	28	V			0.1	SG	4	1
0.51	P	70	V			0.1	SG	1	4
0.59	P	36	V			0.2	SG	2	2
0.52	P	11	V			1	BR	2	4
0.62	P	28	V			0.1	SG	1	1
0.4	P	45	V			0.1	SG	1	4
0.32	P	28	V			0.1	SG	1	1
0.27	P	17	V			0.1	SG	1	1
0.3	P	23	V			0.1	SG	4	1
0.18	P	12	V			0.1	SG	1	1
0.15	P	11	V			0.1	SG	1	1
0.08	P	22	V			0.1	SG	1	1
8877	P	23	V			0.1	SG	4	1
0.06	P	17	V			0.1	SG	1	1
0	P	14	V			0.1	SG	4	1
0.03	P	32	V			0.1	SG	1	1
76.59	P	2	SV			0.2	SG	2	1
8865.8	P	10	V			0.1	SG	1	1
0.72	P	22	V			0.1	SG	1	1
0.68	P	31	V			0.1	SG	1	3
0.37	P	27	V			0.1	SG	1	1
0.28	P	28	V			0.2	SG	4	1
0.18	P	30	V			0.2	SG	1	1
8859.56	P	3	V			0.2	SG	3	3
0.57	P	17	V			0.2	SG	3	3
0.53	P	6	V			0.2	SG	3	3
0.38	P	45	V			0.2	BR	3	3
0.35	P	7	V			0.2	SG	3	3

Depth (ft; top)	Type	Height (mm)	Vertical /sub-vertical	Dip (near 90 °if blank)	Kinematic aperture (mm)		Single/ branch-ing	Termination	
					Min (0.1 if blank)	Max		Top	Base
0.33	P	6	V			0.2	SG	3	3
0.31	P	5	V			0.2	SG	1	3
0.28	P	10	V			0.2	SG	3	3
0.27	P	6	V			0.2	SG	3	3
0.23	P	7	V			0.2	SG	1	1
0.2	P	9	V			0.2	SG	1	1
0.01	P	53	V			?-MISSING FACE	BR	4	2
58.11	P	15	V			0.2	SG	3	3
57.9	P	62	V			0.2	SG	1	3
0.88	P	16	V			0.2	SG	1	1
0.94	P	11	V			0.2	SG	3	3
0.98	P	5	V			0.1	SG	2	1
0.81	P	22	V			0.2	SG	4	2
0.86	P	5	V			0.2	SG	4	2
56.01	P	7	SV			0.2	SG	1	1
0.05	P	485	V		0.1	3	SG	1	4
57.58	P	4	V			0.1	SG	2	1
0.6	P	18	V			0.2	BR	1	1
8855.97	P	3	V			0.1	SG	1	1
0.94	P	7	V			0.1	SG	1	1
0.93	P	3	V			0.1	SG	1	1
0.93	P	20	V		0.2	1	BR	2	4
0.92	P	14	V			0.1	SG	1	1
0.95	P	15	V			0.2	SG	1	1
0.82	P	41	V			0.2	SG	1	3
0.88	P	9	V			0.1	SG	1	1
0.83	P	19	V			0.2	SG	1	1
0.62	P	65	V			0.2	SG	1	1
0.6	P	3	V			0.2	SG	2	2
0.58	P	6	V			0.2	SG	2	2
0.53	P	15	V			0.2	SG	1	1
0.49	P	12	V			0.2	SG	1	1
52.78	P	3	V			0.2	SG	1	2
0.07	P	10	V			0.1	SG	1	1
0.1	P	10	V			0.1	SG	1	1
51.44	P	201	V			0.2	SG	1	1
0.16	P	104	V			0.1	SG	1	1
0.14	P	8	V		0.1	1	SG	2	2
0.2	P	45	V		0.1	1	SG	2	1
8845.85	P	13	V			0.2	SG	3	3

Depth (ft; top)	Type	Height (mm)	Vertical /sub-vertical	Dip (near 90 °if blank)	Kinematic aperture (mm)		Single/ branch-ing	Termination	
					Min (0.1 if blank)	Max		Top	Base
0.95	P	2	V			0.1	SG	2	2
0.96	P	2	V			0.1	SG	2	2
0.89	P	12	V			0.2	SG	2	2
0.79	P	20	V			0.2	SG	2	2
0.71	P	17	V			0.2	SG	2	2
0.77	P	22	V			0.2	SG	2	2
0.7	P	4	V			0.2	SG	2	2
0.65	P	11	V		0.2	0.5	BR	2	2
0.57	P	9	V			0.2	BR	3	1
0.57	P	23	V			0.2	SG	3	1
0.55	P	6	V			0.2	SG	2	2
0.42	P	41	V			0.2	SG	1	3
0.46	P	11	V			0.1	SG	1	1
0.51	P	15	V			0.1	SG	1	1
0.31	P	38	V			0.1	SG	1	1
43.01	P	22	V			0.1	SG	1	1
0.01	P	11	V			0.1	SG	1	2
0.06	P	3	V			0.1	SG	2	2
0.07	P	4	V			0.1	SG	2	2
8819.62	P	22	V			0.2	SG	1	1
0.54	P	30	V			0.2	SG	1	1
0.3	P	18	V			0.2	SG	1	1
14.08	P	108	V			0.2	BR	4	1
0.08	P	40	V		0.1	0.3	SG	4	1
13.45	P	260	V		0.1	0.3	BR	1	1
0.39	P	18	V			0.1	SG	1	4
0.38	P	82	V			0.2	SG	1	1
0.34	P	44	V			0.1	SG	1	1
12.95	P	116	V			0.2	SG	2	1
0.94	P	320	V		0.2	?-MISSING FACE	?-MISSING FACE	1	4
0.94	P	136	V			0.1	SG	1	1
0.98	P	80	V			0.1	SG	1	1
8786.12	P	16	V			0.2	SG	2	1
0.12	P	40	V		0.1	0.5	BR	2	1
0.17	P	8	V			0.2	SG	2	4
0.2	P	5	V			0.2	SG	4	1
0.22	P	17	V			0.2	SG	2	1
0.27	P	20	V			0.2	SG	1	1
8779.82	P	38	V			0.2	SG	1	1
0.53	P	50	V			0.1	SG	1	1

Depth (ft; top)	Type	Height (mm)	Vertical /sub-vertical	Dip (near 90 °if blank)	Kinematic aperture (mm)		Single/ branch-ing	Termination	
					Min (0.1 if blank)	Max		Top	Base
0.59	P	35	V			0.2	SG	1	1
0.58	P	6	V			0.1	SG	1	1
0.47	P	31	V			0.2	SG	4	1
0.11	P	20	V			0.2	SG	1	1
0.19	P	39	V			0.2	SG	2	1
0.32	P	163	V			0.2	SG	2	1
0.35	P	68	V			0.2	BR	1	1
0.58	P	5	V			0.2	SG	2	1
0.07	P	268	V		0.2	4	BR	1	2
8754.45	P	15	SV			0.6	SG	4	3
0.48	P	17	SV			0.6	SG	2	4
53.17	P	136	V			0.2	SG	1	3
0.06	P	8	V			0.2	SG	1	1
0.08	P	9	V			0.2	SG	1	1
0.12	P	11	V			0.2	SG	1	1
0.17	P	10	V			0.2	SG	1	1
0.18	P	108	V		0.2	2	SG	1	1
0.52	P	32	V		0.2	1.8	SG	1	3
0.02	P	18	V			0.2	SG	2	2
0.08	P	22	V			0.3	SG	2	2
0.18	P	36	V		0.1	0.3	SG	1	1
52.98	P	88	V			0.2	SG	1	1
0.95	P	32	V			0.2	SG	1	1
0.92	P	6	V			0.2	SG	1	1
0.88	P	5	V			0.2	SG	1	1
8752.38	P	14	V			0.2	SG	1	1
0.344	P	11	V			0.2	SG	1	1
0.49	P	25	V			0.2	SG	1	1
0.57	P	35	V		0.1	0.3	SG	1	1
0.58	P	325	V			9	BR	1	3
8745.05	P	3	V			0.2	SG	2	2
0.06	P	7	V			0.2	SG	2	2
0.08	P	6	V			0.2	SG	2	2
0.1	P	5	V			0.2	SG	2	2
0.13	P	7	V			0.2	SG	2	2
0.15	P	2	V			0.2	SG	2	2
0.16	P	7	V			0.2	SG	2	2
0.18	P	24	V			0.3	SG	2	2
0.25	P	4	V			0.3	SG	2	2
0.27	P	18	V			0.3	BR	1	2
0.33	P	23	V			0.2	SG	1	1
0.36	P	16	V			0.1	SG	1	1
0.38	P	7	V			0.2	SG	1	1

Depth (ft; top)	Type	Height (mm)	Vertical /sub-vertical	Dip (near 90 °if blank)	Kinematic aperture (mm)		Single/ branch-ing	Termination	
					Min (0.1 if blank)	Max		Top	Base
0.42	P	3	V			0.2	SG	2	2
0.03	P	12	V			0.3	SG	2	2
0.03	P	4	V			0.1	SG	2	2
0.07	P	4	V			0.2	SG	2	2
0.09	P	8	V			0.2	SG	2	2
0.12	P	7	V			0.2	BR	2	1
0.15	P	18	V			0.3	SG	2	2
0.28	P	7	V			0.2	SG	4	1
8744.19	P	3	V			0.2	SG	1	1
0.28	P	4	V			0.2	SG	1	1
0.23	P	31	V			0.2	SG	1	1
0.05	P	3	V			0.1	SG	1	1
0.06	P	7	V			0.2	SG	1	1
43.98	P	27	V			0.2	SG	1	1
0.98	P	2	V			0.3	SG	2	2
0.97	P	3	V			0.2	SG	2	2
0.95	P	3	V			0.2	SG	1	1
0.93	P	5	V			0.2	SG	2	1
0.91	P	6	V			0.2	SG	1	2
0.88	P	5	V			0.3	SG	1	1
0.85	P	8	V			0.3	SG	1	1
0.82	P	20	V			0.5	SG	1	1
0.79	P	10	V			0.5	BR	1	1
0.73	P	17	V			0.5	BR	1	2
0.68	P	10	V			0.2	SG	1	1
39.06	P	7	V			0.1	SG	1	1
8738.98	P	26	V			0.2	SG	1	1
0.88	P	25	V			0.2	SG	1	1
0.84	P	14	V			0.2	SG	2	2
0.75	P	25	V			0.3	SG	2	1
0.68	P	23	V			0.2	SG	2	2
0.67	P	8	V			0.2	SG	2	2
0.65	P	5	V			0.2	SG	2	2
0.62	P	7	V			0.2	SG	2	2
0.6	P	4	V			0.2	SG	3	2
0.73	P	38	V			0.2	SG	4	1
8725.09	P	32	V		0.1	1	SG	1	2
0.13	P	33	V			0.3	SG	1	1
24.54	P	125	V			0.2	SG	1	1
0.58	P	105	V			0.1	SG	1	1
0.38	P	52	V			0.3	SG	4	2
0.52	P	5	V			0.2	SG	2	2
0.55	P	32	V			0.3	SG	2	2

Depth (ft; top)	Type	Height (mm)	Vertical /sub-vertical	Dip (near 90 °if blank)	Kinematic aperture (mm)		Single/ branch-ing	Termination	
					Min (0.1 if blank)	Max		Top	Base
0.62	P	63	V			0.5	SG	2	2
0.82	P	3	V			0.4	SG	2	2
0.83	P	2	V			0.4	SG	2	2
0.84	P	4	V			0.4	SG	2	2
0.85	P	11	V			0.4	SG	2	2
0.89	P	115	V		0.5	1	SG	2	1
8714.02	P+VE	56	V			0.2	SG	2	1
8711.27	P	100	V			0.2	SG	1	1
0.6	P	20	V			0.1	SG	1	1
0.66	P	10	V			0.2	SG	4	1
0.68	P	87	V			0.2	SG	4	4
10.55	P	35	V			0.2	SG	1	4
0.55	P	15	V			0.2	SG	1	4
0.38	P	8	V			0.1	SG	1	1
0.3	P	6	V			0.6	SG	2	2
0.33	P	13	V			0.7	BR	2	1
0.31	P	20	V			1	BR	2	1
0.12	P	15	V			0.2	SG	4	4
0.12	P	18	V			0.2	SG	1	2
0.12	P	19	V			0.2	SG	1	2
0.12	P	20	V			0.3	SG	2	2
0.12	P	26	V			0.3	SG	2	2
8710	P	9	V			0.2	SG	2	1
9.98	P	6	V			0.1	SG	4	2
0.99	P	2	V			0.1	SG	2	2
8.84	P	15	V			0.3	SG	1	1
0.15	P	4	SV			0.1	SG	4	2
8708.01	P	1	V			0.5	SG	3	3
0.02	P	7	V		0.2	1	SG	3	4
0.02	P	3	SV			0.3	SG	1	3
0.04	P	7	V		0.2	0.6	SG	3	3
0.06	P	2	SV			0.2	SG	3	1
7.72	P	16	V			0.2	SG	1	1
6.78	P	7	V			0.6	SG	2	2
5.47	P	29	V			0.1	SG	1	1
0.09	P	4	V			0.1	SG	2	1
0.12	P	19	V			0.1	SG	1	1
4.48	P	50	V			0.8	BR	1	2
0.57	P	12	V			0.1	SG	1	1
0.6	P	7	V			0.1	SG	1	1
0.66	P	43	V			0.1	SG	1	1
0.64	P	3	V			0.2	SG	2	1
0.64	P	9	V			0.2	SG	2	1

Depth (ft; top)	Type	Height (mm)	Vertical /sub-vertical	Dip (near 90 °if blank)	Kinematic aperture (mm)		Single/ branch-ing	Termination	
					Min (0.1 if blank)	Max		Top	Base
0.65	P	18	V			0.1	SG	1	1
0.65	P	11	V			0.1	SG	1	1
8700.17	P	21	V			0.1	SG	1	3
0.24	P	9	V			0.1	SG	3	3
0.28	P	19	V			0.1	SG	1	1
8696.08	P	67	V			0.1	SG	1	1
0	P	87	V			0.1	SG	1	1
8691.79	P	5	V			0.2	SG	2	1
0.81	P	7	V			0.2	SG	2	1
0.83	P	8	V			0.2	SG	2	1
0.44	P	101	V		0.2	1	SG	2	2
0.42	P	7	V			0.2	SG	2	2
0.28	P	8	V			0.2	SG	2	2
0.26	P	5	V			0.2	SG	1	2
0.25	P	5	V			0.2	SG	1	2
0.2	P	20	V			0.2	SG	2	2
0.19	P	44	V			0.7	SG	3	1
90.59	P	45	V			0.2	SG	4	1
0.52	P	49	V			0.1	SG	1	1
0.42	P	8	V			0.2	SG	4	1
89.3	P	40	V		0.1	0.3	SG	1	1
0.43	P	5	V			0.2	SG	2	2
0.44	P	3	V			0.2	SG	2	2
0.12	P	9	V			0.2	SG	1	4
8688.3	P	72	V			0.3	SG	2	1
85.4	VE	13	V			0.1	SG	2	1
0.34	VE+P	23	V			0.1	SG	2	1
0.3	P	10	V			0.1	SG	2	1
0.25	VE	16	V			0.1	SG	2	1
0.23	VE	4	V			0.1	SG	1	1
8675.58	P	22	V			0.1	SG	2	1
0.52	P	19	V			0.1	SG	1	2
0.33	P	55	V			0.1	SG	1	1
0.48	P	32	V			0.1	SG	1	1
0.4	P	39	V			0.1	SG	1	1
74	P	9	V			0.2	SG	4	2
74	P	14	V			0.2	SG	4	2
73.12	P	31	V			0.1	SG	1	1
0.28	P	13	V			0.2	SG	4	4
0.35	P	8	V			0.2	SG	4	2
0.38	P	10	V			0.3	SG	2	2
0.39	P	63	V			0.3	SG	4	4

Depth (ft; top)	Type	Height (mm)	Vertical /sub-vertical	Dip (near 90 °if blank)	Kinematic aperture (mm)		Single/ branch-ing	Termination	
					Min (0.1 if blank)	Max		Top	Base
8673	P	173	V			?-MISSING FACE	SG	4	4
0.62	P	19	V			0.1	SG	4	2
8672.92	P	42	V			0.2	SG	2	1
0.92	P	18	V			0.2	SG	3	4
8667.53	P	15	V			0.2	SG	1	1
0.6	P	13	V			0.1	SG	1	1
0.23	P	10	V			0.2	SG	1	1
0.27	P	71	V		0.2	0.5	SG	1	1
8666.85	P	210	V			0.2	SG	3	2
65.12	P	37	V			0.1	SG	2	1
0.29	P	85	V			0.2	SG	2	2
0.28	P	162	V			0.2	SG	1	1
0.27	P	12	V			0.3	SG	2	2
0.24	P	7	V			0.2	SG	1	1
0.08	P	60	V			0.1	SG	1	1
8665	P	15	V			0.1	SG	1	1
64.85	P	291	V			0.3	BR	2	1
61.5	P	42	V			0.2	SG	2	1
0.42	P	28	V			0.2	SG	2	2
0.22	P	62	V			0.2	SG	2	2
0.21	P	4	V			0.2	SG	2	2
0.04	P	31	V			0.2	SG	1	2
0	P	70	V			0.1	SG	4	1
0.2	P	62	V			0.2	SG	1	1
0.19	P	5	V			0.1	SG	1	1
8660.89	P	56	V			0.2	SG	1	1
0.97	P	65	V			0.2	SG	2	2
0.88	P	5	V			0.2	SG	2	2
0.87	P	5	V			0.2	SG	2	2
0.83	P	10	V			0.2	SG	1	1
0.95	P	11	V			0.2	SG	1	1
0.91	P	4	V			0.2	SG	1	1
0.86	P	15	V			0.2	SG	1	2
0.81	P	5	V			0.2	SG	1	1
8656.55	P	55	V			0.7	SG	1	1
54.89	P	50	V			0.3	SG	2	1
0.59	P	85	V			0.3	SG	1	1
0.84	P	44	V			0.5	SG	1	2
0.84	P	22	V			0.2	SG	1	1
0.97	P	11	V			0.2	SG	1	4

Depth (ft; top)	Type	Height (mm)	Vertical /sub-vertical	Dip (near 90 °if blank)	Kinematic aperture (mm)		Single/ branch-ing	Termination	
					Min (0.1 if blank)	Max		Top	Base
0.82	P	9	V			0.5	SG	1	1
0.72	P	25	V		0.2	0.5	BR	1	1
0.38	P	98	V			0.5	BR	4	1
0.47	P	12	V			0.2	SG	1	1
0.51	P	7	V			0.2	SG	1	1
0.54	P	7	V			0.2	SG	1	1
0.48	P	280	V			0.1	SG	1	1
0.31	P	21	V			?-MISSING FACE	SG	2	2
8644.83	P	61	V		0.2	1	SG	3	3
0.82	P	1	V			0.1	SG	1	1
8636.72	P	100	V		0.1	1.2	BR	1	1
8619.08	P	7	V			0.2	SG	2	1
0.09	P	9	V			0.3	SG	2	1
0.12	P	19	V			0.5	SG	2	1
0.19	P	83	V			0.5	SG	1	1
8617	P	38	V		0.1	1	SG	1	1
16.87	P	38	V		0.1	1	SG	2	1
0.87	P	68	V		0.1	1	BR	1	1
8607	P	102	V			0.5	SG	4	1
8606.73	P	40	V			0.4	SG	4	1
0.51	P	70	V			0.4	SG	1	1
0.42	P	27	V			0.1	SG	1	1
8605.94	P	309	V		0.5	1.5	SG	2	4
0.89	P	9	V		0.2	0.8	SG	2	2
0.87	P	8	V			0.8	SG	2	2
0.84	P	4	V		0.2	0.8	SG	2	1
0.79	P	7	V		0.2	0.8	SG	2	1
0.73	P	17	V		0.1	0.8	SG	1	2
8596.85	P	6	V		0.2	0.5	SG	2	2
0.87	P	5	V			0.2	SG	1	1
0.86	P	38	SV			0.1	SG	1	4
8594.36	P	12	V		0.1	0.5	SG	2	1

Core #5 – Fracture measurement data

Depth (ft; top)	Type	Height (mm)	Vertical /sub-vertical	Dip (near 90 °if blank)	Kinematic aperture (mm)		Single/ branch-ing	Termination	
					Min (0.1 if blank)	Max		Top	Base
9379.68	P	30	V			0.1	SG	1	1
78.12	VE	53	V			0.2	SG	1	4
77.03	VE	50	V			0.1	SG	1	1
76.51	P	8	V	70		0.2	SG	4	2
0.56	P	2	V	70		0.2	SG	2	2
0.57	P	3	V	70		0.2	SG	2	2
0.58	P	4	V	70		0.2	SG	2	2
0.59	P+VE	20	V	70		0.2	SG	2	1
0.64	VE	180	V			0.1	SG	1	1
0.68	VE	150	V			0.1	SG	1	1
0.69	VE	65	V			0.1	SG	1	1
0.75	VE	148	V			0.1	BR	1	4
0.03	VE	73	V	70		0.1	SG	3	1
9374.3	VE	45	V			0.3	SG	1	1
0.48	P+S	105	V			1.5	BR	4	1
0.5	P	9	V			0.2	SG	1	1
0.7	P	25	V			0.2	SG	1	1
0.64	P	9	V			0.1	SG	1	1
0.71	P	7	V			0.1	SG	4	1
0.78	P	10	V			0.1	SG	1	1
0.8	P	9	V			0.1	SG	1	1
0.89	P	25	V			0.3	SG	1	1
0.98	P	12	V			0.3	BR	1	1
0.99	P	5	V			0.1	SG	1	1
73.33	P	2	V	80		0.3	SG	1	1
0.35	P	9	V	80		0.3	SG	1	1
0.38	P	15	V	80		0.3	SG	1	1
0.42	P	5	V	80		0.3	SG	1	1
0.44	P	8	V			0.1	SG	1	1
71.84	P	24	V	70		0.3	SG	1	1
0.83	P	5	V	60		0.2	SG	1	1
0.87	P	7	V	60		0.2	SG	1	1
0.91	P	10	V			0.2	SG	1	1
0.95	P	4	V	80		0.2	SG	1	1
9370.12	P	35	SV	45		0.1	SG	4	1
68.1	P	18	V			0.3	SG	1	1
0.11	P	13	V			0.1	SG	1	1
0.15	P	52	V			0.3	SG	1	1
0.15	P	12	V			0.1	SG	1	1
67.08	VE	40	V			0.1	SG	1	1
0.15	P	7	V	60		0.2	SG	1	1
0.18	P	7	V	60		0.2	SG	1	1

Depth (ft; top)	Type	Height (mm)	Vertical /sub-vertical	Dip (near 90 °if blank)	Kinematic aperture (mm)		Single/ branch-ing	Termination	
					Min (0.1 if blank)	Max		Top	Base
0.19	P	13	V	60		0.2	SG	1	1
0.2	P	5	V	60		0.2	SG	1	1
0.2	P	12	V	60		0.2	SG	1	1
0.13	VE	12	V			0.1	SG	1	1
0.17	VE	12	V			0.1	SG	1	1
0.06	VE	15	V			0.1	BR	1	1
0.1	VE	55	V			0.1	BR	1	1
0.21	VE	12	V			0.1	SG	1	1
0.12	P+VE	45	V			0.1	SG	1	1
67.08	VE	12	V			0.1	SG	1	1
0.1	VE	38	V			0.1	SG	1	1
0.11	VE	18	V			0.1	SG	1	1
0.09	VE	20	V			0.1	SG	1	4
66.76	VE+P	142	V			0.5	SG	3	1
0.72	P	5	V			1	SG	2	3
0.93	VE	22	V			0.1	SG	1	1
0.95	VE	12	V			0.3	SG	4	1
66.12	VE	10	V			0.1	SG	1	1
0.04	VE	20	V			0.1	SG	1	1
0.01	VE	16	V			0.1	SG	1	1
65.93	VE	38	V			0.1	SG	1	4
0.98	VE	24	V			0.1	SG	1	1
0.77	VE	89	V			0.1	BR	1	1
0.82	VE	60	V			0.1	SG	1	1
0.99	VE	17	V			0.1	SG	1	1
0.78	VE	20	V			0.1	SG	1	4
9361	VE	22	V			0.1	SG	1	1
0.08	VE	12	V			0.1	SG	1	1
0.11	VE	20	V			0.1	SG	1	1
0.1	VE+P	25	V			0.1	SG	1	1
0.18	VE+P	22	V			0.1	SG	1	1
0.19	VE	15	V			0.1	SG	1	1
0.33	VE	8	V			0.1	SG	1	1
0.36	P	7	V			0.1	SG	1	1
0.38	P	22	V			0.2	SG	1	1
0.33	VE	10	V			0.1	SG	1	1
0.37	P	45	V	60		0.2	SG	1	1
0.35	P	4	SV	30		0.1	SG	3	1
0.35	P+S	68	V			0.5	BR	3	1
0.35	P	42	V			0.2	BR	3	1
0.32	P	10	V			0.4	BR	3	1
0.39	P	5	SV	50			SG	1	1
0.5	P	7	SV	20			SG	1	1

Depth (ft; top)	Type	Height (mm)	Vertical /sub-vertical	Dip (near 90 °if blank)	Kinematic aperture (mm)		Single/ branch-ing	Termination	
					Min (0.1 if blank)	Max		Top	Base
0.5	P	2	SV	20			SG	1	1
0.49	P	2	SV	10			SG	1	1
0.5	VE	3	SV	40			SG	1	1
9361.55	P+VE	19	V			0.2	SG	1	1
0.38	VE	101	V			0.3	BR	1	1
0.62	P	4	SV	40		0.2	SG	1	1
0.63	P	3	SV	30		0.2	SG	1	1
0.07	P	2	SV	10		1.5	SG	1	1
0.7	P	2	SV	10		0.1	SG	1	1
0.71	P	1.5	SV	10		0.1	SG	1	1
0.72	P	1	SV	10		0.1	SG	1	1
0.71	P	5	V			0.1	SG	1	1
0.72	P	6	V			0.1	SG	1	1
9360.7	VE	10	V			0.3	SG	4	1
0.7	VE	102	V			0.1	SG	3	3
0.69	VE	19	V			0.2	SG	3	3
0.69	VE	17	V			0.3	SG	3	3
0.78	P	30	V			0.1	BR	3	3
0.76	VE	25	V			0.1	SG	1	1
0.73	VE	25	V			0.1	SG	1	1
0.73	VE	7	V			0.1	SG	1	1
0.71	VE	5	V			0.1	SG	1	1
0.81	P	10	V			0.1	SG	1	1
0.83	P	7	V			0.1	SG	1	4
0.8	P	5	SV	45		0.3	SG	1	1
0.78	P	13	V			0.1	SG	1	1
0.82	VE	7	V			0.2	SG	1	1
0.88	P	58	V			0.5	BR	3	1
0.89	VE	20	SV	45		0.1	SG	4	1
0.89	P	7	V			0.1	SG	1	4
0.95	VE	36	V			0.2	SG	1	1
9358.98	VE+P	29	V			1.5	SG	1	1
0.96	VE	3	V			0.1	SG	1	1
0.95	VE	4.5	V			0.1	BR	1	1
0.82	P	10	V			1	SG	1	1
0.32	P	66	V			0.2	SG	1	4
0.42	P	94	V			0.4	BR	1	1
0.32	P	53	V			0.2	SG	1	1
56.02	VE	9	V			0.1	SG	1	1
0.05	VE	17	V			0.1	SG	1	1
55.98	P	86	V			0.2	SG	1	1
9350.11	P	58	V			1	SG	1	1
48.91	P	210	V			1	SG	1	1

Depth (ft; top)	Type	Height (mm)	Vertical /sub-vertical	Dip (near 90 °if blank)	Kinematic aperture (mm)		Single/ branch-ing	Termination	
					Min (0.1 if blank)	Max		Top	Base
0.9	P	11	V			0.1	SG	1	1
47.03	VE	90	V			0.2	SG	1	1
45.8	VE	25	V			0.1	SG	1	1
0.77	VE	35	V			0.1	SG	1	1
46.07	VE	40	V			0.1	SG	1	1
0.03	VE	32	V			0.1	SG	1	1
0.19	VE	30	V			0.1	SG	1	1
0.2	VE	6	V			0.1	SG	1	1
0.3	VE	70	V			0.1	SG	1	1
0.58	VE	42	V			0.2	SG	1	1
0.74	VE	20	V			0.1	SG	1	4
45.78	P	33	V			0.1	SG	1	1
0.77	P	48	V			0.1	SG	1	1
9343.12	P	115	V			1	SG	1	1
0.04	P	33	V			0.2	SG	1	1
42.2	P	19	V			0.4	SG	1	1
41.6	P	72	V			1	SG	3	1
0.85	P	5	V			0.5	SG	1	1
0.87	P	21	V			0.5	SG	1	1
0.22	VE	83	V			0.1	SG	4	1
40.67	VE	145	V			0.1	SG	1	4
0.27	VE	124	V			0.1	SG	1	1
39.55	VE	116	V			0.1	SG	1	1
37.55	P	19	V			0.2	SG	1	1
9330.68	P	145	V		0.5	1	BR	4	1
9329.8	P	100	V			0.3	SG	1	1
0.37	P	50	V			0.6	SG	1	4
9334.25	P	4	V			0.2	SG	1	1
0.32	P	28	V			0.2	SG	1	1
31.02	VE	30	V			0.1	SG	1	2
30.35	P	53	V			0.2	BR	1	1
0.52	P	5	SV			0.3	SG	1	1
0.53	P	7	V			0.5	SG	1	4
9327.79	P	92	V			0.7	SG	1	1
0.56	P	78	V			0.3	SG	1	1
25.65	VE	60	V			1	SG	1	4
0.58	P	7	V			0.4	SG	1	1
0.17	VE	69	V			0.6	SG	1	3
0.12	VE+P	72	V			0.6	BR	1	1
0.11	P	63	V			1	SG	1	1
0.09	P	10	V			0.2	SG	1	1
.24.98	VE+P	122	V			1	SG	1	4
0.96	P	15	V			0.5	SG	1	4

Depth (ft; top)	Type	Height (mm)	Vertical /sub-vertical	Dip (near 90 °if blank)	Kinematic aperture (mm)		Single/ branch-ing	Termination	
					Min (0.1 if blank)	Max		Top	Base
0.95	P	15	V			0.5	SG	1	4
0.91	P	10	V			0.2	SG	1	1
0.85	P	25	V			0.3	SG	1	4
0.54	VE	70	V			0.1	SG	1	1
0.53	VE	50	V			0.1	SG	1	4
9323.55	VE	375	V		0.5	3	BR	4	1
0.41	P	17	V			1	SG	2	2
0.53	P	11	V				SG	2	2
0.15	P	50	V			0.8	SG	4	1
0.89	P	52	V			0.5	SG	4	1
0.57	P	49	V			0.3	SG	1	1
0.43	P	70	V			0.5	SG	4	1
0.83	VE	25	V			0.5	BR	3	1
0.73	P	9	V			0.5	SG	1	3
24.28	VE	20	V			0.3	SG	1	3
23.98	VE	98	V			0.2	SG	1	1
21.4	P	20	V			0.3	SG	1	4
0.46	P	5	SV				SG	4	4
20.38	P	72	V			0.5	SG	1	4
9317.56	VE	90	V			0.5	SG	1	1
0.5	VE	145	V			0.5	SG	1	1
0.4	P	85	V			0.5	BR	1	4
0.42	VE	100	V			1	SG	1	1
0.36	P	89	V			1	SG	1	1
0.43	P	11	V			0.5	SG	1	1
0.41	P	9	V			0.5	SG	1	1
0.17	P	36	V		0.5	1	SG	4	1
0.1	P	15	SV			0.6	SG	4	1
77	VE	52	V			0.5	SG	1	1
9316.7	P	25	V			0.3	SG	1	4
0.25	P	25	V			0.4	SG	1	1
0.18	P	15	V			0.1	SG	1	1
9315.65	VE	25	V			0.5	SG	1	1
0.35	P	39	SV			0.5	SG	1	1
0.37	VE	70	V			0.5	SG	1	1
0.03	P	67	V			0.5	SG	4	4
9310.42	P	15	V			0.1	SG	1	1
9314.74	P+S	355	V			2	SG	3	1
0.57	VE+S	42	V			0.6	SG	1	1
9308.35	P	55	V			1	SG	1	1
7.15	P	17	V			0.3	SG	1	1
0.05	P	40	V			0.8	SG	1	1
5.4	P	20	V			0.5	SG	1	1

Depth (ft; top)	Type	Height (mm)	Vertical /sub-vertical	Dip (near 90 °if blank)	Kinematic aperture (mm)		Single/ branch-ing	Termination	
					Min (0.1 if blank)	Max		Top	Base
0.47	P	55	V			1	BR	4	1
0.6	P	6	V			0.1	SG	4	1
0.25	P	26	V			1.5	SG	3	4
0.31	P	6	SV			0.5	SG	1	4
4.86	P	125	V			1	SG	1	1
0.73	P	17	V			0.5	SG	1	1
0.71	P	18	V			0.5	SG	1	1
5.19	P	10	V			0.3	SG	1	3
0.5	P	5	V			0.5	SG	1	1
0.5	P	27	V		0.5	1	SG	1	1
9304.87	P	120	V			1	SG	1	1
9303.7	VE	109	V			0.5	SG	1	1
0.77	VE	30	V			0.1	SG	1	1
0.85	VE	192	V			0.1	SG	1	1
0.6	P	80	V			0.5	SG	1	1
0.39	P	20	V			0.2	SG	1	1
0.4	P	21	V			0.2	SG	1	1
0.11	VE+P	170	V			0.5	SG	1	1
0	VE	18	V			0.1	SG	4	1
9302.68	VE	186	V		0.2	1	BR	2	4
0.69	VE	40	V			0.8	BR	2	4
0.86	VE	30	V			0.2	SG	1	1
0.72	VE	22	V			0.2	SG	1	1
0.75	VE	25	SV	50		0.3	BR	1	1
0.79	P	16	V			0.2	BR	1	1
0.88	P	22	V			0.5	SG	1	4
0.57	P	25	V		0.2	2	SG	1	2
0.54	P	6	SV	40		0.4	SG	1	4
0.41	VE	17	V			0.2	SG	1	1
0.42	VE+P	40	V		0.2	0.7	BR	1	1
0.38	VE	30	V			0.2	SG	1	4
0.4	VE	55	V			0.5	SG	1	1
9302.15	P+VE	110	V		0.2	1.5	SG	2	1
0.04	P	30	V			1	SG	1	1
1.84	VE	25	V			0.1	SG	1	1
0.7	VE	45	V			0.5	SG	1	1
0.71	VE	50	V			0.5	SG	1	1
0.74	VE	30	V			0.1	SG	1	1
0.73	VE	8	V			0.1	BR	1	1
0.73	VE	47	V			0.3	BR	1	1
0.09	VE	32	V			0.2	SG	1	4
0.02	VE	20	V			0.2	SG	1	1
9301.08	VE	48	V			0.3	SG	1	1

Depth (ft; top)	Type	Height (mm)	Vertical /sub-vertical	Dip (near 90 °if blank)	Kinematic aperture (mm)		Single/ branch-ing	Termination	
					Min (0.1 if blank)	Max		Top	Base
0.3	VE	24	SV			0.5	SG	4	1
0.31	P	25	V			0.3	SG	3	1
9300.86	VE+P	50	V			0.5	SG	3	1
0.93	P	88	V		0.5	1.5	SG	1	1
0.88	VE+P	112	V		0.5	1	BR	1	1
0.97	P	12	V			0.5	SG	1	1
0.58	P	40	V		0.5	3	BR	1	1
0.57	P	20	V		0.5	2	BR	1	1
0.56	P	10	V			1.5	SG	4	1
0.52	VE	8	V			0.3	SG	1	1
0.54	VE	6	V			0.5	SG	1	1
0.51	VE	12	V			0.5	BR	1	4
9300.4	VE	44	V			0.3	SG	1	4
0.38	P	15	V			0.3	SG	1	1
0.4	P	30	V			0.5	SG	1	1
0.25	VE	15	V			0.1	SG	4	1
9299.95	P	19	V			0.5	SG	1	4
0.93	P	14	V			0.5	SG	2	4
0.91	P	10	V			0.5	SG	4	1
0.66	VE	43	V			0.3	SG	1	1
0.6	VE	72	V			0.5	SG	1	1
9299.7	VE+P	81	V			0.6	BR	1	4
0.77	VE	20	V			0.2	SG	1	1
0.77	VE	11	V			0.2	SG	1	1
0.72	VE	12	V			0.2	SG	1	1
0.25	P	23	V			1.5	SG	4	1
0.36	S	20	V			0.5	SG	1	1
0.04	P	25	V			1.5	SG	1	1
9298.87	VE	27	V			0.5	SG	1	4
0.79	P	25	V		0.3	1	SG	1	3
0.75	P	12	V		0.3	1	SG	2	2
9298.62	P+VE	38	V		0.3	1	BR	4	2
0.7	P	7	V			0.5	SG	1	1
97.35	P	9	V			0.2	SG	1	1
0.23	P	9	SV			0.2	SG	1	1
98.57	VE	8	SV			0.2	SG	1	1
0.58	VE	20	SV			0.4	SG	1	1
0.52	VE	39	V			0.5	SG	1	1
0	VE	39	V			0.1	SG	4	1
9297.19	VE	105	V			0.5	SG	1	1
0.03	P	9	V			0.4	SG	1	1
0.07	P	65	V			0.5	BR	1	1
0.15	P	31	V			0.5	BR	1	1

Depth (ft; top)	Type	Height (mm)	Vertical /sub-vertical	Dip (near 90 °if blank)	Kinematic aperture (mm)		Single/ branch-ing	Termination	
					Min (0.1 if blank)	Max		Top	Base
0.25	VE	39	V			0.3	SG	4	1
0.21	P	27	V			0.2	SG	1	1
0.29	VE	70	V			0.2	SG	1	1
0.3	P	7	SV			0.2	SG	1	1
0.28	VE	50	V			0.3	SG	1	1
0.44	VE	30	V			0.2	BR	4	1
0.42	VE+P	60	SV			0.5	BR	1	1
0.8	VE	21	V			0.3	SG	1	1
0.42	VE	14	V			0.2	SG	4	1
0.41	VE	33	V			0.2	SG	1	1
96.6	P	40	V			0.6	SG	3	3
0.6	P	7	V			0.3	SG	3	4
0.28	P	22	V		0.5	1	SG	1	1
0.03	P	20	SV			0.5	SG	4	1
95.85	VE	70	V		0.5	1	SG	1	1
0.31	VE	59	V		0.5	1.5	BR	1	1
0.4	VE	20	V			0.1	SG	1	1
0.48	VE	94	V			0.6	SG	4	1
0	VE	39	V			0.6	SG	4	1
9294.1	P	16	SV			0.2	SG	4	1
0.29	P	6	V			0.3	SG	4	1
0.32	P	12	V			0.5	SG	3	3
0.33	P	154	V			1	SG	1	1
0.45	P	12	V			0.2	SG	1	4
0.62	P	8	SV			0.1	SG	1	1
0.83	P	31	V			0.2	SG	1	4
0.89	P	30	V			0.1	SG	1	4
93.05	P	21	V			0.3	BR	1	1
0.3	P	6	SV			0.5	SG	1	1
0.06	P	17	V			0.5	SG	1	1
0.11	P	5	V			0.5	SG	2	4
0.13	P	13	V			0.5	SG	3	3
0.17	P	8	V			0.5	SG	3	3
0.19	P	7	V			0.5	SG	3	3
0.24	VE	11	SV			0.3	SG	4	1
0.72	P	12	V			0.5	SG	3	3
0.77	P	14	V			0.5	SG	3	3
0.77	P	16	V			0.5	SG	3	3
0.79	P	22	V			0.8	SG	3	3
0.95	VE+P	30	V			0.3	SG	4	1
9297.86	P	19	V		0.2	1	BR	1	1
0.8	P	7	V			0.2	SG	1	4
0.49	VE	13	V			0.5	SG	1	4

Depth (ft; top)	Type	Height (mm)	Vertical /sub-vertical	Dip (near 90 °if blank)	Kinematic aperture (mm)		Single/ branch-ing	Termination	
					Min (0.1 if blank)	Max		Top	Base
0.54	P	11	V			0.2	SG	1	1
0.31	VE	20	V			0.3	SG	1	1
90.21	P	76	V			0.5	SG	1	1
0.13	P	25	V			1	SG	3	3
0.32	P	50	V			0.5	SG	1	1
0.57	VE	4	SV			0.5	SG	1	1
0.6	VE	10	SV			0.2	SG	1	1
0.8	VE	35	V			0.1	SG	1	1
89.85	P	28	V		0.2	1	SG	1	1
0.48	P	32	V			1	SG	3	3
0.51	P	24	V			0.7	SG	4	3
0.52	P	15	V			0.2	SG	3	3
0.4	P	17	SV			0.3	SG	1	1
9288.67	VE	30	V			0.3	SG	1	1
0.93	VE	13	V			0.2	SG	1	4
87.33	VE	80	V			0.5	SG	1	1
0.3	P	9	SV			0.1	SG	1	1
0.38	P	9	V			0.1	SG	1	1
0.2	P	24	V			0.3	SG	1	1
0.1	P	26	V			0.3	SG	1	1
0.03	P	18	V			0.3	SG	1	1
86.98	P	15	V			1	SG	2	1
0.4	VE	50	V			0.1	SG	1	1
0.09	VE	145	SV			0.6	SG	1	1
0.02	VE	13	SV			0.1	SG	1	1
9284.45	VE	183	SV		0.5	1	SG	4	1
83.79	P	5	V			0.3	SG	1	4
0.65	P	10	SV			0.3	SG	1	1
0.58	VE	37	V			0.3	SG	1	1
0.52	VE+P	20	V			0.4	SG	4	1
0.72	P	10	V			0.5	SG	1	1
0.52	VE	20	V			0.2	SG	4	1
0.44	VE	20	V			0.3	SG	1	1
9283.12	VE	10	SV			0.3	SG	1	1
0.08	P	29	V			0.3	SG	1	1
0.02	VE	35	V			0.2	SG	1	1
0	P	25	V			0.1	SG	4	1
0.16	P	3	V			0.2	SG	1	1
0.17	P	6	V			0.2	SG	1	1
0.19	P	10	V			0.2	SG	1	4
9282.68	P	26	V			1	SG	1	1
0.83	VE	44	V			0.2	SG	1	1
0.68	P	9	V			0.5	SG	1	1

Depth (ft; top)	Type	Height (mm)	Vertical /sub-vertical	Dip (near 90 °if blank)	Kinematic aperture (mm)		Single/ branch-ing	Termination	
					Min (0.1 if blank)	Max		Top	Base
0.13	P	25	V			0.2	SG	3	1
80.2	P	90	V		0.5	1	SG	4	1
0.11	P	30	V			0.2	SG	1	1
0	VE	28	SV			0.3	SG	4	1
79.8	VE	2	V			0.1	SG	1	4
79.7	VE	29	V			0.4	SG	1	4
0.69	P	13	V			0.2	SG	1	1
0.64	P	22	V			0.3	BR	3	1
0.58	P	13	V			0.1	SG	1	1
0.59	P	82	V			0.2	SG	2	4
0.58	VE+P	25	V			0.3	SG	1	1
0.3	P	52	V			1	SG	1	1
0.24	P	3	V			0.2	SG	1	1
9278.43	P	30	V			1	SG	1	4
0.47	P	36	V			0.7	SG	1	1
0.26	P	8	V			0.5	SG	1	1
77.09	VE	30	V			0.2	SG	1	4
76.9	VE	320	V			0.2	SG	1	1
0.86	VE	9	V			0.6	SG	1	4
0.82	P	12	V			0.5	SG	1	2
9275.54	VE+P	390	V			0.7	SG	4	1
0.45	P	30	V			0.2	SG	1	1
0.56	P	35	V			0.2	SG	1	4
74.95	P	160	V			0.3	BR	1	4
9268.23	P	255	V			2	SG	1	4
0.22	P	98	V			0.5	SG	4	1
67.79	VE	8	V			0.2	SG	3	1
0.79	P	7	V			0.2	SG	3	1
0.76	VE	20	V			0.3	SG	1	4
0.89	VE	30	V			0.2	SG	1	4
0.86	P+VE	30	V			0.6	BR	1	1
0.86	VE	13	V			0.2	SG	1	1
0.76	P	32	V		0.2	1	BR	3	3
0.87	P	6	V			0.3	SG	1	1
0.69	VE	3	V			0.3	BR	3	1
0.85	P	4	V			0.2	SG	4	1
0.83	P	3	V			0.2	SG	3	1
0.54	VE	10	V			0.2	SG	1	1
0.82	P	10	V			0.2	SG	3	1
0.55	VE+P	20	V			0.3	SG	3	1
0.81	P	8	V			0.3	SG	3	1
0.51	VE	9	V			0.1	SG	1	1
0.8	P	8	V			0.2	SG	1	1

Depth (ft; top)	Type	Height (mm)	Vertical /sub-vertical	Dip (near 90 °if blank)	Kinematic aperture (mm)		Single/ branch-ing	Termination	
					Min (0.1 if blank)	Max		Top	Base
9267.5	VE	19	V			0.5	SG	3	1
0.75	P	4	V			0.3	SG	3	3
0.79	VE	2	V			0.2	SG	3	3
0.79	VE	3	V			0.2	SG	3	3
0.75	VE	4	V			0.2	SG	3	3
0.71	VE	3	SV			0.2	SG	3	4
0.72	P	4	V			0.2	SG	1	3
66.95	P+VE	13	V			0.5	BR	2	4
0.89	VE	1.5	V			0.2	SG	3	2
0.89	P	15	V			0.3	SG	1	1
0.9	VE	3	V			0.1	SG	1	1
0.89	P	21	V			0.3	SG	1	1
0.9	P	3	V			0.1	SG	3	2
0.6	P	30	V			0.5	SG	1	1
0.67	P	20	V			0.2	SG	1	1
0.65	P	10	V			0.2	SG	1	1
0.53	P+VE	32	V		0.5	1	BR	3	1
67.59	P+S	12	V			0.2	SG	1	1
0.57	VE	3	V			0.2	SG	1	1
0.57	VE	18	V			0.2	SG	1	1
0.57	VE	3	V			0.2	SG	1	1
0.5	VE	4	V			0.1	SG	1	1
9267.48	VE	5	V			0.2	SG	1	4
0.44	VE	10	V			0.2	SG	1	1
0.4	P	10	V			0.3	SG	1	1
0.35	P	6	V			0.2	SG	1	1
0.36	P	3	V			0.2	SG	1	1
0.34	VE+P	12	V			0.2	SG	1	1
0.35	VE+P	10	V			0.2	SG	1	1
0.34	VE+P	26	V			0.2	SG	4	5
0.27	VE	23	V			0.2	BR	4	4
9254.02	P	35	V		0.5	1	SG	1	1
53.25	P	7	V			0.5	SG	1	3
0.22	P	9	V			0.3	SG	1	1
0.09	P	35	SV		0.5	2	SG	1	1
0.06	VE+P	37	V			0.2	SG	3	3
50.57	P	18	V			0.5	SG	3	3
0.09	P	30	V			0.3	SG	3	1
48.52	VE	64	V			0.2	SG	1	1
0.41	VE	50	V			0.2	SG	1	1
0.39	VE	50	V			0.2	SG	1	1
0.57	VE	25	V			0.2	SG	1	1
47.38	VE	30	V			1	SG	1	1

Depth (ft; top)	Type	Height (mm)	Vertical /sub-vertical	Dip (near 90 °if blank)	Kinematic aperture (mm)		Single/ branch-ing	Termination	
					Min (0.1 if blank)	Max		Top	Base
46.32	P	60	V			0.2	SG	4	4
0.39	P	46	V			0.2	SG	1	1
0.52	P	23	V			0.3	SG	1	1
0.58	P	48	V			0.5	SG	1	1
0.71	P	63	V			0.5	SG	1	4
9244.84	P	21	V			0.5	SG	1	1
43.87	P	30	V			0.3	SG	1	4
42.56	P	160	V			0.3	BR	1	1
40.56	P	72	V			0.2	SG	3	3
39.29	P	15	V			0.3	SG	4	1
0.56	P	11	V			0.3	SG	1	1
0.58	P	5	V			0.3	SG	1	1
0.58	P	22	V			0.6	SG	1	4
0.64	P	16	V			0.5	SG	1	4
0.7	P	20	V			0.3	SG	1	4
0.77	P	7	V			0.5	SG	1	4
9238.6	P	10	V			0.1	SG	3	3
0.61	P	23	V			0.6	SG	1	1
0.6	P	25	V			0.3	SG	1	1
0.65	P	10	V			0.2	SG	1	1
0.7	P	95	V			1	BR	1	4
0.7	P	39	V			0.2	SG	3	1
0.69	P	30	V			0.2	SG	1	1
0.7	P	24	V			0.2	SG	3	1
0.7	P	15	V			0.2	SG	3	4
0.79	P	22	V			0.2	SG	1	4
0.92	P	13	V			0.3	SG	4	1
0.93	VE	17	V			0.2	SG	4	1
0.93	VE	16	V			0.2	SG	4	3
0.93	VE	18	V			0.2	SG	4	3
0.6	P	13	V			0.1	SG	3	1
9230.07	VE	6	V			0.2	SG	3	3
0.04	VE	9	V			0.1	SG	3	3
0.98	VE	22	V			0.3	SG	4	1
0.49	VE+P	30	V			0.5	SG	3	3
0.47	VE+P	90	V			1	BR	1	4
0.45	VE+P	55	V		0.2	0.5	SG	1	4
0.38	P	28	V			0.5	BR	3	3
0.35	P	25	V			0.6	SG	3	3
0.32	P	12	V		0.2	0.5	SG	1	1
9229.89	VE	7	V			0.5	SG	3	3
0.9	VE	8	V			0.4	SG	3	3
0.74	VE	46	V			0.6	SG	3	3

Depth (ft; top)	Type	Height (mm)	Vertical /sub-vertical	Dip (near 90 °if blank)	Kinematic aperture (mm)		Single/ branch-ing	Termination	
					Min (0.1 if blank)	Max		Top	Base
0.61	VE	110	V			2	BR	4	1
0.14	P	92	V			3	BR	3	4
0.13	VE	32	V		1	0.1	SG	3	1
0.14	VE	38	V			0.1	SG	3	1
0.15	P	2	SV			0.2	SG	1	1
0.32	P	2	SV			0.2	SG	1	1
9236.13	VE+P	17	V			0.5	SG	1	1
0.32	VE	29	V			0.2	SG	4	1
0.33	VE	42	V			0.5	SG	4	1
0.37	VE	24	V			0.3	SG	4	1
0.37	VE	18	V			0.3	SG	4	1
31.04	VE	27	V			1	BR	2	4
0.07	VE	7	SV			0.2	SG	3	1
0.23	VE	25	V			1	SG	4	1
0.5	P	10	V			0.3	SG	3	3
0.53	P	9	V			0.3	SG	3	3
0.54	VE+P	42	V			0.3	SG	3	3
0.56	VE	9	V			0.1	SG	3	3
0.57	P	9	V			0.1	SG	3	3
0.63	VE	3	V			0.2	SG	3	1
0.64	VE	19	V			0.2	SG	1	3
0.66	P	20	SV			0.2	SG	1	3
0.72	VE	7	V			0.1	SG	3	1
0.73	VE	13	V			0.2	SG	1	1
0.73	VE	35	V			0.1	SG	1	4
0.8	P	7	SV			0.1	SG	1	1
0.82	P	25	V			0.1	SG	1	1
9228.31	P	37	V			0.3	SG	1	3
0.33	P	25	V			0.2	SG	1	3
0.32	P	2	V			0.2	SG	1	3
0.23	P	6	V			0.3	SG	3	3
0.22	P	13	V			1	SG	1	1
0.95	P	37	V			0.5	SG	3	3
0.5	P	11	V			0.1	SG	1	1
0.49	P	5	V			0.1	SG	1	1
27.32	VE	5	V			0.1	SG	3	3
26.52	VE+P	110	V			0.1	SG	1	4
24.3	P	17	V			0.1	SG	1	1
0.49	P	15	V			0.2	SG	1	1
0.61	P	12	V			0.2	SG	1	1
23.76	VE+P	100	V			0.2	BR	1	1
0.53	P	47	V			1	SG	1	1
9222.12	VE	10	V			0.2	SG	1	4

Depth (ft; top)	Type	Height (mm)	Vertical /sub-vertical	Dip (near 90 °if blank)	Kinematic aperture (mm)		Single/ branch-ing	Termination	
					Min (0.1 if blank)	Max		Top	Base
0.14	P	10	SV			0.2	SG	1	1
0.31	P	6	SV			0.2	SG	1	1
21.85	P	59	V			?	SG	1	1
0.92	VE	15	V			0.1	SG	4	4
0.96	VE	50	V			0.1	SG	1	1
0.53	VE	5	V			1	SG	1	4
0.33	VE	20	V			3	SG	1	1
0.32	VE	25	V			1	SG	3	1
0.32	P	3	SV			0.2	SG	3	1
0.15	P	13	SV			0.2	SG	1	1
0.15	P	15	SV			0.4	SG	1	1
0.15	VE	10	V			0.1	SG	1	1
0.13	P	23	SV			0.5	BR	1	4
0.13	VE	10	V			0.1	SG	1	1
0.11	P	18	V			0.3	SG	1	4
0.2	P	16	V			0.1	SG	1	1
0.12	VE	17	V			0.1	SG	4	1
9220.42	VE+P	46	V			0.5	SG	4	1
0.57	VE	40	V			0.2	SG	1	1
0.8	VE	7	V			0.2	SG	1	1
0.29	VE+P	26	V			0.2	SG	1	4
9219.82	VE	7	SV			0.1	SG	4	1
0.54	P	4	SV			0.2	SG	4	4
0.49	P	7	SV			0.1	SG	1	4
0.3	P	16	V			0.1	SG	1	1
17.98	P	17	V			0.2	SG	3	1
0.98	P	15	V			0.3	SG	4	1
0.8	P	8	V			0.3	SG	1	3
0.85	P	9	SV			0.2	SG	3	1
0.73	P	13				0.5	SG	1	4
0.75	P	9				0.3	SG	1	4
0.71	VE	4	V			0.1	SG	4	1
0.57	VE	7	SV			0.2	SG	1	1
0.6	VE	8	SV			0.2	SG	4	1
0.05	P	36	V			0.3	SG	1	1
0.1	VE+P	76	V			0.2	SG	1	4
0	VE+P	40	V			0.2	SG	4	1
9216.48	P	8	V			1	SG	4	1
0.51	P	46	V			2	SG	1	4
0.65	P	27	V			0.6	SG	1	1
0.93	P	18	V			0.3	SG	4	4
15.18	VE	15	V			1	SG	4	2
0.4	P	19	V		0.2	1	SG	4	2

Depth (ft; top)	Type	Height (mm)	Vertical /sub-vertical	Dip (near 90 °if blank)	Kinematic aperture (mm)		Single/ branch-ing	Termination	
					Min (0.1 if blank)	Max		Top	Base
14.3	VE+P	55	SV		0.5	2	SG	1	1
0.29	P	11	SV			0.2	SG	4	1
11.7	VE	13	V			0.1	SG	1	1
0.77	VE	7	V			0.2	SG	3	1
0.78	P	15	V			0.2	SG	3	1
0.77	P+VE	55	V			0.2	BR	3	1
0.62	P	10	V			0.2	SG	1	1
0.61	VE	11	V			0.1	SG	1	1
0.2	VE	67	V			0.5	BR	4	3
0.67	VE	7	V			0.1	SG	1	1
0.13	P	18	V			0.5	SG	1	4
0.43	VE	53	V			0.5	BR	1	1
16.42	P	7	V			0.5	SG	3	3
0.41	P	1	SV			0.2	BR	1	1
15.56	VE+P	31	V			0.6	SG	4	1
0.47	P	50	V			0.2	BR	4	1
0.5	VE	46	V			1	SG	4	1
0.58	VE	14	V			0.1	SG	1	1
0.96	VE	8	V			0.1	SG	1	4
0.96	VE	5	V			0.1	SG	1	4
0.92	P	7	V			0.1	SG	1	4
9214.16	P	7	SV			0.1	SG	4	1
0.11	VE	68	V			0.1	SG	1	1
0.13	VE	15	V			0.1	SG	1	1
0.11	VE+P	55	V			0.1	SG	1	1
0.47	VE	26	V			1	SG	1	4
0.81	P	33	V			0.1	SG	1	4
0.81	P	8	V			0.2	SG	1	1
13.69	P	50	V			0.1	BR	4	1
0.8	VE	11	V			0.1	SG	1	1
11.2	P	22	V			0.5	BR	1	1
0.16	P	19	V			0.3	SG	1	1
9210.85	VE	130	V			0.1	SG	4	4
2	P	90	V			1.5	SG	4	1
0.02	P	22	V			0.3	SG	4	1
0.39	VE	45	V			0.2	SG	1	1
10.49	VE	32	V			0.2	SG	1	1
0.56	VE	6	SV			0.1	SG	4	1
0.51	VE	16	V			0.1	SG	1	1
0.57	VE	8	V			0.1	SG	1	1
0.43	VE	48	V			0.1	SG	1	1
0.56	VE	44	V			0.1	SG	1	4
0.67	P	13	SV			1	SG	1	4

Depth (ft; top)	Type	Height (mm)	Vertical /sub-vertical	Dip (near 90 °if blank)	Kinematic aperture (mm)		Single/ branch-ing	Termination	
					Min (0.1 if blank)	Max		Top	Base
0.69	P	3	SV			0.5	SG	1	1
0.51	P	3	SV			0.1	SG	1	1
0.51	P	3	SV			0.2	SG	1	1
0.51	P	4	SV			0.2	BR	1	1
0.5	P	5	SV			0.6	BR	1	1
0.52	P	8	SV			2.5	BR	1	1
9210.16	VE	59	V			0.1	SG	1	4
0.12	VE	9	V			0.2	SG	1	4
0.1	VE	13	V			1.5	SG	1	4
0.05	P	12	V			0.1	SG	1	1
0.01	P	12	V			0.2	SG	1	1
0.07	VE	8	V			0.1	SG	1	1
9.9	VE	57	V			0.2	SG	1	4
0.81	P	65	V			0.2	SG	1	1
0.81	VE	7	V			0.1	SG	1	4
0.89	P	3	SV			1	SG	1	1
0.9	P	2	SV			1	SG	1	1
0.85	VE	11	V			0.2	SG	1	1
0.1	P	16	V			0.1	SG	1	1
0.15	P	11	V			0.1	SG	1	4
8.33	P	19	V			0.1	SG	4	3
0.42	VE	25	V			0.1	SG	3	1
0.69	P	5	V			0.2	SG	1	1
0.7	P	12	SV			0.2	SG	4	1
0.99	P	9	V			0.1	SG	1	1
9208.58	VE	100	V			0.1	SG	1	3
0.8	VE+P	39	V			0.2	SG	4	3
0.88	P	15	V			0.2	SG	4	3
0.86	VE	14	V			0.2	SG	1	3
0.9	P	30	V			0.2	BR	4	3
9196.28	P	12	SV			0.2	SG	1	1
0.48	P	10	SV			0.1	SG	1	1
0.68	P	5	V			0.1	SG	1	1
0.8	P	12	V			0.1	SG	1	1
98	P	9	V			0.1	SG	1	1
0.03	P	14	V			0.1	SG	1	1
0.13	P	7	V			0.1	SG	1	1
0.23	P	5	V			0.1	SG	1	1
0.35	P	11	V			0.1	SG	1	1
0.52	P	4	V			0.1	SG	1	1
0.7	P	7	SV			0.1	SG	1	1
9195.2	P	5	SV			0.1	SG	1	1
0.22	P	5	SV			0.1	SG	1	1

Depth (ft; top)	Type	Height (mm)	Vertical /sub-vertical	Dip (near 90 °if blank)	Kinematic aperture (mm)		Single/ branch-ing	Termination	
					Min (0.1 if blank)	Max		Top	Base
0.25	P	5	SV			0.1	SG	1	1
0.43	P	15	V			0.1	SG	1	1
91.52	P	5	V			0.1	SG	1	1
0.58	P	12	V			0.1	SG	1	1
0.68	P	7	SV			0.1	SG	1	1
0.7	P	4	SV			0.1	SG	1	1
87.08	P	7	SV			0.1	SG	1	4
0.08	P	2	SV			0.1	SG	1	1
9185.26	P	55	V			0.1	SG	1	1
0.35	P	22	V			0.1	SG	1	1
83.95	P	13	V			0.1	SG	1	1
79.6	P	7	V			0.1	SG	1	1
9167.02	VE	19	V			0.2	SG	1	4
0.1	VE	13	V			0.2	SG	1	1
0.23	VE	8	V			0.2	SG	1	4
0.3	VE	30	V			0.2	SG	1	4
66.59	P	57	V			0.1	SG	1	4
0.6	P	80	V			0.1	SG	1	4
0.79	VE	7	V			0.1	SG	1	4
0.83	VE	10	V			0.1	SG	1	1
0.93	VE	11	V			0.1	SG	1	4
9158.97	VE	21	V			0.1	SG	1	1
0.87	P	150	V			0.1	SG	1	4
0.96	VE	30	V			2	SG	2	2
59.17	P	56	V			0.1	SG	1	1
0.35	P	32	V			0.1	SG	1	1
0.3	P	20	V			0.2	SG	4	1
58.6	P	32	V			0.1	SG	1	1
0.81	P	35	V			0.1	SG	1	1
0.82	P	20	V			0.1	SG	1	1
0.95	P	7	V			0.1	SG	1	1
56.52	VE	9	V			1	SG	1	4
9150.37	VE	16	V			0.2	SG	4	1
9128.03	VE	167	V			? - NO LEFT WALL	SG	4	1
9119.79	P	40	V			0.5	SG	1	1
0.1	P	230	V		0.5	1	BR	1	1
0.09	P	15	V			0.2	SG	1	1
9119	P	19	V			0.3	SG	1	1
9118.85	P	40	V			0.3	SG	1	1
0.41	P	58	V			0.4	SG	1	1
0.35	P	25	V			0.5	SG	1	1

Depth (ft; top)	Type	Height (mm)	Vertical /sub-vertical	Dip (near 90 °if blank)	Kinematic aperture (mm)		Single/ branch-ing	Termination	
					Min (0.1 if blank)	Max		Top	Base
0.22	P	75	V			0.5	SG	1	1
0.01	P	185	V			0.5	SG	1	1
22.32	P	10	SV			0.1	SG	1	1
0.49	P	16	SV			0.1	SG	1	1
20.09	P	11	SV			0.1	SG	1	1
9107.55	P	58	V			0.1	SG	1	1
0.76	P	9	V			0.1	SG	1	1
6.05	P	24	V			0.2	SG	1	1
0.09	P	20	SV			0.1	SG	1	1
9114.44	VE+P	42	V			0.1	SG	1	1
0.56	P	14	V			0.1	SG	1	1
0.48	P	12	V			0.1	SG	4	2
0.5	P	7	V			0.1	SG	1	1
9105.02	P	42	V			0.1	SG	1	4
4.9	P	20	V			0.1	SG	4	1
0.42	P	35	V			0.2	SG	1	1
0.35	P	38	V			0.3	SG	1	4
9101.47	P	6	V			0.1	SG	1	1
0.85	P	10	V			0.1	SG	1	1
0.38	P	10	V			0.1	SG	1	1
0.5	P	7	SV			0.1	SG	1	1
0.67	P	6	SV			0.1	SG	1	1
9099.5	VE	19	V			0.2	SG	1	1
9079.12	P	32	V			1	SG	1	4
0.58	P	32	V			0.3	SG	4	1
0.67	P	22	V			0.2	SG	1	1
80.51	P	50	V			0.2	SG	1	4
0.54	P	14	V			0.2	SG	4	1
84.78	VE	142	V			0.2	SG	3	3
0.9	VE	105	V			0.2	SG	4	3
9079.58	P	2	V			0.1	SG	4	1
0.59	P	2	V			0.1	SG	1	1
0.59	P	35	V			0.1	SG	1	4
9078.7	VE	50	V			? - CORE BROKEN	SG	?	?
74.4	P	20	V			? - CORE MISSING	SG	1	4
9058.37	P	11	V			1	BR	1	1
0.45	P+VE	22	V			0.2	SG	1	4

Depth (ft; top)	Type	Height (mm)	Vertical /sub-vertical	Dip (near 90 °if blank)	Kinematic aperture (mm)		Single/ branch-ing	Termination	
					Min (0.1 if blank)	Max		Top	Base
0.4	P	14	V			0.6	SG	3	3
0.44	P	15	V			0.5	SG	3	4
57.43	P	77	V			? - CORE BROKEN	SG	4	4
0.7	P	62	V			? - CORE BROKEN	SG	4	4
0.28	P	8	V			0.2	SG	4	1
0.3	P	14	V			0.2	SG	1	4
0.6	P	4	V			0.3	SG	1	1
0.2	VE	53	V			0.2	SG	3	3
9050.51	P	27	SV			0.5	SG	4	1
0.48	P	13	V			0.2	SG	1	1
0.38	P	20	V			0.1	SG	1	1
49.52	P	228	V			? - CORE BROKEN	SG	4	1
43.56	P	3	V			0.3	SG	1	1
0.58	P	90	V		0.5	1	SG	1	4
9039.56	P	297	V			? - CORE BROKEN	SG	1	1
0.8	P	32	V			0.5	SG	1	4
38.75	P	187	V			? - CORE BROKEN	SG	1	1
36	P	11	SV			0.3	SG	1	3
35.89	P	46	V			0.2	SG	4	3
0.89	P	46	V			0.5	SG	4	1
0.2	P	128	V			0.2	SG	1	4
0.04	P	175	V			0.3	SG	1	4
0.18	VE	7	V			0.1	SG	1	4
34.27	P	460	V			? - CORE BROKEN	SG	1	4

Depth (ft; top)	Type	Height (mm)	Vertical /sub-vertical	Dip (near 90 °if blank)	Kinematic aperture (mm)		Single/ branch-ing	Termination	
					Min (0.1 if blank)	Max		Top	Base
0.3	P	225	V			? - CORE BROKEN	SG	1	4
0.45	P	85	V			0.2	SG	1	4
0.38	P	15	V			0.2	SG	1	1
9031.39	P	105	V			0.3	BR	1	1
30.27	P	32	V			0.2	SG	1	1
0.26	P	32	V			0.2	SG	1	1
0.39	P	5	V			0.2	SG	1	1
9031.77	P	80	V			0.3	SG	1	4
26.85	P	11	V			0.1	SG	1	1
9022.22	P	32	V			0.2	SG	4	1
23.24	P	24	V			0.1	SG	1	1
9004.37	P	100	V			2	SG	1	4
8999	P	230	V			? - CORE BROKEN	SG	1	4
0.54	P	70	V			? - CORE BROKEN	SG	4	?
8992.33	VE	66	V			0.1	SG	1	1
0.63	VE	92	V			0.1	SG	1	4
0.75	P	30	V			0.1	SG	1	1
0.75	P	30	V			0.1	SG	1	1
0.73	P	25	V			0.1	SG	1	4
0.77	P	21	V			0.1	SG	1	4
0.76	P	57	V			0.1	SG	1	1
8971.46	P	18	V			0.2	SG	1	1
8957.93	P	30	V			0.1	SG	1	1
58.07	P	53	V			0.2	SG	1	1
8945.97	P	41	V			0.5	SG	1	1
47.08	P	25	SV			0.1	SG	1	1
0.16	P	20	SV			0.1	SG	1	1
0.21	P	19	SV			0.1	SG	1	1
0.28	P	9	SV			0.1	SG	1	1
46.71	P	40	V			0.1	SG	1	1
0.19	P	19	V			0.1	SG	1	1
0.48	P	8	V			0.1	SG	1	1
0.48	P	28	V			0.1	SG	1	1
8899.39	P	52	V			0.2	SG	1	1

Depth (ft; top)	Type	Height (mm)	Vertical /sub-vertical	Dip (near 90 °if blank)	Kinematic aperture (mm)		Single/ branch-ing	Termination	
					Min (0.1 if blank)	Max		Top	Base
8867.08	P	90	V		0.2	0.5	BR	4	1
8866.58	P	70	V			0.2	SG	1	4
62.7	VE	46	V			0.2	SG	4	4
0.72	VE	52	V			0.2	SG	4	4
0.6	VE	20	V			0.2	SG	4	4
0.6	VE	12	V			0.2	SG	1	1
0.65	P	5	V			0.1	SG	1	1
0.54	VE+P	49	V			0.1	SG	1	1
0.3	P	15	V			0.2	SG	1	1
61.93	VE	5	V			0.2	SG	2	2
8855.15	P	30	V			0.2	BR	1	4
54.55	P	24	V			0.5	SG	4	1
53.38	P	52	V			0.2	BR	1	1
0.29	P	28	V			0.1	SG	1	1
0.21	P	22	SV			0.1	BR	1	1
0.14	P	20	V			0.1	BR	1	1
0.13	P	12	SV			0.1	SG	1	1
49.5	P	78	V			0.2	BR	4	1
8840.4	P	120	V			0.1	BR	1	1
8828.4	P	10	V			0.1	SG	1	1
0.44	P	10	V			0.1	SG	1	1
0.46	P	23	V			0.1	SG	1	1
0.21	P	47	V			0.1	SG	1	1
0.25	P	105	V			0.2	BR	1	1
0.38	P	38	V			0.1	SG	1	1
27.6	P	92	V			? - CORE BROKEN	SG	4	4
8820.83	P	20	V			? - CORE BROKEN	SG	? - CORE BROKEN	
0.86	P	30	V			? - CORE BROKEN	SG	? - CORE BROKEN	
19.12	P	27	V			0.2	SG	1	1
0.62	P	22	V			0.2	SG	1	1
16.25	VE+P	77	V			0.2	SG	4	1
15.62	P	15	SV			0.2	SG	1	1

Core #6 – Fracture measurement data

Depth (ft; top)	Type	Height (mm)	Vertical /sub-vertical	Dip (near 90 °if blank)	Kinematic aperture (mm)		Single/ branch-ing	Termination	
					Min (0.1 if blank)	Max		Top	Base
10312.91	VE	555	V			1	BR	1	1
0.78	VE+P	438	V			1	SG	2	1
0.6	VE	55	V			0.1	SG	4	1
0.9	VE	44	V			0.2	SG	1	1
0.8	VE	83	V			0.2	SG	1	1
0.7	VE	55	SV	45		0.1	SG	1	1
0.75	VE	45	V			0.1	SG	1	1
0.78	VE	42	V			0.1	SG	1	1
0.7	VE	20	V			0.1	SG	1	1
0.41	VE	95	V			0.1	SG	3	1
0.4	VE+P	98	V			0.1	BR	3	1
0.41	VE+P	139	V			0.1	BR	3	1
10313.6	VE	19	V			0.3	SG	2	4
0.88	VE	40	SV	45		0.1	SG	1	1
0.82	VE	50	SV	45		0.1	SG	1	1
0.54	VE	49	V			0.1	SG	1	1
0.02	VE	138	V			0.1	SG	1	1
10311.32	VE+P	110	V			0.1	SG	1	1
0.58	VE	35	V			0.1	SG	1	1
0.68	P	35	V			0.1	SG	1	1
0.3	P	63	V			0.1	SG	1	1
10310.77	P	186	SV	?		0.1	BR	4	1
0.89	P	110	V			0.1	SG	1	1
0.53	P	58	V			1	SG	4	4
10309.89	P	8	V	80		0.1	SG	1	1
0.93	P	7	V	80		0.1	SG	1	1
0.09	P	100	V			0.1	SG	1	1
10308.8	VE+P	175	V			0.4	SG	1	1
0.23	VE	50	V			2	SG	1	1
0.2	VE	10	SV	40		0.2	SG	1	1
10307.67	P+S	153	SV	60		0.3	SG	4	1
0.47	P	25	SV	45		1	SG	1	1
0.48	P	12	V			1	SG	1	1
0.38	P	110	V			2.5	SG	1	1
0.35	P	9	V	70		0.5	SG	1	1
0.09	P	45	SV	45		1	BR	1	1
0.23	P	61	V			1.5	BR	1	1
15	P	86	V			1.5	BR	1	1
10306.84	P+VE	96	V			1	BR	1	1
0.86	P	104	V			0.5	BR	4	1
0.97	P+S	86	SV	?		1	SG	4	1
0.79	P	15	V			1	SG	1	1

Depth (ft; top)	Type	Height (mm)	Vertical /sub-vertical	Dip (near 90 °if blank)	Kinematic aperture (mm)		Single/ branch-ing	Termination	
					Min (0.1 if blank)	Max		Top	Base
10305.42	P	23	SV	?		1	SG	1	1
0.6	P	44	SV	?		1	SG	4	4
10301.2	P	161	V	?		0.3	SG	1	1
10295.59	P	270	V	?		2	SG	1	1
10299.21	P	16	SV	70		0.5	SG	1	1
0.22	P	16	SV	80		0.3	SG	1	1
0.17	P	9	V			0.6	SG	1	1
10281.02	P	70	V			1	SG	1	4
0.22	P+S	11	SV	30		1	SG	4	4
0.24	P	63	V			0.5	SG	1	4
0.37	P	12	V	80		1	SG	1	1
10276.95	P	70	V			1	SG	1	1
0.59	P	83	V	60		1	SG	1	1
0.38	P	72	V			0.5	SG	1	1
0.4	P	10	V			0.1	SG	1	1
0.29	P	38	V			1	SG	1	1
10284.33	P	25	SV	45		0.5	SG	1	1
10274.05	P	235	V			3	SG	1	4
0.7	P	66	SV			1.5	SG	1	4
0.72	P	340	V			0.5	SG	1	1
0.79	P	198	SV			1	SG	4	4
10275.52	P	103	V	80		0.4	SG	1	1
0.44	P	41	V			0.2	SG	1	1
10272.06	VE+P	60	V	70		0.5	SG	1	3
0.32	P	5	V			0.5	SG	2	2
0.31	P	12	V	60		0.5	SG	2	2
10275.94	P	122	V			0.6	SG	1	1
10270.55	P	18	V			0.1	SG	1	1
0.03	P	35	V			0.2	SG	4	1
0.03	P	6	V			0.1	SG	4	1
0.1	P	63	V			0.2	SG	1	1
0.13	P	42	V			0.2	SG	1	1
0.37	P	58	V			0.2	SG	1	1
10265.47	VE	113	V			0.5	SG	1	1
10263.51	P+VE	90	V			0.2	SG	1	1
0.65	VE	65	V			0.1	SG	1	1
10262.97	VE	30	V			0.1	SG	1	1
10261.46	VE	40	V			0.1	SG	1	1
0.5	VE	15	V	80		0.1	SG	1	4
0.39	VE	30	V			0.1	SG	1	1
10260.95	VE+P	62	V			0.1	SG	1	1
0.83	VE+P	36	V			0.2	SG	1	1
0.85	P	42	V			0.2	SG	1	1

Depth (ft; top)	Type	Height (mm)	Vertical /sub-vertical	Dip (near 90 °if blank)	Kinematic aperture (mm)		Single/ branch-ing	Termination	
					Min (0.1 if blank)	Max		Top	Base
10266.3	P	12	V			0.2	SG	1	1
10265.86	P	7	V			0.2	SG	1	1
0.88	P	53	V	80		0.5	SG	1	1
10257.78	P	32	V			0.1	SG	1	1
0.65	P	9	V			0.1	SG	1	1
10251.31	VE	25	V	70		0.1	SG	4	1
0.3	VE	66	V			1.5	BR	4	3
10250.86	VE	12	V			0.1	SG	1	1
0.86	VE	20	V			0.1	SG	1	4
0.28	P	27	V			0.1	SG	1	1
10249.7	VE	12	V			0.1	BR	1	1
0.7	VE+P	13	V			0.2	BR	1	1
0.7	P	18	V			0.1	SG	1	1
10247.37	P	19	V			1	SG	1	4
0.08	P	28	V			1	SG	1	1
0.08	P	25	V			1.5	SG	1	4
10246.27	VE	15	V	80		2.5	SG	2	2
0.3	VE	5	V			1.5	SG	2	2
0.3	VE	10	V			1	SG	2	2
10245.56	VE	7	V			0.5	SG	1	4
0.2	P	16	V			1	SG	4	1
10244.1	VE	11	V			0.2	SG	1	1
0.1	VE	12	V			0.2	SG	1	1
10243.83	P	24	V	70		0.2	SG	1	1
0.63	VE	10	V			0.2	SG	1	1
0.63	P	12	V			0.2	SG	1	1
0.62	VE	15	V			0.2	SG	1	1
0.63	VE	11	V			0.2	SG	1	1
10243.38	VE	14	V			0.2	SG	1	1
0.34	P	20	V			0.2	SG	1	1
0.39	VE	9	V			0.2	SG	1	1
0.22	VE	7	V			0.2	SG	1	1
10242.58	VE	10	V			0.2	SG	1	1
0.6	VE	22	V			0.2	SG	1	1
0.85	P	15	V			0.1	SG	4	1
0.82	VE	19	V			0.1	SG	1	1
0.8	P	7	V			0.1	SG	1	1
0.75	P	7	V			0.1	SG	1	1
0.8	P	14	V			0.1	SG	1	1
0.92	VE	17	V			0.1	SG	1	1
0.93	VE	10	V			0.1	SG	1	1
0.93	VE	10	V			0.1	SG	1	1
10241.15	VE	21	V			0.1	SG	1	1

Depth (ft; top)	Type	Height (mm)	Vertical /sub-vertical	Dip (near 90 °if blank)	Kinematic aperture (mm)		Single/ branch-ing	Termination	
					Min (0.1 if blank)	Max		Top	Base
0.01	VE	120	V			0.1	SG	1	1
10240.02	P	72	V	70		0.1	SG	1	1
0.3	P	38	V	70		0.2	SG	1	1
0.33	P	39	V	70		0.2	SG	1	1
10239.7	P+VE	46	SV	60	0.5	0.5	SG	1	1
10235.02	P	78	SV	50		1	SG	1	1
10233.65	P	210	V	70		0.5	SG	1	1
0.9	P	59	V	80		0.3	SG	1	1
10232.9	P	25	V			0.5	SG	1	1
0.9	P	358	SV	60		0.5	BR	2	1
0.95	P	14	V	80		1	SG	2	1
0.89	P	17	SV	40	0.5	1	SG	2	1
0.82	P	12	SV			1	SG	3	3
0.7	VE	26	V			0.5	SG	1	1
0.7	P	23	SV	60		0.5	SG	1	1
0.68	VE	8	V	70		0.1	SG	1	4
0.31	VE	119	V			0.5	SG	1	1
0.78	P	9	V			0.1	SG	1	1
10231.77	P	90	V		0.5	1.5	BR	2	1
0.65	P	60	SV			0.5	BR	2	1
10231.31	P	40	V		0.5	1	BR	1	1
0.23	P	5	V			0.1	SG	1	1
0.27	VE	12	V			0.1	BR	1	1
0.1	P	123	V			1	SG	1	1
0.02	P	63	V			0.5	SG	1	1
0.26	P	70	V		0.5	1	SG	1	1
0.22	P	70	V			0.5	SG	1	1
10239.75	P	18	V			0.1	SG	1	1
0.84	P	13	SV	40		0.1	SG	1	1
10234.2	P	80	V			0.1	SG	1	1
10232.8	P	5	SV	30		0.3	SG	1	4
0.7	P	4	SV	30		0.1	SG	1	1
0.61	VE	5	SV	40		0.1	SG	1	1
0.6	VE	5	SV	40		0.2	SG	1	1
0.48	VE+S	17	V	80		0.3	SG	1	1
0.5	P	5	SV	60		0.1	SG	1	1
0.51	P	8	SV	40		0.3	SG	1	1
0.51	VE	4	SV	30		0.1	SG	1	1
10232.46	VE	8	SV	30		0.1	SG	1	1
0.48	P	3	SV	30		0.1	SG	1	1
0.49	VE	13	SV	60		0.1	SG	1	1
0.45	VE	4	V	80		0.1	SG	1	1
0.45	VE	4	V	80		0.1	SG	1	1

Depth (ft; top)	Type	Height (mm)	Vertical /sub-vertical	Dip (near 90 °if blank)	Kinematic aperture (mm)		Single/ branch-ing	Termination	
					Min (0.1 if blank)	Max		Top	Base
0.42	VE	4	V	80		0.1	SG	1	1
0.35	P	12	V			0.1	SG	1	1
0.35	VE	9	V			0.1	SG	1	1
0.3	VE	11	V	70		0.1	SG	1	1
0.3	VE	11	V	80		0.4	BR	1	1
0.3	VE	10	V	80		0.1	SG	1	1
0.32	VE	10	V	80		0.2	SG	1	1
0.26	VE	10	V	80		1	SG	1	2
0.25	P	8	V			0.1	SG	1	2
0.25	P	7	V			0.1	SG	1	2
0.25	P	10	V			0.1	SG	1	2
0.16	P	13	SV	50		0.5	BR	1	1
0.16	P	6	SV	?		1	BR	1	1
0.2	VE	5	V			0.1	BR	1	1
10232.09	P	4	SV	30		0.1	SG	1	1
0.08	P	10	V			0.1	SG	1	1
0.08	VE	5	V			0.1	SG	1	1
0.09	P	15	V			0.1	SG	1	1
0.09	VE	11	V			0.1	SG	1	1
0.1	VE	8	V			0.1	SG	1	1
0.1	VE	7	V			0.1	SG	1	1
0.08	S	9	SV	60		0.1	SG	1	1
0.1	VE	4	SV	60		0.1	SG	1	1
0.02	P	5	SV	50		0.3	SG	1	1
0.05	VE	7	V	70		1	SG	1	1
0.02	P	17	SV	50		0.3	BR	1	1
10231.64	VE	14	V			0.5	SG	2	1
0.6	P	25	V	80		0.5	SG	2	1
0.79	VE	68	V			0.1	SG	1	1
0.72	VE	60	V			0.1	SG	1	1
0.6	P	13	V			0.1	SG	2	1
0.6	VE	11	V			0.1	SG	2	1
0.58	VE	42	V			1.5	SG	2	1
10230.97	P	190	SV	?		1	SG	1	1
10228.89	P	22	V			0.5	SG	1	1
0.98	P	26	V			0.3	SG	1	1
0.88	P	22	V			0.5	SG	1	1
0.89	P	39	V			1	SG	1	1
10224.45	P	13	V			0.2	SG	1	1
0.4	P	12	V			0.2	SG	1	1
0.62	P	12	V			0.2	SG	1	1
0.66	P	12	V			0.2	SG	1	1
0.42	VE	4	V	80		0.1	SG	1	1

Depth (ft; top)	Type	Height (mm)	Vertical /sub-vertical	Dip (near 90 °if blank)	Kinematic aperture (mm)		Single/ branch-ing	Termination	
					Min (0.1 if blank)	Max		Top	Base
0.67	P	7	V			0.2	SG	1	1
10224.12	P	177	V			1	BR	1	1
0.14	P	10	V			0.1	SG	1	1
0.1	P	9	V			0.1	SG	1	1
0.04	P	15	SV	?	0.5	1	SG	1	1
10223.4	P	170	V			0.1	SG	2	1
0.4	P	33	V			0.1	SG	2	1
0.95	P	42	V			0.1	SG	1	1
10222.05	VE	10	V			0.1	SG	2	1
10221.79	P	60	V			0.3	BR	1	4
0.8	P	31	V	?		0.1	SG	1	1
0.88	P	33	SV	50		0.2	BR	1	4
0.88	VE	7	V			0.1	SG	1	1
0.43	P	135	V	?		0.5	SG	1	1
0.01	P	120	SV			0.5	SG	1	1
10215.3	P	60	V		0.5	1	SG	1	2
10214.12	P	90	V	70	0.5	1	SG	1	1
0.07	P	25	V	70		0.5	SG	1	1
0.05	P	15	V	70		0.5	SG	1	1
10219.01	P	75	V			0.3	SG	1	1
0.7	P	87	V			0.1	SG	4	4
10211.8	P	40	SV	?	0.5	2.5	SG	2	4
10209	P	275	SV			1	BR	1	1
10207.59	VE	410	V			3	BR	2	1
10207	P	70	SV			1	BR	4	1
10212.55	P	7	SV			0.1	SG	1	1
0.11	P	?	SV			0.1	SG	4	1
10211.73	P	17	V			0.2	SG	1	2
0.35	P	107	SV			0.1	BR	2	1
0.48	P	42	SV			0.1	SG	2	2
0.32	VE	15	V			0.1	SG	1	1
0.33	VE	7	V			0.1	SG	1	1
0.33	VE	4	SV			0.1	SG	1	1
10210.79	P	42	V			0.2	SG	1	1
0.89	P	30	V			0.2	SG	1	1
0.2	P	9	SV			0.1	SG	1	1
0.11	P	14	V			0.1	SG	1	1
0.07	VE+P	55	V			0.2	SG	1	1
10207.22	P	12	V			0.3	SG	1	1
0.22	P	22	V			0.1	SG	1	1
0.31	P	20	V			0.2	SG	1	1
0.4	S	23	V			0.2	SG	1	1
0.35	VE	25	SV			0.1	SG	1	1

Depth (ft; top)	Type	Height (mm)	Vertical /sub-vertical	Dip (near 90 °if blank)	Kinematic aperture (mm)		Single/ branch-ing	Termination	
					Min (0.1 if blank)	Max		Top	Base
10208.9	VE	303	V			3	BR	1	1
10209.29	VE	35	V			1	SG	4	4
0.88	P	23	V			0.4	SG	4	1
10203.82	P	5	SV			0.1	SG	1	1
0.85	P	5	V			0.1	SG	1	1
0.96	P	3	V			0.1	SG	1	1
0.42	VE	5	SV			0.1	SG	1	1
0.35	P	23	V			1	SG	1	1
0.42	P	5	V			0.1	SG	1	1
0.43	P	62	V			0.2	SG	1	1
0.3	VE	15	V			0.1	SG	1	1
0.3	VE	12	V			0.1	SG	1	1
0.3	VE	10	V			0.1	SG	1	1
0.23	VE	30	V			0.1	SG	1	1
0	VE	37	V			0.3	SG	1	1
0.05	VE	15	V			0.1	SG	1	1
10202.95	P	18	V			0.2	SG	1	1
0.22	VE	22	V			0.1	SG	1	1
0.2	P	10	V			0.1	SG	1	1
0.18	P	18	V			0.1	SG	1	1
0.25	P	33	V			1.5	BR	1	3
0.18	VE	13	V			0.1	?	1	1
0.2	VE	48	V			1	?	1	1
0.3	P	20	V			0.2	?	1	3
12	P	26	V			0.1	SG	1	1
0.1	P	10	V			0.1	SG	1	1
0.08	P	7	V			0.1	SG	1	1
0.05	P	22	V			0.1	SG	1	1
10201.76	P	75	V			1	SG	2	1
0.84	P	135	V			0.2	SG	1	1
0.75	P	30	V			1	SG	2	2
0.08	P	12	SV	45		0.1	SG	1	1
0.14	P	51	V			0.1	SG	1	1
0.5	P	52	V	70		0.1	SG	1	1
0.3	P	78	V	70		0.1	BR	1	1
0.2	VE	28	V	70		0.1	SG	4	1
0.4	P	20	SV	50		0.1	SG	4	1
10200.8	P	59	V	70		0.2	SG	1	1
10199.42	VE	43	V			3	SG	1	1
0.4	VE	35	V			0.1	SG	1	1
0.43	VE	20	V			0.1	SG	1	1
0.12	VE	20	V			0.3	SG	1	1
10198.61	P	10	V			0.2	SG	1	1

Depth (ft; top)	Type	Height (mm)	Vertical /sub-vertical	Dip (near 90 °if blank)	Kinematic aperture (mm)		Single/ branch-ing	Termination	
					Min (0.1 if blank)	Max		Top	Base
0.62	P	22	V			0.2	SG	1	1
0.25	P	68	V			1	SG	1	1
10197.85	P	160	V			0.3	SG	1	1
0.42	P	23	V	70		0.2	SG	4	1
10196.6	P	70	V			0.1	SG	1	1
0.26	VE	55	V			0.1	SG	1	1
10195.55	P	36	V			0.2	SG	1	1
10194.86	VE	65	V			0.1	BR	1	1
0.96	P	12	V			0.2	SG	1	1
0.49	P	152	V			0.7	SG	1	1
0.37	VE	34	V			0.2	SG	1	1
0.19	VE	20	V			0.1	SG	1	3
10192.3	VE+P	37	V			0.2	SG	3	1
10189.8	P	27	V			0.5	SG	1	1
10188.52	P	10	V			0.3	SG	1	1
10187.53	VE	30	V			0.1	SG	1	1
0.54	VE	26	V			0.1	SG	1	1
0.6	VE	12	V			0.1	SG	1	1
0.76	P	5	V			0.2	SG	4	1
10186.3	P	25	V			0.2	SG	1	1
10167	P	123	V			0.2	SG	1	1
10165.33	P	33	V			0.2	SG	1	1
10164.12	P	5	V			0.2	SG	1	1
10147.3	P	136	V		0.5	2	SG	1	4
10146.62	P	112	V			1	SG	1	4
10145.77	P	116	V		1	2	SG	4	1
0.62	P	273	V			1	SG	1	1
0.58	VE	12	V			0.1	SG	1	1
0.6	VE	28	V			0.1	SG	1	1
10143	P	23	V			1	SG	1	1
10141.01	P	9	V			0.2	SG	1	1
0.24	P	21	V			0.5	SG	1	1
10095.05	P	7	V			0.5	SG	1	1
0.06	P	1	V			0.5	SG	2	2
0.07	P	4	V			0.5	SG	1	1
0.09	P	10	V			0.2	BR	1	1
10089.55	P	6	SV			0.2	BR	1	1
0.54	P	36	SV			0.5	SG	3	3
10071.9	VE+P	110	V			3	BR	1	1
10075.31	VE+P	160	V			1	BR	1	1
10070	S	17	SV			0.5	SG	1	1
10070.11	P	27	SV			0.2	SG	4	1
10070.3	P	48	SV			0.2	SG	4	1

Depth (ft; top)	Type	Height (mm)	Vertical /sub-vertical	Dip (near 90 °if blank)	Kinematic aperture (mm)		Single/ branch-ing	Termination	
					Min (0.1 if blank)	Max		Top	Base
10073.88	P	10	V			0.1	SG	1	2
0.88	P	8	V			0.1	SG	1	1
10068.8	P	37	V			0.6	SG	1	4
0.38	P	85	V			0.5	BR	1	1
0.1	VE	74	SV			0.5	SG	3	1
0.36	P	35	SV			0.5	BR	1	1
10064.86	P	10	V			0.5	SG	1	3
10061.23	P	10	SV			1	SG	1	1
10065.09	P	128	SV			1	SG	4	1
0.21	P	8	V			0.2	SG	1	1
0.03	P	55	V			0.5	BR	1	1
0.19	P	32	V			0.3	SG	1	1
10064.9	P	5	V			0.5	SG	1	1
0.92	P	8	V			1	SG	1	1
10061.18	P	7	V			0.2	SG	1	1
0.21	P	5	V			0.5	SG	1	1
10058.84	P	65	V	80		0.6	SG	1	1
10047.27	P	70	V			0.1	SG	1	1
0.3	P	25	V			0.1	SG	1	1
0	P	60	V			0.1	BR	1	4
0	P	62	V			0.1	SG	1	1
0.05	P	35	V			0.1	SG	1	1
10046.96	P	6	V			0.1	SG	1	1
0.75	P	70	V			0.1	SG	1	1
0.75	P	120	V			0.1	SG	1	1
0.38	P	110	V			0.1	SG	1	1
0.3	P	221	V			1	BR	1	1
0.4	P	19	V			0.1	SG	1	1
9988.25	VE	45	V			0.5	BR	1	1
0.19	P+S	127	V			0.5	SG	3	3
9985.31	P+S	125	V			0.5	SG	1	1
9985.01	P	2	SV			0.2	SG	1	1
0.02	S	24	SV			0.2	SG	1	1
0.1	S	2	SV			0.2	SG	1	1
0.12	S	7	SV			0.2	SG	1	1
0.13	S	3	SV			0.2	SG	1	1
0.16	S	22	SV			0.2	SG	1	1
9984.58	P+S	122	V			3	BR	1	3
0.55	VE	13	V				SG	4	1
0.32	P+VE	710	V			2	BR	1	1
0.3	VE	3	V			0.2	?	1	1
9938.02	VE	225	V			0.2	BR	1	2
9934.02	P+S	56	V			0.3	SB	1	1

Depth (ft; top)	Type	Height (mm)	Vertical /sub-vertical	Dip (near 90 °if blank)	Kinematic aperture (mm)		Single/ branch-ing	Termination	
					Min (0.1 if blank)	Max		Top	Base
0.17	P+S	96	V			0.3	BR	1	1
9933.04	P	75	V			0.5	BR	1	1
0.29	P	32	V			0.1	SG	4	3
0.29	P	32	V			0.1	SG	4	3
0.71	P+S	155	SV			0.5	SWARM	1	1
0.7	P+S	145	SV		0.5	1.5	BR	2	2
0.45	S	100	SV		1	10	BR	2	4
9931.1	VE	85	V			11	SG	1	2
9929.46	VE+P+S	122	V			0.5	SG	1	1
9914.5	P	?							
9911.85	P	62	SV			0.5	SG	1	1
0.82	P	73	V	70		0.7	SG	1	1
0.21	P	204	SV			1	SG	1	1
0.15	P	85	V			0.2	SG	1	1
9897.78	P	38	V			0.6	SG	1	3
9889.58	P	30	V			0.3	SG	3	1
9885.86	P	38	V	80		0.8	SG	1	4
9869.77	P	8	V			0.4	SG	3	3
9863.2	P	3	V			0.2	SG	3	1
0.22	P	27	V			0.2	SG	1	1
0.18	P	11	V			0.2	SG	1	1
0.23	P	3	V			0.2	SG	1	1
0.19	P	26	V			0.2	SG	1	1
0.18	P	32	V			0.2	SG	1	1
9832.79	P	13	V			1	SG	1	1
9765.25	P	3	V			0.2	SG	1	1
0.27	P	11	V			0.2	SG	1	1
0.52	P	10	V			0.2	SG	1	1
0.52	P	95	V			0.2	SG	1	1

Core #4 – Fracture spacing data

Core #	Box #	Depth (ft; top)	Fracture Count	Spacing (mm)
4	5	9377.05	4	8
				24
				6
		76.9	3	26
				14
		74.72	3	5
				31
		73.42	2	11
		71.9	2	14
4	4	9368.15	3	3
				2
		9366.01	5	21
				2
				17
				10
		9367.17	9	11
				4
				8
				5
				1
				3
				16
				15
				13
4	3	9361.55	3	10
				18
		0.36	6	3
				8
				24
				1
				1.5
		59.8	5	3
				17
				9
				12
				17
		58.43	3	6
				14
		56.1	2	35
4	2	9348.93	2	6
		45.86	2	31
4	1	9341.85	2	2
3	15	9331.1	2	9
3	14	9325.15	3	30
				6

Core #	Box #	Depth (ft; top)	Fracture Count	Spacing (mm)
		24.65	3	25
				13
3	13	9317.5	4	20
				4
				48
		0.1	2	42
		0.7	2	16
3	12	9307.18	2	2
		8.21	2	24
		1.8	4	36
				12
				20
		0.15	4	22
				15
				19
		3.62	2	28
		0.4	3	25
				12
		2.9	3	18
				25
		0.43	5	2
				15
				16
				6
3	11	9301	4	2
				19
				32
		9300.59	3	57
				7
		9301.4	2	33
		9299.79	5	3
				7
				42
				6
		97.37	5	16
				27
				5
				11
		92.8	3	4
				13
3	10	9290.4	2	34
		86.5	2	43
3	9	9282.69	2	7
		79.6	3	26
				17
		0.35	2	22

Core #	Box #	Depth (ft; top)	Fracture Count	Spacing (mm)
		78.5	2	34
		77.15	2	30
3	8	9268.4	2	68
		67.8	6	15
				11
				22
				18
				12
				8
		0.35	4	43
				5
				28
		66.69	3	18
				8
		0.9	4	35
				7
				4
3	6	9249.53	3	11
				7
		48.4	2	47
3	5	9239.95	5	6
				6
				28
				8
		0.7	4	30
				4
				6
		0.59	3	10
				42
3	4	9236.35	4	37
				6
				8
		9230.55	3	11
				35
		0.4	2	69
		0.05	2	48
		9229.2	3	9
				11
		0.85	2	46
		0.8	2	44
3	3	9228.25	2	50
		0.39	2	9
		0.51	2	37
		9221.15	7	10
				8
				8

Core #	Box #	Depth (ft; top)	Fracture Count	Spacing (mm)
				12
				20
				3
		0.42	2	21
		0.36	2	27
		0.2	4	50
				21
				14
3	2	9215.6	4	37
				7
				17
		14.25	2	52
		14.16	3	17
				28
		11.79	3	19
				21
3	1	9210.59	3	42
				7
		0.02	3	57
				19
2	19	9159.2	2	17
		9159	3	16
				17
		58.85	2	6
2	15	9119.1	2	15
		9118.4	3	8
				8
2	14	9114.5	2	12
		9106.08	2	17
2	11	9079.6	2	5
		9085	2	23
2	8	9058.48	2	4
2	6	9034.4	3	23
				8
2	5	9030.3	2	32
2	2	8992.8	5	10
				8
				11
				12
1	6	8828.5	3	13
				27

Core #5 – Fracture spacing data

Core #	Box #	Depth (ft; top)	Fracture Count	Spacing (mm)
2	17	9164.29	5	2
				57
				10
				6
		0.38	4	40
				22
				12
2	16	9162.4	6	7
				3
				26
				1
				6
		0.5	5	8
				3
				25
				10
2	15	9150.5	3	17
				9
		47.05	2	43
2	14	9140.07	6	21
				24
				18
				6
				5
		39.9	7	4
				19
				4
				7
				4
				10
				3
		39.35	2	32
2	13	9135.87	3	47
				6
		0.42	3	23
				4
		27.55	2	6
2	11	9114.9	2	5
2	10	9105.72	5	12
				6
				2
				14
		3.45	4	9
				9
				16

Core #	Box #	Depth (ft; top)	Fracture Count	Spacing (mm)
		2.7	2	24
2	9	9098.7	2	70
		9094.15	3	5
				4
2	8	9089.05	3	3
				12
		85.8	2	15
2	7	9081.5	3	4
				4
		80.45	2	22
		78.4	2	12
		77.39	2	40
		0.34	2	32
2	5	9060.05	2	28
		0.01	2	37
		55.9	2	59
		55.65	2	35
2	4	9051.28	3	7
				10
		47.18	3	36
				22
2	1	9024.2	3	36
				4
		9019.03	2	20
1	51	9019	2	51
		9018.1	2	62
1	50	9017.9	2	31
		0.6	2	16
		0.3	2	72
		12.1	6	26
				4
				4
				3
				33
		11.8	7	2
				28
				3
				16
				20
				12
		10.53	3	20
				28
		0.2	2	21
1	47	8987.1	5	16
				4
				4

Core #	Box #	Depth (ft; top)	Fracture Count	Spacing (mm)
				7
		0.04	7	5
				6
				2
				7
				2
				21
		86.07	9	1
				9
				4
				7
				5
				18
				11
				22
		85.29	7	10
				17
				8
				5
				4
				29
		84.67	4	21
				6
				40
		82.99	6	27
				18
				2
				8
				11
1	46	8981	2	26
		8980.78	6	1
				2
				12
				4
				35
1	45	8970.25	3	43
				6
		69.95	5	48
				2
				4
				2
		68.7	2	32
1	43	8954.65	3	37
				21
		0.4	6	2

Core #	Box #	Depth (ft; top)	Fracture Count	Spacing (mm)
				17
				4
				8
				4
		53	2	15
1	42	8942.9	2	9
		8941.95	2	4
1	41	8936.25	2	15
1	40	8921.64	3	32
				8
		0.54	3	37
				42
1	39	8918.49	4	8
				23
				7
		17.92	3	23
				26
		12.02	2	53
		11.6	3	51
				19
		10.87	2	48
		10.2	2	41
1	38	8909.2	4	8
				24
				40
		8.25	4	21
				13
				13
		6.85	3	11
				9
1	37	8899.9	4	15
				12
				15
		0.65	4	23
				10
				7
				2
		8896.84	3	7
				51
		0.15	2	33
1	36	8891.3	2	32
1	35	8881.46	2	34
		80.3	2	73
		77.65	2	43
		0.05	2	35
1	31	8845.5	3	22

Core #	Box #	Depth (ft; top)	Fracture Count	Spacing (mm)
				4
		8843.05	2	42
1	28	8814.4	2	42
		8814.3	2	44
		13.4	4	23
				12
				6
		13	4	35
				2
				3
1	25	8786.13	2	13
1	24	8776.37	3	19
				13
1	21	8753.28	3	18
				44
		0.1	4	48
				10
				1
1	20	8745.04	2	8
		44.28	2	35
1	18	8725.15	2	46
		24.7	2	42
1	16	8710.14	5	35
				3
				20
				8
		0.35	2	37
1	15	8696.1	2	18
1	14	8691.3	4	24
				2
				23
		8691.22	2	17
		90.65	2	21
1	12	8675.4	2	13
1	11	8665.45	3	15
				5
		0.1	2	9
		64	2	23
1	10	8654.65	3	30
				41
1	6	8617.05	2	24
		16.9	2	30

Core #6 – Fracture spacing data

Core #	Box #	Depth (ft; top)	Fracture Count	Spacing (mm)
2	39	10314	5	8
				7
				2
				4
		10313.62	3	15
				19
		.3 / .2	4	7
				19
				1
		10312.9	6	11
				4
				7
				10
				5
		0.5	3	17
				23
2	38	10311.35	4	9
				23
				14
		10310.9	2	28
		10307.5	3	2
				23
		0.4	3	32
				7
		0.16	4	2
				17
				47
				19
		10307	3	45
				30
2	37	10299.23	2	6
2	35	10281.4	2	36
		0.22	2	25
2	34	10275.55	3	7
				37
		10274.8	4	35
				18
				5
		10270.2	2	18
		0.02	2	7
2	33	10263.75	2	13
		10260.98	3	7
				9
2	32	10250.9	2	23
		10249.75	3	13

Core #	Box #	Depth (ft; top)	Fracture Count	Spacing (mm)
				14
2	31	10247.1	2	34
		10246.06	2	50
		10244.12	2	17
		10243.64	4	18
				16
				19
		0.45	3	37
				12
		10242.81	3	12
				15
		0.6	2	25
2	30	10239.86	2	37
		0.76	2	13
		10234	3	29
				39
		10232.92	3	44
				17
		0.32	4	4
				34
				7
		0.1	7	10
				6
				11
				10
				7
				8
		10231.61	4	23
				37
				8
		0.4	4	8
				23
				12
2	29	10228.95	2	22
		10224.45	3	2
				9
		10223.45	2	5
2	28	10221.84	3	16
				14
		10214.14	2	6
		0.1	2	5
2	27	10210.14	2	36
		0.9	2	33
		10207.22	2	15
		10204.1	2	30
2	26	10203.32	4	18

Core #	Box #	Depth (ft; top)	Fracture Count	Spacing (mm)
				23
				6
		10202.22	3	6
				4
		10201.89	3	6
				4
		10198.3	2	6
2	25	10194.9	2	37
		10187.6	2	23
2	20	10146.65	2	6
		10145.9	2	54
		10145.8	2	45
2	14	10089.55	2	23
2	12	10074.82	2	41
		10073.9	2	19
2	11	10068.43	2	15
		10065.25	2	42
		10064.95	2	51
2	9	10047.37	2	2
		0.1	2	47
		10046.98	4	16
				14
				30
		0.75	4	9
				30
				5
		10042	3	7
				51
2	3	9988.31	2	7
2	2	9985.08	2	35
		0.6	2	24
		0.4	2	15
		0	2	40
1	23	9933.73	3	18
				11
		0.8	2	20
		9934.18	3	7
				3
1	20	9911.85	3	15
				4
		9912	2	15
1	15	9863.21	5	4
				3
				13
				20
1	4	9765.52	2	7

APPENDICES

APPENDIX 3

Fracture Data – Outcrop

In fracture data spreadsheet, fracture types include ptygmatic (P), opening-mode (VE, *sensu* vertical extension fractures), and shear (S) fractures; orientation is denoted as vertical (V) or sub-vertical (SV) to the layering (or bedding) structure; Dip angle is denoted as degree and direction ("L" for "dipping to the left", "R" for "dipping to the right"); mineralization of fractures is denoted as extent and composition of mineralization ("F" for "fully mineralized"); to describe the spatial relationship between fracture tip and layering boundary or bedding plane, fractures are denoted as confined "Y" or not confined "Y" by layering or bedding; for termination styles (three in total), type 1 means the fracture is tapered at top and base, type 2 means the fracture is abruptly terminated at top or base in a random place, and type 3 means the fracture is abruptly terminated at top or base due to lithological variations.

Layering/bedding		Scanline		Fracture type	Vertical or sub-vertical to layering/ bedding	Dip (angle, to the left or right)	Fully sealed? Mine-ralogy?	Height (mm)	Kine-matic aper-ture (mm)	Vertical termination					Lithology
# - Geo-metry	Thick-ness (along fracture; mm)	Length (sum of spacing; m)	Fracture count							Style		Con-fined in bed?	Distance of fracture tip to bedding plane (mm)		
										Top	Base		Top	Base	
1-a - nodular	110	0.364	5	P	V	90	F - calcite	100	1.4	3	1	Y	0	-10	mudstone
1-a - nodular	105	0.364		P	V	90	F - calcite	115	0.75	2	1	N	-30	40	mudstone
1-a - nodular	65	0.364		P	V	90	F - calcite	55	0.75	3	2	Y	0	-10	mudstone
1-a - nodular	80	0.364		P	V	90	F - calcite	50	0.95	3	1	Y	0	-30	mudstone
1-a - nodular	70	0.364		P	V	90	F - calcite	15	0.5	3	1	Y	0	-55	mudstone
1-b - nodular	135	0.536	7	P	V	90	F - calcite	133	1.4	1	?	N	-10	8	mudstone
1-b - nodular	65	0.536		P	V	90	F - calcite	65	0.75	3	3	Y	0	0	mudstone
1-b - nodular	45	0.536		P	V	90	F - calcite	63	1.15	3	1	Y	0	-18	mudstone
1-b - nodular	45	0.536		P	V	90	F - calcite	27	0.4	2	2	N	20	-38	mudstone
1-b - nodular	50	0.536		P	V	90	F - calcite	50	0.5	3	3	Y	0	0	mudstone
1-b - nodular	10	0.536		P	V	90	F - calcite	22	0.5	3	1	Y	0	-18	mudstone
1-b - nodular	35	0.536		P	V	90	F - calcite	25	0.5	3	1	Y	0	-10	mudstone
2 - nodular	95	1.483	9	P	V	70 L	F - calcite	90	1.4	3	1	Y	0	5	mudstone

Layering/bedding		Scanline		Fracture type	Vertical or sub-vertical to layering/ bedding	Dip (angle, to the left or right)	Fully sealed? Mine-ralogy?	Height (mm)	Kine-matic aper-ture (mm)	Vertical termination					Lithology
# - Geo-metry	Thick-ness (along fracture; mm)	Length (sum of spacing; m)	Fracture count							Style		Con-fined in bed?	Distance of fracture tip to bedding plane (mm)		
										Top	Base		Top	Base	
2 - nodular	50	1.483		P	V	90	F - calcite	20	0.75	2	2	Y	-5	-25	mudstone
2 - nodular	55	1.483		P	V	90	F - calcite	30	0.75	2	3	Y	-25	0	mudstone
2 - nodular	70	1.483		P	V	80 L	F - calcite	70	1.15	3	3	Y	0	0	mudstone
2 - nodular	110	1.483		P	V	80 L	F - calcite	50	1.75	2	3	Y	-60	0	mudstone
2 - nodular	40	1.483		VE	V	90	F - calcite	40	1.75	3	3	Y	0	0	mudstone
2 - nodular	60	1.483		P	V	80 L	F - calcite	45	0.33	1	3	Y	-15	0	mudstone
2 - nodular	70	1.483		P	V	90	F - calcite	55	0.62	1	3	Y	-15	0	mudstone
2 - nodular	150	1.483		P	V	90	F - calcite	30	0.4	1	1	Y	-80	-40	mudstone
3 - planar	45	0.175	5	VE	V	90	F - calcite	15	0.95	3	1	Y	-2	-25	chert
3 - planar	45	0.175		VE	V	90	F - calcite	20	0.75	1	3	Y	-25	0	chert
3 - planar	45	0.175		VE	V	80 R	F - calcite	20	0.215	1	3	Y	-5	-20	chert
3 - planar	40	0.175		VE	V	80 R	F - calcite	14	0.265	1	1	Y	-3	-23	chert
3 - planar	70	0.175		VE	V	70 R	F - calcite	50	0.4	1	3	Y	-20	0	chert

Layering/bedding		Scanline		Fracture type	Vertical or sub-vertical to layering/ bedding	Dip (angle, to the left or right)	Fully sealed? Mine-ralogy?	Height (mm)	Kine-matic aper-ture (mm)	Vertical termination					Lithology
# - Geo-metry	Thick-ness (along fracture; mm)	Length (sum of spacing; m)	Fracture count							Style		Con-fined in bed?	Distance of fracture tip to bedding plane (mm)		
										Top	Base		Top	Base	
3 - nodular	107	0.076	3	VE	V	90	F - calcite	30	0.62	1	1	Y	-40	-37	chert
3 - nodular	Proble-matic Data	0.076		VE	V	90	F - calcite	Proble-matic Data	0.62	1	2	Y	Proble-matic Data		chert
3 - nodular	115	0.076		VE	V	90	F - calcite	90	0.62	1	3	Y	-25	0	chert
4 - nodular	110	0.49	7	VE	V	90	F - calcite	60	0.75	1	3	Y	-50	0	chert
4 - nodular	110	0.49		VE	V	90	F - calcite	65	0.4	1	3	Y	-45	0	chert
4 - nodular	60	0.49		VE	V	90	F - calcite	45	0.5	1	3	Y	-15	0	chert
4 - nodular	60	0.49		P	V	70 L	F - calcite	20	0.5	3	1	Y	0	-40	chert
4 - nodular	80	0.49		P	V	80 L	F - calcite	20	0.62	3	2	Y	0	-60	chert
4 - nodular	100	0.49		VE	V	80 R	F - calcite	60	4.5	2	1	Y	0	-40	chert
4 - nodular	110	0.49		P	V	90	F - calcite	45	1.15	3	1	Y	0	-65	chert
5 - nodular	75	Proble-matic Data	10	VE	V	90	F - calcite	25	0.33	1	3	Y	-45	-5	chert
5 - nodular	70			VE	V	90	F - calcite	70	0.265	3	3	Y	0	0	chert

Layering/bedding		Scanline		Fracture type	Vertical or sub-vertical to layering/ bedding	Dip (angle, to the left or right)	Fully sealed? Mine-ralogy?	Height (mm)	Kine-matic aper-ture (mm)	Vertical termination					Lithology
# - Geo-metry	Thick-ness (along fracture; mm)	Length (sum of spacing; m)	Fracture count							Style		Con-fined in bed?	Distance of fracture tip to bedding plane (mm)		
										Top	Base		Top	Base	
5 - nodular	100	Proble-matic Data		VE	V	90	F - calcite	50	0.265	3	1	Y	0	-50	chert
5 - nodular	110			VE	V	90	F - calcite	20	0.265	3	1	Y	0	-90	chert
5 - nodular	120			VE	V	90	F - calcite	45	0.265	3	1	Y	0	-75	chert
5 - nodular	130			VE	V	90	F - calcite	35	0.265	3	1	Y	0	-105	chert
5 - nodular	115			VE	V	90	F - calcite + qtz	100	0.75	3	1	Y	0	-15	chert
5 - nodular	115			P	SV	50 R	F - calcite	75	0.4	1	1	Y	-5	-35	chert
5 - nodular	120			P	SV	50 R	F - calcite	120	0.5	3	3	Y	0	0	chert
5 - nodular	110			VE+P	SV	40 L	F - calcite	85	0.65	2	2	Y	-5	-20	chert
6 - nodular	90	0.25	4	P	V	90	F - calcite+qtz	90	0.95	3	3	Y	0	0	mudstone
6 - nodular	75	0.25		P	V	90	F - calcite	75	0.95	3	3	Y	0	0	mudstone
6 - nodular	80	0.25		P	V	90	F - calcite	80	1.15	3	3	Y	0	0	mudstone
6 - nodular	90	0.25		P	V	80 L	F - calcite+qtz	90	1.15	3	3	Y	0	0	mudstone
7 - nodular	70	0.332	7	VE	V	90	F - calcite	70	0.62	3	3	Y	0	0	chert

Layering/bedding		Scanline		Fracture type	Vertical or sub-vertical to layering/ bedding	Dip (angle, to the left or right)	Fully sealed? Mine-ralogy?	Height (mm)	Kine-matic aper-ture (mm)	Vertical termination					Lithology
# - Geo-metry	Thick-ness (along fracture; mm)	Length (sum of spacing; m)	Fracture count							Style		Con-fined in bed?	Distance of fracture tip to bedding plane (mm)		
										Top	Base		Top	Base	
7 - nodular	100	0.332		VE	V	80 L	F - calcite	50	0.5	1	1	Y	-30	-20	chert
7 - nodular	70	0.332		VE	V	30 L	F - calcite	70	0.75	3	3	Y	0	0	chert
7 - nodular	80	0.332		VE	V	90	F - calcite	40	0.215	3	1	Y	0	-40	chert
7 - nodular	70	0.332		VE	V	90	F - calcite	40	1.15	3	1	Y	0	-30	chert
7 - nodular	65	0.332		VE	V	90	F - calcite	30	1.15	3	1	Y	0	-35	chert
7 - nodular	90	0.332		VE	V	60 L	F - calcite	50	0.5	1	1	Y	-25	-15	chert
8 - nodular	100	0.317	9	P	V	90	F - calcite	40	0.4	1	1	Y	-20	-40	chert
8 - nodular	100	0.317		P	V	70 R	F - calcite	40	0.95	3	1	Y	-30	-30	chert
8 - nodular	100	0.317		VE	V	90	F - calcite	40	1.4	1	3	Y	-40	-20	chert
8 - nodular	80	0.317		VE	V	90	F - calcite	80	0.265	3	3	Y	0	0	chert
8 - nodular	105	0.317		P	V	90	F - calcite	100	0.15	2	3	Y	-5	0	chert
8 - nodular	100	0.317		VE	V	90	F - calcite	35	0.62	1	3	Y	-65	0	chert
8 - nodular	130	0.317		P	V	90	F - calcite	90	4	1	2	Y	-10	-30	chert

Layering/bedding		Scanline		Fracture type	Vertical or sub-vertical to layering/ bedding	Dip (angle, to the left or right)	Fully sealed? Mine-ralogy?	Height (mm)	Kine-matic aper-ture (mm)	Vertical termination					Lithology
# - Geo-metry	Thick-ness (along fracture; mm)	Length (sum of spacing; m)	Fracture count							Style		Con-fined in bed?	Distance of fracture tip to bedding plane (mm)		
										Top	Base		Top	Base	
8 - nodular	115	0.317		P+VE	V	90	F - calcite	105	1.4	1	3	Y	-10	0	chert
8 - nodular	125	0.317		P+VE	V	90	F - calcite	105	0.5	1	3	Y	-20	0	chert
9-a - planar	90	0.393	12	P	V	90	F - calcite	75	2.65	3	2	Y	0	-15	chert
9-a - planar	110	0.393		VE	SV	50 L	F - calcite	70	0.5	3	2	Y	0	-40	chert
9-a - planar	105	0.393		P+VE	V	90	F - calcite	75	0.95	3	1	Y	0	-30	chert
9-a - planar	110	0.393		P	V	90	F - calcite	45	0.5	3	1	Y	0	-65	chert
9-a - planar	115	0.393		P	SV	50 R	F - calcite+qtz	55	1.15	2	1	Y	-20	-40	chert
9-a - planar	60	0.393		P	SV	20 R	F - calcite+qtz	25	3.3	1	3	Y	-35	0	chert
9-a - planar	60	0.393		VE	SV	40 R	F - calcite	40	0.5	1	1	Y	-10	-10	chert
9-a - planar	60	0.393		VE	V	90	F - calcite	25	0.95	1	2	Y	-10	-25	chert
9-a - planar	60	0.393		P	V	90	F - calcite	40	0.95	1	3	Y	-20	0	chert
9-a - planar	60	0.393		P	V	90	F - calcite	45	0.265	1	3	Y	-15	0	chert
9-a - planar	60	0.393		VE	V	90	F - calcite	50	0.175	1	3	Y	-10	0	chert

Layering/bedding		Scanline		Fracture type	Vertical or sub-vertical to layering/ bedding	Dip (angle, to the left or right)	Fully sealed? Mine-ralogy?	Height (mm)	Kine-matic aper-ture (mm)	Vertical termination					Lithology
# - Geo-metry	Thick-ness (along fracture; mm)	Length (sum of spacing; m)	Fracture count							Style		Con-fined in bed?	Distance of fracture tip to bedding plane (mm)		
										Top	Base		Top	Base	
9-a - planar	60	0.393		VE	V	90	F - calcite	45	0.265	1	3	Y	-15	0	chert
9-b - nodular	100	0.228	11	VE	V	80 R	F - calcite	50	0.33	1	3	Y	-50	0	chert
9-b - nodular	105	0.228		P	V	80 L	F - calcite	105	3.3	3	3	Y	0	0	chert
9-b - nodular	100	0.228		VE	V	90	F - calcite	80	0.265	1	1	Y	-15	-5	chert
9-b - nodular	100	0.228		P	V	90	F - calcite	30	0.265	1	1	Y	-10	-60	chert
9-b - nodular	100	0.228		P	V	90	F - calcite	25	0.265	1	1	Y	-5	-70	chert
9-b - nodular	100	0.228		P	V	90	F - calcite	70	0.265	1	1	Y	-10	-20	chert
9-b - nodular	100	0.228		P	V	90	F - calcite	100	0.265	3	3	Y	0	0	chert
9-b - nodular	100	0.228		P	V	90	F - calcite	130	0.265	1	3	N	30	0	chert
9-b - nodular	110	0.228		P	V	90	F - calcite	110	0.265	3	3	Y	0	0	chert
9-b - nodular	100	0.228		P	V	90	F - calcite	70	0.265	1	1	Y	-10	-20	chert
9-b - nodular	110	0.228		VE	V	90	F - calcite	?	1.4	?	2	Y	?	-10	chert
10 - nodular	210	0.126	9	P	SV	40 R	F - calcite	20	0.75	1	3	Y	-190	0	chert

Layering/bedding		Scanline		Fracture type	Vertical or sub-vertical to layering/ bedding	Dip (angle, to the left or right)	Fully sealed? Mine-ralogy?	Height (mm)	Kine-matic aper-ture (mm)	Vertical termination					Lithology
# - Geo-metry	Thick-ness (along fracture; mm)	Length (sum of spacing; m)	Fracture count							Style		Con-fined in bed?	Distance of fracture tip to bedding plane (mm)		
										Top	Base		Top	Base	
10 - nodular	210	0.126		P+S	V	80 L	F - calcite	110	0.33	1	3	Y	-100	0	chert
10 - nodular	210	0.126		P	V	80 L	F - calcite	95	0.62	1	1	Y	-115	-5	chert
10 - nodular	210	0.126		VE	V	80 L	F - calcite	55	0.33	1	2	Y	-120	-35	chert
10 - nodular	210	0.126		VE	V	80 L	F - calcite	12	0.215	1	2	Y	-128	-70	chert
10 - nodular	210	0.126		P	V	80 L	F - calcite	20	0.33	1	2	Y	-120	-70	chert
10 - nodular	210	0.126		P	V	80 L	F - calcite	15	0.33	2	2	Y	-145	-50	chert
10 - nodular	210	0.126		P	V	80 L	F - calcite	80	0.33	1	3	Y	-130	0	chert
10 - nodular	210	0.126		P	V	80 L	F - calcite	110	0.175	1	3	Y	-100	0	chert
11 - nodular	150	0.148	4	P	V	90	F - calcite	95	0.265	1	1	Y	-15	-40	chert
11 - nodular	200	0.148		P	V	90	F - calcite	120	0.75	1	1	Y	-40	-40	chert
11 - nodular	190	0.148		P	V	90	F - calcite	60	0.75	1	1	Y	-60	-70	chert
11 - nodular	190	0.148		P	V	90	F - calcite	25	0.75	1	1	Y	-60	-105	chert
12 - nodular	190	0.8	5	P	V	80 L	F - calcite	30	0.75	1	3	Y	-160	0	mudstone

Layering/bedding		Scanline		Fracture type	Vertical or sub-vertical to layering/ bedding	Dip (angle, to the left or right)	Fully sealed? Mine-ralogy?	Height (mm)	Kine-matic aper-ture (mm)	Vertical termination					Lithology
# - Geo-metry	Thick-ness (along fracture; mm)	Length (sum of spacing; m)	Fracture count							Style		Con-fined in bed?	Distance of fracture tip to bedding plane (mm)		
										Top	Base		Top	Base	
12 - nodular	200	0.8		P	V	80 L	F - calcite	45	0.95	1	3	Y	-155	0	mudstone
12 - nodular	100	0.8		P	V	90	F - calcite	50	0.5	1	3	Y	-50	0	mudstone
12 - nodular	150	0.8		P	V	90	F - calcite	130	1.4	1	3	Y	-20	0	mudstone
12 - nodular	170	0.8		P	V	80 R	F - calcite	105	3.3	2	2	Y	-50	-15	mudstone
13 - nodular	170	0.04	2	P	V	80 R	F - calcite	40	0.62	1	3	Y	-130	0	mudstone
13 - nodular	180	0.04		P	V	90	F - calcite	40	1.4	1	3	Y	-140	0	mudstone
15 - planar	80	0.37	2	P	V	90	F - calcite	80	6.5	3	3	Y	0	0	mudstone
15 - planar	70	0.37		P	V	80 R	F - calcite	52	2.65	2	2	Y	-15	-3	mudstone
16 - nodular	65	0.263	7	VE	V	80 R	F - calcite	57	1.4	3	2	Y	0	-8	chert
16 - nodular	75	0.263		P	V	90	F - calcite	55	0.5	1	1	Y	-5	-15	chert
16 - nodular	75	0.263		VE	V	90	F - calcite	35	0.33	3	1	Y	0	-40	chert
16 - nodular	70	0.263		DE	V	90	F - calcite	17	7	3	1	Y	0	-53	chert
16 - nodular	70	0.263		VE	V	90	F - calcite	25	0.33	3	1	Y	0	-45	chert

Layering/bedding		Scanline		Fracture type	Vertical or sub-vertical to layering/ bedding	Dip (angle, to the left or right)	Fully sealed? Mine-ralogy?	Height (mm)	Kine-matic aper-ture (mm)	Vertical termination					Lithology
# - Geo-metry	Thick-ness (along fracture; mm)	Length (sum of spacing; m)	Fracture count							Style		Con-fined in bed?	Distance of fracture tip to bedding plane (mm)		
										Top	Base		Top	Base	
16 - nodular	65	0.263		DE	V	90	F - calcite	20	4	1	1	Y	-40	-5	chert
16 - nodular	65	0.263		DE	V	90	F - calcite	40	3.3	3	1	Y	0	-25	chert
17 - nodular	170	1.397	6	P	V	90	F - calcite	65	2.65	1	1	Y	-80	-25	mudstone
17 - nodular	130	1.397		P	V	90	F - calcite	65	5	1	3	Y	-65	0	mudstone
17 - nodular	110	1.397		P	V	90	F - calcite+qtz	110	0.75	3	3	Y	0	0	mudstone
17 - nodular	105	1.397		P	V	90	F - calcite	105	2.65	3	3	Y	0	0	mudstone
17 - nodular	130	1.397		P	V	70 R	F - calcite	70	2.65	2	2	Y	-30	-30	mudstone
17 - nodular	125	1.397		P	V	70 R	F - calcite+qtz	50	1.75	1	1	Y	-65	-10	mudstone
18 - nodular	50	0.389	18	VE	V	90	F - calcite	35	0.4	1	1	Y	-5	-10	chert
18 - nodular	55	0.389		P	V	90	F - calcite	13	0.215	3	1	Y	0	-42	chert
18 - nodular	55	0.389		VE	V	90	F - calcite	10	0.5	3	2	Y	0	-45	chert
18 - nodular	55	0.389		P	V	70 R	F - calcite	30	0.265	3	1	Y	0	-25	chert
18 - nodular	55	0.389		P	V	80 R	F - calcite	25	0.265	3	1	Y	0	-30	chert

Layering/bedding		Scanline		Fracture type	Vertical or sub-vertical to layering/ bedding	Dip (angle, to the left or right)	Fully sealed? Mine-ralogy?	Height (mm)	Kine-matic aper-ture (mm)	Vertical termination					Lithology
# - Geo-metry	Thick-ness (along fracture; mm)	Length (sum of spacing; m)	Fracture count							Style		Con-fined in bed?	Distance of fracture tip to bedding plane (mm)		
										Top	Base		Top	Base	
18 - nodular	50	0.389		P	V	90	F - calcite	25	0.265	3	1	Y	0	-25	chert
18 - nodular	55	0.389		P	V	90	F - calcite	55	0.4	3	3	Y	0	0	chert
18 - nodular	55	0.389		P	V	90	F - calcite	30	0.265	3	1	Y	0	-25	chert
18 - nodular	50	0.389		P	V	90	F - calcite	30	0.4	1	1	Y	-10	-10	chert
18 - nodular	45	0.389		P	V	90	F - calcite	30	0.265	1	1	Y	-10	-5	chert
18 - nodular	45	0.389		P	V	90	F - calcite	32	0.265	1	1	Y	-10	-3	chert
18 - nodular	45	0.389		P	V	90	F - calcite	35	0.265	3	1	Y	-5	-5	chert
18 - nodular	50	0.389		P	V	90	F - calcite	30	0.33	1	3	Y	-20	0	chert
18 - nodular	50	0.389		P	V	90	F - calcite	10	0.14	1	1	Y	-30	-10	chert
18 - nodular	70	0.389		P	V	90	F - calcite	15	0.75	1	1	Y	-45	-10	chert
18 - nodular	80	0.389		P	SV	50 R	F - calcite	30	0.4	1	1	Y	-40	-10	chert
18 - nodular	85	0.389		P	V	90	F - calcite	45	0.75	1	3	Y	-40	0	chert
18 - nodular	100	0.389		VE	V	90	F - calcite	45	0.4	1	1	Y	-25	-30	chert

Layering/bedding		Scanline		Fracture type	Vertical or sub-vertical to layering/ bedding	Dip (angle, to the left or right)	Fully sealed? Mine-ralogy?	Height (mm)	Kine-matic aper-ture (mm)	Vertical termination					Lithology
# - Geo-metry	Thick-ness (along fracture; mm)	Length (sum of spacing; m)	Fracture count							Style		Con-fined in bed?	Distance of fracture tip to bedding plane (mm)		
										Top	Base		Top	Base	
19 - nodular	80	0.135	4	P	V	90	F - calcite	10	0.33	3	1	Y	0	-70	mudstone
19 - nodular	80	0.135		P	V	90	F - calcite	80	1.4	1	3	Y	0	0	mudstone
19 - nodular	80	0.135		P	V	90	F - calcite+qtz	50	0.62	1	1	Y	-25	-5	mudstone
19 - nodular	85	0.135		P	V	80 R	F - calcite	30	0.4	1	3	Y	-5	-50	mudstone
20 - nodular	100	0.278	6	P	V	80 L	F - calcite+qtz	45	1.15	3	1	Y	0	-55	chert
20 - nodular	130	0.278		P	V	80 L	F - calcite	45	2.15	1	3	Y	0	-85	chert
20 - nodular	140	0.278		P	V	80 L	F - calcite	60	1.5	2	1	Y	-35	-45	chert
20 - nodular	145	0.278		P	V	90	F - calcite	45	0.265	1	3	Y	-100	0	chert
20 - nodular	125	0.278		P	V	70 L	F - calcite	65	2.15	2	2	Y	-45	-15	chert
20 - nodular	90	0.278		P	SV	40 L	F - calcite	55	0.95	1	3	Y	-35	0	chert
21 - nodular	80	0.08	4	P	V	90	F - calcite	45	0.62	3	2	Y	0	-35	chert
21 - nodular	83	0.08		VE	V	90	F - calcite	25	0.095	1	1	Y	-18	-40	chert
21 - nodular	80	0.08		P	V	90	F - calcite	50	0.62	1	3	Y	-15	-15	chert

Layering/bedding		Scanline		Fracture type	Vertical or sub-vertical to layering/ bedding	Dip (angle, to the left or right)	Fully sealed? Mine-ralogy?	Height (mm)	Kine-matic aper-ture (mm)	Vertical termination					Lithology
# - Geo-metry	Thick-ness (along fracture; mm)	Length (sum of spacing; m)	Fracture count							Style		Con-fined in bed?	Distance of fracture tip to bedding plane (mm)		
										Top	Base		Top	Base	
21 - nodular	90	0.08		P	V	90	F - calcite+qtz	75	?	1	3	Y	-15	0	chert
22 - nodular	155	0.899	8	P	V	80 R	F - calcite+qtz	105	1.4	1	1	Y	-15	-5	mudstone
22 - nodular	105	0.899		P	V	80 R	F - calcite	90	?	1	1	Y	-10	-5	mudstone
22 - nodular	175	0.899		P	V	80 R	F - calcite	85	1.15	1	1	Y	-75	-15	mudstone
22 - nodular	105	0.899		P	V	80 R	F - calcite	97	4	3	1	Y	0	-8	mudstone
22 - nodular	100	0.899		P	V	80 R	F - calcite+qtz	60	0.215	1	1	Y	-20	-20	mudstone
22 - nodular	100	0.899		P	V	80 R	F - calcite	60	0.33	1	1	Y	-35	-5	mudstone
22 - nodular	85	0.899		P	V	80 R	F - calcite	75	?	2	2	Y	-5	-5	mudstone
22 - nodular	110	0.899		P	V	80 R	F - calcite	90	1.75	1	1	Y	-5	-15	mudstone
23 - nodular	35	0.471	14	P	SV	30 R	F - calcite	27	0.75	?	1	?	?	-3	chert
23 - nodular	45	0.471		P	V	90	F - calcite	38	0.62	?	3	?	?	0	chert
23 - nodular	30	0.471		VE	V	80 R	F - calcite	15	0.95	?	1	?	?	-5	chert
21 - nodular	90	0.08		P	V	90	F - calcite+qtz	75	?	1	3	Y	-15	0	chert

Layering/bedding		Scanline		Fracture type	Vertical or sub-vertical to layering/ bedding	Dip (angle, to the left or right)	Fully sealed? Mine-ralogy?	Height (mm)	Kine-matic aper-ture (mm)	Vertical termination					Lithology
# - Geo-metry	Thick-ness (along fracture; mm)	Length (sum of spacing; m)	Fracture count							Style		Con-fined in bed?	Distance of fracture tip to bedding plane (mm)		
										Top	Base		Top	Base	
23 - nodular	50	0.471		P	V	80 R	F - calcite	25	0.4	2	1	Y	-20	-5	chert
23 - nodular	90	0.471		VE	V	80 R	F - calcite	40	0.33	?	3	?	?	-25	chert
23 - nodular	90	0.471		VE	V	90	F - calcite	40	0.33	?	3	?	?	-25	chert
23 - nodular	95	0.471		VE	V	90	F - calcite	12	0.33	1	1	Y	-38	-45	chert
23 - nodular	100	0.471		P	V	70 R	F - calcite	30	1.15	1	1	Y	-55	-15	chert
23 - nodular	100	0.471		P	V	90	F - calcite	30	0.62	1	1	Y	-55	-15	chert
23 - nodular	105	0.471		VE	V	90	F - calcite	18	0.95	2	3	Y	-87	0	chert
23 - nodular	110	0.471		P	V	90	F - calcite	45	0.75	1	1	Y	-40	-25	chert
23 - nodular	110	0.471		P	V	90	F - calcite	98	0.75	3	2	Y	0	-12	chert
23 - nodular	110	0.471		P	V	90	F - calcite	55	0.95	2	1	Y	-10	-45	chert
23 - nodular	105	0.471		P	V	90	F - calcite	55	?	?	?	?	-15	-35	chert
24 - nodular	120	0.133	3	P	V	90	F - calcite	40	2.65	2	2	Y	-3	-77	mudstone
24 - nodular	65	0.133		P	V	90	F - calcite	45	2.15	2	2	Y	0	-20	mudstone

Layering/bedding		Scanline		Fracture type	Vertical or sub-vertical to layering/ bedding	Dip (angle, to the left or right)	Fully sealed? Mine-ralogy?	Height (mm)	Kine-matic aper-ture (mm)	Vertical termination					Lithology
# - Geo-metry	Thick-ness (along fracture; mm)	Length (sum of spacing; m)	Fracture count							Style		Con-fined in bed?	Distance of fracture tip to bedding plane (mm)		
										Top	Base		Top	Base	
24 - nodular	65	0.133		P	V	90	F - black mud	50	0.115	2	2	Y	-5	-10	mudstone

APPENDICES

APPENDIX 4

Rebound Hardness (RHN) Data – MISS/STACK Cores, Outcrop Samples, and Vaca Muerta Plug Samples

Core #1 – Rebound hardness data

Depth (ft)	Average RHN	Individual RHN Measurements				
4481.5	578	596	577	576	568	573
4481.15	709	725	696	697	702	725
4480.5	714	716	703	715	734	701
4479.4	763	755	788	749	765	757
4479.3	550	558	546	538	552	557
4478.5	548	542	559	548	550	543
4477.2	610	610	620	616	602	603
4476.4	621	624	601	630	632	617
4473.5	632	623	642	623	633	641
4472.3	678	667	677	673	683	688
4471.3	710	713	716	712	698	713
4470.65	664	663	665	665	665	663
4469.3	580	583	568	598	569	581
4468.4	559	563	560	546	576	548
4467.35	692	694	691	703	673	698
4466.85	824	813	836	816	817	840
4465.84	692	694	695	674	694	702
4465.75	675	681	691	666	670	667
4465.7	661	661	648	662	650	683
4465.62	673	689	669	669	661	678
4465.47	661	653	665	664	659	666
4465.35	698	694	693	698	707	697
4465.15	683	663	671	665	713	704
4464.15	718	714	723	713	724	714
4463.9	697	696	702	688	695	705
4463.7	714	710	720	712	715	712
4463.6	721	718	722	713	747	705
4463.5	707	702	709	703	718	704
4463.4	684	666	688	688	695	684
4463.22	681	682	684	688	672	680
4460.3	667	659	676	678	661	663
4458.6	644	651	629	649	656	634
4457.35	584	597	570	575	583	596
4456.5	693	686	691	696	700	694
4455.35	608	597	634	607	599	603
4454.35	672	685	672	673	664	668
4453.2	700	700	708	694	703	694
4452.5	649	633	653	660	651	649
4451.4	693	696	702	694	689	682
4450.1	703	703	702	704	705	703
4447.6	666	669	666	658	668	668
4447.35	706	716	694	697	710	712
4447.29	660	668	666	650	649	666
4447.2	653	658	643	664	645	657

Depth (ft)	Average RHN	Individual RHN Measurements				
4446.8	685	685	693	692	671	684
4446.65	823	824	830	820	812	827
4446.55	674	685	678	667	668	672
4446.45	720	727	723	719	713	720
4446.1	675	672	685	674	668	676
4445.92	666	674	662	672	666	654
4445.85	661	676	647	658	669	656
4444.8	754	773	743	773	729	752
4443.6	731	738	733	732	722	732
4443.5	712	724	705	714	703	715
4443.25-left	742	750	737	737	740	748
4443.25-right	784	776	796	773	777	800
4443.24	786	787	784	786	776	798
4442.84	761	761	761	752	770	760
4442.8	803	793	803	806	813	801
4442.72	913	917	915	911	913	909
4442.65	808	788	797	812	832	810
4441.25	828	823	833	824	832	826
4440.4	708	711	702	704	715	706
4440.25	802	785	807	807	804	805
4440.2	693	696	687	693	700	689
4440.1	776	787	768	773	781	773
4440.05	748	744	747	765	743	742
4439.95	743	737	754	740	745	741
4439.8	737	719	744	753	721	748
4438.25	775	797	795	768	761	756
4438.18	769	757	780	787	752	770
4436.3	734	735	733	743	726	732
4436.2	786	779	788	784	784	793
4436.15	788	792	786	787	794	783
4434	807	809	809	799	814	804
4432.8	758	754	770	755	754	757
4432.58	789	799	781	784	796	783
4432.51	793	795	786	799	793	790
4432.45	684	695	694	662	675	693
4432.3	697	700	705	686	702	693
4429.1	639	658	632	636	631	638
4426.2	833	829	823	837	839	837
4424.9	793	802	777	797	797	794
4424.75	796	789	795	801	797	799
4424.65	773	777	770	763	775	782
4423.9	753	763	755	756	742	750
4422.68	785	799	782	786	786	774
4422.6	747	736	739	754	778	730

Depth (ft)	Average RHN	Individual RHN Measurements				
4422.5	697	696	714	692	690	692
4422.45	744	754	748	737	748	733
4422.38	748	764	748	744	736	749
4421.5	690	686	705	694	686	678
4420.4	706	716	704	707	693	708
4420.1	791	802	771	805	786	
4420	859	853	861	861	861	861
4419.9	785	786	780	781	785	793
4419.78	720	711	718	716	722	732
4419.65	761	752	763	748	751	790
4417.7	727	729	722	720	737	725
4416.2	705	704	714	691	691	727
4414.7	788	784	791	783	794	786
4414.6	777	784	753	783	790	774
4411.3	719	717	716	721	727	714
4408.1	880	886	865	880	883	887
4407.1	808	794	814	814	810	806
4405.5	734	740	727	724	751	728
4404.1	747	740	743	750	744	756
4403.65	620	610	630	603	635	623
4402.65	764	769	759	756	768	769
4402.55	809	815	810	809	803	809
4402.42	814	822	814	817	797	819
4402.35	815	816	821	821	797	820
4402.29	711	710	706	717	715	709
4401.2	836	837	842	843	829	830
4399.75	776	773	777	784	774	772
4399.56	746	739	755	739	756	739
4398.5	708	689	709	709	721	710
4396.6	853	857	847	866	856	839
4396.5	772	770	778	782	761	770
4396.43	821	830	815	836	823	800
4396.3	765	761	769	756	765	772
4395.85	729	735	726	724	731	727
4389.5	746	743	746	752	754	737
4388.1	745	750	738	748	739	752
4385.3	713	712	717	713	711	710
4384.7	706	699	710	709	702	710
4382.3	776	766	784	773	776	783
4380.75	820	813	816	825	824	821
4380	737	741	743	734	735	731
4377.57	694	700	688	701	697	684
4377.53	753	744	760	751	753	758
4377.45	738	731	752	738	745	726
4377.35	722	715	710	731	731	722

Depth (ft)	Average RHN	Individual RHN Measurements				
4377.28	752	755	764	760	741	739
4377.15	715	723	702	721	726	705
4375.72	686	698	689	675	682	684
4375.67	703	674	705	684	724	727
4375.63	674	675	676	678	668	672
4375.6	754	743	757	757	758	756
4375.55	682	696	671	672	691	678
4375.49	748	740	747	760	755	737
4375.45	669	668	675	666	661	673
4373.3	728	734	725	722	726	735
4372.48	732	728	729	732	728	741
4372.41	819	835	810	819	809	823
4372.39	626	625	620	629	625	630
4372.32	806	793	824	816	797	802
4371.4	831	830	827	837	831	831
4370.4	660	661	665	658	658	658
4369.8	752	770	746	739	757	750
4368.1	823	820	824	820	821	831
4367.2	597	607	587	597	592	600
4366.65	629	637	623	625	631	627
4365.3	645	651	643	636	642	651
4364.48	660	653	657	661	668	661
4364.41	643	637	636	638	649	654
4364.34	594	604	588	595	594	587
4364.15	632	633	617	635	638	636
4363.3	622	623	621	616	616	634
4362.35	741	736	737	738	747	748
4361.7	717	722	722	708	699	732
4358.1	699	711	686	706	712	681
4356.3	672	669	673	682	677	658
4354.3	722	716	722	723	720	727
4353.9	761	760	769	763	760	754
4353.72	774	777	779	771	770	774
4353.6	738	727	737	738	740	748
4353.45	760	764	761	761	756	758
4352.88	719	701	728	720	717	729
4352.84	742	734	729	745	753	748
4352.8	739	748	741	732	744	729
4352.68	728	725	726	727	730	733
4352.6	741	724	759	752	750	718
4352.02	682	674	674	701	688	673
4350.55	718	719	731	718	708	715
4349.9	703	714	719	697	683	701
4349.4	705	711	707	700	698	707
4346.6	730	720	723	728	740	738

Depth (ft)	Average RHN	Individual RHN Measurements				
4345.7	723	713	717	732	721	730
4345.62	744	735	756	756	741	734
4345.56	696	696	685	722	692	686
4345.5	698	678	708	701	703	702
4344.3	719	717	724	723	716	717
4343.25	712	724	703	709	713	712
4341.25	704	705	714	704	707	688
4340.95	724	739	722	714	722	721
4340.7	783	773	787	783	785	788
4340.62	701	691	699	704	705	707
4340.58	694	693	698	697	700	684
4340.55	656	651	662	658	650	657
4340.25	729	731	732	724	727	732
4339.7	707	712	688	704	710	721
4339.5	702	710	704	698	691	708
4338.3	350	354	370	354	343	330
4337.85	656	675	651	647	656	650

Core #2 – Rebound hardness data

Depth (ft)	Average RHN	Individual RHN Measurements				
5313.75	520	506	509	520	519	545
5313.1	528	546	519	522	535	517
5312.9	610	588	638	590	604	628
5312.65	591	616	573	575	595	595
5310.25	757	761	757	752	755	758
5309.6	702	690	702	696	716	705
5308.9	733	744	719	722	737	744
5308.5	730	731	726	725	728	739
5308.35	725	722	709	734	740	722
5308.25	717	726	707	714	719	718
5308.15	742	744	747	745	743	731
5306.5	789	786	788	784	798	790
5305.35	733	749	734	729	727	724
5302.9	789	790	793	779	800	784
5301	741	733	732	742	733	766
5298.45	762	758	754	770	764	766
5296.7	757	762	761	749	757	756
5294.2	740	739	739	741	739	741
5293.2	747	747	749	746	748	746
5292.6	645	624	636	659	642	665
5292.35	438	435	424	434	445	453
5290.5	689	699	688	691	690	676
5289.55	652	665	639	667	641	649
5288.5	692	702	687	693	677	701
5287.2	702	700	703	705	708	693
5285.55	713	724	722	712	700	706
5283.2	725	727	723	727	723	726
5282.5	669	679	651	696	663	655
5281.4	674	672	678	656	673	693
5281.15	718	725	721	712	718	712
5280.9	739	725	736	723	743	770
5280.72	754	740	758	770	744	756
5280.55	694	691	696	682	696	705
5279.85	718	721	721	723	703	720
5278.4	743	740	739	745	743	748
5277.8	720	720	723	715	724	720
5277.4	707	713	700	708	711	702
5277.16	672	676	643	686	681	673
5276.2	707	701	706	714	708	706
5275.3	729	739	737	726	723	722
5274.6	706	712	714	697	703	705
5272.4	725	718	712	733	726	737
5271.85	646	652	644	662	618	655
5271.78	782	790	790	768	779	782

Depth (ft)	Average RHN	Individual RHN Measurements				
5271.66	710	708	699	710	715	719
5271.6	686	688	696	677	680	691
5271.45	702	704	706	693	704	701
5271.25	758	765	762	759	753	751
5271.12	705	694	714	711	698	707
5270.92	586	589	582	591	583	583
5270.82	840	838	847	836	842	836
5270.74	709	704	718	696	717	709
5268.95	677	685	672	686	674	670
5268.6	749	739	762	760	728	754
5267.1	807	805	793	808	815	815
5265.4	813	801	813	815	816	820
5261.64	671	665	676	662	683	667
5261.55	818	805	832	815	831	808
5261.45	808	812	809	804	809	804
5260.35	746	737	758	740	741	755
5260.1	724	718	720	717	726	739
5258.5	701	705	691	694	704	712
5257.3	701	693	712	695	701	703
5255.2	706	702	699	703	713	714
5253.8	691	696	687	704	685	683
5251.2	730	731	739	730	720	729
5249.75	750	741	749	747	752	762
5249.3	639	635	646	647	642	626
5249.15	664	663	671	668	638	679
5248.9	619	619	632	609	630	607
5248.8	620	635	607	603	632	622
5248.7	664	666	667	655	665	665
5248.5	701	700	700	694	706	703
5247.5	746	745	747	745	748	744
5247.43	733	734	733	729	733	734
5247.38	729	741	725	721	728	729
5247.33	728	713	750	737	726	712
5247.28	750	741	746	754	763	748
5247.15	772	777	775	768	774	765
5247.1	760	742	766	758	775	758
5244.35	781	786	776	783	788	774
5244.3	711	711	710	705	730	701
5244.25	823	822	825	828	826	815
5243.9	813	824	820	814	806	803
5243.75	749	740	751	759	753	741
5243.45	717	717	724	726	706	711
5242.85	729	731	739	703	734	737
5241.2	731	724	730	735	721	746
5240.2	726	726	708	730	754	714

Depth (ft)	Average RHN	Individual RHN Measurements				
5238.65	730	726	730	719	742	731
5237	755	755	762	763	761	735
5234.6	801	798	807	793	797	811
5232.9	701	694	697	702	711	703
5230.91	771	770	773	762	765	783
5230.86	831	831	832	833	833	828
5230.8	835	835	834	842	841	825
5230.72	832	825	836	833	836	832
5230.68	713	719	710	706	706	722
5229.75	736	727	742	740	733	738
5229.35	767	763	768	764	764	774
5228.55	721	747	716	697	715	729
5227.28	747	751	739	774	719	750
5227.23	791	794	792	791	791	787
5227.2	809	805	794	812	820	815
5227.13	635	631	632	644	652	616
5227.1	652	657	659	646	639	659
5225.5	725	730	730	718	721	724
5224.97	796	783	804	802	783	806
5224.87	630	631	631	634	627	627
5224.82	712	707	690	716	720	728
5224.8	798	789	799	806	793	805
5222.85	801	807	804	800	802	793
5220.8	725	712	727	733	726	728
5219.75	741	738	743	753	732	741
5217.7	742	742	744	733	758	734
5215.6	640	650	630	634	642	644
5213.4	728	727	729	732	730	720
5211.6	811	805	821	803	817	809
5209.5	725	727	726	719	729	726
5207.3	729	730	726	725	737	725
5205.5	777	770	774	784	768	791
5205.4	720	720	722	721	726	709
5205.25	819	808	819	822	836	810
5205.11	679	688	688	669	680	671
5204.6	678	665	678	687	683	677
5203.75	663	650	678	649	669	671
5203.55	811	813	812	802	820	807
5203.4	666	677	650	669	667	667
5201.8	801	790	818	792	800	807
5201.7	843	854	826	844	854	839
5201.6	781	781	785	764	782	792
5201.5	686	695	684	685	690	677
5201.4	790	794	776	795	800	787
5201.38	695	714	717	692	681	670

Depth (ft)	Average RHN	Individual RHN Measurements				
5201.35	614	607	620	615	610	617
5200.85	581	591	572	590	589	563
5200.75	827	835	845	806	824	827
5200.55	671	667	658	691	665	676
5200.4	677	673	683	665	673	689
5200.1	602	592	603	616	587	613
5199.8	777	785	770	767	780	782
5199.55	823	795	837	822	821	840
5199.4	781	789	802	775	767	774
5198.75	780	780	777	776	789	778
5198.1	742	739	733	757	734	749
5197.95	829	828	818	834	821	842
5197.85	896	888	901	890	895	907
5197.78	872	874	880	877	865	866
5194.28	645	643	640	654	651	636
5194.23	658	654	658	663	655	662
5194.15	845	837	862	839	851	836
5193.95	864	864	868	863	862	862
5193.85	698	694	691	699	721	684
5191.5	634	635	629	636	645	625
5190.1	804	805	799	805	787	823
5185.7	693	684	693	695	692	701
5184.15	822	826	831	815	813	827
5182.25	806	817	801	804	806	800
5179.15	694	700	679	696	694	703
5178.7	690	675	696	692	697	690
5178.55	830	839	842	831	824	814
5178.45	669	659	666	697	670	654
5176.35	732	738	727	728	740	729
5173.9	799	803	808	782	798	805
5171.4	717	717	711	712	728	719
5170.15	787	776	796	789	786	787
5168.2	782	779	785	783	780	783
5167.5	747	737	756	739	756	745
5166.4	723	719	723	735	717	719
5165.3	679	680	685	678	666	684
5164.5	721	715	723	726	724	717
5163.45	700	702	697	696	703	703
5163.2	732	736	715	733	738	740
5161.93	731	727	724	738	734	731
5161.84	738	740	730	747	737	737
5161.7	763	765	745	761	776	770
5161.5	713	705	736	715	701	707
5161.4	727	727	724	722	728	732
5159.85	734	732	732	730	739	737

Depth (ft)	Average RHN	Individual RHN Measurements				
5157.25	589	587	595	570	610	581
5155.65	677	668	678	701	672	667
5154.9	623	628	626	625	622	612
5153.9	641	651	641	657	630	625
5152.9	672	670	665	676	668	680
5152	715	713	716	718	717	711
5149.8	707	703	708	703	720	703
5149.55	757	761	761	757	761	744
5149.35	739	740	729	735	741	748
5149.15	744	738	747	745	742	750
5148.9	735	737	736	736	725	742
5148.7	741	739	732	746	744	745
5148.5	629	628	635	627	627	629
5148.43	760	769	766	754	764	748
5148.4	755	767	764	736	749	758
5146.8	733	737	732	739	735	723
5145.93	740	749	736	739	737	737
5145.9	759	759	761	765	758	754
5145.88	717	717	732	728	712	696
5145.86	809	797	814	812	812	812
5145.82	784	777	781	789	788	783
5145.78	752	755	754	755	745	752
5145.75	731	725	714	734	743	737
5145.68	718	712	723	715	718	721
5145.66	720	726	726	717	707	722
5145.64	729	729	726	725	733	734
5145.62	728	730	721	730	735	724
5145.59	741	749	739	743	725	750
5145.58	733	736	729	733	739	729
5145.57	733	726	732	739	725	743
5144.1	603	609	610	596	601	598
5143.7	618	628	613	618	615	617
5142.2	722	735	721	713	721	718
5139.8	713	703	715	729	708	712
5139.25	715	714	719	710	722	708
5139.15	729	738	721	722	727	736
5136.6	727	736	734	728	716	723
5135.5	764	763	767	769	762	760
5134.25	757	760	755	761	751	756
5132.75	744	738	743	739	749	750
5132.5	880	876	884	881	886	873
5132.25	797	789	800	805	788	802
5132.2	730	720	731	737	730	734
5132	751	753	746	749	753	755
5131.75	708	712	709	707	707	703

Depth (ft)	Average RHN	Individual RHN Measurements				
5130	745	741	740	749	748	746
5129.75	746	748	748	736	745	754
5129.3	774	776	774	784	771	766
5128.65	721	712	726	730	719	720
5128.55	724	719	719	725	731	728
5128.35	762	752	750	767	769	770
5128.2	793	783	791	796	788	805
5126.15	824	821	826	819	830	823
5125.5	773	778	767	768	776	777
5124.55	887	880	879	866	908	902
5124.45	864	863	852	872	874	860
5123.7	933	932	933	933	935	932
5123.55	909	914	894	918	909	910
5123.15	422	442	411	405	413	440

Core #3 – Rebound hardness data

Depth (ft)	Average RHN	Individual RHN Measurements				
5819.75	509	516	515	502	505	508
5819.65	531	538	540	537	522	517
5818.4	536	518	541	543	527	550
5817.5	539	553	538	526	543	533
5816.8	642	645	644	641	660	621
5816	786	791	786	787	788	776
5815.4	794	795	791	796	790	797
5814.8	729	723	723	722	739	740
5814.55	722	702	746	702	736	726
5814.4	718	728	714	710	724	716
5814.2	724	733	720	717	714	735
5814.05	789	790	796	791	785	783
5814	756	756	761	756	750	756
5813.6	712	709	713	713	717	707
5813.3	713	722	714	708	700	721
5813.25	693	688	691	682	723	681
5813.1	725	721	728	728	729	721
5812.5	764	760	767	770	760	763
5811.7	781	789	786	783	779	767
5811.4	747	759	731	749	741	756
5811.2	764	766	758	769	754	773
5810.7	738	731	733	763	733	730
5810.55	766	758	760	768	759	783
5810.45	888	865	909	897	865	906
5810.25	750	761	754	743	745	748
5810	723	728	723	731	729	703
5809.3	673	698	664	670	662	673
5809.1	672	680	672	678	669	660
5808.85	704	707	712	688	687	724
5808.75	738	733	737	732	751	737
5808.2	659	661	667	641	654	672
5808.1	674	667	685	683	664	672
5807.95	780	774	760	781	796	791
5807.75	708	707	710	696	716	709
5807.4	694	693	701	699	690	687
5807.3	675	678	700	674	657	668
5807.1	709	715	702	702	710	714
5804.8	814	816	817	802	817	818
5804.74	734	725	745	740	716	745
5803.6	757	754	758	756	754	764
5802.5	747	751	754	747	742	741
5801.3	711	697	731	723	697	705
5800.6	817	807	804	813	829	833
5800.4	872	861	864	883	869	881

Depth (ft)	Average RHN	Individual RHN Measurements				
5799.8	794	786	798	796	784	806
5799.72	748	748	740	759	749	744
5799.69	791	787	769	799	797	802
5799.5	779	777	788	781	772	775
5799.46	736	734	747	731	733	735
5798.8	743	717	756	750	750	744
5798.45	819	819	842	814	811	811
5798.25	689	712	682	670	674	709
5798	721	720	690	731	735	728
5797.85	735	730	753	708	744	742
5797.55	790	783	779	811	794	781
5797.42	841	853	847	829	845	833
5795.8	798	808	816	784	781	803
5794.9	762	775	742	752	769	770
5794.55	729	732	740	725	728	718
5794.35	910	898	906	910	919	915
5794.2	700	696	707	688	699	709
5793.9	901	897	904	894	900	909
5793.8	849	843	855	865	847	835
5793.45	782	810	772	788	770	768
5791.3	713	714	720	703	714	715
5790.6	713	706	699	718	715	725
5789.65	718	717	726	712	706	728
5789.45	792	805	771	805	786	792
5788.25	795	798	788	805	785	798
5787.5	791	793	793	789	784	794
5785.6	775	770	771	787	781	764
5783.8	750	749	733	767	761	739
5782.7	732	743	721	726	735	734
5781.3	780	770	777	792	793	766
5779.8	686	685	685	682	683	693
5778.5	764	753	760	774	763	769
5778.36	708	711	713	701	710	705
5778.2	716	716	693	735	718	720
5778.15	765	744	763	772	773	772
5775	781	774	787	767	782	797
5773	787	787	780	795	771	800
5771.3	748	743	752	742	753	748
5770.6	758	757	755	766	749	761
5769.2	760	769	759	763	741	766
5766.7	745	739	746	743	749	747
5765	750	750	745	749	755	750
5763.15	745	747	747	741	746	746
5760.6	734	735	723	738	737	738
5759.7	722	715	721	709	738	725

Depth (ft)	Average RHN	Individual RHN Measurements				
5759.5	737	735	735	742	737	737
5757.66	541	537	531	554	549	535
5757.3	551	545	549	537	560	565
5756.1	684	683	672	697	695	675
5755.5	681	673	686	684	673	687
5754.5	649	654	643	658	652	638
5753.7	711	715	711	708	707	716
5752.2	719	716	725	716	712	725
5751.65	710	713	704	713	707	711
5751.25	643	654	648	631	644	638
5750.6	697	699	698	702	694	692
5749.3	735	733	728	737	734	744
5748.5	624	622	624	629	631	616
5747.1	743	738	748	737	744	747
5746.87	704	697	701	727	699	698
5746.75	749	756	746	744	743	755
5746.65	752	739	759	757	754	753
5746.3	703	695	691	705	730	696
5745.4	703	701	705	703	706	701
5745.2	684	692	671	680	689	687
5745.1	712	712	694	718	724	714
5744.75	739	738	736	738	735	747
5744.4	712	713	714	712	710	710
5742.75	730	741	733	724	722	732
5742.65	732	742	731	715	724	749
5742.5	695	700	700	701	689	685
5741.5	722	701	722	737	723	726
5740.85	780	773	782	783	780	780
5740.75	738	754	735	720	740	740
5740.67	719	719	706	723	725	724
5740.6	662	660	652	680	657	662
5740.45	704	692	722	696	713	697
5738.9	688	694	690	689	686	682
5737.85	736	735	741	735	735	735
5736.5	703	700	704	701	706	702
5735	697	696	699	692	705	694
5733.5	689	702	694	680	682	689
5730.87	759	755	755	757	758	772
5730.8	804	824	800	813	785	798
5730.7	769	766	768	769	769	771
5729.8	794	801	791	790	795	795
5729.7	781	779	781	782	782	783
5729.6	801	799	789	808	805	805
5729.45	770	766	756	771	784	771
5728.9	776	759	777	797	762	785

Depth (ft)	Average RHN	Individual RHN Measurements				
5728.5	663	659	681	668	656	652
5728.2	666	661	668	665	652	684
5727.5	798	786	802	809	786	806
5727.15	777	771	769	788	786	772
5726.85	726	728	712	738	728	726
5726.7	806	811	802	803	800	813
5725.75	712	719	706	719	712	703
5723.22	654	656	663	631	662	656
5723.19	683	677	674	687	692	683
5723.1	723	722	725	720	717	729
5722.95	723	719	725	729	722	718
5722.65	721	722	714	716	723	730
5722.4	768	769	769	770	771	763
5722.1	671	679	668	672	669	668
5721.5	702	706	699	703	698	706
5720.95	739	741	726	756	731	739
5719.5	727	731	713	730	730	732
5719.25	704	721	701	697	705	697
5718.55	753	766	749	757	748	744
5717.5	741	727	744	744	735	755
5717.15	658	649	684	648	658	650
5716.2	662	651	666	665	659	671
5715.5	712	721	714	711	702	713
5713.8	791	788	798	784	792	792
5712.55	716	709	712	727	716	714
5711.6	701	704	702	698	701	702
5710.8	852	835	864	869	842	850
5710.5	568	587	560	547	582	565
5710.3	604	605	617	587	608	603
5709.65	869	897	852	871	844	881
5909.45	799	810	800	812	792	781
5709.25	687	685	687	681	681	701
5709.18	679	670	682	682	685	678
5709.1	684	684	684	682	679	692
5708.92	678	683	678	695	673	660
5708.7	753	752	743	757	757	756
5708.62	710	710	694	714	706	727
5708.55	740	752	742	742	741	723
5708.45	756	754	770	747	752	758
5707.5	818	822	825	812	815	817
5706.95	760	771	760	761	751	757
5706.9	824	831	822	823	830	815
5706.82	787	794	784	765	795	797
5706.75	772	767	778	751	782	780
5706.65	727	740	715	721	719	741

Depth (ft)	Average RHN	Individual RHN Measurements				
5705.75	636	622	645	633	633	646
5705.45	822	811	826	821	828	822
5705.3	635	623	614	651	638	649
5705	701	683	694	722	708	697
5704.7	615	608	617	597	615	636
5704.55	610	614	619	605	596	614
5704.4	887	892	881	885	894	881
5704.25	689	683	688	685	694	694
5703.3	693	684	678	715	706	684
5702.3	647	638	653	657	635	652
5701.65	709	706	706	725	703	704
5701.4	670	660	669	665	677	678
5700.3	752	739	759	758	757	745
5699.3	791	798	795	788	790	786
5698.7	744	733	728	771	752	734
5697.5	716	712	717	721	716	715
5696.8	761	755	763	763	762	764
5694.85	858	849	864	847	879	852
5693.75	870	885	851	873	871	871
5691.1	832	828	835	829	839	828
5689.25	788	780	788	797	787	789
5688.85	707	713	705	705	703	710
5688.72	819	814	825	819	818	821
5688.62	862	865	870	859	852	863
5688.55	864	865	855	874	867	858
5688.48	793	783	791	802	803	785
5687.5	808	803	812	810	813	800
5684.5	766	767	766	763	768	767
5683.4	799	791	790	801	806	807
5680.8	817	811	819	824	808	824
5679.7	777	782	767	782	776	776
5678.35	811	812	811	810	806	815
5676.7	713	706	719	719	711	709
5673.77	737	738	753	724	749	723
5673.74	786	793	788	783	788	778
5673.72	750	736	749	752	757	757
5673.66	690	682	693	688	690	699
5673.62	697	682	699	717	694	695
5673.25	799	794	811	805	791	795
5671.1	805	807	806	801	806	807
5669.7	816	811	806	822	817	822
5668.3	738	733	748	737	740	732
5666.7	724	775	719	697	714	717
5666.2	807	816	818	801	802	799
5665.4	787	782	786	788	794	785

Depth (ft)	Average RHN	Individual RHN Measurements				
5663.75	799	790	798	811	810	785
5661	792	793	797	792	791	788
5659	790	794	776	785	793	804
5657.1	788	785	790	790	787	790
5654.8	837	832	842	834	838	840
5653.5	747	753	750	750	735	747
5651.5	791	787	793	790	788	798
5649.8	787	785	788	786	788	788
5649.07	755	750	735	758	765	768
5648.65	782	805	784	773	777	772
5647.3	825	811	832	834	827	820
5646.65	766	763	771	770	770	758
5643.6	799	811	788	799	798	801
5641.8	754	755	756	755	756	750
5640	838	837	843	839	836	837
5638.5	738	736	732	736	739	747
5636.7	737	736	736	741	742	732
5636.66	778	761	783	773	787	788
5636.6	701	702	701	705	704	692
5636.4	694	695	689	692	686	706
5636.32	877	880	886	873	872	875
5636.26	704	707	710	695	700	710
5634.75	815	813	811	821	819	811
5634.72	805	801	800	804	813	808
5634.65	804	801	798	807	806	808
5634.53	773	775	771	774	774	773
5634.35	789	790	780	793	785	795
5633.45	787	783	788	791	787	788
5632.45	775	785	767	785	777	760
5631.9	739	731	748	733	731	754
5631.65	761	752	741	791	772	748
5631.5	768	767	762	778	770	762
5630.75	674	666	686	660	674	684
5629.55	682	679	685	676	684	686
5628.82	715	708	733	718	707	710
5628.76	784	790	763	787	793	787
5628.65	868	872	854	876	869	871
5628.5	816	805	822	806	837	812
5628.4	752	749	746	768	744	751
5628.24	746	733	758	740	746	752
5628.13	740	743	741	749	739	727
5627.72	708	701	705	715	697	724
5627.6	699	702	695	700	697	703
5627.45	704	692	710	708	701	709
5626.85	649	644	651	668	646	638

Depth (ft)	Average RHN	Individual RHN Measurements				
5626.75	643	636	639	648	642	650
5626.65	762	771	734	756	783	764
5626.6-left	823	824	798	829	837	827
5626.6-right	710	704	716	711	708	710
5626.5	828	826	824	828	827	833
5626.4	872	881	875	872	868	865
5626.15	752	751	755	764	749	743
5625.93	817	821	818	816	811	818
5625.84	762	765	766	755	767	757
5625.8	755	757	761	759	750	748
5625.74	765	756	760	771	770	766
5625.65	685	678	702	681	688	678
5625.52	728	718	706	726	763	725
5625.43	891	897	903	888	889	879
5625.3	734	737	735	717	747	736
5624.9	750	734	755	762	739	761
5624.75	680	671	667	678	705	679
5624.5	888	902	881	900	882	875
5624.35	673	673	665	675	678	674
5624.2	643	648	647	631	639	649
5624.1	857	866	851	860	852	857
5622.7	835	846	819	824	837	851
5622.45	800	796	801	793	800	811
5622.27	753	739	746	771	758	752
5622.15	722	727	727	715	715	727
5621.88	719	716	722	730	714	711
5621.6	844	850	853	844	834	837
5621.45	861	857	863	858	856	869
5621.25	648	643	658	651	653	636
5620.55	737	741	749	737	728	732
5619.9	815	818	822	811	823	800
5619.8	786	799	794	775	776	785
5617.8	751	748	759	759	743	746
5617.7	834	833	832	834	835	835
5615.5	683	678	677	690	684	687
5615.3	792	794	799	791	790	784
5614.7	787	783	789	780	798	786
5614.62	858	862	850	851	860	865
5614.55	786	785	786	788	784	788
5614.45	864	874	865	857	867	859
5614.38	789	784	792	777	785	805
5613.96	813	812	835	805	807	804
5613.7	745	751	755	739	743	739
5613.65	690	690	697	690	695	679

Depth (ft)	Average RHN	Individual RHN Measurements				
5613.55	705	708	711	708	704	696
5613.45	864	866	854	864	870	868
5613.25	680	677	679	685	672	686
5612.9	776	767	773	776	785	777
5612.82	749	733	749	752	760	753
5612.78	699	694	698	706	699	700
5612.7	767	764	768	772	762	767
5612.68	707	696	705	717	719	697
5612.6	766	753	799	756	761	763
5612.4	771	759	779	775	773	769
5612.2	894	890	896	895	887	900
5611.9	705	708	699	702	700	715
5611.85	774	771	780	778	781	758
5611.3	872	865	885	867	893	850
5610.75	905	906	905	898	905	911
5608.5	716	722	730	709	701	718
5606.4	760	754	784	765	761	735
5605.5	811	807	810	812	810	814
5603.5	755	765	759	758	747	748
5602.35	814	828	800	831	802	807
5600.5	783	783	779	786	786	781
5599.45	904	910	896	905	904	906
5599.4	666	666	670	671	655	669
5599.34	597	587	597	617	570	612
5599.2	658	657	656	669	659	651
5598	743	738	754	736	745	742
5596.8	699	689	699	690	716	702
5595.5	791	789	800	787	785	794
5594.5	801	812	796	799	802	795
5592.7	720	712	722	736	725	703
5592	774	773	772	776	776	775
5590.8	820	822	823	835	793	825
5589.6	656	663	652	654	658	654
5588.4	700	704	691	691	719	695
5587.35	789	788	790	790	785	790
5587.2	803	799	798	809	826	783
5587.13	802	799	802	802	801	806
5587.1	698	684	700	696	709	703
5586.5	725	721	725	725	729	726
5584.8	726	727	714	730	724	737
5583.85	706	698	720	713	699	702
5583.7	742	748	743	748	740	730
5583.6	711	706	701	721	725	701
5583.54	786	789	783	789	787	781
5583.46	715	714	712	722	716	711

Depth (ft)	Average RHN	Individual RHN Measurements				
5583.35	680	695	675	671	680	679
5583.2	706	697	693	723	713	704
5581.7	783	802	772	787	765	789
5581.65	811	798	822	826	813	795
5581.4	540	540	534	530	543	552
5580	596	601	601	576	596	608
5578.5	597	596	594	598	596	600
5577.5	683	668	686	687	686	688
5576.1	631	648	636	618	619	636
5574.35	627	617	639	624	627	628
5572	700	698	699	704	700	698
5570.15	648	642	654	635	648	659
5569.8	605	615	607	621	598	582
5568.55	638	644	640	633	633	641
5568.46	715	720	643	719	716	705
5568.43	656	666	670	657	651	638
5568.41	675	685	673	664	670	684
5568.35	671	668	674	678	670	667
5566.4	752	759	755	752	746	746
5563.6	763	758	773	737	774	771
5561.7	733	730	732	737	737	727
5559.5	805	800	810	800	810	803
5558.2	731	734	728	724	736	732
5556.05	781	783	771	784	781	785
5554.4	791	787	789	795	795	788
5552.62	802	800	808	803	787	811
5552.59	780	772	781	779	791	775
5552.58	789	787	790	788	791	
5552.53	799	798	797	800	796	805
5552.5	773	784	773	771	768	771
5552.49	812	820	807	817	805	812
5552.48	817	810	820	822	819	813
5552.47	731	718	729	737	739	733
5550.8	738	737	740	739	739	734
5550.68	730	719	733	722	726	748
5550.64	798	803	802	802	792	790
5550.6	793	790	799	791	793	791
5550.25	823	824	816	829	827	817
5548	790	787	784	792	786	799
5546.62	812	810	807	815	824	806
5546.59	815	814	822	820	806	812
5546.55	796	809	815	784	785	789
5546.54	739	715	739	746	749	744
5546.53	764	765	771	765	754	766
5546.48	774	762	775	768	778	788

Depth (ft)	Average RHN	Individual RHN Measurements				
5546.44	712	700	725	704	714	719
5546.43	734	714	744	710	749	755
5546.38	786	787	796	788	771	788
5546.34	770	783	756	768	772	770
5546.32	808	794	810	811	808	815
5546.29	720	722	719	723	724	714
5546.28	732	733	731	734	731	733
5546.1	790	792	803	780	787	787
5545.35	778	775	788	774	777	777
5545.3	727	725	718	716	751	726
5545.24	807	798	787	813	824	813
5545.21	791	788	789	794	793	790
5545.17	816	808	816	813	827	817
5545.13	795	793	803	789	798	793
5544.65	733	727	737	733	737	733
5544.2	864	867	866	866	866	854
5543.63	779	786	778	778	780	771
5543.58	800	800	783	833	798	786
5543.55	762	758	756	768	763	763
5543.52	783	774	788	767	791	794
5543.47	776	773	775	779	777	777
5543.43	794	781	797	785	810	797
5543.36	793	792	792	787	796	796
5543.3	777	771	772	781	781	781
5542.05	789	785	789	786	786	798
5541.95	789	798	789	792	782	786
5541.88	795	799	792	791	800	793
5539.4	807	801	808	810	804	812
5537.9	775	767	795	770	761	783
5536.6	794	794	797	796	793	789
5532.6	766	765	765	766	759	774
5532.56	712	738	710	711	704	696
5532.52	768	776	760	775	759	769
5532.39	747	752	751	748	752	730
5532.1	785	781	793	777	784	789
5532	766	764	749	762	770	787
5530.85	786	786	779	788	785	794
5527.8	785	797	778	779	777	793
5527.75	749	750	758	737	746	755
5527.6	772	758	770	777	782	773
5527.5	708	707	725	711	693	704
5527.42	736	750	734	720	745	731
5526.05	841	850	836	851	838	832
5524.8	767	761	763	751	773	785
5522.2	799	791	807	801	798	798

Depth (ft)	Average RHN	Individual RHN Measurements				
5520.45	718	718	721	724	719	706
5520.3	764	769	753	759	773	766
5520.1	722	735	708	718	721	729
5519.85	737	730	743	716	740	754
5519.6	706	718	695	710	700	705
5518.3	807	805	814	798	803	815
5517.7	689	680	694	702	677	693
5516.7	710	711	706	723	699	712
5516.4	782	792	779	784	776	779
5516.2	735	738	735	730	737	736
5516.1	725	710	731	710	739	734
5514.5	738	737	744	737	737	737
5512.1	569	573	580	559	561	572
5510.8	655	663	654	660	654	644
5510.5	692	687	692	693	700	690
5509.1	731	740	728	723	732	732
5508.1	711	711	710	708	717	707
5507.9	743	749	739	757	734	735
5507.65	750	756	752	747	743	754
5507.35	686	697	702	680	666	686
5507.15	770	767	774	770	759	779
5506.9	678	688	684	668	671	681
5506.1	738	738	734	743	736	738
5504.35	736	730	741	737	744	728
5504.25	810	800	819	810	807	814
5504.12	734	732	734	736	729	740
5502.4	715	714	713	718	720	710
5500.6	798	801	802	791	794	801
5498.45	745	740	744	738	754	748
5496.7	708	716	706	709	702	705
5495.5	672	683	662	661	688	664

Core #4 – Rebound hardness data

Depth (ft)	Average RHN	Individual RHN Measurements				
9166.5	671	703	682	645	642	681
9165.5	722	721	718	722	728	721
9164.5	694	695	698	696	687	694
9163.35	690	688	688	689	700	686
9161.35	624	618	639	619	611	635
9160.7	724	720	721	734	715	731
9159.8	699	693	705	714	692	693
9156.5	716	724	715	721	710	708
9155.5	671	654	668	658	677	696
9154	739	734	733	747	731	748
9153.5	686	687	704	682	666	691
9152.4	822	819	828	818	830	817
9151.5	707	708	705	702	711	707
9150.5	649	651	644	649	644	659
9150.5	642	640	643	641	639	645
9150	674	673	672	676	675	674
9149	707	698	718	717	695	709
9148.3	712	712	718	706	711	711
9147.5	875	880	873	873	868	880
9146.5	839	835	840	834	846	841
9145.4	783	784	779	780	791	779
9144	674	670	683	669	684	663
9143.2	766	752	788	751	761	780
9142.6	767	758	767	765	776	770
9141.5	747	748	741	724	762	760
9140.7	734	743	714	731	738	745
9140.32	780	766	794	763	789	789
9140.2	884	884	881	890	886	880
9140.07	840	839	818	851	836	858
9139.9	832	835	819	841	822	843
9139.75	761	759	765	761	762	758
9138.3	756	765	752	755	762	747
9137.5	627	614	626	640	611	644
9136.85	705	705	709	707	704	700
9136.3	701	696	690	699	712	707
9135.42	726	727	722	730	728	722
9135.4	718	715	722	713	720	721
9135.25	670	649	690	665	674	671
9134.4	680	664	695	684	667	691
9133.7	870	870	879	870	852	878
9133.55	685	677	686	682	690	689
9133.5	663	656	655	659	664	680
9132.5	702	703	700	703	704	700
9131.6	657	674	657	651	649	655

Depth (ft)	Average RHN	Individual RHN Measurements				
9129.5	667	663	672	662	670	666
9128.4	690	704	687	676	696	689
9127.55	678	681	675	672	686	678
9127.5	690	686	699	694	687	682
9126.4	725	723	724	720	729	731
9125.5	732	737	730	726	738	729
9124.8	714	711	710	721	713	713
9124.55	667	673	662	668	666	666
9124.1	670	660	676	678	656	679
9123.5	662	654	654	662	666	672
9122.5	690	682	700	694	687	685
9121.5	670	671	673	664	675	668
9120.2	716	709	714	719	717	719
9119.7	719	714	719	718	724	721
9118.3	698	704	697	691	700	700
9117.55	703	697	722	697	709	689
9116.4	701	698	702	706	696	701
9114.9	722	726	727	726	709	720
9114.8	698	702	681	712	703	693
9113.5	716	718	721	725	711	707
9112.6	729	725	730	736	721	731
9111.7	704	707	705	701	706	702
9110.5	682	683	682	683	678	686
9109.5	701	687	702	687	701	726
9108.8	720	715	727	718	725	717
9108.3	707	711	705	703	710	707
9107.3	729	723	724	735	733	729
9106.5	743	735	741	751	741	745
9105.45	834	825	827	839	839	840
9105	752	746	756	748	757	751
9104	686	682	697	678	689	683
9103.3	760	750	768	766	758	760
9102.65	759	755	750	774	768	750
9102.56	740	744	727	748	739	742
9102.5	771	741	782	769	782	782
9102.5	745	760	738	760	748	720
9101.5	741	743	738	731	753	739
9100.5	664	653	666	650	668	682
9099.5	751	741	758	742	747	765
9098.7	648	660	613	663	651	652
9098.3	707	707	697	708	708	714
9097.5	679	665	680	673	686	689
9096.5	717	722	712	714	719	718
9095.5	687	699	684	698	665	689
9094.6	702	688	714	703	700	704

Depth (ft)	Average RHN	Individual RHN Measurements				
9093.4	632	636	615	640	628	641
9092.3	681	670	697	683	674	681
9091.5	703	715	702	680	717	699
9090.4	697	694	687	702	704	700
9089.9	696	687	699	693	701	701
9089.5	675	667	665	679	677	685
9089.45	700	702	689	695	707	705
9089.2	724	724	719	721	716	741
9089.2	723	724	722	729	722	720
9089.05	718	714	712	715	712	735
9088.8	711	706	707	704	722	718
9087.5	676	661	681	682	679	677
9085.9	701	701	696	703	705	702
9085.8	704	709	712	699	702	700
9085.6	674	670	672	671	684	672
9085.5	701	703	699	704	703	696
9083.5	724	729	717	717	735	721
9082.5	738	743	739	738	738	734
9081.5	702	711	683	697	714	703
9081.5	692	704	699	687	678	692
9080.6	748	757	747	742	746	748
9077.8	758	762	761	755	754	760
9076.78	671	675	672	664	679	664
9076.75	656	651	659	643	669	657
9076.7	737	745	737	729	735	737
9076.2	812	826	797	787	836	816
9075.8	867	874	859	867	875	862
9075.4	766	783	767	771	743	767
9074.4	789	774	806	797	780	788
9074	663	658	655	666	656	678
9073.5	663	680	648	665	660	661
9072.4	716	719	720	723	709	710
9071.5	703	707	698	705	708	699
9070.6	758	752	761	760	759	758
9069.5	744	745	744	735	751	745
9068.75	644	651	637	636	646	650
9067.5	744	751	745	744	737	744
9066.6	743	740	743	746	738	748
9065.3	694	686	706	697	684	699
9064.7	697	692	715	690	690	697
9064.2	653	664	652	651	645	651
9063.25	643	638	635	645	660	636
9062.4	749	738	749	764	743	753
9060.2	703	695	700	714	704	700
9060.16	698	695	701	695	697	700

Depth (ft)	Average RHN	Individual RHN Measurements				
9060.11	713	714	713	715	710	715
9060.05	717	711	720	709	727	717
9060.04	693	687	694	691	684	708
9060.02	728	730	701	734	739	734
9060.01	728	738	719	726	732	723
9059.95	704	693	711	699	716	703
9059.5	763	757	747	772	780	757
9058.6	741	752	741	745	731	737
9056.8	744	737	753	746	749	736
9055.4	738	750	747	738	732	722
9054.45	775	766	770	777	782	778
9053.8	763	760	769	767	760	760
9053.15	747	723	741	765	758	747
9052.3	770	768	768	773	777	764
9051.5	672	677	681	662	679	662
9051.35	751	740	740	749	754	770
9051.32	767	742	785	776	759	775
9051.28	737	731	732	732	747	743
9051.24	724	730	728	726	716	720
9051.2	729	735	732	736	712	728
9051.15	673	670	676	666	677	675
9050.8	790	791	792	784	803	782
9050.3	863	878	875	856	845	861
9049.8	654	638	657	683	646	647
9049.5	676	695	683	662	653	687
9048.5	723	721	731	723	715	723
9048.1	717	719	714	715	721	716
9048.1	712	708	711	713	720	708
9047.3	769	785	784	767	759	749
9047.18	751	752	751	735	747	768
9046.7	729	728	737	729	727	722
9045.5	733	723	737	736	746	724
9045.1	646	642	655	639	639	657
9044.8	617	612	608	635	626	605
9044.3	535	541	535	534	521	544
9043.2	613	630	611	617	610	596
9042.3	646	647	626	656	665	638
9041.6	572	580	573	564	569	573
9040.6	637	632	650	635	625	644
9039.5	621	608	634	613	608	642
9039.4	638	632	635	630	649	645
9039.25	805	808	795	775	826	821
9039.2	866	843	851	895	873	868
9039	717	722	713	706	725	721
9038.4	733	729	723	743	738	731

Depth (ft)	Average RHN	Individual RHN Measurements				
9037.5	715	703	724	717	720	711
9036.4	894	903	907	881	907	870
9035.3	618	618	616	612	621	621
9034.5	703	693	709	703	703	705
9034	690	682	690	690	703	683
9033.2	702	698	708	693	704	707
9032.1	693	694	692	692	695	694
9031.3	639	640	645	635	637	639
9030.5	704	706	705	696	702	710
9029.2	676	675	671	676	682	677
9027.5	681	706	672	671	681	676
9026.5	610	617	597	615	600	621
9025.4	679	669	684	677	675	688
9024.2	677	668	685	690	660	681
9024.2	701	701	702	704	694	702
9018.8	803	797	797	817	803	803
9018.3	825	820	821	829	817	837
9017.9	738	735	740	740	740	733
9017.6	700	689	702	705	695	707
9017.3	720	706	715	720	731	730
9016.35	731	724	739	734	726	730
9015.5	674	662	673	678	682	676
9014.5	694	694	700	691	694	693
9013.45	685	691	696	672	677	687
9011.35	680	681	678	679	683	679
9011.2	579	581	583	584	570	576
9010.65	666	673	674	665	661	655
9010.6	675	677	676	677	673	670
9010.53	709	708	714	716	705	702
9010.28	709	707	711	713	712	704
9010.2	705	711	700	708	701	706
9010.05	690	695	684	683	692	697
9009.4	677	671	662	681	683	688
9008.5	651	651	654	649	652	649
9007.6	634	646	625	625	643	630
9006.6	659	666	663	658	657	652
9006.25	638	620	650	638	645	638
9006.1	615	611	609	613	626	614
9005.5	689	694	691	691	684	684
9004.25	628	618	631	642	627	624
9003.8	667	671	665	655	669	675
9002.5	726	729	735	713	725	730
9002	663	654	668	658	673	664
9001.6	748	748	742	746	756	746
9001.35	750	755	748	752	747	746

Depth (ft)	Average RHN	Individual RHN Measurements				
9001.1	697	700	694	712	696	682
9001.06	740	750	737	730	747	736
9000.85	703	705	702	703	700	707
9000.5	701	704	695	700	689	718
8998.65	712	689	719	716	717	721
8998.45	804	806	804	808	798	804
8997.95	728	706	729	723	764	720
8997.8	909	886	914	915	918	912
8997.73	755	744	757	751	753	770
8997.5	710	703	710	712	726	699
8996.87	658	655	643	660	662	669
8996.7	683	670	696	671	682	697
8996.5	682	671	692	695	666	684
8996.35	771	773	783	761	772	767
8995.5	817	818	821	817	813	818
8994.6	709	706	725	705	710	700
8993.6	720	720	712	708	727	734
8992.5	785	776	784	817	768	778
8990	714	722	720	707	716	707
8989.7	746	743	749	750	746	742
8987.7	814	805	814	816	815	822
8987.1	854	867	868	849	845	841
8986.74	835	819	843	831	839	841
8986.5	915	916	917	913	919	910
8986.39	873	886	875	873	862	870
8986.37	873	866	879	876	880	862
8986.1	905	905	891	895	917	916
8986.07	905	902	907	912	913	889
8986	885	888	869	888	893	888
8985.55	850	852	850	848	844	856
8984.67	869	870	872	879	869	855
8984.55	724	735	736	715	720	712
8984.52-right	728	736	731	727	724	723
8984.52-left	802	801	810	805	792	802
8984.5	858	863	866	839	866	857
8984.49	804	777	819	813	813	800
8984.46	865	863	870	852	873	866
8984.43	855	851	853	856	855	858
8984.38	852	844	856	860	846	853
8984.2	876	887	874	860	882	878
8984.15	896	895	902	901	893	887
8984.15	882	916	873	888	870	862
8984.11	867	865	873	891	856	849
8984.07	926	933	926	923	927	922

Depth (ft)	Average RHN	Individual RHN Measurements				
8984	909	912	905	900	917	909
8983.5	924	926	919	927	926	921
8981	906	898	911	909	897	914
8980.6	643	645	646	651	638	635
8979.5	549	536	547	537	551	575
8979.5	701	707	696	703	705	695
8978.6	543	550	549	537	542	537
8978.4	716	726	714	707	738	693
8978	581	570	559	604	580	592
8977.5	624	633	652	621	604	609
8976.5	676	672	686	684	661	675
8976.2	774	777	774	782	769	768
8975.4	636	652	629	621	639	638
8974.5	749	750	750	750	746	747
8973.9	702	725	693	702	702	688
8973.25	663	674	659	661	659	660
8972.5	631	633	641	626	626	628
8971.5	667	672	658	660	674	671
8970.6	690	685	691	696	691	686
8968.5	656	659	655	648	651	665
8968.25	648	634	657	641	646	660
8967.5	701	698	697	693	707	710
8966.3	740	746	734	730	746	743
8965.2	712	706	706	733	719	697
8964.7	731	731	728	731	732	734
8964.2	771	771	776	766	768	775
8962.75	710	695	714	705	726	710
8961.5	775	773	783	781	769	770
8960.5	724	722	724	722	726	727
8960.16	696	690	697	701	694	699
8959.5	679	676	677	682	681	678
8959.45	713	711	718	712	709	715
8959.4	701	701	702	701	701	700
8959.33	730	727	718	722	764	719
8959.29	726	726	729	729	725	722
8959.27	710	707	713	717	709	705
8959	765	758	762	769	766	770
8958.1	736	737	740	736	737	729
8956.7	693	690	703	696	689	688
8956.45	718	707	719	717	717	730
8955.5	707	711	699	707	702	715
8953.1	703	706	696	710	703	702
8953	730	714	747	733	742	715
8950.7	788	786	795	777	801	783
8949.6	726	734	713	728	727	729

Depth (ft)	Average RHN	Individual RHN Measurements				
8949.58	724	735	727	720	720	720
8949.55	732	734	730	731	727	738
8949.54	738	744	740	748	727	732
8949.53	748	732	760	743	736	771
8949.5	731	739	727	729	734	726
8947.5	755	747	750	753	757	766
8946.7	698	704	695	694	691	707
8945.4	726	731	718	723	729	727
8945	716	731	715	702	708	722
8942.9	688	679	686	693	690	692
8942.8	738	761	741	737	721	729
8941.9	685	676	689	701	678	680
8941.7	762	765	761	763	761	758
8940.9	726	730	730	719	732	720
8939.6	684	670	689	702	683	676
8939.55	665	675	672	657	658	664
8939	740	742	734	757	742	724
8938.86	722	721	721	732	720	718
8938.8	717	721	716	717	721	710
8938.75	721	722	720	724	721	719
8938.7	716	721	709	721	719	709
8938.65	722	717	730	724	722	718
8938.55	732	726	733	728	736	736
8935.6	702	709	702	692	708	700
8935.3	712	709	712	719	719	703
8934.35	702	696	695	709	703	706
8933	727	724	725	723	730	735
8932.3	734	726	739	738	730	738
8931.4	669	675	669	667	661	674
8930.7	718	711	721	723	723	711
8929.65	715	713	720	719	706	718
8929.3	716	714	717	714	716	718
8928.8	749	758	734	748	750	755
8928.6	737	727	733	743	743	740
8928.5	751	770	755	743	751	738
8926.6	681	680	672	688	690	674
8925.3	592	566	590	611	591	601
8924.5	630	631	619	639	641	618
8923.65	671	683	637	687	666	681
8922.5	704	698	708	713	694	706
8921.85	725	724	713	734	725	728
8921.67	690	696	688	687		
8921.64	691	686	682	697	696	694
8921.62	688	698	699	684	681	677
8921.57	689	687	689	689	692	688

Depth (ft)	Average RHN	Individual RHN Measurements				
8921.55	652	639	659	658	668	638
8921.35	683	677	670	696	692	681
8919.4	681	681	678	680	679	686
8918.3	746	757	748	743	738	742
8915.7	785	782	779	793	781	790
8914.4	717	708	713	730	716	717
8913.45	747	745	766	743	737	743
8912.5	757	763	766	741	759	755
8911.45	704	710	714	696	701	699
8911	679	683	680	688	676	670
8910.93	684	694	688	668	690	680
8910.87	700	713	693	702	689	701
8910.65	689	694	678	683	691	701
8910.6	676	672	672	689	679	666
8910.55	703	722	702	702	698	691
8910.35	698	687	707	696	693	706
8910.2	708	711	704	706	710	711
8910.15	697	692	703	683	700	706
8909.6	652	639	653	646	658	665
8909.55	698	706	698	706	690	692
8908.55	700	701	712	703	704	682
8908.1	681	695	674	670	680	688
8905.65	689	690	684	688	696	686
8904.5	800	820	820	785	788	788
8903.55	763	759	754	777	758	768
8902.9	650	639	652	675	645	641
8902.4	648	663	646	635	644	651
8901.3	771	773	760	789	775	757
8900.3	836	841	839	812	850	837
8900	734	747	741	733	738	712
8899.94	804	801	809	812	786	814
8899.92	717	715	724	721	712	714
8899.9	777	769	774	787	772	785
8899.88	745	748	744	745	748	739
8899.85	776	780	785	773	771	771
8899	719	727	720	711	725	713
8898.5	817	823	798	812	834	816
8896.84	785	796	786	769	786	786
8896.3	758	766	761	757	752	752
8894.7	720	711	727	717	725	719
8894.4	702	701	698	703	700	706
8893.3	729	719	732	734	720	741
8892.9	733	736	722	722	775	710
8892.6	643	622	618	670	659	645
8892.2	712	720	713	713	710	706

Depth (ft)	Average RHN	Individual RHN Measurements				
8891.4	681	692	672	685	683	674
8891.4	672	672	681	680	667	660
8891.3	706	707	722	696	712	692
8891.27	707	698	698	709	715	713
8891.25	694	705	699	698	693	673
8891.2	704	688	702	694	709	725
8891.15	701	706	706	708	690	694
8890.81	747	748	763	747	736	739
8890.8	772	776	771	770	768	774
8890.77	754	747	763	753	762	747
8890.73	766	766	769	768	751	774
8890.4	628	631	625	610	630	642
8889.7	649	658	650	647	648	642
8888.5	694	681	695	693	697	702
8887.7	780	781	785	781	774	779
8886.6	697	699	690	702	696	697
8886.2	588	573	601	581	594	591
8885.7	630	620	634	623	636	637
8885.3	726	738	711	739	713	727
8884.4	694	694	702	696	690	690
8883.55	725	711	712	736	732	736
8883.45	702	700	720	711	693	688
8883.25	696	687	702	698	695	700
8882.6	752	758	728	772	715	789
8881.8	686	685	696	688	686	675
8878.5	754	756	768	755	739	753
8877.85	711	708	715	706	717	711
8877.65	709	704	706	715	714	704
8877.6	705	705	698	704	712	706
8876.8	677	685	664	670	682	684
8876	712	712	703	710	724	710
8875.5	705	693	701	694	700	736
8874.5	735	736	734	738	724	744
8873.2	715	713	706	703	726	728
8872.5	737	732	736	739	740	737
8871.5	721	728	718	708	730	723
8870.65	707	714	711	691	703	717
8869.35	708	699	704	720	710	707
8868.25	727	728	722	725	740	722
8866.4	663	684	671	644	651	666
8865.55	697	688	697	697	701	700
8864.55	712	709	708	705	738	701
8863.5	739	728	733	747	742	744
8862.6	730	705	741	737	724	741
8861.5	739	722	742	742	737	751

Depth (ft)	Average RHN	Individual RHN Measurements				
8860.6	728	704	722	748	731	737
8859	730	735	726	737	722	729
8858.5	744	715	751	752	750	753
8857.5	709	708	710	707	706	716
8856.5	698	686	707	697	704	697
8855.5	756	747	747	764	760	761
8854.6	757	755	759	751	750	770
8853.25	743	752	735	752	739	739
8852.3	730	732	735	730	733	721
8851.4	686	689	679	699	682	681
8850.5	756	766	763	753	756	742
8849.5	769	765	757	773	774	774
8848.55	722	698	714	734	735	730
8847.5	739	739	742	731	737	744
8846.5	718	713	725	713	721	718
8845.85	729	730	722	727	737	727
8845.8	725	729	726	726	721	723
8845.75	736	739	728	737	736	741
8845.68	658	653	657	649	684	647
8845.65	724	725	723	737	712	725
8845.62	697	684	707	722	688	682
8845.5	690	695	684	699	686	686
8845.5	686	684	671	685	697	692
8845.4	742	739	747	738	749	735
8845.35	725	733	717	738	721	715
8844.35	697	691	699	695	698	702
8843.45	729	731	750	713	706	744
8842.5	728	731	726	721	728	732
8841.7	681	679	677	683	691	677
8840.7	713	720	719	718	700	708
8839.7	739	746	740	739	739	730
8839	713	698	716	724	710	718
8838.5	719	715	713	731	724	711
8836.85	703	694	708	691	712	712
8835.5	673	674	668	669	670	685
8834.5	679	673	687	681	678	675
8833.6	674	662	676	695	675	663
8832.5	666	662	669	654	674	671
8831.5	681	709	672	686	675	661
8830.5	674	679	665	681	666	677
8828.5	654	658	652	652	659	648
8827.35	637	650	640	630	623	641
8826.5	659	652	662	652	665	663
8825.6	589	582	587	587	599	590
8824.35	586	591	585	568	592	593

Depth (ft)	Average RHN	Individual RHN Measurements				
8823.7	575	588	570	571	570	577
8822.4	570	576	571	574	566	561
8821.4	547	549	540	540	549	555
8820.55	512	522	508	521	508	503
8819.7	715	711	715	717	711	720
8819	688	663	689	700	694	693
8818.9	631	623	640	621	639	630
8816.5	771	773	762	764	778	779
8815.75	563	563	573	563	536	579
8815.2	746	769	763	732	736	730
8814.5	735	731	737	737	740	732
8814.5	730	730	714	754	726	728
8814.4	719	724	710	719	719	725
8814.3	708	709	712	694	716	710
8813	672	668	677	669	678	670
8812.92	658	650	652	673	649	664
8812.2	715	708	716	704	729	720
8811.6	719	725	708	703	718	739
8811.3	582	585	586	593	565	582
8810.4	590	574	592	597	575	610
8809.6	592	590	620	587	579	585
8808.6	536	539	547	533	522	540
8806.4	584	597	577	584	583	581
8805.5	584	604	580	560	599	577
8803.5	576	557	583	578	569	591
8802.6	596	597	588	623	574	597
8801.4	680	687	683	664	673	692
8800.6	671	667	666	673	672	675
8799.7	691	694	688	688	691	692
8798.6	659	648	662	670	668	649
8797.5	681	684	668	681	686	688
8796.6	680	680	681	682	667	688
8795.5	685	679	683	683	692	689
8794.5	698	689	693	711	697	701
8793.5	682	689	678	686	687	672
8792.5	669	663	682	665	659	676
8791.5	689	678	689	686	699	692
8790.5	705	701	712	716	689	706
8789.6	696	691	695	705	699	691
8788.6	691	689	683	695	693	696
8787.5	683	675	683	693	685	681
8786.5	687	685	693	684	678	696
8786.3	686	682	689	692	680	686
8786.13	694	696	694	687	691	701
8786.1	679	675	690	666	686	677

Depth (ft)	Average RHN	Individual RHN Measurements				
8785.5	714	727	695	741	693	713
8784.5	709	719	702	707	710	709
8783.5	708	711	705	695	710	717
8782.5	689	694	687	682	693	687
8781.6	667	674	657	667	666	670
8780.5	710	694	718	715	711	713
8779.4	673	663	673	661	687	682
8778.5	708	706	714	692	709	719
8776.5	682	675	678	686	678	691
8775.3	719	721	724	724	709	716
8774.5	702	711	686	702	721	691
8774	675	671	670	672	686	676
8773.5	690	708	680	668	688	706
8772.7	684	678	686	686	685	685
8771.7	703	691	716	701	712	696
8770.5	691	699	687	694	688	688
8769.5	681	686	680	677	684	678
8768.6	680	670	689	682	682	679
8767.5	671	679	677	676	635	689
8766.4	622	612	617	616	639	628
8765.75	620	622	620	610	624	623
8765.3	621	620	626	616	619	622
8764.45	660	664	654	667	654	663
8763.25	630	616	631	625	649	630
8762.7	663	659	665	667	662	662
8761.5	709	698	694	712	728	714
8760.7	686	690	690	686	683	682
8759.7	675	682	659	675	678	682
8759	688	683	682	695	689	691
8758.8	696	691	711	681	699	700
8758.4	717	710	710	712	716	735
8758.2	709	719	713	730	686	697
8757.5	729	729	734	722	737	724
8756.5	724	725	728	725	724	717
8755.4	696	693	695	695	697	700
8754.7	697	697	696	696	705	692
8754	694	692	699	693	690	696
8753.3	705	698	701	696	723	705
8753.28	696	699	695	689	700	696
8753.1	693	691	690	682	702	701
8752.5	701	697	702	711	697	697
8751.5	729	728	729	728	730	728
8750.7	727	723	728	732	725	727
8749.5	730	727	729	736	725	731
8748.25	719	708	717	721	720	730

Depth (ft)	Average RHN	Individual RHN Measurements				
8746.5	716	722	719	716	708	714
8745.5	711	709	707	717	715	706
8744.5	660	680	648	658	660	652
8744.28	693	699	690	685	699	693
8743.85	697	711	693	682	684	715
8743.8	703	688	706	704	704	713
8743.55	682	692	679	682	685	670
8743.25	709	711	715	694	711	716
8742.5	632	614	649	636	612	651
8741.5	661	669	660	648	649	679
8740.5	724	731	721	725	720	721
8739	676	681	670	687	664	676
8738.65	700	697	686	706	701	710
8738.2	642	656	663	631	635	625
8738	707	716	715	707	690	708
8737.5	715	725	704	710	705	732
8737.2	707	699	726	697	708	705
8736.5	668	660	676	670	674	658
8735.5	674	688	678	677	666	661
8734.6	684	670	706	684	686	675
8733.7	699	709	697	691	695	705
8733.25	690	686	695	697	686	688
8732.4	629	639	621	624	626	634
8731.8	699	690	698	699	706	702
8731.45	725	719	733	737	718	718
8730.5	753	761	753	742	754	753
8729.6	644	630	646	652	646	646
8728.7	693	683	697	710	692	683
8728.5	682	677	699	663	685	687
8728.1	699	697	694	695	701	710
8727.35	732	721	721	737	738	743
8726.25	728	724	723	722	731	739
8725.4	727	731	733	728	725	716
8725.4	726	718	725	742	737	706
8725.15	733	744	735	731	724	730
8724.7	716	715	714	728	708	715
8724.5	713	713	712	711	712	717
8724.45	720	722	717	723	724	716
8724.3	725	715	734	724	730	720
8724.2	711	721	701	721	710	704
8723.35	677	676	687	676	666	680
8722.2	717	721	714	704	728	717
8721.2	709	707	711	718	702	709
8720.6	712	713	721	712	710	704
8719.7	736	737	728	746	725	744

Depth (ft)	Average RHN	Individual RHN Measurements				
8719.4	770	771	767	768	775	767
8718.6-mud	603	592	613	611	609	588
8718.6-burrow	645	637	669	639	629	651
8718.5	767	759	783	751	763	777
8716.6	712	717	719	714	704	705
8715.5	744	754	752	739	742	731
8715.2	748	749	740	754	737	761
8711.55	705	705	713	719	705	684
8710.5	751	753	748	745	753	755
8710.5	756	760	752	744	760	762
8710.35	744	757	747	740	734	740
8710.25	725	726	722	724	727	728
8710.14	747	756	735	745	750	747
8710.1	735	743	722	737	740	734
8708.65	733	737	731	734	735	727
8707.5	834	836	836	829	838	829
8706.3	706	707	717	693	709	706
8705.4	733	725	739	743	722	736
8704.6	756	752	744	761	757	768
8703.7	765	767	772	763	774	747
8703.25	777	785	794	774	773	760
8702.5	776	766	783	780	776	777
8702.2	723	712	723	718	735	726
8701.5	733	714	735	748	737	730
8701.2	725	721	721	734	716	733
8700.4	778	777	767	783	783	781
8699.85	744	733	752	738	749	749
8699.4	723	726	716	703	727	742
8698.25	780	775	781	781	778	784
8697.5	777	783	784	774	780	763
8697.2	753	763	748	737	750	766
8696.5	765	758	766	755	765	780
8696.1	717	718	723	715	718	712
8696.1	696	704	711	699	683	685
8695.8	718	722	727	720	721	702
8695.4	714	698	713	712	740	706
8694.5	761	750	777	765	748	763
8693.6	758	776	752	757	742	762
8693.4	828	829	829	827	826	831
8692.6	758	760	757	760	753	760
8692.3	704	706	703	698	709	702
8691.7	690	675	684	674	711	707
8691.65	699	702	696	700	691	707
8691.4	741	758	746	727	740	736

Depth (ft)	Average RHN	Individual RHN Measurements				
8691.3	790	773	805	793	786	794
8691.15	756	751	748	752	772	755
8690.3	808	809	801	815	813	804
8689.85	792	800	792	792	790	786
8689.3	656	673	657	643	658	650
8688.7	729	733	706	722	736	750
8688.65	737	737	740	740	729	739
8688.45	737	756	745	729	721	732
8688.4	786	768	784	789	798	789
8688.25	756	744	748	786	762	741
8686.5	745	733	756	759	731	745
8685.7	744	737	741	741	752	749
8685.2	704	712	704	702	701	702
8684.3	689	701	683	686	684	689
8683.25	361	348	355	366	368	368
8682.7	703	684	716	700	714	703
8682.4	721	726	702	712	737	728
8681.5	708	701	717	718	697	705
8680.4	737	737	736	734	738	741
8679	690	685	691	680	694	698
8678.5	720	729	720	720	714	717
8677.7	704	702	704	705	701	706
8676.5	708	707	707	703	715	707
8675.8	708	709	703	705	716	708
8675.5	712	721	709	709	715	708
8675.4	712	708	734	698	712	709
8675.3	707	707	711	709	705	701
8674.6	697	688	691	695	716	694
8674	721	714	719	728	723	720
8673.5	729	733	730	729	727	724
8672.6	739	733	742	744	740	736
8671.9	672	687	676	667	647	683
8671	662	667	660	670	668	647
8670.3	689	695	666	692	699	691
8669.8	629	626	648	612	631	626
8669.2	707	687	704	710	714	719
8668.5	724	721	728	723	717	730
8667.5	711	706	715	709	720	706
8666.3	719	710	721	726	720	719
8665.9	720	720	722	722	713	722
8665.3	722	723	720	727	720	721
8665.2	734	733	735	736	735	729
8665.1	733	732	734	732	731	734
8664.9	720	722	718	721	716	723
8664.8	737	738	736	736	737	736

Depth (ft)	Average RHN	Individual RHN Measurements				
8664.6	715	727	714	714	709	713
8664.2	675	678	677	669	686	663
8663.7	726	725	723	728	728	724
8663	713	713	733	696	711	712
8662.6	716	714	728	719	702	716
8662.2	711	706	708	705	720	717
8661.2	720	725	718	719	715	722
8660.5	705	683	713	712	712	703
8659.5	716	724	712	714	716	716
8658.7	718	707	723	722	724	715
8656.9	705	709	704	711	692	710
8656.85	703	702	703	705	696	709
8656.65	692	707	688	695	688	682
8656.65	717	711	723	718	716	715
8656.5	712	707	702	712	711	726
8655.7	718	714	722	730	710	716
8655.2	719	715	722	714	721	724
8654.65	685	685	679	680	694	688
8654.6	711	713	711	714	704	712
8654	690	695	700	699	671	683
8653.5	722	729	724	726	718	715
8652.5	715	712	709	715	719	721
8651.5	704	705	710	701	704	699
8650.9	711	714	708	715	705	712
8650.6	699	710	695	697	696	697
8649.5	702	694	696	701	706	711
8648.5	698	696	694	697	707	697
8647.2	708	702	703	713	711	710
8646.5	698	698	694	700	694	703
8645.6	698	694	705	702	700	688
8645.08	686	695	684	684	686	683
8644.92	713	708	713	714	712	717
8644.78	698	701	697	698	698	696
8644.2	709	714	702	713	712	705
8643.25	691	696	688	689	686	694
8642.5	696	692	698	697	696	699
8641.5	702	707	701	694	698	712
8640.6	703	711	702	698	708	698
8640.2	694	690	697	689	701	692
8639.3	707	705	717	712	689	710
8639.2	708	694	701	717	710	716
8638.9	707	718	687	707	705	719
8638.68	613	592	634	599	614	625
8638.35	692	686	694	692	699	688
8637.7	710	717	712	706	714	702

Depth (ft)	Average RHN	Individual RHN Measurements				
8637.3	697	700	685	698	695	705
8636.5	668	669	673	652	696	652
8635.4	638	655	659	620	621	634
8634.3	650	651	655	648	639	655
8634	724	731	728	724	721	717
8633.5	658	651	674	651	657	657
8632.75	545	556	547	541	550	533
8632.45	566	583	580	552	549	565
8631.5	680	691	677	682	668	683
8630.4	664	665	654	663	671	666
8629.5	644	641	640	637	647	653
8629.1	591	592	587	599	589	586
8628.5	695	694	697	689	701	694
8628.3	728	728	733	722	727	728
8626.5	692	686	696	694	696	690
8625.5	688	688	684	689	688	693
8624	689	683	694	700	681	686
8623.3	695	699	691	701	683	699
8622.4	705	706	710	693	713	705
8621.6	626	622	628	619	627	636
8621.2	688	689	690	685	686	689
8620.6	702	706	695	705	700	702
8619	707	703	707	700	713	710
8618.5	717	714	719	727	711	712
8618	719	717	700	718	729	732
8617.6	663	658	668	658	659	670
8617.14	667	663	667	666	670	671
8617.05	668	659	673	679	649	680
8616.7	657	663	656	644	669	651
8616.4	670	678	670	662	673	666
8615.4	681	692	678	672	673	688
8614.4	720	718	720	709	726	729
8614.1	646	652	654	635	630	657
8613.3	655	659	649	656	650	659
8612.5	700	690	699	697	704	710
8611.5	712	710	711	710	712	719
8610.5	706	709	708	709	706	696
8609.5	703	704	699	702	704	708
8609	692	693	689	692	696	690
8608.5	713	714	716	713	710	712
8607.5	704	698	712	706	698	705
8606.3	689	687	684	696	690	686
8605.3	711	711	708	715	712	709
8604.5	717	711	714	723	717	720
8603.25	689	684	693	682	692	692

Depth (ft)	Average RHN	Individual RHN Measurements				
8602.4	677	682	679	674	677	675
8601.4	673	674	662	677	670	684
8600.3	675	665	684	684	672	671
8599.5	678	672	683	677	677	679
8599.1	696	699	689	700	704	686
8598.5	691	696	685	693	703	679
8596.5	651	653	662	647	645	646
8595.5	640	625	648	641	651	633
8594.5	698	693	680	707	706	704
8594.2	719	725	720	714	708	728
8593.6	422	426	424	400	435	424
8593.3	522	547	514	512	510	525
8592.6	552	556	558	557	554	536
8592.2	568	557	571	566	568	577
8591.8	745	726	738	755	752	756
8591.2	712	691	735	696	723	715

Core #5 – Rebound hardness data

Depth (ft)	Average RHN	Individual RHN Measurements				
9924.1	730	730	722	727	731	740
9923.95	810	800	811	810	816	811
9923.8	652	645	642	657	662	656
9923.65	804	803	808	806	805	796
9923.35	552	550	542	562	561	543
9821.15	662	650	665	664	663	668
9388.6	759	765	749	769	752	758
9386.5	619	624	633	608	629	600
9385.7	727	731	734	713	734	722
9384.5	751	751	760	752	747	744
9383.4	658	652	650	650	667	669
9381.4	610	604	631	614	607	592
9380.5	787	750	805	762	810	806
9379.9	747	734	735	742	769	755
9377.05	680	685	677	686	688	666
9376.65	773	793	777	760	766	769
9376.6	767	791	778	759	755	752
9376.5	759	769	763	763	737	764
9376.4	787	791	768	788	787	802
9376.1	889	886	892	888	886	894
9375.85	770	770	766	777	771	765
9375.5	895	892	908	895	885	897
9375.15	760	765	755	763	761	755
9374.9	758	759	752	745	771	761
9374.72	830	826	840	833	821	828
9374.5	824	833	839	809	819	821
9374.35	804	797	792	802	800	829
9374.2	818	824	819	826	815	808
9373.6	798	790	802	802	808	790
9373.5	734	722	724	734	751	740
9371.9	728	717	736	734	717	738
9371.85	758	734	751	760	779	766
9371.5	726	721	720	738	726	724
9370.75	763	765	767	763	765	754
9370.5	764	766	761	763	761	767
9370.3	749	749	749	753	748	746
9370.1	758	761	760	748	760	761
9369.5	746	755	754	747	742	734
9368.5	762	760	755	768	767	761
9368.5	769	768	778	757	779	764
9368.15	835	832	850	832	834	828
9367.85	764	762	770	759	757	772
9367.5	835	841	835	829	849	822
9367.45	824	816	818	824	853	809

Depth (ft)	Average RHN	Individual RHN Measurements				
9367.17	900	909	904	872	903	913
9367.1	915	920	906	920	924	906
9366.3	871	863	872	868	880	871
9366.01	875	879	875	876	887	859
9365.85	861	845	871	861	853	876
9365.7	633	626	613	650	634	641
9365.3	694	706	708	685	677	696
9364.5	706	713	702	706	698	711
9363.5	716	721	726	690	734	709
9362.8	625	650	637	592	633	611
9362.4	680	675	654	692	692	685
9361.9	699	696	704	699	706	691
9361.55	819	823	811	824	823	813
9361.5	884	892	886	893	878	873
9361.36	859	821	869	864	873	867
9360.8	859	839	871	868	860	857
9360.55	602	590	600	600	614	607
9360.5	628	631	621	622	623	645
9359.8	646	645	641	647	652	644
9359.5	684	675	673	692	687	694
9358.5	709	697	701	701	711	734
9358.43	753	771	750	746	763	735
9357.5	661	666	654	667	659	657
9356.5	687	685	709	695	670	676
9356.1	664	643	635	679	684	678
9355.25	714	704	719	716	717	715
9354.5	686	697	686	682	681	686
9354.1	678	667	695	678	680	671
9353.5	697	704	696	684	692	708
9351.5	688	694	689	678	682	695
9350.5	692	702	670	707	683	699
9349.8	718	719	718	716	720	717
9349.5	717	714	723	716	710	721
9348.93	713	717	713	712	711	714
9348.8	705	706	709	711	710	691
9348.5	686	663	684	673	709	701
9347.5	737	736	737	733	735	746
9346.5	681	679	678	666	689	692
9346	765	773	766	762	770	753
9345.1	762	773	760	755	760	763
9344.25	709	702	698	716	716	713
9343.55	760	755	760	759	762	763
9343.5	735	737	726	740	730	743
9343.3	730	732	741	722	728	729
9343.15	782	785	779	789	781	774

Depth (ft)	Average RHN	Individual RHN Measurements				
9343.05	765	757	769	756	766	775
9342.5	687	688	685	697	675	690
9341.85	700	704	698	699	698	699
9341.8	735	711	731	739	749	743
9341.4	715	718	718	705	716	718
9340.2	715	713	720	714	713	715
9339.4	709	707	707	701	716	713
9338.6	716	710	716	724	708	723
9338.2	713	705	720	711	711	716
9337.6	706	704	711	714	693	708
9336.3	719	730	692	726	724	725
9335.5	725	719	723	727	726	728
9334.5	754	731	747	773	750	767
9333.25	765	764	770	775	751	766
9331.5	751	752	735	759	749	759
9330.5	773	780	777	772	767	767
9329.5	778	772	778	776	782	783
9328.5	747	741	748	736	755	756
9327.5	763	774	745	775	753	766
9326.5	741	730	725	757	754	741
9325.95	737	741	740	738	717	749
9325.8	829	824	838	823	823	839
9325.65	768	789	777	745	759	769
9325.5	727	730	739	712	746	707
9325.5	737	715	733	733	749	754
9325.15	785	790	802	779	776	776
9325.1	774	772	778	767	778	773
9324.65	696	708	698	686	701	686
9324.5	710	711	706	698	731	705
9324.3	700	693	698	711	700	700
9323.5	762	758	767	761	763	760
9323.3	752	751	742	759	753	757
9323	678	674	680	685	672	677
9322.7	667	659	661	664	670	680
9322.4	696	696	689	701	704	688
9322.25	657	661	659	656	660	651
9321.5	811	823	810	808	802	812
9320.5	797	802	799	789	806	788
9319.4	716	717	720	715	710	717
9318.5	638	623	635	637	649	647
9317.85	698	719	684	694	695	699
9317.7	685	687	674	706	674	683
9317.5	771	778	766	785	761	766
9317.5	771	769	771	763	771	782
9317.1	708	720	715	698	702	707

Depth (ft)	Average RHN	Individual RHN Measurements				
9316.95	730	731	710	728	738	741
9316.8	903	892	910	907	902	906
9316.65	738	734	741	737	740	740
9316.5	700	697	697	702	698	707
9316.45	714	703	717	720	709	720
9316.3	844	827	860	856	841	838
9315.9	790	783	788	792	793	796
9315.8	711	717	711	705	705	718
9315.5	677	686	672	668	685	673
9315.5	686	682	671	697	689	692
9315.2	722	726	712	707	717	748
9314.95	720	720	719	730	717	715
9314.85	703	700	698	715	696	706
9314.8	697	690	697	698	706	694
9314.5	847	844	853	849	842	847
9314.4	854	858	850	862	856	845
9313.8	677	676	680	668	688	674
9313.5	683	676	686	684	677	693
9313.4	693	699	697	692	692	687
9313.1	701	711	695	693	694	711
9311.6	808	801	795	805	812	826
9311.1	839	828	840	842	843	841
9310.5	685	688	690	685	676	685
9309.9	740	731	734	735	755	744
9309.6	774	776	762	769	781	781
9309.3	772	775	778	762	777	769
9308.95	819	815	822	815	825	
9308.9	788	785	784	786	793	791
9308.8	775	774	771	771	785	774
9308.8	771	772	759	779	775	772
9308.7	752	756	754	751	747	754
9308.65	741	741	744	733	738	750
9308.6	756	736	772	763	749	762
9308.55	743	731	750	745	728	761
9308.5	749	747	750	752	742	754
9308.45	748	745	742	751	758	743
9308.35	722	701	728	719	727	733
9308.3	689	709	667	684	723	664
9308.21	707	716	729	691	692	709
9308.1	723	715	717	727	721	734
9307.5	732	721	731	747	730	729
9307.3	710	714	706	714	713	704
9307.18	764	762	762	758	773	764
9306.8	731	733	726	731	742	724
9306.5	740	741	725	744	745	744

Depth (ft)	Average RHN	Individual RHN Measurements				
9305.5	827	819	821	830	838	825
9305	756	754	760	748	762	756
9304.5	684	684	685	682	684	687
9303.62	625	624	627	623	634	619
9303.5	663	664	672	662	658	658
9303.45	834	815	847	843	834	829
9303.4	725	735	718	726	721	725
9303.3	729	728	717	730	728	741
9302.8	838	826	846	860	826	832
9302.5	857	860	857	854	857	857
9302.43	860	859	857	863	857	866
9302.4	723	726	712	722	728	726
9302.1	704	712	707	702	708	692
9301.95	750	740	753	743	786	728
9301.95	750	740	753	743	786	728
9301.85	851	833	854	846	863	857
9301.85	851	833	854	846	863	857
9301.7	723	717	714	721	725	736
9301.7	723	717	714	721	725	736
9301.6	719	711	719	716	728	720
9301.4	811	813	809	811	809	813
9301.2	910	920	896	911	907	918
9301.15	921	927	922	912	922	921
9301.1	878	876	882	875	885	872
9300.75	805	807	802	791	815	808
9300.35	822	817	817	829	824	825
9300.25	731	726	732	731	731	735
9300.25	744	744	737	751	740	748
9299.9	747	747	760	745	743	741
9299.79	852	851	864	843	856	848
9299.7	766	763	769	773	767	760
9299.7	754	749	750	758	750	763
9299.5	734	734	726	739	736	733
9299.35	751	755	746	739	764	749
9299.33	737	732	749	735	724	744
9299.2	818	821	817	822	817	813
9299.1	753	757	753	742	753	758
9299	826	833	823	823	825	826
9298.95	832	833	828	837	835	829
9298.4	832	829	836	837	829	830
9298.1	781	793	787	793	778	755
9297.62	743	735	740	740	739	759
9297.5	880	886	898	869	864	883
9297.37	882	882	872	891	882	884
9297.1	743	744	749	743	740	741

Depth (ft)	Average RHN	Individual RHN Measurements				
9296.5	762	770	753	760	760	768
9296.4	770	770	769	772	772	766
9296.35	746	733	754	747	745	749
9296.2	739	744	742	737	726	748
9295.5	730	732	742	727	724	723
9294.2	774	778	771	781	762	776
9293.8	751	767	760	725	737	766
9291.5	718	711	726	709	683	730
9290.5	743	756	720	741	755	741
9287.5	858	864	856	859	855	856
9287	741	735	748	737	720	763
9286.5	682	699	674	683	686	669
9284.5	690	689	683	694	696	689
9283.5	855	836	860	862	863	852
9282.8	755	752	757	748	763	756
9282.69	773	775	777	776	763	774
9282.4	720	704	727	730	722	715
9281.5	782	768	794	797	772	777
9281.1	788	788	793	789	787	785
9280.4	706	713	701	708	702	705
9279.8	717	702	710	721	732	718
9279.6	761	753	769	758	754	773
9279.4	765	786	758	769	759	755
9279.35	756	738	772	754	758	759
9278.8	788	786	789	791	788	786
9278.6	744	738	736	748	750	750
9278.5	769	770	769	765	770	773
9278.4	790	788	791	791	792	789
9278.25	734	735	725	720	755	734
9277.9	700	705	703	691	712	690
9276.8	705	702	709	709	698	707
9275.8	691	699	691	680	687	700
9275	697	715	691	683	699	696
9274.6	672	664	662	672	681	683
9273.5	694	688	693	698	685	707
9271.5	683	687	682	683	681	681
9270.5	704	694	703	716	704	702
9269.3	750	746	746	763	741	755
9268.9	721	714	714	733	729	715
9268.4	775	765	775	787	778	770
9267.8	866	864	868	872	865	859
9267.35	822	814	818	823	814	840
9267.25	798	813	768	810	794	805
9266.9	818	824	816	807	820	822
9266.7	839	849	829	834	855	826

Depth (ft)	Average RHN	Individual RHN Measurements				
9266.69	831	832	831	826	831	833
9266.4	699	689	704	695	700	708
9266.3	727	728	732	745	717	714
9265.5	594	607	592	580	588	601
9264.5	596	590	604	584	598	604
9263.5	657	658	666	647	665	651
9262.5	703	706	692	685	718	713
9261.5	683	683	679	670	684	699
9260.5	715	706	717	710	724	720
9259.5	582	570	592	572	595	583
9258.5	610	618	606	630	594	601
9257.5	625	631	634	615	630	615
9256.25	670	661	677	685	675	652
9255.5	653	649	663	652	647	656
9254.5	690	684	693	709	692	673
9253.5	714	725	729	707	693	717
9251.5	691	694	683	694	687	699
9250.5	658	632	665	645	668	681
9249.5	673	680	683	686	663	652
9248.9	659	676	658	661	655	647
9248.5	695	697	681	698	705	693
9248.4	695	696	694	695	693	698
9248.2	687	680	679	694	693	688
9247.5	669	681	659	647	683	675
9246.2	677	688	666	666	680	685
9245.25	708	699	683	709	733	717
9244.5	695	683	711	682	680	719
9244.1	713	696	715	723	718	715
9243.6	708	716	717	702	712	694
9243.2	680	668	681	667	675	710
9242.3	697	678	718	697	686	708
9241.8	728	737	729	714	727	733
9241.2	748	748	747	749	748	749
9240.7	766	766	769	764	768	765
9240.3	773	774	764	772	778	777
9240	768	769	772	775	765	758
9239.8	726	713	727	738	732	722
9238.7	733	733	738	731	733	732
9238.1	788	788	788	788	786	
9237.7	705	704	725	686	721	687
9237.2	658	643	642	663	660	681
9236.5	721	717	726	707	726	727
9235.7	721	715	722	722	732	713
9235.3	703	690	713	708	703	703
9234.25	639	639	645	632	638	642

Depth (ft)	Average RHN	Individual RHN Measurements				
9233.5	694	710	689	686	686	700
9233.1	712	719	703	713	714	713
9231.6	759	772	760	734	762	766
9230.6	727	719	736	723	733	724
9230.1	710	703	707	703	735	703
9230.05	710	702	721	698	725	706
9229.85	788	788	786	796	792	780
9229.76	754	751	755	754	754	756
9229.6	732	729	727	729	740	734
9228.8	761	762	764	758	764	759
9228.55	736	735	738	740	733	736
9228.51	705	705	696	708	712	702
9228.45	707	706	699	706	713	713
9228.4	688	691	680	685	692	692
9228.3	702	696	705	691	705	714
9228.25	695	696	696	698	698	685
9227.5	706	697	701	707	718	709
9226.5	705	710	704	711	695	707
9225.8	710	707	699	719	720	705
9225.4	872	878	870	867	882	861
9224.6	744	742	741	742	745	749
9224.2	663	654	665	671	666	660
9223.9	804	796	802	814	812	796
9223.9	804	796	802	814	812	796
9223.75	646	650	634	640	653	654
9223.75	646	650	634	640	653	654
9223.65	770	773	777	759	783	760
9223.65	770	773	777	759	783	760
9223.55	536	573	532	541	514	518
9223.55	536	573	532	541	514	518
9223.25	577	544	593	575	593	582
9222.5	564	555	564	557	581	561
9221.5	696	699	692	687	703	699
9221.5	710	695	705	712	734	706
9221.42	730	726	722	733	726	742
9221.4	724	722	734	719	713	734
9221.3	640	652	643	643	634	628
9221.28	662	661	656	656	665	670
9221.2	870	867	862	879	878	866
9221.2	877	873	881	877	877	875
9221.12	650	642	659	652	644	654
9220.5	701	700	704	704	698	701
9219.4	814	828	826	794	782	839
9219.2	642	645	633	650	639	642
9219	793	808	805	797	772	783

Depth (ft)	Average RHN	Individual RHN Measurements				
9218.85	728	748	734	709	735	715
9218.6	711	709	707	722	699	719
9218.5	697	676	704	713	685	706
9218.4	669	699	664	659	660	663
9217.7	868	868	876	859	870	868
9217.1	857	858	864	853	852	857
9216.7	692	686	690	692	696	697
9216.3	731	727	728	715	745	738
9215.7	692	689	686	696	688	700
9215.6	854	847	855	861	849	856
9215.5	842	848	844	834	843	842
9214.5	642	635	652	629	656	639
9214.37	708	705	709	714	710	700
9214.25	888	891	879	885	891	892
9214.14	707	710	707	706	710	703
9214.1	695	695	689	705	689	695
9213.6	678	665	682	680	685	679
9211.8	694	696	694	687	694	699
9211.4	724	705	714	715	739	747
9210.59	870	875	875	862	875	863
9210.5	814	804	819	817	822	810
9210.02	692	694	696	685	695	688
9210	706	705	703	714	700	708
9209.8	593	588	592	591	592	600
9209.5	543	533	542	552	537	549
9209.45	555	557	542	572	553	549
9208.9	694	692	684	698	705	692
9208.56	692	699	680	699	700	684
9208.2	668	665	671	667	677	661
9207.4	664	660	661	655	664	681
9206.71	635	647	633	628	638	629
9205.5	629	634	616	634	636	627
9204.6	662	665	647	673	653	674
9204.2	671	658	677	663	674	682
9203.5	695	692	699	694	694	695
9202.64	690	686	700	695	687	681
9200.95	652	648	656	649	647	659
9200.5	688	699	695	685	695	668
9199.5	650	647	651	646	660	644
9198.5	676	654	683	692	681	670
9197.5	676	674	662	684	682	680
9196.25	633	635	626	650	620	635
9195.5	692	688	693	703	686	688
9194.5	682	688	684	674	678	688
9193.5	683	682	694	678	673	687

Depth (ft)	Average RHN	Individual RHN Measurements				
9191.6	714	717	726	716	705	707
9191.2	554	563	545	567	553	541
9190.25	611	605	617	596	619	619
9189.9	674	680	679	668	670	672
9189.6	665	660	649	673	670	672
9189	709	706	702	721	712	702
9188.5	658	653	657	664	654	661
9188.1	571	558	574	574	568	582
9187.5	710	716	700	719	707	707
9186.5	662	672	665	683	642	649
9185.25	687	693	693	680	689	680
9185.25	683	682	671	662	700	701
9184.5	637	631	625	662	631	638
9183.9	719	714	723	713	725	722
9183.5	663	655	658	654	668	680
9182.5	615	629	611	612	619	604
9181.9	668	688	675	661	660	655
9181.5	675	681	668	659	694	674
9180.5	678	682	684	665	671	690
9179.25	636	641	621	644	637	635
9178.5	638	658	668	612	630	624
9177.5	689	691	689	691	680	695
9176.5	694	703	693	702	684	686
9175.5	707	712	690	710	706	717
9174.25	680	689	688	685	672	666
9173.8	666	670	665	670	646	680
9173.5	706	697	704	703	720	706
9173.1	677	679	685	674	671	678
9171.5	680	688	682	697	670	661
9170.5	676	675	667	685	681	671
9169.5	615	618	626	622	615	592
9168.4	640	632	644	636	636	654
9167.7	693	675	695	704	696	693
9167.4	671	656	665	680	679	677
9166.3	706	710	703	704	711	702
9165.6	693	688	693	691	700	693
9165.2	687	678	709	684	676	686
9164.5	669	671	672	668	670	666
9163.25	695	692	689	694	711	688
9162.5	649	643	664	650	648	641
9161.2	656	649	644	653	684	651
9160.2	694	716	688	694	687	684
9159.8	746	719	749	753	761	749
9158.8	716	702	707	710	733	730
9157.8	723	724	730	728	720	715

Depth (ft)	Average RHN	Individual RHN Measurements				
9156.5	715	700	712	715	731	715
9155.5	722	733	717	704	740	718
9154.5	736	731	730	732	734	753
9152.25	706	728	695	689	717	700
9151.9	693	693	694	689	694	693
9151.5	725	721	728	716	726	733
9150.6	709	717	719	683	711	715
9149.7	692	687	685	695	698	697
9148.5	691	689	680	692	688	704
9147.3	668	666	663	679	676	656
9146.5	730	736	723	708	746	737
9145.5	692	684	685	703	694	693
9144.5	691	686	699	682	695	693
9143.4	730	726	735	740	720	729
9142.9	700	686	704	691	703	716
9141.25	731	740	734	712	730	741
9140.5	696	696	711	700	696	675
9139.5	692	710	698	694	681	677
9138.5	698	697	722	687	700	684
9137.5	669	646	687	668	669	674
9136.5	710	709	733	700	710	699
9135.25	644	658	649	627	657	630
9134.8	684	662	684	692	689	692
9134.2	619	610	634	613	611	626
9133.9	646	652	632	646	650	648
9133.4	701	703	687	715	715	684
9133.1	702	697	699	706	703	705
9131.8	701	690	706	711	695	704
9130.6	770	763	779	762	763	785
9129.5	662	641	669	671	669	658
9129	730	738	722	724	730	737
9128.5	776	778	782	771	765	786
9127.5	713	699	721	706	716	725
9127.1	761	773	756	751	748	777
9126.5	677	668	686	663	689	679
9125.6	680	692	689	675	669	675
9124.25	659	637	675	650	673	658
9123.5	707	711	684	715	722	701
9122.5	708	691	728	709	721	693
9121.5	715	696	715	703	730	733
9120.5	721	718	748	710	700	729
9119.65	697	705	701	713	681	687
9118.5	658	640	683	669	648	650
9117.4	637	664	652	632	621	615
9116.5	658	687	644	658	667	633

Depth (ft)	Average RHN	Individual RHN Measurements				
9115.5	655	642	654	676	658	644
9114.75	658	646	670	661	653	661
9114.6	643	629	631	644	640	670
9114.5	706	719	711	702	712	687
9114.4	642	653	653	641	634	627
9113.25	663	653	643	668	686	667
9111.9	673	662	683	685	659	674
9111.5	496	489	502	488	502	498
9111.2	604	591	584	618	624	602
9110.5	425	439	402	428	411	446
9109.6	586	614	577	591	569	581
9108.25	618	604	630	627	608	620
9107.8	599	620	600	586	590	598
9107.4	512	495	512	520	508	524
9106.6	558	559	552	539	567	571
9105.9	692	700	694	706	679	680
9104.7	715	701	731	703	720	718
9103.8	690	690	691	697	689	681
9103.5	557	560	533	565	549	576
9102.7	570	579	552	577	577	564
9102.25	503	511	512	492	515	487
9101.5	642	635	637	636	633	668
9100.5	660	645	659	684	669	644
9099.2	645	627	671	632	639	656
9098.8	641	639	654	649	632	631
9097.9	633	635	623	636	632	641
9097.25	646	638	649	669	629	644
9096.5	685	673	688	681	686	699
9095.5	605	596	590	604	630	607
9094.7	681	688	668	694	675	681
9094.3	661	671	665	670	668	633
9093.6	668	662	673	656	671	679
9093.1	627	605	621	622	638	647
9091.25	680	689	689	662	681	678
9090.5	705	699	702	704	717	703
9089.5	692	686	697	698	683	697
9088.4	671	651	689	663	688	663
9087.5	636	637	630	636	636	643
9086.25	683	667	703	679	681	686
9085.5	717	711	721	692	728	735
9085.1	707	692	715	701	717	710
9084.6	709	711	701	718	711	706
9084.1	741	726	750	758	742	731
9083.1	662	639	677	666	651	675
9082.6	540	539	535	552	553	522

Depth (ft)	Average RHN	Individual RHN Measurements				
9082.2	722	713	712	719	723	743
9081.3	679	672	669	681	684	690
9080.25	697	691	691	706	719	678
9079.8	742	740	723	749	750	747
9079.75	721	720	740	724	716	705
9079.6	746	745	752	751	746	736
9078.1	716	717	725	711	705	721
9077.9	717	721	716	725	705	717
9076.1	713	721	741	700	704	697
9075	692	712	692	675	695	687
9074.9	719	706	712	744	715	717
9074.5	774	778	785	762	778	767
9073.5	726	708	728	720	739	737
9071.9	783	786	791	776	788	776
9071.5	730	736	710	726	722	754
9071	636	642	623	648	648	620
9070.5	567	562	564	565	564	579
9070	701	714	735	686	694	676
9069.6	717	718	701	727	711	726
9068.55	713	710	723	716	710	708
9067.9	734	707	737	733	752	741
9067.5	700	704	703	694	713	685
9066.4	732	744	760	721	716	718
9065.8	695	696	697	695	700	689
9065.3	778	765	762	781	799	782
9064.8	744	722	769	739	751	740
9064.25	636	628	614	645	639	652
9063.5	697	693	706	689	685	713
9062.2	693	703	708	681	681	693
9061.8	714	714	722	710	718	706
9060.5	625	611	604	629	623	657
9059.6	662	651	652	685	665	658
9058.25	754	757	745	752	756	758
9057.3	822	817	805	841	836	809
9056.5	593	582	588	587	600	607
9055.4	742	721	734	756	749	752
9055.1	784	770	795	780	786	788
9054.7	773	771	774	775	767	778
9053.25	719	721	730	726	710	707
9051.2	702	717	680	703	712	699
9050.5	734	744	735	723	738	730
9049.6	687	679	681	686	692	697
9049.2	622	630	633	613	623	611
9048.5	523	511	528	527	536	514
9047.25	667	665	677	672	650	669

Depth (ft)	Average RHN	Individual RHN Measurements				
9046.7	756	741	764	774	767	735
9046.2	528	525	524	526	515	552
9044.8	677	689	688	690	652	668
9043.6	695	672	689	699	706	709
9042.8	659	656	653	652	666	666
9042.25	642	656	642	634	631	648
9041.5	713	694	735	696	719	719
9040.5	681	667	682	692	676	688
9039.5	658	645	681	658	651	655
9038.6	675	663	668	670	687	685
9038.1	542	544	563	539	537	526
9037.6	465	470	450	464	473	467
9037.2	584	588	582	594	579	575
9035.5	717	715	725	710	711	723
9034.4	659	648	676	656	650	663
9033.5	710	716	721	719	700	696
9031.7	700	698	705	702	693	704
9031.2	674	698	671	655	649	695
9030.5	613	615	625	603	603	618
9030.5	654	643	661	670	638	656
9030.3	704	692	713	706	703	708
9030.15	577	601	573	564	581	567
9030	548	542	542	546	550	562
9029.5	510	503	524	500	520	503
9029.2	621	637	622	613	626	606
9028.4	662	643	671	675	656	663
9028.1	532	554	539	538	520	509
9027	553	556	548	546	575	542
9026.5	526	536	516	511	554	512
9025.8	673	670	681	656	689	670
9025.3	412	430	404	400	396	429
9022.8	488	465	491	476	506	504
9022.3	715	709	714	714	698	739
9021.5	714	703	725	720	706	716
9020.25	703	691	700	691	715	718
9019.5	693	691	691	690	691	701
9018.9	616	614	592	624	626	624
9017.2	699	696	699	704	699	699
9016.5	693	692	708	695	682	687
9015.8	622	606	633	627	631	613
9015.1	605	606	617	597	606	599
9014.4	552	544	570	543	543	560
9013.4	642	653	636	644	632	643
9011.5	607	624	586	587	623	613
9010.4	635	638	640	643	631	623

Depth (ft)	Average RHN	Individual RHN Measurements				
9009.9	653	660	678	653	646	628
9009.25	541	533	517	548	556	552
9008.6	501	501	520	494	514	478
9007.5	507	519	509	515	494	496
9006.9	557	539	574	565	558	549
9006.5	648	640	649	632	656	665
9005.5	706	696	710	709	709	705
9004.3	696	678	703	700	697	702
9003.6	709	704	704	710	708	718
9002	660	647	652	662	668	673
9001.5	684	680	689	686	681	686
9000.5	692	691	689	702	685	693
8999.5	723	714	723	723	723	733
8998.25	568	572	562	561	575	569
8997.9	634	615	638	636	636	646
8997.6	539	536	550	542	542	524
8997.1	517	510	521	522	515	517
8996.6	576	583	590	561	579	566
8995.8	595	588	589	614	586	598
8995.3	694	683	699	695	691	700
8994.7	579	594	574	572	573	582
8991.6	631	639	622	630	625	637
8990.7	678	681	674	684	676	675
8989.3	689	687	705	679	684	689
8988.7	639	633	647	640	627	648
8987.7	727	713	726	735	734	726
8987.25	620	621	623	635	613	606
8986.8	699	690	725	695	679	706
8986.4	654	653	657	636	658	665
8986.1	698	695	721	689	697	686
8985.6	717	742	720	719	696	708
8985	649	653	654	651	638	651
8984.5	440	429	458	446	436	429
8983.4	710	701	720	719	700	709
8982.5	709	701	717	703	710	715
8982	677	694	670	675	672	673
8981.25	630	630	616	620	631	654
8980.4	620	630	620	622	615	613
8979.4	613	612	606	596	630	623
8979	640	628	659	631	636	647
8978.5	608	605	610	624	593	608
8978.2	617	620	617	624	603	620
8977.3	541	553	542	535	542	531
8975.7	680	690	684	661	686	680
8975.3	626	616	634	637	622	619

Depth (ft)	Average RHN	Individual RHN Measurements				
8974.4	642	640	624	650	651	645
8973.5	560	561	558	569	560	554
8971.4	589	610	577	583	572	601
8970	513	515	500	519	521	510
8969.5	609	615	601	618	609	601
8968.8	614	614	614	601	625	615
8968.4	605	605	600	600	611	608
8967.5	635	640	626	632	651	627
8967.1	690	681	688	687	699	697
8966.7	663	672	657	653	664	670
8966.3	621	610	620	618	618	640
8965.9	601	608	595	599	601	604
8964.9	598	589	608	593	610	588
8964.2	570	563	569	574	561	581
8963.6	617	622	620	621	611	610
8962.9	645	630	639	650	657	649
8962	631	640	615	648	631	621
8961.4	589	571	586	588	598	604
8960.5	550	550	562	541	540	556
8959.6	622	614	629	622	624	622
8958.5	668	667	674	658	675	666
8957.6	575	581	575	562	580	
8956.9	612	604	616	611	618	609
8956.4	701	718	694	701	697	695
8955.5	699	695	710	683	710	695
8954.25	624	635	627	619	626	612
8953.7	706	703	719	704	712	691
8953.3	670	663	674	668	675	668
8951.5	613	615	604	613	616	619
8950.4	652	642	649	662	651	656
8950.1	690	690	693	685	702	679
8949.2	697	688	702	688	701	706
8948.25	662	631	657	685	662	676
8947.5	676	670	670	670	679	689
8947	655	644	658	656	657	662
8946.5	612	624	614	610	610	601
8945.5	657	659	661	650	655	659
8944.5	651	652	645	659	640	657
8943.25	622	612	625	624	631	618
8942.5	674	671	670	678	670	679
8941.6	681	693	675	678	687	672
8940.6	696	695	699	699	693	696
8939.9	689	686	682	691	690	692
8939.5	634	631	630	631	643	
8938.2	579	586	575	570	581	581

Depth (ft)	Average RHN	Individual RHN Measurements				
8937	597	594	601	581	605	602
8936.7	673	660	678	671	675	679
8936.3	764	767	757	763	778	756
8935.4	746	745	750	743	745	746
8934.5	742	744	752	729	737	746
8934.1	690	687	695	688	693	688
8932.59	672	670	665	683	670	674
8932.25	692	705	678	677	702	697
8931.3	721	704	724	713	728	736
8930.5	701	707	718	690	685	706
8929.5	721	714	726	729	715	722
8928.5	725	725	734	721	718	
8927.5	723	707	716	723	727	741
8926.25	707	707	703	709	716	701
8925.5	695	700	688	690	698	699
8924.4	711	703	722	708	696	726
8923.5	712	705	706	733	698	716
8922.4	706	721	719	702	696	693
8921.25	682	671	681	695	675	686
8920.5	728	712	738	709	735	745
8919.5	720	723	721	722	716	716
8918.5	718	710	723	716	724	716
8917.5	639	657	633	630	638	639
8916.5	665	677	658	669	659	660
8915.25	634	636	633	652	620	628
8914.5	717	705	709	722	735	713
8913.5	725	735	712	721	722	737
8911.5	730	729	736	722	734	730
8910.25	681	690	684	686	676	668
8909.5	675	672	690	665	673	
8908.5	719	709	712	720	720	734
8907	706	688	701	721	721	699
8906.5	724	716	730	723	728	725
8905.5	689	692	701	690	686	676
8904.3	689	691	685	694	688	687
8903.23	731	725	734	721	745	732
8902.5	714	712	709	722	713	716
8901.5	753	757	761	758	746	741
8900.5	705	711	698	695	715	707
8899.25	728	721	717	724	742	737
8898.5	729	724	732	724	715	749
8897.5	737	735	731	729	746	746
8896.5	747	747	754	744	740	752
8895.7	753	743	774	747	758	745
8895.3	559	560	548	539	576	573

Depth (ft)	Average RHN	Individual RHN Measurements				
8894.8	586	580	593	583	588	588
8894.1	633	643	621	617	641	642
8893.25	720	712	712	735	717	725
8891.2	743	732	748	749	734	751
8890.5	735	726	734	731	742	742
8889.5	740	736	747	740	739	739
8889	750	733	763	749	754	752
8888	658	646	662	656	667	661
8887.5	693	680	695	700	690	699
8886.5	731	710	746	731	717	751
8885.5	719	707	718	722	721	726
8884.5	696	704	699	665	719	692
8883.5	678	651	684	676	682	695
8882.25	688	688	674	700	682	695
8881.5	694	705	679	698	700	686
8880.5	725	747	736	708	717	718
8879.5	709	701	709	711	714	711
8878.5	712	718	716	702	717	705
8877.25	705	723	692	701	703	708
8876.5	743	733	755	737	752	739
8875.5	764	763	774	740	771	771
8874.8	753	752	751	752	764	747
8874.2	694	706	685	692	687	702
8873.65	540	544	540	523	550	543
8871.3	577	579	559	578	581	586
8870.6	633	639	634	639	627	624
8869.8	568	577	566	557	572	568
8869.2	608	609	598	619	604	608
8868.5	580	583	573	583	582	577
8867.8	576	572	569	582	587	572
8867.4	719	715	726	721	718	717
8866.3	703	701	705	709	698	704
8865.5	607	595	599	622	601	620
8864.6	615	586	613	635	632	607
8863.2	647	647	646	643	654	647
8862.7	744	740	753	740	751	738
8862	720	713	726	718	715	727
8861.6	741	731	752	753	729	739
8860.3	700	706	705	706	693	692
8859.9	733	720	733	717	740	753
8859.4	725	728	736	722	718	720
8858.6	744	742	749	736	749	744
8857.7	748	748	748	751	744	751
8856.7	750	747	749	745	761	747
8855.25	722	719	712	740	710	728

Depth (ft)	Average RHN	Individual RHN Measurements				
8854.7	703	711	695	693	707	710
8853.5	728	727	721	731	728	733
8851.4	722	716	716	722	725	733
8850.4	729	731	726	728	724	737
8848.4	714	710	704	719	715	724
8847.5	730	705	735	737	733	740
8846.8	749	743	751	749	751	752
8846.4	735	733	743	729	734	737
8845.7	706	703	703	708	703	711
8845.4	722	724	720	725	716	727
8843.7	730	737	729	727	725	734
8842.4	741	753	730	744	731	746
8841.3	753	751	753	756	752	755
8841.1	741	734	729	761	743	737
8840.7	707	702	716	710	707	700
8840.5	732	734	730	733	730	731
8840.2	742	733	746	741	739	749
8839.8	723	717	720	731	727	719
8839.1	711	704	705	718	718	708
8838.8	689	689	690	693	686	688
8838.1	669	662	683	655	666	678
8837.5	730	715	732	743	733	727
8836.9	748	745	748	750	743	752
8836.4	645	636	662	643	641	643
8835.4	631	642	627	626	632	628
8834.9	742	759	755	730	737	727
8834.5	742	748	747	747	730	738
8834.2	716	711	728	704	721	717
8833.65	662	661	674	658	654	665
8831.4	691	696	699	685	693	681
8830.3	714	719	714	717	715	706
8829.4	746	743	753	747	743	744
8828.7	741	731	741	755	740	739
8826.4	736	724	738	730	736	753
8825.3	741	727	746	741	756	736
8824.4	726	712	742	731	724	720
8823.4	731	723	729	735	727	742
8823	706	702	718	703	700	708
8822	697	713	697	688	687	702
8821.3	687	671	682	690	682	709
8820.5	708	711	719	696	718	694
8819.7	696	699	700	687	711	681
8818.8	704	696	713	717	692	704
8817.5	744	745	750	749	740	738
8816.6	690	694	689	693	688	684

Depth (ft)	Average RHN	Individual RHN Measurements				
8816	697	696	695	696	698	702
8815.5	674	673	655	687	696	658
8815.1	676	685	656	672	689	679
8814.5	686	685	685	697	690	673
8813.4	565	566	563	571	569	556
8810.6	696	707	694	700	686	695
8810.2	645	645	633	650	662	637
8809.5	633	639	634	634	625	631
8808.5	654	641	656	660	655	659
8807.6	669	667	678	669	664	668
8806.3	656	652	659	657	654	660
8805.25	670	671	656	676	671	678
8804.5	712	710	706	712	718	715
8803.5	418	395	434	430	423	406
8802.55	526	501	536	537	528	526
8802.4	480	486	476	482	486	471
8801.6	523	530	530	523	513	521
8800.35	610	625	592	606	588	639
8799.25	584	555	590	603	575	595
8798.3	727	728	740	722	717	727
8797.6	452	449	454	445	470	441
8796.9	534	532	533	536	539	530
8796.7	759	775	750	742	768	759
8796.5	749	757	732	771	745	739
8796.2	410	406	411	419	410	405
8795.8	335	343	332	342	323	333
8795.4	327	320	306	350	330	327
8795.15	444	443	456	430	444	447
8794.75	709	715	711	704	720	694
8794.5	562	537	566	562	584	561
8794.35	511	507	512	508	509	518
8794.25	471	483	470	475	463	463
8793	354	384	338	344	341	362
8792.5	551	536	554	556	556	552
8792.2	550	545	557	535	557	557
8791.9	537	524	537	545	546	534
8791.7	456	472	460	436	458	454

Core #6 – Rebound hardness data

Depth (ft)	Average RHN	Individual RHN Measurements				
10316.1	323	323	302	349	311	
10314.5	629	655	638	604	640	633
10313.5	591	563	590	585	579	610
10313.3	694	697	693	696	698	686
10312.6	635	636	632	641	645	
10312.2	443	414	447	468	471	413
10311.8	654	656	684	631	665	633
10311.4	668	685	685	686	673	646
10311.35	714	710	719	714	712	717
10310.5	712	718	719	685	721	715
10310.3	763	761	778	746	762	769
10309.5	770	789	785	742	758	775
10308.9	932	918	940	938	923	941
10308.5	753	732	769	752	746	765
10308.4	665	655	677	658	683	651
10308.3	684	698	676	670	710	667
10308.2	733	748	737	729	723	730
10307.5	821	813	817	823	831	819
10307.4	838	836	842	837	840	835
10307.2	778	752	791	784	787	785
10307.16	741	748	743	740	746	730
10307	809	804	815	804	810	810
10306.6	793	795	796	804	776	795
10306.5	758	737	767	751	780	773
10305.5	703	692	724	708	692	697
10304.5	715	694	737	705	703	737
10304	771	778	765	771	763	780
10303.7	710	689	713	714	706	728
10303.4	634	638	652	639	601	640
10303.2	744	730	759	727	752	752
10302.5	694	661	700	695	706	709
10301.5	764	748	779	769	778	748
10301	735	722	737	740	754	721
10300.6	684	667	715	669	667	691
10299.7	617	596	622	611	607	649
10299.4	691	693	693	696	689	683
10299.23	678	678	677	678	682	677
10298.2	680	678	689	675	677	682
10297.2	719	712	733	702	726	721
10296.5	711	704	723	694	723	709
10295.7	688	684	686	674	700	677
10295.4	718	725	726	704	714	722
10295.1	651	631	674	627	656	666
10294.5	676	653	684	661	686	697

Depth (ft)	Average RHN	Individual RHN Measurements				
10292.3	685	687	673	690	696	677
10291.5	681	675	686	681	687	676
10290.5	798	807	788	784	801	812
10289.5	582	558	598	603	586	567
10288.5	757	763	762	749	736	774
10287.7	645	619	658	643	665	638
10287.2	748	757	736	740	770	736
10286.5	693	696	698	693	692	694
10285.5	687	704	702	667	710	716
10284.5	733	731	721	685	710	688
10283.5	688	663	685	702	690	701
10282.6	687	678	692	681	702	684
10281.5	645	660	629	634	658	643
10281.15	671	669	665	669	676	674
10280.9	657	655	671	651	658	650
10280.3	826	834	854	820	806	818
10279.5	683	690	692	696	662	665
10278.5	819	793	834	823	806	839
10277.4	711	696	727	720	676	727
10277.25	760	755	763	765	754	764
10277.1	785	788	763	789	790	795
10276.95	782	779	790	782	778	780
10276.7	790	804	787	788	787	785
10276.5	779	762	787	790	783	771
10276.4	808	814	805	804	812	806
10275.5	694	707	688	696	675	705
10275.2	778	786	775	771	780	780
10274.8	773	772	763	777	780	773
10274.6	785	804	780	781	776	784
10274.5	779	776	786	772	777	786
10274.3	792	790	799	780	796	794
10274.15	779	783	776	778	779	778
10274.05	761	762	768	758	755	762
10273.5	626	617	638	640	637	600
10272.9	701	692	703	697	700	715
10272.43	766	761	762	779	763	764
10272.35	795	787	798	793	804	794
10272.29	786	771	795	783	785	795
10272.23	814	814	801	814	823	817
10272.2	818	822	823	807	812	825
10272.05	760	760	768	747	764	762
10271.7	706	712	694	694	700	732
10271.2	803	788	812	814	812	790
10270.5	749	735	760	744	749	755
10270.2	740	741	750	734	738	739

Depth (ft)	Average RHN	Individual RHN Measurements				
10269.5	651	658	665	643	636	651
10268.8	662	652	659	675	653	669
10268.5	670	643	682	679	660	685
10268.3	671	655	678	672	675	677
10267.4	634	638	640	633	629	629
10267.4	618	610	625	601	625	628
10266.5	753	762	758	740	747	760
10266.4	775	773	777	767	772	786
10266.2	706	703	715	690	711	712
10265.7	678	678	687	689	668	669
10265.5	558	551	562	572	537	569
10265.2	592	577	594	608	583	598
10263.75	888	911	864	904	878	884
10263.5	781	769	763	775	785	811
10263	820	817	839	818	817	819
10262.75	631	620	629	633	628	645
10261.2	743	723	767	743	752	728
10261.1	822	823	837	813	822	813
10260.9	812	817	828	809	787	820
10260.8	744	746	744	745	747	737
10260.7	750	748	765	740	738	761
10260.2	870	872	871	876	851	879
10260.1	880	876	876	893	878	886
10259.5	720	712	717	713	722	737
10259.35	676	691	686	677	660	668
10259.2	719	722	715	710	723	724
10259	611	623	612	595	618	608
10258.92	708	708	707	705	700	720
10258.7	614	586	620	629	620	615
10258.6	792	789	799	814	782	777
10258.2	779	755	801	783	779	779
10257.85	737	741	736	734	738	737
10257.7	849	864	849	866	868	832
10257.15	793	814	791	778	807	776
10256.5	666	673	666	660	674	659
10256.5	583	564	594	594	587	577
10256.4	676	682	677	671	667	681
10255.3	764	789	756	754	763	756
10254.9	811	805	816	813	809	814
10254.7	762	766	786	761	753	744
10254.3	756	746	755	765	756	759
10253.5	700	689	717	693	705	699
10252.2	707	707	702	712	717	695
10251.9	680	656	687	685	686	687
10251.2	613	625	619	580	620	621

Depth (ft)	Average RHN	Individual RHN Measurements				
10250.9	845	852	848	847	843	835
10250.85	656	649	648	653	679	651
10250.6	639	630	649	638	639	637
10250	702	684	704	706	704	713
10249.5	705	700	708	705	709	702
10248.5	706	696	705	700	714	717
10247.2	791	786	796	787	796	788
10247.1	870	864	882	874	861	870
10247.05	907	906	909	906	904	909
10246.7	745	725	752	746	759	741
10246.34	790	793	788	787	794	789
10246.3	747	746	748	755	745	740
10246.23	812	808	809	815	816	813
10246.2	798	786	802	806	798	799
10246.15	806	807	805	808	810	799
10246.06	735	738	735	729	740	733
10246.05	760	759	767	748	769	759
10245.5	787	782	793	809	785	768
10244.5	788	791	787	788	781	792
10244.25	753	758	749	759	752	745
10244.12	696	689	702	687	699	701
10244.05	700	696	700	701	698	703
10243.64	699	701	692	702	707	693
10243.6	679	679	682	675	683	675
10243.5	656	645	671	676	661	628
10243.45	800	818	795	791	787	811
10243.22	704	696	694	714	705	712
10243.15	690	688	695	691	688	686
10242.9	691	686	694	693	694	686
10242.81	691	693	687	690	693	692
10242.35	725	722	737	731	701	736
10242.1	741	738	738	758	711	759
10241.6	755	779	759	779	732	726
10241	688	694	698	689	675	686
10240.6	676	674	688	657	668	697
10240.2	689	713	699	671	671	689
10239.92	752	752	756	747	754	750
10239.86	777	777	778	776	778	775
10239.76	736	741	737	737	731	735
10239.7	648	665	647	642	629	655
10239.5	698	685	716	703	683	702
10238.5	687	663	679	695	694	702
10237.2	609	605	610	603	632	593
10236.5	656	637	670	671	658	645
10235.5	689	680	698	701	673	694

Depth (ft)	Average RHN	Individual RHN Measurements				
10234.6	734	723	747	723	736	743
10234.5	739	736	727	746	738	749
10234.3	764	761	772	765	762	758
10234.1	774	780	775	772	774	771
10233.5	754	734	765	759	761	753
10233.1	777	776	781	778	776	773
10232.92	772	756	783	766	771	784
10232.32	838	851	812	853	829	844
10232.15	801	784	776	813	815	815
10232.1	788	791	781	787	786	794
10231.64	861	875	868	860	856	846
10231.5	887	885	890	883	890	887
10231.4	911	918	915	919	907	894
10230.85	653	654	655	643	661	651
10230.5	545	540	574	531	528	552
10229.5	583	553	600	567	591	605
10229.2	660	677	660	654	660	650
10228.95	700	695	692	710	699	705
10228.85	698	697	684	698	705	706
10228.5	685	680	706	679	690	670
10227.2	734	722	758	742	718	728
10226.5	665	659	672	679	631	686
10225.5	654	628	655	642	680	666
10224.8	712	720	707	721	698	712
10224.55	767	775	765	769	744	783
10224.55	745	743	753	733	766	730
10224.5	688	679	666	707	695	692
10224.45	708	703	710	709	709	708
10224.35	720	722	720	716	716	725
10224.2	699	699	695	710	697	696
10224.1	645	621	653	654	673	623
10223.95	686	688	691	694	681	678
10223.85	688	691	683	680	693	692
10223.5	624	608	638	630	623	623
10223.3	717	719	711	718	716	719
10222.2	695	689	702	710	701	675
10222.15	711	702	716	705	730	701
10221.84	714	710	707	714	712	725
10221.6	691	693	689	689	695	691
10221.5	681	682	696	686	665	677
10221.4	698	703	700	699	690	700
10219.9	745	729	760	753	735	748
10219.5	693	670	698	708	684	703
10218.5	661	655	655	689	654	650
10217.2	666	657	681	684	641	667

Depth (ft)	Average RHN	Individual RHN Measurements				
10216.5	676	673	678	691	687	650
10215.5	725	725	731	714	729	726
10214.8	739	729	729	752	740	746
10214.5	705	705	702	713	699	704
10214.4	677	673	677	673	655	707
10214.14	715	718	706	714	719	720
10214.1	701	696	699	697	712	701
10214	668	670	684	649	689	648
10213.6	722	724	731	733	714	706
10212.2	761	756	782	774	751	744
10211.5	705	703	714	707	690	712
10210.9	795	806	802	789	789	791
10210.8	782	784	783	780	775	786
10210.5	762	754	770	755	781	751
10210.4	773	767	775	772	775	774
10210.14	817	819	815	823	816	813
10209.4	664	674	681	654	660	653
10208.5	612	628	628	617	594	592
10207.3	841	852	848	848	832	825
10207.22	875	879	871	879	872	874
10207.2	865	861	881	862	837	883
10206.85	831	835	833	830	833	824
10206.5	740	740	741	748	730	741
10205.6	694	667	706	708	690	700
10204.4	823	822	828	817	827	819
10204.4	810	804	817	817	792	822
10204.1	826	830	825	819	810	846
10203.6	767	769	759	762	777	768
10203.5	775	759	792	778	777	769
10203.32	891	897	885	893	891	890
10203.2	733	723	731	725	745	741
10203.08	887	879	887	894	881	895
10202.22	728	722	729	733	729	726
10202.2	730	777	801	691	699	680
10201.89	784	774	814	782	781	770
10201.6	764	765	764	762	765	763
10201.5	730	727	734	727	729	733
10201.5	724	717	728	723	724	726
10201.3	793	787	800	780	797	799
10201.15	714	704	718	719	717	711
10200.5	721	693	731	738	742	703
10199.5	899	895	900	902	901	895
10198.5	758	728	767	769	761	763
10197.2	749	760	759	742	735	750
10196.5	666	660	669	675	650	674

Depth (ft)	Average RHN	Individual RHN Measurements				
10195.4	723	721	730	725	728	711
10194.7	745	743	749	751	731	751
10194.1	817	794	804	818	834	833
10193.5	710	716	704	711	706	711
10192	733	724	737	742	742	718
10191.5	759	759	763	766	738	770
10190.5	720	702	719	728	720	731
10189.5	690	671	685	701	683	710
10188.5	702	704	698	711	704	693
10187	670	674	686	678	668	644
10186.5	660	657	660	658	637	686
10185.5	617	622	628	631	606	599
10184.5	611	615	620	590	610	621
10183.5	616	596	645	622	594	622
10182.2	686	675	657	706	707	684
10181.5	695	689	697	706	680	702
10180.5	650	639	645	660	640	668
10179.5	670	675	668	676	672	657
10178.5	673	658	673	670	681	685
10177.2	674	663	681	679	687	660
10176.5	664	666	651	675	671	659
10175.5	677	695	676	660	672	681
10174.65	684	667	677	696	684	697
10173.6	738	737	726	745	736	744
10172.3	634	659	629	632	622	627
10171.5	726	751	718	727	717	717
10170.5	611	617	588	616	634	602
10169.5	711	696	713	717	716	712
10167.25	730	729	733	732	728	727
10166.5	721	718	722	720	737	708
10165.7	542	530	542	535	547	555
10165.2	704	675	714	723	709	697
10164.7	564	565	563	564	574	553
10164.2	669	667	679	675	650	674
10163.5	689	711	684	682	684	686
10162.25	712	724	695	716	707	716
10161.5	678	687	666	684	672	680
10160.5	704	717	728	695	686	695
10159.5	649	651	650	637	645	662
10158.5	681	685	673	707	677	663
10157.25	703	699	709	714	701	694
10156.5	650	620	652	661	651	668
10155.9	723	724	719	728	721	724
10155.4	696	682	692	717	685	702
10154.5	679	666	686	675	703	664

Depth (ft)	Average RHN	Individual RHN Measurements				
10153.5	697	694	696	715	682	697
10152.9	625	613	637	637	600	636
10152.5	629	630	646	628	615	626
10152	676	683	680	673	660	682
10151	704	705	688	711	705	711
10150.5	698	675	720	712	700	684
10149.5	667	669	652	649	675	688
10148.7	696	673	692	687	714	712
10148.1	721	715	724	734	731	701
10147.95	724	727	707	733	724	728
10147.7	739	734	741	739	740	741
10147.5	717	718	715	710	715	725
10147.3	714	700	713	728	703	724
10147.25	702	699	705	707	704	697
10147.2	738	737	741	737	741	735
10146.65	732	731	739	733	732	726
10146.5	700	699	713	715	690	681
10146.4	718	710	708	715	725	733
10145.9	704	698	699	713	698	714
10145.65	708	713	723	703	693	710
10145.6	710	708	717	716	710	701
10145.5	705	702	699	713	707	703
10144.5	704	693	695	708	722	701
10143.5	703	676	720	713	700	707
10143.1	721	727	729	698	734	719
10143.03	733	736	737	731	736	727
10142.9	734	746	734	723	737	732
10142.5	681	658	705	702	667	675
10142.25	713	699	702	706	747	710
10141.7	734	737	744	730	719	739
10141.2	737	745	731	743	721	746
10140.7	734	731	742	739	739	720
10139.5	727	740	739	729	701	725
10138.5	716	739	711	699	716	717
10137.3	704	701	716	704	705	694
10136.5	680	673	688	702	666	670
10135.5	709	710	696	726	699	716
10134.5	691	670	682	712	682	708
10134	640	638	645	659	635	623
10133.4	679	658	682	708	686	662
10132.7	713	698	737	706	724	699
10132.25	657	653	661	672	643	658
10131.5	708	715	717	718	693	697
10130.6	651	659	635	620	669	672
10130.1	562	542	567	579	566	558

Depth (ft)	Average RHN	Individual RHN Measurements				
10129.5	646	631	624	665	637	674
10128.5	625	619	634	632	619	620
10128	725	734	727	748	704	710
10127.25	722	692	728	741	735	714
10126.9	566	569	570	580	538	572
10126.5	729	713	731	741	738	721
10125.5	736	745	745	730	722	740
10125	572	571	566	584	564	576
10124.4	727	714	713	743	742	725
10123.5	735	735	741	740	723	735
10122.25	678	683	688	686	666	665
10121.5	716	725	716	683	729	729
10120.2	692	669	697	710	683	703
10119.6	644	649	640	660	635	635
10119.3	636	639	648	640	626	625
10118.8	675	680	683	676	665	672
10117.4	661	669	667	664	653	651
10116.9	551	532	541	549	566	569
10116.2	527	516	531	525	536	526
10115.5	685	691	680	680	706	669
10114.5	680	681	701	699	664	654
10113.6	669	681	678	682	647	656
10113.25	618	620	614	625	598	635
10112.25	636	640	628	648	635	629
10111.2	644	670	642	637	630	641
10110.9	544	546	569	531	547	528
10110.4	628	606	606	640	648	650
10109.5	672	688	664	671	675	703
10108	636	638	650	631	624	635
10107.3	437	432	469	425	411	446
10107	668	670	674	677	667	653
10106.5	647	635	646	644	662	650
10105.5	661	659	678	669	652	646
10104.9	634	624	635	663	629	619
10104.25	643	632	636	654	639	653
10103.5	657	667	679	630	662	647
10102.7	663	643	653	646	683	689
10102.25	660	651	657	655	673	656
10101.5	710	688	703	737	693	729
10100.5	656	678	653	648	635	666
10099.5	617	607	636	605	633	604
10098.5	665	669	681	675	658	642
10097.35	707	691	704	722	689	728
10096.5	702	692	694	715	702	708
10095.5	749	729	752	755	758	751

Depth (ft)	Average RHN	Individual RHN Measurements				
10095	696	701	691	685	706	696
10095	683	660	680	690	703	683
10094.5	747	755	736	758	734	752
10094.5	737	728	740	735	744	737
10093.5	613	617	617	607	612	611
10093.5	597	588	606	609	603	578
10092.8	660	639	672	664	653	670
10092.5	666	667	662	667	667	668
10092.25	659	654	671	669	658	644
10091.7	677	671	686	687	678	665
10091.6	690	686	695	692	689	688
10091.2	721	714	727	720	718	725
10090.5	722	715	742	729	717	707
10090.2	770	776	777	771	763	764
10090	720	723	727	727	730	694
10089.7	770	775	769	790	758	756
10089.6	801	794	817	800	798	798
10089.55	774	774	781	773	774	766
10089.53	767	774	767	763	761	772
10089	640	639	617	641	657	647
10088.3	662	699	651	650	646	662
10087.25	699	673	703	690	710	721
10086.5	654	684	671	640	641	633
10085.5	666	653	671	688	665	654
10084.5	595	585	597	616	586	593
10083.5	668	663	648	675	686	666
10083	667	678	674	678	646	658
10082.4	653	651	672	652	647	645
10081.8	623	624	622	633	621	616
10081.3	689	679	687	709	688	683
10080.8	622	621	633	602	634	619
10080.3	657	630	656	660	672	668
10079.7	601	590	600	628	604	581
10078.5	688	717	679	695	685	664
10077.25	682	683	693	682	670	
10076.5	660	633	660	671	671	665
10075.5	687	684	692	699	667	692
10074.5	702	696	722	691	699	704
10073.96	776	771	755	787	785	784
10073.9	734	742	732	730	725	740
10073.86	692	694	696	683	701	688
10073.5	636	621	643	671	627	618
10072.4	729	733	711	728	741	733
10072.25	743	729	741	759	759	727
10072.15	737	731	747	726	735	744

Depth (ft)	Average RHN	Individual RHN Measurements				
10071.7	645	640	660	664	629	633
10071.5	645	643	663	642	646	632
10070.5	694	696	698	699	692	687
10069.5	827	808	851	832	799	843
10068.5	648	659	638	658	628	658
10067.25	641	643	657	647	616	644
10065.7	767	757	766	769	770	775
10065.5	704	705	710	718	708	679
10065.2	760	757	762	771	748	762
10064.95	799	803	800	795	808	788
10064.8	772	772	770	775	772	769
10064.5	701	685	700	719	697	704
10063.7	608	610	622	614	613	582
10063.2	632	610	640	623	641	644
10062.45	685	657	670	694	705	697
10061.5	708	698	720	701	726	694
10060.5	597	597	611	592	604	582
10059.5	581	604	585	570	572	573
10058.9	680	665	680	681	691	683
10058.3	598	588	604	619	592	587
10057.7	552	543	570	544	573	529
10057.25	662	643	664	642	675	688
10056.5	700	696	707	701	695	700
10055.5	673	682	672	663	689	661
10054.5	682	675	690	688	686	670
10053.5	683	672	691	690	692	652
10052.25	651	637	661	671	658	630
10051.5	684	687	690	705	670	670
10050.3	560	547	560	577	547	569
10049.9	594	600	591	586	585	608
10049.4	625	609	637	626	638	613
10048.8	667	665	662	673	668	668
10048.2	630	628	646	635	628	614
10047.7	670	674	665	677	668	665
10047.5	692	685	703	687	688	695
10047.37	745	722	757	749	756	741
10047.25	648	634	665	668	647	624
10047.1	747	733	753	748	752	750
10046.98	651	652	656	650	651	645
10046.75	747	747	741	747	748	752
10046.5	710	703	713	732	708	693
10046.35	726	721	744	738	732	696
10046.2	624	618	633	631	628	610
10045.5	598	586	588	605	601	610
10044.8	587	591	579	583	587	593

Depth (ft)	Average RHN	Individual RHN Measurements				
10044.3	515	506	522	506	514	527
10043.5	533	530	556	519	553	509
10042.35	618	597	614	629	628	621
10041.8	632	650	629	639	635	608
10041.3	637	612	652	611	647	663
10040.8	604	605	601	607	603	602
10040.2	479	487	459	480	471	496
10039.5	544	531	544	554	545	546
10038.5	612	619	630	608	596	609
10037.8	645	652	647	638	641	646
10037.3	643	627	627	652	659	648
10036.6	587	586	593	593	583	580
10035.9	608	602	617	627	604	589
10035.3	587	560	602	590	593	592
10034.5	553	545	565	568	542	544
10033.5	608	598	608	591	621	624
10032.25	621	619	615	629	632	609
10031.5	573	559	572	567	581	584
10030.5	591	579	607	583	614	572
10029.5	537	533	543	516	556	537
10028.5	577	579	573	577	574	583
10027.3	634	620	633	646	632	638
10025.5	570	550	565	570	579	588
10024.5	623	623	621	629	621	619
10023.5	494	497	491	487	511	485
10022.25	614	611	609	630	617	603
10021.5	627	636	622	621	630	628
10020.5	599	581	585	629	590	610
10019.6	601	587	603	606	611	596
10019.1	612	602	634	601	614	610
10018.5	622	635	629	636	609	599
10017.25	576	599	588	561	571	559
10016.5	609	582	630	615	611	609
10015.5	634	636	647	621	632	633
10014.5	699	675	717	697	726	678
10013.5	546	543	560	565	529	532
10012.9	692	686	703	703	683	687
10012.25	499	503	497	505	500	491
10011.5	671	648	659	694	664	688
10010.5	611	630	613	617	601	596
10009.5	685	664	702	682	710	668
10008.5	575	592	569	568	566	581
10007.25	677	660	672	681	696	
10006.8	664	674	651	644	662	690
10006.3	454	440	452	445	470	463

Depth (ft)	Average RHN	Individual RHN Measurements				
10005.5	609	594	635	603	600	611
10004.7	580	583	572	575	582	587
10003.5	701	709	710	695	708	682
10002.25	616	614	603	613	624	626
10001.4	523	511	539	506	545	514
10000.5	594	595	574	617	602	583
10000.1	445	430	421	443	464	467
9999.5	524	512	543	538	504	523
9998.9	574	573	585	574	571	569
9997.25	461	456	463	468	471	446
9996.5	461	459	479	462	445	458
9996	506	489	508	508	524	501
9995.5	711	688	713	718	720	714
9994.5	667	657	662	662	672	680
9993.5	658	646	658	665	672	651
9992.25	610	608	605	622	592	622
9991.5	652	629	648	660	650	671
9991.1	682	685	683	683	677	681
9990.6	673	669	683	674	676	663
9989.7	615	614	621	609	618	612
9989.2	656	645	660	671	648	658
9988.6	664	664	659	655	667	675
9988.42	636	657	632	634	632	624
9988.31	625	622	616	614	656	617
9988.3	681	678	674	679	688	685
9988.1	668	662	676	664	674	665
9987.9	660	650	659	659	662	670
9987.45	665	668	668	665	673	653
9987	676	669	673	679	680	680
9986.5	665	663	684	665	652	663
9986.1	637	637	631	642	632	645
9986	675	683	675	667	682	668
9985.6	633	631	634	631	634	633
9985.47	709	709	709	707	710	711
9985.4	689	694	712	667	703	670
9985.3	677	668	685	683	685	665
9985.08	702	684	708	696	701	719
9984.6	672	643	674	676	679	688
9984.5	694	686	699	691	687	706
9984.2	536	533	542	542	529	533
9984.1	563	547	579	587	565	535
9983.5	647	638	632	669	670	624
9982.25	644	646	638	635	651	652
9981.5	559	543	566	558	557	570
9981	469	465	464	494	448	473

Depth (ft)	Average RHN	Individual RHN Measurements				
9980.5	509	513	528	485	516	501
9979.5	532	530	551	518	528	532
9978.5	569	562	592	578	540	575
9977.15	585	586	587	582	584	585
9976.8	583	561	595	599	577	583
9976.3	540	517	536	554	556	535
9975.7	556	556	541	532	567	584
9974.6	579	591	588	582	565	570
9973.3	553	561	566	552	542	544
9972.5	573	567	586	589	565	559
9972	596	604	608	596	594	576
9970.6	496	493	492	485	506	504
9968.5	613	596	616	610	623	620
9967	592	605	608	600	574	572
9966.5	551	547	561	538	551	557
9965.7	625	631	643	641	608	603
9964.5	676	661	662	681	689	688
9964.2	665	657	662	656	667	684
9963.5	650	627	652	631	674	668
9962.35	685	686	687	697	675	682
9960.5	708	718	677	704	721	720
9959.4	564	552	574	583	536	573
9958.7	656	658	649	659	646	668
9958.54	510	510	522	500	505	514
9957.15	642	631	622	621	673	663
9956.8	504	508	486	496	510	518
9956.5	530	513	540	530	514	552
9955.7	603	587	607	585	636	599
9955.3	502	498	524	508	501	479
9954.6	664	644	669	652	696	659
9953.5	532	537	525	550	510	539
9953	639	634	644	625	659	634
9952.15	558	552	555	553	561	569
9951.5	691	687	700	696	689	684
9950.6	521	510	526	526	521	524
9950.2	525	529	543	540	489	524
9949.5	495	488	499	495	480	512
9948.5	563	534	578	580	564	557
9947.15	517	512	512	515	531	514
9946.7	502	497	509	485	524	496
9946.2	555	529	563	572	562	551
9945.5	565	563	570	551	570	570
9944.5	612	601	626	610	618	606
9943.5	549	531	560	561	542	552
9942	528	525	510	525	551	529

Depth (ft)	Average RHN	Individual RHN Measurements				
9941.5	538	553	528	523	545	543
9940.6	536	509	539	528	554	551
9939.7	564	547	562	582	575	552
9939.1	723	727	723	706	733	727
9938.8	725	718	735	731	712	730
9938.5	534	528	561	522	542	517
9937.8	700	685	707	695	697	716
9937	469	437	460	471	488	489
9936.3	524	531	510	501	540	539
9935.8	711	714	720	725	701	696
9934.6	674	666	656	690	679	678
9934.18	695	694	691	695	693	704
9933.8	673	667	667	677	677	676
9933.7	652	639	665	634	646	676
9932.6	668	662	676	664	669	668
9932	699	698	711	697	702	685
9931.1	701	702	709	685	722	686
9930.6	539	530	561	546	517	540
9930.2	561	556	571	555	552	573
9929.6	695	670	693	715	692	703
9928.4	658	645	637	637	682	687
9927	695	692	687	678	718	701
9925.7	684	683	689	690	679	679
9924.6	713	686	736	714	699	732
9923.5	506	497	514	530	505	482
9922	600	618	601	589	607	584
9921.5	617	611	620	608	625	623
9920.5	594	600	594	590	582	603
9919.5	560	560	540	558	581	563
9918.5	467	458	458	467	477	474
9917.9	739	715	736	741	744	757
9917.6	422	399	450	421	430	411
9917	728	699	739	752	719	733
9915.8	726	717	722	714	741	737
9915.4	497	489	503	493	498	500
9915.2	459	451	478	436	451	479
9914.7	681	653	688	682	686	694
9914.2	671	660	671	664	682	680
9913.5	613	591	622	607	630	617
9912.2	688	686	690	689	690	687
9912	658	649	648	654	667	
9911.85	686	688	694	689	676	683
9911.7	681	689	676	679	679	680
9911.4	691	687	708	693	682	683
9911.3	709	715	718	693	712	709

Depth (ft)	Average RHN	Individual RHN Measurements				
9910.5	705	708	703	709	707	698
9910.25	734	734	732	737	726	742
9909.25	583	560	615	579	568	595
9908.5	556	536	578	531	573	561
9907.7	564	542	576	578	578	548
9907	629	624	629	634	632	625
9906.5	556	521	553	563	558	586
9905.6	418	429	427	406	436	393
9904.5	490	505	504	468	489	486
9903.3	530	509	517	532	542	552
9902	439	414	453	445	443	439
9901.6	374	389	369	395	383	336
9900.1	726	718	732	708	734	736
9899.8	718	714	733	724	714	704
9898.5	706	695	706	701	708	718
9897.8	647	633	631	661	667	642
9897	649	635	643	639	661	667
9896.3	386	402	391	397	388	354
9895.2	721	714	726	716	722	729
9894.5	719	728	710	720	715	722
9893.9	678	683	697	667	673	669
9892.15	380	376	378	368	400	378
9891.4	494	466	504	483	504	514
9890.7	781	772	790	794	765	782
9889.4	702	701	696	700	703	710
9889	682	684	679	678	688	680
9888.6	724	718	743	725	718	714
9887.8	672	671	690	677	657	664
9887.15	688	680	719	683	679	681
9885.5	709	691	712	711	717	715
9885.1	711	691	709	695	734	724
9884.7	407	385	417	424	417	391
9883.6	532	539	535	518	564	503
9882.15	635	636	646	630	633	630
9881.5	543	558	541	538	516	564
9880.4	446	412	432	462	480	444
9879.8	450	439	454	449	447	463
9879.4	439	421	417	465	430	462
9878.5	570	564	560	586	568	570
9877.15	703	703	684	709	724	696
9876.8	554	552	549	548	555	565
9876.3	660	657	666	660	653	666
9875.2	583	584	591	561	596	584
9874.3	615	613	620	624	615	604
9873.8	577	559	587	586	578	575

Depth (ft)	Average RHN	Individual RHN Measurements				
9872.35	509	507	508	502	512	515
9871.5	534	551	510	540	536	534
9870.4	541	544	537	527	549	550
9869.5	504	487	518	502	510	502
9869.1	574	569	591	579	556	573
9868.8	592	589	600	582	608	582
9867.35	614	602	612	616	614	625
9866.5	620	602	620	628	629	621
9865.5	608	605	600	604	614	616
9864.8	529	528	513	525	539	541
9864.2	603	585	622	623	591	592
9863.5	643	635	640	657	648	634
9863.35	659	666	662	641	666	659
9863.21	680	672	673	685	686	685
9863.1	610	621	602	606	603	
9862.15	536	534	547	544	533	523
9861.5	545	536	558	542	535	554
9860.5	594	593	602	594	590	590
9859.7	587	599	600	575	591	572
9859.1	614	614	611	614	616	616
9858.5	655	651	661	654	652	656
9857.15	660	663	669	656	656	656
9856.8	675	669	656	669	692	689
9856.2	534	526	550	508	531	557
9855.5	519	520	518	495	549	515
9854.5	544	548	538	526	553	554
9853.5	592	587	594	597	593	587
9852.15	635	636	639	645	622	634
9850.5	668	674	658	688	665	655
9850	681	670	670	680	693	693
9849.5	675	675	687	650	686	677
9848.5	551	547	583	533	546	548
9847.8	580	580	585	578	587	568
9847.15	589	596	578	567	606	597
9846.5	554	554	551	537	566	563
9845.5	570	567	580	578	547	577
9844.5	603	615	608	575	600	615
9843.5	564	555	585	560	562	559
9842.15	563	538	582	559	568	569
9841.2	565	571	567	548	563	576
9840.5	566	566	559	569	570	567
9839.5	577	576	569	593	579	569
9838.5	578	565	588	579	579	580
9837.2	506	483	511	509	515	514
9836.5	513	511	501	514	511	529

Depth (ft)	Average RHN	Individual RHN Measurements				
9835.9	581	582	590	586	569	578
9835.5	682	682	685	684	681	678
9835.3	707	706	708	709	708	704
9834.7	689	692	695	685	686	688
9834.5	669	668	670	659	674	672
9834.14	536	530	527	544	523	555
9833.9	483	483	483	472	488	490
9832.15	591	576	585	594	601	599
9831.5	684	662	690	685	672	709
9830.5	710	722	725	703	699	701
9829.6	681	648	687	679	699	692
9829	668	667	684	682	648	658
9828.5	654	632	662	656	641	681
9827.7	458	485	460	460	442	444
9827.15	475	487	489	479	455	465
9826.5	500	490	497	494	508	511
9825.5	580	583	584	582	579	573
9824.9	597	572	613	619	602	579
9824.3	704	688	731	692	683	727
9823.8	663	677	653	677	655	655
9823.1	682	695	694	685	668	668
9822.2	495	492	501	493	492	
9821.5	508	484	496	514	527	521
9820.1	515	511	509	525	514	514
9819.6	547	562	565	530	545	533
9818.5	515	516	525	507	519	508
9817.15	689	679	707	695	677	687
9816.1	610	581	614	614	617	625
9815.6	693	694	690	694	697	692
9814.5	662	654	649	663	663	682
9813.7	763	758	776	768	741	772
9813.4	443	437	442	442	445	450
9813.1	567	582	538	580	555	580
9812.45	481	499	483	479	472	474
9811.2	534	525	543	543	521	540
9810.6	628	621	628	617	636	637
9809.9	646	640	633	660	636	660
9809.1	707	700	705	705	699	725
9808.5	725	733	726	715	736	716
9807.5	537	529	567	528	539	524
9807.15	754	766	739	752	739	773
9805.9	363	373	375	342	365	359
9805.5	389	395	403	380	382	383
9805	696	710	700	681	692	696
9804.5	477	472	492	465	475	480

Depth (ft)	Average RHN	Individual RHN Measurements				
9803.2	687	687	676	685	685	704
9802.55	420	411	425	405	426	431
9801.8	397	372	408	414	385	405
9801.1	734	750	706	724	754	735
9800.7	545	546	543	536	551	548
9799.8	545	545	528	579	535	536
9798.7	514	523	510	513	518	506
9797.1	443	432	441	432	456	452
9796.5	438	431	435	428	454	441
9795.5	531	542	524	509	536	544
9795.1	440	420	441	456	442	442
9794.6	417	401	413	423	446	400
9793.5	496	498	495	492	498	496
9792.15	493	490	502	490	499	485
9791.5	521	515	534	516	520	519
9790.5	522	522	521	519	533	517
9789.7	437	419	436	437	440	454
9789.1	539	523	555	545	527	544
9788.5	544	531	576	545	525	
9787.15	711	693	706	712	730	716
9786.5	708	711	683	734	716	696
9785.7	694	680	691	686	694	718
9785.3	595	595	598	597	591	596
9785	515	527	511	508	518	509
9784.5	355	367	334	356	366	353
9783.5	465	466	463	462	474	461
9782.5	421	424	426	419	426	412
9782.2	472	465	473	484	454	482
9781	682	688	680	672	665	707
9780.7	632	605	634	643	631	645
9780.2	604	607	615	583	583	632
9779.5	414	406	420	393	438	412
9778.1	416	416	428	411	411	416
9777.2	571	562	548	584	587	572
9776.5	582	610	572	581	582	563
9775.5	541	535	544	514	562	551
9774.5	517	514	521	527	524	497
9773.5	513	509	520	535	503	500
9772.35	579	590	574	577	582	571
9771.5	391	368	413	383	407	385
9770.5	413	407	425	416	402	415
9769.5	402	388	396	401	415	411
9768.5	563	569	556	558	563	568
9767.35	371	364	382	356	375	377
9766.5	431	428	433	434	425	435

Depth (ft)	Average RHN	Individual RHN Measurements				
9765.8	426	429	426	417	408	448
9765.52	418	411	405	429	416	430
9765.2	405	397	415	382	406	423
9764.7	747	732	758	743	750	750
9764.2	440	441	441	440	440	439
9763.7	444	437	449	439	451	446
9763	461	434	474	474	453	472
9762.7	740	732	757	724	747	738
9762.2	379	375	351	396	387	385
9760.5	720	703	743	749	706	699
9759.8	782	781	790	782	778	780
9759.3	435	437	434	404	450	450
9758.5	453	441	439	441	474	469
9757.6	466	472	462	462	452	483
9757.2	689	691	685	681	693	694
9756.1	459	460	448	450	466	470
9755.5	488	492	510	490	476	472
9754.5	478	477	492	481	475	465
9753.5	449	444	471	441	450	441
9752.7	493	470	489	486	512	508
9752.2	604	602	603	598	619	600
9751.6	668	677	682	672	645	666
9751	460	452	462	436	465	484
9750.3	679	679	680	669	680	687
9749.6	440	425	449	460	417	447
9749	455	438	475	470	457	435
9748.5	496	505	509	475	505	486
9747.2	486	477	483	489	490	491
9746.5	450	447	455	452	451	444
9745.5	491	487	502	484	493	489
9744.8	626	643	644	606	602	633
9743.3	538	541	561	528	535	524
9742.7	566	565	564	571	566	563
9742.25	608	615	584	633	608	599
9741.5	461	459	463	458	460	467
9740.6	473	486	468	458	478	473
9740.2	449	437	430	445	468	463
9739.5	347	357	360	331	350	335
9738.8	403	410	410	388	402	404
9737.3	576	584	588	574	564	571
9737.2	495	482	498	485	504	504
9736.6	663	664	669	650	665	665
9736.5	668	667	672	674	668	661
9736.15	526	508	536	519	532	537
9735.5	431	441	424	435	419	438

Depth (ft)	Average RHN	Individual RHN Measurements				
9734.5	352	355	363	339	356	348
9733.5	465	456	469	489	455	458
9732.15	466	468	460	456	469	476

Outcrop samples – Rebound hardness data

Sample #	Lithology	Average RHN	Individual RHN Measurements				
F1	chert	852	865	831	866	848	850
F1	mudstone	646	651	654	648	634	642
F2	mudstone	661	665	665	656	662	659
F3	chert	890	905	900	855	896	893
F4	chert	940	948	949	940	928	936
F5	chert	956	961	965	949	949	957
N1	chert	913	897	936	898	926	907
N2	mudstone	677	679	678	675	675	680
N3	chert	918	924	924	923	916	902
N4	chert	940	938	949	937	937	938
N5	mudstone	665	669	658	665	666	668
N6	mudstone	668	677	664	672	664	664
N7	chert	892	876	905	889	892	897
N8-1	chert	847	846	855	849	848	836
N8-2	mudstone	590	591	585	581	605	588
N9	chert	930	941	922	935	921	931
3-2-1	chert	915	915	898	925	927	909
4-1	chert	897	902	898	877	890	919
5-1	chert	933	937	941	936	921	930
6-1	mudstone	662	664	657	671	660	657
7-1	chert	886	878	863	900	903	885
11-1	chert	885	890	893	889	870	883
11-2	mudstone	684	687	684	685	686	677
14-1	chert	864	873	862	862	843	878
15-1	mudstone	620	626	626	617	616	615
17-1	mudstone	680	663	682	683	692	681
19-1	mudstone	675	674	669	675	682	675
21-1	mudstone	687	689	687	689	681	695

Vaca Muerta plug samples – Rebound hardness data

Plug #	Average RHN	Individual RHN Measurements					Notes
1v	324	321	306	342	334	319	
3h	292	296	276	281	286	320	at "top"
3h	284	287	274	287	287	285	at "base"
5v	541	547	548	545	520	545	
5v	544	549	547	548	534	543	
5v	547	547	542	546	542	560	
7v	254	263	246	281	246	236	
7v	254	253	240	254	229	295	
8v	247	240	220	257	260	256	
9v	409	415	410	417	411	393	
9v	328	322	343	319	329	327	
10v	322	308	335	314	318	337	
10v	339	335	352	335	346	329	
13h	411	398	408	386	453	410	
13h	414	429	407	424	386	423	
14v	476	447	483	482	488	481	
14v	467	471	471	478	459	458	
15v	482	478	478	482	484	489	
18h	462	453	449	457	468	484	
19d	447	448	444	466	444	435	
20h	367	349	389	347	357	392	
21v	388	388	398	398	382	376	
22v	555	559	558	558	548	554	
23v	339	346	337	323	333	356	
24h	529	534	531	524	535	521	
25h	553	561	553	552	556	543	
26h	493	468	472	527	486	510	
35v	373	376	355	376	368	392	
36h	489	495	492	480	484	493	
38h	434	433	428	441	453	417	
40h	451	432	446	470	473	434	
42h	491	502	496	496	483	479	
44h	473	501	477	445	486	458	
50h	403	412	393	417	419	373	
52h	367	368	375	352	361	378	
54h	382	371	375	372	394	397	
55v	444	440	449	443	437	452	
56h	576	572	588	578	569	574	
57v	306	282	314	312	322	298	
58h	272	302	272	261	270	256	
59v	510	523	538	493	493	501	
60h	502	503	502	493	502	510	
62h	283	291	307	258	275	285	
63v	450	443	451	454	440	462	

Plug #	Average RHN	Individual RHN Measurements					Notes
64h	535	532	532	540	533	539	
66h	535	505	534	536	545	555	
67v	455	466	466	455	450	440	
68h	560	561	562	553	573	553	
69v	344	349	320	356	355	339	
72h	597	605	596	592	596	596	
73v	490	494	467	505	477	507	
74h	336	329	343	345	326	337	
76h	576	578	568	580	570	584	
80h	374	365	396	365	387	355	
87v	559	547	552	558	583	555	at black side
87v	464	484	483	447	441	467	at yellow side
88h	606	596	634	597	598	603	at "top"
88h	581	573	582	571	613	566	at "base"
90v	521	521	509	500	515	559	
91h	517	527	518	514	513	512	
94v	391	394	397	394	373	396	
103h	444	449	457	444	433	436	
104v	425	443	413	436	398	433	
105h	468	478	472	463	461	465	at non-fractured side; gray @ center
106v	434	438	432	424	438	438	
107h	417	426	415	412	407	423	
108v	530	534	534	514	536	534	at gray, grainy side
108v	470	461	489	482	443	474	at black, muddy side
109h	606	608	603	605	601	611	at non-fractured side
110v	636	640	634	634	629	643	
111h	668	670	673	655	665	675	at non-vuggy side
111h	676	669	686	684	668	675	at vuggy side (not @ vug)
112v	573	574	578	571	566	574	
113h	597	594	591	599	601	601	at non-fractured side
114v	587	589	587	591	580	589	
115h	555	555	555	552	558	553	
117h	490	485	494	494	491	485	
118v	349	342	365	360	357	320	
119h	523	517	515	515	531	537	
122v	478	472	476	478	485	478	
123h	488	485	484	506	481	484	
124v	497	501	496	512	493	482	
126v	441	450	436	433	431	455	
127h	436	490	401	413	473	402	
130v	528	522	536	522	535	526	

Plug #	Average RHN	Individual RHN Measurements					Notes
131h	548	552	558	550	536	545	
132v	485	473	477	496	484	497	
133h	536	541	532	535	536	536	
135h	542	544	545	541	541	537	
136v	494	480	490	479	488	532	
137h	498	498	503	499	491	499	
138v	533	538	543	531	523	532	
139h	623	622	628	623	626	618	
140h	531	533	532	527	528	533	
141h	555	543	566	556	555	553	
144v	565	572	567	564	559	563	
145h	550	556	556	544	547	549	
147h	564	569	563	564	567	559	
148 (a)v	418	426	410	420	419	414	
148 (b)v	326	324	316	325	349	318	
153h	343	329	348	339	354	344	at non-fractured side
158v	445	445	446	443	451	439	
159h	376	394	376	367	358	386	
160v	340	339	339	337	338	349	at yellow side
160v	404	404	419	403	393	401	at black side
161h	476	464	468	468	489	492	at non-fractured side
164v	459	443	479	445	432	495	
165h	498	512	500	496	489	494	
166v	556	563	560	576	550	529	sandy
167h	604	593	619	583	608	616	sandy
168v (a)	325	320	334	335	327	309	sandy
173d	409	422	413	403	412	395	at non-fractured side
180h	542	541	547	541	544	538	
181d	480	477	479	477	477	488	
185d	448	447	461	454	444	435	
186h	507	496	512	499	520	507	
188d	525	525	530	523	517	530	
189d	671	668	671	676	665	673	at black side
189d	662	646	647	680	687	652	at fracture cement side
190h	567	557	581	581	551	564	at "top"
190h	566	570	562	570	568	559	at "base"
192 (v?)	630	614	634	635	631	634	at black side
192 (v?)	583	587	588	598	563	580	at fracture cement side
193d	649	641	661	652	634	659	at black side
193d	620	611	632	638	618	601	at fracture cement side

Plug #	Average RHN	Individual RHN Measurements					Notes
196d	473	472	471	485	474	464	at "top" - in black portion, not in gray lamination
197h	463	465	464	468	465	453	
199d	366	360	354	374	359	383	at more complete side - laminated
200d	316	331	318	313	325	295	
201d	418	394	405	440	450	400	
202d	351	334	348	358	362	353	
203d	471	469	471	474	470	469	
204h	345	339	338	366	343	341	at non-fractured side
206d	514	521	527	508	514	499	
207h	462	466	450	438	471	485	fractures seem to develop during testing
209d	440	430	444	451	450	424	
210d	429	423	432	436	418	437	
211d	482	495	461	472	501	481	
212d	527	523	530	521	535	528	
213d	507	503	514	504	514	500	
214d	433	436	450	414	431	435	
215d	495	474	497	523	494	487	at non-fractured side
216d	404	393	425	397	425	378	
218h	415	409	419	419	414	415	
220 (va)	435	436	440	426	442	433	
222d	313	299	326	308	339	291	
230d	332	325	344	345	332	312	
241d	537	527	542	537	548	529	at gray sandy side
241d	507	511	500	521	502	501	at black muddy side
D-02	484	469	461	507	465	519	"beef" fracture-fill?
D-05	538	536	543	536	538	538	
D-08	527	533	529	518	532	522	
D-12	507	503	503	509	519	501	at non-fractured side
D-11	510	510	507	511	517	506	
D-06	510	502	505	518	506	521	
D-09	468	448	457	473	479	485	
D-10	571	570	569	575	567	573	
D-07	552	540	555	560	561	543	

VITA

Yulun Wang

Candidate for the Degree of

Doctor of Philosophy

Thesis: SEQUENCE STRATIGRAPHY, FRACTURE CHARACTERIZATION, AND REBOUND HARDNESS ANALYSIS OF THE UNCONVENTIONAL "MISSISSIPPIAN LIMESTONE"/STACK PLAY, NORTH-CENTRAL OKLAHOMA, USA

Major Field: Geology

Biographical:

Education:

Completed the requirements for the Doctor of Philosophy in geology at Oklahoma State University, Stillwater, Oklahoma in December, 2019.

Completed the requirements for the Master of Science in geology at the University of Tulsa, Tulsa, Oklahoma in 2014.

Completed the requirements for the Bachelor of Science in Petroleum Geology at Jilin University/College of Earth Sciences, Changchun, China in 2012.

Experience: Geology intern, Tiptop Oil and Gas/SINOPEC (Oklahoma City, Oklahoma), 2016 Summer

Professional Memberships: American Association of Petroleum Geologists (AAPG), American Rock Mechanics Association (ARMA), Houston Geological Society (HGS), Society for Sedimentary Geology (SEPM)